

Sustainable Aviation

Melih Cemal Kuşhan

Selim Gürgen

Mehmet Alper Sofuoğlu *Editors*

Materials, Structures and Manufacturing for Aircraft

 **SARES**
INTERNATIONAL SUSTAINABLE AVIATION
AND ENERGY RESEARCH SOCIETY



Springer


Sustainable Aviation

Series Editors

T. Hikmet Karakoc , Faculty of Aeronautics and Astronautics, Eskisehir Technical University, Eskisehir, Turkey

The Information Technology Research and Application Center, Istanbul Ticaret University, Turkey

C Ozgur Colpan , Department of Mechanical Engineering, Dokuz Eylul University, Buca, Izmir, Turkey

Alper Dalkiran , School of Aviation, Süleyman Demirel University, Isparta, Turkey

The Sustainable Aviation book series focuses on sustainability in aviation considering all aspects of the field. The books are developed in partnership with the International Sustainable Aviation Research Society (SARES), and include contributed volumes consisting of select contributions to SARES international symposiums and conferences, as well as cutting edge monographs and professional books focused on all aspects of sustainable aviation. The series aims at publishing state-of-the-art research and development in areas including, but not limited to:

- Green and renewable energy resources and aviation technologies
- Aircraft engine, control systems, production, storage, efficiency and planning
- Exploring the potential of integrating renewables within airports
- Sustainable infrastructure development under a changing climate
- Training and awareness facilities with aviation sector and social levels
- Teaching and professional development in renewable energy technologies and sustainability


More information about this series at <https://link.springer.com/bookseries/16670>


Melih Cemal Kuşhan • Selim Gürgen
Mehmet Alper Sofuoğlu
Editors


Materials, Structures and Manufacturing for Aircraft

 Springer

Editors

Melih Cemal Kuşhan 
Aeronautical Engineering
Eskişehir Osmangazi University
Eskişehir, Turkey

Selim Gürgen 
Aeronautical Engineering
Eskişehir Osmangazi University
Eskişehir, Turkey

Mehmet Alper Sofuoğlu 
Mechanical Engineering
Eskişehir Osmangazi University
Eskişehir, Turkey

ISSN 2730-7778

ISSN 2730-7786 (electronic)

Sustainable Aviation

ISBN 978-3-030-91872-9

ISBN 978-3-030-91873-6 (eBook)

<https://doi.org/10.1007/978-3-030-91873-6>

© The Editor(s) (if applicable) and The Author(s), under exclusive license to Springer Nature Switzerland AG 2022

This work is subject to copyright. All rights are solely and exclusively licensed by the Publisher, whether the whole or part of the material is concerned, specifically the rights of translation, reprinting, reuse of illustrations, recitation, broadcasting, reproduction on microfilms or in any other physical way, and transmission or information storage and retrieval, electronic adaptation, computer software, or by similar or dissimilar methodology now known or hereafter developed.

The use of general descriptive names, registered names, trademarks, service marks, etc. in this publication does not imply, even in the absence of a specific statement, that such names are exempt from the relevant protective laws and regulations and therefore free for general use.

The publisher, the authors and the editors are safe to assume that the advice and information in this book are believed to be true and accurate at the date of publication. Neither the publisher nor the authors or the editors give a warranty, expressed or implied, with respect to the material contained herein or for any errors or omissions that may have been made. The publisher remains neutral with regard to jurisdictional claims in published maps and institutional affiliations.

This Springer imprint is published by the registered company Springer Nature Switzerland AG
The registered company address is: Gewerbestrasse 11, 6330 Cham, Switzerland

Contents

1	Aluminum-Lithium Alloys in Aircraft Structures	1
	Esad Kaya, Mohammad Rauf Sheikhi, Selim Gürgen, and Melih Cemal Kuşhan	
2	Metal Foams and Their Applications in Aerospace Components	27
	Cihat Ensarioglu, Altug Bakirci, Huseyin Koluk, and M. Cemal Cakir	
3	Advanced Polymers in Aircraft Structures	65
	Dipen Kumar Rajak, Pratiksha H. Wagh, Ashwini Kumar, Ajit Behera, and Catalin I. Pruncu	
4	Advanced Fibrous Composites for Aircraft Application	89
	Mahdi Hasanzadeh and Shahram Mahboubi Zadeh	
5	Natural Composites in Aircraft Structures	113
	Lata Samant, Fábio A. O. Fernandes, Seiko Jose, and Ricardo J. Alves de Sousa	
6	Aeroengines: Principles, Components, and Eco-friendly Trends	127
	Mohammad Rauf Sheikhi, Hakan Aygun, and Onder Altuntas	
7	Landing Gear Systems in Aircraft	153
	Erdem Tunca, Hasim Kafali, Goksel Keskin, and Melih Cemal Kuşhan	
8	Manufacturing and Maintenance Operations for Bladder-Type Aircraft Fuel Tanks	181
	Tamer Saraçyakupoğlu	
9	Structural Health Monitoring Method for In Situ Inspection of Landing Gears	211
	Gökhan Haydarlar, Mesut Tekkalmaz, and Mehmet Alper Sofuoğlu	

10 Major Units and Systems in Aircraft	239
Tamer Saraçyakupoğlu	
11 Vibration-Assisted Machining of Aerospace Materials	259
Ramazan Hakkı Namlu and Bahram Lotfi Sadigh	
12 Potential of Incremental Forming Techniques for Aerospace Applications	293
Ricardo J. Alves de Sousa, D. G. Afonso, F. Rubino, and A. K. Behera	
13 Welding of Dissimilar Materials in Aerospace Systems	317
Seyed Reza Elmi Hosseini, Fábio A. O. Fernandes, António B. Pereira, and Zhuguo Li	
14 Design, Analysis, and Production of Lattice Structures Through Powder Bed Fusion Additive Manufacturing	345
Ozgur Poyraz, Evren Yasa, Fatma Nur Depboylu, and Feza Korkusuz	
15 Application of Wire Arc Additive Manufacturing for Inconel 718 Superalloy	367
G. K. Sujan, Huijun Li, Zengxi Pan, Daniel Liang, and Nazmul Alam	
Index	411

Chapter 1

Aluminum-Lithium Alloys in Aircraft Structures



Esad Kaya, Mohammad Rauf Sheikhi, Selim Gürgen,
and Melih Cemal Kuşhan

Nomenclature

CYS	Compressive yield strength
DT	Damage-tolerance properties
E	Modulus of elasticity
ISS	International space station
L	Longitudinal loading direction
LT	Long transverse loading direction
SSSS	Supersaturated solid solution
TL	Transverse loading direction
TS	Tensile strength
VIAM	Russian Scientific Research Institute of Aviation Materials

Subscripts

B	$\text{Al}_{7.5}\text{Cu}_4\text{Li}$ phase
1	Al_2CuLi phase
2	Al_6CuLi_3 phase

E. Kaya (✉)

Department of Mechanical Engineering, Eskişehir Osmangazi University, Eskişehir, Turkey
e-mail: esatkaya@ogu.edu.tr

M. R. Sheikhi

Faculty of Aeronautics and Astronautics, Eskişehir Technical University, Eskişehir, Turkey

S. Gürgen · M. C. Kuşhan

Department of Aeronautical Engineering, Eskişehir Osmangazi University, Eskişehir, Turkey

© The Author(s), under exclusive license to Springer Nature Switzerland AG 2022

M. C. Kuşhan et al. (eds.), *Materials, Structures and Manufacturing for Aircraft*, Sustainable Aviation, https://doi.org/10.1007/978-3-030-91873-6_1

Greek

- α Al-Li equilibrium phase
- β' Al_3Zr phase
- θ Al_2Cu phase
- δ Al_3Li phase

1.1 Introduction

In the aviation industry, improvements in structural efficiency, fuel savings, and carrying capacity are important in terms of weight reduction. Weight reductions could be occurring by novel mechanical design changes or improvements in material properties. These kinds of improvements seem to be marginal compared to those achievable with the use of newer materials with lower densities. Today, Al–Li alloys with their new generation are being developed. These new type alloys are characterized by superior strength and modulus of elasticity, especially lower density. Hence, it is interesting in the fabrication of daily and future aircraft technology as it is a lightweight structural material [1, 2].

Figure 1.1 shows the effect of mechanical properties of materials on weight reduction. As seen in the chart, the use of low-density material is the most important factor in weight reduction. Nowadays, low cost is a priority for the production and development of aircraft. The main ways to reduce the cost per flight are low fuel consumption engine designs and weight reduction using ultralight materials. It is

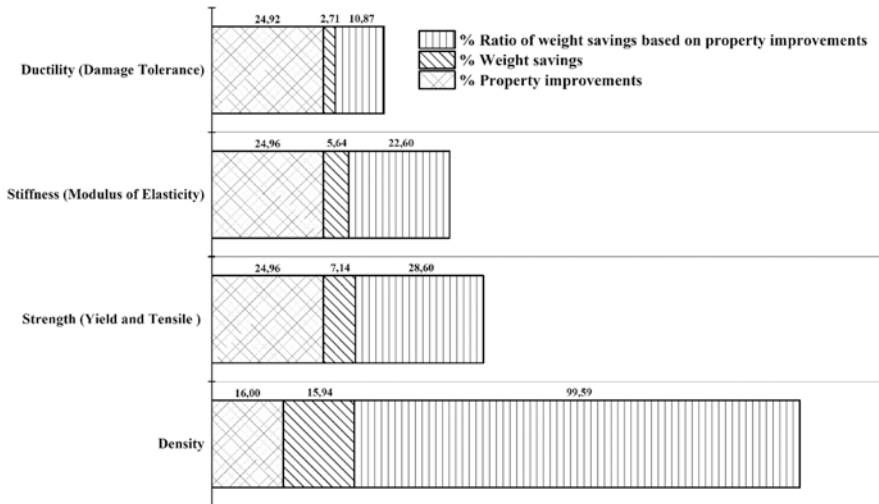


Fig. 1.1 Effect of mechanical properties on weight reduction

therefore important to add Li and similar low-density elements into conventional Al alloys for aviation.

The modern design solutions of aviation engineering are the development of novel industrial production and therefore, the use of new structural materials is required in the design of new generation civil and combat aircraft. One of the basic structural materials in aircraft is Al alloys. Contemporary researches continue into the development of Al alloys to maximize the weight-to-strength ratio. One of the methods to improve this parameter is to design low-density alloys. For this reason, scientific studies have turned their focus to Li, which has a density of 0.536 g/cm^3 . At this point, it is noteworthy that Li is the lightest metal element. The produced Al–Li alloys are investigated under three basic generations. The development of these advanced alloys started in the 1920s and still continues today [1, 2].

Table 1.1 shows the chemical contents of Al–Li alloys for different generations. As seen in the table, there is no direct restriction on Li ratio in the first-generation alloys. The second-generation alloys contain Li more than 2 wt%. It seems that increasing the Li ratio provided the density of the alloy to decrease. However, studies show that these alloys have quite weakness in fracture toughness, thermal shock resistance, and dynamic impact toughness [2–6]. The Li content of the third-generation alloys is less than 2 wt%. In comparison to the other generations, Mn and Zn have been added to the alloys. It is known that the static and dynamic corrosion resistance of the material is increased with the effect of Zn added to the alloys [6, 7].

The first generation is VAD23 (USSR) and X2020 (USA) variants covering the 1920s and 1960s. The first alloys were produced based on the Al–Cu–Li system as such in VAD23 (USSR) and X2020 (USA) variants. These alloys have been used in the production of different parts of military aircraft. As a good example of this case, X2020 was used military seaborne airplanes without incident for years. USSR variant, VAD23, was used in the parts of the TU-144 supersonic commercial airliner. Adding a unit of Li to Al reduces the density by approximately 3%. Moreover, with the addition of Li, the module of elasticity of the Al alloy increases by approximately 6% [2, 9–11]. These alloys are 3% lighter and 8% harder than conventional 2024 and D16 Al alloys. In addition, they retain their high strength at elevated temperatures (up to $175 \text{ }^\circ\text{C}$). One of the other breakthroughs in the development of Al–Li alloys was made by the scientists from the All-Russian Scientific Research Institute of Aviation Materials (VIAM). With their research, a large group of Al–Mg–Li alloys has been hardened by aging heat treatment [1]. Figure 1.2 shows the use of a first-generation Al–Li alloy, 1420 on Mig-29 M fighter as a fuel tank.

The second-generation Al–Li alloys cover the years between 1960 and 1980. This generation is produced by two different methods. These methods are powder metallurgy and casting. Both methods have their advantages and disadvantages over each other [12, 13]. Production with powder metallurgy provides flexibility in chemical content, mechanical alloying, and rapid solidification in structures. However, this method has a high-cost and low-production capacity. Casting is a cheaper and effective method in producing large ingots. However, the equipment used in the Al–Li casting process is limited and highly expensive. The obtained chemical structures are limited compared to the production by powder metallurgy. Examples of

Table 1.1 Chemical contents and density of Al–Li alloys [8]. Reprinted by permission from Elsevier

Alloys	Li	Cu	Mg	Ag	Zr	Sc	Mn	Zn	Density (g/cm ³)	Introduction to service
<i>First generation</i>										
2020	1.2	4.5					0.5		2.71	Alcoa 1958
1420	2.1		5.2		0.11				2.47	Soviet 1965
1421	2.1		5.2		0.11	0.17			2.47	Soviet 1965
<i>Second generation (Li ≥ 2 wt%)</i>										
2090	2.1	2.7			0.11				2.59	Alcoa 1984
2091	2.0	2.0	1.3		0.11	0.17			2.58	Pechiney 1985
8090	2.4	1.2	0.8		0.11				2.54	EAA 1984
1430	1.7	1.6	2.7		0.11				2.57	Soviet 1980s
1440	2.4	1.5	0.8		0.11				2.55	Soviet 1980s
1441	1.95	1.65	0.9		0.11				2.59	Soviet 1980s
1450	2.1	2.9			0.11				2.60	Soviet 1980s
1460	2.25	2.9			0.11	0.09			2.60	Soviet 1980s
<i>Third generation (Li < 2 wt%)</i>										
2195	1.0	4.0	0.4	0.4	0.11				2.71	LM/Reynolds 1992
2196	1.75	2.9	0.5	0.4	0.11		0.35	0.35	2.63	LM/Reynolds/McCook Metals 2000
2297	1.4	2.8	0.25		0.11		0.3	0.5	2.65	LM/Reynolds 1997
2397	1.4	2.8	0.25		0.11		0.3	0.1	2.65	Alcoa 2002
2098	1.05	3.5	0.53	0.43	0.11		0.35	0.35	2.70	McCook Metals 2000
2198	1.0	3.2	0.50	0.4	0.11		0.5	0.35	2.69	Reynolds/McCook Metals/Alcan 2005
2099	1.8	2.7	0.30		0.11		0.3	0.7	2.63	Alcoa 2003
2199	1.6	2.6	0.20		0.11		0.3	0.6	2.64	Alcoa 2005
2050	1.0	3.6	0.40	0.4	0.11		0.35	0.25	2.70	Pechiney/Alcan 2004
2296	1.6	2.45	0.6	0.43	0.11		0.28	0.25	2.63	Constellium/Alcan 2010
2060	0.75	3.95	0.85	0.25	0.11		0.3	0.4	2.72	Alcoa 2011
2055	1.15	3.7	0.4	0.4	0.11		0.3	0.5	2.70	Alcoa 2011
2065	1.2	4.2	0.5	0.3	0.11		0.4	0.2	2.70	Constellium 2012
2076	1.5	2.35	0.5	0.28	0.11		0.33	0.3	2.64	Constellium 2012

produced parts from the second-generation alloys are secondary important structural components. Leading-edge parts produced from 2090 series could be found in Airbus A330 and A340. Payload adapter parts made from 8090 series in Agusta Westland EH101 helicopters can be given as another example [13]. Figure 1.3 represents the use of the second-generation Al–Li alloys on Agusta Westland EH101.

The third-generation Al–Li alloys are designed in the late 1980s by Pickens [15] for Lockheed Martin. The main purpose of the design is to develop cryogenic tanks suitable for low-density aviation applications. Variants containing Li up to 1.3 wt% have been developed with subsequent investigations. For microstructural improvements, a chemical-containing structure of 4.6Al 6.3Cu 1.3Li 0.4Ag 0.4Mg 0.14Zr

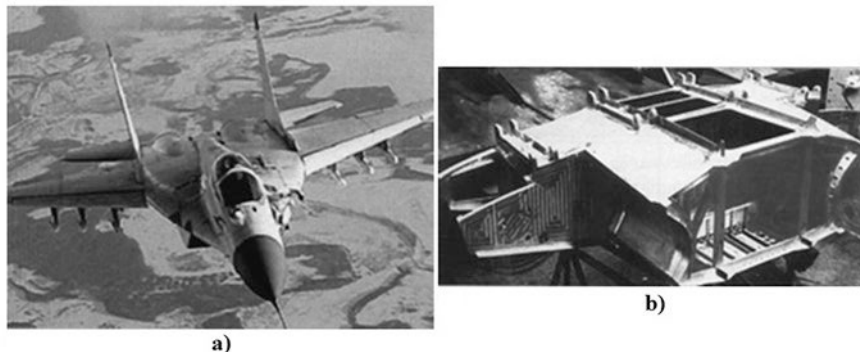


Fig. 1.2 The use of a first-generation Al–Li alloys (a) on Mig-29 M fighter and (b) its welded fuel tank [1]. Reprinted by permission from Taylor & Francis



Fig. 1.3 8090T852 alloys as structural parts on the Agusta Westland EH101 [14]. Reprinted by permission from Elsevier

0.06Fe 0.03Si, which was named as Weldalite, was created. By applying a uniform T1 temperature, the alloy can provide a yield strength of approximately 700 MPa. The third-generation alloys contain a Li content of less than 2 wt%. Rioja et al. [16] increased the static and dynamic corrosion resistance of Weldalite alloy by adding Zn. The third-generation alloys could be used in either exoatmospheric or atmospheric platforms. Alloy 2195 was used in the construction of ultralight tanks in the space shuttles of the international space station (ISS). The alloys 2297 and 2397 were used in the production of bulkheads in the F-16 fighter [7, 13]. By using Al–Li alloys in structural applications, the weight of composites or metallic structures can

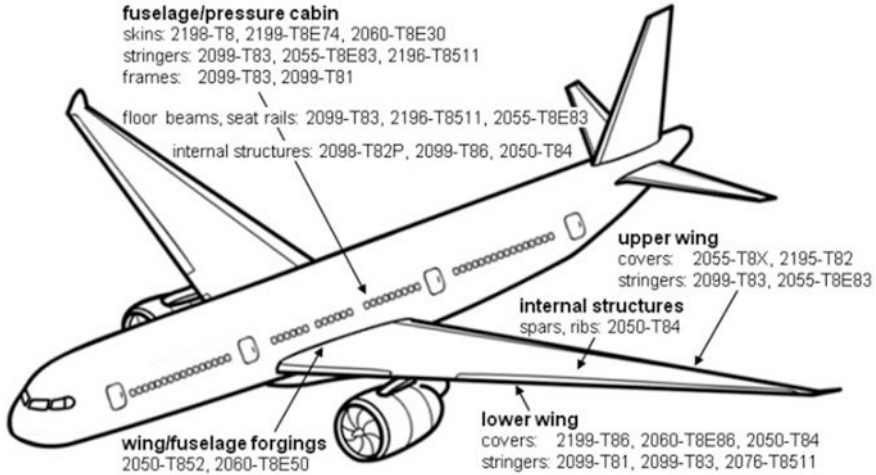


Fig. 1.4 Recommended applications of the third-generation Al-Li alloys for an airliner [8]. Reprinted by permission from Elsevier

be reduced. Al-Li alloys offer some significant improvement in mechanical properties in comparison to conventional Al alloys. The main motivation for the development and use of Al-Li alloys is the improvements in specific strength (strength-to-density) and rigidity (modulus of elasticity-to-density) achieved by the addition of Li. Figure 1.4 shows the recommended application areas of the third-generation Al-Li alloys for an airliner.

1.2 Production of Al-Li Alloys

The production of the first two generation Al-Li alloys has some drawbacks due to the high reactivity of Li together with inadequate technology. These drawbacks lead to low production rates for the casting method. With the developed technology in the 1990s, the production of Al-Li alloys by casting method has been more effective and safer. Furthermore, due to the low Li ratio in comparison to the first and second generation, the third-generation Al-Li alloys could be produced more easily by casting method. Similar to the other conventional Al alloys, Al-Li alloys are primarily melted and cooled in a reverberatory furnace environment. Afterward, thermo-mechanical treatment is applied to the ingots. The casting of Al-Li alloys requires very low impurities and an extremely high argon atmosphere as well. Due to the high reactivity of Li, electrolysis process is required to be included in the molten metal [6, 17–19].

After the casting and homogenization process, Al-Li alloys can be processed in hot forming, cold forming, and superplastic forming processes. In addition to the given manufacturing methods, the third-generation alloys of Weldalite family can

be manufactured by friction stir welding, friction welding, laser beam welding, and inert gas welding methods [6, 19]. Forged machine parts exhibit superior features compared to cast products in terms of mechanical properties. However, the casting method provides both economical and mass anisotropy for complex geometry parts [6, 13].

1.3 Microstructural Properties of Al–Li Alloys

It is reasonable to use the scanning electron microscopy and optical microscopy techniques to get the most accurate results from microstructural investigations of Al–Li alloys. In addition, phase diagrams are important for the characterization of chemical content. The presence of Li makes the Al–Li alloys important in terms of material properties. Hence, the formation kinetics of Li and the other element content compounds should be determined precisely. The ductility of the alloy decreases as the amount of Li increases. The main reason for the decreasing ductility is the formation of δ' (Al₃Li) phase in the microstructure. Figure 1.5a shows the Al–Li binary phase diagram. When the diagram is examined, there are α -Al, δ (Al–Li), δ' (Al₃Li), and α -Li phases. The addition of the Li element reduces the density and enhances the strength [20]. As a result of the planar shear motion of the particles of this phase, stress concentrations occur and consequently, the ductility decreases. Figure 1.5b shows the possible chemical compositions and phases in Al–Li–X alloys. The physical metallurgy of Al–Li alloys is quite complex due to the elements in the alloy. Consequently, formed precipitates by aging heat treatment can be found in various chemical compositions and types. The main strengthening mechanism in the Al–Li alloy system is based on forming precipitates from supersaturated solid solution (SSSS).

Similar to the commonly produced Al aviation alloys, the third-generation Al–Cu–Li alloys provide superior mechanical properties due to the precipitates in their microstructures. Strength in alloys is controlled by the formation of an intra-grain

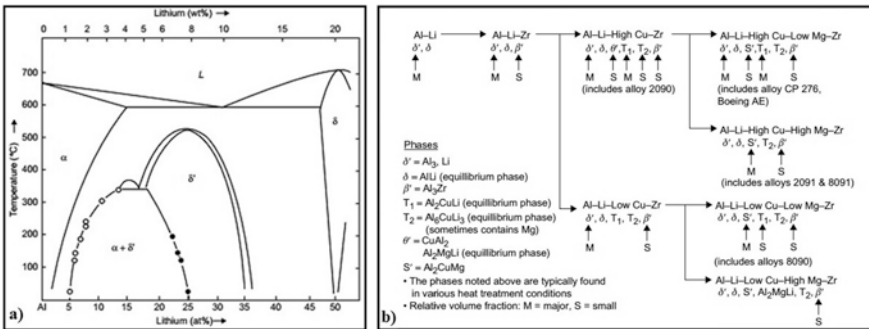


Fig. 1.5 (a) Al–Li phase diagram [21] and (b) possible phase compositions for Al–Li–X systems [22]. Reprinted by permission from Elsevier

precipitate whereas toughness is controlled by precipitation occurring at the grain boundaries [19, 23]. Besides, the corrosion resistance of the alloy depends on some specific precipitated formations within the microstructure. Table 1.2 gives some of the elements that could be found in the microstructure of the third-generation Al–Li alloys and their effects on the material properties. These elements can be transformed into strength-enhancing microstructural forms in three different ways. These are precipitates, dispersoids and intermetallics, which could be observable as different chemical contents and regions in the microstructure of the alloys. Together with these properties, these formations directly affect the mechanical properties of the alloys [19]. Figure 1.6 shows the schematic of different formations in the Al–Li microstructures.

Some elements can be added to the microstructure to increase the ductility of the alloy. One of these elements is Cu. With the addition of Cu, high strength precipitates of θ' (Al₂Cu) and T₁(Al₂CuLi) are formed as well as toughness enhancing precipitates of T₂(Al₆CuLi₃). Unlike the T₁ phase, the T₂ phase is heterogeneously nucleated at dislocations and grain boundaries. However, excessive precipitation of the T₂ phase in grain boundaries has a detrimental effect on toughness. The T₂ phase is more ductile than the T₁ phase. In this case, heat treatment (precipitation hardening, aging) parameters should be determined concerning the mechanical properties required by the structural part. Al–3Li–2Cu–0.2Zr alloy could be considered as an example of this case. This alloy includes θ (Al₂Cu), T₂(Al₆CuLi₃), and T₁(Al₂CuLi) phases in the microstructure. As a result of metastable cooling and solidification, a small amount of T₁(Al₂CuLi) phase is formed. Hence, the optimization of heat treatment parameters is essential for a properly designed microstructure [6, 24]. Other elements that can be included in Al–Li alloys are Zr and Sc. These elements affect the grain refinement while increasing the possibility of Al–Zr–Sc–Li precipitate formations. The precipitates provide better intergrain and intragrain coherence in the microstructure. This behavior increases the material strength as the movement of dislocations gets difficult. β' (Al₃Zr) is another phase that could be formed in the

Table 1.2 Effect of alloying elements on the material properties of Al–Li alloys [19]. Reprinted by permission from Elsevier

Alloying element	Effects on material properties
Li and Mg	Density reduction, solid solution, and precipitation strengthening
Cu	Solid solution and precipitation strengthening
Ag	Nucleation agent, coats the T ₁ precipitate, increases raw material cost
Zn	Solid solution strengthening and corrosion resistance
Zr, Sc, Mn and Cr	Formation of dispersoids and control of the grain size and texture
Fe and Si	Impurities that form intermetallics, detrimental to mechanical properties
Ti and B	Grain refiner
Na and K	Present as impurities

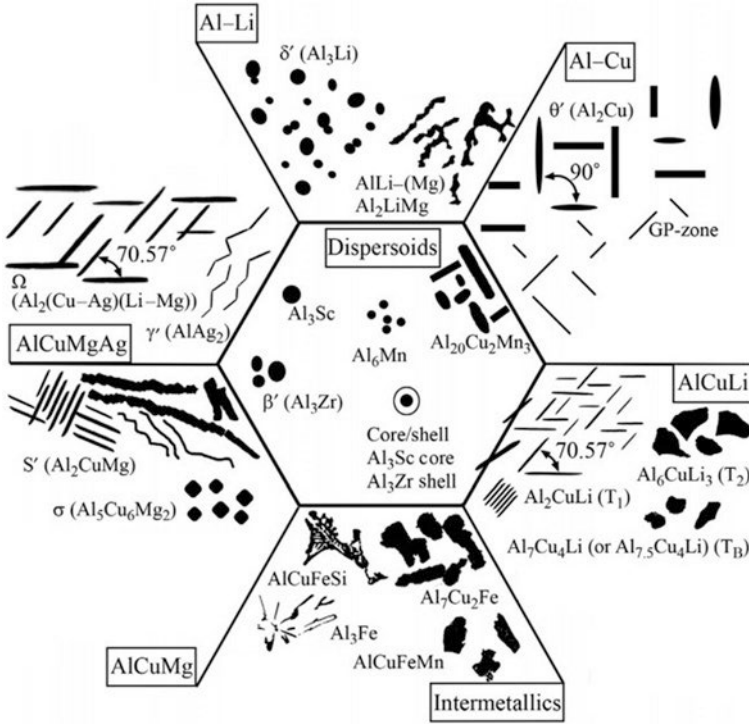


Fig. 1.6 Schematic representation of different formations in the microstructure of Al-Li alloys [19]. Reprinted by permission from Elsevier

microstructure. It is an intermetallic compound with low ductility and resistance to recrystallization [25]. Alloying elements such as Mg, Ag, and Zn are often added to the third-generation Al-Cu-Li alloys as provide T_1 phase to nucleate [19]. The dissolved elements are primarily segregated. Subsequently, they accelerate the nucleation of the T_1 phase [19, 26, 27]. Gumbmann et al. conducted comparative researches on the effect of Mg in Al-Li-Cu alloys [28–31]. They stated that the addition of one of the three elements or a combination of them affects the precipitation kinetics of Al-Li-Cu alloys. It was observed that Mg accelerates the precipitation kinetics. Mg effect is very effective in the early stages of the precipitation process and furthermore, directly affects the precipitation sequence in the nucleation stage. Besides, the elements Ag and Zn accelerate the precipitation kinetics; however, they have no effect on the precipitation sequence. Mg is the most important alloying element in comparison to Ag and Zn. Early studies [29, 32–34] showed that the addition of Mg dramatically increases the nucleation of the T_1 phase. This is due to the Mg atoms straining in the Al lattice. In another study, it was determined that at least 0.1 wt% Mg should be added to increase the nucleation of the T_1 phase [29]. Itoh et al. [33] found that the T_1 phase can precipitate in octahedral spaces (also known as secondary defects and vacancy-rich clusters) and monolayer

Guinier–Preston regions for the Mg-containing alloys. For the Mg-free alloys, the precipitates occur only in the dislocation loops. On the other hand, the high price of raw Ag restricts the usage as it increases the production cost. Alternatively, combination of Mg and Ag is reasonable for tailoring the chemical composition. The dual use of these elements accelerates the nucleation kinetics of the T_1 phase. Due to this fact, Al–Cu–Li alloys including Ag and Mg contents exhibit higher tensile strengths [19, 34, 35]. Ag leads to the redistribution of T_1 phase at the interface of Al matrix. Thus, by creating a diffusion barrier, it prevents T_1 phase plates from coarsening. This behavior improves the thermal stability of Al–Cu–Li alloys as well [19, 26, 36]. Similar to Ag, Zn accelerates the precipitation of T_1 phase in the microstructure of the third-generation Al–Li alloys [37–39]. Gable et al. [39] investigated the effect of Zn element on grain coarsening of T_1 phase in Al–2.7Cu–1.8Li alloy. It was noted that alloys with Zn content exhibit lower rate of grain coarsening at 300°C. This is related to the presence of Zn element in T_1 phase, which provides homogenization in Al matrix. In addition, Zn improves the corrosion resistance of Al–Cu–Li alloys as is the case with Ag [16, 19]. Another element as a grain size controller is Mn. The addition of Mn increases ductility while prevents abnormal grain growths. As given in Table 1.1, Mn is frequently used in the third-generation Al–Li alloys. This element forms $Al_{20}Cu_2Mn_3$ compounds if present with Cu in the microstructure. The formed precipitates restrict shear and thereby hindering the dislocation movements. They also prevent the grain coarsening during precipitating and, therefore, materials with high damage tolerance are obtained. Mn-containing precipitates control the grain size during the cooling and heating stages during precipitation hardening. However, Mn content above a certain limit lowers the Cu ratio in the microstructure by forming a precipitate. This formation has some detrimental effects on the aging process [40]. Additional T_B phase ($Al_{7.5}Cu_4Li$) occurs as a result of excessive Mn addition. T_B phase affects the toughness of Al–Li alloys. Since it is formed by a peritectic reaction, it shows a rare presence in the microstructure. Mn forms primary solid solution phases. These phases prevent grain growth during precipitation. The addition of Mn has no direct effect on the yield strength of the alloy. But the excessive addition decreases ductility due to the grain refinement. Figure 1.7 shows the optical microstructural images of an Al–3Li–2Cu–0.2Zr casting alloy with and without Mn contents. It is seen that the grain size of the Mn-free alloy is coarser than that including Mn. The grain refinement occurs when $Al_{20}Cu_2Mn_3$ precipitates lower the solidification point and prevent the grain to grow. These types of formations have an effect on the recrystallization and texture control during solidification or high-temperature aging [5, 41].

1.4 Mechanical Properties of Al–Li Alloys

Structural components in aircraft are subjected to different types of loading during flights. These loads could be either mechanical such as tensile, compression, shear, and fatigue or chemicals such as corrosion and corrosion stress cracking. Hence, the

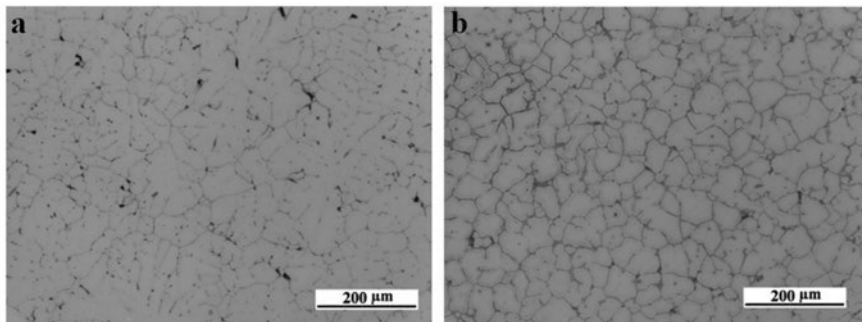


Fig. 1.7 The effect of Mn addition to as-cast Al-3Li-2Cu-0.2Zr: (a) 0% and (b) 1.2% [40]. Reprinted by permission from Elsevier

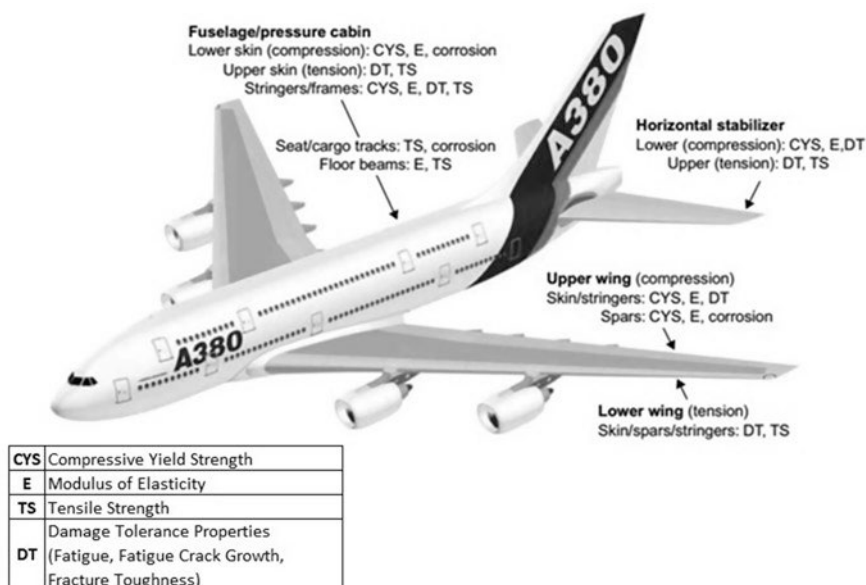


Fig. 1.8 Mechanical loads on the main structures of an aircraft [8]. Reprinted by permission from Elsevier

environmental and operating conditions should be taken into account in the material selection for structural parts. Figure 1.8 shows the types of loadings acting on different parts of an aircraft [42]. As can be seen from the image, the upper wing structures are forced by compression, shear, and dynamic impacts while the lower wing structures are exposed to high tensile and deflection. Due to deformation and deflection, damage tolerance is always required for entire wing structures. In addition to the mechanical loadings, corrosion could be seen in entire parts of an aircraft but it mostly encounters in fuselage and spars [13].

Strength of Al–Li alloys, such as overall strength, deformation behavior, fatigue resistance, fracture toughness, corrosive, and noncorrosive fracture behavior, is affected by metallurgical and processing properties, which are characterized as chemical composition, precipitates, precipitate-free zones, grain boundary characteristics, processing condition, thermomechanical history, structural part geometry, etc. [2, 13, 42, 43]. The addition of Li into Al alloys results in high ductility and high strength combinations. Figure 1.9 shows the mechanical properties of Al–Li alloys with different chemical compositions. As shown in the chart, superior mechanical properties are obtained in Al–Li–Cu–Mg–Zr alloys, which are among the second-generation Al–Li alloys. Despite this fact, these alloys are produced by lowering the Li content and thereby yielding new alloys that are categorized in the third generation. Mechanical properties of Al–Li–Cu–Mg–Zr alloys have been investigated in several studies. Table 1.3 gives the well-known mechanical properties of commercial Al–Li alloys. It is seen that the designed low-density alloys have higher yield strength than most of the steels. Of the new generation alloys, alloy 2090 is designed as an alternative to alloy 7075T6. Alloy 2090 has a lower density and higher hardness compared to alloy 7075T6 as well as possessing superior corrosion-resistant characteristics [6, 13]. Alloy 2091 is produced for aviation parts that require high damage tolerances. It has 8% less density and 7% modulus of elasticity than alloy 2024T3. 8090 is another commercial Al–Li alloy designed as an alternative to the alloy 2014T6 to benefit from its lower density and higher modulus of elasticity [13].

One of the major drawbacks for the first-generation Al–Li alloys is low ductility. The second-generation Al–Li alloys have a challenge of anisotropy that results in very low yield strengths and dense delaminations, especially in the direction of 45° to the rolling direction. The development of the third-generation Al–Li alloys by lowering the Li content as well as the innovative process techniques enable the alloys to exhibit isotropic behavior. In addition to this improvement, the third-generation Al–Li alloys show equivalent tensile strength behavior for all cross

Fig. 1.9 Strength versus ductility for various types of Al–Li alloys [17]. Reprinted by permission from Springer Nature

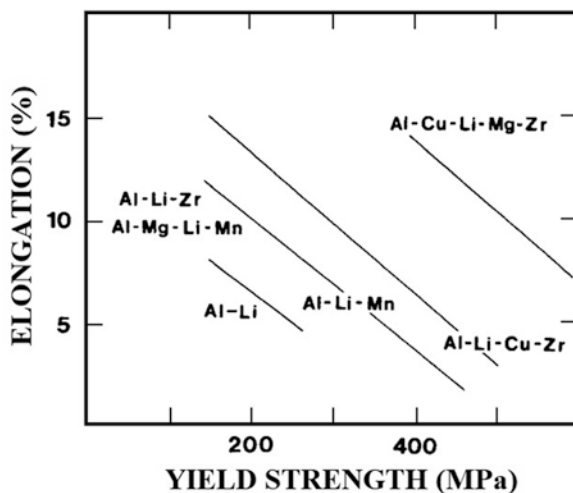


Table 1.3 Mechanical properties of commercial Al–Li alloys [46]

Alloy	Density (g/cm ³)	Total elongation (%)	Modulus of elasticity (GPa)	Tensile strength (MPa)	Fracture toughness (MPa m ^{1/2})
2090	2.59	5	76	525	49
2091	2.58	12	75	460	>100
8090	2.54	7	77	490	75

sections and in-planes. Considering the tensile strength values, it is possible to mention that the third-generation Al–Li alloys leave behind the first- and the second-generation alloys and naturally the traditional Al alloys as well [2, 5, 43–45].

Fatigue behavior of materials is one of the most important properties, especially for aircraft materials. Fatigue behavior can be categorized into two main groups that are low cycle and high cycle fatigue behavior. Low cycle fatigue behavior of Al–Li alloys is affected by microstructural properties and partially by crystallographic structures. One of the most important microstructural effects is the amount of Li in the chemical composition. Li-containing precipitates and volumetric ratio, size, distribution, aging process parameters directly affect the low cycle fatigue behavior of Al–Li alloys [42, 47–49]. It is known that the low cycle fatigue resistance of the first- and the second-generation Al–Li alloys is lower than that of the conventional Al alloys. Figure 1.10 shows the low cycle fatigue resistance of the first- and the second-generation Al–Li alloys as well as comparing those of the conventional Al alloys. As can be seen in the graph, alloys 2024T4 and 7075T6 have superior low cycle fatigue resistance in comparison to the first- and the second-generation Al–Li alloys.

High cycle fatigue resistance of Al–Li alloys increases with solid solution hardening and coarsening of δ' (Al₃Li) precipitates. Thermomechanical processes, including artificial aging and cold processing, contribute to the increase of high cycle fatigue resistance in the alloys. Previous studies showed that all generations of Al–Li alloys have almost equivalent high cycle fatigue resistance with some minor deviations. Al–Li alloys do not exhibit significantly better high cycle fatigue behavior compared to the conventional Al alloys [49–51]. Figure 1.11 represents the comparison of the high cycle fatigue resistance of the third-generation Al–Li alloys and conventional Al alloys. It can be seen that high cycle fatigue resistance performances are quite similar for the conventional Al and the third-generation Al–Li alloys.

It has been determined that the fatigue crack growth rate in the second-generation Al–Li alloys is lower than that of the conventional Al alloys [53]. The main reason for this phenomenon is defined by “crack tip shielding.” Rough fracture surfaces lead to fatigue cracks to close and consequently a decrease in crack driving force. However, this behavior seems to be in a good manner. It is associated with unacceptably high anisotropic mechanical properties [42]. Since anisotropy problems are eliminated in the third-generation Al–Li alloys, a less rough fracture surface is detected in the investigations [42, 54]. The third-generation Al–Li alloys exhibit better fatigue crack growth properties than the first- and the second-generation Al–Li alloys. They also surpass the conventional Al alloys in terms of fatigue crack

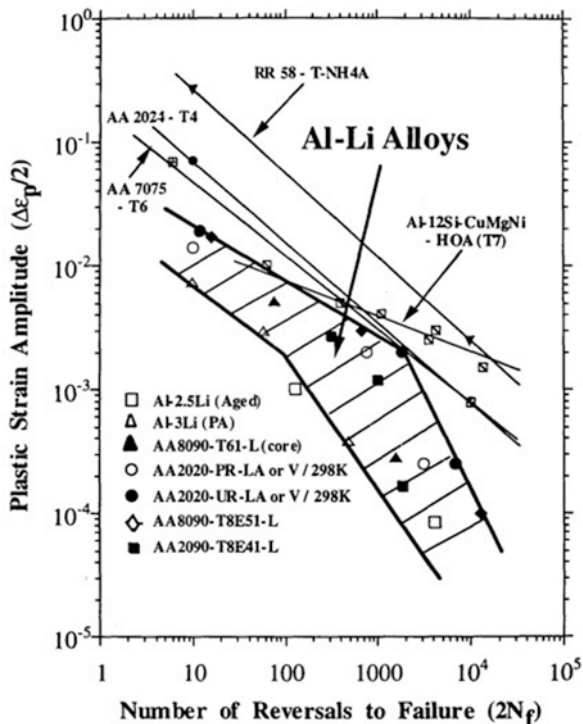


Fig. 1.10 Comparison of the low cycle fatigue resistances for Al-Li and conventional Al alloys in terms of plastic strain amplitude [48]. Reprinted by permission from Taylor & Francis

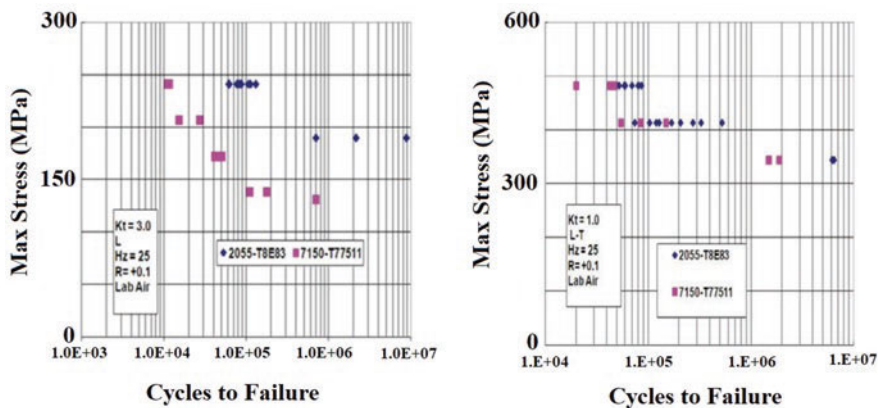


Fig. 1.11 High cycle fatigue life as a function of maximum stress for conventional 7150T77511 and the third-generation Al-Li alloy 2055T8E83 [52]. Reprinted by permission from Springer Nature

growth resistance. As a result of the tests applied to the materials by different researchers, it was observed that the third-generation Al–Li alloys have superior fatigue crack growth properties. An important study confirming this situation was carried out by Karabin et al. [55]. In this study, the length of the formed crack in the aircraft parts was investigated depending on the number of simulated flights. As a result of the research, it was predicted that the life span of the parts made from the Al–Li alloys 2199 and 2060 would be longer compared to that of the conventional Al alloys. Figure 1.12 shows the experimental results comparing various alloys in terms of fatigue crack growth.

Fracture toughness is another critical material property for aerospace applications. It is one of the features that limit the utilization of the first- and the second-generation Al–Li alloys. Plane strain fracture toughness for short transverse is very low in the second-generation Al–Li alloys (Plate type alloy 8090T81 can be shown as an example). Such problems have been solved in the third-generation Al–Li alloys as such in the alloys 2050 and 2060. Plane stress fracture toughness and R-curve values for sheet and plate type third-generation Al–Li alloys are better than those of the second-generation Al–Li alloys for similar strength values. Figure 1.13 shows the R curves of the second- and the third-generation Al–Li alloys (8090T86, 2060, and 2199) and those of the conventional Al alloys (2X24 series). As can be seen in the chart, the second-generation Al–Li alloy 8090T86 shows lower performance compared to the conventional Al alloys, while the third-generation alloys 2060 and 2199 have superior fracture toughness resistance [42].

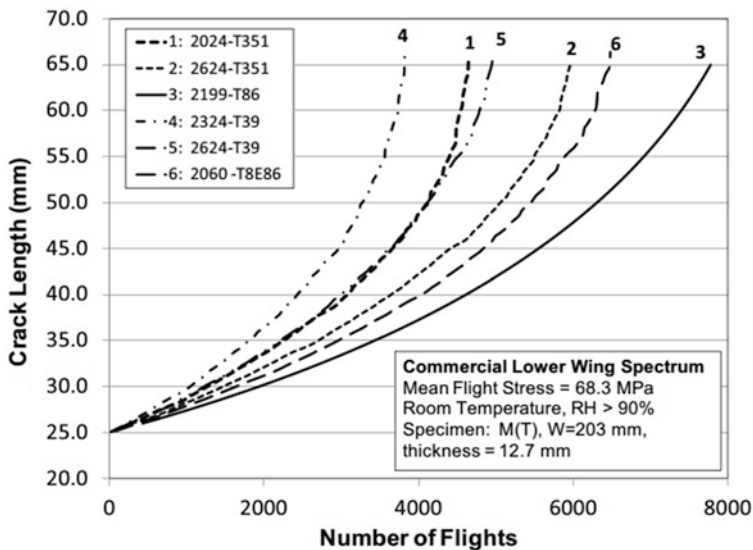


Fig. 1.12 Fatigue crack growth behavior for Al–Li and conventional Al alloys in the simulated flights [55]. Reprinted by permission from Springer Nature

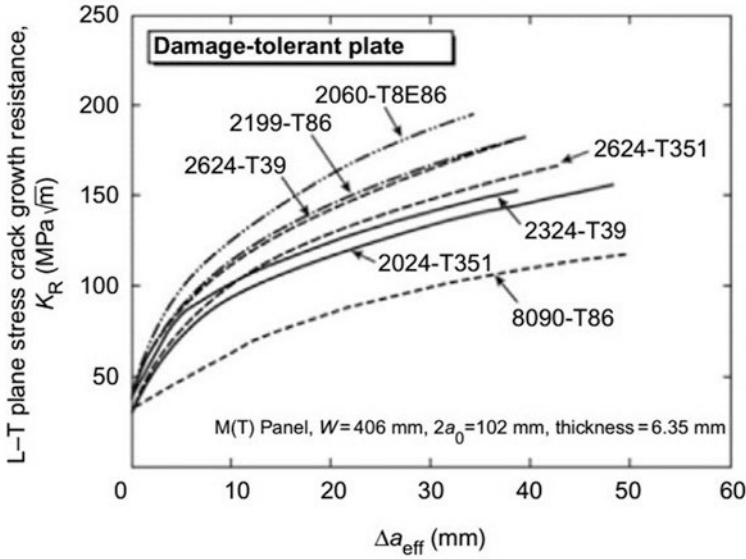


Fig. 1.13 The R-curve comparison of the second- and the third-generation Al–Li alloys (damage-tolerant plate type 8090 and 2060, 2199), conventional Al alloys (damage-tolerant 2X24 series) [56]. Reprinted by permission from Elsevier

1.5 Corrosion Properties of Al–Li Alloys

Corrosion is an important complication both for conventional Al and Al–Li alloys. Corrosion resistance is affected by multiple criteria such as chemical content, grain boundary, and aging heat treatment parameters, etc. The first-generation Al–Li alloys have quite high corrosion resistance and, therefore, have been used properly in aircraft structures. However, the second-generation Al–Li alloys are very vulnerable to intergranular corrosion. This drawback is more evident especially in the alloys with high Cu and Mg contents. Together with Cu and Mn contents, aging heat treatment is known to affect the susceptibility to intergranular corrosion. The lowest intergranular corrosion resistance is observed in the overaged alloys. Peak-aged condition leads to mild corrosion resistance in the alloys, while the highest corrosion resistance is observed in the alloys with under-aged conditions. If aging process is carried out at low temperatures, intergranular corrosion resistance is considerably enhanced in the third-generation Al–Li alloys, which is more than that in the second-generation Al–Li alloys. Furthermore, the addition of Zn element increases the corrosion resistance of the third-generation Al–Li alloys [5, 42, 54].

Stress corrosion cracking is a common problem for the second-generation Al–Li alloys. In contrast to intergranular corrosion, stress corrosion crack resistance increases by increasing aging condition. The second- and third-generation Al–Li alloys exhibit similar stress corrosion crack resistance. Due to the low Li content of the third-generation Al–Li alloys, as well as the Zn and Ag content, they provide

higher stress corrosion crack resistance compared to the conventional Al alloys. Another factor that provides enhanced stress corrosion cracking resistance is the peak-aged condition. However, stress corrosion crack resistance varies depending on material thickness. The aforementioned results about the stress corrosion cracking resistance are valid for the material thicknesses up to 30 mm. The required thermomechanical treatment and multistage aging applications change for thicker parts. For this reason, grain boundaries in microstructures should be optimized according to the desired level of stress corrosion crack resistance [42, 54].

1.6 Applications of Al–Li Alloys in Aircraft Structures

Al–Li alloys are used in different fields of aerospace sector. The alloys make ground in either spacecraft or aircraft applications. In aircraft applications, main sections are fuselage, upper wing and lower wing for Al–Li alloys.

1.6.1 Fuselage

High strength, fatigue, and crack resistances are always desired in aircraft fuselage designs [13]. One of the most commonly used alloys in airframe construction is Al–Li based alloys of 2199 and 2060. These alloys provide high fatigue strength and lightweight compared to the conventional Al alloys. Figure 1.14 shows the comparison of Al–Li alloys with conventional Al alloys. As can be seen in the chart, Al–Li alloys have superiority in all mechanical properties. Moreover, approximately 5% reduction is achieved in the densities. In addition, yield strength and fracture toughness strength are enhanced in Al–Li alloys.

Aircraft fuselage supporting beams and elements are exposed to high compression and tensile stresses [13]. For this reason, 7055 and 2024 series Al alloys are used in the production of these parts. Al–Li alloys of 2055 and 2099 are alternative materials to be used for these parts. Figure 1.15 shows the comparison of the mechanical properties of conventional Al and Al–Li alloys. It is seen that conventional 7055 series and 2055 Al–Li series alloys exhibit almost the same strength values. However, it is seen that Al–Li alloys are 5% lower in density. For 2099 series, while the density decreases by 7%, the strength of the alloy also decreases. Compressive modulus of elasticity and corrosion resistance of both Al–Li alloys is better than those of the conventional alloy. When the alloys used in the body frame (2024T42 and 2099T83/81) are compared, it is seen that the alloys and applied heat treatments are different. Using Al–Li alloys, density reduction is about 5.4% while providing higher strength limits.

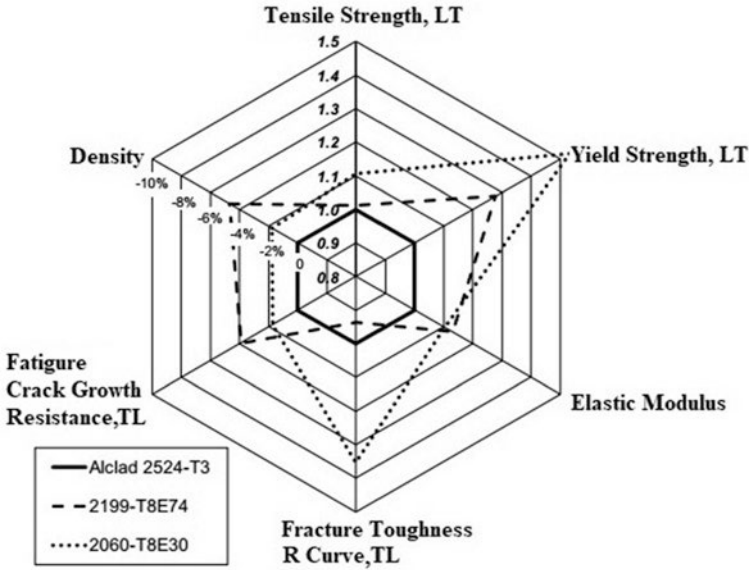


Fig. 1.14 Comparison of Al-Li and conventional Al alloys in terms of mechanical properties [57]. Reprinted by permission from Springer Nature

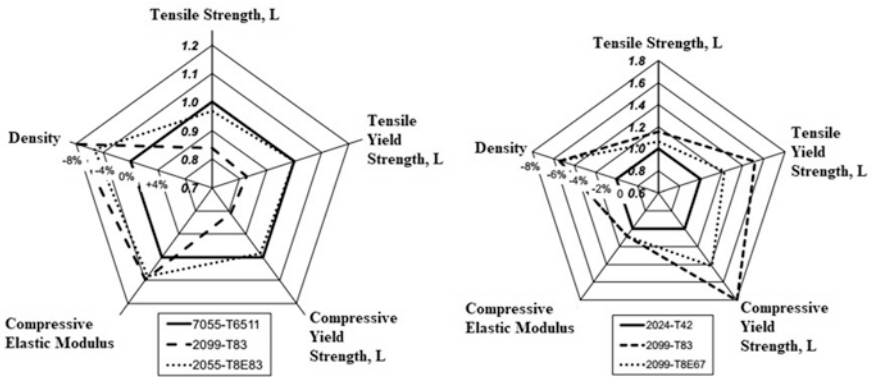


Fig. 1.15 Comparison of Al-Li and conventional Al alloy in terms of mechanical properties [57]. Reprinted by permission from Springer Nature

1.6.2 Upper Wing Structures

Due to the physics of the flight phenomenon, upper wing structures must be resistant to compression strength, fracture toughness, and torsional loadings [6, 13]. Figure 1.16 shows the variation of the specific yield strength and modulus of elasticity values for the conventional Al alloys and Al-Li alloys over the years. By

developing new alloys and heat treatments, a general increase regime is observed over the years. With the use of Al–Li alloys, it is seen that this increase has been even more dramatic. Figure 1.17 shows the mechanical properties of conventional Al and Al–Li alloys produced in sheet metal form. Conventional alloys of 7055T7751 and 7255T7751 exhibit similar mechanical properties. The mechanical properties (tensile, compressive yield strength, and fracture toughness) of 7075T7651 alloy are approximately 25–30% lower while the density is higher with a ratio of 2%. The new generation 2055 Al–Li alloy performs equivalent performance in all mechanical properties in addition to its lower density of about 6%. Figure 1.18 shows the comparison of conventional extruded 7XXX series and Al–Li alloys. It is seen that the density of alloy 2055 is 6% lower than that of 7XXX series whereas compressive modulus of elastic and fracture toughness is higher than the conventional one.

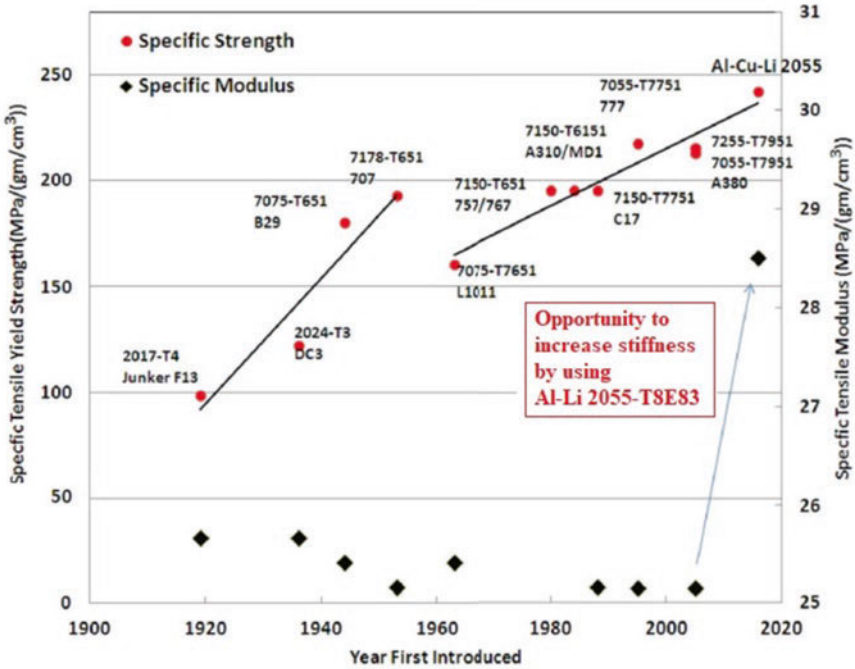


Fig. 1.16 Comparison of specific yield strengths and elastic modulus for conventional Al and Al–Li alloys [52]. Reprinted by permission from Springer Nature

Fig. 1.17 Mechanical properties of sheet form conventional Al and Al-Li alloys [52]. Reprinted by permission from Springer Nature

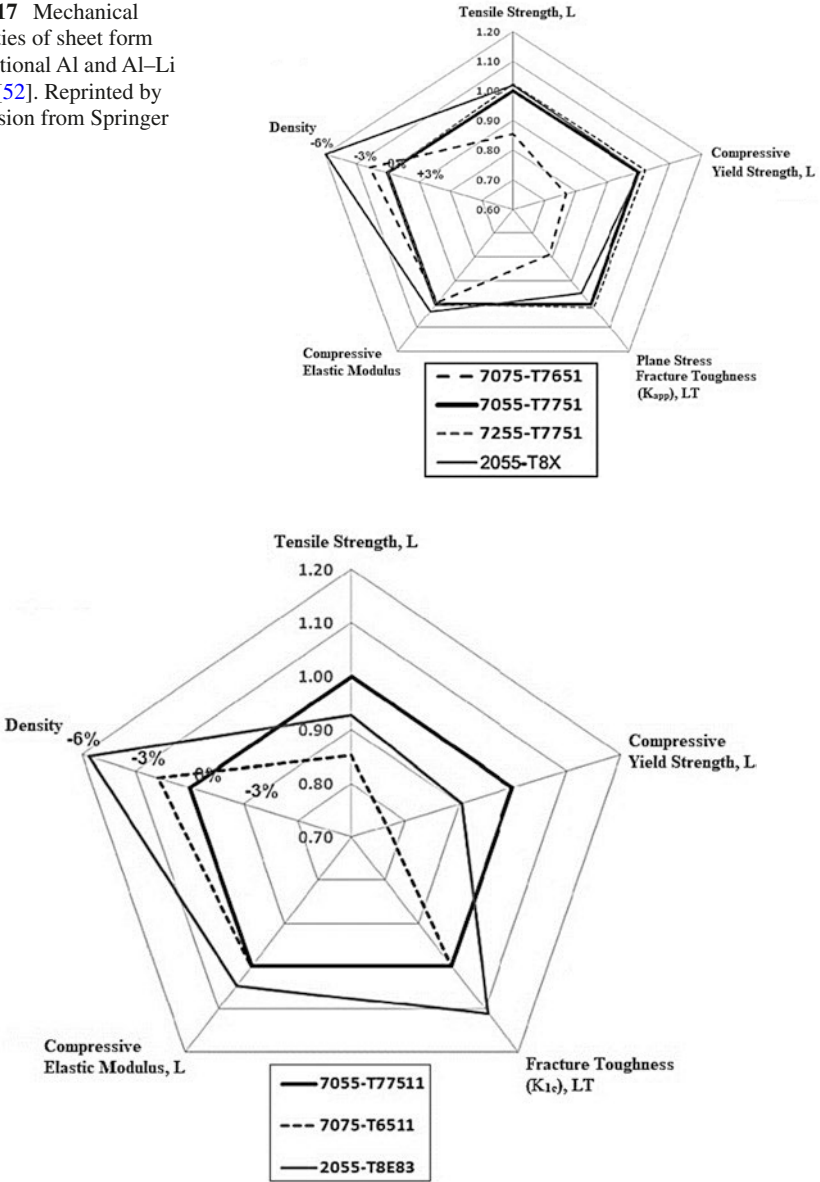


Fig. 1.18 Mechanical properties of extruded form conventional Al and Al-Li alloys [52]. Reprinted by permission from Springer Nature

1.6.3 Lower Wing Structures

Lower wing structures used in aircraft are made of materials with high strength and

damage tolerance. For this purpose, natural aging (T3XX) heat treatment is generally used for 2X24 series alloys. Today, three Al-Li alloys are considered as an alternative candidate to the conventional Al alloys. These candidates are 2199T86, 2060T8E86, and 2050T84 alloys. Plate type 2199 and 2060 Al-Li alloys have been developed for lower wing structures [55]. 2050 series has been developed to replace the alloy 7050T7451 [58, 59]. Figure 1.19a shows the comparison of the mechanical properties of Al-Li alloy 2199T86 and conventional alloys of 2024 and 2624. It is seen that alloy 2199T86 provides enhanced mechanical properties while lowering the density about 5%. A similar case is observed in high strength Al alloys as shown in Fig. 1.19b. It is clear that alloy 2060T8E86 has a lower density and higher mechanical properties than the conventional alloys of 2324 and 2624.

1.7 Conclusions

The third-generation Al-Li alloys are candidates for aircraft structures as challenging alternatives to conventional Al alloys and carbon fiber composites. These alloys have superiority in terms of modulus of elasticity, specific strength, corrosion resistance, stress corrosion crack resistance, hardness, and density. For this reason, these alloys have started to be used in various applications instead of the conventional Al alloy series of 2XXX and 7XXX. The main feature that makes Al-Li alloys popular is low density. In addition to this advantage, equivalent or better mechanical properties in comparison to the conventional alloys make these alloys desirable for aircraft applications. The most important reason for the increase in hardness and modulus of elasticity is T₁ type nano-sized precipitates in the alloy microstructure. Despite these benefits, many problems are encountered in the production of Al-Li alloys due to the Li content. These problems have created some milestones in the development of Al-Li alloys such as first, second, and third generations. Due to inadequate

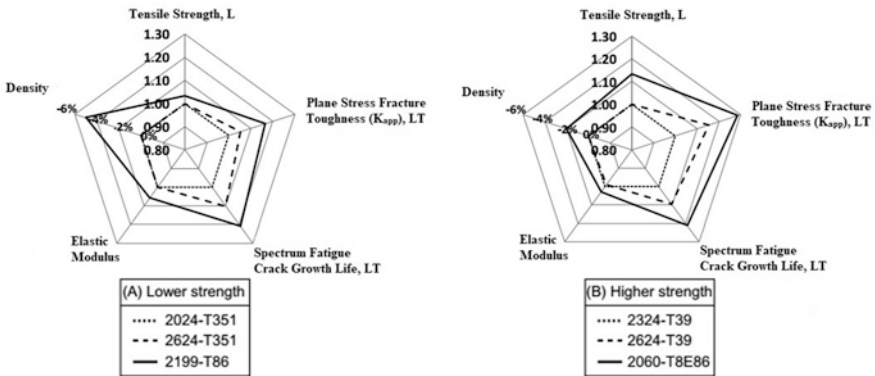


Fig. 1.19 Mechanical properties of plate type conventional Al and Al-Li alloys [55]. Reprinted by permission from Springer Nature

technology, some problems occurred in the first- and the second-generation alloys. However, by the developing technology, the third-generation Al–Li alloys are designed with superior mechanical properties along with high corrosion resistance. In order to achieve further improvements, additional elements such as Mg, Zn, and Mn are used in Al–Li alloys. These elements have a grain refining effect, which improves the mechanical properties drastically. Al–Li alloys have been developed by pioneer aviation companies such as Airbus, Boeing, Lockheed Martin, Mikoyan Gurevich, and Tupolev for the production of aircraft components. In near future, the prevalence of these alloys is expected to increase in aircraft applications.

References

1. Olga Grushko, B. O., & Ovchinnikov, V. (2016). Brief history of aluminum–lithium alloy creation. In *Aluminum-lithium alloys* (1st ed., pp. 1–10). CRC Press.
2. Prasad, N. E., Gokhale, A. A., & Rao, P. R. (2003). Mechanical behaviour of aluminium–lithium alloys. *Sadhana: Academy Proceedings in Engineering Sciences*, 28(1–2), 209–246.
3. Ekvall, J. C., Rhodes, J. E., & Wald, G. G. (1982). Methodology for evaluating weight savings from basic material properties. In P. R. Abelkis & C. M. Hudson (Eds.), (pp. 328–341). ASTM International.
4. Pasang, T., Lynch, S., & Moutsos, S. (2006). Challenges in developing high performance Al–Li alloys. *International Journal of the Society of Materials Engineering for Resources*, 14, 7–11.
5. Rioja, R. J., & Liu, J. (2012). The evolution of Al–Li base products for aerospace and space applications. *Metallurgical and Materials Transactions A: Physical Metallurgy and Materials Science*, 43(9), 3325–3337.
6. Öztürk, F., Kılıç, S., & Kacar, İ. (2018). *Havacılık Endüstrisinde Yeni Trend: Al–Li Alaşımları*. Gazi Üniversitesi Mühendislik–Mimarlık Fakültesi Dergisi.
7. Kobayashi, K., Ohsaki, S., Kamio, A., & Tsuji, Y. (1992) Effect of Zn addition on corrosion resistance of 2090 and 2091 alloys. *Aluminum Lithium*, 2.
8. Wanhill, R. J. H., & Bray, G. H. (2014). Aerostructural design and its application to aluminum–lithium alloys. In *Aluminum-lithium alloys* (pp. 27–58).
9. Sankaran, K. K., & Grant, N. J. (1980). The structure and properties of splat-quenched aluminum alloy 2024 containing lithium additions. *Materials Science and Engineering*, 44(2), 213–227.
10. Peel, C., Evans, B., Baker, C., Bennett, D., Gregson, P., & Flower, H. (1984). The development and application of improved aluminium–lithium alloys. *Aluminum-Lithium Alloys*, II, 363–392.
11. Westwood, A. R. C. (2013). New materials for aerospace industry. *Materials Science and Technology*, 6(10), 958–961.
12. Quist, W., Narayanan, G., & Wingert, A. (1983). Aluminum–lithium alloys for aircraft structure—An overview. *Aluminum-Lithium Alloys*, II, 313–334.
13. Prasad, N. E., Gokhale, A. A., & Wanhill, R. J. H. (2014). *Aluminum-lithium alloys processing, properties, and applications*.
14. Pasang, T., Symonds, N., Moutsos, S., Wanhill, R. J. H., & Lynch, S. P. (2012). Low-energy intergranular fracture in Al–Li alloys. *Engineering Failure Analysis*, 22, 166–178.
15. Pickens, J. R. (1990). Recent developments in the weldability of lithium-containing aluminum alloys. *Journal of Materials Science*, 25(7), 3035–3047.
16. Rioja RJ, Cho A, Pretz PE (1990) *Al–Li alloys having improved corrosion resistance containing Mg and Zn*. USA Patent.

17. Starke, E. A., Sanders, T. H., & Palmer, I. G. (2013). New approaches to alloy development in the Al-Li system. *JOM*, 33(8), 24–33.
18. Kamaludeen, M., Renganathan, N. G., Sundaram, M., & Vasu, K. I. (1987). Aluminium-lithium alloy by fused salt electrolysis. *Bulletin of Electrochemistry*, 3(2), 143–145.
19. Dorin, T., Vahid, A., & Lamb, J. (2018). Aluminium lithium alloys. In *Fundamentals of aluminium metallurgy* (pp. 387–438).
20. Wright, W. J., & Askeland, D. R. (2021). *The science and engineering of materials*.
21. Prasad, N. E., & Ramachandran, T. R. (2014). Phase diagrams and phase reactions in Al–Li alloys. In *Aluminum-lithium alloys* (pp. 61–97).
22. Starke, E. A. (2014). Historical development and present status of aluminum–lithium alloys. In *Aluminum-lithium alloys* (pp. 3–26).
23. Decreus, B., Deschamps, A., Donnadieu, P., & Ehrström, J. C. (2013). On the role of microstructure in governing fracture behavior of an aluminum–copper–lithium alloy. *Materials Science and Engineering A*, 586, 418–427.
24. Hu, L., Zhan, L., Shen, R., Liu, Z., Ma, Z., Liu, J., & Yang, Y. (2017). Effects of uniaxial creep ageing on the mechanical properties and micro precipitates of Al-Li-S4 alloy. *Materials Science and Engineering A*, 688, 272–279.
25. Giummarra, C., Thomas, B., & Rioja, R. (2007). *New aluminum-lithium alloys for aerospace applications*. Paper presented at the Proceedings of the 3rd International Conference on Light Metals Technology, Saint-Saveur, Québec, Canada.
26. Araullo-Peters, V., Gault, B., Geuser, F., Deschamps, A., & Cairney, J. M. (2014). Microstructural evolution during ageing of Al–Cu–Li–x alloys. *Acta Materialia*, 66, 199–208.
27. Duan, S. Y., Le, Z., Chen, Z. K., Gao, Z., Chen, J. H., Ming, W. Q., Li, S. Y., Wu, C. L., & Yan, N. (2016). Li-atoms-induced structure changes of Guinier–Preston–Bagaryatsky zones in AlCuLiMg alloys. *Materials Characterization*, 121, 207–212.
28. Gumbmann, E., de Geuser, F., Lefebvre, W., Sigli, C., & Deschamps, A. (2014). The influence of Mg and Ag on the precipitation kinetics and the formation of the T₁ phase in Al-Cu-Li alloys. *Materials Science Forum*, 794-796, 945–950.
29. Gumbmann, E., De Geuser, F., Deschamps, A., Lefebvre, W., Robaut, F., & Sigli, C. (2016). A combinatorial approach for studying the effect of Mg concentration on precipitation in an Al–Cu–Li alloy. *Scripta Materialia*, 110, 44–47.
30. Gumbmann, E., Lefebvre, W., De Geuser, F., Sigli, C., & Deschamps, A. (2016). The effect of minor solute additions on the precipitation path of an Al Cu Li alloy. *Acta Materialia*, 115, 104–114.
31. Gumbmann, E., De Geuser, F., Sigli, C., & Deschamps, A. (2017). Influence of Mg, Ag and Zn minor solute additions on the precipitation kinetics and strengthening of an Al-Cu-Li alloy. *Acta Materialia*, 133, 172–185.
32. Huang, B. P., & Zheng, Z. Q. (1998). Independent and combined roles of trace Mg and Ag additions in properties precipitation process and precipitation kinetics of Al–Cu–Li–(Mg)–(Ag)–Zr–Ti alloys. *Acta Materialia*, 46(12), 4381–4393.
33. Itoh, G., Cui, Q., & Kanno, M. (1996). Effects of a small addition of magnesium and silver on the precipitation of T₁ phase in an Al-4%Cu-1.1%Li-0.2%Zr alloy. *Materials Science and Engineering A*, 211(1–2), 128–137.
34. Gilmore, D. L., & Starke, E. A. (1997). Trace element effects on precipitation processes and mechanical properties in an Al-Cu-Li alloy. *Metallurgical and Materials Transactions A: Physical Metallurgy and Materials Science*, 28(7), 1399–1415.
35. Murayama, M., & Hono, K. (2001). Role of Ag and Mg on precipitation of T₁ phase in an Al-Cu-Li-Mg-Ag alloy. *Scripta Materialia*, 44(4), 701–706.
36. Kang, S. J., Kim, T.-H., Yang, C.-W., Lee, J. I., Park, E. S., Noh, T. W., & Kim, M. (2015). Atomic structure and growth mechanism of T₁ precipitate in Al–Cu–Li–Mg–Ag alloy. *Scripta Materialia*, 109, 68–71.
37. Guinel, M. J., Brodusch, N., Sha, G., Shandiz, M. A., Demers, H., Trudeau, M., Ringer, S. P., & Gauvin, R. (2014). Microscopy and microanalysis of complex nanosized strengthening

- precipitates in new generation commercial Al-Cu-Li alloys. *Journal of Microscopy*, 255(3), 128–137.
38. Kilmer, R. J., & Stoner, G. E. (1991). Effect of Zn additions on precipitation during aging of alloy 8090. *Scripta Metallurgica et Materialia*, 25(1), 243–248.
 39. Gable, B. M., Pana, M. A., Shiflet, G. J., & Starke, E. A., Jr. (2002). The role of trace additions on the coarsening behavior in Al-Li-Cu-X alloys. *Materials Science Forum*, 396-402, 699–704.
 40. Chen, A., Zhang, L., Wu, G., Sun, M., & Liu, W. (2017). Influences of Mn content on the microstructures and mechanical properties of cast Al-3Li-2Cu-0.2Zr alloy. *Journal of Alloys and Compounds*, 715, 421–431.
 41. Proton, V., Alexis, J., Andrieu, E., Delfosse, J., Deschamps, A., De Geuser, F., Lafont, M.-C., & Blanc, C. (2014). The influence of artificial ageing on the corrosion behaviour of a 2050 aluminium–copper–lithium alloy. *Corrosion Science*, 80, 494–502.
 42. Prasad, N. E., Gokhale, A. A., & Wanhill, R. J. H. (2016). Aluminium-lithium alloys. In *Aerospace materials and material technologies* (Aerospace materials) (Vol. 1). Springer.
 43. Prasad, N. E. (1993). *In-plane anisotropy in the fatigue and fracture properties of quaternary Al-Li-Cu-Mg alloys*. Banaras Hindu University.
 44. Eswara Prasad, N., & Malakondaiah, G. (1992). Anisotropy of mechanical properties in quaternary Al-Li-Cu-Mg alloys. *Bulletin of Materials Science*, 15(4), 297–310.
 45. Peters, M., Eschweiler, J., & Welpmann, K. (1986). Strength profile in Al-Li plate material. *Scripta Metallurgica*, 20(2), 259–264.
 46. Matweb. (2021). *Aluminum lithium alloy*. Retrieved from <http://www.matweb.com/>.
 47. Eswara Prasad, N., Malakondaiah, G., Kutumbarao, V. V., & Rama Rao, P. (2013). In-plane anisotropy in low cycle fatigue properties of and bilinearity in Coffin-Manson plots for quaternary Al-Li-Cu-Mg 8090 alloy plate. *Materials Science and Technology*, 12(7), 563–577.
 48. Eswara Prasad, N., & Rama Rao, P. (2013). Low cycle fatigue resistance of Al–Li alloys. *Materials Science and Technology*, 16(4), 408–426.
 49. Eswara Prasad, N., Srivatsan, T. S., Wanhill, R. J. H., Malakondaiah, G., & Kutumbarao, V. V. (2014). Chapter 11—Fatigue behavior of aluminum–lithium alloys. In N. Eswara Prasad, A. A. Gokhale, & R. J. H. Wanhill (Eds.), *Aluminum-lithium alloys* (pp. 341–379). Butterworth-Heinemann.
 50. De, P. S., Mishra, R. S., & Baumann, J. A. (2011). Characterization of high cycle fatigue behavior of a new generation aluminum lithium alloy. *Acta Materialia*, 59(15), 5946–5960.
 51. Chen, J., Madi, Y., Morgeneyer, T. F., & Besson, J. (2011). Plastic flow and ductile rupture of a 2198 Al–Cu–Li aluminum alloy. *Computational Materials Science*, 50(4), 1365–1371.
 52. Denzer, D. K., Rioja, R. J., Bray, G. H., Venema, G. B., & Colvin, E. L.H. Weiland, A. D. Rollett, & W. A. Cassada (Eds.). *The evolution of plate and extruded products with high strength and fracture toughness, ICAA13 Pittsburgh, Cham, 2016//2016* (pp. 587–592). Springer International Publishing.
 53. Wanhill, R. J. H., & Bray, G. H. (2014). Chapter 12—Fatigue crack growth behavior of aluminum–lithium alloys. In N. Eswara Prasad, A. A. Gokhale, & R. J. H. Wanhill (Eds.), *Aluminum-lithium alloys* (pp. 381–413). Butterworth-Heinemann.
 54. Holroyd, N. J. H., Scamans, G. M., Newman, R. C., & Vasudevan, A. K. (2014). Chapter 14—Corrosion and stress corrosion of aluminum–lithium alloys. In N. Eswara Prasad, A. A. Gokhale, & R. J. H. Wanhill (Eds.), *Aluminum-lithium alloys* (pp. 457–500). Butterworth-Heinemann.
 55. Karabin, L. M., Bray, G. H., Rioja, R. J., & Venema, G. Al-Li-Cu-Mg-(Ag) products for lower wing skin applications. In H. Weiland, A. D. Rollett, & W. A. Cassada (Eds.), *ICAA13 Pittsburgh, Cham, 2016//2016* (pp. 529–534). Springer International Publishing.
 56. Lynch, S. P., Wanhill, R. J. H., Byrnes, R. T., & Bray, G. H. (2014). Chapter 13—Fracture toughness and fracture modes of aerospace aluminum–lithium alloys**© 2013 Commonwealth of Australia. In N. Eswara Prasad, A. A. Gokhale, & R. J. H. Wanhill (Eds.), *Aluminum-lithium alloys* (pp. 415–455). Butterworth-Heinemann.

57. Magnusen, P. E., Mooy, D. C., Yocum, L. A., & Rioja, R. J. (2012). Development of high toughness sheet and extruded products for airplane fuselage structures. In: *ICAA13: 13th international conference on aluminum alloys*. pp. 535–540.
58. Lequeu, P. (2008). Advances in aerospace aluminum summaries of presentations by Alcan Aerospace personnel during ASM's AeroMat 2007 conference. Al-Li alloys are highlighted. *Advanced Materials and Processes*, 166(2), 47.
59. Lequeu, P., Smith, K. P., & Daniélou, A. (2009). Aluminum-copper-lithium alloy 2050 developed for medium to thick plate. *Journal of Materials Engineering and Performance*, 19(6), 841–847.

Chapter 2

Metal Foams and Their Applications in Aerospace Components



Cihat Ensarioglu, Altug Bakirci, Huseyin Koluk, and M. Cemal Cakir

2.1 Introduction

Light weighting is a target that almost all designers are responsible. By reducing the weight, energy efficiency increases due to the decreasing energy consumption. In addition, vehicle performance increases with increasing acceleration [1]. Material substitution is a method to achieve light weighting. For instance, mechanically, a material with higher specific strength (strength/density) (such as aluminum foam instead of polymer foam) can be used. Besides material substitution, lower weight constructions can be obtained by changing the shape (e.g., using a lattice structure) or by developing composite structures [2].

As an example, instead of a single steel plate, a composite construction with the same stiffness value and an 83% lower weight can be obtained by using two aluminum sheets with aluminum foam between them (AFS/aluminum foam sandwich). A similar reduction in weight (77%) can be achieved with a CFRP/carbon fiber-reinforced plastic composite structure. However, the cost of this material is approximately four times compared to that of AFS [1]. Also, AFS can have similar bending stiffness values as an aluminum honeycomb sandwich structure of the same weight [3].

There are many porous materials such as bone and wood in nature. Studies have been recorded since the mid-twentieth century on making metals porous by imitating nature. Developed methods can also be used in obtaining functionally graded structures because that the density of the products can to some extent be adjusted [4].

C. Ensarioglu (✉) · A. Bakirci · M. C. Cakir
Department of Mechanical Engineering, Bursa Uludag University, Nilufer, Bursa, Turkey
e-mail: cihatensari@uludag.edu.tr; altugbakirci@uludag.edu.tr

H. Koluk
ALUPAM AS, Bursa, Turkey

Porous metals attracted attention after being used against high shock-wave pressures in the 1950s, and studies on aluminum foam production for aircraft technology began. As a result of the increasing number of studies on porous metals, continuous improvements are achieved in production methods and material properties. There is a conference originated in Europe (MetFoam), dedicated to developments in this field and being held regularly since 1999. In addition to these improvements, the ability of porous metals to meet ever-rising and often conflicting expectations increases the interest in this material group [5]. As of 2019, when the total use of metal foams in different industries is approximately compared, the industries where they are used the most are automotive (31%) and aerospace/defense (20%) [6].

Although many other metals can be turned into a metal foam, still the most study is on aluminum and its alloys. Aluminum foam materials combine light weightiness, high mechanical energy absorption, good sound absorption, nonflammability, low thermal conductivity, and electromagnetic shielding [7].

Metal foams are classified as open cell if their cells are open to each other and closed cell if they are closed to each other (Fig. 2.1).

2.2 Primary Processing

Basically, there are possibilities of making metals porous while they are in four different forms (Table 2.1): Solid (powder, fiber, sphere), liquid (melt), gas (vapor), ion [10]. Closed-cell porous structures can only be formed by some liquid metal methods (Fig. 2.2). In these methods, it is the surface tension (which occurs in liquid state) that allows the formation of cells that are almost completely closed [11]. An exception to this situation is syntactic metal foams. Fully closed cells in these structures are generated with hollow, place-holder elements that remain in the structure after manufacturing [12]. Another exception is the studies on the production of closed/open-cell metal foams with the help of 3D printing technology [13], which has been started to be employed for metallic material manufacturing, too.

Although many of the porous metals are commonly referred to as metal foam, “metal foam” literally defines materials formed by the dispersion of gas bubbles in

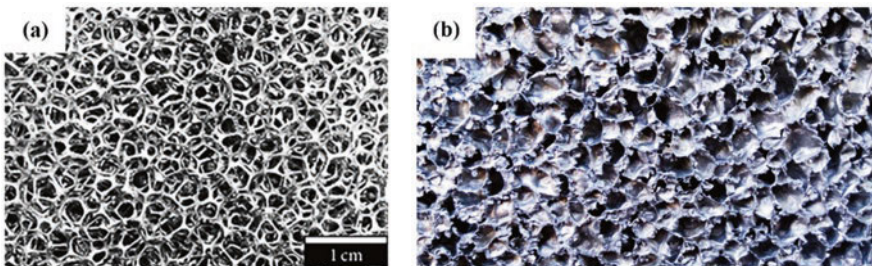


Fig. 2.1 Metal foams: (a) open cell [8] Reprinted by permission from Elsevier, (b) closed cell [9], (Courtesy of AluPam).

Table 2.1 Porous metal production methods [10]. Reprinted by permission from Elsevier

POROUS METAL PRODUCTION					
Form of Metal (during porosity generation)					
Solid (Powder, Fiber, Sphere)	Liquid (Melt)		Gas (Vapor)	Ion	
form of porosity					
open cell		open cell or closed cell		open cell	
porosity generation method					
sintering	powders or fibers	foaming <i>(literally "metal foam")</i>	direct (using gas or blowing agent)	vapor deposition (condensation on a cold polymer precursor)	electro-deposition (onto a polymeric foam)
	powders compacted with space-holders		indirect (using blowing agent)		
	hollow spheres	gasar (eutectic system of liquid metal + H ₂ gas)			
	powders consolidated in rod form				
	powder mixture (reaction sintering)				
gas entrapment (expansion of gas in a solid metal powder compact)	casting	investment casting (replicating a polymer foam)			
		using space-holders			
slurry foaming (expansion of a mixture of metal powders, blowing agents and reactives)	spray forming (collecting spray metal on a substrate)				

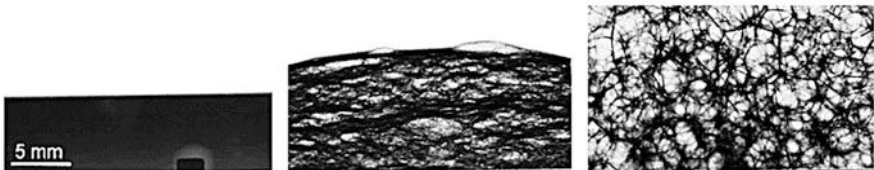


Fig. 2.2 Expansion stages of a metal foam, monitored by X-ray radioscopy [14]. Reprinted by permission from AIP Publishing

liquid metal [10]. Even though aluminum is the most common material that is foamed; zinc, magnesium, gold, copper, tin, brass, lead, nickel, and even steel can also be made into this form [15].

The idea of producing metal foam materials with macroscopic cells was embodied in a series of patents received in the 1950s. There was a second activity in this area in the 1980s; since these dates, many scientific studies have been conducted and the results have been published, some companies have commercialized metal foam materials by establishing small-scale production lines [16]. It was only possible in the early 2000s for these materials to become a niche market where productions are made at 1000 kg/h capacities [10].

In **closed-cell** metal foam production methods (Table 2.2), where liquid metal is foamed, if a bubble formation mechanism (injecting gas or introducing a

Table 2.2 Elements and steps in direct and indirect metal foaming methods [16]. Reprinted by permission from Wiley

METAL FOAM PRODUCTION				
Foaming Method				
Direct Foaming		Indirect Foaming		
bubble formation method				
gas injection	blowing agent decomposition		blowing agent decomposition	
material preparation				
pre-alloyed/elementary bulk metal(s)		pre-alloyed/ elementary powder metal(s)		precursor
		blowing agent addition		
		mixing		
		consolidation (pre-forming)		
melting				
particle addition for viscosity and stability				
mixing				
gas injection	blowing agent addition			
forming				
pulling onto a conveyor after expansion	collecting/injecting into a mold during expansion	free expansion in a container	expansion in a mold or between sheets	free expansion in a container
solidification				
some companies and (“their products”)				
Cymat (Canada) (“SAF”)		Applied lightweight materials/alm (Germany) (“AFS”)		
Foamtech (Korea) (“Lasom”)		Alulight (Austria) (“Alulight”)		
Hütte Kleinreichenbach/HKB (Austria) (“Metcomb”)		Fraunhofer-Institute (Germany) (“Foaminal”)		
Shinko-Wire (Japan) (“Alporas”)		Gleich-IWE (Germany)		
AluPam (Turkey)		Schunk (Germany)		

gas-releasing agent) is activated when the metal becomes molten, these methods are called direct foaming. If the bubbles are formed spontaneously due to the melting of a previously prepared structure (precursor), these methods are called indirect foaming [17]. In this second method, pores may start to emerge before the structure is completely melted, even if it is not desired [18].

Although naming indirect foaming method of metals as “PM/powder metallurgical foaming method” is common, this can be evaluated as a mumpsimus. The reason is that the similarity of two methods ends at the end of the consolidation stage. The next stage in indirect metal foaming is melting and no sintering stage is included.

Pore structure is predetermined in some porous metallic materials. For instance, in investment casting method, a metal replica of an open-cell polymer structure is produced. On the other hand, in metal foams, the pore structure is formed almost freely, even some control mechanisms have been developed. In addition, the pores are subject to deteriorations such as drainage (liquid flowing over the foam boundaries and accumulating at the bottom) and coalescence (loss of the foam boundaries).

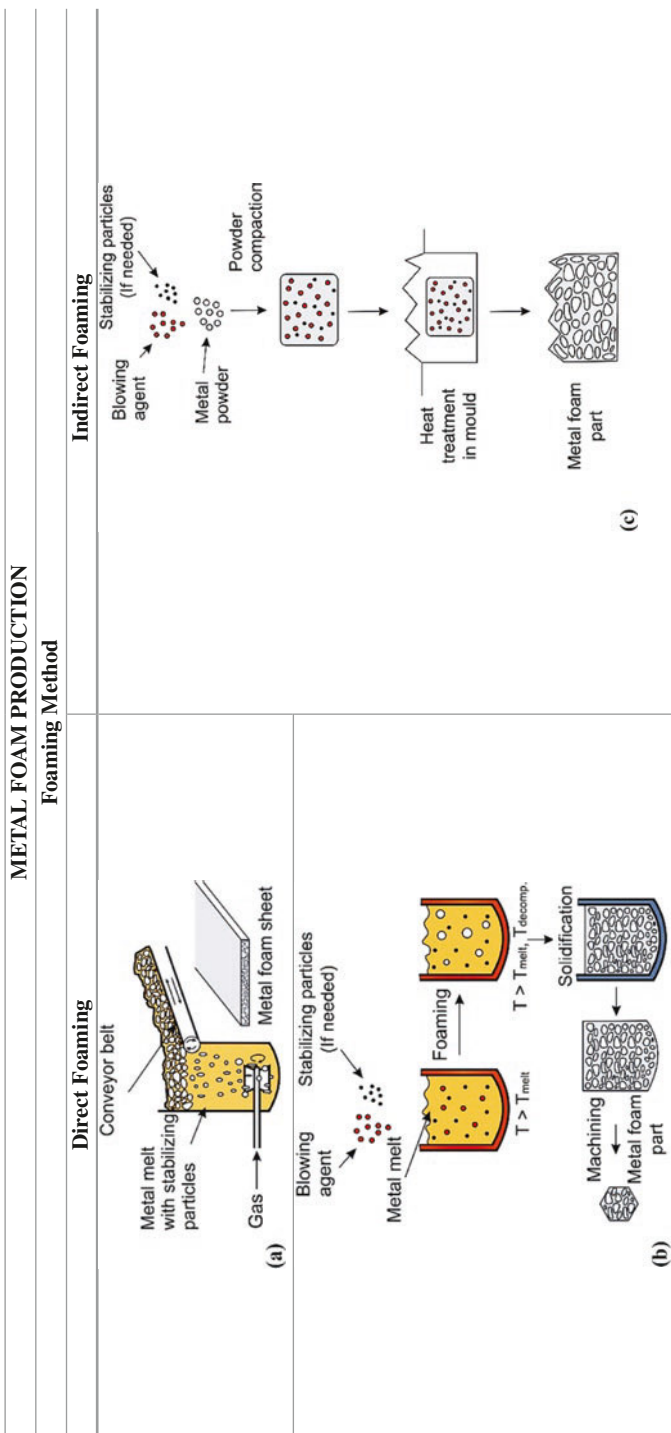
There are some requirements for the foam structure to form and keep its form (Table 2.3). According to this, there is a need for a source to generate gas bubbles, a force to keep the bubbles in the structure, and a mechanism that stabilizes the bubbles.

The source which generates gas bubbles in molten metal is a mechanism that injects gas from a rotating propeller or a vibrating nozzle in the gas injection method. In this way, usually air, alternatively nitrogen or argon gas, is sent into the mixture in a fine and homogeneous manner. Another source of gas formation is the so-called blowing agents, which cause gas emergence when decomposed at high temperatures [19]. For a matrix of Al or its alloys, TiH_2 and CaCO_3 compounds are the most popular blowing agents. This type of gas formation can be used in both direct and indirect methods. In direct methods, it is ensured that the blowing agent is dispersed into the molten metal. In indirect methods, the blowing agent is added to the precursor material in a homogeneous manner before melting [20].

The gas bubbles formed tend to leave the molten metal rapidly due to the buoyant force. In order to prevent this in direct foaming methods, the viscosity of the liquid is increased. For this purpose, ceramic particles such as SiC , Al_2O_3 , TiB_2 are added to the molten metal [22]. Another method is to add elements that will form a ceramic compound (in situ ceramic particle formation). For this, the addition of elements such as Ca or Al in an oxygen-containing medium has yielded good results [11]. It has been observed that viscosity can be increased up to five times with the help of Ca addition [19].

These particles, which increase the viscosity, are also effective in stabilizing the bubbles. There is a correlation between viscosity and foam stability. However, viscosity is not a reason for foam stability; it is only considered to be an indication of the presence of hard particles. Many studies have shown that melts without hard particles do not form metal foam. It was also found that there is a proportionality between the oxide content and the total value of the inner surface areas of the cells. When the ratio of these particles remains too low, the surface tensions increase and the foam structure deteriorates. SiC has come to the fore with its ability to delay

Table 2.3 Metal-foaming methods: (a–b) Direct methods, (c) indirect method [21]. Reprinted by permission from The Royal Society of Chemistry



bubble coalescence for a long time, to cover foam films (boundaries that will become walls when solidified) without getting stuck in the bubbles, and to allow the formation of very thin foam films [16].

In some cases, the addition of blowing agent can both generate bubbles and lead to their stabilization. An example for this is the use of CaCO_3 as a blowing agent for direct foaming of aluminum and its alloys. As a result of the reaction of Al (or Al alloy) and CaCO_3 , (besides the CO_2 gas that provides foaming) hard particles such as CaO and Al_2O_3 are formed and act as stabilizers. Such a mechanism does not occur in the use of TiH_2 blowing agent [23].

The indirect foaming method involves the compression of mixed powder materials (“pre-alloyed powder + blowing agent” or “alloying elements + blowing agent”). The purpose of this stage is to increase the density of the powder mixture (min. 94% of the theoretical density [24]) so that it is ensured that the blowing agent is embedded in the metal matrix and that it is made difficult for the bubbles to escape from the structure by reducing the porosity as much as possible [10]. Another function of the compression stage is to break down the oxide layers on the metal powders. As a result, the broken oxide particles increase the stability of the metal foam (when the metal becomes liquid); also, the breaking of the oxide shells on the powder metals improves the combining of powder particles [25]. Even the oxide content on as-received powders could be sufficient to obtain a successful expansion [26].

Although metal foam production methods do not involve very complex process steps, when the process parameters and the material content (alloying elements, hard particles, blowing agent, etc.) are not precisely controlled, the quality of the product obtained changes significantly [27]. As mentioned previously, the impact of the compression process on foaming in indirect foaming methods can be given as an example.

Another example is the need to ensure that gas bubbles or blowing agent particles sent into the liquid metal are dispersed homogeneously in direct foaming methods. One method developed to enable homogeneous distribution of the blowing agent is two-stage foaming. In one version of this method, the matrix metal is brought to a temperature above its solidus temperature but below the decomposition temperature of the blowing agent and mixing is performed. Afterward, foaming occurs when the intermediate product (can be called precursor material), obtained by cooling and shaping in molds, is brought to about melting temperature [10]. In another version (FORMGRIP), an Al-based matrix is brought to a temperature above its melting temperature and TiH_2 (blowing agent) is mixed in pretreated (oxidized) condition, ensuring limited decomposition. Casting and cooling take place thereafter, yielding a precursor material. The second stage is similar to that of the former version [28]. In fact, these two two-stage foaming versions, which are modifications of direct foaming, turn into indirect foaming methods since the metal foam is produced by baking a precursor. In another method developed for homogeneous distribution, a eutectic metal alloy with a low melting temperature is liquidized and the blowing agent is added into this liquid and mixing is performed. After solidification, a structure is formed in which the blowing agent is embedded. This structure is added homogeneously into a suitable liquid metal (with a higher melting

temperature) and foaming occurs, achieving the desired alloy foam. As a result, a more homogeneous foam structure is attained [10].

On the other hand, it is an advantage that the mixture can be prepared at room temperature before melting in the indirect method; but the decomposition of the blowing agent before the metal matrix melts is a problematic situation that needs improvement. For this reason, the melting temperature of the metal matrix and the decomposition temperature of the blowing agent are tried to be brought as close as possible [29]. Addition of alloying elements (lowering the melting temperature) and pretreatment of the blowing agent (providing oxidation by means of annealing, thus, increasing the decomposition temperature) are two examples for this purpose [30].

The properties such as type, size, and ratio of oxides that will provide stability should also be carefully selected. While the ratio is too low, it decreases the stability of the structure; while being too high makes the material difficult to expand by increasing the viscosity too much. In addition, using a very high oxide ratio increases the brittleness of the product obtained. While too small particle sizes make mixing difficult, too big sizes make it difficult to cover the bubbles and cause the stability to decrease [11].

After the maximum expansion is achieved, the foam structure deteriorates within seconds. For this reason, the foaming time is also an important parameter that needs to be carefully adjusted. The final density and foam structure, arising from the production parameters (foaming time, foaming temperature, mixing time, etc.), determine the mechanical, thermal, acoustic performances of the product.

Direct foaming methods are the most suitable ones for mass production. The materials produced in the form of sheets, slabs, or blocks are used as they are or after they are processed into the desired shape by secondary operations [10]. Alternatively, the desired shape can be obtained by guiding the material into a mold in the foaming stage (either by the action of the buoyant force [16] or by using a customized injection machine [31]). Indirect foaming method (foaming powder compact precursors) could also be used in mass production effectively by employing continuous furnaces, which would involve conveyors to transfer precursors from foaming to cooling stages [10].

Sandwich structures (e.g., AFS) can be produced by placing metal foam materials (in the form of slabs or sheets, produced by direct or indirect methods) between two metal sheets (aluminum or steel). One way to construct sandwich products is using adhesives [32]. In an alternative way, two metal sheets are rolled by placing a precursor material between them, subsequently, they are shaped by deep drawing if necessary, and finally, the precursor is foamed as a result of heating. This method forms a metallurgical bond between the sheets and the metal foam core [10].

An application applied in the indirect foaming method is to foam the precursor inside a hollow structure, which also results in a metallurgical bond [33]. Using precursor materials with a shape adapting the shape of the hollow structure ensures more successful filling of the cavities while foaming [10].

As stated previously, although **open-cell** metallic structures are not metal foams in the literal sense of the word, they are often considered in the metal foam material group. In addition to their functional properties, when compared to their

alternatives, high strength, high melting point, and nonflammability properties make these materials preferred. Open-cell metal foams find applications in energy storage (e.g., battery electrodes, fuel cell membranes), thermal management (e.g., heat exchangers, radiative cooling systems), electromagnetic shielding, filtering, and so on [34].

Since the 1920s, a wide range of production processes has been developed for open-cell metal foams [35]. The intended application dictates the structure and the form of open-cell metal foam. Generally, to be produced in the desired form, open-cell metal foams need a pattern. Reticulated structures (sponges), space holders, and additive manufactured geometries are the most common patterns, which are made of mostly polymers. Additive manufacturing can even be used to produce directly open-cell metal foams themselves [9]. Some of the open-cell metal foam production methods will be described subsequently.

One of the common liquid state methods is investment casting, which generates a metallic copy of a polymer sponge. Wax could be used to increase the wall thicknesses of the sponge. The process is suitable for most of the metals [36]. It starts by trapping the polymer foam in a slurry, which will become the metal casting mold after dried. The material of this mold has to be heat resistant and should be selected such that the mold can easily be dissolved or dispersed at the end of the process. Then the composite structure, containing the polymer foam and the slurry, is dried and heated to remove the polymer foam by evaporation or melting, resulting in a structure with cavities. It serves as a mold in the metal casting stage. The mold may need to be fired to endure the casting temperature and pressure. In some evolved processes, these three operations can occur concurrently [37]. By the act of gravity, or in some cases by applying pressure, the target metal is filled into the mold cavities. Then the mold is dissolved with some chemicals or just water. Final product appears almost the same as the polymer sponge. The phases of the process are shown in Fig. 2.3. It is possible to obtain an open-cell metal foam with 80–97% porosity using this method [10].

Polymer foam in the method above may be replaced with lattice structure. Porous metals with such a regular lattice structure are also called periodic cellular metal. Polymer fragments may be glued together to form a lattice. The lattice can also be constructed on 3D printers with PLA, ABS, or other filaments. Since the structure of a lattice block is not stochastic like that of a polymer foam, it may be possible to

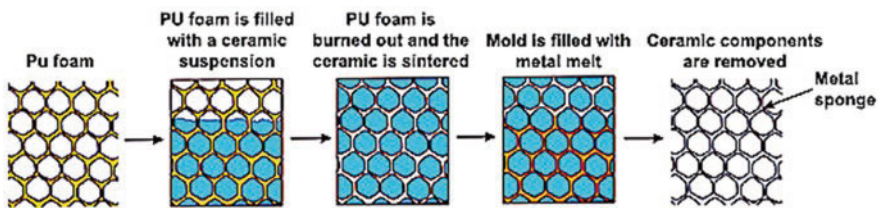


Fig. 2.3 Producing open-cell metal foams by investment casting [21]. Reprinted by permission from The Royal Society of Chemistry

manufacture metal foams with more consistent and repeatable mechanical properties. As a result of the regular pattern, it is quite easy to predict their behavior [38].

Producing open-cell metal foams with the method called supergravity infiltration is also a viable casting option (Fig. 2.4). The term “supergravity” represents the accelerations, which are much greater than gravitational acceleration ($a \gg g$), applied to the particles. In such a condition, mass and heat transfer, and reaction rates increase [39]. In supergravity infiltration method, supergravity fields are where the detrimental effect of surface tension in molten metal during infiltration can be minimized or even removed, yielding complete formation of the intended open-cell foam. The supergravity fields are generated by centrifuge effect. A mold made of plaster can be used. Increasing the gravity coefficient improves the product quality by allowing molten metal to penetrate into cavities more easily [40].

However, in this and similar methods, the metal foam can get deformed when releasing it from the mold. Using a dissolvable preform material such as NaCl is more practical. By leaching with water, the final foam can be obtained without damaging it [41].

One of the most cost-effective ways of open-cell metal foam production in liquid state is employing space holders. In this method, infiltration casting technique is used (Fig. 2.5). An essential step in this method is dissolving of the space holders in a solvent, which is water in most cases. Pearl grain sugar, saccharose [42], coarse grain salt, ultra-coarse granule sodium bicarbonate, tapioca starch [43], carbamide [44], potassium chloride [45, 46], potassium sorbate, potassium bromide [47], coarse ground calcium carbonate, magnesium sulfate can be used as space holders [9, 48–50]. To enable the molten metal to leak through the gaps; pressure, load, or vacuum may be used. The form and the volume of the porosity are generated by

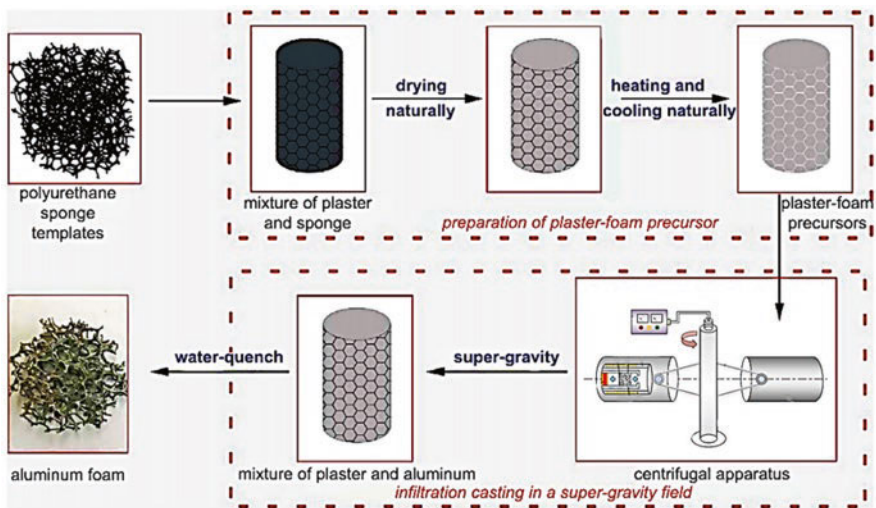


Fig. 2.4 Producing open-cell metal foams by supergravity infiltration [39, 40]. Reprinted by permission from Elsevier

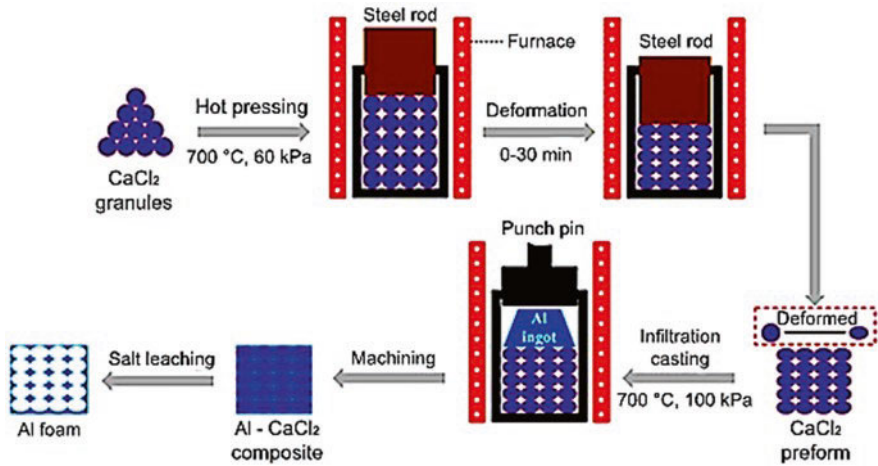


Fig. 2.5 A process for producing open-cell metal foams by using space holders [52]. Reprinted by permission from Elsevier

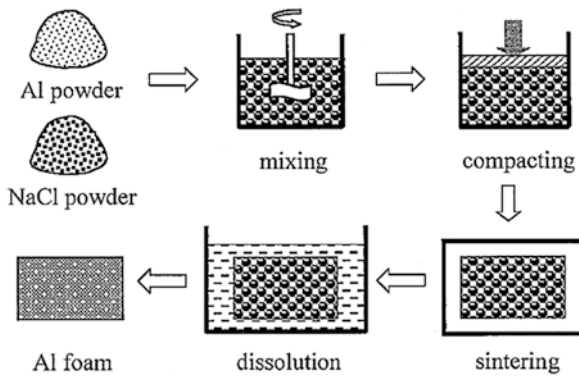


Fig. 2.6 A process for producing open-cell metal foams by using sintering and space holders [55]. Reprinted by permission from Elsevier

space holders. The contact points of the space holders provide the interconnections between the cells, which also make the removal of the space holders possible. A porosity of 65–80% can be achieved [51]. Space holders can cause corrosion, so it is critical to consider their compatibility with the metal foam material.

Solid-state processes for open-cell metal foam production include methods that combine powder metallurgy and the use of space holders (Fig. 2.6). First step is mixing the powders and space holders. The compression for the packaging process is then performed at a pressure that does not cause the space holders to break but slightly deforms them. If the space holders are polymers like cellulose, polyurethane, polyvinyl, or polystyrene [53], the compact is preheated to remove them from the structure before the sintering process, since evaporation of them at sintering

temperature can cause structural damage [52]. If dissolvable space holders are preferred, materials mentioned in infiltration casting method could be used. The total porosity in this process is between 60 and 80% [10].

Another powder-based process is the slurry method. The powder is transformed into a viscous slurry and coated on polymer reticulated sponge walls. The slurry is dried after being coated upon the sponge. At a proper temperature, the polymer is extracted and sintering is then performed to obtain a metal foam [54]. Since the structure is fragile, the operations should be carried out with caution. This process produces relatively poor metal foams, both in terms of strength and microstructure (Fig. 2.7).

In vapor deposition method, a solid pattern structure is required to define the geometry of the metal foam. As polymer patterns, reticulated polyurethane foams or lattice blocks may be used. The basic principle is that metal particles in vapor phase condense on cold surfaces of a pattern structure in a vacuum chamber. There are several techniques to evaporate metals. Physical evaporation (resistance, inductive, arc, electron beam, laser techniques) or chemical evaporation can be utilized [9, 56]. The density and the application time of the metal vapor can be used to predict the thickness of the film. It is possible to produce nickel foams effectively by applying a coating at low temperatures (above 120 °C) using nickel tetracarbonyl gas, which decomposes at these temperatures and generates nickel (the coating material) and carbon monoxide [57]. After the coating process, the substrate is carefully removed (thermally or chemically). Performed concurrently or subsequently, a high-temperature sintering treatment is a common practice, aiming densification of the connections [58]. It is possible to obtain metal foams with a very high purity and cells with diameters of 0.4–6 mm. They have a macroscopic shape (Fig. 2.8) that is somewhat similar to that of electrodeposition foams, described subsequently. Incofoam is a commercially available nickel foam made in this manner [10].

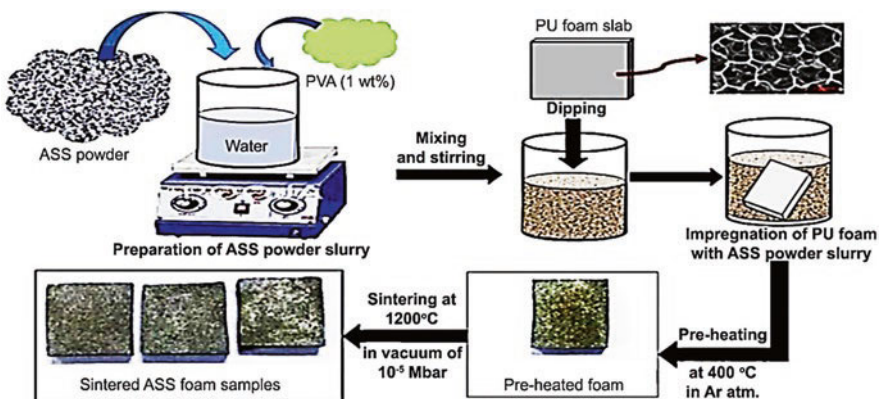
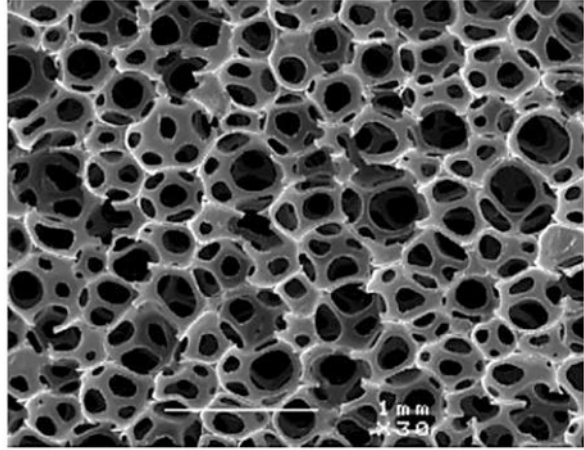


Fig. 2.7 A process to produce open-cell ASS/Austenitic Stainless Steel foams by slurry method [54]. Reprinted by permission from Elsevier

Fig. 2.8 A sample metal foam produced by vapor deposition [57]. Reprinted by permission from Wiley



Metal ions in an electrolyte solution are deposited on an open-cell polymeric foam in electrodeposition technique. The metal structure deposited replaces the polymer foam in the process. Metallic deposition methods do not work well with aluminum [9]. On the other hand, the electrodeposition method can be employed to coat an aluminum foam with copper [59]. The surface to be coated has to be conductive in order to achieve electrodeposition. Polymer pattern foams are covered in a graphite slurry or carbon black to obtain a thin conductive layer. Spraying the slurry onto the polymer pattern is another way to attain conductivity. The pattern foam acts as the cathode for the electrolyzed metal. In the electrolysis process, the metal is deposited on this cathode. As a final step, the polymer is removed from the finished product (Fig. 2.9). Generally, nickel or nickel–chromium alloys but also copper is preferred to be deposited in this way [60]. Retimet (Dunlop, UK), Celmet (Sumitomo Electric, Japan), and Recemat (SEAC, the Netherlands) are commercial foams produced by electrodeposition process [10].

Technological advances have resulted in significant improvements in additive manufacturing. Metal powders which are used in layered printing technology allow for direct printing of metal foams. Laser sintering or direct energy deposition with a powder bed may be used to produce metal foams. However, these processes are not effective in obtaining aluminum foams [62]. High reflectivity and thermal conductivity of aluminum make the operation complicated [9]. Studies have been conducted in which aluminum foams produced using laser powder bed fusion technique were compared to those produced by common methods [63]. Besides, patterns used in abovementioned open-cell foam production methods can be generated using additive manufacturing techniques. PLA, ABS, photosensitive resin, or another 3D printing material can be used.

For aluminum foams, Table 2.4 summarizes some representative properties.

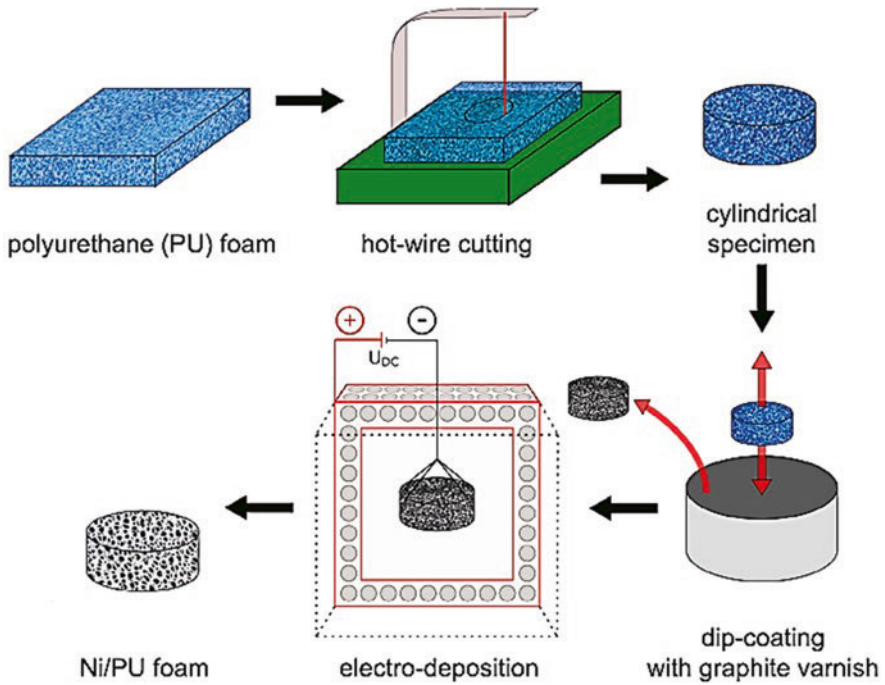


Fig. 2.9 A process for producing open-cell metal foams by electrodeposition. (This example does not include the common final step, namely, pattern removal) [61]. Under the Creative Commons license

Table 2.4 Some representative properties of Al foams [64–67]. Modified from [65] by permission from Wiley

Property		Range of Values	
Density (g/cm ³)	Relative density (%)	0.07–1	2–35
Young's modulus (modulus of elasticity) (MPa)		20–12,000	
Compressive strength (MPa)		0.04–14	
Tensile yield strength (MPa)		0.04–20	
Tensile strength (MPa)		0.05–30	
Densification strain (–) (for 0.4–0.5 g/cm ³)		0.65–0.70	
Volumetric energy absorption (MJ/m ³) (at 50% strain) (for 0.4–0.5 g/cm ³)		2.5–3.75	
Specific heat capacity (J/kg.K)		830–950	
Thermal conductivity (mW/m.K)		300–35,000	
Sound absorption coefficient (–)	open-cell	up to 0.99	
	closed-cell	up to 0.85	

2.3 Secondary Processing

Secondary operations of metal foams are of high significance since they help these materials to be applicable [68]. Thus, these processes, which turn metal foams into useful products, will be reviewed and the purpose of their use will be cited briefly.

Secondary operations of metal foams can be listed in five main groups:

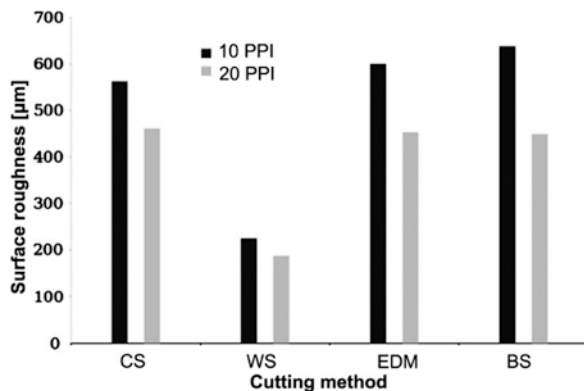
- Cutting
- Forming
- Joining
- Finishing
- Coating.

In cutting processes, it is desired that the metal foam maintains the form of its cells after the operation. The methods generally used in cutting metal foams can be given as band sawing, circular sawing, wire sawing, diamond sawing, chemical milling, EDM (electrical discharge machining), laser cutting, and water-jet cutting [67, 69–72]. While each method has some advantages, there are also some weaknesses and various difficulties. For instance, in EDM processes, it is possible to ensure that the cells do not deteriorate, but the cost and the speed of the operation should also be evaluated. As another example, if an open-cell metal foam press-fitted in a heat exchanger is considered, the wire-sawing method is more effective in reducing the macroscopic surface roughness (quality of the walls/struts regarding their distance to the cutting plane) compared to circular sawing, band sawing, and EDM (Fig. 2.10) [69].

In a study where the laser cutting method was applied on 9 mm thick closed-cell aluminum foams, some problems due to overheating were encountered. However, it was concluded that laser cutting provided burr-free and parallel-sided cutting operations without damaging the cells [71].

As to forming, foaming of powder metal precursors in a mold or press-forming during foaming of precursors was carried out [73, 74]. Metal foam sheets can also be formed after foaming, in regard to ease of application and cost. To give the

Fig. 2.10 Comparison of four cutting methods according to macroscopic surface roughness: Circular sawing (CS), wire sawing (WS), electrical discharge machining (EDM), band sawing (BS) [69]. Reprinted by permission from Elsevier



desired shape, various operations such as V-bending, roll forming, stamping, forging, and laser forming can be applied [32, 75–77]. Some forming process results for AFSs are given in Fig. 2.11.

Although bending, forging, and stamping processes are thought to deteriorate the foam structure substantially, foam core could maintain its cellular structure, if the process is applied carefully [32]. There are some potential defects that affect and limit the forming processes of foam sandwich panels. Core fracture/crack, delamination/debonding (at the core–face sheet interface), and face tearing can be listed as the most encountered ones (Fig. 2.12) [78, 79]. Joining techniques have an important role in the forming ability of metal foam sandwiches [80].

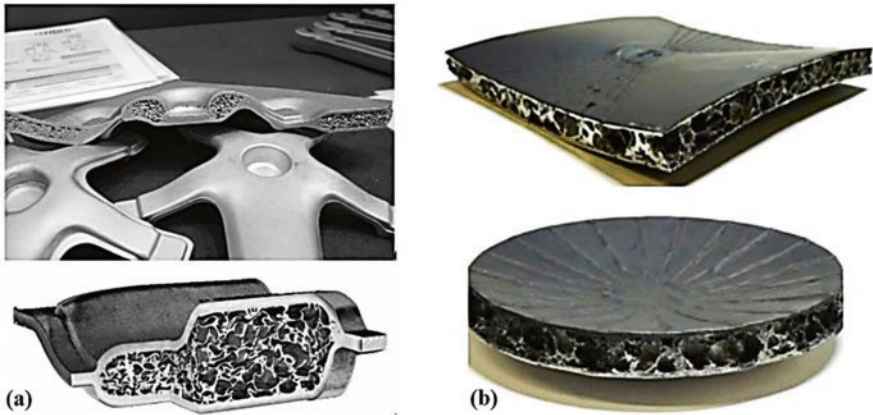


Fig. 2.11 (a) AFS materials: Forged [32] (Reprinted by permission from Wiley Online Library) and (b) Laser-formed [75]. Reprinted by permission from Elsevier

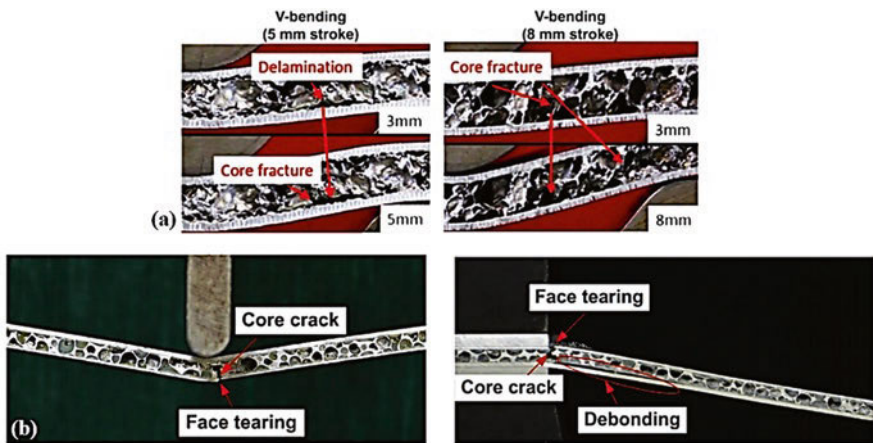


Fig. 2.12 Some AFS forming defects during: (a) V-bending [79], (b) Clamped beam bending [78]. Reprinted by permission from Elsevier

Various difficulties could be encountered when joining individual metal foams or metal foam sandwich panels. Generally, these difficulties arise from the deformation sensitivity of the foam and the limited surface area available for joining. Figure 2.13 shows the joint surface conditions for two sample joining operations.

For sandwich panels, three scenarios exist on joining: Joining two sandwich panels, joining a sandwich panel to another material, joining the face sheets with the foam core (adhesive or metallurgical joining). Joining the face sheets metallurgically with the foam core (e.g., by soldering) results in higher strengths against peeling, when compared to adhesive joining (Fig. 2.14). Some of the joining techniques (exemplified in Fig. 2.15) for metal foam structures in the literature are soldering, brazing, diffusion welding, friction stir welding, laser welding, bonding, and fastening (threaded, riveted, pinned) [78, 81–91].

There are also innovative solutions such as joining two aluminum foam sheets by using a foamable filler (aluminum-silicon alloy), which was melted and foamed by applying concentrated solar energy [93]. Another example is a fluxless soldering method for closed-cell aluminum foams using surface self-abrasion (back and forth motion of the foams in the presence of a solder alloy between them) [92]. To choose an appropriate joining method, the load condition (axial tension/compression, bending, shear, peel, cleavage, or combined) and the material in use should be known. Results of tensile shear tests under oscillating and static loads for various joining methods applied to Al foam + metal sheet structures are given in Fig. 2.16.

Although welding or similar methods seem like ideal joining techniques for sandwich structures, they involve a heat input. Heat-applying methods can cause material structure to alter. Besides, these methods and also adhesive methods necessitate rigorous preparation steps. Other processes, such as inlays, require advanced manufacturing. These drawbacks could be eliminated by mechanical joining methods described in [89, 90]. In a study [90], the best mechanical joining solutions for sandwich structures have been proposed (Fig. 2.17).

Some aluminum foam manufacturers claim that secondary operations are facilitated by manipulating the properties of the material. ALUHAB has been shown to be ideal for processes like slicing, milling, turning, and cogging since it does not

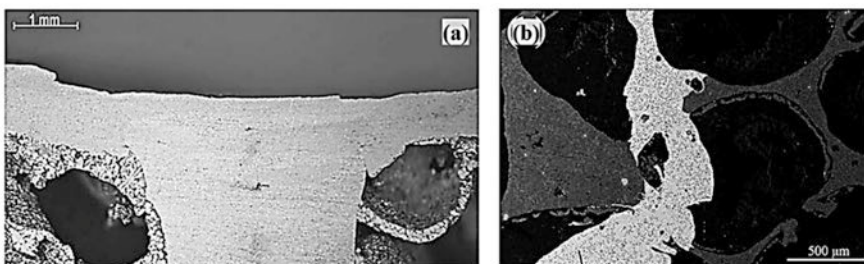


Fig. 2.13 Some joint surface conditions after: (a) Friction stir welding of two AFSs (to obtain a butt weld) (by inserting an extruded aluminum profile) [85] and (b) surface self-abrasion fluxless soldering of two closed-cell aluminum foams [92]. Reprinted by permission from Elsevier

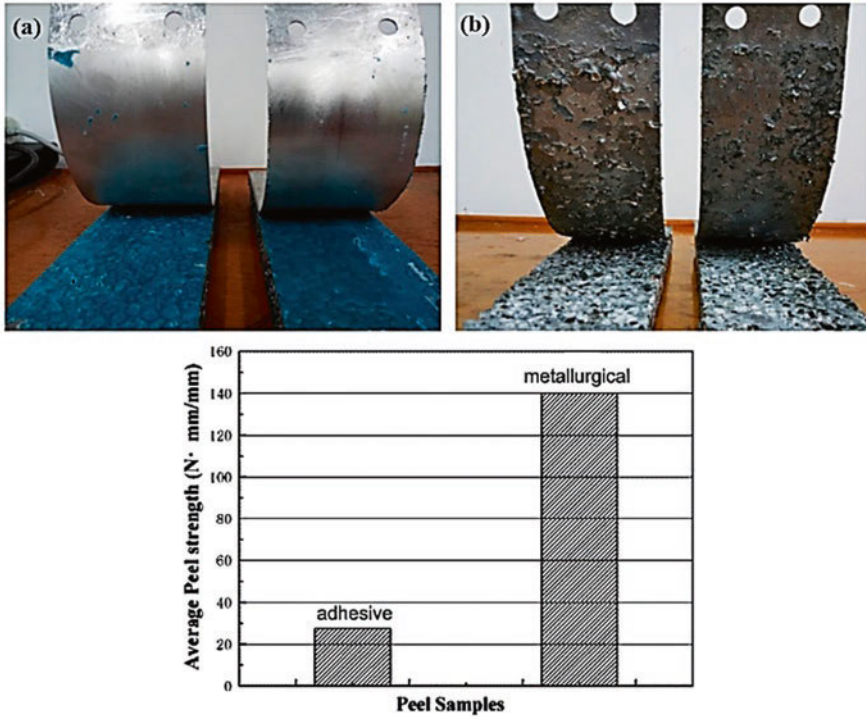
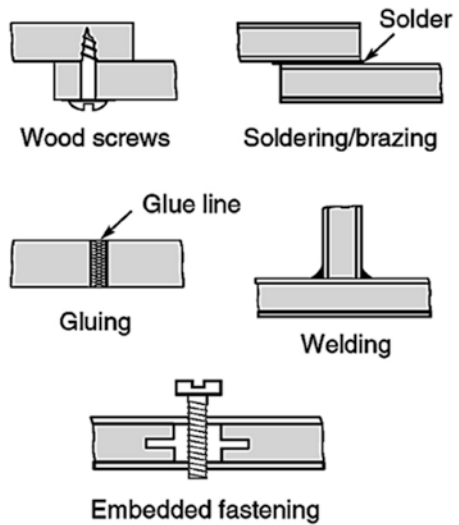


Fig. 2.14 Comparison of: (a) adhesive and (b) metallurgical joining [83]. Under the Creative Commons license

Fig. 2.15 Some methods for joining metal foam structures [67]. Reprinted by permission from Elsevier



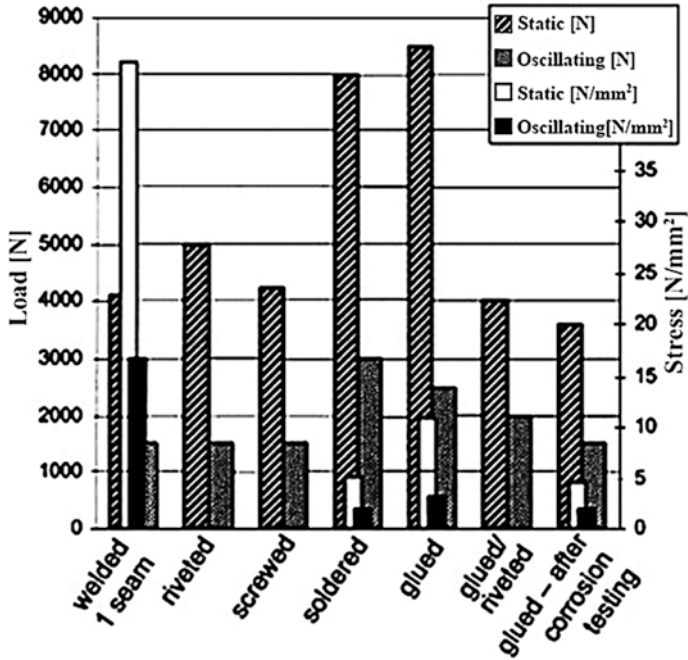


Fig. 2.16 Failure loads/stresses of Al foam + metal sheet structures for some joining methods [88]. Reprinted by permission from Wiley

disintegrate during the process. This type of metal foam is easy to drill, holds the screw steadily, and the wood screw can be driven into it without threading [94].

Burrs and other surface defects may occur as a result of the processes. These problems are a bit more complicated in metal foams. Because, when processed, negative burr formation (smearing) can be observed in metal foam structures. Surfaces with defects could cause the succeeding processes such as joining or coating to be unsuccessful. Edge quality is also an important property for product functionality, safety, price, and appearance. Increased or changed friction, increased wear on moving or stressed parts, interferences in assemblies, turbulent flow, and reduced formability are just a few of the issues which can be caused by poorly finished edges.

Generated burrs could get embedded into the cells of metal foam products, which would make it difficult to remove them. Therefore, achieving a surface with minimum burr formation is of high significance when machining metal foams. In this context, ultrasonic milling has been proposed to be an alternative to conventional milling, in a study [95] where ALUHAB specimens (a closed-cell aluminum foam, mentioned previously) were machined (Fig. 2.18).

Corrosion occurrence on metal foams may induce functionality losses. In some cases, electrical isolation or even aesthetic improvements may also be requested. For such reasons, metal foams may need to be coated with various materials and

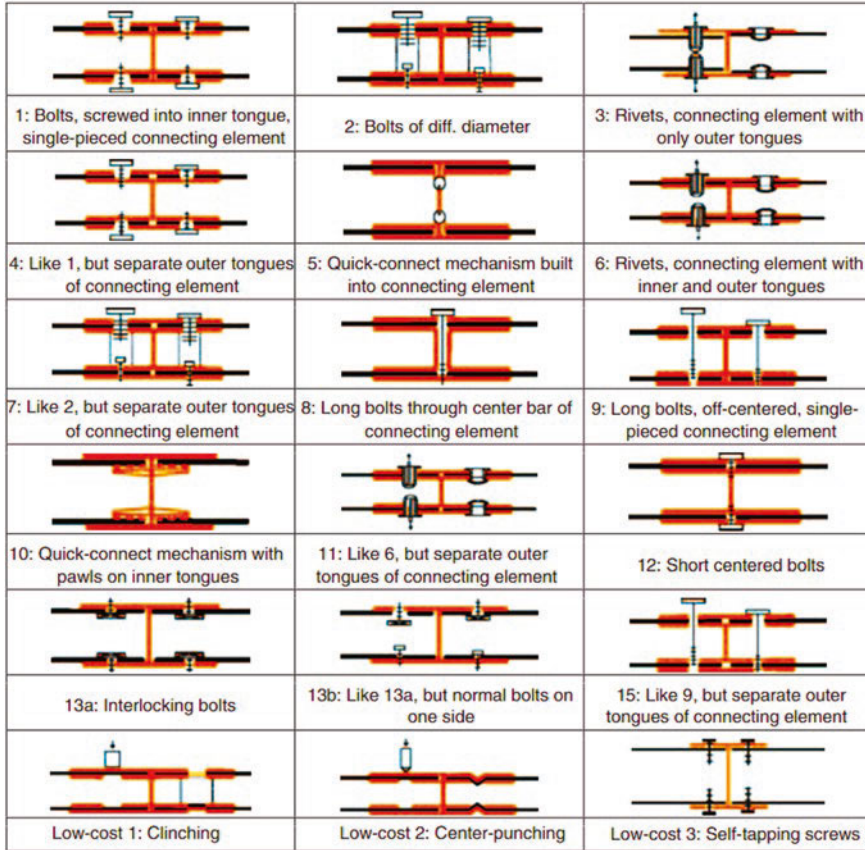


Fig. 2.17 The configurations proposed as the best ways for mechanical joining of sandwiches [90]. Reprinted by permission from SAGE

methods. The effect of coating on mechanical properties of metal foams was also investigated. For this purpose, closed-cell aluminum foam sheets were coated with various porcelain enamel coating systems and 4-point bending tests, also indentation tests were performed. The results indicated that the enamel coating strongly affected the Young's modulus of elasticity of the foam sheets and enhance the stiffness of them. Bending tests showed that the cracks on the samples initiated at the points where the coating was thinner (Fig. 2.19) [96].

Besides vitreous enamel coating mentioned previously, which provides resistance to both corrosive and thermal effects, an acrylic cathaphoretic deposited paint, which has the ability to achieve a protective and homogeneous paint layer even with complex geometries, is also a viable option for metal foams. In a study, both these coatings prevented deterioration after an exposure of 850 h in accelerated corrosion tests. As to the uncoated samples, corrosion products were encountered after about

Fig. 2.18 Macroscopic comparison of conventional and ultrasonic milling in terms of smearing [95]. Reprinted by permission from Elsevier

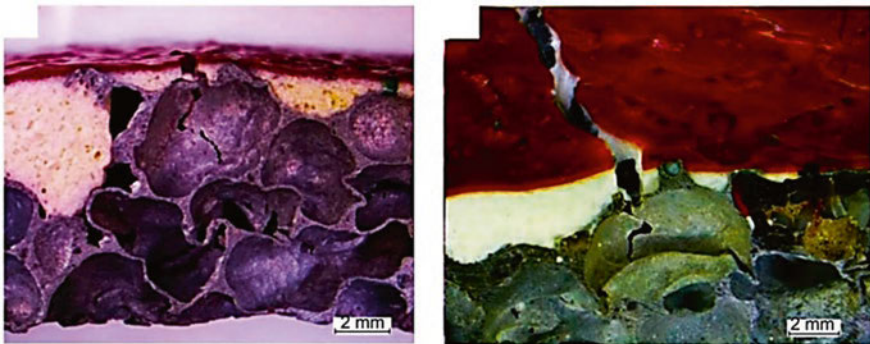
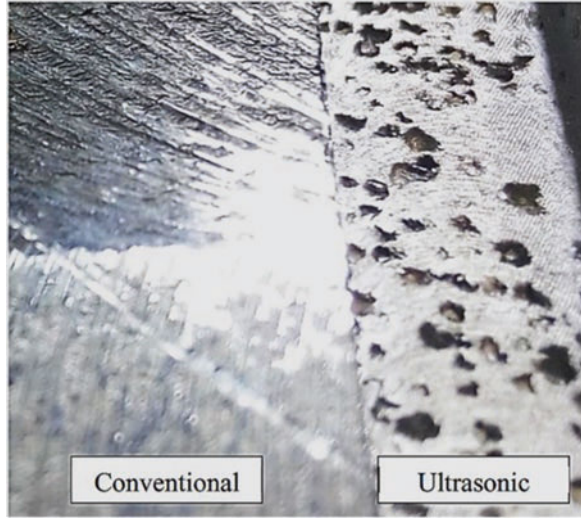


Fig. 2.19 Crack initiations on enamel coated closed-cell aluminum foams [96]. Reprinted by permission from Taylor & Francis

360 h. In the light of the findings, it is possible to conclude that both of the examined layers are ideal for protecting the aluminum foam [97].

2.4 Aircraft Applications

The use of aluminum foam material in the aircraft industry can bring along more efficient exploitation of material and energy resources, as well as the economic benefits of light weighting. Traditional parts such as stamped steel can be replaced with alternative parts generated using aluminum foam. These changes will serve the goal of lower fuel consumption, which is the priority of the aircraft [98]. For

instance, every 1 kg of weight reduction in the fuselage provides a reduction of approximately one million Euros in 25 years in terms of fuel costs. This gain will increase as fossil fuel prices rise [50]. The use of aluminum, which was 81% by weight in the Boeing 747, decreased to 20% in the Boeing 787. The proportion of composites, on the other hand, has reached 50% [99].

In this context, sandwich composite structures, which can be shaped in three dimensions and contain metal foam core, can also fulfill the requirements of light weighting and safety [100]. Nowadays, besides aluminum honeycomb sandwich structures and aluminum + FRP/fiber-reinforced plastic structures in laminated form, AFS structures have also started to be used as flooring elements or interior fixture elements in aircrafts [1]. In addition, sandwich structures containing titanium foam and sandwich structures containing aluminum foam have been used by Boeing in the tail booms of aircrafts and helicopters [6].

Duocel foams, open-cell metal foams produced by ERG Aerospace Corporation, have some commercial implementations in aircraft industry. “Breather plugs” (used in Lockheed Martin C-130 Hercules military transport aircraft) for equalization of pressure during rapid changes in altitude and “air/oil separators” (used in Rolls Royce Trent 1000 turbofan engine of Boeing 787) for utilization in engine gear-boxes are two examples (Fig. 2.20) [101].

Multifunctional materials are economically advantageous. This advantage can reach the highest values in the aerospace applications [50]. In this context, sandwich structures, which contain metal foam and stand out with their low densities, not only meet mechanical requirements such as specific strength and energy absorption, but also have functions such as absorbing the vibration/sound and insulating heat, which are generated by the turbines. Their life-cycle costs are low; also recycling is possible for these materials [102]. It can be said that the long and costly validation of new materials and the current popularity of fiber-reinforced composites have slowed the spread of metal foam-containing materials in this industry [50].

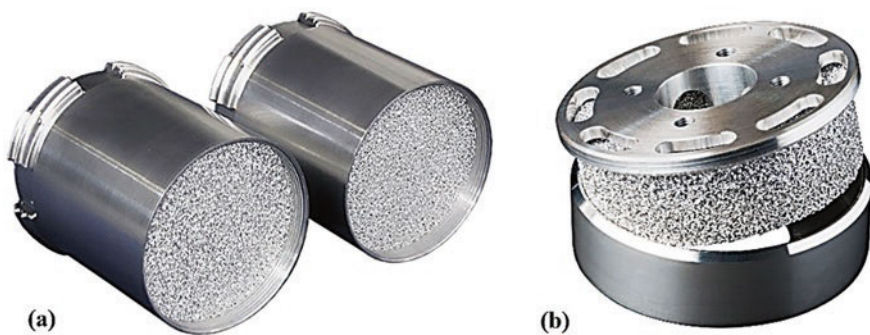


Fig. 2.20 Some commercial applications of Duocel (an open-cell metal foam) in aircraft industry: (a) In breather plugs and (b) in air/oil separators [101]. Reprinted by permission from ERG Aerospace Corporation

The performance of AFS materials in mechanical energy absorption is remarkable due to the characteristic behavior of the aluminum foam material used in the core. While the aluminum foam material performing mechanical absorption, it operates at an almost constant stress value (plateau stress) during the large deformation experienced until it reaches its densification point. This feature makes it an effective material against crash and blast [102].

Where AFS materials can be used in the aerospace industry can be listed as follows: Luggage containers, premixed combustion chambers (as sound absorbers), heat sinks of electronic devices, aircraft elevators bringing aircrafts from the hangar to the takeoff area in aircraft carriers (as a structural element) [103], floor and drop ceilings, cargo pallets, passenger seat pallets [104]. In AFS panels, the face sheets and the core can be joined using adhesives or metallurgical bonding. For AFSs, using adhesives may be disadvantageous due to the maximum temperature resistance of approx. 220 °C, thermal expansion, moisture absorption, and low elasticity modulus [7].

In military aviation applications, aluminum foams (especially closed cell) can provide considerable improvements in the performance of some equipment. Examples are aircraft carrier deck, bulletproof composite armor, airborne buffer table, and lightweight missile manhole cover. When an AFS structure is employed as flight deck in an aircraft carrier (Fig. 2.21a), the rebound effect which occurs in aircraft landing is reduced by more than 50%. This secures a smooth glide and makes it possible that the tailhook of the aircraft engages the cable of the arresting gear system (located on the aircraft carrier) and the aircraft is arrested. It would also enhance the blast resistance and antimissile combat capability. AFSs can also be employed together with aluminum foam-filled columns, as shown in Fig. 2.21b. In heavy equipment airdrop missions, the equipment attached to a parachute is expected to land safely. Russian airborne equipment of 20 tons can be dropped in a smooth and safe manner by using a parachute and a buffer table involving aluminum foam-filled columns of 500 mm height [105].

Studies have been carried out on metal foam materials to absorb vibration and sound in aircraft. An active vibration control system has been introduced for an aerobatic aircraft wing using closed-cell aluminum foam structures in a study. They carried out both numerical and experimental tests building a scaled model (Fig. 2.22).

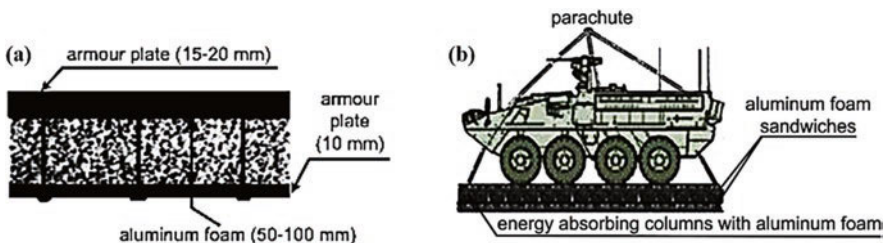


Fig. 2.21 Military applications: (a) Flight deck of an aircraft carrier and (b) buffer table for airborne equipment [105]. Under the Creative Commons license

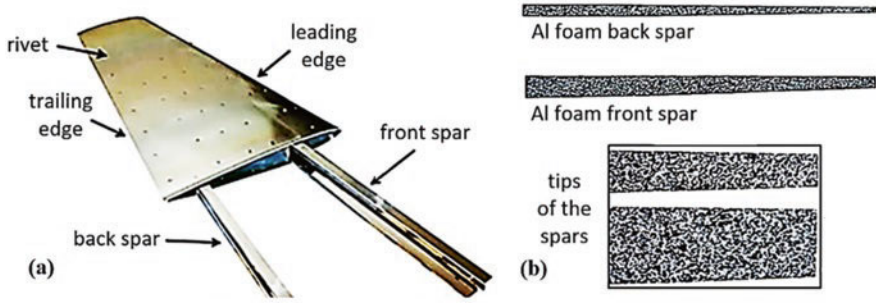


Fig. 2.22 (a) Wing elements and (b) Al foam as substitute material for spars [106]. Under the Creative Commons license

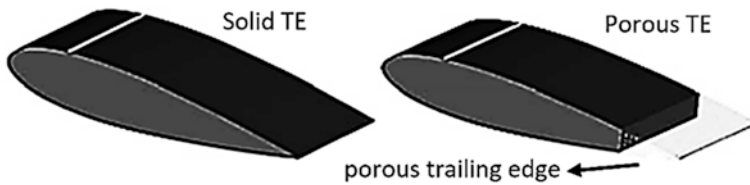


Fig. 2.23 Porous trailing edge (TE) concept [109]. Reprinted by permission from Cambridge University Press

The total wing was modeled virtually, including a velocity feedback control system. Two different materials were employed (glass fiber-reinforced epoxy and aluminum foam) as wing spars and compared with respect to the effectiveness of the controller. The use of aluminum foam for the wing's spars decreased the wing's settling time by 83% [106].

The sound transmission loss characteristics of sandwich aircraft panels were examined in another research. They compared the performances of commonly used aerospace cores such as honeycomb, triangular, closed-cell aluminum foam, and Rohacell foam (a commercial PMI/PolyMethacrylimide based closed-cell foam) with various (aluminum, titanium, and epoxy carbon laminate) face sheets. It was stated that a desirable sound transmission loss level can be achieved by varying the density of foam and the type of face sheets [107].

Acoustic absorptive materials, withstanding high temperatures, were aimed to be developed in a study in order to reduce internal noise caused by turbo engines. As a result, two types of metallic materials were suggested: Open-cell metal foams and metallic fiber materials. It was determined that for open-cell foam, high porosity results in more space for sound waves to pass through the material, therefore, inducing less reflection and more absorption [108].

The use of open-cell foam materials as a means of reducing turbulent boundary-layer trailing edge noise has been suggested too (Fig. 2.23). The researchers studied the aeroacoustics of a porous trailing edge made of Ni–Cr–Al open-cell metal foam. A NACA 0018 airfoil was examined numerically with three different configurations

of trailing edges: A baseline solid trailing edge, a completely porous trailing edge, and a blocked-porous version. They discovered two noise reduction mechanisms on a trailing edge of open-cell metal foam, allowing to improve the noise reduction capability even further [109]. Open-cell metal foams have also been used to control the flow and related aerodynamic noise in various other applications. They greatly decreased the aerodynamic noise produced by airfoils, tubes, aeroengines, and axial/centrifugal fans in experimental studies [110].

In aircrafts, metal foams can also be used against the effects of collisions with foreign objects. There is always a risk of a soft body impact (such as rubber) or a hard body impact (such as runway debris) in consequence of these collisions. Since the materials used on the exterior surfaces of aircrafts can vary depending on the area of use, different materials from metal to glass are studied in the researches about collisions with foreign objects [111]. In this context, especially for bird strikes, the aerospace industry has exploited cellular materials like metallic/organic foams and hollow sphere assemblies [112].

Due to their potential for severe damage and accidents, collisions between birds and an aircraft pose a significant threat to aviation, both in safety and cost issues. Average bird strike rates in civil aviation are given in Table 2.5. Large front components like the radome and nose, the leading edges, and the engines are being the target of the majority of bird strikes. Since 1960, 23 of the 30 accidents involving hull losses and casualties have occurred as a result of one or more engines struck by birds. An average of 101 h aircraft downtime per strike has been reported in the United States. Table 2.6 shows the reported repair and indirect costs arising from bird strikes in the United States from 1990 to 2018 [113].

Between 1990 and April 2021, the US Air Force recorded 244,341 bird/wildlife strikes on aircraft around the world, with a total cost of \$779,892,099 for civilian and military aircraft [114]. The majority of bird strikes occurred while the aircrafts are takingoff or landing. To develop structures resisting these impacts, studies where the leading edges and leading edge flaps of the wings have been strengthened with closed-cell aluminum foam have been conducted (Fig. 2.24) [115]. In general, although the proportion of fiber-reinforced composites in aircraft fuselage construction has increased nowadays, metallic materials are still used in areas exposed to strikes by foreign objects [116].

Table 2.5 Average rate of bird strikes per 10,000 aircraft movements for some countries [113]. Under the Creative Commons license

Country	Bird Strike Rate	Period
Australia	7.76	2008–2017
Canada	3.51	2008–2018
France	3.95	2004–2013
Germany	4.42	2010–2018
UK	7.76 (all) 4.62 (confirmed)	2012–2016
USA	2.83	2009–2018

Table 2.6 Bird/wildlife strike induced costs in the United States (1990–2018) [113]. Under the Creative Commons license

Cost Type	Total/Average	Reported Cost (US \$)
Repair costs	total	4.6 M
	average	158,573
Indirect costs	total	726,044
	average	25,036
Total costs	total	5.3 M
	average	183,609

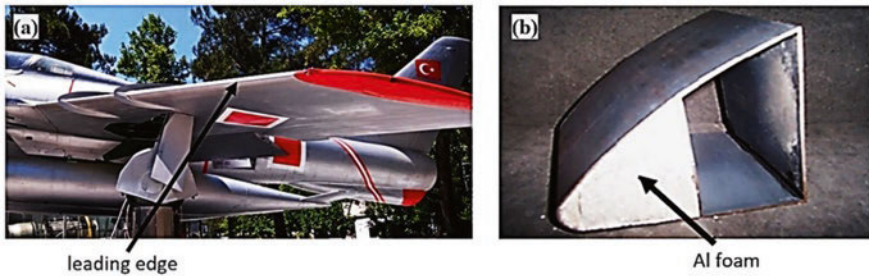


Fig. 2.24 (a) Leading edge and (b) an Al-foam-filled leading edge [117]. Reprinted by permission from Elsevier



Fig. 2.25 Wildlife strike to an aircraft, damaging its radome and leading edges [119, 120]. Courtesy of The Aviation Herald

An aircraft damaged from its radome shield is shown in Fig. 2.25. Although the radome shield was made of a honeycomb structure, it did not provide sufficient protection. In a study using AFS panels, experimental (by using real birds) and numerical investigations have been performed in order to determine the behavior of AFS panels against bird strike. The motivation of the study was that this type of a structure could be used to protect the radome bulkhead section from bird penetration into the cockpit. They tried various core (AlSi7Mg0.5 foam) thicknesses, core densities, and impact velocities (140–190 m/s) in order to compare the amount of penetration (Fig. 2.26) [111]. In another study, a gas gun was used to generate the impact of a bird strike [118].

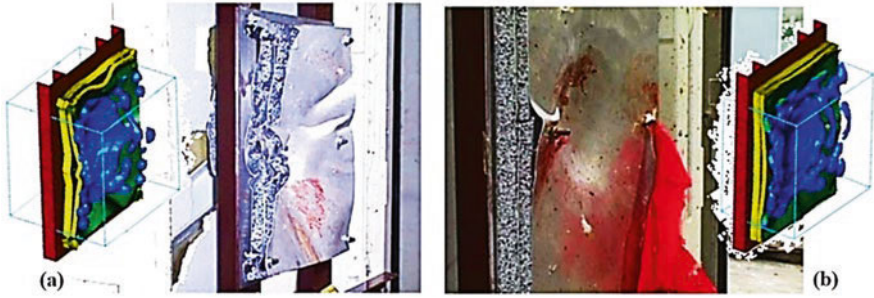


Fig. 2.26 Deformed states of sandwich panels after bird strike simulations (both experimental and numerical) for: (a) 0.15 g/cm^3 , (b) 0.3 g/cm^3 core densities [111]. Reprinted by permission from Elsevier

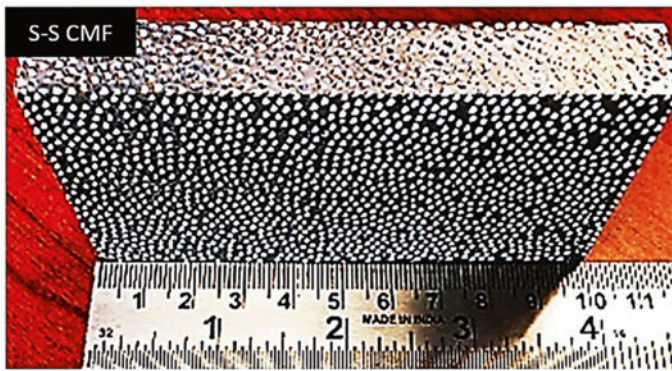


Fig. 2.27 An image of an epoxy-infused S-S CMF composite developed [122]. Reprinted by permission from Elsevier

Besides bird strikes, weather conditions can pose a threat to the safety of an aircraft. For instance, even a short transition from a hail zone can cause deteriorations such as depression, cracks, and holes. Therefore, important elements such as leading edge, radome, and engine can be damaged. In a numerical study, the mechanical performances of eight different sandwich structures were analyzed in a way that they were exposed to hail effect at different velocities. The core parts of sandwich structures consisted of different designs such as corrugated metal sheet, pyramidal lattice, and metal foam. As a result, the best design in terms of energy absorption has been the aluminum foam reinforced tetrahedral core [121].

A composite material comprising a stainless steel open-cell metal foam (S-S CMF) infused with a hydrophobic epoxy resin (Fig. 2.27) was introduced in a study. A vacuum-assisted thermal infusion process was employed. S-S CMF was produced using a powder metallurgy technique and infused thereafter. The final product was used as the leading edge of aircraft wings. The aim was to protect the edges from three-dimensional disturbances due to insect adhesion, ice accretion, and



Fig. 2.28 (a) A metal foam sandwich panel (17-4 PH stainless steel foam core + 17-4 PH face sheets). (b) The engine fan model where the sandwich panel was used and numerically analyzed [123]. Reprinted by permission from SAGE

particle wear. This, in turn, would improve performance, safety, and fuel efficiency, with an overall product density similar to that of aluminum [122].

Another composite material involving a nonaluminum metal foam, but this time in sandwich form, was designed and produced to be used in aircrafts by a research group. It was obtained by a 17-4 PH/Precipitation-Hardened stainless steel open-cell foam (having high strength and high toughness) and two face sheets of the same material in dense form (Fig. 2.28). This composite structure was employed as an engine fan blade and compared to a solid titanium blade, with respect to vibration characteristics and design requirements. In the study, skin thickness and core volume were varied. The vibration analysis revealed that substantial weight/cost savings can be achieved without having unacceptable resonant frequencies. This innovative design exhibited a competitive performance while having a significantly lower cost and lightweight [123].

As a different sort of exploitation, open-cell metal foams have been employed to generate electricity (micro-energy harvesting) from the surroundings of an aircraft. Based upon this idea, harvesting of thermal fluctuations in the fuselage during a flight and their transformation into electricity (by using thermoelectric effect) was modeled and simulated numerically, and reported by a researcher. The model involved a thermoelectric generator (TEG) and (as a heat reservoir) a phase change material (PCM) combined with each other, aiming to boost electricity generation. It was concluded that open-cell metallic foam inside the PCM enhanced the effective conductivity, allowed larger volumes of heat storage units, and increased the heat transfer between the TEG and PCM; thus, increased the electric power generation [124, 125].

2.5 Spacecraft Applications

Besides their multi-functionality, also the high temperatures and stresses in aerospace applications make metal foams feasible materials in spacecraft industry. Existing utilizations of the cylindrical shells involving metal foams in missile/spacecraft hulls, storage tanks, and nuclear reactor shells indicate the potential of

these materials. There are many researches on buckling and vibration of these shell structures [4]. Metal foams are suitable to be used for mechanical energy absorbing in space vehicle landing pads and for reinforcement of load-bearing structures in satellites [10]. Moreover, metal foams could be employed in high-temperature applications such as transpiration-cooled rocket nozzles, heat shielding for exhaust [108], heat sinks, filtration, and PEM/proton-exchange membrane fuel cells [126]. Metal foams could play a greater role in the design of spacecrafts in the future [3].

For spacecrafts and satellites, there is always a collision risk with hypervelocity space debris and meteoroids. Critical components have to be protected against these impacts by using appropriate structures, without causing substantial increase in weight. In this context, hypervelocity impact tests of open-cell Al foams were performed in various studies, being supported by NASA and ESA [127].

When compared to metallic honeycombs, metal foams are competitive in mechanical performance and advantageous by not having channeling cells (which are impairing MMOD/micro-meteoroids and orbital debris shielding) [128]. The gas trapped in the porosities of a closed-cell foam could expand and burst the cell walls due to the changing ambient pressure in high amounts, during the spacecraft launch. These deformations could bring about unexpected results. Therefore, open-cell foams are better suited to the spacecraft components [127].

A modified version for the representative shielding element (against MMOD) of the ISS/International Space Station was developed employing an open-cell foam instead of honeycomb structure in a study. Total weight was kept equal with the original structure. The ballistic limit equation, which was derived by using the data from the hypervelocity impact tests conducted by the researchers, resulted that for 3 km/s, the critical projectile diameter increased by 15%. The performance gain was predicted to be higher with the increase in impact obliquity [129].

NASA published an article evaluating the shielding performance of sandwich panel configurations having open-cell aluminum foam core(s), comparing them with alternative sandwich panel configurations (aluminum honeycomb core, Trussgrid 3D aluminum honeycomb core, nonmetallic honeycomb core) (Fig. 2.29). The effects of foam parameters, core thickness, and face sheet thickness were examined, too. Also, a ballistic limit equation was developed for the foam core sandwich panels. According to this equation, at both normal and oblique strikes, the foam core panel resulted in a superior performance with respect to the honeycomb core panel [128].

The effect of elevated temperatures on the penetration behavior of AFSs was evaluated in a numerical study. The developed model was validated with experiments and could be employed in aerospace structural designs. Numerical results showed that when increasing the temperature from room temperature to 300 °C, the decreases in energy absorption and peak force were 29.9% and 31.8%, respectively. Another result was that the decreases in these characteristics were linear when the numerical tests were carried out in various temperatures by increasing the temperature 100 °C each time [126].

Utilizing metal foam core sandwich panels, Pohltec Metalfoam manufactured a prototype of a conical adapter for the Ariane rocket. This prototype, having a

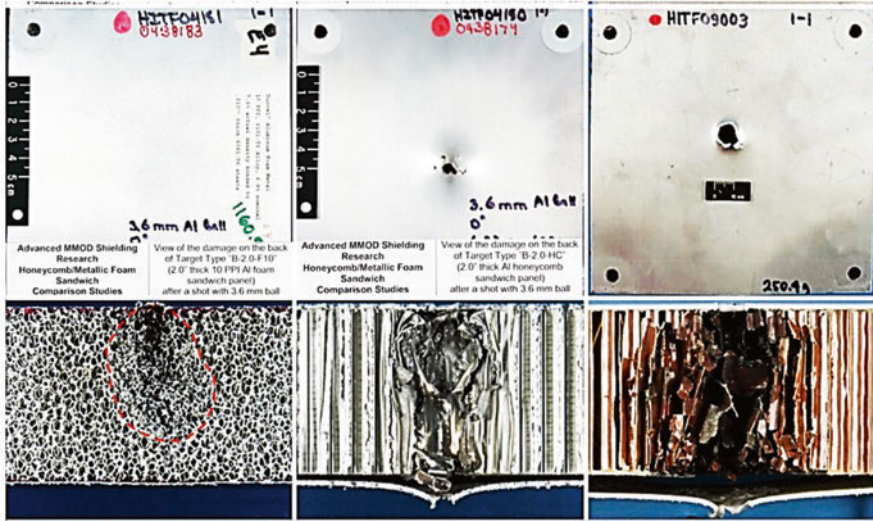


Fig. 2.29 The deformed states of three sandwich panel configurations, having a 2.0" total thickness, after an impact of a 3.6 mm diameter projectile at ~ 6.8 km/s with 0° : With an open-cell Al foam core (40 pores per inches), with an Al honeycomb core, with a nonmetallic honeycomb core, respectively from left to right. (The upper images show the rear face sheet deformation) [128]. Courtesy of NASA

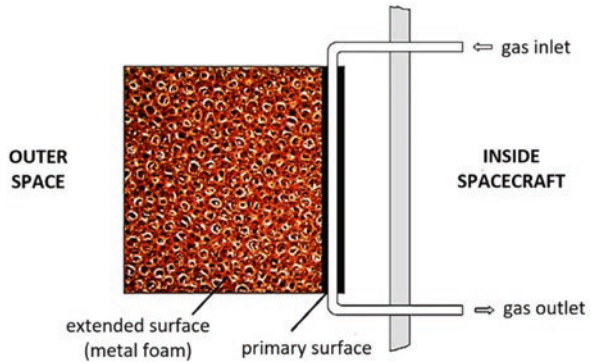
diameter bigger than 4 m and including welded and curved AFS panels, exhibited an exceptional performance because of the good vibration damping property of AFS panels [130].

Ensuring an efficient heat dissipation in spacecrafts and space-based equipments (e.g., lunar probes) is a challenging issue. Heat sinks such as space radiators and water sublimators are employed for this task. Open-cell aluminum foam is an ideal solution for this type of applications [131].

An open-cell Al foam (Duocel) heat exchanger produced by ERG Aerospace Corporation has been used both for heat exchanging and air filtration in a space shuttle and ISS. Filtration was achieved by granulated chemicals supported by the Al foam so as to absorb and remove CO_2 and moisture. The system rotates periodically to emit the CO_2 and the moisture into space, therefore, functions without stopping servicing a long time. Duocel have also been utilized to provide heating and cooling uniformly in satellite cryogenic tanks, as well as isothermalization and baffling in solid cryogenic coolers of space-based infrared optical devices [50].

Radiation heat transfer is dominant in cooling of the systems located in spacecrafts. Passive cryogenic radiators having extended heat transfer surfaces are suitable for this condition. High porosity open-cell metal foam, possessing a low density and high surface area density, could be an alternative material (Fig. 2.30) to be used as a passive cryogenic radiator [132]. Interactive surface area for radiation is higher in open-cell metal foams, due to their high porosity. Heat transfer performances of a copper and an aluminum open-cell foam, each having a pore density of 20 PPI/

Fig. 2.30 The concept of a radiative cooling system was designed and tested in a study [132]. Reprinted by permission from Taylor & Francis



Pores per Inch (with corresponding porosities of 94.9% and 90.3%, respectively) and intended to be used as passive cryogenic radiators, have been evaluated in a study. As a common practice, performance characteristic was taken as surface area/cooling capacity. According to the experimental and theoretical results, the aluminum foam was found to be more successful than the copper foam in cooling [133]. In a theoretical study, radiative cooling performance of aluminum foam fins (with a 20 PPI pore density and a 90% porosity) was concluded to be ten times higher, when compared to that of solid aluminum fins [134].

Gamma-ray shielding in spacecrafts and satellites could be another application for metal foams. Open-cell metal foams have been proposed to be used instead of perforated beam screens, employed in high synchrotron radiation particle accelerators of the CERN Large Hydrogen Collider [135].

References

1. Gokhale, A. A., Prasad, E., & Basu, B. (2019). *Light weighting for defense, aerospace, and transportation*. Springer Nature.
2. Council, N. R. (2012). *Application of lightweighting technology to military aircraft, vessels, and vehicles*. National Academies Press.
3. Thoma, K., Schäfer, F., Hiermaier, S., & Schneider, E. (2004). An approach to achieve progress in spacecraft shielding. *Advances in Space Research*, 34(5), 1063–1075.
4. Toan Thang, P., Nguyen-Thoi, T., & Lee, J. (2020). Mechanical stability of metal foam cylindrical shells with various porosity distributions. *Mechanics of Advanced Materials and Structures*, 27(4), 295–303.
5. Selivanov, V. V., Silnikov, M. V., Markov, V. A., Popov, Y. V., & Pusev, V. I. (2021). Using highly porous aluminum alloys and honeycomb structures in spacecraft landing gear. *Acta Astronautica*, 180, 105–109.
6. Rajak, D. K., & Gupta, M. (2020). *An insight into metal based foams: Processing, properties and applications*. Springer.
7. Ubertalli, G., Ferraris, M., & Bangash, M. K. (2017). Joining of AL-6016 to Al-foam using Zn-based joining materials. *Composites Part A: Applied Science and Manufacturing*, 96, 122–128.

8. Wan, T., Liu, Y., Zhou, C., Chen, X., & Li, Y. (2021). Fabrication, properties, and applications of open-cell aluminum foams: A review. *Journal of Materials Science and Technology*, 62, 11–24.
9. Aluminium Foam. (2021). Retrieved from <http://www.alupam.com/>.
10. Banhart, J. (2001). Manufacture, characterisation and application of cellular metals and metal foams. *Progress in Materials Science*, 46(6), 559–632.
11. Banhart, J. (2000). Manufacturing routes for metallic foams. *The Journal of The Minerals, Metals & Materials Society*, 52, 22–27.
12. Szlancsik, A., Katona, B., Kemény, A., & Károly, D. (2019). On the filler materials of metal matrix syntactic foams. *Materials*, 12(12).
13. Atalay, S., Bayri, N., Kaya, H., İzgi, T., & Kolat, V. S. (2018). Al-Si-Mg foam produced by 3D printer. *Adıyaman University Journal of Science*, 8(1), 13–23.
14. Banhart, J., Stanzick, H., Helfen, L., & Baumbach, T. (2001). Metal foam evolution studied by synchrotron radiography. *Applied Physics Letters*, 78(8), 1152–1154.
15. Babcsán, N., Banhart, J., & Leitmeier, D. (2003). Metal foams—Manufacture and physics of foaming. In *Advanced metallic materials 2003: Proceedings of the international conference*. Bratislava: Institute of Materials & Machine Mechanics Slovak Academy of Science.
16. Banhart, J. (2006). Metal foams: Production and stability. *Advanced Engineering Materials*, 8(9), 781–794.
17. Avinash, G., Harika, V., Sandeepika, C., Kumar, R., & Gupta, N. (2019). Porosity control in aluminium foams using different additives. *Materials Today: Proceedings*, 18, 1054–1057.
18. Rack, A., Helwig, H. M., Büttow, A., Rueda, A., Matijašević-Lux, B., Helfen, L., ... Banhart, J. (2009). Early pore formation in aluminium foams studied by synchrotron-based microtomography and 3-D image analysis. *Acta Materialia*, 57(16), 4809–4821.
19. Banhart, J. (2000). Metallic foams: Challenges and opportunities. In *Eurofoam2000* (pp. 13–20). MIT-Verlag Bremen.
20. Kevorkijan, V. (2010). Low cost aluminium foams made by CaCO₃ particulates. *Association of Metallurgical Engineers of Serbia AMES*, 16(3), 205–219.
21. Kränzlin, N., & Niederberger, M. (2015). Controlled fabrication of porous metals from the nanometer to the macroscopic scale. *Materials Horizons*, 2(4), 359–377.
22. Uzun, A., & Turker, M. (2015). The effect Of B₄C addition on pore morphology of the AlSi7 foams. *Journal of the Faculty of Engineering and Architecture of Gazi University*, 30(3), 523–532.
23. Soloki, A., & Esmailian, M. (2015). Carbonate-foaming agents in aluminum foams: Advantages and perspectives. *Metallurgical and Materials Transactions B: Process Metallurgy and Materials Processing Science*, 46(2), 1052–1057.
24. Kennedy, A. R. (2002). Effect of compaction density on foamability of Al-TiH₂ powder compacts. *Powder Metallurgy*, 45(1), 75–79.
25. Ramirez, A. M. M., Vintila, R. R., & Drew, R. A. L. (2019). Morphology of aluminum alloy foams produced with dolomite via partial sintering of precursors. *Materials*, 12(10).
26. Asavavisithchai, S., & Kennedy, A. R. (2006). The effect of compaction method on the expansion and stability of aluminium foams. *Advanced Engineering Materials*, 8(9), 810–815.
27. Ensarioğlu, C., & Çakır, M. C. (2015). Investigating the Influence of Alloying Elements on the Foamability and the Morphology of Aluminum Foams. In *The Advances in Materials and Processing Technologies (AMPT 2015)*. Madrid, Spain.
28. Gergely, V., Degischer, H. P., & Clyne, T. W. (2000). Recycling of MMCs and production of metallic foams. *Comprehensive Composite Materials*, 3, 797–820.
29. Matijasevic, B., & Banhart, J. (2006). Improvement of aluminium foam technology by tailoring of blowing agent. *Scripta Materialia*, 54(4 SPEC. ISS), 503–508.
30. Ensarioğlu, C. (2014). *Alüminyum Köpük Malzemelerin Toz Metalürjisi Yöntemi ile Üretiminde Üretim Parametrelerinin Malzemenin İşlenebilirliği Üzerindeki Etkilerinin İncelenmesi*. Bursa Uludağ University.

31. Koerner, C. (2008). *Integral foam molding of light metals: Technology, foam physics and foam simulation*. Springer.
32. Banhart, J., & Seeliger, H. W. (2008). Aluminium foam sandwich panels: Manufacture, metallurgy and applications. *Advanced Engineering Materials*, 10(9), 793–802.
33. Banhart, J. (2003). Aluminum foams: On the road to real applications. *MRS Bulletin*, 28(4), 290–295.
34. Shi, Z. L., & Szpunar, J. A. (2018). The introduction of thin open-cell metal foams and their wider engineering applications. *Materials Science Forum*, 933, 112–122.
35. Lefebvre, L. P., Banhart, J., & Dunand, D. C. (2008). Porous metals and metallic foams: Current status and recent developments. *Advanced Engineering Materials*, 10(9), 775–787.
36. Yamada, Y., Shimojima, K., Sakaguchi, Y., Mabuchi, M., Nakamura, M., Asahina, T., ... Higashi, K. (1999). Processing of an open-cellular AZ91 magnesium alloy with a low density of 0.05 g/cm³. *Journal of Materials Science Letters*, 18, 1477–1480.
37. Fischer, S. F., Schüler, P., Fleck, C., & Bührig-Polaczek, A. (2013). Influence of the casting and mould temperatures on the (micro)structure and compression behaviour of investment-cast open-pore aluminium foams. *Acta Materialia*, 61(14), 5152–5161.
38. Carneiro, V. H., Rawson, S. D., Puga, H., Meireles, J., & Withers, P. J. (2020). Additive manufacturing assisted investment casting: A low-cost method to fabricate periodic metallic cellular lattices. *Additive Manufacturing*, 33.
39. Wen, X., Bao, Q., Guo, L., & Guo, Z. (2021). The introduction of super-gravity into optimization separation of bismuth and zinc from crude bismuth melt. *Chemical Engineering and Processing—Process Intensification*, 160.
40. Chang, K., Gao, J. T., Wang, Z., & Guo, Z. C. (2018). Manufacturing 3-D open-cell aluminium foam via infiltration casting in a super-gravity field. *Journal of Materials Processing Technology*, 252, 705–710.
41. Wang, Z., Gao, J., Chang, K., Meng, L., Zhang, N., & Guo, Z. (2018). Manufacturing of open-cell aluminium foams: Via infiltration casting in super-gravity fields and mechanical properties. *RSC Advances*, 8(29), 15933–15939.
42. Jakubowicz, J., Adamek, G., & Dewidar, M. (2013). Titanium foam made with saccharose as a space holder. *Journal of Porous Materials*, 20(5), 1137–1141.
43. Mansourighasri, A., Muhamad, N., & Sulong, A. B. (2012). Processing titanium foams using tapioca starch as a space holder. *Journal of Materials Processing Technology*, 212(1), 83–89.
44. Aida, S. F., Zuhailawati, H., & Anasyida, A. S. (2017). The effect of space holder content and sintering temperature of magnesium foam on microstructural and properties prepared by Sintering Dissolution Process (SDP) using carbamide space holder. *Procedia Engineering*, 184, 290–297.
45. Dehghan-Manshadi, A., Chen, Y., Shi, Z., Bermingham, M., StJohn, D., Dargusch, M., & Qian, M. (2018). Porous titanium scaffolds fabricated by metal injection moulding for bio-medical applications. *Materials*, 11(9), 1–13.
46. Shbeh, M. M., & Goodall, R. (2016). Open pore titanium foams via metal injection molding of metal powder with a space holder. *Metal Powder Report*, 71(6), 450–455.
47. Mat Noor, F., Zain, M. I. M., Jamaludin, K. R., Hussin, R., Kamdi, Z., Ismail, A., ... Taib, H. (2014). Potassium bromide as space holder for titanium foam preparation. *Applied Mechanics and Materials*, 465–466, 922–926.
48. Mondal, D. P., Barnwal, A., & Diwakar, V. (2017). Effect of strain rate and relative density on the compressive deformation of open cell Ti6Al alloy foam through P/M route. *Journal of Applied Mechanical Engineering*, 6(6).
49. Jain, H., Mondal, D. P., Gupta, G., & Kumar, R. (2021). Effect of compressive strain rate on the deformation behaviour of austenitic stainless steel foam produced by space holder technique. *Materials Chemistry and Physics*, 259.
50. García-Moreno, F. (2016). Commercial applications of metal foams: Their properties and production. *Materials*, 9(2), 20–24.

51. Kennedy, A. (2012, August). Porous metals and metal foams made from powders. *Powder Metallurgy*.
52. Wan, T., Liu, Y., Zhou, C., Ding, X., Chen, X., & Li, Y. (2021). Fabrication of high-porosity open-cell aluminum foam via high-temperature deformation of CaCl₂ space-holders. *Materials Letters*, 284, 129018.
53. Zhu, J., Liu, J., & Yang, S. (2019). *Ceramic foam filter and manufacturing method thereof*.
54. Jain, H., Kumar, R., Gupta, G., & Mondal, D. P. (2020). Microstructure, mechanical and EMI shielding performance in open cell austenitic stainless steel foam made through PU foam template. *Materials Chemistry and Physics*, 241.
55. Zhao, Y. Y., & Sun, D. X. (2001). Novel sintering-dissolution process for manufacturing Al foams. *Scripta Materialia*, 44(1), 105–110.
56. Tian, Q. H., & Guo, X. Y. (2010). Electroless copper plating on microcellular polyurethane foam. *Transactions of Nonferrous Metals Society of China (English Edition)*, 20, 283–287.
57. Poserin, V., Marcuson, S., Shu, J., & Wilkinson, D. S. (2004). CVD technique for Inco nickel foam production. *Advanced Engineering Materials*, 6(6), 454–459.
58. Queheillalt, D. T., Hass, D. D., Sypeck, D. J., & Wadley, H. N. G. (2001). Synthesis of open-cell metal foams by templated directed vapor deposition. *Journal of Materials Research*, 16(4), 1028–1036.
59. Antenucci, A., Guarino, S., Tagliaferri, V., & Ucciardello, N. (2015). Electro-deposition of graphene on aluminium open cell metal foams. *Materials and Design*, 71, 78–84.
60. Duan, D. L., Li, S., Ding, X. J., & Jiang, S. L. (2008). Preparation of Ni–Cr alloy foams by electrodeposition technique. *Materials Science and Technology*, 24(4), 461–466.
61. Felten, M., Fries, M., Pullen, A., Proud, W. G., & Jung, A. (2020). Investigation of strain-rate effects in Ni/PU hybrid foams under low-impact velocities. *Advanced Engineering Materials*, 22(7), 1–9.
62. Luo, H. (2019). Preparation of foamed aluminum and its application in China. *Journal of Physics: Conference Series*, 1347(1).
63. Matheson, K., Cross, K., Javahery, I., Plumb, J., & Spear, A. (2016). Comparison of conventional open-cell aluminum foam and its additively manufactured twin. *Materials Science and Technology Conference and Exhibition 2016, MS and T 2016*, 2, 745–752.
64. Gale, W. F., & Prorok, B. C. (2004). Non-conventional and emerging metallic materials. In *Smithells metals reference book* (Eighth.). Elsevier.
65. Marx, J., & Rabiei, A. (2017). Overview of composite metal foams and their properties and performance. *Advanced Engineering Materials*, 19(11), 1–13.
66. Akseli, I. (2005). *The application of aluminum foam for the heat and noise reduction in automobiles*. İzmir Institute of Technology.
67. Ashby, M. F., Evans, A. G., Fleck, N. A., Gibson, L. J., Hutchinson, J. W., & Wadley, H. N. G. (2000). *Metal foams: A design guide*.
68. Sığırtaç, T., Çakır, M. C., Uğuz, A., & Ensarioğlu, C. (2012). Alüminyum Köpük Malzemelerin İkincil İşlemleri Ve Bu İşlemlerin Sonlu Elemanlar Yöntemi İle Modellenmesi. In 3. *Ulusal Tasarım İmalat ve Analiz Kongresi (TİMAK)* (pp. 160–174). Balıkesir, Turkey.
69. De Jaeger, P., T'Joene, C., Huisseune, H., Ameer, B., De Schampheleire, S., & De Paepe, M. (2012). Assessing the influence of four cutting methods on the thermal contact resistance of open-cell aluminum foam. *International Journal of Heat and Mass Transfer*, 55(21–22), 6142–6151.
70. Meng, K. P., Chai, C. G., Sun, Y. L., Wang, W., Wang, Q. Y., & Li, Q. M. (2019). Cutting-induced end surface effect on compressive behaviour of aluminium foams. *European Journal of Mechanics/A Solids*, 75, 410–418.
71. Yilbas, B. S. (2018). *The laser cutting process. The laser cutting process: Analysis and applications*. Elsevier.
72. Ozturk, M., & Dogan, B. (2019). Enhancement of heat exchangers with metal foams. *World Journal of Environmental Research*, 9(1), 15–28.

73. Banhart, J. (2013). Light-metal foams—History of innovation and technological challenges. *Advanced Engineering Materials*, 15(3), 82–111.
74. Hangai, Y., Ohashi, M., Nagahiro, R., Amagai, K., Tomaru, T., Utsunomiya, T., & Yoshikawa, N. (2019). Press forming of aluminum foam during foaming of precursor. *Materials Transactions*, 60(11), 2464–2469.
75. Changdar, A., & Chakraborty, S. S. (2021). Laser processing of metal foam—A review. *Journal of Manufacturing Processes*, 61, 208–225.
76. Paunoiu, V., Quadri, F., Cataragiu, A., & Santo, L. (2015). Laser forming of aluminium metal foam panels. In *The annals of “Dunarea De Jos” University Of Galati Fascicle V, Technologies in machine building*.
77. Contorno, D., Filice, L., Fratini, L., & Micari, F. (2006). Forming of aluminum foam sandwich panels: Numerical simulations and experimental tests. *Journal of Materials Processing Technology*, 177(1–3), 364–367.
78. Zhang, J., Qin, Q., Han, X., & Ai, W. (2016). The initial plastic failure of fully clamped geometrical asymmetric metal foam core sandwich beams. *Composites Part B: Engineering*, 87, 233–244.
79. Weiss, M., Abeyrathna, B., & Pereira, M. (2018). Roll formability of aluminium foam sandwich panels. *International Journal of Advanced Manufacturing Technology*, 97(1–4), 953–965.
80. D’Urso, G., & Maccarini, G. (2012). The formability of aluminum foam sandwich panels. *International Journal of Material Forming*, 5(3), 243–257.
81. Chen, N., Feng, Y., Chen, J., Li, B., Chen, F., & Zhao, J. (2013). Vacuum brazing processes of aluminum foam. *Xiyou Jinshu Cailiao Yu Gongcheng/Rare Metal Materials and Engineering*, 42(6), 1118–1122.
82. Khokhlov, M., Ishchenko, D., & Khokhlova, J. (2016). Peculiarities of forming diffusion bimetallic joints of aluminum foam with a monolithic magnesium alloy. *Journal of Magnesium and Alloys*, 4(4), 326–329.
83. Yao, C., Hu, Z., Mo, F., & Wang, Y. (2019). Fabrication and fatigue behavior of aluminum foam sandwich panel via liquid diffusion welding method. *Metals*, 9(5), 1–11.
84. Peng, P., Wang, K., Wang, W., Huang, L., Qiao, K., Che, Q., ... Cai, J. (2019). High-performance aluminium foam sandwich prepared through friction stir welding. *Materials Letters*, 236, 295–298.
85. Bušić, M., Kožuh, Z., Klobčar, D., & Samardžić, I. (2016). Friction stir welding (FSW) of aluminium foam sandwich panels. *Meta*, 55(3), 473–476.
86. Banhart, J., Schmoll, C., & Neumann, U. (1998). Light-weight aluminium foam structures for ships. *Proc. Conf. Materials in Oceanic Environment*, 1, 55–63.
87. Nowacki, J., Krajewski, S., & Grabian, J. (2014). Problems of aluminum foam soldering. *Przegląd Spawalnictwa—Welding Technology Review*, 86(1).
88. Bernard, T., Bergmann, H. W., Haberling, C., & Haldenwanger, H. G. (2002). Joining technologies for Al-foam-Al-sheet compound structures. *Advanced Engineering Materials*, 4(10), 798–802.
89. Castanie, B., Bouvet, C., & Ginot, M. (2020). Review of composite sandwich structure in aeronautic applications. *Composites Part C: Open Access*, 1.
90. Feldhusen, J., Warkotsch, C., & Kempf, A. (2009). Development of a mechanical technology for joining sandwich elements. *Journal of Sandwich Structures and Materials*, 11(6), 471–486.
91. Joesbury, A. M. (2015). *New approaches to composite metal joining*. Cranfield University. Retrieved from <https://dspace.lib.cranfield.ac.uk/handle/1826/10009>
92. Wan, L., Huang, Y., Huang, T., Lv, Z., & Feng, J. (2016). Interfacial behavior and mechanical properties of aluminum foam joint fabricated by surface self-abrasion fluxless soldering. *Journal of Alloys and Compounds*, 671, 346–353.

93. Cambronero, L. E. G., Cañadas, I., Ruiz-Román, J. M., Cisneros, M., & Corpas Iglesias, F. A. (2014). Weld structure of joined aluminium foams with concentrated solar energy. *Journal of Materials Processing Technology*, 214(11), 2637–2643.
94. Babcsan, N., Beke, S., Makk, P., Szamel, G., & Kadar, C. (2014). Pilot production and properties of ALUHAB aluminium foams. *Procedia Materials Science*, 4(1997), 127–132.
95. Líska, J., Kun, K., & Líska, K. (2016). MMC materials ultrasonic machining and its economic aspects. *Procedia Engineering*, 149, 245–256.
96. Rossi, S., Bergamo, L., Calovi, M., & Fontanari, V. (2019). Effect of enamel coatings on the mechanical properties of aluminium foams. *Mechanics of Advanced Materials and Structures*, 26(13), 1130–1139.
97. Rossi, S., Fedel, M., Da Col, L., Deflorian, F., & Petrolli, S. (2017). Coatings to increase the corrosion behaviour of aluminium foam. *Surface Engineering*, 33(6), 405–409.
98. Huang, Y., Gong, J., Lv, S., Leng, J., & Li, Y. (2012). Fluxless soldering with surface abrasion for joining metal foams. *Materials Science and Engineering A*, 552, 283–287.
99. Gloria, A., Montanari, R., Richetta, M., & Varone, A. (2019). Alloys for aeronautic applications: State of the art and perspectives. *Metals*, 9(6), 1–26.
100. Duan, X., Dai, Z., Xu, R., Mao, R., & Song, B. (2019). The preparation methods and application of aluminum foam. In *Light metals 2019* (pp. 501–504).
101. ERG Aerospace Applications. (2020). Retrieved from <http://ergaerospace.com/applications>.
102. Raeisi, S., Kadkhodapour, J., & Tovar, A. (2019). Mechanical properties and energy absorbing capabilities of Z-pinned aluminum foam sandwich. *Composite Structures*, 214, 34–46.
103. Lu, T. (2002). Ultralight porous metals: From fundamentals to applications. *Acta Mechanica Sinica/Lixue Xuebao*, 18(5), 457–479.
104. Oana, B., Florea, R. M., Buz, A., Roman, C., & Carcea, I. (2013). Manufacturing and characterization of stabilized aluminum foams. *International Journal of Modern Manufacturing Technologies*, V(1), 17–24.
105. Yao, G.-C., Luo, H.-J., & Cao, Z.-K. (2015). The manufacturing technology of aluminum foam material and some special equipments. In *Proceedings of the 2015 international conference on material science and applications (ICMSA)* (pp. 869–874). Atlantis.
106. Ali, A. A., Mahmood, H. Y., & Saeed, M. W. S. (2018). Implementation of vibration suppression on an aircraft wing using velocity feedback controller. *Association of Arab Universities Journal of Engineering Sciences*, 25(2), 45–64.
107. Arunkumar, M. P., Pitchaimani, J., Gangadharan, K. V., & Lenin Babu, M. C. (2017). Sound transmission loss characteristics of sandwich aircraft panels: Influence of nature of core. *Journal of Sandwich Structures and Materials*, 19(1), 26–48.
108. Paun, F., Gasser, S., & Leylekian, L. (2003). Design of materials for noise reduction in aircraft engines. *Aerospace Science and Technology*, 7(1), 63–72.
109. Teruna, C., Manegar, F., Avallone, F., Ragni, D., Casalino, D., & Carolus, T. (2020). Noise reduction mechanisms of an open-cell metal-foam trailing edge. *Journal of Fluid Mechanics*, 898.
110. Xu, C., Mao, Y., & Hu, Z. (2018). Numerical study of pore-scale flow and noise of an open cell metal foam. *Aerospace Science and Technology*, 82–83, 185–198.
111. Hanssen, A. G., Girard, Y., Olovsson, L., Berstad, T., & Langseth, M. (2006). A numerical model for bird strike of aluminium foam-based sandwich panels. *International Journal of Impact Engineering*, 32(7), 1127–1144.
112. Heimbs, S. (2012). Energy absorption in aircraft structures. In *1st international workshop on hydraulic equipment and support systems for mining (IWHM)*, pp. 1–10. Retrieved from http://www.heimbs-online.de/Heimbs_2012_IWHM.pdf.
113. Metz, I. C., Ellerbroek, J., Mühlhausen, T., Kügler, D., & Hoekstra, J. M. (2020). The bird strike challenge. *Aerospace*, 7(3), 1–20.
114. FAA Wildlife Strike Database. (2021). Retrieved from <https://wildlife.faa.gov/search>.
115. Liu, J., Li, Y., Yu, X., Gao, X., & Liu, Z. (2018). Design of aircraft structures against threat of bird strikes. *Chinese Journal of Aeronautics*, 31(7), 1535–1558.

116. Why are the B787 leading edges made from aluminum? (2020). Retrieved from https://aircraft-technic.com/aviation_technology/why-are-the-b787-leading-edges-made-from-aluminum.
117. Reglero, J. A., Rodríguez-Pérez, M. A., Solórzano, E., & de Saja, J. A. (2011). Aluminium foams as a filler for leading edges: Improvements in the mechanical behaviour under bird strike impact tests. *Materials and Design*, 32(2), 907–910.
118. Zhou, J., Liu, J., Zhang, X., Yan, Y., Jiang, L., Mohagheghian, I., ... Charalambides, M. N. (2019). Experimental and numerical investigation of high velocity soft impact loading on aircraft materials. *Aerospace Science and Technology*, 90, 44–58.
119. 5 May 2015—Nevsehir (Turkey) THY B737. (2021). The Aviation Herald. Retrieved from <http://avherald.com/h?article=485d4116>.
120. 3 December 2015 Bandar Seri Begawan bird strike. (2021). The Aviation Herald. Retrieved from <http://avherald.com/h?article=490d1e37>.
121. Li, S., Jin, F., Zhang, W., & Meng, X. (2016). Research of hail impact on aircraft wheel door with lattice hybrid structure. *Journal of Physics: Conference Series*, 744(1).
122. Robbins, S. J., Marx, J., Grady, Z. A., Rabiei, A., & Palmieri, F. L. (2019). *Polymer-filled metal foams for contamination resistant aircraft leading edges*.
123. Min, J. B., Ghosn, L. J., & Lerch, B. A. (2015). A study for stainless steel fan blade design with metal foam core. *Journal of Sandwich Structures and Materials*, 17(1), 56–73.
124. Madruga, S. (2021). Modeling of enhanced micro-energy harvesting of thermal ambient fluctuations with metallic foams embedded in Phase Change Materials. *Renewable Energy*, 168, 424–437.
125. Madruga, S. (2019). Thermoelectric energy harvesting in aircraft with porous phase change materials. *IOP Conference Series: Earth and Environmental Science*, 354(1).
126. Xi, H., Tang, L., Luo, S., Liu, Y., Jiang, Z., & Liu, Z. (2017). A numerical study of temperature effect on the penetration of aluminum foam sandwich panels under impact. *Composites Part B: Engineering*, 130, 217–229.
127. Zhang, X., Wang, R., Liu, J., Li, X., & Jia, G. (2018). A numerical method for the ballistic performance prediction of the sandwiched open cell aluminum foam under hypervelocity impact. *Aerospace Science and Technology*, 75, 254–260.
128. Ryan, S., & Christiansen, E. L. (2015). *Hypervelocity impact testing of aluminum foam core sandwich panels* (NASA/TM–2015–218593). Houston, TX, USA.
129. Ryan, S., Hedman, T., & Christiansen, E. L. (2010). Honeycomb vs. foam: Evaluating potential upgrades to ISS module shielding. *Acta Astronautica*, 67(7–8), 818–825.
130. Exerowa, D., Gochev, G., Platikanov, D., Liggieri, L., & Miller, R. (2018). *Foam films and foams: Fundamentals and applications*. CRC Press. Taylor & Francis Group.
131. Gao, L., Li, Y., Xu, H., Zhang, X., Yuan, M., & Ning, X. (2019). Numerical investigation on heat-transfer and hydromechanical performance inside contaminant-insensitive sublimators under a vacuum environment for spacecraft applications. *Energies*, 12(23).
132. Dixit, T., & Ghosh, I. (2018). Experimental and numerical modeling of metal foam passive radiator at low temperatures. *Experimental Heat Transfer*, 31(5), 425–435.
133. Dixit, T., & Ghosh, I. (2017). Cooling capacity of high porosity open-cell metal foams as passive cryogenic radiators. *Cryogenics*, 84, 81–88.
134. Tisha, D., & Indranil, G. (2017). Prospective of employing high porosity open-cell metal foams in passive cryogenic radiators for space applications. *IOP Conference Series: Materials Science and Engineering*, 171, 012048.
135. Dixit, T., & Ghosh, I. (2016). Radiation heat transfer in high porosity open-cell metal foams for cryogenic applications. *Applied Thermal Engineering*, 102, 942–951.

Chapter 3

Advanced Polymers in Aircraft Structures



**Dipen Kumar Rajak, Pratiksha H. Wagh, Ashwini Kumar, Ajit Behera,
and Catalin I. Pruncu**

3.1 Introduction

Engineering materials can be classified as composites, metals, nonmetals, and ceramics. Metals lose their strength at much higher temperatures than polymer materials. Considering ceramic materials, they have the potential to have a high temperature, thermal expansion characteristics, and good strength, but the only drawback is their brittleness so that they cannot be employed for the development of structural materials. Therefore, composite materials come into existence in view of the shortcomings of all materials. Recently, polymer composite materials have been the major choice of all aircraft design engineers because they can meet the high-performance requirement and ability to design material characteristics. This

D. K. Rajak

Department of Mechanical Engineering, Sandip Institute of Technology and Research Centre,
Nashik, Maharashtra, India

P. H. Wagh

Department of Mechanical Engineering, G. H. Raison Institute of Engineering and
Technology, Pune, Maharashtra, India

A. Kumar

Department of Mechanical Engineering, Faculty of Engineering and Technology, SGT
University, Gurugram, India

A. Behera

Department of Metallurgical and Materials Engineering, National Institute of Technology,
Rourkela, India

C. I. Pruncu (✉)

Design, Manufacturing and Engineering Management, University of Strathclyde,
Glasgow, Scotland, UK

e-mail: catalin.pruncu@strath.ac.uk

material provides excellent strength to weight ratio, wear resistance under severe environmental conditions, ability to meet intensive dimensional stability, moderate thermal expansion characteristics rapid growth cycle, and excellent fracture and fatigue resistance. In the sectors like military, with the use of polymer composite materials to produce fighter aircraft frames, significant amounts of weight loss have been achieved [1–3]. In addition, polymer composites found about 80% of recent vehicles for satellites, including many important satellite components such as, cylinder support structures antennas, hive structures, solar array substrates, instrument panels, and so on. Solid boosters of the space shuttle contain 30 tons of graphite-reinforced epoxy composites even the growth of micron-thickness films will ultimately enable some types of spacecraft, such as solar cells [4]. The material used in the manufacturing of the structural parts has to carry the load, which is acted upon the frames of the aircraft starting from the takeoff till the landing. In U.S. F14 and F15 fighter planes, the composite material was used for the first time before 30 years in the skin of empennages [5]. Now the primary and secondary parts of the aircraft polymer composite material include wings, center wing box, flap track panels, landing gear doors, engines cowlings, horizontal tailplane, tail cone, outer flaps, upper deck floor beams, vertical tailplane, etc. as shown in Fig. 3.1 [6]. Some of the metals like nickel-metal alloys are replaced with the carbon fiber–reinforced composite in the application of high-pressure turbines components like jet engine fan blades which were resulted in 5% reduction in fuel consumption than other comparable engines [7]. Researchers had proved that traditional materials are having many of the drawbacks and large amount of money is wasted in maintenance, repair, and operation of aircraft, whereas the composites material is providing excellent strength and other properties which will last for larger period. Even some of the researchers were also discovered that metals are facing so many problems in manufacturing complex design shapes; however, matrix and reinforced composite can be

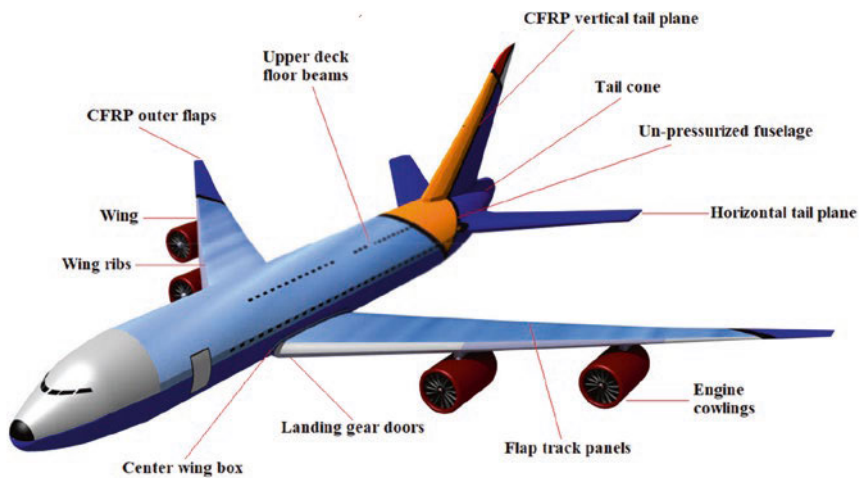


Fig. 3.1 Aircraft components produced from polymer composite materials

Table 3.1 Composite materials used in various aircraft

Type of the aircraft	Name of the aircraft
Fighter aircraft	AV-8B, F16, F14, F18, YF23, F22, JSF, UCAV, Europe Harrier, GR7, Gripen JAS39, Mirage 2000, Rafael, Eurofighter, Lavi, EADS Mako, Mig29, Su series
Bomber/transport aircraft	KC135, C17, 777, 767, MD11, A320, A340, A380, Tu204, ATR42, Falcon 900, A300–600
General aviation	Piaggio, Starship, Cirrus SR 20, and SR22
Rotary aircraft	V22, Eurocopter, Comanche, RAH66, BA609, EH101, Super Lynx 300, S92

manufactured in any type of critical shape and they are more appropriate than the metals. The prime role of the matrix and the reinforced material is that it can be effortlessly mold in any type of complex shape and can hold good strength, mechanical properties, and stiffness. As the composite materials are the hybrid materials obtained from the combination of two or more materials which will provide advanced properties that is the reason the utilization of composite material in aerospace industry is reached up to more than 50% [8–10]. In the past, the composite material was used by only military aircraft but due to the technological development, it is used in commercial planes also. Presently, composite material has become an excellent replacement for metal components. Taking the example of Airbus 320, the use of composite material has reduced the weight of the airplane up to 800 kg and more than 20% of the airframes were made of composite material [11]. Even some of the well-known examples where composite material was used like in European fighter plane, Harrier AV-8B, A320, A380, rotor hubs and blades of helicopter, propeller, Boeing 787, etc. Table 3.1 depicts a type of aircraft whose components are made with the help of composite materials, which are given subsequently. Presently the polymer composite materials are widely used in fighter planes for the manufacturing of the parts like the wing skins, flappers, forward fuselage, and also other parts that are labeled in Fig. 3.1. The percentage distribution of the composite material is like 40% for the structural parts, 75% for the exterior parts, etc. [12, 13]. The use of polymer-based composite is rapidly increasing in the aviation parts related market instead of metal as the maintenance costs reduce. This review will focus on various types of polymer composites in the field of aviation, components, and manufacturing process, etc.

3.2 Polymer Composites in Aircraft

Polymer composite materials are the materials in which one compulsory element is a polymer. It is a type of composite in which the fibers or other small particles are inserted into it and that insertion of the fibers is called as reinforcement. The selection of the matrix and the reinforcement mainly depends on the type of application,

properties, manufacturing process, and cost-effectiveness. The polymer matrix composites are the most innovative composites. This type of composite consists of fiber-reinforced polymer thermosetting or thermoplastic, also the materials can be molded in many shapes and dimensions, the classification of thermoplastic and thermosetting polymer matrix is as shown in Fig. 3.2 with their structure [14–16]. The commonly used thermoplastic and thermosetting polymer matrices are listed below:

- PEEK (poly-ether-ether-ketone)
- PEI (Polyetherimide)
- PPS (Polyphenylene sulfide)
- Polyester
- Vinyl ester
- Epoxy

In recent times, the polymer composite is in more demand due to its improved mechanical and tribological properties with more amount of weight saving. This composite has the fastest processing cycle and even at very high temperature polymer composite material cannot be stretched or compressed also excellent fracture and fatigue resistance. The unwavering urge of the aircraft manufacturers and industry to improve the enactment of military and commercial aircraft pointers to improvement of better high-performance structural materials. Among the current aircraft components, composite materials are a type of material that plays an important role. Due to the outstanding rigidity, strength, density ratio, and excellent physical characteristic polymer composite are in the focus of aircraft parts or component manufacturing industry. The most common type of fibers used in the aviation is the carbon and glass fiber. Carbon fiber is having improved properties than the glass fiber but the only drawback is the cost. Carbon fiber–reinforced plastics (CFRP) are the primary and most significant material used in aerospace sector at the earliest. Now in the latest models of thin and wide structure civil aircraft, more than 50% of the construction components are led by their excellent rigidity, strength, and weight

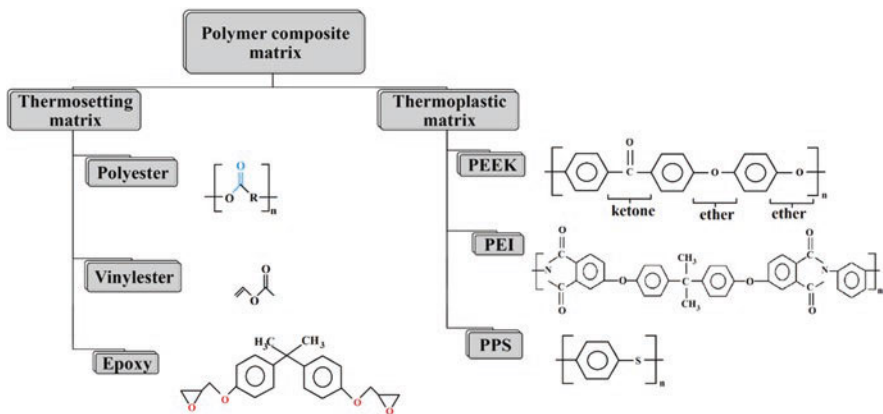


Fig. 3.2 Classification of thermoplastic and thermosetting polymer matrix

ratio. Now the major focus of the manufacturing industry is to prepare the thin-ply fiber from the spread tow fibers. The fibers are permeable to low density and strong uniform fiber–matrix reaction. The primary markets for these components were racing cars and sports-related equipment, but now there is an attraction toward the aircraft industry. The CFRP material is being employed for the inside seats of Airbus A350 aircraft by aircraft overhaul and maintenance firm Hong Kong Aircraft Engineering [13–19].

3.3 Structural Components in Aircraft

Aircraft manufacturers, which allow the production of composite structures for the future of the aircraft, contribute to the correction of the current production of the aircraft. The advantages of using composites in construction applications have been identified in many technical studies. Currently, technology development programs are being implemented to correct known shortcomings and make necessary improvements. The aircraft's parts were made using various materials and assembled using bolts, nuts, screws, rivets, and special adhesives. The design of the aircraft is designed in such a way that it can carry loads and withstand various stresses. Each part of the aircraft had different forms of complex loads. The layout of the aircraft is mostly made based on the wing structure. The aircraft can be steered around the transverse, longitudinal, and vertical axis by deflecting the control surface. These controls represent the pilot's articulated or moving landing surfaces to the aircraft's position during takeoff, flight, and landing. They can be operated either by the pilot or by connecting to the chain using foot pedals and a control stick or steering wheel. The important components of an aircraft were listed subsequently:

3.3.1 *Engine Fan Blades*

Composite material is currently found in many commercial applications of turbofan engines shown in Fig. 3.3 due to its low cost, enhancement in efficiency, and less weight. Recently, the composite fan blade manufacturing is the greatest innovation in the aircraft industry. As carbon fiber is mostly chosen by the design engineer for the manufacturing of composite material. The main reason to prefer the carbon fiber in the fan blade is its weight, durability, and efficiency. This carbon fiber–reinforced composite blades are used because they have the ability to withstand usual fatigue without failure and can be easily retained and repair. The use of polymer composite has reduced the weight of the engine fan blades up to 159 kg along with enhancement in mechanical and tribological properties [20, 21]. The strength of the engine fan blades mainly depends on the fiber orientation, only the specific direction of the fiber orientation will give the higher strength and this decision depends on the designer. Presently, the fibers with unidirectional tow are normally used by holding

Fig. 3.3 3D sketch of engine fan blades

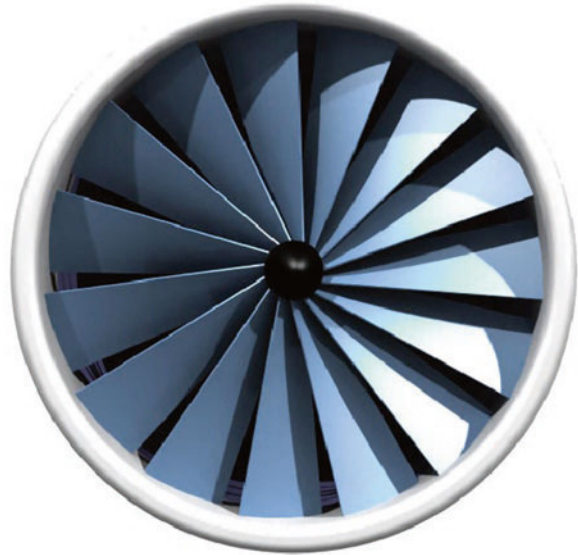


Table 3.2 Properties of a recommended polymer matrix composite [24]

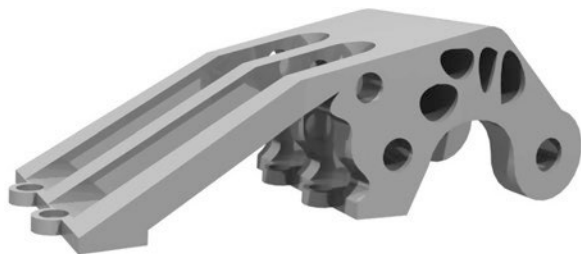
Properties	Value
Tensile strength	99.3 MPa
Tensile modulus	4090 MPa
Elongation at yield	4.4%
Fracture toughness	3.51 MPa-m ^{1/2}
Density	1.272 g/cc
Viscosity	1900 cP at 129–149°C
Moisture absorption at equilibrium	3.1%

the layer together for some preferred performance. The composite fan blades can be worked in the higher temperature also by using proper epoxy resin. There is a huge enhancement in the engine performance due to the use of fiber reinforcement composite in the manufacturing of blades. Some of the researchers had done the 3D modeling analysis by using the design software and it is concluded that comparing with the materials like carbon fiber, glass fiber, and aluminum alloy carbon fiber had shown less stress with more safety material [22]. As the advantages of the composite materials were focused but they are having some drawbacks in the form of vibration damping, but this drawback can also be overcome by some of the researcher and observed that by adopting the piezoelectric vibration damping can considerably diminish vibration of aircraft engine composite fan blades [23]. The properties of a recommended polymer matrix composite for the manufacturing of airplane engine fan blades are given in Table 3.2.

3.3.2 Brackets

Aircraft component manufacturing is now becoming a challenge to manufacture the parts with more amount of weight saving. As all the parts from the main body to small components all are replaced with the composite material. Focusing on the aircraft brackets as shown in Fig. 3.4, they support the structure as they are employed to hold the two components one above the other. Brackets used in aircraft are employed for many types of applications like fuel tank, fuselage frame installation, engine mounts, and landing gears. Considering the molded bracket, the polymer used for manufacturing is PEEK (poly-ether-ether-ketone), which has reduced the weight up to 40% with cost-effectiveness and presently employed in the Bombardier's C-Series, Global, and Learjet aircraft. Also, the manufacturing cost is also reduced as there is no extra machining and painting process due to the complex shape of the mold, similarly decrease of scrap and manufacturing cycle time. The brackets of the aircraft are of three types and can be used according to the category of application like class A, class B, and class C. Class A brackets are in the primary structure, for removing the structure class B is used, and for the attachment of the tertiary structure class C. Till now many books are published to give the advantages and disadvantages of the composite material but steps to design the composite material for specific type of component manufacturing is yet not published. So, for this reason, focus is on the finite element analysis (FEA), by using FEA prediction can be done for the material failure and strength [25–27]. The researcher named Mun et al. had prepared a design model for the design and analysis of composite material as it works on the following three steps like analysis, discretization, and laminated modeling. This model will give the exact recognition of stress sharing on certain areas and will help to develop the superior composite material and structure [28, 29]. Properties that are used to check the bonding of composite material for the brackets are shear bond strength, flexural strength test, and polymerization contraction stress [28].

Fig. 3.4 Bracket used in aircraft



3.3.3 Interiors

Interior of the aircraft must have to promote the maximum safety and comfort for the passengers. The need to build airplane composite interior which will provide lightweight, airy, and comfortable with cost reduction. The interior of the aircraft includes electrical panels, seating arrangement, galleys, aircraft structure, entertainment devices, cabin avionics, etc. The future of composite material in the aircraft industry for the application of interior components is going on increasing in regional aircraft, general aviation, commercial aircraft, military aircraft, and helicopters. The introduction of composite window frames and the application of composite thermo-plastic applications to aircraft interior had developed styles that directly affect the flexibility of composites in the aircraft industry. As compared to the glass fiber, carbon fiber–reinforced composite observed highest demand in the application like window frames and seat components as shown in Fig. 3.5 [30, 31]. In case of turbulence or at the time of emergency landing the upper storage, compartment may subject to highly dynamic loads so to overcome this drawback one of the researchers Heimbs et al. prepared a model, which will correlate the simulation and experimental data with the help of numerical method to manufacture the interior components of the airplane [32]. The most widely used resins for the applications of aircraft interior are [CYCOM 2400-1](#), [CYCOM 6070](#), [CYCOM 2265](#), [CYCOM 2290](#), [CYCOM 919](#), and [MTM 82S](#). Table 3.3 gives the properties of two of them, while Fig. 3.6 shows the yearly growth of composites in aircraft interior [33–35].

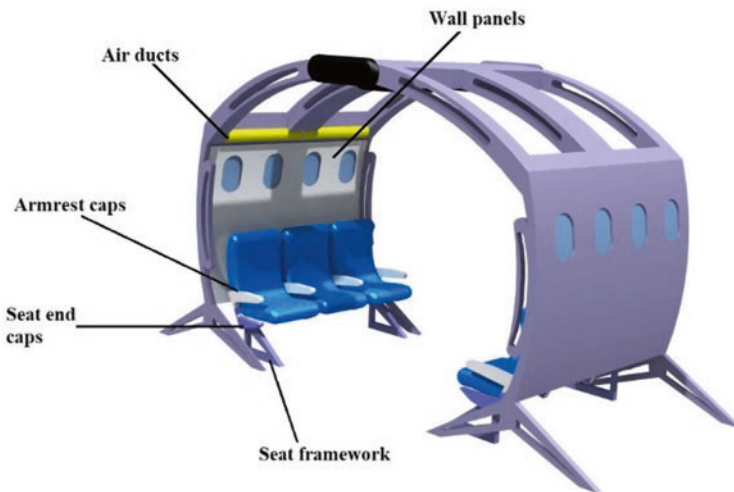


Fig. 3.5 Interior of an airplane

Table 3.3 Some resins for the application of aircraft interior components [33]

(CYCOM 6070) Phenolic composite laminates, glass				
Properties	Test temperature	7781/1581 Fiberglass fabric 8HS	120/220 Fiberglass fabric 4HS	Test method
0° Tensile strength (MPa)	-55°C	507	428	ASTM D 638
	24°C	414	369	
	82°C	352	407	
0° Compressive strength (MPa)	-55°C	407	507	ASTM D 695
	24°C	338	479	
	82°C	273	397	
0° Flexural strength (MPa)	55°C	493	579	ASTM D 790
	24°C	486	490	
	82°C	445	438	
0° Flexural modulus (GPa)	-55°C	27	25	ASTM D 790
	24°C	25	25	
	82°C	26	24	
(CYCOM 2400-1) Autoclave cured laminate				
Properties	Glass style 7781	Carbon 3K T650 8HS	Test method	
0° Tension strength (MPa)	441	924	ASTM D 638	
0° Tension modulus (GPa)	24.8	64.1	ASTM D 638	
0° Compression strength (MPa)	524	717	ASTM D 695	
0° Compression modulus (GPa)	28.3	61.4	ASTM D 695	

3.3.4 Nacelles

The nacelle is an important part of the aircraft as shown in Fig. 3.7, which is also called as covering, as it is separate from fuselage which grips the fuel or other equipment with engine. The nacelles boost airflow and safeguard the engine. Also, it supports to diminish noise and contributes to aircraft braking through integrated thrust reversers. The structure that environs the aircraft engine has fate in its inherent complexity as the shape of the aircraft nacelle is smooth. Composite nacelles are especially design to decrease the weight of the aircraft with improved engine fuel economy and supporting noise regulation. Presently most of all the aircraft are now employing composite nacelles due to its excellent properties and benefits. There are three main components of the nacelle like fan cowl, thrust reverser, and inlet. The fan base is the central part of the nacelle and it is generally prepared as a couple of hinged doors with or next to a pylon. The fan cover door engine affords access to the looking after of the assembled systems on the fan case. In most recent jet engines, the gearbox assembly is organized on a next to the fan case. That arrangement describes the region below the fan. The inlet is also the most advanced part of the

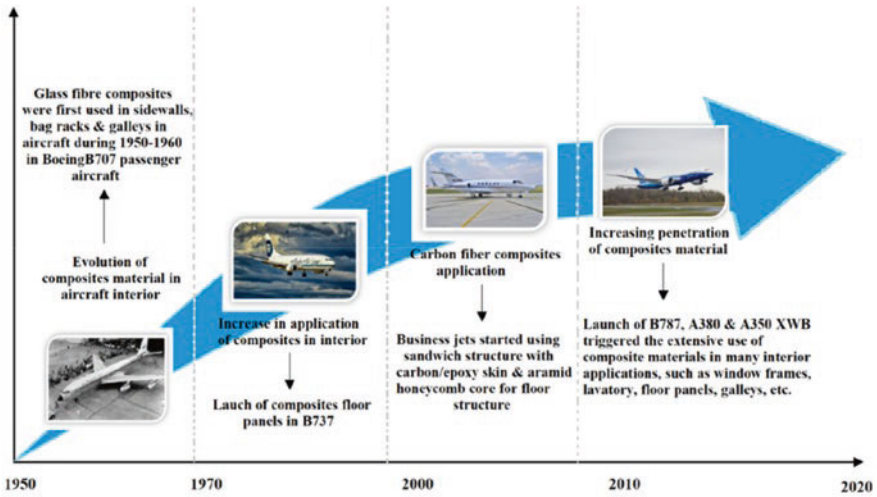


Fig. 3.6 Yearly growth of composites in aircraft interior

Fig. 3.7 3D sketch of nacelles used in aircraft



nacelles as it is connected to the engine fan case. As the inlet geometry is aerodynamically adapted to cruise conditions, it can operate in high angles of protruding engine axes in airflow next to kin. The main function of the inlet is to deliver air directly to the engine. The last and very important part of the nacelle is the thrust reverser which helps to diminish the landing distance of the airplane. It is also used to reduce the wear of the tires and provides excess power to the pilot at the time of stopping the plane in wet and icy platform [36–39]. So, some of the researchers like Dudziak et al. revealed in his research that the structure of the airplane nacelles is design in such a way that the high temperature will not affect the components as the design is made of solid laminated structure and it is part in two sections like sandwich structure in the rear part and solid laminated structure in the front part [40].

The two important resin mostly used for nacelles manufacturing are bismaleimides and polyimide its properties are given in Table 3.4.

3.3.5 Wings

The main and important part of the airplane is wing shown in Fig. 3.8 as it has to govern the rolling and pitching action so it has to be created by different types of components. The structure of the wing is commonly hollow from the inside. At present, wings are made of composite material carbon fiber fabric that is coated and molded with resin. However, the way these materials are placed varies according to the work. To create the wing, design engineers use digital simulation and modeling software, to check the number of possible formations to create a digital arrangement paperback of layers. According to the National composite center (NCC), there may be 14,000 possible combinations of laying and cutting for a single wing skin with 150 layers. The wing of the airplane is also called as airfoil that makes a lift when moving speedily in air. By considering different types of aerodynamic properties the designer had prepared different types of wings. These types of wings are available with many a type of shapes and can be attached in many types of the angles to the main frame of the airplane. At the time of takeoff, the wings of the aircraft lift it into the air. The special design of wings for any aircraft depends on many factors including weight and size of the aircraft, use of airplanes, desired rate of climb, desired speed in landing and flight, and takeoff. The wings of the aircraft are often of full-size design. This means that they are constructed in such a way that they do not require any outward bracing. They are supported internally by structural

Table 3.4 Mechanical properties of resin used to manufacture nacelles [41, 42]

Properties	Value
Bismaleimides	
Tensile strength at 25°C	85 MPa
Tensile modulus	3.63 GPa
Flexural strength	
25°C	143 MPa
150°C	87 MPa
180°C	72 MPa
Flexural modulus at 25°C	4 GPa
Elongation	3%
Polyimide	
Modulus of elasticity	500 MPa
Compressive strength	25,000 MPa
Shearing strength	70 MPa
Tensile strength	300 MPa

Fig. 3.8 3D design of an aircraft wings

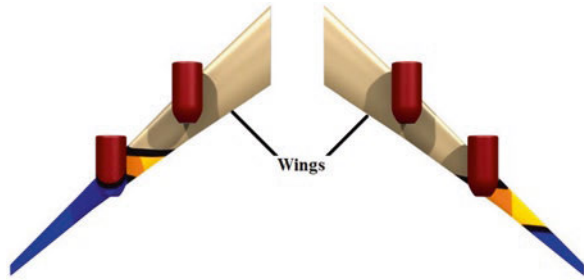


Table 3.5 Properties of resin used for wings [48]

Properties	Value
Tensile strength	70 MPa
Tensile modulus	3.1 GPa
Tensile elongation	6.3%
Flexural strength	139 MPa
Fracture modulus	3.2 GPa
Fracture elongation	3.3%
Fracture toughness	0.9 MPa.m ^{1/2}
Elastic shear modulus	1.2 GPa
Cured resin density	1.22 g/cm ³

members and plane skin. So, there are nine types of wings like rectangular, tapered, elliptical, delta, ogive, trapezoidal, swept back, forward, and variable swept wing as it can be used according to the type of application [43–46]. Some of the researchers are working on the fluttering speed due to variation in fiber arrangement angle, thickness of fiber, and differences in material, hence concluding that by making the computational efficient probabilistic flutter model better results can be achieved [47]. Table 3.5 gives detail about the resin properties of CYCOM 890 used for the manufacturing of aircraft wings.

3.3.6 Fuselage

The fuselage is the central and very important part of the airplane where the seating of the passenger is arranged as shown in Fig. 3.9. The part looks like central tube-shaped that's why it is called as fuselage; also, it can hold all the parts of the airplane together. The fuselage is very long and hollow to reduce the weight of the airplane, the exact shape of the fuselage depends on the application for which that aircraft is used. If we consider passenger airplane then long fuselage is employed to transfer number of passengers at one time, likewise to reduce the drag associated with high-speed streamlined fuselage is used and for fighter planes slim fuselage is used

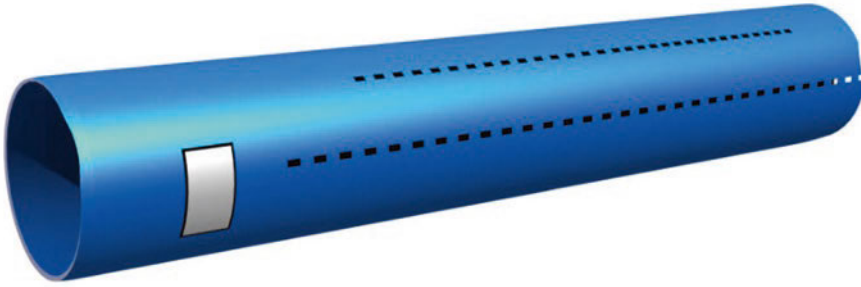


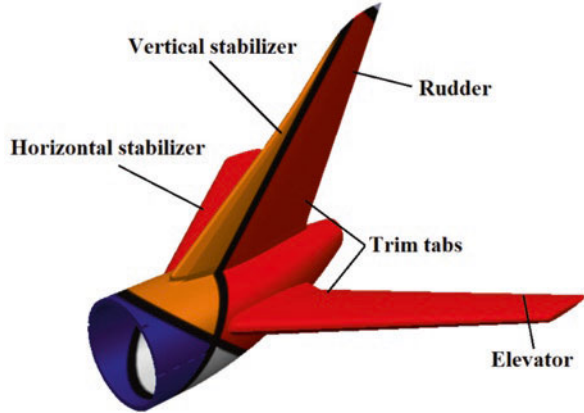
Fig. 3.9 Fuselage of an airplane

[49–52]. According to the size of the fuselage for particular application, the door size also changes. As the passenger aircraft has a smaller door as compared to the fighter aircraft, so at the time of considering the loads, smaller doors can transmit the load around the door. Pressure and volume are the main important things that work consequently in aircraft. If the fuselage is depressed because of the pressure difference, the floor will be loaded and if the fuselage is pressurized, there will be no compressive load on the floor. The basal frame of the fuselage hardly has diverse spaces; this is entitled double-bubble fuselage [53]. A researcher like Quadman et al. provided a method for calculating the post-buckling and buckling load stiffness of orthotropic sheets at the junction of compression and shear, and this proposed method is used to estimate the reverse factors and is used to design the airplane fuselage structure of this concern [54]. Presently, the airplane fuselage is made of carbon fiber–reinforced polymer composite to improve all the properties with cost-effectiveness.

3.3.7 Empennage

Empennage is commonly known as the tail assembly of an aircraft. From Fig. 3.10, all the parts like vertical stabilizer, horizontal stabilizer, elevators, trim tabs, and rubber of the tail section were clearly shown. The horizontal and vertical stabilizers are fixed but the elevator, rubber, and trim tabs are movable which is used to control the vertical/horizontal rotation of an aircraft and it is operated by the pilot. In some aircraft, a cockpit is a unit used to control the overall trim of the aircraft, so that the entire horizontal surface of the tail can be installed and adjusted. These designs are commonly referred to as stabilizers, flying tails, or tail boards. Aircraft tail, directions, and balance mechanism, as well as a tool for the control panel and maneuvering on the aircraft. The stress that occurs in an empennage is removed like the stress in a wing. Flexural, torsional, and shear strengths created by the loaded air pass from one element to another. Every element absorbs some of the stress and it will be shared with other element. As the stress exceeds its limit, then it starts transmitting

Fig. 3.10 Empennage of an airplane



to the fuselage section. Recently, the aircraft component manufacturing companies are now focusing on the new version of the empennage made of composite material for the existing aircraft. As the scientists conclude in their research, empennage elements made of composite materials show a significant improvement in the laboratory conditions of using composites in comparison with secondary structures. They are considered one of the horizontal stabilizers for decorating the Boeing 737 and Douglas DC-10 and a stabilizer of lateral stability in the vertical position. It is made of a composite stabilizer, which weighs 92.53 kg, which reduces the weight by 22% compared to metals [55].

3.4 Manufacturing Processes for Aircraft Composites

The manufacturing of composite plays a very important role at the time of designing any type of component. From the point of view of manufacturing modern fiber-reinforced composites, the main thing is to recognize that both the material and structure are made at the same time. Any defects that occur during the manufacturing process directly affect the strength and rigidity of the material and structure. Many of the manufacturing process have come into existence from the last three decades like automated tape-layup process, resin transfer molding, automated fiber placement, vacuum-assisted resin transfer molding, pultrusion, filament winding, autoclave, etc. All of the above methods have numerous things in common: that the reinforcements have been placed in the desired shape, in the tool or mold, the resin and fibers placed under high temperature and pressure to cure the resin, and the shape that will be removed from the product after the resin has cured.

3.4.1 Automated Tape Layup

The most well-founded automated manufacturing techniques for a composite are automatic tape laying. In this process, the unidirectional tapes are loaded at a partial slope and the delivery of different sizes using the loaded roller system is subject to the complexity of the fabricated part. The process diagram is as shown in Fig. 3.11 where the tapes are partially pre-bonded with adhesive resin from thermoplastic continuous strands in one direction. Further, tapes are wrapped around the reel so that they fit into the construction system. The forage unit pulls the tape from the roll and places it in the desired position on the robotic work platform or semifinished component. There, the glue is melted by heating with a laser to increase the grip. In this process, step-by-step, high-intensity continuous fiber structures are established by automated fiber placement. The single wide tape is up to 300 mm which may generally use to manufacture the part-like skin of airplane wings. The researchers, Comer et al., presented in their study that by using the automated tape layup process, the enhancement in the mechanical properties was obtained when compared to the autoclave process [56].

3.4.2 Resin Transfer Molding

It is a low temperature and low-pressure method, where the thermosetting resin is transfer into the closed mold to obtain superior quality of surface finish with improved dimensional accuracy of the composite. The process diagram is as shown in Fig. 3.12 where the mold is traditionally coated with a gel, if necessary. The mold is sealed and the reinforcement is located in the mold. Further, the resin is inserted under pressure using special inserted tools and the part is treated with mold. Reinforcement may be in the form of pattern cut roll stock material. The preform is a reinforcement that is made into a precise shape in a specific method and can be speedily molded. This process can be done under atmospheric temperature; also, the

Fig. 3.11 Automated tape laying process

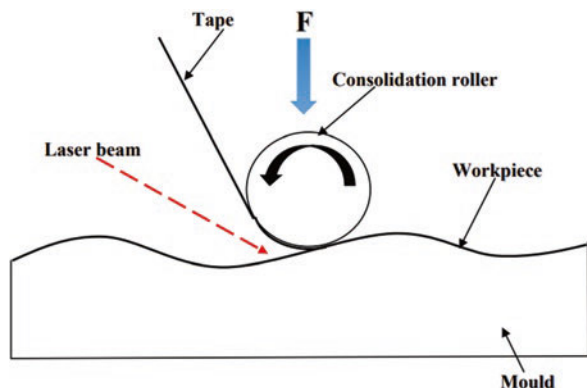


Fig. 3.12 Resin transfer molding

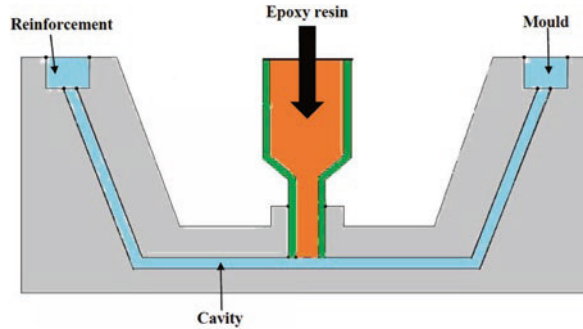
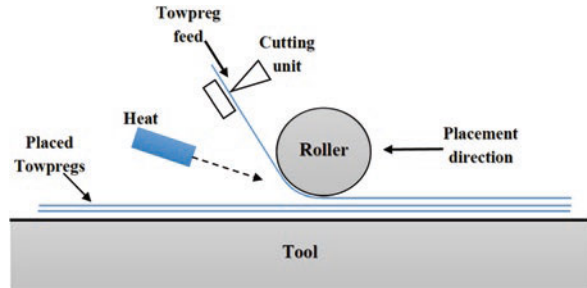


Fig. 3.13 Automated fiber placement



heated molds are necessary to accomplish fast curing time and product stability. The clamp can be completed with a circumferential clamp or press clamp [57].

3.4.3 Automated Fiber Placement

Automated fiber placement is an industrial method as shown in Fig. 3.13 that prescribes the precise placement of continuous fiber tapes for the manufacturing of multilayered composite products. In this process, usually 3–13 mm width narrow strip of tape is feed for the product to be manufactured. Tapes are fed into the head through a tape feeding system, which consists of multiple bobbins or spools with tape. These spools typically have around 1000 m of tape per bobbin. These tapes are properly placed by AFP machines according to a computer program, which is defined to provide optimal alignment of the fibers based on the expected operating load of the part being manufactured to the final product. The tape-laying head is connected to a robot, which directs the head to the correct position during the process. This process is generally used in the application related to the aircraft industry like fuselage tubs, cows with small edges, and many small/large structural parts [58].

3.4.4 Vacuum-Assisted Resin Transfer Molding

Vacuum-assisted resin transfer molding procedure as shown in Fig. 3.14 makes practice of vacuum to support resin flow in the fiber layers that are enclosed inside a mold tool protected by a vacuum bag. It is usually a top open molding device employed for the manufacturing of composite parts. In this process, the vacuum bag is placed to the top of the mold tool to regulate the continuous flow of low-pressure resin flow from one side to the other side. The composite fiber contours are compressed under the vacuum bag when the vacuum extracts air from the preform and the vacuum-assisted resin transfer molding machine on-ratio of the metered and mixes the degassed air-free resins. This process provides 60–70% fiber to resin proportion with a near-zero pore content. The most important application associated with this process is the parts manufactured like landing gears doors of airplane, turbine blades, fuselage area, etc. [59, 60].

3.4.5 Pultrusion

The pultrusion process is an extremely automated continuous fiber laminating process that produces high fiber block shapes with a fixed cross section. Having a high fiber block area is an excellent process for the production of structural components that give greater strength to the weight ratio. The process is as shown in Fig. 3.15 begins with the backing of carbon and glass fiber as a reinforcement in the form of roving. The material is drawn into the in-feed region where it is precisely formed to the required shape and capped with a resin matrix. The resin matrix can be used like epoxy, polyester, or vinyl ester for this process. Further, the impregnation reinforcement is pulled into the hot extrusion dye from the in-feed region. The cured profile that exits the die is indorsed to cool before turning and the towing units pull against each other. Puller units rotate by hand-over-hand motion, requiring a return stroke to pull smoothly at a constant speed rather than pulling force. From the pulling

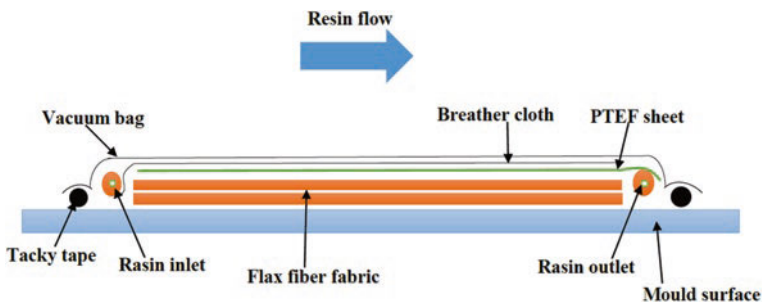


Fig. 3.14 Vacuum-assisted resin transfer molding

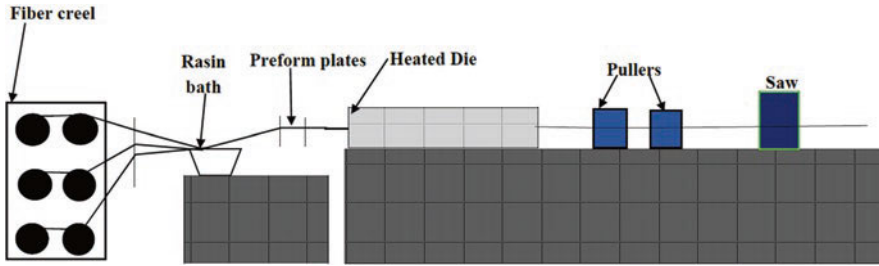


Fig. 3.15 Pultrusion process

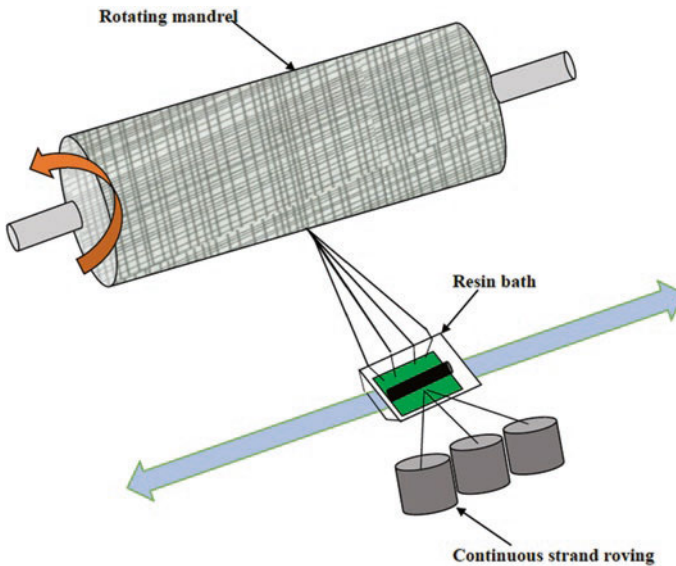


Fig. 3.16 Filament winding process

units, the profile is seen in the flying cutoff where it is cut to the necessary length [61, 62].

3.4.6 Filament Winding

The filament winding process is as shown in Fig. 3.16 produces hollow structures of unbelievable strength. In this process, the cross-weaving lines of the glass, carbon, or other fiber are added into the resin matrix, this process is used to manufacture the products that are suitable for various aircraft and other related applications. This process consists of two main components like fixed steel mandrel and carriage arm which will rotate horizontally up and down. With the help of the traveling arm

comprises of winding center which includes glass, carbon, or the mixture both are allocated on the mandrel. As the mandrel rotates, the rowing's form a composite surface on the mandrel. The particular orientation of the composite matrix is determined by the travel speed of the vehicle and the rotational speed of the mandrel, both of which are automatic. The fibers are embedded in a resin and then reinforced with fiber to form the final composite material before facing to the mandrel. The disadvantage of using a filament winding is that the mandrel is often encircled to the windings. If the cladding is made of metal or polymer, then it is used as a real problem and can be an integral part of the project, but more often than not the development has been chipped off, as the parts are eventually dismantled [63, 64].

3.4.7 Autoclave Process

In today's many applications, autoclave processes as shown in Fig. 3.17 and injection molding machines are the most often used a necessary process for the aviation industry. These processes use a pre-impregnated unidirectional plies or woven cloths that can be partially cured. The only drawback is that the prepreg can be stored in the freezer to prevent the resin from escaping. Several layers of prepreg are applied to the surface using a predetermined fiber orientation to create the desired thickness, and then coated with a layer of separation film, breathing cloth, and using a vacuum cleaner bag or silicon pressure on the bag. The air escapes from the bag to create a vacuum, and the instrument, which is heated under high temperature and pressure to cure the resins. In this process, number of layup is done and after every three to four layers there is a need to remove the air which is accumulated in the layers. This removal of air prevents the layer or the material from delamination as well as determines the thickness and dimensions. The correct shape of the cycles and the appropriate hydrostatic pressure of the hand, while the curing time, are the two main requirements for succeeding good results. As compared to other processes

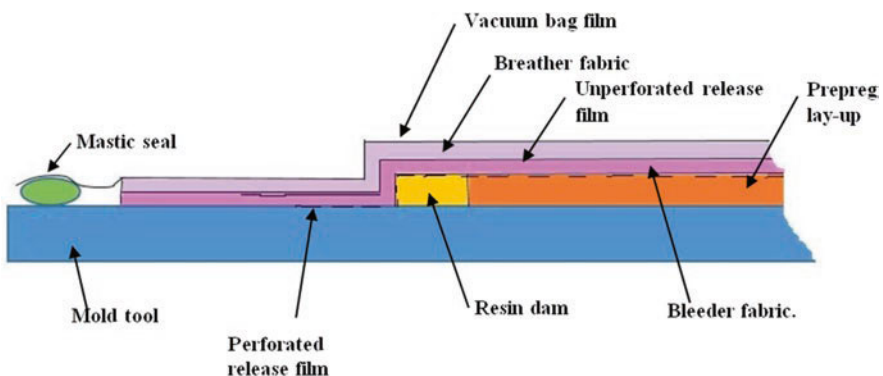


Fig. 3.17 Autoclave process for composite manufacturing

the efficiency of the machine is quite less, as more time and labor are required for bagging, stacking, and disassembling process. In addition, in the capital, the costs will be huge, and this will not limit the use of large buildings in which these costs may be required [65–67].

3.5 Conclusions

In this review article, the important thing that display is the proper selection of polymer for certain application is really important as the airplane has to sustain various types of loads and related properties when it is in running condition. As for the designing of aircraft wings, proper selection of material is very essential otherwise there is a problem with the fluttering speed. Even the fiber orientation will play a very important role at the time of manufacturing engine fan blades to diminish the vibration-related problems. The fuselage is the central part of the airplane so it should be designed in such a way that it has to carry the whole weight of the passengers. The manufacturing process for the development of aircraft components is already discussed in detail; the proper selection of the manufacturing process depends on the type of part to be manufactured. As aviation is the most advanced engineering branch so the two important things that should be considered while designing or selecting the polymer are reliability and safety. There is always a need to make polymer composite material that will provide unique properties with cost-effectiveness, because the designing of aircraft or its component is always a challenge as it requires tremendous care otherwise the significances will be hazardous and extreme.

3.6 Future Scope

In this review article, all the polymer components related to the aircraft applications are discussed in detail with their properties. By reviewing the article, the importance of composite materials is highlighted in the field of the aircraft industry. The next future of composite is bright and challenging which will present the products with extra lightweight and more efficient. In coming years, the whole aircraft will be manufactured with composite only instead of metals. At present, some of the aircraft parts are made of metals and some of the composite, which has directed to the production of important constituents by the practice of bonding and curing processes that completely restrict the practice of fasteners. In upcoming years, the focus is not only on the strength and life of the composite but also on the cost reduction. There is a need to develop the extra smart composite material so it can be used in any sort of application and also it can be fabricated in a very complex shape.

References

1. Njuguna, J., & Pielichowski, K. (2003). Polymer nanocomposites for aerospace applications: Properties. *Advanced Engineering Materials*, 5(11), 769–778.
2. Williams, G., Trask, R., & Bond, I. (2007). A self-healing carbon fibre reinforced polymer for aerospace applications. *Composites Part A: Applied Science and Manufacturing*, 38(6), 1525–1532.
3. Irving, P. E., & Soutis, C. (2019). *Polymer composites in the aerospace industry*. Woodhead Publishing.
4. Pan, Z., Wang, M., Chen, J., Shen, B., Liu, J., & Zhai, J. (2018). Largely enhanced energy storage capability of polymer nanocomposite utilizing a core-satellite strategy. *Nanoscale*, 10, 16621–16629.
5. Oliver, L. I., Anderson, T. R., & Robert, R. H. (2006). Predicting U.S. jet fighter aircraft introductions from 1944 to 1982: A dogfight between regression and TFDEA. *Technological Forecasting and Social Change*, 73(9), 1178–1187.
6. Ghori, S. W. (2018). *Sustainable composites for aerospace applications* || *The role of advanced polymer materials in aerospace*. pp. 19–34.
7. Alemour, B., Badran, O., & Hassan, M. R. (2019). A review of using conductive composite materials in solving lightning strike and ice accumulation problems in aviation. *Journal of Aerospace Technology and Management*, 11(1), 219–219.
8. Vasile, B. S., Birca, A. C., Surdu, V. A., Neacsu, I. A., & NicoarĂf, A. I. (2020). Ceramic composite materials obtained by electron-beam physical vapor deposition used as thermal barriers in the aerospace industry. *Nano*, 10(2), 370.
9. Zhang, X., Chen, Y., & Hu, J. (2018). Recent advances in the development of aerospace materials. *Progress in Aerospace Science*, 97, 22–34.
10. Soutis, C. (2020). *Polymer composites in the aerospace industry* || *Aerospace engineering requirements in building with composites*, pp. 3–22.
11. Freeman, W. T. (1993). The use of composites in aircraft primary structure. *Composites Engineering*, 3(7–8), 767–775.
12. Suhara, P., & Mohini, S. (2007). Injection-molded short hemp fiber/glass fiber-reinforced polypropylene hybrid composites—Mechanical, water absorption and thermal properties. *Applied Polymer*, 103(4), 2432–2441.
13. Di, S. R. (2015). Fibre optic sensors for structural health monitoring of aircraft composite structures: Recent advances and applications. *Sensors*, 15(8), 18666–18713.
14. Yadav, R., Tirumali, M., Wang, X., Naebe, M., & Kandasubramanian, B. (2019). Polymer composite for antistatic application in aerospace. *Defence Technology*, 16, 107–118.
15. Ma, Y., Yang, Y., Sugahara, T., & Hamada, H. (2016). A study on the failure behavior and mechanical properties of unidirectional fiber reinforced thermosetting and thermoplastic composites. *Composites: Part B*, 99, 162–172.
16. John, D., & Muzzy, A. O. (1984). Thermoplastic vs. thermosetting structural composites. *Polymer Composites*, 5(3), 169–172.
17. Dhinakaran, V., Surendar, K. V., Hasunfur Riyaz, M. S., & Ravichandran, M. (2020). Review on study of thermosetting and thermoplastic materials in the automated fiber placement process. *Materials Today: Proceedings*, 27, 812–815.
18. Yao, Y., Wang, J., Lu, H., Xu, B., Fu, Y., Liu, Y., & Leng, J. (2015). Thermosetting epoxy resin/thermoplastic system with combined shape memory and self-healing properties. *Smart Materials and Structures*, 25(1), 015021.
19. Haque, A., & Jeelani, S. (1992). Environmental effects on the compressive properties: Thermosetting vs. thermoplastic composites. *Journal of Reinforced Plastics and Composites*, 11(2), 146–157.
20. George, M. (2012). Aero engines lose weight thanks to composites. *Reinforced Plastics*, 56(6).
21. Amoo, L. M. (2013). On the design and structural analysis of jet engine fan blade structures. *Progress in Aerospace Science*, 60, 1–11.

22. Mehar, A. K. (2020). Transient effect of aircraft propeller blade by using composites. *International Journal of Engineering Research & Technology*, 9(8), 1–6.
23. Min, J. B., Duffy, K. P., Choi, B. B., Provenza, A. J., & Kray, N. (2013). Numerical modeling methodology and experimental study for piezoelectric vibration damping control of rotating composite fan blades. *Computers and Structures*, 128, 230–242.
24. Colvin, G. E., & Swanson, S. R. (1990). Mechanical characterization of IM7/8551-7 carbon/epoxy under biaxial stress. *Journal of Engineering Materials and Technology*, 112(1), 61.
25. Srinivas, Y. P., Ramalingam, T., Bari, B. S., & Sharada, P. C. (2020). Development of composite mounting bracket for aerospace applications. *Materials Today: Proceedings*, 26, 1356–1359.
26. Holmes, M. (2017). Aerospace looks to composites for solutions. *Reinforced Plastics*, 61(4), 237–241.
27. Koli, D. K., Agnihotri, G., & Purohit, R. (2015). Advanced aluminium matrix composites: The critical need of automotive and aerospace engineering fields. *Materials Today: Proceedings*, 2(4–5), 3032–3041.
28. Mun, W. C., Rivai, A., & Bapokutty, O. (2014). Design and analysis of an aircraft composite hinge bracket using finite element approach. *Applied Mechanics and Materials*, 629, 158–163.
29. Thuis, H. G. S. J., & Biemans, C. (1997). Design, fabrication and testing of a composite bracket for aerospace applications. *Composite Structures*, 38(1–4), 91–98.
30. Marsh, G. (2013). Composites poised to transform airline economics. *Reinforced Plastics*, 57(3), 18–24.
31. Scarponi, C., Santulli, C., Sarasini, F., & Tirillò, J. (2017). Green composites for aircraft interior panels. *International Journal of Sustainable Aviation*, 3(3), 252.
32. Heimbs, S., Vogt, D., Hartnack, R., Schlattmann, J., & Maier, M. (2008). Numerical simulation of aircraft interior components under crash loads. *International Journal of Crashworthiness*, 13(5), 511–521.
33. Retrieved March 23, 2021, from <http://www.matweb.com/search/GetMatlsByTradename.aspx?navletter=C&tn=CYCOM%C2%AE>.
34. Retrieved March 26, 2021, from <https://www.stratasydirect.com/industries/aerospace/3d-printing-transforming-aircraft-interiors>.
35. Retrieved March 26, 2021, from <https://www.lucintel.com/aircraft-interior-composites-market.aspx>.
36. Kozaczuk, K. (2017). Engine nacelles design—Problems and challenges. *Proceedings of the Institution of Mechanical Engineers, Part G: Journal of Aerospace Engineering*, 231(12), 2259–2265.
37. Kalagi, G. R., Patil, R., & Nayak, N. (2018). Experimental study on mechanical properties of natural fiber reinforced polymer composite materials for wind turbine blades. *Materials Today: Proceedings*, 5(1), 2588–2596.
38. Kidangan, R. T., Venkata, K., & Balasubramaniam, K. (2020). Detection of dis-bond between honeycomb and composite facesheet of an Inner Fixed Structure bond panel of a jet engine nacelle using infrared thermographic techniques. *Quantitative InfraRed Thermography Journal*, 1–15.
39. McGarel, W., & Campbell, K. (1990). SAE Technical Paper Series [SAE International Aerospace Technology Conference and Exposition—(OCT. 01, 1990)] SAE Technical Paper Series, *Development of Composite Materials Applications to Production Nacelle Component Structures*, 1.
40. Dudziak, J., Guła, P., Gawlik, A., & Kondracki, J. (2017). Design and manufacture of nacelles for small turboprop aircraft. *Proceedings of the Institution of Mechanical Engineers, Part G: Journal of Aerospace Engineering*, 231(12), 2239–2247.
41. Santhosh Kumar, K. S., Reghunadhan Nair, C. P., Sadhana, R., & Ninan, K. N. (2007). Benzoxazine–bismaleimide blends: Curing and thermal properties. *European Polymer Journal*, 43(12), 5084–5096.

42. Der-Jang, L., Kung-Li, W., Ying-Chi, H., Kueir-Rarn, L., Juin-Yih, L., & Chang-Sik, H. (2012). Advanced polyimide materials: Syntheses, physical properties and applications. *Progress in Polymer Science*, 37(7), 907–974.
43. Haddadpour, H., Kouchakzadeh, M. A., & Shadmehri, F. (2008). Aeroelastic instability of aircraft composite wings in an incompressible flow. *Composite Structures*, 83(1), 93–99.
44. Smith, F., & Grant, C. (2006). Automated processes for composite aircraft structure. *Industrial Robot: An International Journal*, 33(2), 117–121.
45. Wölcken, P. C., & Papadopoulos, M. (Eds.). (2015). *Smart intelligent aircraft structures (SARISTU): Proceedings of the final project conference*. Springer.
46. Retrieved March 26, 2021, from <https://eandt.theiet.org/content/articles/2020/03/making-future-aircraft-wings-through-composites-manufacturing/>.
47. Manan, A., & Cooper, J. (2009). Design of composite wings including uncertainties: A probabilistic approach. *Journal of Aircraft*, 46(2), 601–607.
48. Retrieved March 26, 2021, from <https://www.eaircraftsupply.com/MSDS/93251Cytac%20CYCOM%20890%20RTM%20tds.pdf>.
49. Mou, H., Xie, J., & Feng, Z. (2020). Research status and future development of crashworthiness of civil aircraft fuselage structures: An overview. *Progress in Aerospace Science*, 119, 100644.
50. Richard, D., Raimund, R., Rolf, Z., & Klaus, R. (2006). COCOMAT—Improved material exploitation of composite airframe structures by accurate simulation of postbuckling and collapse. *Composite Structures*, 73(2), 175–178.
51. Mabson, G., Flynn, B., Ilcewicz, L., & Graesser, D. (1994). [American Institute of Aeronautics and Astronautics 35th Structures, Structural Dynamics, and Materials Conference—Hilton Head, SC, U.S.A. (18 April 1994–20 April 1994)] 35th Structures, Structural Dynamics, and Materials Conference—*The use of COSTADE in developing composite commercial aircraft fuselage structures*.
52. Zimmermann, R., & Rolfes, R. (2006). POSICOSS—Improved postbuckling simulation for design of fibre composite stiffened fuselage structures. *Composite Structures*, 73(2), 171–174.
53. Al-Ahmed, S., & Fielding, J. P. (1999). Vulnerability prediction method for use in aircraft conceptual design. *The Aeronautical Journal*, 103(1024), 309–315.
54. Quatmann, M., & Reimerdes, H. G. (2011). Preliminary design of composite fuselage structures using analytical rapid sizing methods. *CEAS Aeronautical Journal*, 2(1–4), 231–241.
55. Bohon, H. L. (1982). Opportunities for composites in commercial transport structures. *Advanced Materials Technology, NASA, CP-2251*, 1–27.
56. Comer, A. J., Ray, D., Obande, W. O., Jones, D., Lyons, J., Rosca, I., O’Higgins, R. M., & McCarthy, M. A. (2015). Mechanical characterisation of carbon fibre–PEEK manufactured by laser-assisted automated-tape-placement and autoclave. *Composites Part A: Applied Science and Manufacturing*, 69, 10–20.
57. Laurenzi, S., & Marchetti, M. (2012). Advanced composite materials by resin transfer molding for aerospace applications. *Composites and Their Properties*, 197–226.
58. Denkena, B., Schmidt, C., & Weber, P. (2016). Automated fiber placement head for manufacturing of innovative aerospace stiffening structures. *Procedia Manufacturing*, 6, 96–104.
59. Nguyen, N. Q., Mehdikhani, M., Straumit, I., Gorbatikh, L., Lessard, L., & Lomov, S.V.(2017). Micro-CT measurement of fibre misalignment: Application to carbon/epoxy laminates manufactured in autoclave and by vacuum assisted resin transfer moulding. *Composites Part A: Applied Science and Manufacturing*, 104, 14–23.
60. Chensong, D. (2008). A modified rule of mixture for the vacuum-assisted resin transfer moulding process simulation. *Composites Science and Technology*, 68(9), 2125–2133.
61. Kathleen, V. V., & Paul, K. (2001). Thermoplastic pultrusion of natural fibre reinforced composites. *Composite Structures*, 54(2–3), 355–360.
62. Miller, A. H., Dodds, N., Hale, J.M., & Gibson, A.G. (1998). High speed pultrusion of thermoplastic matrix composites. *Composites Part A: Applied Science and Manufacturing*, 29(7), 0–782.

63. Abdalla, F. H., Mutasher, S. A., Khalid, Y. A., Sapuan, S. M., Hamouda, A. M. S., Sahari, B. B., & Hamdan, M. M. (2007). Design and fabrication of low cost filament winding machine. *Materials and Design*, 28(1), 234–239.
64. Lossie, M., & Van Brussel, H. (1994). Design principles in filament winding. *Composites Manufacturing*, 5(1), 5–13.
65. Hubert, P. (2012). Manufacturing Techniques for Polymer Matrix Composites (PMCs). In *Autoclave processing for composites*, (pp. 414–434).
66. Wang, Q., Wang, L., Zhu, W., Xu, Q., & Ke, Y. (2017). Design optimization of molds for autoclave process of composite manufacturing. *Journal of Reinforced Plastics and Composites*, 36, 1564–1576.
67. Park, S. Y., Choi, C. H., Choi, W. J., & Hwang, S. S. (2018). A comparison of the properties of carbon fiber epoxy composites produced by non-autoclave with vacuum bag only prepreg and autoclave process. *Applied Composite Materials*, 26, 187–204.

Chapter 4

Advanced Fibrous Composites for Aircraft Application



Mahdi Hasanzadeh and Shahram Mahboubi Zadeh

Nomenclature

AF	Aramid fiber
CF	Carbon fiber
CFRP	Carbon fiber–reinforced polymer composites
CNTs	Carbon nanotubes
CVD	Chemical vapor deposition
FRP	Fiber-reinforced polymer or plastics
FRPC	Fiber-reinforced polymer or plastic composites
GF	Glass fiber
GFRP	Glass fiber–reinforced polymer composites
HDPE	High-density polyethylene
LDPE	Low-density polyethylene
LLDPE	Linear low-density polyethylene
MWCNT	Multi-walled carbon nanotubes
NF	Natural fiber
PE	Polyethylene
PEEK	Polyether ether ketone
PET	Polyethylene terephthalate
PI	Polyimide
PL	Polyester
PMMA	Poly(methylmethacrylate)

M. Hasanzadeh (✉)
Department of Textile Engineering, Yazd University, Yazd, Iran
e-mail: m.hasanzadeh@yazd.ac.ir

S. M. Zadeh
Department of Materials Science and Engineering, Islamic Azad University, Science and Research Branch, Tehran, Iran

PP	Polypropylene
PS	Polystyrene
PU	Polyurethane
PVC	Polyvinyl chloride
PVD	physical vapor deposition
RTM	Resin transfer molding
TPCs	Thermoplastic composites
UHMWPE	Ultrahigh molecular weight polyethylene
VARTM	Vacuum-assisted resin transfer molding

4.1 Introduction

The use of fibrous composites in the manufacture of aircraft parts developed around the 1980s, due to their superior properties such as high specific modulus and high specific strength. But it took several years for buildup of confidence in this new class of materials and their use in aircraft structures as compared to their metallic counterparts like aluminum and its alloys [1–3]. In recent years, owing to the advancements made in material design and manufacturing technology, increasing attention has been paid to polymer-based fibrous composites as compared to metals and their alloys. Generally, reducing the weight of the structure with simultaneous increase of the strength and stiffness are considered as most important goals for the development and application of fibrous composite materials in aircraft structures.

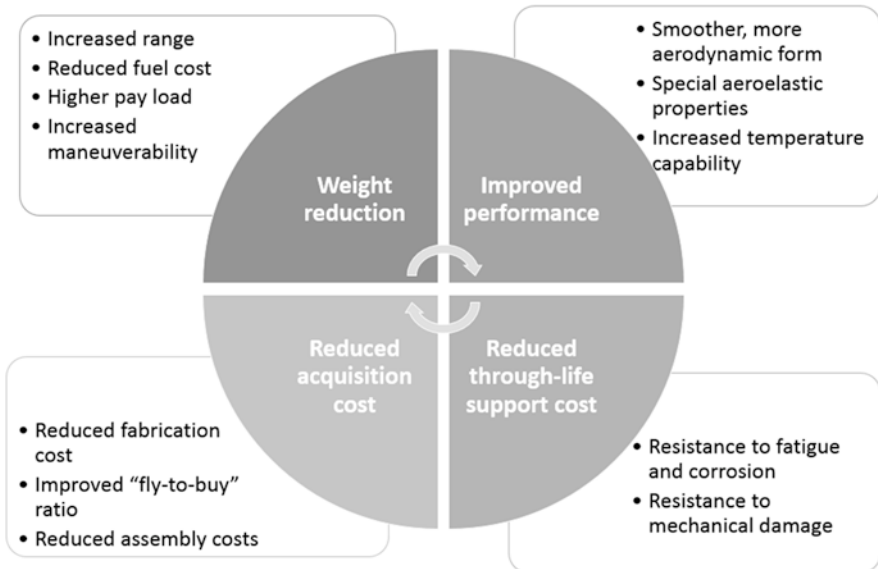


Fig. 4.1 The criteria for manufacturing and application of new materials in the aircraft industry

Other important factors in choosing new fibrous composite materials are durability, their resistance to cyclic stress, and their endurance against environmental degradation and damage [4, 5]. Figure 4.1 summarizes the criteria for manufacturing and application of new materials in aerospace industry, along with their implications and benefits.

Fibrous composite materials generally consist of fiber as a reinforcement and matrix as a binder. The matrix transfers the applied stress to the fibers by holding them together and filling the voids between them [6].

This chapter reviews the design, fabrication, and development of fibrous composite structures for aircraft applications. The properties, advantages, and drawbacks of fibrous composites for application in aircraft structures are also presented, along with the discussion on various fibrous preforms and their production methods.

4.2 Fibrous Composite Structures

4.2.1 *Fibrous Materials*

Several fibrous materials have been used for composite fabrication. Among several fibers that are used in various applications, only those fibers that exhibit high strength, stiffness, heat resistance, or chemical resistance are suggested for the fabrication of composite materials used in aircraft structures [5, 7–9]. These fibers, termed as high-performance fibers, generally exhibit higher tenacity and higher modulus than standard fibers. Carbon, aramid, and glass fibers are the most important high-performance fibers utilized for the fabrication of aircraft composites.

Carbon fibers are the most common high-performance fibers. They have been widely used in high-tech industries particularly in aircraft applications. Polyacrylonitrile (PAN) and pitch are the most common precursors for producing carbon fibers. The properties of carbon fibers depend on their carbon source.

Aramids are another type of high-performance fibers generally synthesized using aromatic diamines and diacids. They are categorized into two categories, i.e., the meta-aramid fiber (Nomex) which is highly resistant to temperature and chemical degradation, and the para-aramid fiber (Kevlar) with high tensile strength, modulus, and toughness. Meta- and para-aramid fibers are generally used for heat-resistant clothing and ballistic protection composites, respectively.

Glass fiber is another conventional fiber that is mostly used for the fabrication of composite materials. There are various types of glass fibers according to the percentage of ingredients. E-glass and S-glass are the two most common glass fibers with general-purpose glass for low electrical conductivity, and for high strength applications, respectively.

Ultrahigh molecular weight polyethylene (UHMWPE) fiber is generally manufactured through gel spinning process and is composed of very long chains of polyethylene with a very high degree of orientation and crystallinity. UHMWPE fibers exhibited high strength and high resistance to abrasion and chemicals. These

features make these fibers a suitable candidate for many applications such as body armor and climbing ropes. Table 4.1 compares the physical properties of several high-performance fibers [10–14].

4.2.2 Fibrous Architectures

A fiber, as the most important group of one-dimensional reinforcements, can form various types of 1D, 2D, and 3D fibrous architectures. These architectures are generally classified in different ways either based on the dimensions, the textile processing techniques, or based on the chemical structure and nature. The fibrous materials which have been considered useful in aircraft applications include carbon fibers, glass fibers (E-glass, S-glass), and aramid fibers [15]. The carbon/epoxy and glass/phenolic composites are the most common fibrous composite structures used in aircraft applications. The former is used in major load-bearing structures, while the latter is used in cabin furnishings and amateur-built aircraft structures. These fibrous composites are formed laminated structures, which are produced by bonding together. The required strength for a particular structure is attained by adjusting the thickness of the laminate [11, 16–18].

Several fibrous architectures have been used for the fabrication of composite structures, including woven, knitted, and braided fabrics in 2D and 3D structures [7, 13, 19–25]. Table 4.2 summarizes the characteristics of fibrous architectures based upon their type and textile processing technique.

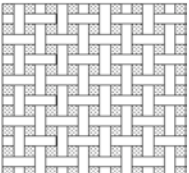
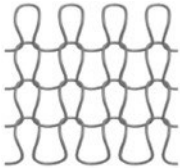


Nonwoven Fabrics

Nonwoven fabric is defined as sheet, web, or batt structures made of entangled fibers or continuous filaments bonded together by using mechanical, chemical, or thermal means. The nonwoven properties such as strength, flexibility, porosity, and

Table 4.1 Specific properties of common high-performance fibers [5]

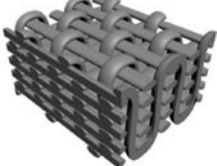

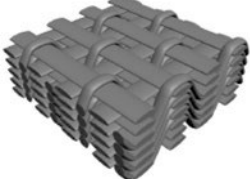



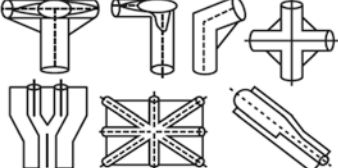
Fiber	Young's modulus (GPa)	Tensile strength (GPa)	Elongation (%)	Density (g/cm ³)
E-glass	70	2–3.5	2.5	2.5
S-glass	86	4.57	2.8	2.5
Carbon	40–230	4	1.4–1.8	1.4
Kevlar (aramid)	63–67	3–3.15	3.3–3.7	1.4
Basalt	89	4.84	3.15	2.7
SiC	190	2.8	–	2.3
Nylon 6 (dry)	18–40	4.2–5.7	28–45	1.14
Polyethylene (dry)	–	4.4–7.9	8–35	0.94–0.96

Table 4.2 The characteristics of fibrous architectures [7, 23]

Dimension	Fibrous architectures	Different structures	Schematic
2D	Woven fabric	<ul style="list-style-type: none"> • Plain • Twill • Satin 	
	Knitted fabric	<ul style="list-style-type: none"> • Weft-knitted • Warp-knitted 	
	Braided structures	<ul style="list-style-type: none"> • Diamond • Regular • Hercules 	
	Non-woven		



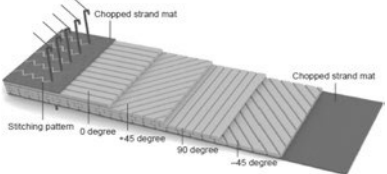

(continued)

Table 4.2 (continued)

Dimension	Fibrous architectures	Different structures	Schematic
3D	3D solid woven fibrous structures	Orthogonal	
		Through-thickness angle interlock	
		Layer-to-layer angle interlock	
		Fully interlaced	
3D hollow woven fibrous structures	3D hollow woven fibrous structures	Spacer structure	
		Honeycomb structure	
3D nodal woven fibrous structures	3D nodal woven fibrous structures		

(continued)

Table 4.2 (continued)

Dimension	Fibrous architectures	Different structures	Schematic
	3D braided structures		
Hybrid architectures	Combining woven and knitted fabrics		 <ul style="list-style-type: none"> → Stitching thread → Woven fabric → Knitted fabric → Knitted fabric → Woven fabric → Stitching thread
	Combining nonwoven fabric and DOS		 <p>Chopped strand mat</p> <p>Stitching pattern: 0 degree, +45 degree, 90 degree, -45 degree</p> <p>Chopped strand mat</p>
	Hybrid co-woven-knitted structure		 <ul style="list-style-type: none"> Warp inserted yarn Weft inserted yarn 1 × 1 rib stitch Unit cell

density are controlled by the extent of bonding. Mechanical bonding includes needle punching, stitchbonding, and hydroentanglement techniques in which the fibers are entangled by reciprocating barbed needles, stitching yarns, and high-velocity water jets, respectively. Chemical bonding applies adhesive binders to the web, while in thermal bonding heat and pressure are applied.

Woven Fabrics

Woven fabric is generally formed by interlacing two or more sets of yarns. The yarns that run along the length of the fabric are called warp and ones that are normal to the direction of the warp are referred to as weft. The warp and weft yarns can be interlaced in various weave structures, including plain, twill, and satin weaves. In 2-D weave structures, the warp and weft yarns are interlaced at an angle of 90°. The plain weave is the simplest woven structure with relatively good fabric stability in which each warp yarn alternately crosses over and under each weft yarn. Twill and satin weaves are other common weave structures, in which each weft yarn goes over and under multiple warp yarns. A reduced amount of interlacing and fewer

intersections with more open construction are characteristics of twill and satin weave structures. They have a lower degree of interlacing, lower fiber crimp, and better packaging density than the plain weave. The drapability, formability, and in-plane properties of these structures are also better than the plain weave. Compared to 2D weave structures, triaxial weaves involving three sets of yarns with an angle of 60° possess exceptional mechanical properties in several directions. A basket weave has two or more warp yarns interlacing with two or more weft yarns, forming closer structures. These weaving structures exhibit high shear resistance as the interlacing points are fixed into the fabric. However, their reinforcing efficiency is less when compared with absolutely straight fibers, due to the periodic out-of-plane undulation of the fibers in the woven structures. A number of hybrid structures can be formed by woven fabrics. For example, a woven fabric could be made from aramid fibers in the warp direction and carbon or glass fibers in the weft direction. Hybrid structures are synthesized to meet the desired conditions from the perspective of required properties and/or cost constraints.

Knitted Fabrics

Knitted fabric is formed by interlacing loops, as the basic construction unit, in the transverse or longitudinal direction. Two types of knitted structures are weft-knitted and warp knitted. In weft-knitted structures, the loops are formed along the fabric width, while in warp-knitted fabrics the loops are in the longitudinal directions. The weft-knitted have four primary structures including plain, rib, interlock, and purl. The length of the yarn in a loop and the total number of loops in a given fabric area are the most important parameters of knitted structures for composite applications. Weft-knitted fabrics are commonly used in the clothing industry, while warp-knitted structures are suitable for manufacturing composite structures. These structures possess high energy absorption and dissipation, due to the high extensibility under tension, which makes them suitable for composite applications. The knitted structures with inserted weft yarns (weft-inserted warp-knitted) are in special interest for technical applications.

Braided Fabrics

A braided fabric is produced by orthogonally interlacing two or more sets of yarns in a diagonal formation, resulting in an integral structure in a tabular form. Generally, there are three braided structures: diamond, regular, and hercules. The most common and simplest braided structure is the regular braid. The braid angle, cover factor, and the volume percent of longitudinal yarns in the structure are the most important parameters of braided structures. The braid angle, which is the angle of intertwining, can vary between 10° and 80° . Due to the size of braiding machines, the widths of braided fabric are normally limited compared to woven fabrics. Hence, they are suitable for manufacturing components with small cross sections.

Three-Dimensional Textiles Preforms

Two-dimensional textile laminates have lower impact damage resistance and through-thickness mechanical properties, which make their application in aircraft structures rather questionable. Three-dimensional textiles exhibit improved inter-laminar properties and damage tolerance through-the-thickness reinforcement. They can be woven, knitted, or braided and formed to near-net shape with complex architecture. They also improve the 3D structural homogeneity and provide better through-thickness mechanical properties. Their specific properties such as inter-laminar shear force, mechanical, and thermal stability are expressed along all three spatial axes. The waste of expensive materials and manufacturing costs, particularly for complex-shaped components, is also reduced in 3D architectures. Therefore, tremendous attention has been paid to 3D fibrous architectures for manufacturing composite structures [25–30].

3D fibrous architectures with various geometrical features could be constructed through weaving technology. They are generally classified into four categories; solid, hollow, shell, and nodal (Fig. 4.2). The orthogonal, angle-interlock, and fully interlaced weaves are the most common architectures of solid 3D woven structures. 3D hollow woven structures are also of two types; spacer structure and honeycomb structure. 3D shell woven structures can be created generally by using different weaving patterns, resulting in double curvatures in fabric. 3D nodal fabrics are also a network structure joined by different tubular members for special application. The complex near-net shaped preforms, with tailored properties for specific applications, could be produced through 3D weaving. These structures exhibit better

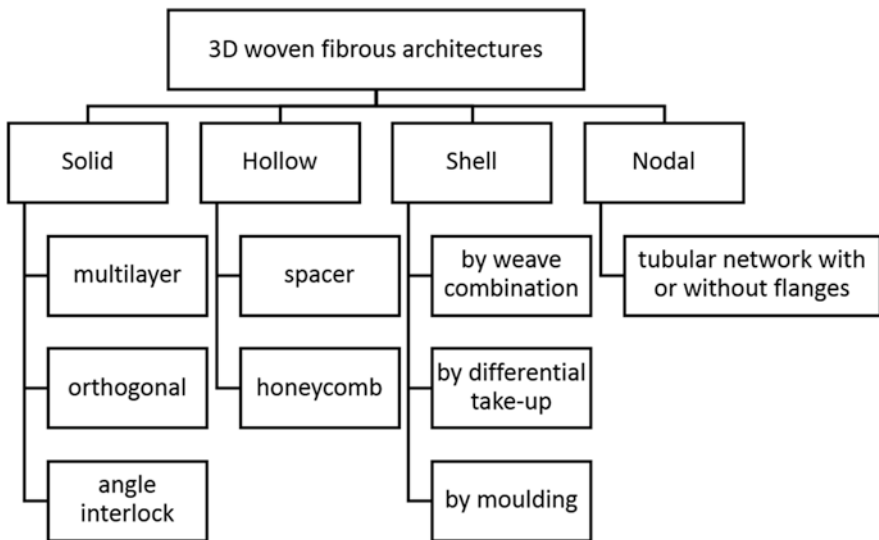


Fig. 4.2 Classification of 3D woven fibrous architectures

delamination resistance, higher tensile strain-to-failure values, and higher interlaminar fracture toughness.

3D knitted fabrics are generally produced by integrally weft-knitting and multi-axial warp-knitting (MWK) processes. The net-shape tubular structures could be easily produced by weft-knitting; however, due to the low mechanical performance, their wide-scale application in composite structures is limited. On the other hand, multi-axial warp-knitted structures are considered more promising for composite applications. Multi-axial warp-knitted structures, also known as non-crimp structures, consist of straight and in-plane fibers that are bonded by a through-the-thickness loop system. The non-crimp nature of MWK structures confirms the effective translation of yarn-to-fabric strength properties. 3D knitted fibrous structures exhibit better formability, and more complex near-net-shape preforms could be produced through 3D knitting processes. About 30% reduction in yarn materials is justifiable, which could provide lower specific density with higher energy absorption properties. They have good dimensional stability allowing facile handling in the composite manufacturing processes. Close fiber packing and dense structures provide higher fiber volume fraction and low resin consumption. Hence, the composite exhibits good mechanical properties.

3D braided fabrics are produced by the intertwining or orthogonal interlacing of two or more yarn systems to form an integral structure. These structures are capable of manufacturing near-net-shape preforms with high damage-resistant properties. A wide variety of complex structural shapes could be manufactured by 3D braiding, providing axial, flexural, and torsional resistance. The process could be automatically controlled leading to the increasing production and quality of preforms. Better delamination resistance is also observed in 3D braided composites.

4.2.3 *Matrices*

Different types of matrices could be used in composite materials, including polymers, ceramics, and metals. Polymeric matrices are generally used for the fabrication of fibrous composites [31–33]. They protect the fibers from the environment and bond fibers together to prevent the failure of adjacent failed fibers. They also transfer the applied load into and out of the fibers [34]. There are two main types of polymer matrices, i.e., thermoplastics and thermosets [31, 35, 36]. Table 4.3 summarizes the physical characteristics of thermoplastic and thermoset matrix. Epoxy, unsaturated polyester, vinyl ester, and phenolics are the main thermosetting matrices, while polypropylene (PP), polyethylene (PE), polyamide (PA), polyester (PET), polystyrene (PS), polyetheretherketone (PEEK), polyetherketone (PEK), and polyimide are some thermoplastic matrices. Thermosetting polymers are generally formed with three-dimensional crosslinking networks, by curing in the presence of heat and pressure. They generally have relatively low failure strains, resulting in poor resistance to mechanical impact damage. Fabrication of composites at relatively low temperatures and pressures is the main advantage of thermosetting

Table 4.3 Physical characteristics of thermoplastic and thermoset polymer matrices

Polymer matrix		Density (g/cm ³)	Elongation (%)	Tensile strength (MPa)	Young's modulus (GPa)	Impact strength (J/m)
Thermoplastic	Polyether ether ketone (PEEK)	1.3–1.35	2–130	100	3.5–4.4	70–20
	Polyethylene	0.9–1	350	20–35	0.7–1.4	1064
	High-density polyethylene (HDPE)	0.9–1.0	150.0	14.5–38	0.4–1.5	26.7–1028
	Low-density polyethylene (LDPE)	0.94–0.96	90–800	40–78	0.055–0.38	≥854
Thermoplastic	Polystyrene (PS)	1.04–1.06	1–2.5	25–69	4–5	1.1
	Polypropylene (PP)	0.899–0.920	15–700	26–41.1	95–1.77	21.4–267
	Polyethylene terephthalate (PET)	1.5–1.6	300	55–159	2.3–9	–
	Polyether ketone (PEK)	1.2–1.4	20	100–110	3.5	–
	Poly(methyl methacrylate) (PMMA)	1.1–1.2	2.5	72.4	3	–
	Polypropylene (PP)	0.9–1.3	80	35.8	1.6	–
	Polyvinyl chloride (PVC)	1.3–1.5	50–80	52–90	3–4	–
Thermoset	Epoxy (EP)	1.2–1.4	1–6	50–110	2.5–5	0.3
	Polyester	1.1–1.4	2	35–95	1.6–4.1	0.15–3.2
	Phenolic	1.2–1.4	–	35–60	2.7–4.1	–

polymers. Despite thermosetting matrices, the process of thermoplastic ones is reversible. Hence, short processing times, unlimited shelf-life, and thermoformability are the advantages of thermoplastic matrices over thermosetting resins. However, they are generally more expensive. Thermoplastic polymers have much higher strains to failure and are suitable for aircraft applications, particularly in areas subject to mechanical damage. Processing with thermoplastic polymers is based on resin-fiber infusion and prepreg techniques. Generally, the fibers are coated with resin followed by consolidation under high temperature and pressure. Table 4.4 compares the advantages and limitations of thermoplastic and thermoset polymer matrices.

4.2.4 Fabrication of Fibrous Composites

Figure 4.3 shows the schematic criteria for the development of high-performance fibrous composites. Orienting the fibers in the matrix in appropriate direction and optimum proportion is the key factor for the fabrication of fibrous composite structures with desired mechanical properties. The forming process should also produce suitable shape as well as desired properties of the structure. The fibers should disperse evenly throughout the matrix without significant voiding. The appropriate infiltration of aligned fibers with a liquid matrix is the simplest method for satisfying the requirements. This method is known as liquid molding, which is subcategorized into several methods according to the process conditions. Another common method is known as prepreg (pre-impregnated), in which the sheets of aligned fibers are pre-coated with matrix precursor and the resulting matrix will be formed by curing (for thermoset resin) and consolidation under appropriate conditions of temperature.

There are several techniques for the fabrication of fibrous composite materials [17, 21, 37–40]. Laminating woven fabrics or aligned fibers sheets with oriented fibers in appropriate direction are the main approaches for fabricating aircraft structures. The methods used for manufacturing fibrous composites are dependent upon the type of matrix, i.e., thermosetting or thermoplastic polymers. For instance, the methods such as hand layup, resin transfer molding (RTM), autoclave molding, compression molding, filament winding, resin infusion, and pultrusion are the most commonly used techniques for thermosetting polymers. On the other hand, injection molding and thermoforming are generally used for thermoplastic matrix. The form of fibrous materials, their volume fraction, the dimension, and shape of composite structure are other important factors for determining the manufacturing technique. Table 4.5 summarizes the advantages and disadvantages of common fabrication methods.

Table 4.4 Comparison of thermoplastic and thermoset polymer matrices

	Thermoset	Thermoplastic
Advantages	<ul style="list-style-type: none"> • Low resin viscosity • Good fiber wetting • Strong durable chemical bond • Resistance to chemical and environmental conditions 	<ul style="list-style-type: none"> • Fast processing • Recyclable • Re-processable • Post-formable • Tough • Resistance to humidity and harsh environment • No curing required
Disadvantages	<ul style="list-style-type: none"> • Brittle • Nonrecyclable • Not post-formable • Curing required 	<ul style="list-style-type: none"> • Poor melt flow • Weak adhesive bond
Manufacturing technique	<ul style="list-style-type: none"> • Resin transfer molding • Filament winding • Pultrusion 	<ul style="list-style-type: none"> • Injection • Compression • Extrusion

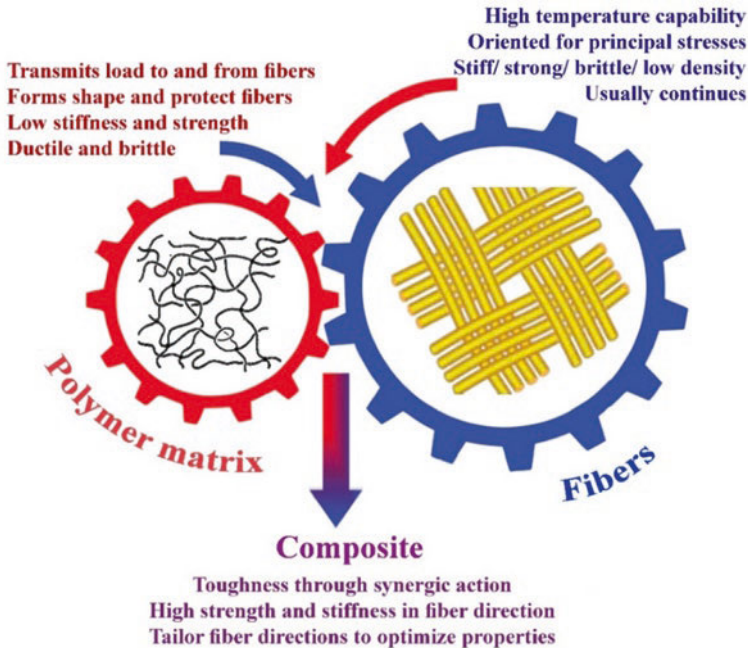


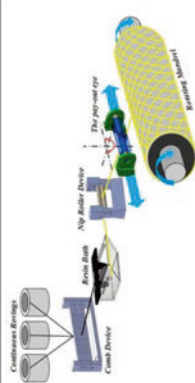
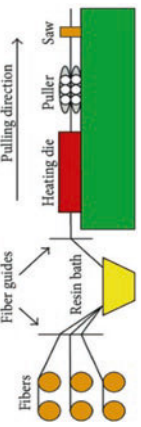
Fig. 4.3 Schematic criteria for the development of high-performance fibrous composites

The simplest and most common manual technique for manufacturing fibrous composite is hand layup, in which no expensive equipment is required. First, surface-release agents are applied on the surface of the mold for easy removal of molded products. Then, the fibrous reinforcement is placed within the mold, followed by the application of polymer matrix on the surface of fibrous structures. After removing the entrapped air, the procedure is repeated until the appropriate number of reinforcement layers are laid and the desired thickness is achieved. Finally, the product is cured followed by removing it from the mold. Utilizing autoclave, as a high temperature and pressure vessel, could enhance the curing of polymer matrix and removing the air bubbles. Easy fabrication of large and complex parts in a very short time is the main advantage of the hand layup technique. On the other hand, the necessity of low viscosity of resin for workability and skill-dependent quality is considered the main limitation of this technique. To overcome the limitations, vacuum bagging process is considered as an extension of the wet layup process. The vacuum bagging process is carried out by sealing a plastic film over the wet laidup laminate and onto the tool followed by extracting the air under the bag by applying vacuum. Then the laminate cures and the resin are spread throughout the laminate evenly. Absorption of extra resin by laminates and better volume fraction of fiber to resin can be achieved by this approach.

Another most popular manufacturing technique is resin transfer molding consisting of male and female parts. The fibrous reinforcements are stacked inside the

Table 4.5 Comparison of different composite manufacturing techniques [5, 7]

Technique	Advantages	Disadvantages	Schematic representation
Hand layup	<ul style="list-style-type: none"> • Low-cost tools • Versatile (wide range of product) 	<ul style="list-style-type: none"> • Time-consuming • Inconsistency • Skill-dependent quality • Easy air bubble forming • Health risks 	
Pre-preg forming	<ul style="list-style-type: none"> • Controlling the orientation of fiber • Consistency • High productivity 	<ul style="list-style-type: none"> • Limited shelf time • Delamination 	
Pressure molding	<ul style="list-style-type: none"> • Wide range of shape • Integrate parts • Consistency • Structural stability 	<ul style="list-style-type: none"> • High cost of the instrument • Time-consuming • Expensive molds 	
Vacuum bagging	<ul style="list-style-type: none"> • Simple design • Any fiber/matrix combination • Better quality for the cost 	<ul style="list-style-type: none"> • Low pressure • Inconsistency • Low speed 	
Resin transfer molding	<ul style="list-style-type: none"> • Low resultant void • Tooling cost comparatively low • Uniform thickness and fiber loading • Producing near shape molding • Automated process • Both sides finished • Using low-pressure injection • Good surface finishing on both sides 	<ul style="list-style-type: none"> • Long curing time • Hard for intricate part • High scrap rate • high cost • Lack of repeatability 	

Technique	Advantages	Disadvantages	Schematic representation
Filament winding	<ul style="list-style-type: none"> • High production rate • Reproducibility • Continuity of fiber over the whole structure • Cost-effectiveness 	<ul style="list-style-type: none"> • Limited spinning speed • The limited shape of the product • Insufficient surface finish 	
Pultrusion	<ul style="list-style-type: none"> • Automated process • High speed • Versatile cross-sectional shape • Continuous reinforcement • Less amount of scrap • Minimum kinking of material 	<ul style="list-style-type: none"> • The complex design of the die • Expensive die • Insufficient curing and fiber wetting • Mainly thermoset matrix 	

female part of the mold. After closing the male part, the polymer matrix is pumped into the mold cavity and filled. Finally, the resin is allowed to cure and the composite structure is removed after the opening of the mold. The procedure could be assisted by a vacuum to remove the entrapped air and facilitate the wetting of the fabric with a polymer matrix. When this process is assisted by vacuum, it is termed as VARTM (vacuum-assisted resin transfer molding). Manufacturing complex and high-performance structures with a suitable surface finish are the advantages of RTM. However, high scrap rate, high cost, and lack of repeatability particularly for complex shapes are the main disadvantages of this technique.

Filament winding is used for producing fibrous composite structures with a cylindrical shape. Fiber rovings are impregnated with polymer matrix followed by winding on a rotating mandrel. Up to 70% fiber volume fraction can be obtained by this method. The direction and pattern of winding can be controlled through the fiber feeder and speeds of the mandrel, respectively. The final properties of the composite structure are adjusted by the fiber volume ratio and winding angle. The main advantages of this process are high production rate, reproducibility, continuity of fiber over the whole structure, and cost-effectiveness. Moreover, the orientation of continuous fibers and their best layup, to meet the desired stress condition, can be accurately controlled. However, the winding angles and insufficient surface finish are the main drawbacks of this approach.

Manufacturing long composite profiles of constant cross section are generally performed through pultrusion. The fibers are impregnated with a polymer matrix by pulling from a creel through a resin bath. Then, the treated fibers are pulled through a heated die for curing. This method is fast and a high fiber volume fraction can be achieved. High production speed, less amount of scrap, and minimum kinking of material are the main advantages, while the fiber rupturing, complex design of die, and insufficient curing and fiber wetting are the limitations of this technique.

4.2.5 Interface of Fiber and Matrix

The fiber–matrix interface plays a critical role in composite performance. Transferring the load from matrix to fibrous reinforcement and distributing it across the composite structure is the main role of the fiber–matrix interface. Chemical bonding, intermolecular interactions, and mechanical interlocking are the main approaches for providing the fiber–matrix interface. It is known that diffusive and electrostatic adhesions are not common in polymer composites. One of the most common types of adhesion in polymer composites is physical adhesion, on account of Van der Waals force, arising from the intermolecular forces between the fibers and polymer matrix. Chemical adhesion, as the strongest form of adhesion, represents chemical bonding between the fibers and polymer matrix. Mechanical adhesion refers to the interlocking and entanglement of fibers

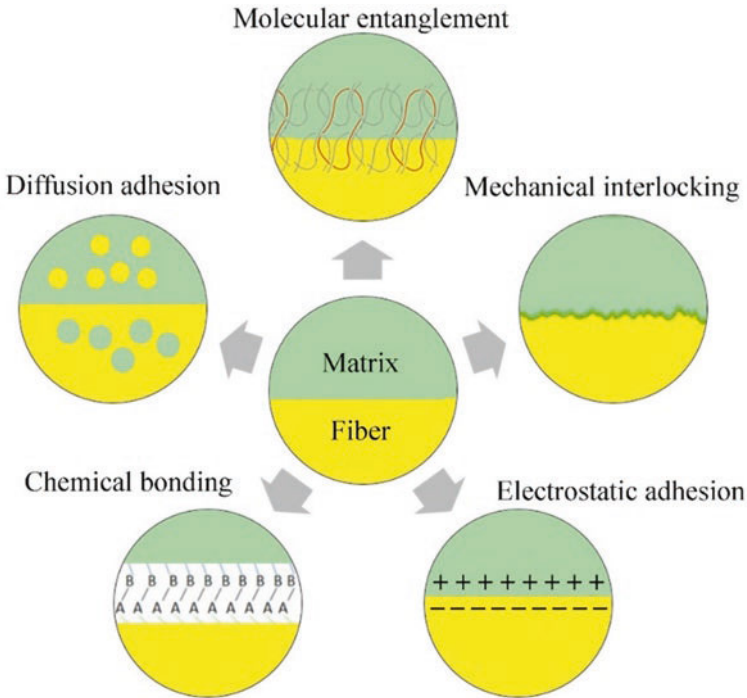


Fig. 4.4 Schematic representation of chemical bonding, molecular entanglement, mechanical interlocking, diffusion adhesion, and electrostatic adhesion between the matrix and the fibers

functional chains and polymer matrix. Figure 4.4 shows the schematic representation of the fiber–matrix interface.

Several methods have been developed to enhance the interfacial strength of fibers and matrix like surface coating, plasma treatment, and chemical modification of fibrous reinforcement [12, 41–43]. For instance, better fiber–matrix bonding can be attained by coating the fiber surface. The common coating techniques such as electrodeposition, chemical vapor deposition (CVD), sputtering, physical vapor deposition (PVD), etc. have been explored by the researchers.

The compatibility and adhesion of fiber to matrix can also improve through the chemical modification of fibers. For instance, the strength of glass fiber-reinforced composites has been enhanced through silane modification, which acts as a bridge between fibers and polymer matrix. Alkali treatment of natural fibers also enhanced the fiber–matrix interfacial strength by removing the impurities and increasing the roughness of the fiber surface, thereby leading to an improved mechanical interlocking between the fibers and matrix. Graft copolymerization and modification with different chemicals are also reported by the researchers to enhance the fiber–matrix bond strength.

4.3 Properties of Fibrous Composites

4.3.1 Mechanical Behavior

It is well-known that the mechanical behavior of fibrous composites is significantly different compared to the traditional metallic structures. For instance, fibrous composites, due to the different laminating structures and multiple laminate plies, might fail in bending under tensile loads, while an equivalent metal structure might fail in tension [12]. Although the metals are generally ductile and will deform before failure, the composite structures are generally brittle and a little deformation may occur before failure.

The failure of fibrous composites under tension has no common signs on the macroscopic scale. However, on the microscopic scale, each fibrous composite exhibits common characteristics indicating their failure under tension. For example, the fracture surface of composite structures is generally rough. In the case of aligned fiber in the direction of tensile load, the fractured fibers are generally pulled out from the fracture surface. The individual fibers, breaking and pulling out from the matrix, lead to the fiber pullout. The phenomenon that the fibers do not break during the tensile loading and the matrix itself fails is called fiber bridging. The length of pulledout fibers is dependent on the environmental and loading conditions on composite structures during the failure. If the fibers are not aligned in the tensile loading direction, the failure occurs often in the matrix rather than the fibers. The failure generally occurs between the fibers at the fiber–matrix interface. The matrix failure usually causes hackles, indicating the shear failure of the matrix.

In the case of compression loadings, the kink bands are generally formed in fibers representing the compression failure (Fig. 4.5). The poor compression strength properties of fibers, particularly when the compressive load approaches the critical level, kink bands occur due to plastic buckling. These kink bands are often associated with matrix splitting and occur at high-stress concentration points in the matrix, such as fiber–matrix interface and between plies.

The bending failure of fibrous composite structures generally exhibits common characteristics of tension and compression around the neutral bending axis. The side

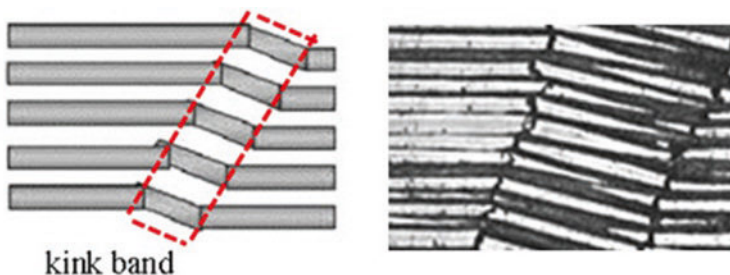


Fig. 4.5 Fiber kinking damage mode

under tension contains pulledout fibers, while the side in compression is generally flat. The difference between the tension and compression sides of fibrous composite structures is an indicator of bending failure.

Fatigue is another failure occurring in fibrous composite structures. Although fatigue is generally identified in traditional aircraft metals rather than composites, it could also occur in some fibrous composites. Fatigue fracture becomes more visible with repeated loading of fibrous composites. The surfaces of fatigue fracture rub against each other, thereby dispersing the broken fibers throughout the area under load. The localized stress concentration zones form by breaking more fibers, leading to the fiber–matrix debonding. In the case where the fatigue damage is not clearly identified, matrix cracking will occur. Increasing the matrix cracking leads to reducing the fatigue life.

4.3.2 Types of Mechanical Tests

Generally, the analysis used for investigating the mechanical properties of fibrous composite structures is similar to those for analysis of other materials. However, the special characteristics of fibrous composites such as material anisotropy, adhesive bonding, and different failure mode, make their mechanical analysis more complex. Several approaches have been suggested to conduct the mechanical test on fibrous composite structures, including static tensile, impact, compressive, shear, and flexural loading. Mechanical testing is carried out based on ASTM standards for fibrous composite specimens, i.e., tensile (ASTM D3039), compressive (ASTM D3410M), shear (ASTM D5379M and ASTM D5379M), and flexural (ASTM D790) testing. The interlaminar properties of the fibrous composite are also included in tensile, compressive, and shear tests. Further, mechanical analysis is also carried out for special characterization or determination of the performance of fibrous composites under critical conditions, including multiaxial, fatigue, creep, impact, and high-rate loading as well as stress and failure analysis [44–47].

The static analysis is a standard tensile test for measuring the strength or stiffness of composite materials, under tensile loading. For analysis of long-term strength and strain stability of the composite structure, the static test may be continued for weeks or months. This long duration test is also known as creep test. To investigate the resistance of fibrous composites to degradation and failure under cyclic and varying loading, the static test is repeated under cyclic and low-frequency loads. Different types of loading could be applied to composite structures, including tension, compression, reverse shear at constant amplitude or specific loading, and the simulated actual loading conditions. The impact or ballistic resistance of composite materials is generally measured under dynamic loads. The dynamic test can also be conducted using an impactor or penetrator with different geometries or under tension, compression, shear, or flexural loadings.

4.4 Fibrous Composites in Aircraft Applications

The lightweight and superior mechanical properties of fibrous composites make them suitable for aircraft and aerospace applications. The fibrous composite exhibits competitive properties such as high static strength, fatigue performance, toughness, and resistance to high temperatures, and impact in comparison to common materials [2, 16, 48, 49]. Development in the field of aircraft composites has led to increase in the component performance, while reducing their costs and weight [1, 3]. The high density and low stiffness of glass fibers and the high moisture adsorption of aramid fibers have restricted their use in aircraft composites. Hence, carbon fibers have been used in manufacturing major parts of aircraft composites. Different fibrous structures such as woven, knitted, and braided have been utilized for producing composites components. Among different polymer matrices, epoxy resin is extensively used as the matrix material due to its good mechanical properties and durability. Carbon fiber/phenolic and carbon-carbon composites are suggested for nozzles such as exit cone and throat elements, because of their high specific mechanical properties as well as high thermal resistance. Carbon-carbon composites are suitable for high temperature and ablative conditions. Low thermal expansion, good thermal conductivity, high heat capacity, and wear resistance are other properties of carbon-carbon composites.

The first airliners which utilized fibrous composites for aircraft structures were Airbus A310 and A300-600. The major structures such as vertical fins, wing loading edge, and fairings are manufactured from carbon fiber composites. The application of fibrous composites in A320, A330, and A340 families exhibit improved aerodynamics and reduced fuel consumption [4]. The application of woven carbon fibers in Embraer ERJ 170 inboard flaps, the Embraer ERJ190 outboard flaps and wing stubs, and the Boeing 737e300 winglets has also been reported. The impregnation of complex preforms made by warp-knitted skins and braided profiles stitched together in an RTM process is an example of knitted structure in aircraft applications. Directionally oriented carbon fiber structures have also been utilized in Airbus A380 rear pressure bulkhead (RPB), Airbus A400M cargo door, Airbus A380 flap track diaphragms, side shells, and straps. Braided structures have been developed for applications in several components such as aircraft propellers, rocket launchers, aircraft fuselage frames, and helicopter rotor blade spars. However, further development was restricted due to the limitation of most of the industrial braiding machines for producing braided structures with large cross sections.

The higher in-plane mechanical properties of 2D fibrous structures than 3D textile preforms have led to more demand for the application of 2D structures in the aircraft industry. The out-of-plane impact resistance of 3D textile composite structures, as an important characteristic for developing aircraft composites, can be enhanced with the yarn orientation in the thickness direction. Hence, the development of 3D fabrics for aircraft components offers a great advantage due to their resistance to delamination fracture. These structures are also low cost due to the elimination of the labor-intensive laminating process. Considering the advantages

of 3D fibrous architectures such as woven, knitted, and braided structure, increasing attention has been paid to their application in the aircraft industry. Among different 3D fibrous structures, MWK carbon fibers are a suitable candidate for application in aircraft composite, not only due to the similar mechanical properties to those of unidirectional preregs but also their beneficial through-the thickness reinforcement. Introducing in-plane yarns without crimping, is the main advantage of MWK structures, which provides better yarn-to-fabric property translation efficiency. Several components such as aircraft skin, tail units, fuselage paneling, leading edges on wings and rudders, engine paneling, rotor blades, and ballistic protection have been developed using MWK fibrous composites. Multiaxial carbon fiber fabrics were impregnated using resin film infusion followed by an autoclave process and developed for the Airbus A380 rear pressure bulkhead. The 3D woven composite structures have found applications in several aircraft structures such as turbine engine thrust reversers, rotors, rotor blades, insulation, structural reinforcement and heat exchangers, rocket motors, nozzles and fasteners, engine mounts, T-section elements for primary fuselage frame structures, and multiblade stiffened panels.

4.5 Conclusions

Fibrous composite materials have received increasing attention for application in several industries such as aerospace, automotive, civil, sports, medicine, and particularly in aircraft. This chapter focused on the design, fabrication, and application of different fibrous architectures such as woven, knitted, braided, nonwoven, and hybrid structures in the aircraft industry. A multilayered composite structure construction, based on two-dimensional textile preforms, is traditionally used for the production of composite materials. Despite the advantages of 2D fibrous structures, the lack of through-the-thickness fibers and consequently poor out-of-plane properties such as interlaminar strength, made their application in aerospace and aircraft applications rather questionable. Increasing the number of layers is also labor-intensive and time-consuming. 3D woven, knitted, and braided fibrous architectures providing yarn oriented in the thickness direction, provided high out-of-plane properties. They also possess many advantages not only in performance viewpoint but also in economical features. Hence, the application of 3D fibrous architectures is beneficial for aircraft components and has attracted great attention. The main drawback of these structures is the high production costs due to the limitations in machining technology. The application of fibrous composite structures in aircraft applications will increase by new developments in fiber and matrix systems, enhancement in the fiber–matrix interfacial strength, and application of nanostructures reinforcement.

References

1. Taylor, R. (2008). *Fibre composite aircraft: Capability and safety*. Australian Government-Australian Transport Safety ... (Vol. AR-2007-02). Retrieved from <http://scholar.google.com/scholar?hl=en&btnG=Search&q=intitle:Fibre+composite+aircraft+?+capability+and+safety#0>.
2. Soutis, C. (2005). Fibre reinforced composites in aircraft construction. *Progress in Aerospace Sciences*, 41(2), 143–151. <https://doi.org/10.1016/j.paerosci.2005.02.004>
3. Pantelakis, S. (2020). Historical development of aeronautical materials. In *Revolutionizing aircraft materials and processes* (pp. 1–19). Springer. https://doi.org/10.1007/978-3-030-35346-9_1
4. Dutton, S., Kelly, D., & Baker, A. (2004). *Composite materials for aircraft structures* (2nd ed.). <https://doi.org/10.2514/4.861680>
5. Karaduman, N. S., Karaduman, Y., Ozdemir, H., & Ozdemir, G. (2017). Textile reinforced structural composites for advanced applications. In *Textiles for advanced applications*. Intechopen. <https://doi.org/10.5772/intechopen.68245>
6. Egbo, M. K. (2020). A fundamental review on composite materials and some of their applications in biomedical engineering. *Journal of King Saud University - Engineering Sciences*, 33(8), 557–568. <https://doi.org/10.1016/j.jksues.2020.07.007>
7. Jinlian, H. (2008). *3-D fibrous assemblies: Properties, applications and modelling of three-dimensional textile structures*. Elsevier. <https://doi.org/10.1533/9781845694982>
8. Thostenson, E. T., Ren, Z., & Chou, T. W. (2001). Advances in the science and technology of carbon nanotubes and their composites: A review. *Composites Science and Technology*, 61(13), 1899–1912. [https://doi.org/10.1016/S0266-3538\(01\)00094-X](https://doi.org/10.1016/S0266-3538(01)00094-X)
9. Ilcewicz, L. B., Hoffman, D. J., & Fawcett, A. J. (2000). Composite applications in commercial airframe structures. In *Comprehensive composite materials* (pp. 87–119). Elsevier. <https://doi.org/10.1016/b0-08-042993-9/00137-6>
10. Sinclair, R. (2015). Understanding textile fibres and their properties: What is a textile fibre? In *Textiles and fashion: Materials, design and technology* (pp. 3–27). Elsevier. <https://doi.org/10.1016/B978-1-84569-931-4.00001-5>
11. Dong, C., & Davies, I. J. (2015). Flexural strength of bidirectional hybrid epoxy composites reinforced by e glass and T700S carbon fibres. *Composites Part B: Engineering*, 72, 65–71. <https://doi.org/10.1016/j.compositesb.2014.11.031>
12. Xu, N., Lu, C., Zheng, T., Qiu, S., Liu, Y., Zhang, D., ... Liu, G. (2021). Enhanced mechanical properties of carbon fibre/epoxy composites via in situ coating-carbonisation of micron-sized sucrose particles on the fibre surface. *Materials & Design*, 200, 109458. <https://doi.org/10.1016/j.matdes.2021.109458>
13. Dhand, V., Mittal, G., Rhee, K. Y., Park, S. J., & Hui, D. (2015). A short review on basalt fiber reinforced polymer composites. *Composites Part B: Engineering*, 73, 166–180. <https://doi.org/10.1016/j.compositesb.2014.12.011>
14. Li, X., Tabil, L. G., & Panigrahi, S. (2007). Chemical treatments of natural fiber for use in natural fiber-reinforced composites: A review. *Journal of Polymers and the Environment*, 15(1), 25–33. <https://doi.org/10.1007/s10924-006-0042-3>
15. Erden, S., & Ho, K. (2017). Fiber reinforced composites. In *Fiber technology for fiber-reinforced composites* (pp. 51–79). <https://doi.org/10.1016/B978-0-08-101871-2.00003-5>
16. Soutis, C. (2019). Aerospace engineering requirements in building with composites. In *Polymer composites in the aerospace industry* (pp. 3–22). <https://doi.org/10.1016/B978-0-08102679-3.00001-0>
17. Andréasson, N., Mackinlay, C. P., & Soutis, C. (1997). Tensile behaviour of bolted joints in low temperature cure CFRP woven laminates. *Advanced Composites Letters*, 6(6), 143–147. <https://doi.org/10.1177/096369359700600601>
18. Hassan, M. H., Othman, A. R., & Kamaruddin, S. (2017). A review on the manufacturing defects of complex-shaped laminate in aircraft composite structures. *International Journal*

- of Advanced Manufacturing Technology*, 91(9–12), 4081–4094. <https://doi.org/10.1007/s00170-017-0096-5>
19. Ishak, F. A., Izzat Wan Zaludin, W. M., Mahmud Zuhudi, N. Z., & Mohd Aris, K. D. (2020). A physical characterisation for the preliminary fabrication of natural woven fabric prepreg and their composites. In *Lecture notes in mechanical engineering* (pp. 575–585). Springer. https://doi.org/10.1007/978-981-15-4756-0_51
 20. Soutis, C., & Spearing, S. M. (2002). Compressive response of notched, woven fabric, face sheet honeycomb sandwich panels. *Plastics, Rubber and Composites*, 31(9), 392–397. <https://doi.org/10.1179/14658010225006369>
 21. Andréasson, N., Mackinlay, C. P., & Soutis, C. (1998). Experimental and numerical failure analysis of bolted joints in CFRP woven laminates. *Aeronautical Journal*, 102(1018), 445–450.
 22. Stig, F., & Hallström, S. (2012). Spatial modelling of 3D-woven textiles. *Composite Structures*, 94(5), 1495–1502.
 23. Liu, Y., de Araujo, M., & Hu, H. (2016). Advanced fibrous architectures for composites in aerospace engineering. In *Advanced composite materials for aerospace engineering* (pp. 17–58). Elsevier. <https://doi.org/10.1016/b978-0-08-100037-3.00002-x>
 24. Kiss, P., Stadlbauer, W., Burgstaller, C., & Archodoulaki, V. M. (2020). Development of high-performance glass fibre-polypropylene composite laminates: Effect of fibre sizing type and coupling agent concentration on mechanical properties. *Composites Part A: Applied Science and Manufacturing*, 138, 106056. <https://doi.org/10.1016/j.compositesa.2020.106056>
 25. Saboktakin, A. (2019). 3D textile preforms and composites for aircraft structures: A review. *International Journal of Aviation, Aeronautics, and Aerospace*, 6(1). <https://doi.org/10.15394/ijaaa.2019.1299>
 26. Hufenbach, W., Gude, M., & Ebert, C. (2009). Hybrid 3D-textile reinforced composites with tailored property profiles for crash and impact applications. In *Special Issue on the 12th European Conference on Composite Materials, ECCM 2006* (Vol. 69, pp. 1422–1426). <https://doi.org/10.1016/j.compscitech.2008.09.033>.
 27. Sugun, B. S., & Sundaram, R. (2015). 3D composites: Opportunities & challenges. *Journal of the Indian Institute of Science*, 95.
 28. Chen, X., Sun, Y., & Gong, X. (2008). Design, manufacture, and experimental analysis of 3D honeycomb textile composites, part II: Experimental analysis. *Textile Research Journal*, 78(11), 1011–1021. <https://doi.org/10.1177/0040517507087683>
 29. Mountasir, A., Hoffmann, G., Cherif, C., Löser, M., & Großmann, K. (2015). Competitive manufacturing of 3D thermoplastic composite panels based on multi-layered woven structures for lightweight engineering. *Composite Structures*, 133, 415–424. <https://doi.org/10.1016/j.compstruct.2015.07.071>
 30. Borba, N. Z., Kötter, B., Fiedler, B., dos Santos, J. F., & Amancio-Filho, S. T. (2020). Mechanical integrity of friction-riveted joints for aircraft applications. *Composite Structures*, 232, 111542. <https://doi.org/10.1016/j.compstruct.2019.111542>
 31. Ngo, T.-D. (2020). *Composite and nanocomposite materials—From knowledge to industrial applications*. Intechopen. <https://doi.org/10.5772/intechopen.80186>
 32. Li, Y., Wang, Q., & Wang, S. (2019). A review on enhancement of mechanical and tribological properties of polymer composites reinforced by carbon nanotubes and graphene sheet: Molecular dynamics simulations. *Composites Part B: Engineering*, 160, 348–361. <https://doi.org/10.1016/j.compositesb.2018.12.026>
 33. Borah, J. S., & Kim, D. S. (2016). Recent development in thermoplastic/wood composites and nanocomposites: A review. *Korean Journal of Chemical Engineering*, 33(11), 3035–3049. <https://doi.org/10.1007/s11814-016-0183-6>
 34. Singh, A. K., Bedi, R., & Kaith, B. S. (2019). Mechanical properties of composite materials based on waste plastic—A review. *Materials Today: Proceedings*, 26, 1293–1301. <https://doi.org/10.1016/j.matpr.2020.02.258>
 35. Mazumdar, S. K. (2001). *Composites manufacturing: Materials, product, and process engineering*. CRC Press.

36. Ku, H., Wang, H., Pattarachaiyakoo, N., & Trada, M. (2011). A review on the tensile properties of natural fiber reinforced polymer composites. *Composites Part B: Engineering*, 42(4), 856–873. <https://doi.org/10.1016/j.compositesb.2011.01.010>
37. Gutowski, T. G. (1997). Advanced composites manufacturing. *Advanced composites manufacturing*. [https://doi.org/10.1016/s0025-5408\(00\)00291-9](https://doi.org/10.1016/s0025-5408(00)00291-9)
38. Mallick, P. K. (1997). *Composites engineering handbook*. CRC Press. <https://doi.org/10.1201/9781482277739>
39. Seferis, J. C., Hillermeier, R. W., & Buheler, F. U. (2000). Prepregging and autoclaving of thermoset composites. In *Comprehensive composite materials* (pp. 701–736). <https://doi.org/10.1016/b0-08-042993-9/00169-8>
40. Polatov, A. M., Ikramov, A. M., Pulatov, S. I., & Gaynazarov, S. M. (2020). Numerical modeling of the stress state of constructions from fibrous composites. *Journal of Physics: Conference Series*, 1479. <https://doi.org/10.1088/1742-6596/1479/1/012100>
41. Lee, G.-W. (2002). Effects of surface modification on the resin-transfer moulding (RTM) of glass-fibre/unsaturated-polyester composites. *Composites Science and Technology*, 62(1), 9–16.
42. Kalia, S., Kaith, B. S., & Inderjeet Kaur, E. (2011). *Cellulose fibers: Bio-and nano-polymer composites: Green chemistry and technology*. Springer Science & Business Media.
43. Kim, T. J., Lee, Y. M., & Im, S. S. (1997). The preparation and characteristics of low-density polyethylene composites containing cellulose treated with cellulase. *Polymer Composites*, 18(3), 273–282. <https://doi.org/10.1002/pc.10281>
44. Uslu, E., Gavgali, M., Erdal, M. O., Yazman, Ş., & Gemi, L. (2021). Determination of mechanical properties of polymer matrix composites reinforced with electrospinning N66, PAN, PVA and PVC nanofibers: A comparative study. *Materials Today Communications*, 26, 101939. <https://doi.org/10.1016/j.matcomm.2020.101939>
45. Khan, Z. I., Arsad, A., Mohamad, Z., Habib, U., & Zaini, M. A. A. (2019). Comparative study on the enhancement of thermo-mechanical properties of carbon fiber and glass fiber reinforced epoxy composites. In *Materials today: Proceedings* (Vol. 39, pp. 956–958). Elsevier BV. <https://doi.org/10.1016/j.matpr.2020.04.223>
46. Kim, J., Cha, J., Chung, B., Ryu, S., & Hong, S. H. (2020). Fabrication and mechanical properties of carbon fiber/epoxy nanocomposites containing high loadings of noncovalently functionalized graphene nanoplatelets. *Composites Science and Technology*, 192, 108101. <https://doi.org/10.1016/j.compscitech.2020.108101>
47. Wu, P., Liu, L., & Wu, Z. (2020). Synthesis of Diels-Alder reaction-based remendable epoxy matrix and corresponding self-healing efficiency to fibrous composites. *Macromolecular Materials and Engineering*, 305(10), 2000359. <https://doi.org/10.1002/mame.202000359>
48. Matthews, F. L., Davies, G. A. O., Hitchings, D., & Soutis, C. (2000). *Finite element modelling of composite materials and structures*. Woodhead Publishing. <https://doi.org/10.1533/9781855738928>
49. Soutis, C., Filiou, C., & Pateau, V. (2000). Strength prediction of fiber reinforced plastics with a hole under compression-tension. *AIAA Journal*, 38(1), 110–114. <https://doi.org/10.2514/2.929>

Chapter 5

Natural Composites in Aircraft Structures



Lata Samant, Fábio A. O. Fernandes, Seiko Jose,
and Ricardo J. Alves de Sousa

5.1 Introduction

Composites consist of two or more physically distinct combinations to produce aggregate properties based on their constituents. These materials have good mechanical properties per unit weight and can be manufactured in any form according to suitability [1]. Multifunctional and eco-friendly composite materials have attracted more researchers and manufacturers to meet the increasing demand of sustainable products. To feed this demand, continuous work has been done on strengthening the ground for composite material.

Green marketing, cleaner production, sustainability, and change of cognitive values of consumers and lawmakers have led to environment-friendly production. Composite materials are being developed and redesigned to improve and adapt conventionally manufactured products while also bringing new products to market sustainably and responsibly [2]. These multifunctional materials have been developed to match the needs of a certain application and offer remarkable physicomaterial properties. Characteristics such as high strength, high modulus, low density, exceptional fatigue resistance, creep resistance, and so on provide design opportunities for the mechanical engineers. Many efforts are being made toward eco-friendly and

L. Samant

G. B. Pant University of Agriculture and Technology, Pantnagar, Uttarakhand, India

F. A. O. Fernandes (✉) · R. J. Alves de Sousa

TEMA: Centre for Mechanical Technology and Automation, Department of Mechanical Engineering, University of Aveiro, Aveiro, Portugal

e-mail: fabiofernandes@ua.pt

S. Jose

ICAR-Textile Manufacturing and Textile Chemistry Division, Central Sheep and Wool Research Institute, Avikanagar, Rajasthan, India

biodegradable materials for the future of composite products because of worldwide environmental agitation and raising awareness of sustainable resources.

The shift toward natural materials in composites has resulted in lower greenhouse gas emissions and a smaller carbon footprint. These are suitable alternatives for substituting or reducing the use of petroleum-based materials [3]. Using natural composite materials that reduce construction waste and increase energy efficiency would be a better solution to the concept of sustainability [4]. Natural composites are, to a certain extent, eco-friendly or green.

Natural renewable resources that reduce carbon footprint are green composites. While materials that have one of the constituents, either fiber or matrix, from non-renewable resources are partly eco-friendly composites [2]. Non-biodegradable predominant fiber-reinforced plastics such as glass, carbon, and aramid fibers reinforced with synthetic thermoplastic and thermosetting resins are hazardous to the environment since they are derived from finite resources [5]. Therefore, to reduce the environmental impact of conventional composite materials, bio-based fibers as reinforcement are getting more attention these days [6].

Advantages of using natural fibers reinforcing materials embrace environment-friendly, low density, low cost, and good mechanical properties [7], Jute [8], coconut [9], hemp [10], pineapple [11, 12], kenaf [13], flax [14, 15], sisal [16], are some important natural fibers used in research and development of the natural fiber composites system. In contrast, natural fiber materials in reinforcements come with some critical shortfall characteristics that are hydrophilicity, poor moisture resistance, and weak fiber/matrix adhesion. But these drawbacks have significant room for improvement using innovative resins, additives, coatings, and surface modification techniques of fibers [17, 18].

Together with the natural fiber flooded market, the approach toward the replacement of a large amount of petroleum-based polymer by natural resins has reduced dependence on petrochemicals, and their cost allows manufacturers to promote a greener product. Bio-resin has a favorable lifecycle profile to the environment that contributed to its emergence in the field of composites. Some of these natural polymer resins are starch, lignin, polylactic acid, furan resins, and super Sap epoxy [19].

In semi-structural and structural applications such as aerospace, vehicles, sports technology, electronics, and plastics, natural fiber-reinforced polymer matrix composites have achieved commercial success. 100% bio-based composites with superior mechanical properties can be made utilizing natural fibers and naturally produced resins, and they can be used for more structural reasons [18]. For instance, Fernandes et al. [15] developed laminate composites based on flax fibers and super Sap epoxy resin to substitute fiberglass laminate composites with matrixes based on synthetic epoxy resin, which showed good impact toughness (Fig. 5.1).

Due to the necessity for enhanced fuel efficiency, corrosion resistance, and fatigue resistance, composite materials are widely employed in the aerospace, marine, and automotive industries [20]. The recent developments in natural composites for aircraft were not the first steps in the use of natural materials for this application. Pioneering work was carried out by the Wright Brothers (1903), who employed wood and natural-based fabrics on their Flyer 1. Wooden structures did



Fig. 5.1 Flax fibers laminates with cured super Sap (bio-based) epoxy resin matrix and cork core

persist until World War II, plywood–balsa–plywood sandwich laminates incorporated in the fuselage of some aircraft [21]. In 1940, balsa-cored sandwich laminates were developed incorporating untwisted flax fibers and having a phenolic resin as the matrix [22]. High strain rate testing of laminate composites has gained significant importance in recent years of material research because these materials are commonly used in lightweight structural applications and there are many cases where the mechanical properties of composite materials are notably reliant on the strain rate. Natural fiber composites have improved in performance thanks to advances in fiber selection, extraction, treatment, interfacial engineering, and composite manufacturing.

5.2 Natural Composites in Aerospace Industry

The first use of composite materials in aircraft was about 30 years ago where boron-reinforced epoxy composite was used for the structure of the tail assembly of the U.S. F14 and F15 fighters. The aerospace industry and manufacturers are relentless in their efforts to improve the performance of commercial and military aircraft as knowledge and technology advances [23]. When it comes to heavier-than-air machines, weight is a major consideration, and designers have worked tirelessly to push the limits of lift-to-weight ratios. Weight loss has been aided significantly by composite materials [24]. The use of metal and alloys-based materials is subsequently replaced by composites for different industrial applications. Fiber–metal laminates such as aluminum/boron/epoxy, titanium/carbon fiber/epoxy, and aramid/aluminum/epoxy are used as aerospace structural material. Although the metal layer is used to improve the impact performance, the rate of moisture absorption increases

in the case of fiber metal hybrid composites, presenting also low fracture toughness [25]. On contrary, properties such as high specific strength, stiffness, fracture toughness, good oxidation resistance, and corrosion are some of the reasons for the high demand for composites in the industry [26].

Despite the structural benefits of synthetic fiber composites such as carbon fiber composites and glass fiber composites, they have several drawbacks, including high raw material costs and significant environmental effects due to their non-recyclability and non-degradability. The danger of sustainability and life cycle assessment (LCA) is imposed on aircraft made with these sorts of composites [27]. Stringent regulations and standards have forced the change toward eco-friendliness. The Advisory Council for Aviation Research and Innovation in Europe (ACARE) released the Flightpath 2050 report, which focuses on the use of recyclable and environmentally friendly materials in aviation technologies to reduce carbon emissions and reliance on crude oil-based products [28].

Natural composites used in aircraft have still to overcome several challenges before being widely used in this industry. This is particularly true for critical structural components. Additionally, challenges such as the requirements of safety standards, from fire retardancy to crash safety standards, are barriers to the wider adoption of natural composites by the aerospace industry. Nevertheless, natural fibers have found their way into commercial aircraft, for instance, in-cabin components and other interior components due to their lightweight and strong nature [29].

5.3 Aerospace Component from Natural Fibers

Boeing's 787 Dreamliner, shown in Fig. 5.2, is the first commercial aircraft in which structural materials are made of composite materials rather than aluminum alloys. There has been seen a shift from the use of alloys to the use of synthetic fibers



Fig. 5.2 Usage of composites in Boeing 787 Dreamliner structure [67]. Reprinted by permission from Elsevier

(fiberglass, carbon composites) to the promotion of the green approach of using hybrid composites (natural fibers/synthetic fibers).

As interest in sustainability and “green” interiors grows, a European project called “Cayley” has brought together Boeing Research and Technology Europe (Madrid, Spain), Invent GmbH (Braunschweig, Germany), Aimplas (Valencia, Spain), and Lineo (St. Martin du Tilleul, France) to develop eco-friendly interior panels made of renewable polymers and flax fibers. These interiors are reported to be 35% lighter than carbon fiber/epoxy prepreg tapes [30]. Fiber reinforcements have a broad application spectrum that includes every sort of modern engineering structure. They can be found in a wide range of airplanes, helicopters, spacecraft, boats, ships, and offshore platforms, as well as automobiles, chemical processing equipment, sporting products, and civic infrastructure including buildings and bridges [31]. Flax composites have a high specific tensile and flexural modulus, making them a promising sustainable material for aircraft, transportation, and light-weight building [32]. The mechanical properties of bio-based resin composites with flax fibers as reinforcements can meet the requirements of an aircraft’s interior structures [29]. Biodegradable banana fiber and epoxy resin composites are being used for low-strength applications. Considering the advantages of natural fibers, these are being used in aircraft as interlines in the seats, panels, etc. Ramie/PLA composites can be used in aerospace applications to replace composites that use glass fiber and petroleum oil-based resins, improving energy efficiency and solution sustainability [33]. Hemp/epoxy composites can compete with and replace glass/epoxy composites in ultra-light aircraft, thereby broadening the range of environmentally acceptable composites [34]. Coir has the potential to be used as a component in aircraft materials that are impact resistant [35]. Both the bamboo/coir epoxy resin composite and the bamboo/coir epoxy resin composite have superior impact resistance when used together. Hemp, kenaf, flax, and other bast fibers are utilized as reinforcement for aircraft interior structures such as seat cushions, cabin linings, and parcel shelves. Pilots’ cabin doors and door shutters are made of jute fiber-reinforced polyester/epoxy [36–38].

In another study, the authors analyzed the dielectric and mechanical properties of five types of natural fibers for radome development viz., banana, bamboo, oil palm, kenaf, pineapple leaf fibers [39]. Hybrid kenaf/glass fiber-reinforced polymer composites showed their potential for this application through their resistance to rain erosion and due to their mechanical performance. More recently, Ilyas et al. [40] also investigated and found the potential application of natural fiber reinforced polymer composites in the radome. These structures are typically manufactured by resin injection molding (RIM).

Boegler et al. [41] found that ramie fiber-reinforced polylactic acid (PLA) and epoxy resin-made wing box could be a sustainable option to replace the conventional aluminum alloy wing box. Natural fiber-based thermoset and thermoplastic panels were found to have the needed flame and heat resistance above conventional sandwich panels [42]. Composites-based high-performance goods must be light-weight while also being robust enough to withstand high loads, such as tails, wings, and fuselages for aerospace structures [43]. The future of the composite industry

relies on the material source that can work together following the environmental concerns, with strengthening research on the performance of natural fiber-reinforced composites and their sustainability, it is likely to guarantee their long-term growth, as well as innovative products and new applications on the horizon.

5.4 Natural Fibers in Aerospace Applications and Their Properties

Alonso-Martin et al. [42] patented publication asserts that the aircraft interior panels made from natural fiber-reinforced panels for secondary structure in the cabin would result in a weight reduction of 200–500 kg constituting a reduction of 2500–6500 tons of CO₂ emissions for panels made from inorganic resin. Additionally, during their lifetime, a reduction of 100–250 kg for the thermoplastic resin panels, which corresponds to a reduction of 1300–3250 tones in CO₂ emissions was estimated for panels made of thermoplastic resin. Comparable mechanical properties of kenaf and glass fiber having tensile strength, tensile modulus, and elongation at failure, 930 MPa, 53 GPa, and 53; 1.6%, 2000–3500 MPa, and 70 GPa 2.5–3.0%, respectively, help to improve the rain erosion resistance and mechanical properties for radome applications.

Boegler et al. [41] compared the mass of a wing made of aluminum alloy of the 7000 series (7000–8829 kg) to a wing made of ramie fiber-based composites (7576 kg), which resulted in a weight reduction of the wing box without compromising structural integrity. Sandwich structures were made with diglycidyl ether of bisphenol-A (DGEBA) and glucufuranoside-based trifunctional epoxy (GFTE) matrices cured by curing agent, jute fiber reinforcement, and polymethacrylimide foam as the core for prospective airplane interior flooring applications. The sandwich composites' bending strength and modulus were found to be substantially higher with GFTE than with DGEBA [44].

Bio-composites, rather than nonrenewable composites, improve the plane's sustainability [45]. Bio-composites have a bright future ahead of them and using renewable and sustainable resources is crucial for their integration into aircraft. Biomass valorization is needed for a better aviation environmental footprint. However, as far as falling weight impact properties are concerned, the possibility that offered quite significant results is the use of bio-based thermosets as the matrix for natural fiber composites, such as soy oil methacrylates reinforced with jute fibers [46]. In another example, the application of a hemp fabric/epoxy composite in an electronic rack of a helicopter [47] and Naca cowling of an acrobatic ultralight airplane [34] showed better results. In the case of sisal/polypropylene composites, the addition of magnesium hydroxide and zinc borate offered a satisfactory fire retardancy effect without affecting the mechanical properties [48].

5.5 Natural Resins in Aerospace Applications and Their Properties

The carbon fiber reinforcement offers stiffness and strength to the composite, while the epoxy matrix provides ductility [49]. Carbon fibers and epoxy are unsatisfactory as aircraft structural materials on their own. Natural fibers and epoxy resin, when mixed as a composite, these can produce a high-performance structure with a wide range of desirable qualities.

One of the current priorities in composites incorporating natural materials for aircraft structures is to substitute the traditional epoxies [21]. In addition to new formulations of epoxy resins for the manufacturing of natural composites with superior performance [50, 51], the introduction of nanofillers into bio-based epoxy matrixes has been explored to improve the mechanical properties. Examples of nanofillers incorporated with success are silicon carbide nanoparticles, carbon nanotubes, and nanoclays, which improved the thermal, mechanical, and conductive performance of the cured thermosets [21].

Dinesh et al. [52] created composites of an epoxy matrix, pineapple fiber, and wire mesh with a PF/SS/PF/SS stacking sequence with 1.0vol percent nano-silica, achieving a normalized strength of 98%. Epoxy composites are a superb alternative material for autos, structure, surveillance micro aircraft, and domestic appliance manufacturing industries with high economic value due to their high fatigue and fracture toughness and high penetration resistance against drop load. In comparison to traditional reinforcements, flax-based epoxy has the potential to reach high specific strength [53]. Various types of natural fillers are used with bio-resin to enhance the mechanical strength and reduce the cost of the material and make the resultant material competitive to synthetic composites. In Table 5.1, a few of the natural fillers and bio-resins are mentioned that are being used in the natural fiber composites.

Table 5.1 List of common bio-resins and natural fillers for natural fiber composites

Natural fibers	Natural resins	Natural fillers
Hemp	Soy oil	Nanoclay
Flax	Wheat gluten	Graphite filler
Kraft Pulp	Cashew nut shell	Cellulose nanofibers
PALF	Starch	Rice husk
Cork	Lignin	Wheat husk
Kenaf	Polylactic acid	Coir
Jute	Furan resins	Palm kernel shell
Ramie	Super sap epoxy	Wood chip

5.6 Natural/Synthetic Hybrid Composites for Aerospace Applications

The complete replacement of synthetic fiber composites employed in aircraft by natural solutions is still not possible, mainly due to the disparity of some properties. Therefore, hybrid composites composed of two discontinuous phases, both natural/synthetic fibers, have been the smart way of increasing the natural material content in aircraft composites [36, 54, 55]. Additionally, hybrid composites make it possible to explore demanding applications in the aerospace sector, going beyond interior panels, by developing lightweight hybrid composites for aircraft structural applications.

To achieve excellent properties and improve the sustainability of the solutions, hybrid composites are usually developed through the combination of natural and synthetic materials. These materials with combined properties have extensive engineering applications. In hybrid composite materials, a combination of excellent properties such as tensile modulus, compressive strength, and impact strength can be achieved, which therefore increases the efficiency, performance, and extensibility of the materials.

Hybrid composites are widely used in commercial airplanes. Unlike other vehicles, airplane manufacture places a larger emphasis on safety and weight reduction, which is accomplished by using materials with high specific characteristics [56]. Modern aircraft are designed to meet performance, properties, environmental standards, and safety. A hybrid composite from natural fiber exhibits weight reduction compared to steel/carbon. By exploring these renewable materials, it increases the recyclability percentage of components in the automotive and aircraft. Combined natural and synthetic materials result in environmentally friendly and sustainable components to fulfill the growing demand for composites worldwide [57].

ECO-COMPASS (Ecological and Multifunctional Composites for Aircraft Interior and Secondary Structures) is a Horizon 2020 research and innovation activity (RIA) initiative involving Europe and China. The major goal of this project was to design and test environmentally friendly multifunctional composites for use in the aviation industry. Overall, it focused on the development of environmentally friendly structures for application in aircraft. Figure 5.3 depicts the collection of materials and technologies based on natural composites developed aircraft within the ECO-COMPASS project scope [58].

Although several efforts have been made to incorporate natural fibers in composites, additional research is still necessary to uncover the potential of these natural materials. For instance, although the potential of ramie fibers has not been completely exploited, its high tensile strength is an indicator that it can be used in various products, for example, through its blending with synthetic fibers [59]. According to Romanzini et al. [60], a larger ramie fiber content in hybrid composites resulted in lower weight composites and higher water absorption. By increasing the fiber content, the composites' mechanical properties, such as impact and interlaminar shear strength, were improved. With carbon fiber hybridization, the flexural strength

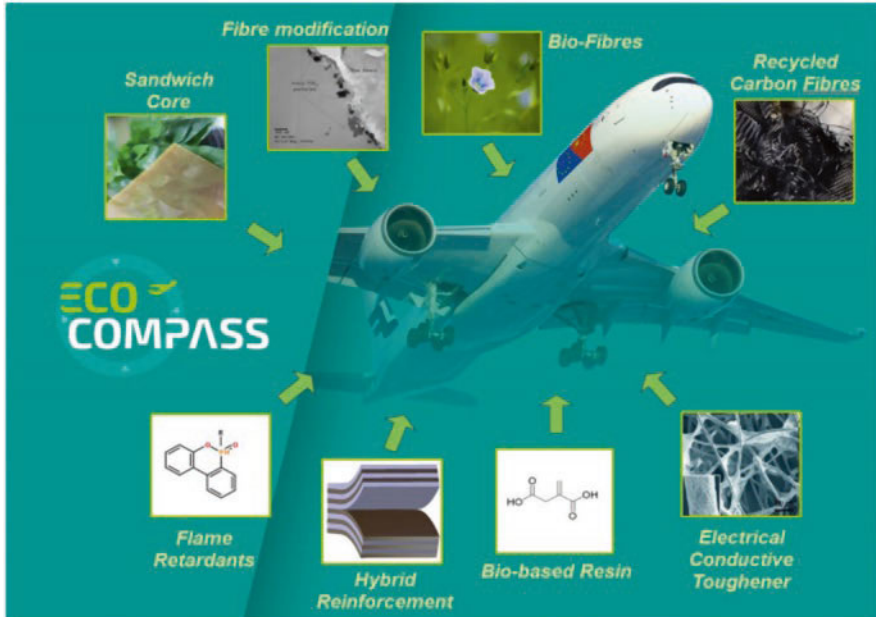


Fig. 5.3 Examples of materials and technologies under investigation in ECOCOMPASS

Table 5.2 Comparison of mechanical properties of bio and synthetic fiber composites

Composite	Tensile strength	References
Carbon/glass/epoxy	58 GPa	[62]
Glass/epoxy	48 GPa	[62]
Carbon/epoxy	110 GPa	[62]
Glass laminate	63 MPa	[63]
Kenaf and glass fiber	65.29 MPa	[64]
Jute and Sisal	66.77 MPa	[65]
Jute and glass fiber	75.68 MPa	[65]
Sisal composite	56.36 MPa	[66]

and modulus of a plain flax/epoxy composite increased from 95.66 MPa to 425.87 MPa and 4.78 GPa to 17.90 GPa, respectively. Carbon fiber hybridization onto flax/epoxy composites can contribute a significant improvement in impact damage behavior and flexural strength and modulus [61]. Brief mechanical properties of bio and synthetic composites are mentioned in Table 5.2 to depict the combined effect to reduce the environmental impact in comparison to completely synthetic composites.

5.7 Conclusions, Challenges, and Future Outlook

Transportation industries functioned to assist mobility of goods and people whether by land, air, or sea, such as automotive, trains, aircraft and ships, etc. Due to the depletion of inorganic materials such as petroleum and other mineral sources, the world is changing, and green materials are at the forefront. As a result, switching to biocomposite materials can meet the expectations for sustainability in the transportation industry by shifting to renewable, recycled, and lightweight materials while taking into account the needs of each type of vehicle. Significant weight reductions can be obtained by switching the materials of some of the heavier vehicle components to high-performance natural fiber composites, contributing to lower fuel consumption and CO₂ emissions.

The ever-increasing carbon footprint and shortage of raw materials push people to think about sustainability, recycling, and the circular economy. As a result, bio-based substitutes are likely to outperform traditional materials. Natural fiber-reinforced composites, particularly those based on bio-based and thermoplastic matrices, are one of the most environmentally friendly materials that could eventually replace glass fiber reinforced plastics (GFRP).

Although the potential of natural composites in transportation has been demonstrated, especially in the automotive sector, the aircraft industry faces many challenges to successfully incorporate these without failing critical requirements. Natural fibers offer advantages and disadvantages when used in composites. They have downsides in terms of performance, behavior in polymeric matrix systems, and processing. Natural fibers' physical qualities do not match in a single fiber or bulk; this inconsistency is a flaw in nature. Depending on the climatic condition, harvesting season, soil conditions, etc., these variations may differ. Additionally, natural fibers have low thermal stability (~200 °C depending on the fiber). Exposure to higher temperatures leads to harmful properties alteration caused by their degradation.

The natural fiber is hydrophilic that constrains its use in the higher ratio in technical applications. The low fiber-matrix adhesion affinity makes the bond weaker and thereby affecting its overall performance. Surface functionalization and treatment of fiber are methods to improve the interface interaction. Sensitivity to humidity and high moisture absorption leads to damage or rupture of the composites. The chemical heterogeneity of the natural fiber makes it a less ideal material for application in aerospace industries. Susceptibility to rotting and high chances of microbial growth can limit its use. These fallbacks can be overcome by modification of the fiber surface and product modifications.

With rising fuel costs and environmental pressure, the aerospace industry, like other industries, is facing sustained implications to improve performance. Understanding the increasing concern for the environment and hike in raw material cost and supply, aircraft production/manufacturing can be reduced by component substitution with comparable alternatives. The aircraft industry ensures that any opportunity to reduce operating costs is explored and exploited wherever possible to

be ahead of competitors. Viewing the progress in composite construction techniques, airplanes with high quality and improved mechanical properties can be developed using natural composite materials.

Independently of the nature of the material, currently, reuse and recycle are two main concepts present in any industry since resources are finite. The aerospace industry is no exception, and the management of wastes generated by end-of-life aircraft components must be addressed. Depending on the composite, there are challenges in its disassembly. Natural composites application expansion in aircraft is an active field of research, motivated by the clear environmental benefits, and focused on improving its performance to meet the different types of safety standards.

Acknowledgments This work was supported by the projects UIDB/00481/2020 and UIDP/00481/2020—FCT—Fundação para a Ciência e a Tecnologia; and CENTRO-01-0145-FEDER-022083—Centro Portugal Regional Operational Programme (Centro2020), under the PORTUGAL 2020 Partnership Agreement, through the European Regional Development Fund.

References

1. Sen, T., & Reddy, H. J. (2011). Application of sisal, bamboo, coir and jute natural composites in structural upgradation. *International Journal of Innovation, Management and Technology*, 2(3), 186.
2. Mitra, B. C. (2014). Environment friendly composite materials: Biocomposites and green composites. *Defence Science Journal*, 64(3), 244.
3. Gholampour, A., & Ozbakkaloglu, T. (2020). A review of natural fiber composites: Properties, modification and processing techniques, characterization, applications. *Journal of Materials Science*, 55(3), 829–892.
4. Humphreys, M. (2003). *The use of polymer composites in construction*.
5. Vilay, V., Mariatti, M., Taib, R. M., & Todo, M. (2008). Effect of fiber surface treatment and fiber loading on the properties of bagasse fiber–reinforced unsaturated polyester composites. *Composites Science and Technology*, 68(3–4), 631–638.
6. Santhosh, J., Balanarasimman, N., Chandrasekar, R., & Raja, S. (2014). Study of properties of banana fiber reinforced composites. *Int. J. Res. Eng. Technol*, 3(11), 144–150.
7. Jeyanthi, S., Jeevamalar, J., & Jancirani, J. (2012). *Influence of natural fibers in recycling of thermoplastics for automotive components*.
8. Rana, A. K., Mandal, A., & Bandyopadhyay, S. (2003). Short jute fiber reinforced polypropylene composites: Effect of compatibiliser, impact modifier and fiber loading. *Composites Science and Technology*, 63(6), 801–806.
9. Brígida, A. I. S., Calado, V. M. A., Gonçalves, L. R. B., & Coelho, M. A. Z. (2010). Effect of chemical treatments on properties of green coconut fiber. *Carbohydrate Polymers*, 79(4), 832–838.
10. Gironès, J., López, J. P., Mutjé, P., Carvalho, A. J. F. D., Curvelo, A. A. D. S., & Vilaseca, F. (2012). Natural fiber-reinforced thermoplastic starch composites obtained by melt processing. *Composites Science and Technology*, 72(7), 858–863.
11. Kengkhetkit, N., & Amornsakchai, T. (2012). Utilisation of pineapple leaf waste for plastic reinforcement: I. A novel extraction method for short pineapple leaf fiber. *Industrial Crops and Products*, 40, 55–61.
12. Jose, S., Salim, R., & Ammayappan, L. (2016). An overview on production, properties, and value addition of pineapple leaf fibers (PALF). *Journal of Natural Fibers*, 13(3), 362–373.

13. Yuhazri, M., & Sihombing, H. (2010). A comparison process between vacuum infusion and hand lay-up method toward kenaf/polyester composite. *International Journal of Basic & Applied Sciences.*, 10, 54–57.
14. Bledzki, A. K., Mamun, A. A., Lucka-Gabor, M., & Gutowski, V. S. (2008). The effects of acetylation on properties of flax fibre and its polypropylene composites. *Express Polymer Letters*, 2(6), 413–422.
15. Fernandes, F. A. O., Tavares, J. P., de Sousa, R. A., Pereira, A. B., & Esteves, J. L. (2017). Manufacturing and testing composites based on natural materials. *Procedia Manufacturing*, 13, 227–234.
16. Gupta, M. K., & Srivastava, R. K. (2016). *Properties of sisal fibre reinforced epoxy composite*.
17. Dittenber, D. B., & GangaRao, H. V. (2012). Critical review of recent publications on use of natural composites in infrastructure. *Composites Part A: Applied Science and Manufacturing*, 43(8), 1419–1429.
18. Nair, K. M., Thomas, S., & Groeninckx, G. (2001). Thermal and dynamic mechanical analysis of polystyrene composites reinforced with short sisal fibres. *Composites Science and Technology*, 61(16), 2519–2529.
19. DoroudgarianNewsha. (2016). *High performance bio-based composites: Mechanical and environmental durability*. PhD Thesis. UPC, Departament de Ciènciadel Materials iEnginyeriaMetal·lúrgica.
20. Shekar, H. S., & Ramachandra, M. (2018). Green composites: A review. *Materials Today: Proceedings*, 5(1), 2518–2526.
21. Soutis, C., Yi, X., & Bachmann, J. (2019). How green composite materials could benefit aircraft construction. *SCIENCE CHINA Technological Sciences*, 62(8), 1478–1480.
22. Soutis, C. (2015). Introduction: Engineering requirements for aerospace composite materials. In *Polymer composites in the aerospace industry* (pp. 1–18). Woodhead Publishing.
23. Quilter, A. (2004). *Composites in aerospace applications, aviation pros*. Retrieved from <https://www.aviationpros.com/engines-components/aircraft-airframe-accessories/article/10386441/composites-in-aerospace-applications>.
24. Johnson, T. (2020). *Composites in aerospace*. ThoughtCo. Retrieved from [thoughtco.com/composites-in-aerospace-820418](https://www.thoughtco.com/composites-in-aerospace-820418).
25. Vlot, A., & Gunnink, J. W. (Eds.). (2011). *Fibre metal laminates: An introduction*. Springer Science & Business Media.
26. Toozandehjani, M., Kamarudin, N., Dashtizadeh, Z., Lim, E. Y., Gomes, A., & Gomes, C. (2018). Conventional and advanced composites in aerospace industry: Technologies revisited. *Am. J. Aerosp. Eng.*, 5, 9–15.
27. Potes, F. C., Silva, J. M., & Gamboa, P. V. (2016). Development and characterization of a natural lightweight composite solution for aircraft structural applications. *Composite Structures*, 136, 430–440.
28. European commission report, Flightpath 2050 Europe's Vision for Aviation. (2011). Retrieved from <https://ec.europa.eu/transport/sites/transport/files/modes/air/doc/flightpath2050.pdf>.
29. Amiri, A., Burkart, V., Yu, A., Webster, D., & Ulven, C. (2018). The potential of natural composite materials in structural design. In *Sustainable composites for aerospace applications* (pp. 269–291). Woodhead Publishing.
30. Black, S. (2015). *Looking to lighten up aircraft interiors? Try natural fibers!* Retrieved from <https://www.compositesworld.com/articles/looking-to-lighten-up-aircraft-interiors%2D%2D-with-natural-fibers>.
31. Shrive, N. G. (2006). The use of fibre reinforced polymers to improve seismic resistance of masonry. *Construction and Building Materials*, 20(4), 269–277.
32. Panzera, T. H., Jeannin, T., Gabriion, X., Placet, V., Remillat, C., Farrow, I., & Scarpa, F. (2020). Static, fatigue and impact behaviour of an autoclaved flax fibre reinforced composite for aerospace engineering. *Composites Part B: Engineering*, 197, 108049.
33. Wang, C., Ren, Z., Li, S., & Yi, X. (2018). Effect of ramie fabric chemical treatments on the physical properties of thermoset polylactic acid (PLA) composites. *Aerospace*, 5(3), 93.

34. Scarponi, C. (2015). Hemp fiber composites for the design of a Naca cowling for ultra-light aviation. *Composites Part B: Engineering*, *81*, 53–63.
35. Affandi, N. B., Rafie, A. S. M., Basri, S., Romli, F. I., Abdul Majid, D. L. A., & Mustapha, F. (2011). A preliminary study on translational kinetic energy absorption using coconut-fiber (coir) sheets as a potential impact-worthy constituent in advanced aerospace material. In *Key engineering materials* (pp. 1028–1033). Trans Tech Publications Ltd..
36. Arockiam, N. J., Jawaid, M., & Saba, N. (2018). Sustainable bio composites for aircraft components. In *Sustainable composites for aerospace applications* (pp. 109–123). Woodhead Publishing.
37. Gopinath, A., Kumar, M. S., & Elayaperumal, A. (2014). Experimental investigations on mechanical properties of jute fiber reinforced composites with polyester and epoxy resin matrices. *Procedia Engineering*, *97*, 2052–2063.
38. Subash, T., & Pillai, S. N. (2015). Bast fibers reinforced green composites for aircraft indoor structures applications: Review. *Journal of Chemical and Pharmaceutical Sciences*, *7*, 305–307.
39. Haris, M. Y., Laila, D., Zainudin, E. S., Mustapha, F., Zahari, R., & Halim, Z. (2011). Preliminary review of biocomposites materials for aircraft radome application. In *Key engineering materials* (pp. 563–567). Trans Tech Publications Ltd..
40. Ilyas, R. A., Sapuan, S. M., Norizan, M. N., Atikah, M. S. N., Huzaifah, M. R. M., Radzi, A. M., et al. (2019). Potential of natural fibre composites for transport industry: A review. In *Prosiding Seminar Enau Kebangsaan 2019; Institute of Tropical Forest and Forest Products (INTROP)*; Universiti Putra Malaysia: Bahau, Malaysia; pp. 2–11.
41. Boegler, O., Kling, U., Empl, D., & Isikveren, A. T. (2015). *Potential of sustainable materials in wing structural design*. Deutsche Gesellschaft für Luft-und Raumfahrt-Lilienthal-Oberth eV.
42. Alonso-Martin, P. P., Gonzalez-Garcia, A., Lapena-Rey, N., Fita-Bravo, S., Martinez-Sanz, V., & Marti-Ferrer, F. (2012). *Green aircraft interior panels and method of fabrication*. European Patent EP2463083A2, 13.
43. Balakrishnan, P., John, M. J., Pothan, L., Sreekala, M. S., & Thomas, S. (2016). Natural fibre and polymer matrix composites and their applications in aerospace engineering. In *Advanced composite materials for aerospace engineering* (pp. 365–383). Woodhead Publishing.
44. Niedermann, P., Szebényi, G., & Toldy, A. (2015). Characterization of high glass transition temperature sugar-based epoxy resin composites with jute and carbon fibre reinforcement. *Composites Science and Technology*, *117*, 62–68.
45. Chen, J. T., Abdullah, L. C., & Tahir, P. M. (2019). Biomass valorization for better aviation environmental impact through biocomposites and aviation biofuel. In *Structural health monitoring of biocomposites, fibre-reinforced composites and hybrid composites* (pp. 19–31). Woodhead Publishing.
46. Dhakal, H. N., Skrifvars, M., Adekunle, K., & Zhang, Z. Y. (2014). Falling weight impact response of jute/methacrylated soybean oil bio-composites under low velocity impact loading. *Composites Science and Technology*, *92*, 134–141.
47. Scarponi, C., & Messano, M. (2015). Comparative evaluation between E-glass and hemp fiber composites application in rotorcraft interiors. *Composites Part B: Engineering*, *69*, 542–549.
48. Jarukumjorn, K., & Suppakarn, N. (2009). Effect of glass fiber hybridization on properties of sisal fiber–polypropylene composites. *Composites Part B: Engineering*, *40*(7), 623–627.
49. Czél, G., Pimenta, S., Wisnom, M. R., & Robinson, P. (2015). Demonstration of pseudo-ductility in unidirectional discontinuous carbon fibre/epoxy prepreg composites. *Composites Science and Technology*, *106*, 110–119.
50. Dai, J., Peng, Y., Teng, N., Liu, Y., Liu, C., Shen, X., et al. (2018). High-performing and fire-resistant biobased epoxy resin from renewable sources. *ACS Sustainable Chemistry & Engineering*, *6*(6), 7589–7599.

51. Li, C., Liu, X., Zhu, J., Zhang, C., & Guo, J. (2013). Synthesis, characterization of a rosin-based epoxy monomer and its comparison with a petroleum-based counterpart. *Journal of Macromolecular Science, Part A*, 50(3), 321–329.
52. Dinesh, T., Kadirvel, A., & Hariharan, P. (2020). Role of nano-silica in tensile fatigue, fracture toughness and low-velocity impact behaviour of acid-treated pineapple fibre/stainless steel wire mesh-reinforced epoxy hybrid composite. *Materials Research Express*, 6(12), 125365.
53. Bos, H. L., Van Den Oever, M. J. A., & Peters, O. C. J. J. (2002). Tensile and compressive properties of flax fibres for natural fibre reinforced composites. *Journal of Materials Science*, 37(8), 1683–1692.
54. Jawaid, M. H. P. S., & Khalil, H. A. (2011). Cellulosic/synthetic fibre reinforced polymer hybrid composites: A review. *Carbohydrate Polymers*, 86(1), 1–18.
55. Sathishkumar, T. P., Naveen, J. A., & Satheeshkumar, S. (2014). Hybrid fiber reinforced polymer composites—A review. *Journal of Reinforced Plastics and Composites*, 33(5), 454–471.
56. Gururaja, M. N., & Rao, A. H. (2012). A review on recent applications and future prospectus of hybrid composites. *International Journal of Soft Computing and Engineering*, 1(6), 352–355.
57. Jawaid, M., & Siengchin, S. (2019). Hybrid composites: A versatile materials for future. *Applied Science and Engineering Progress*, 12(4), 223–223.
58. Bachmann, J., Yi, X., Gong, H., Martinez, X., Bugada, G., Oller, S., et al. (2018). Outlook on ecologically improved composites for aviation interior and secondary structures. *CEAS Aeronautical Journal*, 9(3), 533–543.
59. Jose, S., Rajna, S., & Ghosh, P. (2017). Ramie fibre processing and value addition. *Asian Journal of Textile*, 7(1), 1–9.
60. Romanzini, D., Lavoratti, A., Ornaghi, H. L., Jr., Amico, S. C., & Zattera, A. J. (2013). Influence of fiber content on the mechanical and dynamic mechanical properties of glass/ramie polymer composites. *Materials & Design*, 47, 9–15.
61. Chapman, M., & Dhakal, H. N. (2019). Effects of hybridisation on the low velocity falling weight impact and flexural properties of flax-carbon/epoxy hybrid composites. *Fibers*, 7(11), 95.
62. Prabhakaran, D., Andersen, T. L., Markussen, C. M., Madsen, B., & Lilholt, H. (2013, July). Tensile and compression properties of hybrid composites—A comparative study. In *Proceedings of the 19th International Conference on Composite Materials (ICCM19)* (pp. 1029–1035). Canadian Association for Composite Structures and Materials.
63. Olusegun, D. S., Stephen, A., & Adekanye, T. A. (2012). Assessing mechanical properties of natural fibre reinforced composites for engineering applications. *Journal of Minerals and Materials Characterization and Engineering*, 11(1), 780–784.
64. Sapiai, N., Jumahat, A., & Mahmud, J. (2015). Flexural and tensile properties of kenaf/glass fibres hybrid composites filled with carbon nanotubes. *Jurnal Teknologi*, 76(3).
65. Cavalcanti, D. K. K., Banea, M. D., Neto, J. S. S., Lima, R. A. A., Da Silva, L. F. M., & Carbas, R. J. C. (2019). Mechanical characterization of intralaminar natural fibre-reinforced hybrid composites. *Composites Part B: Engineering*, 175, 107149.
66. Badrinath, R., & Senthilvelan, T. (2014). Comparative investigation on mechanical properties of banana and sisal reinforced polymer based composites. *Procedia Materials Science*, 5, 2263–2272.
67. Georgiadis, S., Gunnion, A. J., Thomson, R. S., & Cartwright, B. K. (2008). Bird-strike simulation for certification of the Boeing 787 composite moveable trailing edge. *Composite Structures*, 86(1–3), 258–268.

Chapter 6

Aeroengines: Principles, Components, and Eco-friendly Trends



Mohammad Rauf Sheikhi, Hakan Aygun, and Onder Altuntas

6.1 Introduction

Jet engines are one of the favorite sources of shaft power up to the present time. They are comparatively clean and more efficient than other common sources, and their working principle is especially applicable to aircraft propulsion. With the increasing use of gas turbine engines in civil aviation, the emission of pollutants from these engines has also increased sharply. According to the International Energy Agency, aviation is probably the most difficult transport sector to decarbonize, due to its cost and size [1]. From airlines to aircraft manufacturers and airports, the aviation industry has taken steps to implement environmentally friendly practices to combat climate change. In 2019, Etihad Airways powered a commercial flight using a jet and a biofuel blend made from a plant called Salicornia, which grows in the Abu Dhabi desert. Sustainable jet fuel can be made from plants, algae, used cooking oil, and even municipal waste, and the trend seems to be taking off [2]. Carbon emissions from aviation were around 2.5% of global emissions in 2018. If that sounds like a small ripple, consider [1]. From 2013 to 2018, CO₂ emissions from commercial flights increased by 32% [3], which is expected to triple as the global travel industry begins to grow [4]. In 2019, 4.5 billion passengers traveled by air [5], while the number of international tourists increased by 4% to reach 1.5 billion [6]. The main countries whose travelers contribute the most to CO₂ emissions are the United States, China, the United Kingdom, Japan, and Germany. In total, the top ten

M. R. Sheikhi (✉) · O. Altuntas

Faculty of Aeronautics and Astronautics, Eskisehir Technical University, Eskisehir, Turkey

e-mail: mohammadraufsheikhi@eskisehir.edu.tr; oaltuntas@eskisehir.edu.tr

H. Aygun

Department of Airframe and Powerplant Maintenance, Firat University, Elazig, Turkey

e-mail: haygun@firat.edu.tr

countries are responsible for 60% of aviation CO₂ emissions [3]. A return flight from London to New York generates more than a ton of carbon dioxide per passenger [7]. This is what the average Paraguayan citizen spends in a year [8]. A growing number of travelers in Europe and the United States are already reducing their air travel due to environmental concerns, which could hamper passenger growth. The aviation industry also wants to improve fuel efficiency—that is, the distance an aircraft can travel on one gallon of fuel. Airbus and Boeing, the two biggest names in the industry, already produce more efficient jets, like the Airbus A350 XWB and the Boeing 787 Dreamliner. In addition to cheap planes, there are also other great solutions. Electric planes have also made an appearance in recent years, whether they are hybrid jets powered by fuel and battery, or fully electric planes. Prototypes such as the Aviation Alice are expected to enter commercial service in the coming decades. However, one of the biggest challenges electric aircraft face is the battery. They are still relatively heavy for aviation. Pound for pound, jet fuel is about 14 times the usable energy of a new lithium battery. In 2009, the International Air Transport Association set strategic goals for the aviation industry, including zero-emission growth from 2020 and a reduction in net air traffic. 50% CO₂ emissions by 2050 compared to 2005 levels [9]. In 2016, the International Aviation Carbon Offsetting and Reduction Plan, or CORSIA, was also implemented [10].

The development of new advanced gas turbine engines with unique features, low fuel consumption, and reduced emissions is not possible without the effective use of critical new technologies. Critical engine technologies are technologies that improve the quality of competitive engines based on the integration of new materials, new technological processes, design solutions, and test methods [11]. With the continued growth of air traffic and the growing public concern for anthropogenic contribution and population growth, we need to find a good solution to this problem and the following can be the most important factors in controlling the emission of pollutants by aircraft:

- The number of operations should be reduced
- The aircraft design and type must be changed
- The way planes fly must be changed with new rules and procedures

It seems unlikely that the number of operations could be reduced. However, changing the type of aircraft is a difficult and time-consuming task. This appears to be a temporary solution. It is therefore recognized that emphasis should be placed on assessing the feasibility of flying the aircraft differently and establishing new or changed operating rules and procedures that reduce the impact of aircraft operations on the environment and climate change. Therefore, trajectory optimization could be an easy solution to implement. At the same time, in new aircraft designs, the use of high-performance and lightweight materials can be considered as one of the important factors in reducing fuel consumption and ultimately pollutants. Lightweight design is a concept widely studied and used in many industries, particularly in aerospace applications, and is associated with the concept of green aviation. An effective way to increase fuel efficiency and reduce fuel consumption is to reduce aircraft mass, as less air mass requires less lift and thrust. For instance, Boeing 787, with a

20% weight reduction resulted in a 10–12% improvement in fuel economy [12]. In addition to reducing environmental impact, in-flight performance improvements such as improved acceleration, increased strength and structural rigidity, and improved safety performance can be achieved through a lightweight design. The use of new generation composites in different parts of the aircraft can reduce the weight of the aircraft to an acceptable level. In recent years, we have witnessed the increasing use of new generation composites in aircraft fuselages. Compared to the fuselage, the use of these composites in the aircraft engine has been less due to the high operating temperature of the internal parts of the engine. Recently, leading companies in the manufacture of aircraft engines have used the use of high-strength composite materials in cold parts of aircraft engines, such as fans in turbofan engines and engine covers, etc., which can reduce the weight of aircraft engines. This chapter provides a summary of the aircraft propulsion and materials used in aero gas turbine engines. First, the evaluation and classification of aircraft engines are reviewed. The specifications of the integrated materials and systems used in the gas turbine engine are considered. Recent developments of materials used in aero gas turbine engines and eco-friendly aeroengines materials are briefly discussed.

6.2 Brief Historical Overview and Classification of Aeroengines

According to the words of Roman Aulus Gellius, a wooden bird was one of the earliest devices that efficaciously applied the principles needed for propulsion. Until the seventeenth century, the principle of action–reaction was not stated as a scientific law. About 300 years after this story (in the first century AD), another Greek, the Heron of Alexandria, who invented the steam turbine, has taken the first step of propulsion. The name of his device is aeolipile (also known as a Heron’s Engine). According to the notes of Hero [13], the construction of the aeolipile, which looked like a rocket reaction engine, and the first-recorded steam engine (As shown in Fig. 6.1).

Heron mounted a ball on a kettle. A fire under the kettle turned the water into steam, and the gas flowed through pipes to the ball. Two L-shaped tubes on opposite sides of the ball let the gas escape and gave the ball a thrust that made it rotate [13]. After Heron’s great invents, many designs and works were done, such as Lagari Hasan Celebi launched with a rocket from Istanbul in 1633 [15], the turbine concept of Giovanni Branca in 1629, the original gas turbine engine designed by John Barber in 1791, etc. Henri Giffard built an airship in 1852. It was the first successful flight (flew at a speed of 10 km/h to cover about 30 km) in aviation history. In 1894, Maxim’s gigantic biplane had a connection with a ground by a railed track, was a pioneer. These developments have been the harbinger of modern aviation. The Wright brothers invented and built the airplane. They made the world’s successful flight in the world on December 17, 1903. The Wright brothers made the first

Fig. 6.1 Hero's Aeolipile [14]. Under the Creative Commons license



controlled, sustained flight of a powered aircraft, which is a heavier-than-air, in Kitty Hawk, North Carolina. Between 1904 and 1905, they technologically advanced their flying machine into the first practical fixed-wing aircraft. This is the first to invent aircraft controls that made the fixed-wing flight possible. There are several scientists and engineers to the developed concept of the jet engine (air-breathing engines both with compressor and without compressor) [16].

In the note of the English scientist Frank Whittle, he wrote that gas turbines could be used in the reinforcement of an aircraft in 1920. Ten years after this acceptance, he has patented the first turbojet, which has an axial compressor and centrifugal compressor. His jet engine was the pioneer of gas turbine engines. In 1939, German Hans von Ohain patented a turbojet engine, and he used it in Henkel engine. Against the linear flow of Whittle's design, Hans von Ohain's turbojet is reverse flow. One of the pioneers was Secondo Campini, an Italian engineer, wrote a report about jet propulsion for the Italian Air Ministry in 1932, then he developed his idea in 1940. The first flight of Campini's mechanical compressed jet engine took place at 270 km between Rome and Milan. Another pioneer was German Hans von Ohain. He designed his jet engine idea, and this aircraft flew in 1939. The first passenger aircraft powered by turboprops was British Vickers Viscount, which was tested in 1948; the first aircraft powered by turbojet was De Havilland Comet, which was tested in 1949.

On the other hand, René Lorin, who is a French aerospace engineer, patented his idea for the world's first ramjet in 1913. But his design was not finalized. In 1933, when René Leduc wanted to patent his invention (known nowadays under the name of "pulsejet"), he discovered the publication of René Lorin. In the following years, he built his idea and was able to demonstrate the practical application of this theory

in 1936. René Leduc terminated the new concept of the pulsejet engine that René Lorin had first begun as a ramjet engine [13, 17]. Meanwhile, after Schmidt, a German scientist designed the pulsejet engine in 1928, the Germans used this engine in the V-1 flying bomb in 1942.

In the design of aeroengines, designers strive to meet several requirements, listed below.

- High thrust (also highest power) at low weight
- Low fuel consumption
- The lowest engine mass/volume/dimension to obtain specific engine performance
- High reliability
- High operational and maintenance technology
- High controllability

6.3 Engine Classification

It is seen those various classifications (airframe, tail, landing system, engine type, etc.) are made for aircraft by considering the design and life processes. The payload to be carried by aircraft directly affects the classifications. For example, the number of passengers will increase the number of seats for the cabin, and the body structure will cause us to classify it as a narrow/wide body. Another example is that less/more cargo (passenger or cargo) to be carried will cause less/more power required for the aircraft to fly, and thus a classification according to engine type [18]. The engine is an essential element for lighter/heavier-than-air aero vehicles (aircraft, airplanes, helicopters, rockets, etc.). Both to move or accelerate an aero vehicle and to overcome drag forces, and a driving force is required, which is usually provided by an aeroengine. Mainly, force to move an aeroengine can be produced as mechanical (with propeller) or thermal (without propeller). With a propeller engine, the air is accelerated by rotating propeller blades. These are airfoil-like surfaces arranged at an angle to the incoming air, which accelerate the air in their plane of rotation purely mechanically downstream. The propeller is driven either by an internal combustion engine (piston engine) or by a gas turbine (turboprop or turboshaft engines). In the case of a jet engine, propulsion is generated in the form of thermal acceleration. It is based on a thermodynamic basis cycle, a fast gas jet is generated within the jet engine, and this is ejected against the direction of movement of the engine. Aeroengines can be subdivided in different ways. Aeroengine classification is given in Fig. 6.2.

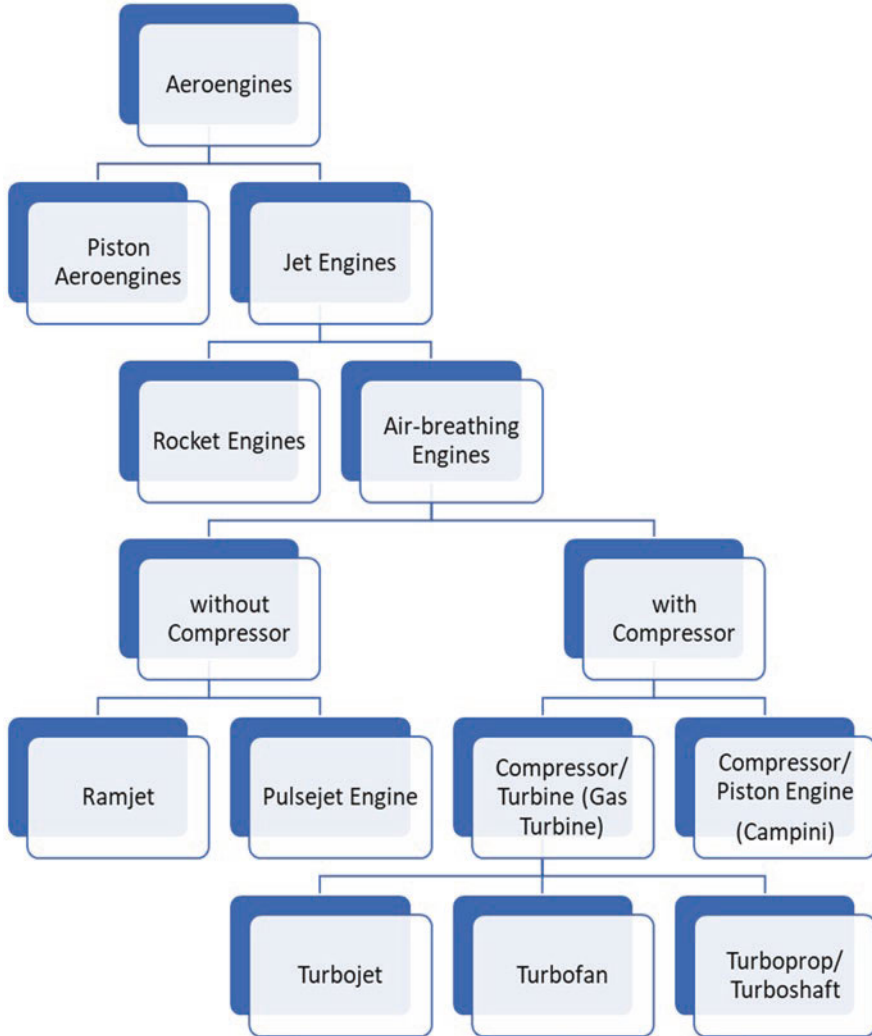


Fig. 6.2 Classification of aeroengines

6.4 Piston Aeroengines

While jet propulsion had been used to produce a forced aircraft, piston aeroengines were used in the first manned aircraft. Piston aeroengines are a combination of an internal combustion engine and a propeller. So, it can call a piston-prop engine as shown in Fig. 6.3. Three-quarters of the total number of aircraft in the world are piston-prop aircraft. The most important reason for this is that it is the most economical aircraft type that a private pilot license can use. Other usage areas of piston-props can be listed as a special purpose, training, ambulance, spraying, etc. While

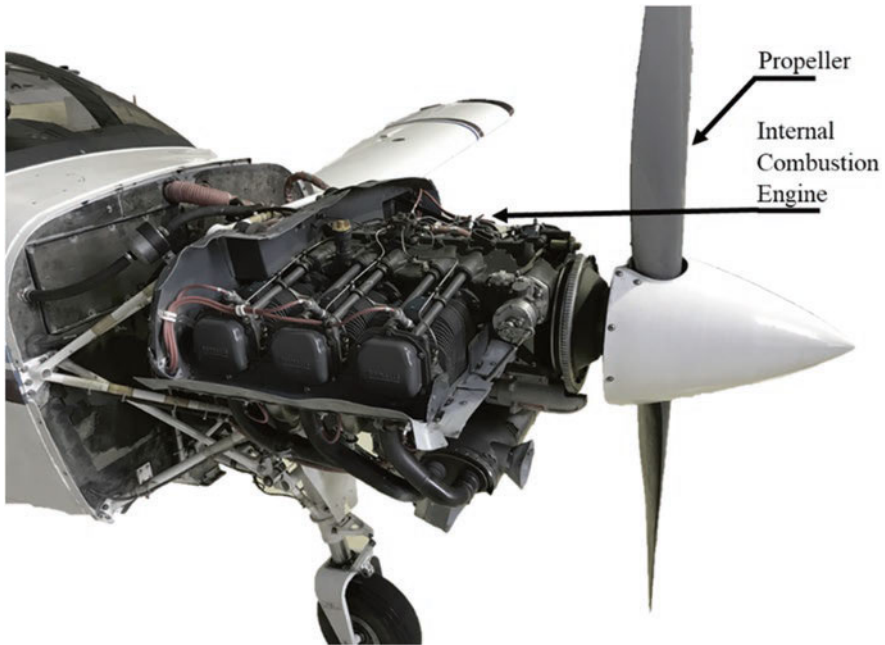


Fig. 6.3 Piston-prop Engine (Piston Aeroengine)

the use of reciprocating engines in ground vehicles goes back 150 years, their use in aircraft goes back to 100 years [18–20].

Internal combustion engines fall into three main categories, compression ignition engines (Diesel Cycle), spark-ignition engines (Otto Cycle), and rotary engines. The basic components of a reciprocating engine are a crankcase, cylinder, pistons, connecting rods, valves, a valve actuation mechanism, and a crankshaft. The valves and spark plugs are in the head of each cylinder. One of the valves is in a passage leading from the induction system. The other is in a passage that leads to the exhaust system. Each cylinder has a moving piston that is connected to a crankshaft via a connecting rod.

6.5 Jet Engines

A jet propulsion engine ventures a column of air backward at too high a speeds. Jet Engines are grouped into two rocket engines and air-breathing engines. While the rocket engine is a part of jet engines, it cannot directly draw air from outside. The combustion process occurs in a closed container. Then, burning gases flow out of the nozzle at high speed. The rocket carries its oxidizer and fuel (solid or liquid) for combustion (both independent of the atmosphere). Rocket is an advantage for

non-atmospheric flight. Ramjet engine, which is an air-breathing engine, may be either of the subsonic or supersonic types. So, it is proper for atmospheric flight. Ramjet does not need a compressor or a turbine. Enough increase is achieved by slowing down the high-speed air flowing into the diffuser (ram effect). For the ramjet to operate, the aircraft must already be in flight at a sufficient speed. The combustion products exiting the combustion chamber are expanded through the nozzle to produce thrust.

Pulsejet, a straightforward jet engine, has three main parts, which are intake, combustion chamber, and acoustically resonant exhaust pipe. The aerial view takes place intermittently. Thus, the combustion occurs in pulses. Compared with continuous thrust, pulsejet has found limited applications [21]. Another air-breathing engine type, commonly used nowadays, is the gas turbine engine. There are three types of gas turbines: turbojet, turbofan, and turboprop/turboshaft.

6.5.1 Turbojet Engines

The turbojet engine comprises an inlet, compressor, combustion chamber, turbine, and exhaust, as shown in Fig. 6.4 the inlet is a sample duct form, which is an opening and first meeting point of a turbojet engine. After the inlet section, the compressor section meets the air. At the end of this section, the air is now compressed. Then, compressed air is delivered to the combustor (generally combustion chamber). While compressed air enters the combustion chamber, fuel is injected into the first zone of the combustion chamber. In a steady-state continuous situation, mixed compounds are ignited (at relatively constant pressure) by sparkplugs, which are in the combustion chamber. To continue the burning process, the correct air–fuel mixture is important. Only about 25% of the air is used for the combustion process. The rest of the air (approx. 75%) is mixed with the combustion products (exhaust gas) to cool down before the gases enter the turbine section. The main power is created in the turbine section. While the burned air moves to the cold zone (atmosphere conditions), it bumps the turbine blades. Due to its aerodynamic structure, the turbine blades rotate. The turbine power up the compressor and auxiliary equipment. Because of the differences in the velocity, mass, and pressure from zero to the end, the thrust is created to push the jet engine forward. In brief, the thrust is created by the exhaust air is released much faster speed than when it entered [21, 22]. An afterburner section is an extra combustion part used on some turbojet engines, generally those on supersonic aircraft. Its target is to get larger thrust, normally for supersonic flight, takeoff, and maneuver positions. Afterburning inserts extra fuel into a combustor in the jet pipe at the back of the turbine, “reheating” the exhaust gas [23].

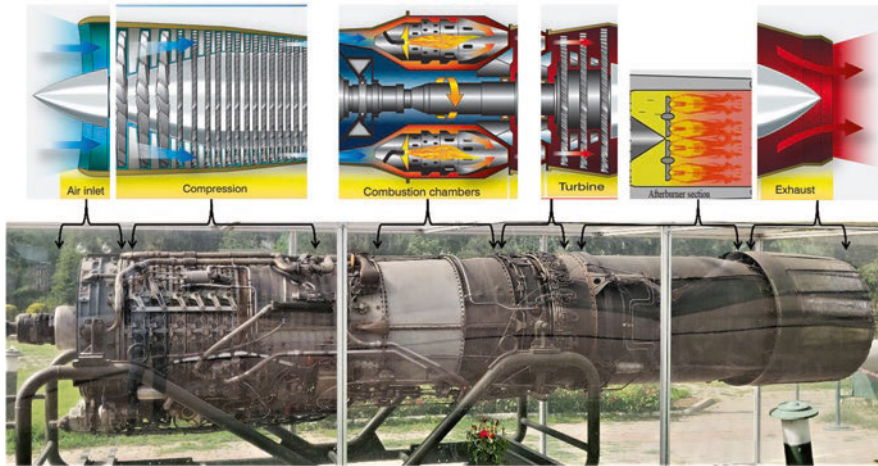


Fig. 6.4 General Electric J79 afterburning turbojet engine [20]. Under the Creative Commons license

6.5.2 Turbofan Engines

The turbofan engine is like a turbojet engine, except for a fan section. The fan section is mounted at the front (rarely at the rear) of the engine. It is simultaneously working with the compressor section. It rotates at the same speed as the compressor or maybe mechanically geared down. Also, the fan draws in more air than a turbojet compressor because the inlet has a larger area. While some of the entrance air passes throughout the compressor, the rest of the air passes outside of the core engine (compressor-combustion chamber-turbine). Compared to the turbojet, the rest of the air helps to decrease the noise level and to increase thrust. Extra thrust allows the turbofan aircraft to take off at a much higher gross weight. Because the air is not heated by burning fuel for thrust, the turbofan engine has lower fuel consumption [21, 22]. As can be seen in Fig. 6.5, the air usually driven by the fan does not pass through the central working core of the engine. The amount of airflow from the fan bypass to the core flow of the engine is the bypass ratio.

6.5.3 Turboprop/Turboshaft Engines

The turboprop and the turboshaft engines have the core engine (basic turbojet engine: compressor, combustion chamber, and turbine), except propeller or rotor blades. While the turboprop engine is used for aircraft (horizontal located; horizontal operation), the turboshaft engine is used for helicopters (vertical located; both horizontal and vertical operations). As shown in Fig. 6.6, rotor blades and gearbox are additional parts for the core in the turboshaft engine. Here, while a huge part of

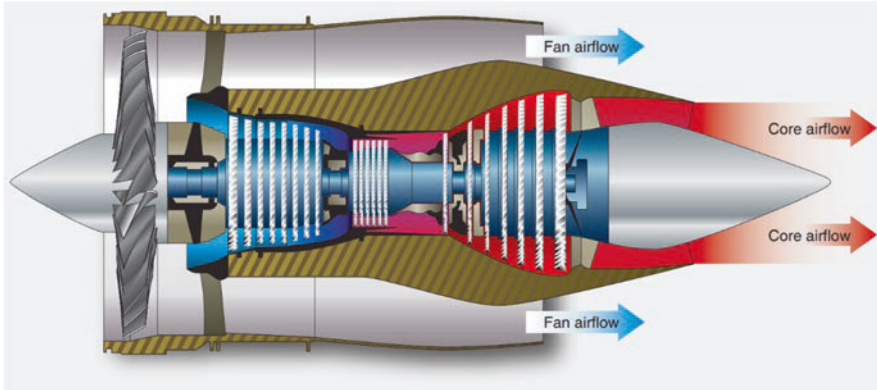


Fig. 6.5 Turbofan engine [24]. Under the Creative Commons license

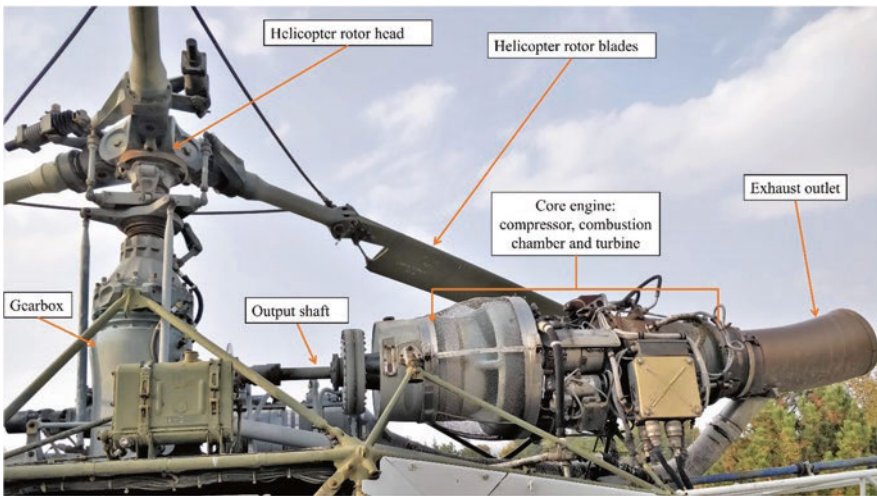


Fig. 6.6 French Alouette 318 C turboshaft engine [25]. Under the Creative Commons license

thrust is created by the rotation of the propeller, the rest of thrust is produced by exhaust gases (about 8%) [21, 22]. Compared to turbofans, turboprops have more efficient at flight speeds less than 650 km/h (400 mph; 350 knots) because the jet velocity of the propeller (and exhaust) is comparatively low. Present-day turboprop aircraft operate at almost the same speed as small regional jet aircraft but burn two-thirds of the fuel per passenger. However, compared to a turbojet a propeller or turboshaft aircraft can fly at a lower ceiling.

6.6 Benefits of New Materials for Gas Turbine Engines

From the past to date, the improvements in aircraft engineering and material engineering have reflected enhancements of jet engine performance. Namely, jet engines have experienced a large of design changes on their important components so far. The reasons for this could be ranked as advances in material technology, cooling technology for turbine blades, and aerodynamic design technology for a compressor and a turbine. According to Fig. 6.7, fuel efficiency has gradually increased since 1940 [26].

As another method to enhance the thermal efficiency of the jet engine is to increase the overall pressure ratio and turbine inlet temperature of the jet cycle. These design changes directly could be associated with advancements in material and cooling technology. Figure 6.8 demonstrates the temperature capacity of turbine material over 50 years. A nickel-based superalloy is usually employed for the construction of a high-pressure turbine. Considering the past 70 years, at the early jet age, the turbine inlet temperature had been achieved to 1000 K for the Whittle engine. However, recently, it increases up to the level of 1800 K for Trent 900. Namely, it should be noted that the reason for these changes lies in the fact that manufacturing technology for the superalloys that are employed in the turbine blades have enhanced from wrought to directionally solidified and single-crystal alloys [27].

As can be understood from the trend, only moderate enhancements have been achieved so far and it is likely to be continued. It is projected that an important

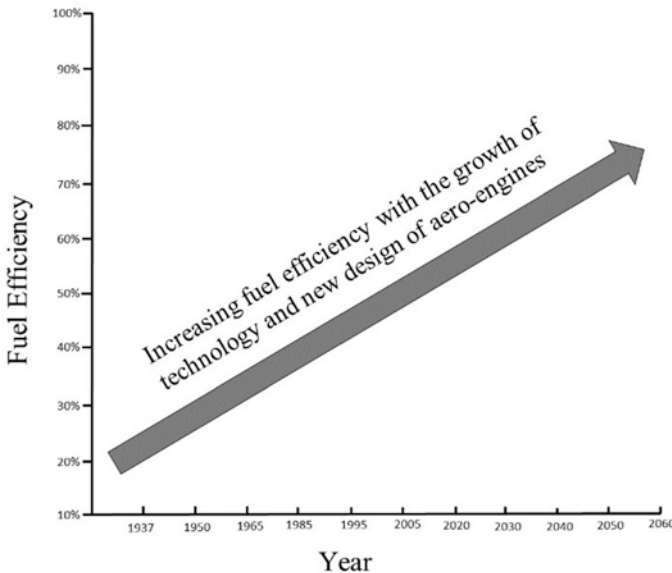


Fig. 6.7 Progress in aeroengines fuel efficiency

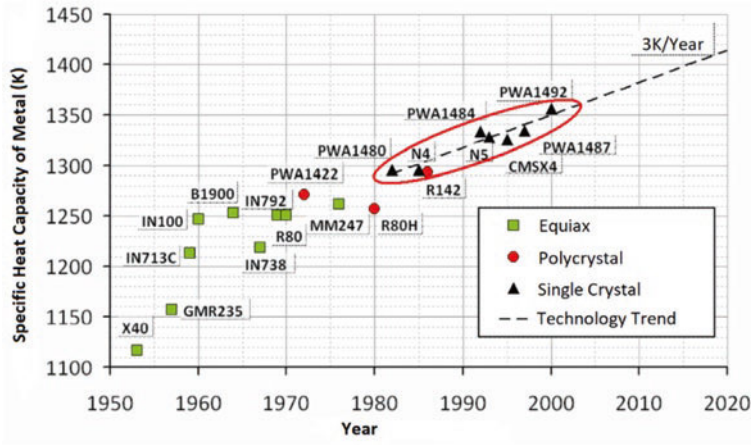


Fig. 6.8 Progress in aeroengines metal heat capacity [27]. Under the Creative Commons license

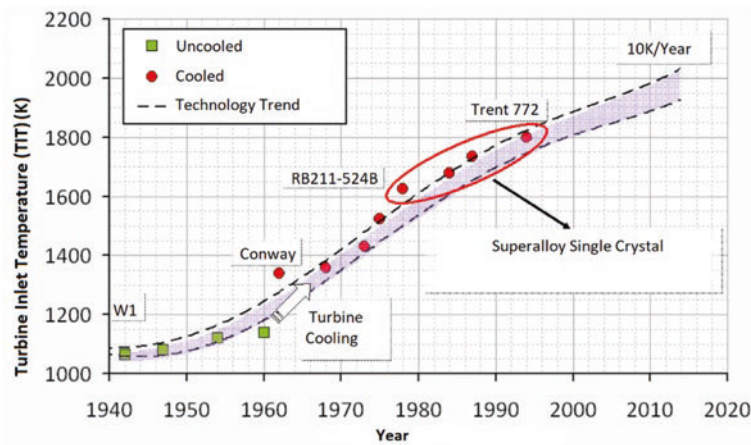


Fig. 6.9 Progress in aeroengines turbine inlet temperature [27]. Under the Creative Commons license

improvement in the field will result from the common usage of ceramics. However, realizing this is still required by more performing research. Considering Fig. 6.9, turbine material technology has been subjected to a limited enhancement rate (roughly 3 [K/year]). However, the design changes of aero engine have led to a substantial rise in turbine inlet temperature over the last 60 years (roughly 10 [K/year]). This case is given in Fig. 6.9 for engines designed for long-haul applications. It should be noted that the application of cooling and Thermal Barrier Coatings (TBC) in turbine designs has the major reason behind these improvements in turbine inlet temperature.

6.7 Materials Used in Aero-gas Turbine Engine Components

Considering the development of aircraft materials, it is required to largely be improved. However, this issue regarding material performance has sparked many organizations and universities to be studied and improved. If it can be achieved, decreasing fuel cost, and performing safe flights depend on the achievement degree of the material performance with high technology. It can be noted that usage of titanium and composite is prone to be preferred more since these leads to decrease the overall weight of the engine thereby the fuel efficiency. Especially, the studies about composite have been gradually increased. It is projected that these materials will be adopted in the major engine pairs. The main goal of the composite to prefer is to considerably save fuel cost [21]. Current and future materials used in different parts of a turbofan engine are presented in Fig. 6.10.

6.7.1 Fan Section

Generally, both fan blades and fan disks of jet engines have been manufactured from titanium, usually forged Ti-6Al-4V. These materials make the component upgrade mechanical properties. Namely, ultimate tensile strength, fatigue resistance, and ductility of the fan component could have been achieved thanks to the forging and machining of titanium alloy. There is a difference between the engines with the smaller diameter and the larger diameter. For The former, solid titanium blades are used whereas for the latter, hollow titanium blades with SPF/diffusion bonding process are used [29]. Fan blades with lengths more than 1 m can be manufactured from polymer matrix composites (PMCs). Especially, GE90, GENx, and GE9x engines incorporate these composite blades due to their being lightweight, stiff, and superior fatigue life. Having a bonded leading edge of Ti-6Al-4V, 23 PMC blades allows the engine to continue its running without catastrophic failure in case of a bird-ingestion event. To obtain greater fatigue capability, the construction of fan disks can be made of higher strength titanium alloys. For this aim, Ti-6Al-2Mn-4Zr-2Sn can be adopted. However, it should be noted that these alloys are heavier and have more complex processes due to chemistry and higher strength.

Generally, fan blades consist of titanium, aluminum, and stainless steel. The reason why titanium is employed is that it has a high strength to weight ratio, corrosion resistance, and creep resistance. However, the constituents of fan blades are different from the engine to the engine. For example, Carbon Fiber Reinforced Plastic composite (CFRP) is employed in the construction of fan blades (see Fig. 6.10) for the GENx engines with titanium leading edge of blades (manufactured from Ti-6Al-4V alloys) since this material can resist the impact forces in case of bird strikes. There are several lamellar structures such as TiAl and Ti Al-3 phases in Ti-6Al-4V. These structures are effective to prevent rapid creep and fatigue crack growth. Considering below approximately 800 C, Ti-6Al-4V alloys demonstrate

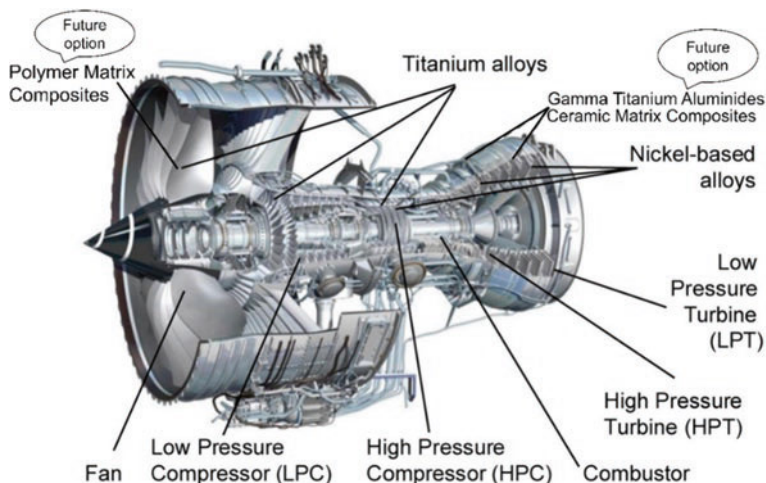


Fig. 6.10 Current and future materials used in different parts of the gas turbine engine [28]. Reused by permission from Elsevier

favorable behavior at high-temperature strength. Furthermore, in terms of design, the newly forward-swept wing types of the blade initialize to be employed thanks to 3D technology related to aerodynamic design. This case leads to a decrease in the number of fan blades from 22 to 18 since the high aerodynamic performance could be obtained with this design approach [15].

Fan case is generally composed of titanium, Aluminum, and CFRP since these components are generally the heaviest part of the engine. CFRP is employed for those of the GENx engines. There are laminated fiber fabrics in these composite cases. Thus, Fan cases could be manufactured as about half weight compared with the conventional metal cases. Both the weight reduction and the safety requirements are achieved thanks to the case with composite materials. Besides, the high resistance against damage, fatigue, and corrosion could be obtained with CRFP. In short, cast aluminum 2219 or stainless steel were typically employed to produce fan cases. However, PMC fan cases have emerged in recent years since they lead to saving weight and show higher corrosion resistance as well as added stiffness.

6.7.2 Compressor Section

Considering the function of the compressor, it compresses air coming from the Fan for turbofan engines. The increasing pressure of air accompanies its rising temperature. Therefore, the material used in this section must withstand high-temperature effects. For this aim, Fe-, Ni-, and Ti-based alloys are generally adopted. Considering the GENx engines having high compression ratios, the importance of this issue becomes more serious. Such as fan sections, Ti-6Al-4V alloys are employed in the

low-pressure compressor blades as well as several high-pressure compressor blades. The remaining parts of high-pressure compressor blades (see Fig. 6.13b) are manufactured from Ni-based superalloys such as Hastelloy X. The several stages of the high-pressure compressor have been manufactured from Ti-based alloys such as Ti-6242 (Ti-6Al-2Sn-4Zr-2Mo) in recent years due to its light material. Furthermore, airfoils and disks of the low-pressure compressor are manufactured from titanium alloys such as Ti-6Al-4V whereas nickel-based superalloys are used at the aft portion of the high-pressure compressor due to high thermal stress which titanium alloys cannot withstand thermal stress. For the early forward stages of the compressor, it should be noted that titanium alloys such as Ti-17 and Ti-6Al-2Mn-4Zr-2Sn (Ti-6-2-4-2) are employed. Lastly, the usage of cast superalloys and powder superalloys can be required for creep and fatigue resistance.

6.7.3 Combustor Section

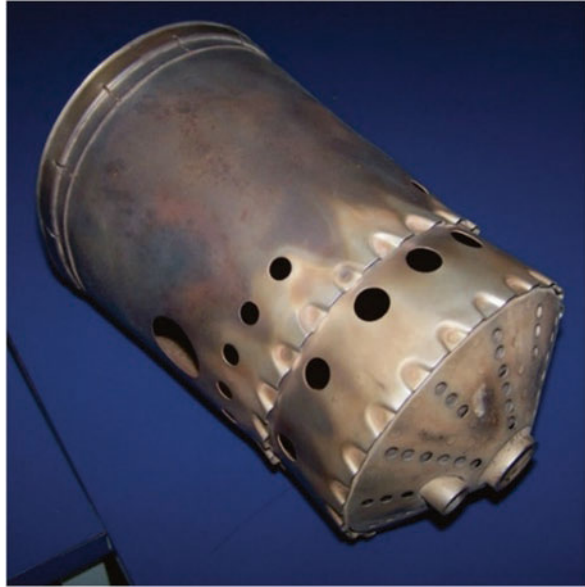
The compressed air is delivered to the combustor where the air is mixed with fuel to perform the combustion. After that process, gases with a high temperature and high energy are produced to move aircraft forward. This section is required to be composed of heat-resistant alloys such as Co- and Ni-based superalloys since more than 1000 °C of temperature could be measured in the combustor. Table 6.1 shows the materials used in the combustor. The mechanical properties of the superalloys are enhanced by introducing several additives to them. Each of these additives has the aim used for in it. For example, Aluminum (Al) and Titanium (Ti) could be preferred for strength whereas Molybdenum (Mo), Tungsten (W), and Rhenium (Re) are selected to enhance high-temperature strength. As for Chromium (Cr), it is selected for corrosion resistance.

The outer case of the combustor is exposed to high thermal and pressure loads affecting it. In this context, a nickel-based superalloy, such as alloy 718 or Waspaloy is adopted for this component. To obtain added strength, these outer cases are generally made as ring rolled. Cobalt sheet material such as HS188 or nickel-based superalloy such as Hastelloy X is used for the inner liner that prevents the combustion flame from directly contacting the case. Hastelloy X has unusual resistance to

Table 6.1 Materials used in the combustor [30]. Under the Creative Commons license

Alloys	Composition	Considerations
Nimonic 263	Ni20Cr20Co0.4Fe6Mo2.1Ti0.4Al0.06C	Nickel-base superalloy
Hastelloy X	Ni22Cr1.5Co1.9Fe0.7W9Mo0.07C0.005B	Nickel-base superalloy
HA188	Co22Cr22Ni1.5Fe14W0.05C0.01B	Cobalt-base superalloy
617	54Ni22Cr12.5Co8.5Mo1.2Al	Nickel-base superalloy
230	55Ni22Cr5Co3Fe14W2Mo0.35Al0.10C0.015B	Nickel-base superalloy; values for Co, Fe, and B are upper limits.

Fig. 6.11 Can-type combustion chamber [24]. Under the Creative Commons license



oxidizing, reducing, and neutral atmospheres. Recently, SiC/SiC ceramic matrix composite (CMC) that is newly commercialized has been adopted for the liner. New cobalt alloys are promising a significant potential for the liner, but they have not yet been commercialized. Figure 6.11 shows the can-type combustion chamber is normal of the class used on turboshaft engines.

6.7.4 Turbine Section

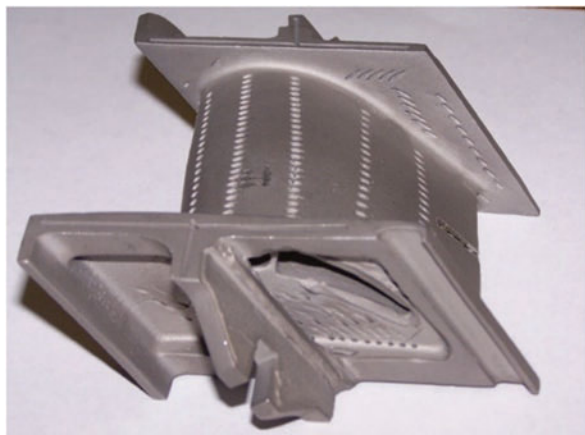
Increasing the operating temperature in the turbine section of gas turbine engines is generally seen as the key role to become greater efficient, and for that reason, new materials are required. They rotate at high rates; so, they need to maintain heavy mechanical loads, and they need to work at temperatures above 1100 °C. These materials should preserve great mechanical resistance in a large range of temperatures [31]. The complex shape of the turbine blades needs to use materials that be able to easily take on complex forms.

The function of the Turbine section is to rotate the compressor and fan as well as the accessory gearbox through the shaft. In the turbine section, power is produced by impinging burnt gases to turbine blades. In this context, these blades are subjected to the factors of the highest temperature and pressure. Due to high loads affecting the turbine unit, these components can withstand factors of creep, fatigue, and corrosion. Therefore, Ni-based superalloys are employed for the manufacturing of turbines. However, the components that are subjected to low pressure and temperature could be manufactured from stainless steels, Co-, and Ni-based

superalloys. It could be noted that the turbine blades of the latest engines are typically exposed to temperature varying between 1200 °C and can reach 1500 °C. To enhance temperature strength, thermal barrier coating could be used such as cooling passages design, zirconia. Heat barrier coating, like ceramic coating, and airflow cooling assistance retain the turbine blades and inlet nozzles cooler. This allows the exhaust temperature to make greater, increasing the efficiency of the aeroengines. Turbine blade with cooling holes as shown in Fig. 6.12. Also, high-temperature corrosion resistance could be improved using Ni–Co–Cr–Al–Y alloys [30]. The high-pressure turbines (HPT) take place between the combustor and the low-pressure turbine. The highest gas-path temperature impinges on HPT blades. This temperature varies between 1350 and 1450 °C or higher for modern jet engines. These ranges could lead to melting the nozzles and blades with nickel-based superalloys [15]. Blades can be the most sensitive part because they are needing the best material properties. When considering the turbine section of the GENx-1B, its two high-pressure stages are composed of TiAl alloys to decrease weight, whereas Ni-based superalloys such as Rene 77 are employed in the rest of the low-pressure stages and high-pressure stages.

Co- and Ni-based superalloys are the common superalloys for the gas turbine. The early-stage, materials of the gas turbine blade were made of Co-based superalloys. Getting bigger off the γ' volume division, to achieve higher creep strength led to the accessibility of alloys such as IN 100 and Rene 100 for aero gas turbine engine blades. However, Ni-based superalloys initialize to be preferred instead of Co-based ones after their development. The reasons for this replacement could be diversified. Firstly, it is a superiority of Clarke's number of Nickel elements. Clarke number illustrates the content of the chemical elements on the surface of the earth as a weight percentage. Namely, the material of Nickel is more abundant than Cobalt. Secondly, Nickel crystal structure is another reason for using it. This property makes the material be moderate strength and ductility. Thirdly, Ni-based superalloys have strength, high resistance against fatigue, oxidation, and corrosion at a

Fig. 6.12 Aeroengine turbine blade cooling holes [24]. Under the Creative Commons license



high-temperature level due to their outstanding mechanical properties resulting in to be applied to the mostly engine turbine blades [30]. Directional solidification (DS) techniques enable the Solidification of materials with grains aligned in a specific direction and single-crystal (SC) castings each of the particle boundaries is eliminated from the microstructure and an SC with a controlled direction is made in an airfoil form. Specifically, directional, and single-crystal structures are formed to make better the mechanical and metallurgical properties of the cast materials at high-temperature applications [32]. Table 6.2 shows the materials used in aero gas turbine engines.

It is projected that the application of Ti–Al-based alloys for jet engines will become widespread for some units having less stringent damage tolerance requirements. Turbine blades of the GE CF6-80C2 turbofan have been manufactured from a cast Ti-47Al-2Cr-2Nb alloy. Figure 6.13 illustrates the aeroengines low-pressure turbine and compressor blades (that consists of 98 blades in GE CF6-80C2). Each one has a length of 50 cm, and, at 217 g. Compared with a conventional nickel-based superalloy blade, the weight of these blades is only about 55% of conventional ones. Reducing the weight of the turbine blade due to Ti–Al alloy would lead to the lighter weight design of the whole turbine Also, it is noteworthy that the light blades impose lower centrifugal forces on the turbine disk (as depicted in Table 6.3) [33]. Considering the GE90 turbofan, usage of these Ti–Al alloys could result in saving weight more than 150 kg. However, due to cost constraints, for low-pressure turbine blades from Ti–Al alloy, the casting route is implemented. Also, the cost issue led to a delay in the production of Ti–Al blades.

6.7.5 *Shaft*

The function of the shaft is to transmit power from the turbine to the compressor as well as the accessory gearbox. Since the shaft is exposed to high-speed rotation under low and high-temperature loads, material properties related to the shaft should be designed for high-temperature strength, high fatigue strength, and toughness. To enable high reliability, the materials for use in the shaft are steels with high cleanliness such as Ti-6Al-4V alloys, Fe-, and Ni-based superalloys. Especially, Cr-Mo-V steels, Inco-718, and Maraging steels (GE1014) are commonly employed. As for the Maraging steel, it is of high strength involving 18–25% of Ni. Also, the Maraging steels possess fatigue strength at a high level (~2200 Mpa or more). These have been employed in the TRENT1000, GE90-115B, and GENx engines. Figure 6.14 shows the turbine shaft of a gas turbine engine. Shafts are sensitive against oscillations and using new damping materials can reduce the damage caused by oscillations. To damp the aircraft engine oscillations from the fuselage and reduce the vibration effects from wings to the engine, which leads to intense damage, it can use polyurethane elastomer materials or cork composites dampers in the connecting parts of the engine with the airframes that are good options to impact and vibration resistance [34, 35].

Table 6.2 Conventionally cast nickel-base, DS nickel-base, DS superalloys used in aeroengines turbine blades [30]. Under the Creative Commons license

Alloys	Composition	Considerations
Rene 77	53.5Ni15Cr18.5Co3.2Mo3.5Ti4.25Al0.08C0.015B	Nickel-base superalloys
Udimet 700	59Ni14.3Cr14.5Co4.3Mo3.5Ti4.3Al0.02Zr0.08C0.015B	Nickel-base superalloys
IN 100	60.5Ni10Cr15Co3Mo4.7Ti5.5Al0.06Zr0.18C0.014B	Nickel-base superalloys
MAR-M200	59.5Ni9Cr10Co12.5W1.8Nb2Ti5Al0.05Zr0.15C0.015B	Nickel-base superalloys
M 22	71.3Ni5.7Cr2Mo11W3Ta6.3Al0.6Zr0.13C	Nickel-base superalloys
MAR-M200 + Hf	Ni8C9Co12W2Hf1Nb1.9Ti5.0Al0.03Zr0.13C0.015B	Nickel-base superalloys
TMD-103	59.8Ni3Cr12Co2Mo6W5Re6Ta0.1Hf6Al	Nickel-base superalloys
DS MAR M-200 + Hf	59.5Ni9Cr10Co12.5W2Hf1.8Nb2Ti5Al0.05Zr0.15C0.015B	DS-first generation
CM247LC	61.7Ni8.1Cr9.2Co0.5Mo9.5W3.2Ta1.4Hf0.7Ti5.6Al0.01Zr0.07C0.015B	DS-first generation
DMD4	66.8Ni2.4Cr4Co5.5W6.5Re8Ta1.2Hf0.3Nb5.2Al0.07C0.01B	DS-third generation
PWA1422	59.2Ni9Cr10Co12W1.5Hf1Nb2Ti5Al0.1Zr0.14C0.015B	DS-first generation
PW1480	62.5Ni10Cr5Co4W12Ta1.5Ti5Al	SC-first generation
PWA1484	59.4Ni5Cr10Co2Mo6W3Re9Ta5.6Al	SC-second generation
CMSX10	69.6Ni2Cr3Co0.4Mo5W6Re8Ta0.03Hf0.1Nb0.2Ti5.7Al	SC-third generation
DMS4	67Ni2.4Cr4Co5.5W6.5Re9Ta0.1Hf0.3Nb5.2Al	SC-fourth generation
TMS 196	59.7Ni4.6Cr5.6Co2.4Mo5.0W6.4Re5.6Ti0.1Hf5.6Al5.0Ru	SC-fifth generation

Fig. 6.13 Aeroengine's turbine and compressor blades: (a): turbine blades (b): compressor rotor blades [24]. Under the Creative Commons license

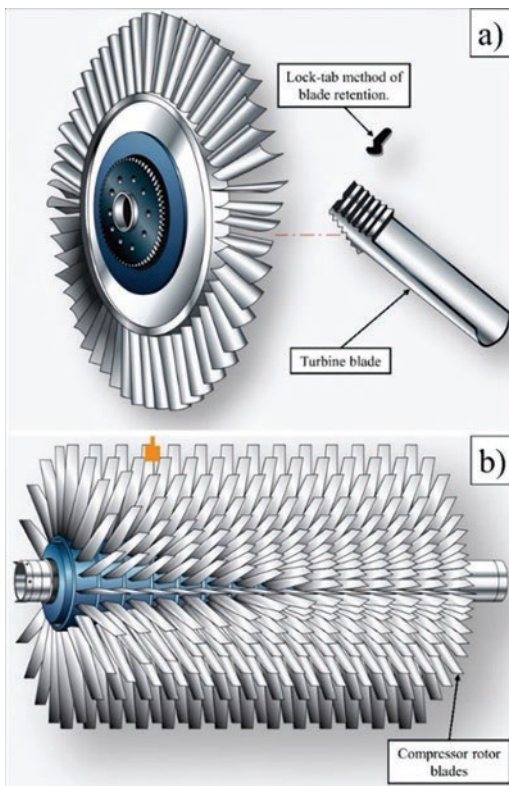


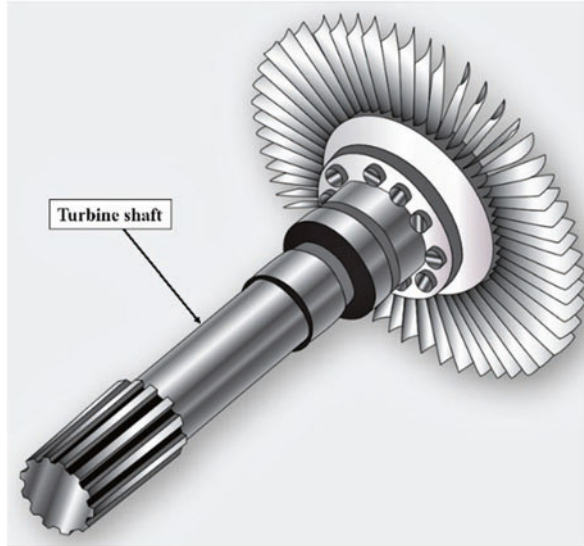
Table 6.3 Reducing the weight of turbine blades

LPT with nickel-based superalloy blade	LPT with the titanium aluminide blade
The weight of one blade is 394 g	The weight of one blade is 217 g
Weight of 98 blades for one stage is $394 \times 98 = 38.66$ kg	Weight of 98 blades for one stage is $217 \times 98 = 21.26$ kg
The weight of whole LPT blades with four stages is = 154.64 kg	Weight of whole LPT blades with four stages is = 85 kg

6.8 Eco-friendly Aeroengines

Global industry becomes larger and international interchange is growing, overall air traffic has consistently increased despite several economic catastrophes. Due to the technology development and the effort to increase fuel efficiency, aircraft is an even more convenient option as international transportation as well as domestic transportation [36]. For this reason, the aircraft is an attractive transportation method and an even stiffer increase in air traffic in the future is expected. Hence, it is crucial to think about sustainable design when it comes to future commercial aircraft. Nowadays, the new focus on preparation for an eco-friendly world has resuscitated

Fig. 6.14 Aeroengine turbine shaft [24]. Under the Creative Commons license



interest in natural materials. However, it is timely to think about whether the asserted advantages of these materials can be justified quantitatively. Life Cycle Assessment (LCA) is an environmental evaluation method which, according to ISO 14040:2006, “considers the all life cycle of a product from raw material extraction and acquisition, through energy and material production and manufacturing, to use and end-of-life treatment and final disposal” [37]. This method can be used as an approved method of environmental indicators for evaluating the materials used in aircraft (as well as other applications) in terms of minimal damage to the environment. In this section, we examine the impact of three types of widely used materials in the cold parts of the aircraft engines from the LCA perspective [38].

One of the contemporary approaches is to aim for weight reduction in aero engines, is using low-density polymer composites to replace weighty materials [39]. To give recognition to examples in the aeroengines area, leading companies in the manufacture of advanced aircraft engines, the use of ultra-advanced composites in fan blades has increased for the front part of the engine [40]. Aside from the obstacles that aero-engine material designers would encounter when incorporating composite materials into their manufacturing, the issue of sustainability is also concerning. Despite the fact that these materials allow for significant weight reduction, resulting in lower fuel consumption during use, composites typically include complex material architectures with higher asking prices, non-eco-friendly chemicals (epoxy resin-based composites), and hazardous working environments [41]. To design more sustainable manufacturing items, it is, therefore, necessary to consider its whole life cycle, from cradle to grave including both environmental and social features [42]. Most studies of the effects of aircraft composites on the environment have been carried out without covering the social and economic aspects and have shown that during their lifespan, composites are more eco-friendly than base metal

materials due to reducing emissions. Therefore, to ensure the greater sustainability of future engines, aircraft engine material designers need a more comprehensive approach to combining sustainability in aircraft engine design [38].

In the past, the main goals in the aerospace sector for the implementation of composites instead of conventional structural materials like metals were weight reduction, cost reduction, better performance. The emphasis has now shifted towards environmental design parameters. Accordingly, the current drivers are fuel consumption reduction, emissions (CO₂, NO_x) reduction, noise reduction. To arrive at these objectives, smaller and more effective aeroengines have been grown, producing smaller thrust and thus for force stability, the aircraft needs to make less drag [43]. Given that the overall shape and form of the aircraft are the same, the drag forms stay unchanged, the reduction should come from induced drag. Once more for the force balance, with less lift, reduced drag, and the same payload, the weight of the aircraft structure needs to be reduced [43]. Some of the structural applications of a polymer matrix reinforced composite can be found in the cold part of the commercial aircraft engine [44].

P. L. Y. Léonard and colleagues investigated the sustainability of composites in aero-engine components. Prediction models that relate an aircraft's fuel consumption and weight have been created to analyze the consequences of weight reduction on an aircraft and fuel saved throughout a product's life-cycle. Each case is modeled in "regular" and "light" editions, with the "light" variant weighing 100 kg less and reducing aircraft weight leading to reducing aircraft fuel consumption. The materials chosen for their research include complete aluminum alloys, full titanium alloys, and composite hybrid components (titanium, composite, steel). Based on their results, composite and titanium components have similar environmental impacts regarding manufacturing, however, aluminum components have a lower impact. The findings of LCA on aero-engine components revealed that metallic and composite components had very similar effects [45].

6.8.1 Environmental Impacts of Aeroengine Materials

For a sustainable approach, researchers should improve the structure of aircraft with the lightest materials. Lighter material ensures fuel savings and a more environmentally friendly aircraft. The results are not limited to this saving. Improvement in lightness means material improvement. In this context, the selection of more environmentally friendly materials will of course make the engine environmentally friendly. According to the LCA application, the normalized effect values of some hazardous are listed in Table 6.4. Altuntas designated that the normalized effect values, scaled in the same unit, show which material may be more environmentally friendly [46].

As given in Table 6.4, environmental impact parameters for some aeroengine materials. According to Table 6.4, the reducing weight of turbine blades indicates that while the LPT with nickel-based superalloy blade has a 0.57 nkg normalized

Table 6.4 Normalized effect values for aeroengine materials

Material	Normalized effect value (nkg)
Al	2.63E-05
Al (contains 3% of magnesium)	8.61E-04
Titanium–Al alloy	5E-03
Cd	4.88
Ni	4.2E-03
Ferronickel (25% Ni)	1.7E-03
Super alloy (Nickel based with iron–chromium)	3.7E-03

affect value, the LPT with the titanium aluminide blade has 0.43 nkg. The new blade material technology is both lighter and more environmentally friendly.

Acknowledgments The authors would like to thank the editors of the book Prof. Melih Cemal Kuşhan, Dr. Selim Gürgen, and Dr. Mehmet Alper Sofuoğlu.

References

- Jacob Teter, P. L. F., Bains, P., Lo Re, L., & Aviation. (2020). International Energy Agency official website. <https://www.iea.org/reports/tracking-aviation-2020>.
- Abideen, Z., et al. (2014). Sustainable biofuel production from non-food sources—An overview. *Emirates Journal of Food and Agriculture*, 26(12), 1057–1066.
- Graver, B., Rutherford, D., & Zheng, S. *CO₂ emissions from commercial aviation: 2013, 2018, and 2019*. Int Council Clean Transport report. Retrieved from <https://theicct.org/sites/default/files/publications/CO2-commercial-aviation-oct2020.pdf>.
- Environment, I.C.A.O.I., ICAO 2019 Environmental Report. (2019). Retrieved from [https://www.icao.int/environmental-protection/Documents/ICAO-ENV-Report2019-F1-WEB%20\(1\).pdf](https://www.icao.int/environmental-protection/Documents/ICAO-ENV-Report2019-F1-WEB%20(1).pdf).
- Group, A.T.A. (2012). *Aviation benefits beyond borders*. ATAG, Geneva.
- UNWTO, W. *International tourism highlights, 2019 edition*. Retrieved from <https://www.e-unwto.org/doi/pdf/10.18111/9789284421152>.
- Nele Erdmann, J. A., Möller, K., Zeller, H., & Burghaus, K. (2020). Annual Report 2019.
- EDGAR—Emissions Database for Global Atmospheric Research. Retrieved from <https://edgar.jrc.ec.europa.eu/>.
- Thomas, V., & Burgess, S. (2015). *International Air Transport Association Vision 2050 Report Assessment*. Retrieved from <https://commons.erau.edu/cgi/viewcontent.cgi?article=1176&context=aircon>.
- ICAO, Carbon Offsetting and Reduction Scheme for International Aviation (CORSA). (2016). Retrieved from <https://www.icao.int/environmental-protection/CORSA/Pages/default.aspx>.
- Nozhnitsky, Y. A. (2018). The problem of ensuring reliability of gas turbine engines. In *IOP conference series: Materials science and engineering*. IOP Publishing.
- Marino, M., & Sabatini, R. (2014). Advanced lightweight aircraft design configurations for green operations. In *Proceedings of the practical responses to climate change conference*, Melbourne, Australia.
- Schmidt, W. (1899). *Hérons von Alexandria Druckwerke und Automatentheater*, Griechisch und Deutsch Herausgegeben. WS book., Trans. Leipzig, Saxon, Deutschland: Druck und Verlag von BG Teubner. Retrieved February 22, 2015.

14. Shearer, S. A., & Vogt, G. L. (2020). *Rockets: Educator's guide with activities in science, technology, engineering and mathematics*. Retrieved from <https://files.eric.ed.gov/fulltext/ED510854.pdf>.
15. Karabag, S. G. (2015). History of science and medicine in Turkish history secondary school textbooks. *International Journal of Environmental and Science Education*, 10(2), 287–300.
16. Romanowski, D. A., & Keiser, M. A. (2010). *The legacy of flight: Images from the archives of the smithsonian national air and space museum*. Bunker Hill Pub.
17. Ricco, P. (2001). *The difficult beginning*. Retrieved from <http://aerostories.free.fr/constructeurs/leduc/page7.html>.
18. Altuntas, O., & Govce, M. (2018). *Hava Araçlarında Piston-prop Motorlar*. Palme Publisher.
19. Pulkrabek, W. W. (2004). *Engineering fundamentals of the internal combustion engine*. Pearson Publisher.
20. University, E. T. (2021). *Faculty of aeronautics and astronautics*. Retrieved from http://ecas.anadolu.edu.tr/fotograflar_teknik_birimler.html.
21. Torenbeek, E. (2013). *Synthesis of subsonic airplane design: An introduction to the preliminary design of subsonic general aviation and transport aircraft, with emphasis on layout, aerodynamic design, propulsion and performance*. Springer Science & Business Media.
22. Mattingly, J. D. (1996). *Elements of gas turbine propulsion* (Vol. 1). McGraw-Hill New York.
23. El-Sayed, A. F. (2008). *Aircraft propulsion and gas turbine engines*. CRC Press.
24. U.S. Department of Transportation, F.A.A., Flight Standards Service, Aviation Maintenance Technician Handbook–Powerplant (FAA-H-8083-32A). (2018). Federal Aviation Administration.
25. University, A. Anadolu University Aviation Park. (2017). Retrieved from <https://havacilik-parki.anadolu.edu.tr/hava-ara%C3%A7lar%C4%B1m%C4%B1z>.
26. Board, A. F. S., & N.R. Council. (2007). *Improving the efficiency of engines for large non-fighter aircraft*. National Academies Press.
27. Kyprianidis, K. G. (2011). *Future aero engine designs: An evolving vision*. IntechOpen Publisher.
28. Klocke, F., et al. (2014). Turbomachinery component manufacture by application of electrochemical, electro-physical and photonic processes. *CIRP Annals*, 63(2), 703–726.
29. Boyer, R., et al. (2015). Materials considerations for aerospace applications. *MRS Bulletin*, 40(12), 1055–1066.
30. Benini, E. (2011). *Advances in gas turbine technology*. IntechOpen Publisher. <https://doi.org/10.5772/664>
31. Duhl, D., & Thompson, E. (1977). Directional structures for advanced aircraft turbine blades. *Journal of Aircraft*, 14(6), 521–526.
32. Zhao, Q., et al. (2015). *Methods for directional solidification casting*. Google Patents. Retrieved from <https://patents.google.com/patent/US20150231696A1/en>.
33. Leyens, C. (2004). Advanced materials and coatings for future gas turbine applications. In *24th international congress of the aeronautical sciences*.
34. Gürgen, S., & Sofuoğlu, M. A. (2021). Smart polymer integrated cork composites for enhanced vibration damping properties. *Composite Structures*, 258, 113200.
35. Shamsadinlo, B., et al. (2020). Numerical and empirical modeling of peak deceleration and stress analysis of polyurethane elastomer under impact loading test. *Polymer Testing*, 89, 106594.
36. Button, K. (2008). The impacts of globalisation on international air transport activity. In *Guadalajara: Global Forum on Transport and Environment in a Globalising World*. Retrieved from <https://www.oecd.org/greengrowth/greening-transport/41373470.pdf>.
37. Standardization, I.O.f. (2006). *Environmental management: Life cycle assessment; Principles and framework* (Vol. 14044). ISO. Retrieved from <https://www.iso.org/standard/38498.html>.
38. Scelsi, L., et al. (2011). Potential emissions savings of lightweight composite aircraft components evaluated through life cycle assessment. *Express Polymer Letters*, 5(3).

39. Soutis, C. (2005). Fibre reinforced composites in aircraft construction. *Progress in Aerospace Sciences*, 41(2), 143–151.
40. Marsh, G. (2012). Aero engines lose weight thanks to composites. *Reinforced Plastics*, 56(6), 32–35.
41. Chua, M. H., et al. (2015). Understanding aerospace composite components' supply chain carbon emissions. In *Proceedings of the Irish manufacturing conference (IMC32)*, Belfast, UK.
42. Garetti, M., & Taisch, M. (2012). Sustainable manufacturing: Trends and research challenges. *Production Planning & Control*, 23(2–3), 83–104.
43. McIlhagger, A., Archer, E., & McIlhagger, R. (2015). Manufacturing processes for composite materials and components for aerospace applications. In *Polymer composites in the aerospace industry* (pp. 53–75). Elsevier.
44. Toozandehjani, M., et al. (2018). Conventional and advanced composites in aerospace industry: Technologies revisited. *American Journal of Aerospace Engineering*, 5(1), 9–15.
45. Léonard, P., & Nylander, J. (2020). Sustainability assessment of composites in aero-engine components. In *Proceedings of the design society: DESIGN conference*. Cambridge University Press.
46. Altuntas, O. (2020). Lead emissions from the use of leaded avgas in Turkey. *Aircraft Engineering and Aerospace Technology*, 93(3), 493–501.

Chapter 7

Landing Gear Systems in Aircraft



Erdem Tunca, Hasim Kafali, Goksel Keskin, and Melih Cemal Kuşhan

7.1 Introduction

Landing gears are the elements that provide contact with the ground during the landing and takeoff phases and their movements on the ground (during taxi), the friction resistance is minimized, and they best absorb the loads caused by the horizontal and vertical movements of the aircraft. Figure 7.1 shows the landing gear contacting to the ground.

Landing gear forms the main support of an airplane in contact with the ground. Generally, although the landing gears are wheeled, the landing gears of the aircraft can be ski or float type in operations to be carried out on ground such as water or snow. Landing gears are designed in a retractable manner in order not to disturb the aerodynamic flow in the air in many aircraft used in passenger transportation today, such as military jets and business jets. However, the fixed landing gear is used in light aircraft. Both fixed landing gear and retractable landing gear use the three-point configuration. The most important issue during the movement of the aircraft on the ground is the ability to steer the aircraft. A three-point configuration is used to enable aircraft to perform their movements on the ground more stable without increasing their weight. The three-point configuration consists of main landing gear, two on the right and left, and auxiliary landing gears, one on the nose or tail of the

E. Tunca · H. Kafali (✉)

School of Civil Aviation, Muğla Sitki Kocman University, Muğla, Turkey
e-mail: hasimkafali@mu.edu.tr

G. Keskin

Eötvös Loránd University, Budapest, Hungary

M. C. Kuşhan

Department of Aeronautical Engineering, Eskisehir Osmangazi University, Eskisehir, Turkey



Fig. 7.1 The landing gear of the aircraft standing in the parked position on the ground [1]. Reprinted by permission from Lufthansa Technik AG

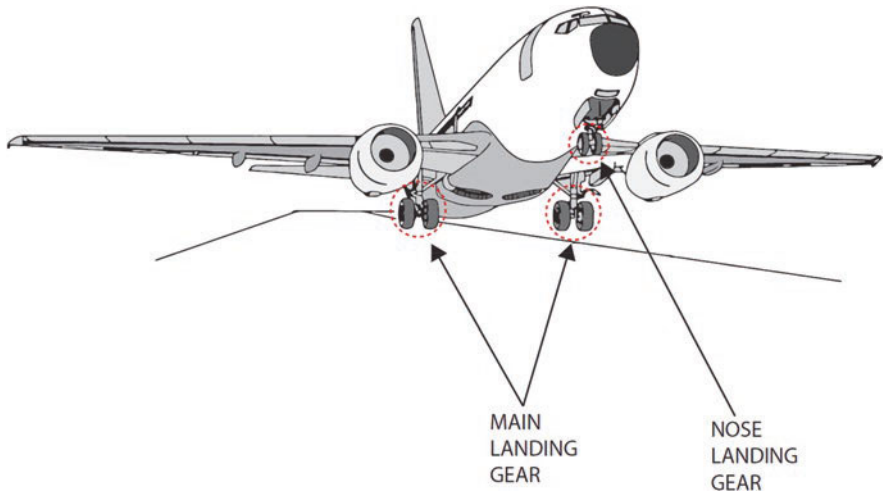


Fig. 7.2 Three-point configuration of Boeing 737–800 aircraft landing gear

aircraft. Figure 7.2 shows the landing gear configuration of the Boeing 737–800 aircraft [2, 3].

The main landing gear is responsible for carrying the main loads during and after landing. Auxiliary landing gears guide the plane on the ground and reduce the load on the main landing gears by assisting the main landing gears in carrying the landing loads.

Landing gear should be designed considering the following items [4]:

- It must be able to absorb the loads arising from the weight and movement of the aircraft without damaging the aircraft structure, without damaging the strut structures.

- An aircraft taking off should accelerate and reach the climb speed as soon as possible. In order to provide this situation, wheels that will minimize the friction on the ground should be used.
- The retraction process of the landing gear should be as short as possible in order to reduce the parasite drag that occurs during takeoff as soon as possible.
- When the wheel of the plane touches the ground, it carries the kinetic energy of both horizontal and vertical velocity components. During landing, the landing gear must be able to resist these loads.
- In addition to resisting these loads, it must be able to perform effective braking and ensure safe deceleration and stopping when necessary.
- It should allow the aircraft to maneuver easily during its movement on the ground.
- It should be pulled or pushed with special towing vehicles when necessary.
- It should contain enough wheels to effectively distribute the weight of the aircraft so that it does not damage the taxiways and runways.

7.1.1 Landing Gear Layouts

When the history and development of aircraft are examined, many different types of landing gear have been used. There are three types of landing gear patterns commonly used in airplanes. These are as follows;

- Tail wheel landing gear (tail wheel/tailedragger/conventional)
- Nose wheel landing gear (tricycle)
- Tandem/bicycle type landing gear

Designers generally use one of these three types of the layout shown in Fig. 7.3, although it varies according to the area where the aircraft will be used and the loads it will carry [7]. In very special cases, these designs may vary. Table 7.1 gives the advantages and disadvantages of nose wheel landing gear and tailwheel landing gear. Tandem type landing gears are applications where the number of wheels is increased in order to reduce the load on each wheel. It may be impossible to place the landing gear inside the wing in aircraft designs where the number of wheels

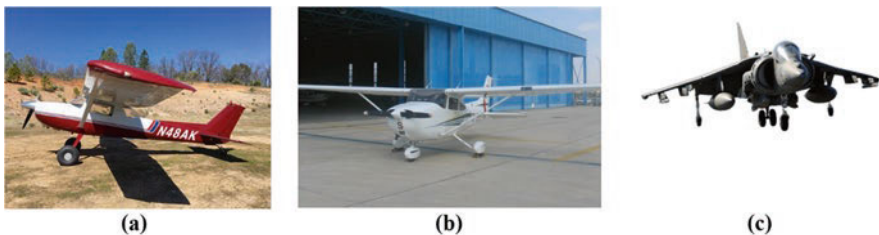


Fig. 7.3 Main landing gear layouts; (a) tailwheel landing gear, (b) nose wheel landing gear, and (c) tandem/bicycle-type landing gear [5, 6]. Reprinted by permission from Skywagons and Faculty of Aeronautics and Astronautics at Eskişehir Technical University

Table 7.1 Advantages and disadvantages of nose wheel landing gear and tailwheel landing gear

	Advantages	Disadvantages
Nose wheel	<ul style="list-style-type: none"> • It allows easier maneuvers as it is more stable dynamically on the ground • Provides better ground control in crosswind situations, which is one of the most dangerous situations during landing • Like tailwheel landing gear, the cockpit is not angled upwards, providing better visibility to the flight crew • Also, since the cockpit is not angled upwards, it provides convenience in passenger entry and exit • More stable during braking than tailwheel landing gear. It does not cause the nose of the aircraft to tip over during hard braking and provides a safer braking • Since the main landing gear first touches the ground during landing, and then the nose landing gear touches the ground, it reduces the lifting force that may occur by tilting the nose down when the main landing gear touches the ground, and a safer landing is achieved • Less bounces/jumps occur after the ground touch occurs • Better acceleration before take-off, as it has a smaller angle of attack compared to tailwheel landing gear 	<ul style="list-style-type: none"> • High structural weight due to three landing gear struts that can bear high loads • In addition to the structural weight, the landing gears that can carry high loads are quite expensive • The malfunctions that may occur in the shimmy system that allows the wheel at the nose to move steadily while landing and when the aircraft is on the ground can cause very harmful consequences • Nose wheel landing gear is exposed to heavier loads than tailwheel landing gear • Difficulties may be experienced during the design and maintenance phase, as it has a more complex steering mechanism • If it has a retractable landing gear system, it can be difficult to retract the nose wheel as it is usually in a limited area • In very heavy braking, the loads on the main landing gear may be discharged, which may cause slipping or skidding

(continued)

Table 7.1 (continued)

	Advantages	Disadvantages
Tail wheel	<ul style="list-style-type: none"> • Since there is much less load on the wheel at the tail, only the main landing gear consists of struts that can carry high loads. This provides an advantage in terms of less structural weight • Landing gear, which can carry less high loads in number, requires less cost • It is more suitable for rugged lands and fields. It is preferred in light aircraft construction that is, in education, entertainment, agricultural, spraying, firefighter, and similar types of aircraft, in terms of structure lightness and economy • Its connections are made to the body and wings more easily • Since there is a wheel on the tail, the high angle of attack created increases the drag force in the air during landing and the need for brakes decreases • It has a lighter tail wheel as it is encountered with lower ground loads due to its usage areas • It has a simpler steering mechanism • Eliminates the landing gear placement problems as there is engine and engine-related equipment and often fuel tanks in the nose of the aircraft in light single-engine aircrafts 	<ul style="list-style-type: none"> • The pilot does not have a good view of the front and therefore cannot move safely on the ground • Maximum braking is not possible due to the danger that the plane will always stand on the nose during braking • Since there is a wheel in the tail, the high angle of attack created may cause the aircraft to bounce off the ground during landing • When the aircraft is standing on the ground, the cabin floor is tilted and the movement of passengers and cargo is difficult • Dynamically on the ground it is more difficult to maneuver on the ground as it is more unstable • Provides weaker direction control in crosswind situations, which is one of the most dangerous situations during landing

should be too high. In such cases, wheels with an increased number of wheels are placed one after the other in the fuselage of the aircraft. The Antonov AN-225 aircraft with such a design is shown in Fig. 7.4 [4, 8].

7.2 Fixed and Retractable Landing Gears

The landing gears used in aircraft can be divided into two subcategories: fixed landing gears and retractable landing gears. Most small, single-engine light aircraft use fixed landing gear, except in special cases. The fixed landing gear is mounted on the

Fig. 7.4 Antonov AN-225 aircraft using tandem type landing gear to reduce the loads on the wheels



fuselage of the aircraft and creates aerodynamically parasitic drag as they cannot be taken in during the flight. In order to eliminate parasitic drag, systems have been designed to retract the landing gears and keep them inside and extend them during landing. However, since these systems cause an increase in weight, the weight increase in small and relatively slow aircraft cannot be tolerated by the reduction of parasite drag, so fixed landing gear is used in small aircraft. Airflow is regulated by adding aerodynamic fairings/housings on the wheels to reduce this parasitic drag that occurs in light aircraft. In addition, fixed struts that house the landing gear are also produced in aerodynamic form, thus helping to reduce parasite drag. Figure 7.5 shows such an application [2, 4].

The increase in the speed capability of the aircraft causes an increase in the parasitic drag caused by the landing gear. Therefore, mechanisms that retract the landing gears inside are used, which allow the landing gears to be kept inside the fuselage or wing partitions during flight. There are cowlings covering the landing gear slots in order to prevent the flow of the airstream to be disturbed after the landing gear is retracted inside the fuselage or under the wing. Thanks to these cowlings, the drag force is reduced to less. In some aircraft, the cowling is not used, considering that the cowlings that cover the landing gear housings cause an increase in weight. Figure 7.6 shows the landing gear housings of the Boeing 737 aircraft. Landing gear doors that cover the main landing gear slots are not used on the Boeing 737 aircraft. These systems, which enable the opening and closing of the landing gears, work hydraulically [2, 4].

Although they vary according to designs and needs, landing gear generally consists of the following components;

- Struts
- Shock absorbers
- Tires
- Rims
- Braking systems
- Extend/retract mechanism
- Controls and indicators
- Steering mechanism for nose landing gear

Fig. 7.5 A sample application for wheel fairings

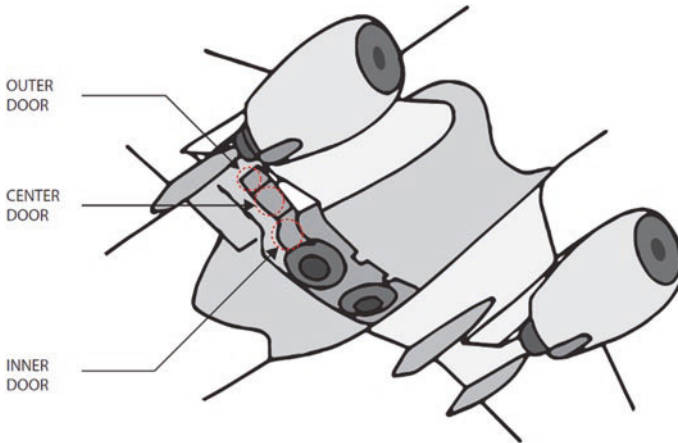


Fig. 7.6 Application used in Boeing 737 aircraft main landing gear housings

7.3 Struts

As mentioned earlier, in addition to the duty of the landing gear to support the aircraft in ground motion, the forces arising from the landing on an aircraft during landing should be controlled by the landing gear. This can be done in two ways [2, 9];

1. The shock energy generated by the landing is distributed to the whole body. Thus, without sudden load on a single point, the magnitude of this load is changed and spreads more slowly throughout the body.
2. The shock energy generated during the landing is absorbed by converting it into heat energy.

7.3.1 *Spring Steel Struts*

Many aircraft using fixed landing gear use struts made of flexible spring steel, aluminum, or composite materials that counteract the impact of the landing and distribute it to the fuselage at a non-harmful size and speed. The struts bend to meet the load during landing and transfer the forces from the landing to the body while

Fig. 7.7 Spring steel strut [5]. Reprinted by permission from Skywagons website



returning to its original position. Made of composite materials, these landing gear supports are lighter, more flexible, and resistant to corrosion and wear [2, 9]. Figure 7.7 shows these landing gear.

7.3.2 *Rigid Struts*

Its use in aircraft landing gear applications dates back to early times. Before spring steel struts were developed, aircraft used rigid and welded landing gear struts made of steel. Unlike spring steel struts, shock energy is transmitted directly to the body in these struts originating from the landing. The use of pneumatic tires alone helps to alleviate impact loads relatively. Aircraft using skid-type landing gear often use this type of landing gear struts [2, 9].

7.3.3 *Bungee Cord*

The use of bungee cords is common in landing gear that does not have impact-absorbing structures. During landing, the strut assembly can be stretched by the landing load. Bungee cords are placed between the rigid airframe and the strut assembly. Bungee cords absorb the load by transmitting the load received from the strut to the fuselage at a level that will not damage it [2, 9].

7.3.4 Shock Struts

This strut type has real shock absorption. This damping is achieved by converting the shock energy generated by the effect of the landing into heat energy. This method, which is used to absorb and distribute the shock effect, is one of the most used methods in aviation. This method can be used for any size aircraft. Shock strut structures are hydraulically operated structures that support the aircraft in ground movements and protect the structure during landing. These systems should be regularly inspected and maintained in order to have a long life and not to disturb the safety while landing. There are many different shock absorber designs depending on the usage areas of the aircraft and the loads they carry. Although the designs differ, the working principles are basically the same. In principle, these pneumatic/hydraulic struts use compressed air or nitrogen together with hydraulic fluid to absorb and distribute shock loads. The strut structure consists of a telescopically nested cylinder or tube with closed outer ends. Of these cylinders, the upper part is fixed to the aircraft and is stationary, the lower cylinder is called the piston. The piston moves into and out of the upper cylinder, absorbing the shock effect. The lower chamber is always filled with hydraulic fluid while the upper chamber is filled with compressed air or nitrogen. An orifice element that allows the hydraulic fluid in the lower chamber to enter the upper chamber when the strut is compressed under load, is positioned between two cylinders. A metering pin is used to control the velocity of this flow in many strut structures. The fluid flow rate is not constant during the compression effect on the descent. This speed is controlled automatically by the taper of the measuring pin in the orifice. Figure 7.8 basically shows the structural elements inside the strut and the situations of these elements at the start and end of the landing. In some types of struts, a metering tube is used. Basically, the working principle is the same as for struts containing measuring pins. Holes on the measuring tube control the hydraulic fluid passage from the lower chamber to the upper chamber [2–4, 10].

The pressure that occurs during compression and the limited amount of hydraulic fluid that is allowed to pass through the orifice cause warming. This is the transformed form of the impact energy generated during the heat descent. Energy converted into heat is discharged through the strut structure. After the landing gear becomes jammed, the struts will want to quickly return to their original state. This situation may cause an impact or damage to the struts. A check valve or recoil pipe located in the strut restricts the flow of hydraulic fluid and slows down the movement while the landing gear returns to the state it only carries the weight of the aircraft after the first touch. Thus, a damaging situation is prevented [2, 3].

The top cylinder of a landing gear strut generally includes a valve assembly. Although it varies by design, this valve is located on or near the cylinder. These valves in Fig. 7.9 are located in order to supply hydraulic fluid to the strut and to supply air/nitrogen as specified by the manufacturer [2, 3].

In order to keep the piston and wheels, which are the basic elements of the strut, in line, there are torque connections on most of the struts (usually nose landing gear

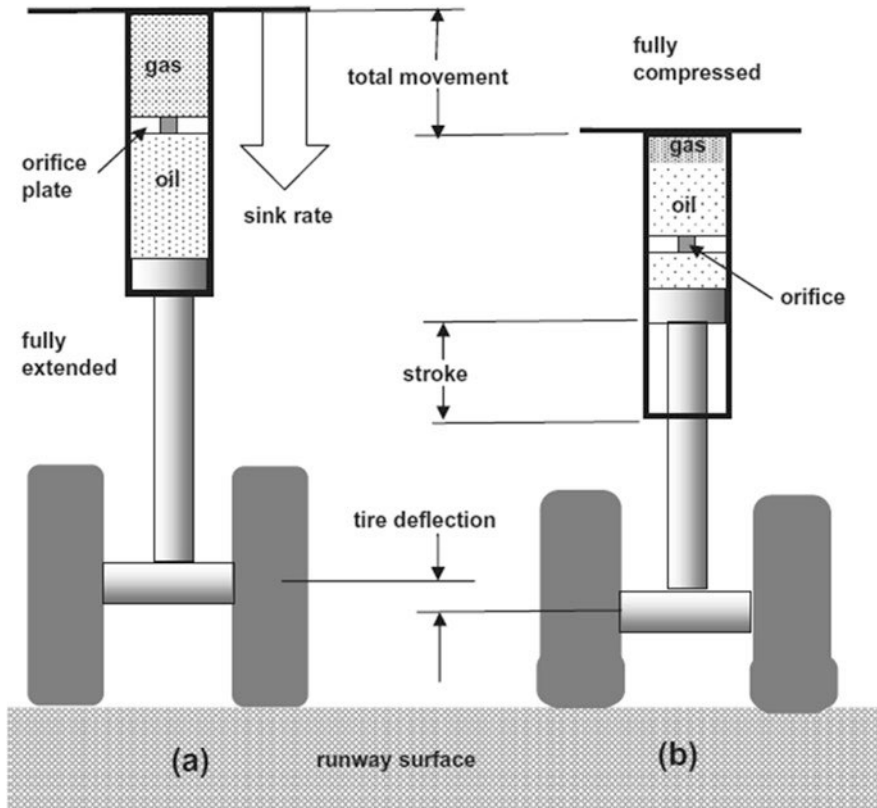


Fig. 7.8 (a) The situation in which contact with the ground first begins and (b) the situation in which contact with the ground occurs completely [10]. Reprinted by permission from Elsevier

struts). While one end of these connections is connected to the fixed upper cylinder, the other end is connected to the mobile lower cylinder. Thanks to the connections made, the wheels remain aligned and the rotation of the roller is prevented. These connections on the front landing gear of the Boeing 737 aircraft are shown in Fig. 7.10 [3].

Centering cams are used in the strut structure so that the landing gear wheels can contact the ground flat in the nose landing gear strut. While the upper cylinder has protrusions belonging to this centering cam, the lower cylinder has recesses belonging to this centering cam. Thus, the cam protrusions in the upper cylinder combine and lock with the recesses in the lower cylinder, ensuring that the wheels are aligned. In addition to the centering cams, the nose landing gear has an external shimmy damper structure. Thanks to this structure, the wheel is prevented from moving unstable during landing and creating unsafe situations. The Shimmy damper system dampens the vibrations that occur with the contact of the wheel on the ground and prevents the wheel from vibrating left and right. This system can be found not only

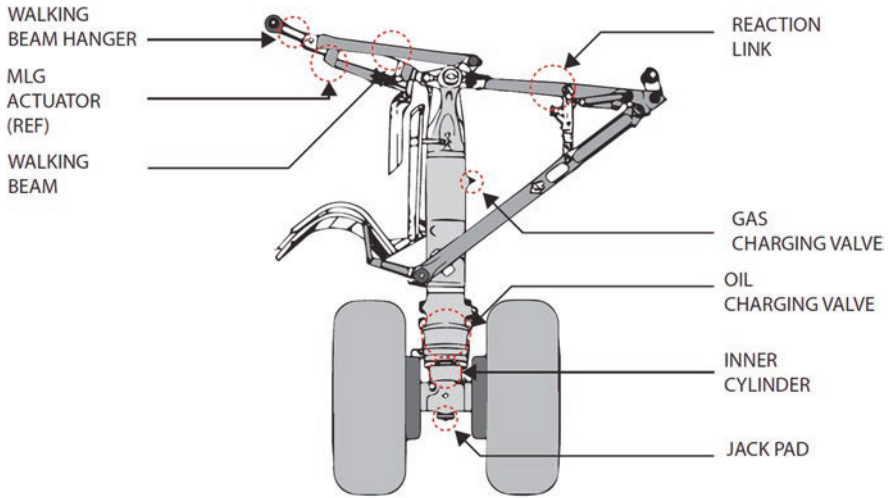


Fig. 7.9 Valves and some connections of Boeing 737 aircraft right main flight gear strut

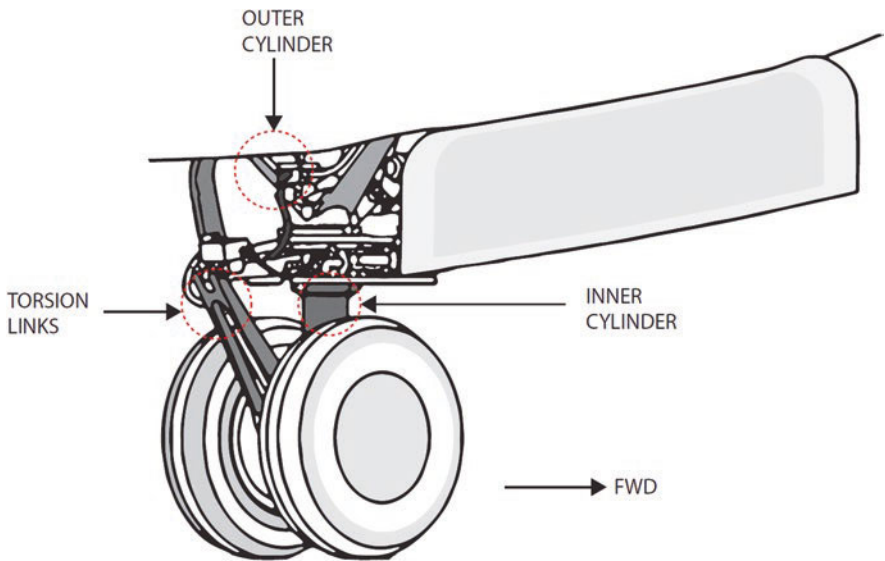


Fig. 7.10 Torque connection at the front landing gear strut of Boeing 737 aircraft

in nose gear but also in the main landing gear. Figure 7.11 shows the centering cams and structures of the shimmy damper system [2].

In cases where the aircraft need to move without starting the engine on the ground, the aircraft are towed by towing vehicles. For towing vehicles to tow the aircraft, the vehicle must be connected to the landing gear on the aircraft by means of a linkage. In order to make these connections, there are towing connection points

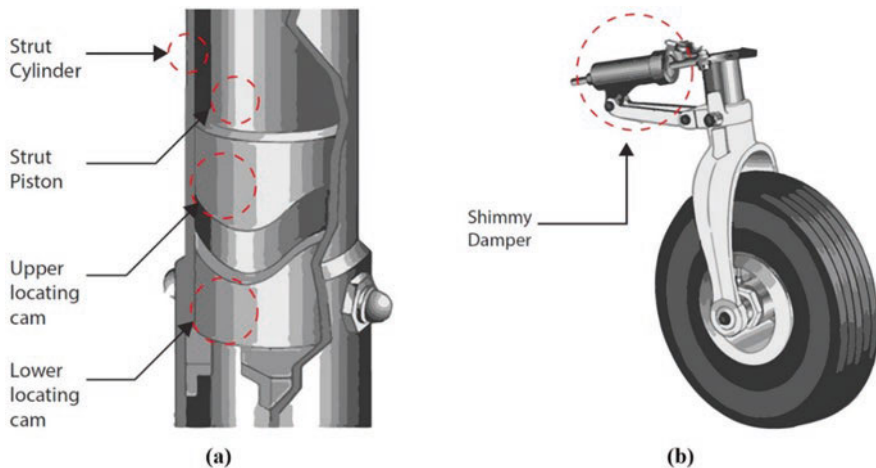


Fig. 7.11 (a) Mechanism of centering cams and (b) shimmy damper system

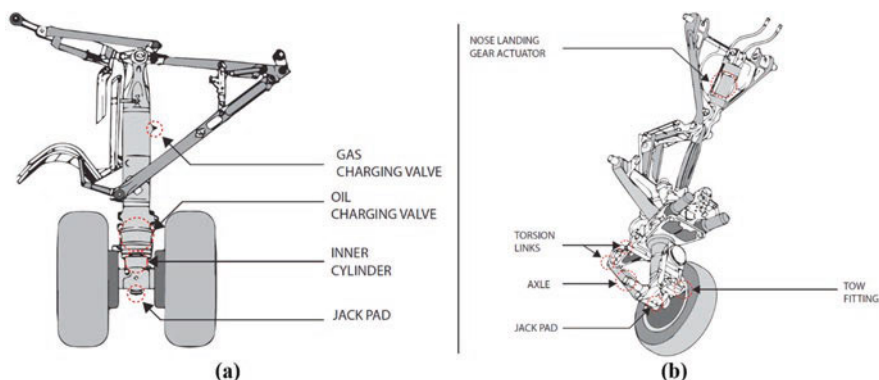


Fig. 7.12 Boeing 737 aircraft landing gear attachment points: (a) main landing gear and (b) nose landing gear

in the nose landing gears in many aircraft, although they differ from aircraft to aircraft. In addition to the towing points, there are jack points on the main landing gear and nose gear. Figure 7.12 shows the jack and towing connection points on the main and nose landing gears of the Boeing 737 aircraft [2, 3].

7.4 Wheels

Wheels and tires are one of the most basic and vital parts of landing gear. Thanks to the tires mounted on the wheels, the wheels bear the weight of the aircraft during takeoff, landing, and ground movements. Although wheels are generally produced

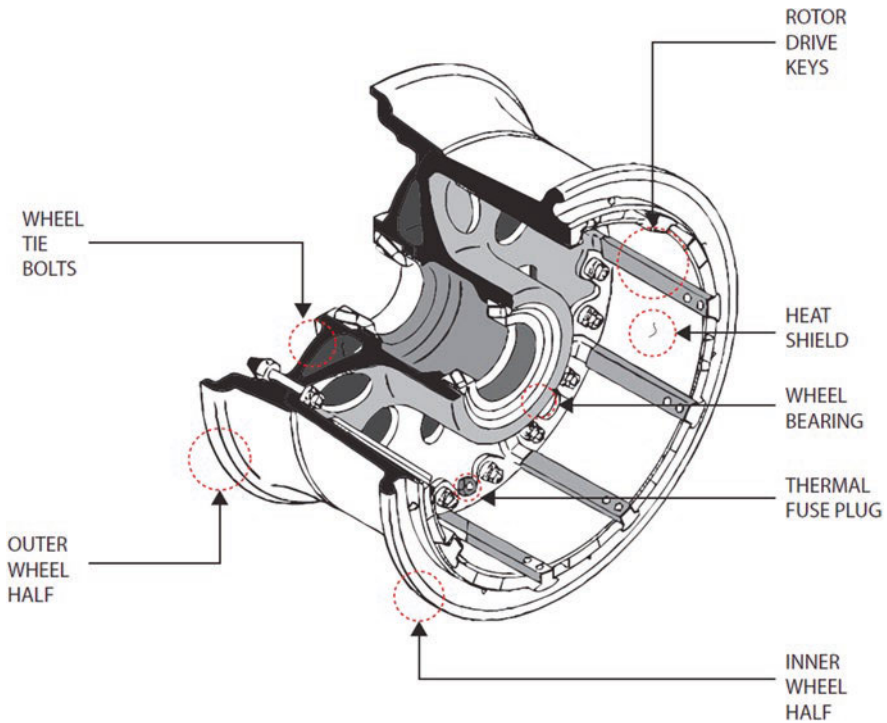


Fig. 7.13 Wheel structure of modern landing gear

from light and strong aluminum alloys, some of them can be produced from magnesium alloys. Aluminum wheels are slightly heavier, but their ability to be manufactured cheaper and their good corrosion resistance make them attractive. However, both have similar performance ratings. Early aircraft wheels were produced in one piece, just like automobiles. As seen in Fig. 7.13, the wheels are generally composed of two halves mounted together with bolts. Some innovative designs can also be used in a single-piece configuration, as they are easy to manufacture and maintain. Tubeless wheels are used in modern aircraft. The place where the wheel actually touches the rim is called the bead seat area. It is an important area that meets significant tensile loads from the tire during landing [2–4].

Inner and outer wheel structures are not the same as they require different element connections. The main reason for this is that the inner wheel half must accommodate the rotors of the aircraft brakes on both main landing gear wheels and must have a vehicle to drive them. The inner wheel half can be distinguished from the outer wheel structure as it has a brake mounting feature. In addition to the brake mounting, the inner wheel half may contain one or more thermal plugs. If hard braking occurs after landing, the excessive temperature increase in the discs causes an increase in tire temperature and pressure. This increase can increase to a level that will damage the wheel and tire assembly, causing them to explode. The thermal

plug is filled with a low melting alloy. Before tire and wheel temperatures reach their puncture level, the plug melts and evacuates the tire air. After the thermal plug melts, this tire and wheel must be replaced before the aircraft is taken back to flight. Wheels that sweat around the replaced tire and wheel should also be inspected for signs of various damage. A heat shield is placed on the brake rotor to protect the wheel and tire elements against overheating and prevent unsafe situations. There is also an over-air safety plug that will release all the air in the tire in the event of over-inflating the inner wheel half. The outer wheel half is joined with the inner wheel half to form the wheel assembly on which the tire is mounted. The outer bearing and end of the existing axle are covered in order not to be affected by contaminants. The outer wheel half provides a suitable location for the valve stem used to inflate and lower these tubeless tires. In varieties that can differ in design, the outer wheel half may contain a hole through the inner wheel half through which a valve extension can pass [2-4].

7.5 Braking Systems

After the First World War, the increase in the speed and complexity of the aircraft and the increase in the use of smooth, coated runways revealed the necessity of brake systems for aircraft. Since the braking systems enable the aircraft to slow down and stop in a short time after landing, these systems must work properly. They keep the aircraft steady on the ground during engine start-up, during engine speeding up, and during engine speed tests on the ground. In most aircraft, the brake units are located on the wheels of the main landing gear. Brake units are not included in the nose landing gear. Generally, brake systems use the connections provided mechanically or hydraulically to the rudder pedals. The pilot activates the brakes on the main landing gear wheels by applying pressure to the upper parts of the rudder pedals. For example, if the pilot puts pressure on the right rudder pedal, the brake on the right main landing gear wheel will be activated, if the left rudder pedal is pressed, the brake on the left main landing gear wheel will be activated, or by applying pressure on both pedals, he can activate the brakes on the two main landing gear. Basically, brake systems work on the principle that the friction created with the applied force converts the existing kinetic energy into heat energy. During braking, a large amount of heat is generated in the brake discs, so the brakes must be constantly inspected, maintained, and adjusted for effective operation. Disc brakes are generally used in modern aircraft. As the wheel rotates, the existing disc or discs also rotate, but when pressure is applied to the rudder pedals to brake, the fixed bit puts pressure on the caliper disc units and makes them resist turning. Aircraft size, weight, and landing speed affect the structure and design of the disc brake system. Single, double, or multiple disc brake types are widely used. Segmented rotor brakes are used in large aircraft. The use of carbon discs is increasing in modern aircraft [2, 3].

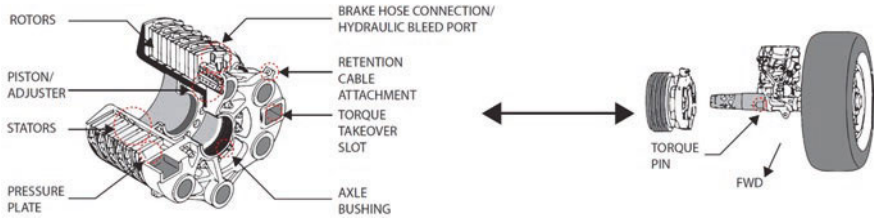


Fig. 7.14 Detailed structure of the Boeing 737 aircraft brake assembly

When slowing the rotation of the wheels in large and high-performance aircraft, the great heat that will occur can cause problems. Segmented rotor disc brakes have been developed to distribute this high heat better. Most of them contain a large number of elements that help control and distribute heat. Segmented rotor disc brakes are heavy-duty brakes specially adapted for use with high-pressure hydraulic systems. In this brake system, an example of which is given in Fig. 7.14, braking is carried out by a series of high friction fixed brake pads in contact with rotating segments. The rotors are designed as slit or gaped sections in order to allow the heat to dissipate more easily and thus to cool more easily [2, 3].

The segmented brake assembly consists of a carrier, a piston and piston cover gasket, a pressure plate, an auxiliary stator plate, rotor segments, brake plates, automatic adjusters, and a support plate. The carrier assembly and brake housing with torque pipe are the basic units of this brake system. Other components of the brake are mounted on this part and the landing gear strut is also connected to this part. Most segmented rotor disc brakes have a large number of individual cylinders machined into the brake housing and the same number of pistons as the number of cylinders driving these cylinders. Often these cylinders are fed by two different hydraulic sources so that if one source fails, the system can operate sufficiently. There is a pressure plate to fit the stator drive sleeves or torque tube spine. This non-rotating high-strength steel has a circular form and a notched structure on the inner frame. An insulator is used between the piston head and the pressure plate to prevent the heat generated in the brake discs from being transferred. The pressure plate transfers the motion in the pistons to the rotor and stator stack, which is used to slow the rotation of the wheels. In most braking systems, the brake lining material attached directly to the pressure plate comes into contact with the first rotor in this stack to transmit the movement of the piston or the pistons. There can also be an auxiliary stator plate with brake lining material on the opposite side of the pressure plate. When the brakes are applied, the successive rotor and stator are compressed under hydraulic pressure to the support plate of the brake assembly. The support plate is a heavy steel plate bolted to the torque tube. In most cases, the backing plate is attached to the brake lining material and is in contact with the last rotor in the stack. The detailed structure of segmented rotor disc brakes is shown in Fig. 7.15 [2, 3].

The segmented multi-disc brake system has provided reliable service for many years in the aviation system. Carbon disc brakes have been developed over time to make these brakes lighter and dissipate the resulting friction heat quickly and safely.

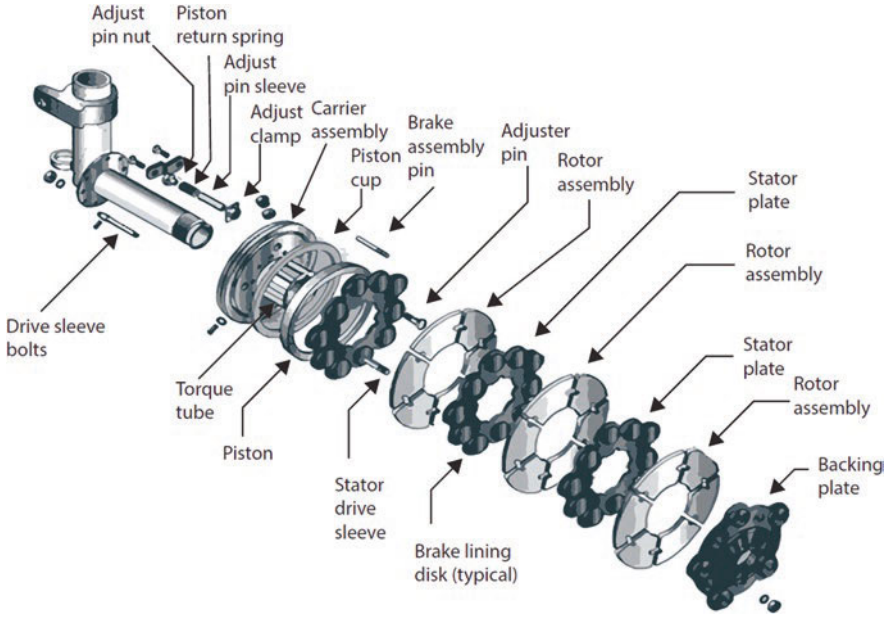


Fig. 7.15 Detailed structure of segmented rotor disc brakes

Table 7.2 Weight savings achieved after the use of carbon discs in some Boeing aircraft models

Aircraft model	Weight saving (kg)
737-600/700	250
737-600/700/700IGW/800/900/900ER	320
757	249
767	363
MD-10 freighter	443

It is named like this because carbon fiber materials are used in the materials that make up the brake rotors. Carbon brakes are about 40% lighter than conventional brakes. Carbon fiber discs are considerably thicker than sintered steel rotors, but despite their thickness, they are extremely light. In addition to their lightness, they can withstand 50% higher temperatures than steel component brake discs. Carbon brakes have been shown to withstand two to three times the heat of a steel disc brake in non-aircraft applications. Carbon rotors dissipate heat faster than steel rotors, maintaining their strength and dimensions at high temperatures. In addition to these advantages, carbon brakes last 20–50% longer than steel brakes, which means they require less maintenance. The only disadvantage of carbon brakes is their high production costs [2, 3, 11]. Weight savings achieved after the use of carbon discs in some Boeing aircraft models are shown in Table 7.2.

7.6 Tires

Aircraft tires are the elements that provide the necessary handling for braking and stopping, which are responsible for meeting the weight of the aircraft while on the ground. Although they are generally tubeless, there are also types with inner tubes. The tires help absorb the landing shock by helping the shock absorbers in the struts. In addition, it reduces the rigidity of operations during takeoff, postlanding ground movements, and taxi movements [2]. Aircraft tires are classified in various ways according to the following items:

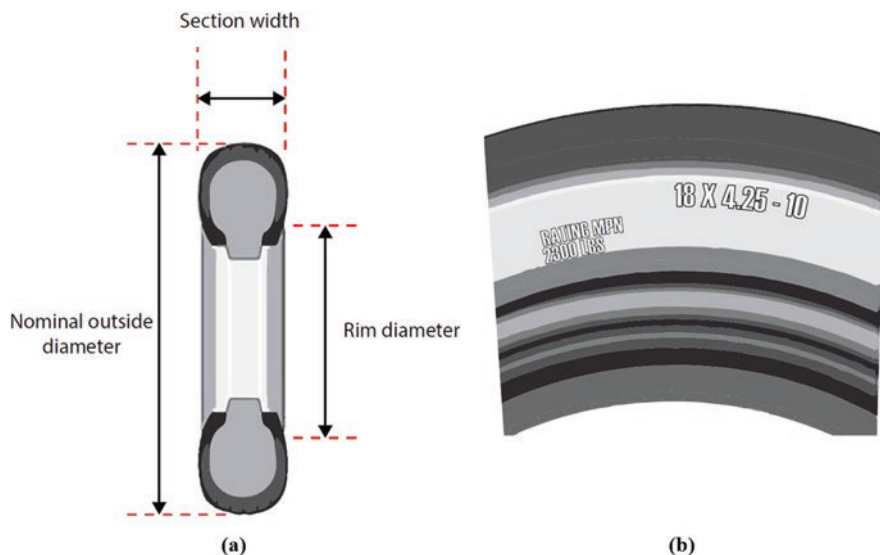
- Type
- Ply rating
- Tubeless/tubed
- Bias-ply tire
- Radials

7.6.1 Type Classification

While there are nine types of tires, only Types I, III, VII, and VIII are still in production. Type I tires are flat profile tires not used in the modern aviation fleet, they can be found on older aircraft. Type I tires are specified only by their nominal overall diameter in inches and are used on fixed landing gear aircraft. Type III tires are considered as general aviation tires. They are generally used in light aircraft with a landing speed of less than 160 mph (140 knots) per hour. Type III tires are regarded as relatively low-pressure tires. They are tires with small rim diameters compared to the overall width of the tire. They are identified by a number two system. In this numbering system, the first number is the nominal section width of the tire and the second number is the diameter of the rim designed to be mounted on the tire. Type VII tires are high-performance tires found on jet aircraft. They are inflated at high pressure and can carry high loads. Type VII tires have a narrower cross section than Type III tires. Type VII aircraft tires are identified by a number two numbering system. The first number indicates the nominal overall diameter of the tire, while the second number indicates the section width. An X symbol is used between these two numbers. Type VIII tires are also used in high-performance jet aircraft and are inflated to very high pressures. These tires have a relatively low profile and are suitable for very high loads. The three-part nomenclature combination is used to describe the tire. Tires are a combination of Type III and Type VII nomenclature using general tire diameter, section width, and rim diameter. In the three-part combination, the symbols X and “-” are used where they are. Bias tires use similar designation terminology, while radial tires use the letter R instead of the “-” symbol. Table 7.3 shows tire types, pressures, usage areas, and speed limits. Figure 7.16 shows the geometric properties of the tire and gives an example of the Type VIII tire notation [2, 4].

Table 7.3 Aircraft tires by type

Type	Pressure	Usage area	Knot ground speed
Type I	Low	Piston engined	Low
Type III	Low	Piston engined	<140
Type VII	High	Jet engined	140–195
Type VIII	Very high	Jet engined	183–204

**Fig. 7.16** (a) Criteria determining tire dimensions and (b) identification of Type VIII tires

7.6.2 Ply Rating

Rubber layers are reinforcing fabrics covered with rubber, placed inside the tire to provide strength. While the number of layers used previously was directly related to the load that the tire can carry, today tire strength has become independent of the layer with the techniques and innovative materials developed in tire-making techniques. However, the layer grade is used to convey the relative strength of an aircraft tire [2, 4].

7.6.3 Tubeless/Tubed

As stated above, aircraft tires can be in tubed or tubeless form. A specially designed liner is used to hold the air in tires without an inner tube. This liner is not required for tires with inner tubes because the inner tube holds this air. There is the word “tubeless” on the sidewalls of tubeless tires. If this statement is missing, it contains a tube inside the tire [2, 4].

7.6.4 Bias Ply or Radial

A classification can be made according to the direction of the layers used in tire construction, which is divided into curved or radial. Conventional aircraft tires are cross-ply (cross-belted bias ply) tires. Depending on the rotation direction of the tire, the angle of the plies varies between 30° and 60°. In this way, it provides a more flexible structure for tires. Radial tires are used in some modern aircraft. The layers of the radial tire are laid at 90° angles according to the rotation direction of the tire. Thanks to this configuration, it is ensured that the tires undergo less deformation when carrying high loads [2, 4].

7.7 Components of Tire

Unlike automobile or truck tires, aircraft tires do not have a load-bearing responsibility over a long working period. Aircraft tires must absorb the high impact loads that occur during landing and must be able to operate at high speeds during the takeoff/landing phases. Components of the aircraft tire are shown in Fig. 7.17 [2].

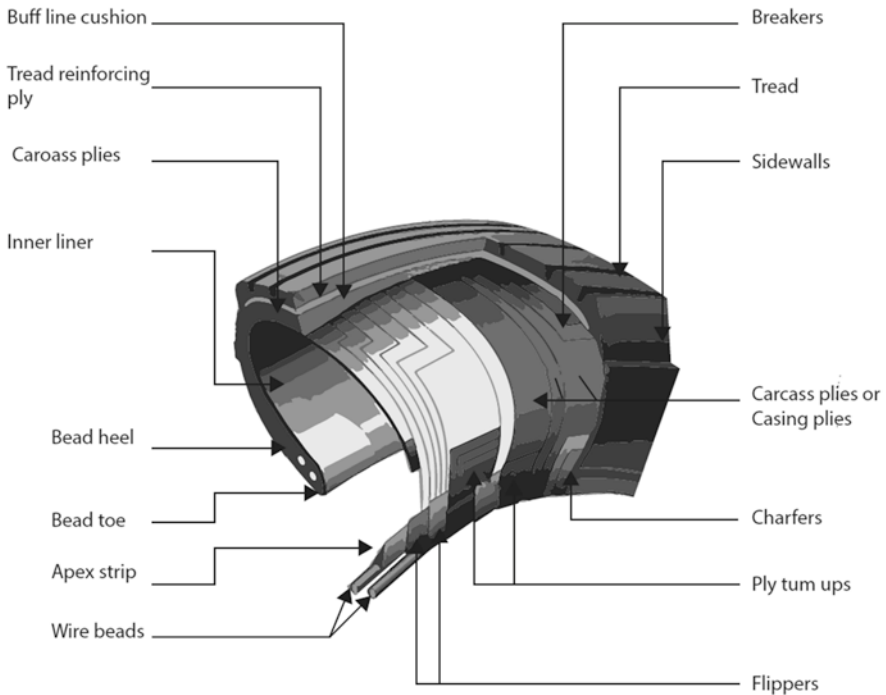


Fig. 7.17 Components of aircraft tires

7.8 Extend: Retract System and Controls

In the previous sections, it was mentioned that the landing gears can be fixed or extendable-retractable. The landing gear is equipped with collapsible mechanisms to eliminate parasitic drag during flight. These mechanisms are generally operated hydraulically. However, electric-hydraulic pumps are also widely used. The extend-retract system consists of the following elements [2, 3];

- Actuating cylinders
- Selector valves
- Uplocks
- Downlocks
- Sequence valves
- Priority valves
- Tubing
- Other conventional hydraulic system components

These elements work in conjunction with each other to allow the landing gear and the covers that contain the landing gear to be properly and sequentially retracted and extended. It is extremely important that the system works correctly and without errors. When the extending command is given to the landing gear, firstly the doors of the landing gear are opened by taking the command, then the landing gear struts are opened. The doors of the nose landing gear are mechanically connected and do not require hydraulic power. Some struts may have a design directly linked to the doors. When commanded in these designs, doors and struts are opened together at the same time. Figure 7.18 shows the general operating diagram of the Boeing 737 aircraft landing gear control system [3].

There are many critical factors during the assembly and extending of the retractable landing gear. These include the factors of locking the landing gear after unlocking and removing this lock while retracting, unlocking when the re-unlocking is completed, and releasing the landing gear when the re-unlocking state is to be performed. Exposure of landing gear to harsh environments (such as mud, ice, etc.) can sometimes cause malfunctions in the operation of these systems. Air loads that occur due to the aircraft moving in the air during opening or closing in the air cause loads on this system. The mechanism design to be made should be carried out by considering these loads [3].

Information about the landing gear extending and retracting system for the Boeing 737 aircraft is given below. A command in the cockpit must be given to unfold or retract the landing gear. Before moving this lever, the control lever on the control must be pulled out. After the control is given, the push-pull cable is operated and this cable runs the forward quadrant. The forward quadrant is located under the floor of the flight compartment. The control lever assembly has a lever locking mechanism actuated by the lever locking solenoid. The existing lever lock prevents accidental assembly of landing gear while the aircraft is on the ground. When the

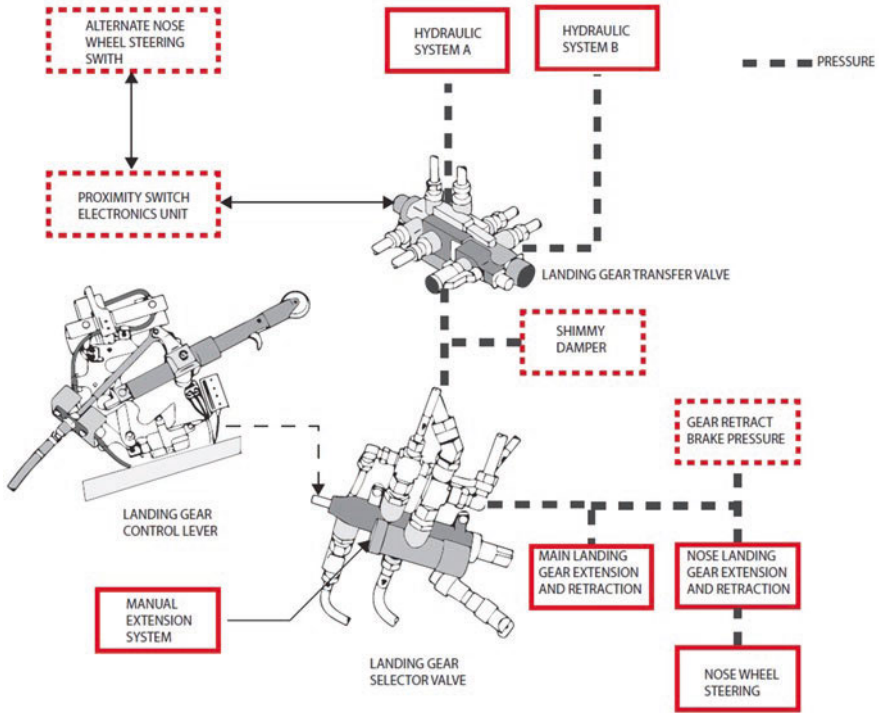


Fig. 7.18 General operating diagram of the Boeing 737 landing gear control system

aircraft takes off, the solenoid is powered electrically and allows the unlocking to be removed for the landing gear to be retracted [3].

As shown in Fig. 7.19, the landing gear control lever has three positions as up, off, and down. When the landing gear control lever is lowered, the down position switches are given the off position. After the switches come to the off position, the position indicator system uses this signal to turn on the red landing gear position lamps. When the landing gear control lever is lifted up, the up position switches are turned off. When the switches are turned off, the antiskid system is stopped [3].

As seen in Fig. 7.20, hydraulic system A for Boeing 737 aircraft provides pressurization for the main landing gear extending and retracting functions. The hydraulic system B provides backup pressurization only for the retracting function. The landing gear transfer valve in the system controls the source of pressure (Hydraulic System A or Hydraulic System B) to provide pressure to the main landing gear. As mentioned before, the shimmy damper present in the system reduces the vibrations of the main landing gear. The Shimmy damper system is connected to the return line between the landing gear selector valve and the landing gear transfer valve. The landing gear selector valve provides up and down pressure to retract or extend the main landing gear. The landing gear control lever controls this valve. With the upstream pressure provided, the backup system and the landing gear retraction

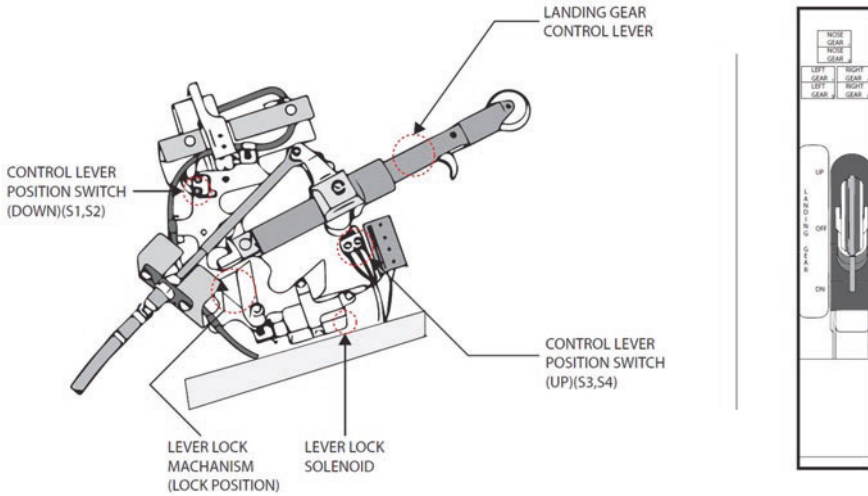


Fig. 7.19 Boeing 737 aircraft landing gear control arm and its internal structure

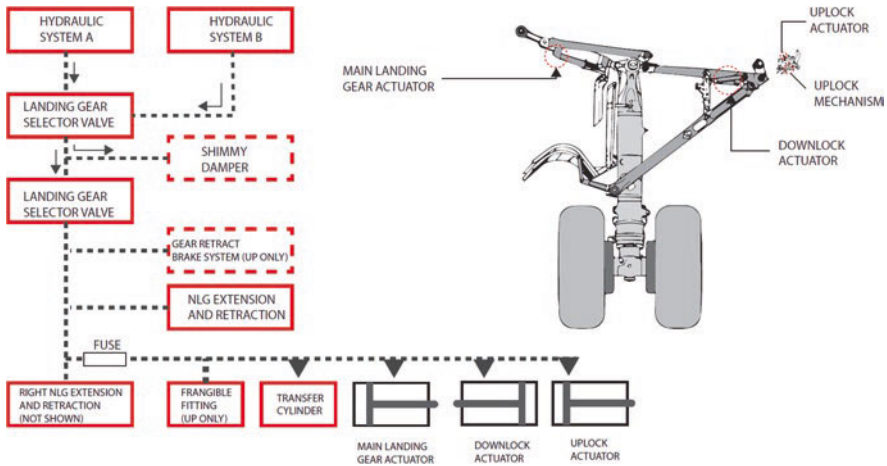


Fig. 7.20 Boeing 737 aircraft main landing gear opening-gathering mechanism system diagram

brake system are pressurized. With this braking, the rotation of the wheel is stopped during the retraction of the main landing gear. Figure 7.21 shows the opening and closing conditions of the Boeing 737 aircraft main landing gear [3].

As seen in Fig. 7.22, for the Boeing 737 aircraft, the hydraulic system A provides pressurization to extend and retract the nose landing gear. The hydraulic system B only provides pressurization to retract the nose landing gear. The landing gear transfer valve controls the hydraulic system from which the pressure source to the nose landing gear comes from. The landing gear selector valve provides up or down pressure for opening or collecting. The landing gear selector valve operates the landing

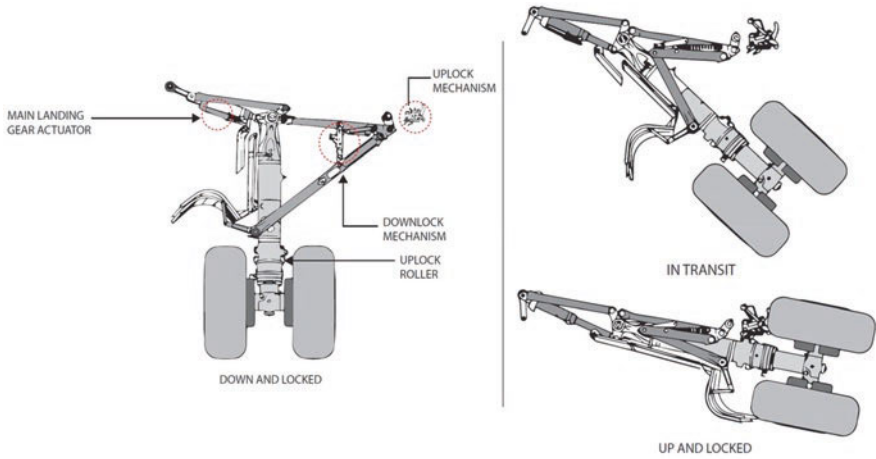


Fig. 7.21 The opening and closing conditions of the Boeing 737 aircraft main landing gear

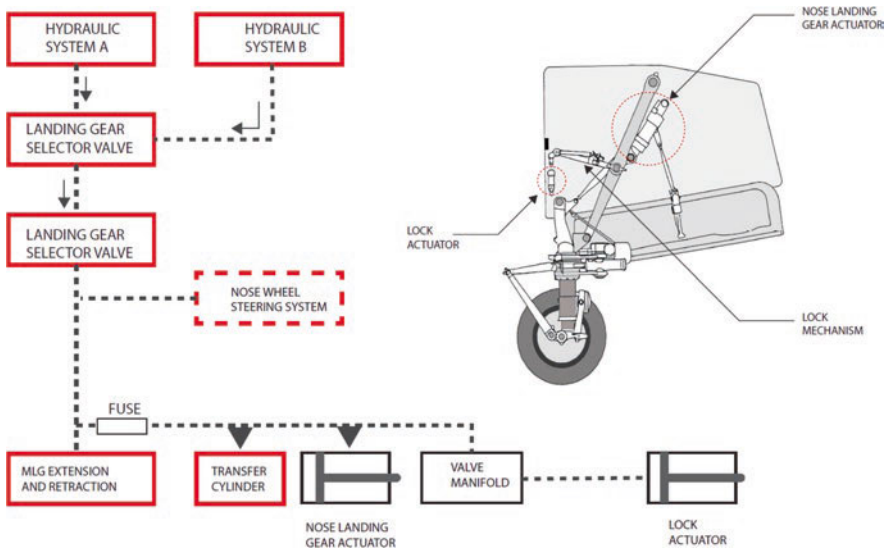


Fig. 7.22 Boeing 737 aircraft nose landing gear opening-collecting mechanism system diagram

gear control lever located in the cockpit. The pressure given to the system also pressurizes the nose wheel steering mechanism. Figure 7.23 shows the opening and closing conditions of the Boeing 737 aircraft main landing gear [3].

When the hydraulic system pressure cannot be provided to extend the landing gear or when normal extending cannot be achieved for some other reason, the landing gear can be opened by using the manual landing gear extension system to extend the main landing gear and nose gear. This system works independently from the

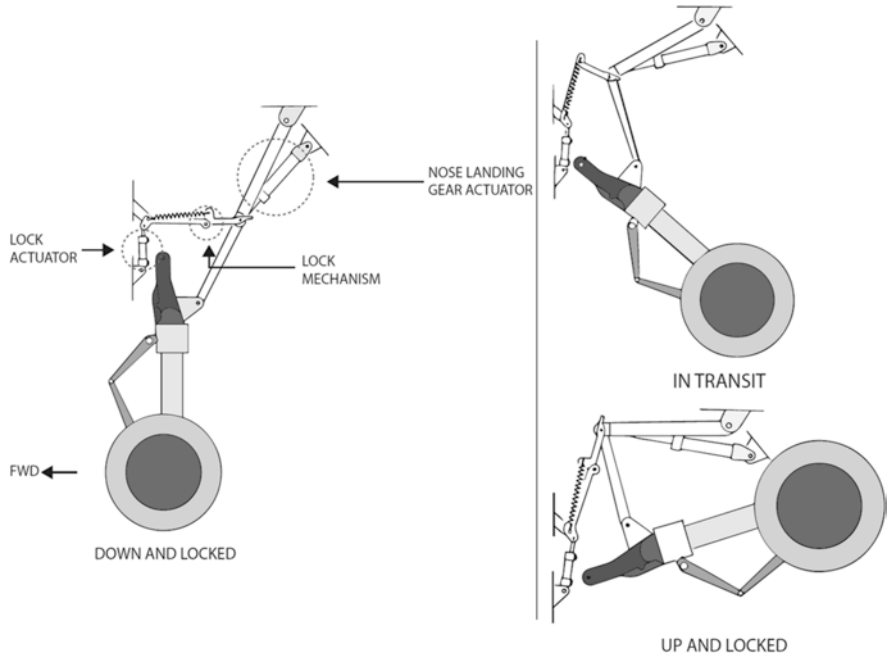


Fig. 7.23 The opening and closing conditions of the Boeing 737 aircraft nose landing gear

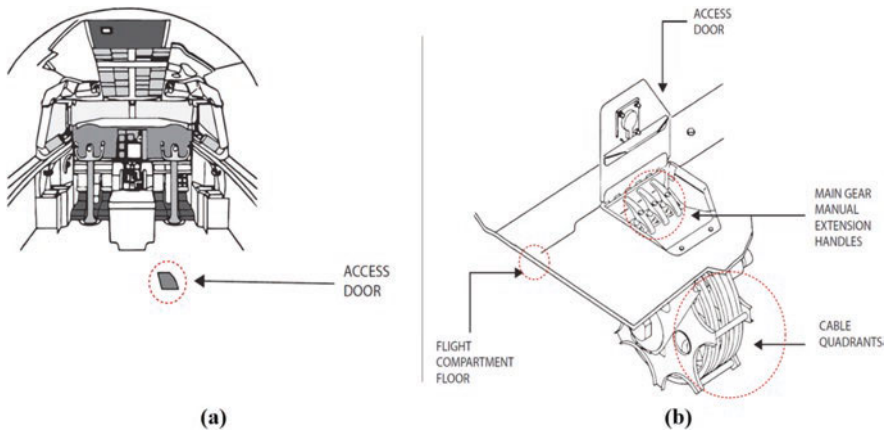


Fig. 7.24 Boeing 737 aircraft landing gear manual opening system, (a) cockpit position, and (b) control arms

normal extension and retraction system. As shown in Fig. 7.24, there are three handles in the cockpit for manual extension, one for each landing gear, in total. The manual system is only for extension the landing gear, it does not have a function such as retracting the landing gear [3].

7.9 Nose Wheel Steering Mechanism

Today, many aircraft have a nose wheel steering mechanism on the nose wheels that can be guided from the cockpit. This mechanism allows the aircraft to be directed during their movement on the ground. In addition to the nose wheel steering mechanism, aircraft can be directed by controlling the rudder with rudder pedals during ground movements. In some aircraft, different braking forces can be applied to the brakes on the main landing gear to provide guidance in taxi movements. Nose wheel steering can be achieved through simple mechanical connections connected to the rudder pedals in small and relatively lighter aircraft. Large and heavy aircraft use a power source for nose wheel steering due to their mass and need for positive control. Although there are different designs for the nose wheel steering system in large aircraft, most of them share similar features and components. Usually in the cockpit, a small steering wheel placed on the left side wall provides direction to the nose wheel. In some aircraft, it is possible to turn this system on or off. In Fig. 7.25, the nose wheel steering mechanism for Boeing 737 aircraft is given as an example below [2, 3].

Inputs taken from the steering wheel or from the rudder pedals go to the metering valve through the control cables. This creates input via the summing mechanism to move the steering metering valve. Thus, hydraulic pressure is allowed to go from the rotary valves to the steering actuators. Actuators apply pressure to move the nose gear wheels between 0 and 78°. When the wheels are in the desired position, the summing mechanism brings the metering valve to the neutral position and thus stops the hydraulic pressure on the actuators. Actuators keep the wheels in their current position [2, 3].

7.10 Tail Skid

The tail skid structure protects the stabilization of the aircraft and the fuselage structure in order not to be damaged as a result of excessive elevator control during landing and takeoff. Tail skid structure is a structure located under the fuselage in the horizontal stabilized part of the aircraft and is controlled with the landing gears. When the landing gear is extended, the tail skid is open, while the landing gear is retracted, the tail skid is closed. There is a wear shoe on the tail skid. As the wear shoe touches the runway, it absorbs the tail strike. The warning sign in the tail skid structure indicates when the tail skid should be changed. Figure 7.26 shows the tail skid structure for the Boeing 737 aircraft [2, 3].

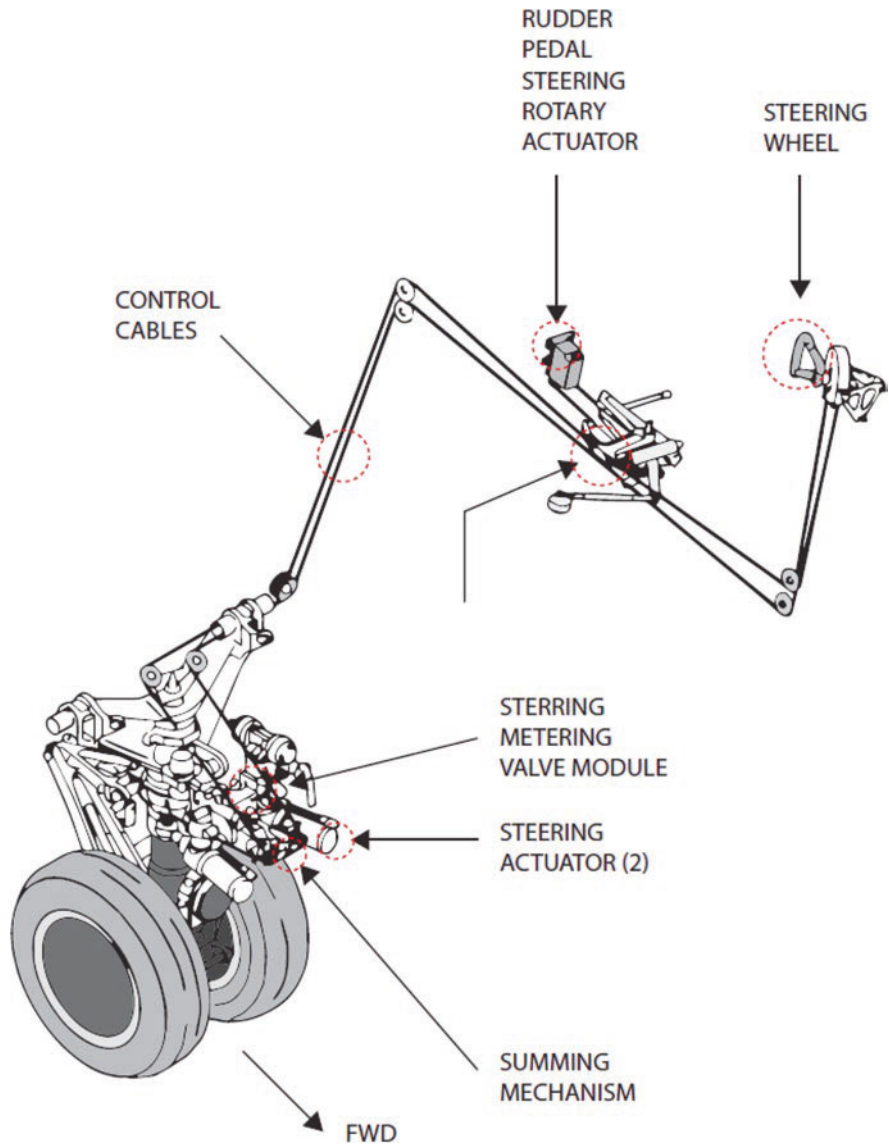


Fig. 7.25 Boeing 737 aircraft nose wheel steering mechanism

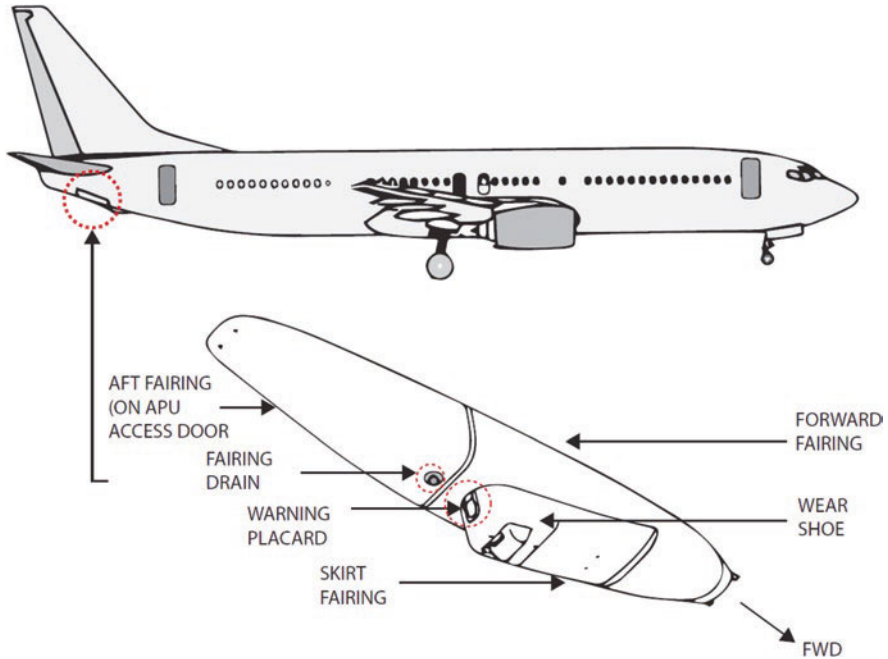


Fig. 7.26 Boeing 737 tail skid structure

References

1. Lufthansa Technik AG Website. Retrieved from <https://www.lufthansa-technik.com/landing-gears>.
2. US Department of Transportation. (2012). Landing gears. In: Aviation maintenance technician handbook- airframe volume 2, Federal Aviation Administration, .
3. The Boeing Company 737-600/700/800/900 Aircraft Maintenance Manual. (2002). Chapter 32—Landing gear.
4. Gudmundsson, S. (2014). The anatomy of the landing gear. In *General aviation aircraft design: Applied methods and procedures* (pp. 547–580). Butterworth-Heinemann.
5. Skywagons Website. Retrived from <http://www.skywagons.com/airplanes-for-sale/1973-cessna-150150-taildragger-sold-n48ak>.
6. Eskisehir Technical University Faculty of Aeronautics and Astronautics Website. Retrieved from http://ecas.anadolu.edu.tr/fotograflar_ucak_filosu.html.
7. U.S. Department of Defense Website. Retrieved from <https://dod.defense.gov/OIR/gallery/igphoto/2001248081/>.
8. Insider Website. Retrived from <https://www.businessinsider.com/antonov-an-225-mriya-worlds-largest-cargo-plane-history-details-2020-4>.
9. BoldMethod Website. Retrieved from <https://www.boldmethod.com/learn-to-fly/systems/how-the-4-types-of-landing-gear-struts-work/>.
10. Sforza, P. (2014). Landing gear design. In *Commercial airplane design principles* (pp. 251–300). Butterworth-Heinemann.
11. Allen, T., Miller, T., & Preston, E. (2009). Operational advantages of carbon brakes. *Boeing Aero Magazine QTR*, 3(09), 16–18.

Chapter 8

Manufacturing and Maintenance

Operations for Bladder-Type Aircraft Fuel Tanks



Tamer Saraçyakupoğlu

8.1 Introduction

Air vehicles are highly-engineered machines designed to operate in excessive conditions. During a long-range cruise flight at the flight level of 33.000 ft, a commercial passenger aircraft floats in an environment where the outside temperature varies from -55 to -60°C while outside pressure is lower than mean sea level (MSL). While flying in these extraordinary conditions, the environmental control system (ECS) of the aircraft keeps the cockpit and cabin at a livable level. The ECS also adjusts the temperature and pressure of the cargo department and electronic bay as necessary.

It is obvious that the design of an airplane varies in compliance with the specification of the mission. Out of question, the level of the risk can differ for military and passenger aircraft [1]. The air vehicles contain different kinds of fluids to support their flights for ensuring the mission. In general, pneumatic, hydraulic and fuel are the fluids needed for the flight and ground operations of an aircraft. Undoubtedly, every fluid works in the system synchronized with the features of the relevant component. Since they are not solid matters, the fluids are generally being impacted by the maneuvers. Undoubtedly, the movement of the fluids varies depending on the type of aircraft. So the design of the fluid components does. For example, for an aerobatics aircraft, the lubrication and the fuel system should meet the requirements of the reverse flight while it is not mandatory for commercial passenger aircraft. In another example, ECS that shown in Fig. 8.1 should be implemented into the commercial passenger aircraft while a simpler one can be used for light sport airplanes (LSA) [2].

T. Saraçyakupoğlu (✉)

Department of Aeronautical Engineering, Istanbul Gelisim University, Istanbul, Turkey

e-mail: dr.tamer@tamersaracyakupoglu.com.tr

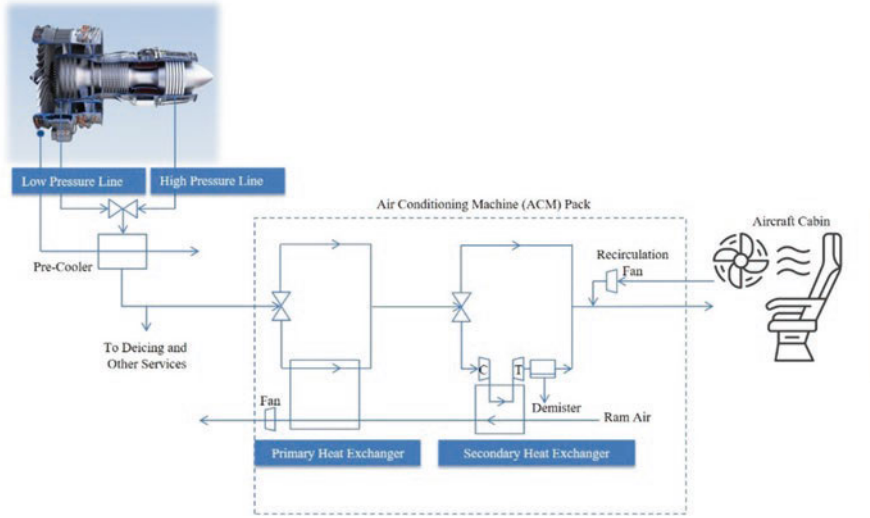


Fig. 8.1 Aircraft environmental control system (ECS)

The airworthiness authorities are the decision makers that approve designs and products considering the flight and ground safety issues. They release the rules and regulations for ensuring public health at the global level for certification of air vehicles. Literally, the military-based certification and civilian-based certification processes have different steps. But, independent from military or civilian, the aircraft and engine manufacturers perform many tests during design and manufacturing and phases to meet these precisely-prepared requirements [3, 4].

Although it doesn't have a direct impact on the crew and passengers as ECS does, the aircraft fuel systems are designed to meet the stiff and meticulously prepared regulations since it influences the performance of the flight. The sloshing effect may be hazardous if it is not designed properly considering the 3-axis movements. The acceleration, deceleration, ascend, descend, rolling, and yawing maneuvers' characteristics are shaped by the impact of the slosh effect augmented by the fuel amount. The need to account for the effects of fuel leakage in the tank caused by large and unexpected changes in aircraft attitude adds to the challenge. To some degree, this can be mitigated by compartmentalizing the fuel by using a greater number of smaller tanks or adding baffles inside the tank to slow the rate of fuel movement across the tank. This technique will introduce different levels between the baffles before the attitude stabilizes and the fuel level equalizes, and it may be necessary to calculate the fuel surface separately inside each compartment.

An air vehicle's weight varies from light to heavy, depending on the number of cockpit and cabin crew, fuel, and payloads that consist of passenger and cargo. Among these members, only fuel dramatically changes during flight. As the aircraft flies, the engines consume the fuel, and hence the weight of the plane decreases. On the contrary, sometimes especially military airplanes fill their tanks from refueling

aircrafts such as KC-135 to increase the flight time. Besides some large body airplanes use fuel jettison systems as their fuel load is substantially higher than the maximum landing weight. Consequently, the amount of fuel changes during flight. It is worth noting that, as the weight of fuel changes the “cg” may displace and deteriorate the flight performance. It concludes with the flight instability. During the cruise flight of certain aircraft, the fuel management system (FMS) actively controls the longitudinal “cg” by automatically moving fuel between the fore and aft tanks. That’s why the locations and the volume of the fuel tanks are important for flight safety. Typically, the wings and the volume between the wings are selected as the layout of the fuel tanks for a commercial passenger aircraft as shown in Fig. 8.2.

The ability of the lateral flight controls to offset any fuel load-induced rolling moment due to a lateral “cg” change must be understood from the start in terms of lateral stability. This issue must also be addressed in terms of the entire flight envelope and all aircraft configurations. A flight-critical fuel lateral balance system must be provided if roll control power is inadequate to sustain the worst-case lateral “cg” change. As a result, the fuel system design team must ensure that important design problems like these are identified by the aircraft design team at the earliest stages of the design, such as the conceptual design phase.

For the military air vehicles, the wings are mainly used for carrying the ammunition attached to the launchers and the electronic pods on the pylons, therefore the inner-fuel capacity may be limited compared to the commercial passenger airplanes. These loads may result in additional aerodynamic and body forces contributing to the existing, torsion, shear, and bending. Besides, the thrust and the weight of the engines affect either the wings or fuselage depending on their locations. The hard-points are the reinforced areas for increasing the carriage capacity of the wings. Since almost any available space has vital importance over fuel storage, the free-form and unusual shaped fuel tanks are usual in military aviation. For example,

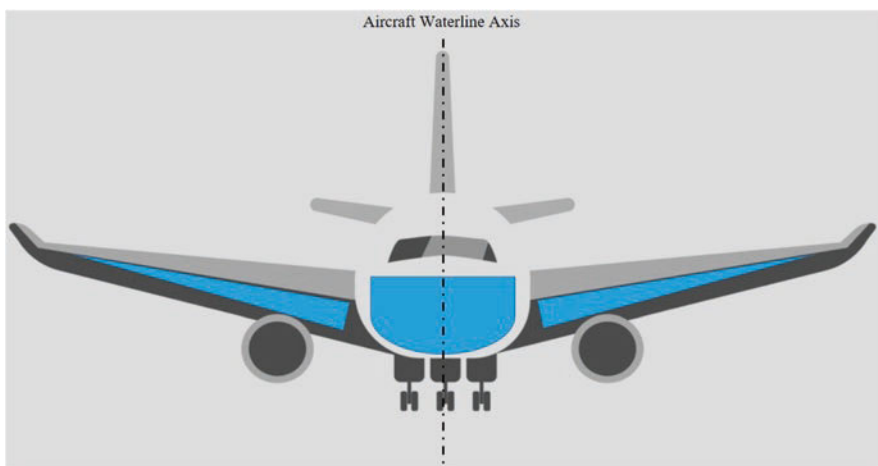


Fig. 8.2 The layout of the fuel tanks of a commercial passenger aircraft

L-shaped fuel tanks are adapted to the place underneath the pilot seats. Besides the inner type fuel tanks, in order to increase the cruising range, auxiliary fuel tanks are installed outside the military airplanes. The mentioned tanks are external replaceable ones, called as “drop tanks” and “conformal tanks.”

8.2 Aircraft Fuel System

For the aircraft to satisfy its operating range specifications, a considerable amount of fuel must be carried on board. The maximum fuel capacity is the value that provides information about the volume of fuel that an aircraft can carry. Table 8.1 gives information about the maximum fuel capacity of some common commercial passenger air vehicles.

When it is compared with the weight of a mid-class family car that has 50 lt (~35 kg) the amounts will be clearer. The overall fuel weight to total aircraft gross weight ratio in many large transport airplanes can be as high as 50%. In comparison, the average car has a ratio of about 5%.

It is noteworthy that, particularly for the light aircraft category, the wing configuration has a direct impact on the fuel system. The high-wing configuration might rely on a gravity-feed fuel system, while a low-wing configuration may require an additional electrical/mechanical fuel pump [5, 6]. A special reserve tank called as a collector tank is connected to each fuel tank in the gravity-fuel tank configuration. The main purpose of the collector fuel tank is to feed the engine continuously via engine pumps. The collector tanks ensure that three-axis movement of the airplane will not result in a drop in fuel pressure which may stop the engine run. Besides, the gravity-fuel tank configuration each tank has a float-type sensor to detect the level of the fuel quantity. The collector tanks are located just below the engine, pumping the fuel to the engine’s injector manifold is necessary [5]. That’s why during engine start and for the critical flight stages such as takeoff and sometimes climb the electrical fuel pump is switched on. During the cruise and descent phases of the flight, the mechanical pump may be operated particularly. Using the fuel-selector-handle, the pilot selects the tanks in the light aircraft category. This mechanism is totally different for airplanes heavier than light aircraft segments. Since the fuel system has crucial importance on flight safety, the airworthiness authorities push the aircraft

Table 8.1 Maximum fuel capacity of some common commercial passenger aircraft

Aircraft type	Maximum fuel capacity (tones)
Boeing 737-800	18.2
Airbus A320-200	16.9
Boeing 747-400	151.7
Airbus A380	323.5

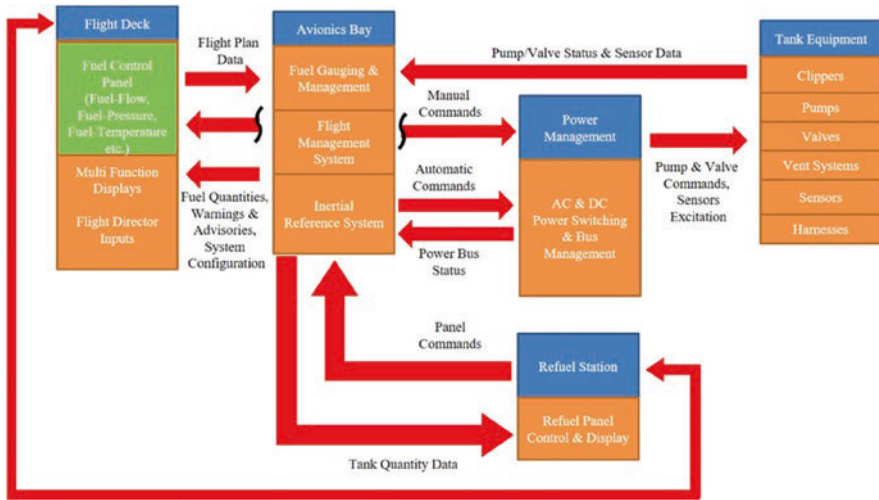


Fig. 8.3 Fuel system typical schematic of a commercial passenger aircraft

manufacturers to install a more robust and fully-automated fuel system. In Fig. 8.3, the fuel system typical schematic of a commercial passenger aircraft is shown. As it is seen in the “Fuel System Typical Schematic of a Commercial Passenger Aircraft” the fuel system is divided into the following subsystems: engine feed, fuel storage, refuel, and defuel, fuel transfer, engine feed line fuel pressurization, vent systems, fuel jettison, in-flight refueling, and others. It is noteworthy that instant mutual data transfer is crucially important in every step. For example, for maintaining the constant rolling angle during a steep turn maneuver fuel pumps should pump the fuel to the opposite direction to prevent the gravity effect. Besides, it is not necessary to underline that, the pilots need on-time information about fuel quantity in flight deck [6]. In conclusion, for managing the huge amount of fuel in terms of fuel consumption, refueling and fuel jettison operations require a proper system architecture as shown in Fig. 8.3.

To allow safe diversion and landing following a rotor burst case, the fuel system designer/manufacturer must ensure that continued safe flight for several hours on the remaining operating engine or engines is possible. In this manner, the implementation of automated fuel balancing is essential for commercial passenger airplanes. Depending on the type of aircraft, different types of fuel tanks are used. In this sense, the rotor burst problem is more than just a tank position problem; it’s also a device design problem, since possible damage to the tank, fuel lines, and electrical power supplies must all be considered. Also as it was described before, fuel tanks’ location and the volume may change the location of “cg” and affect the flight stability. With this regard, the position and “cg” of the stored fuel, in-flight stability is an issue that must be considered.

8.2.1 Aircraft Fuel System Component Requirements

In this section, the aircraft fuel system component requirements will be described in detail. These requirements are taken from most widely referred to general aviation regulations such as British Civil Airworthiness Authority (BCAA), CAP 482.

General

- (a) Each fuel system should be constructed and arranged in such a way that the fuel will flow at a speed and pressure to ensure proper operation of the engine functions under normal conditions.
- (b) Each fuel system should be arranged in such a way that each engine draws fuel from a single tank, except when the inside of the tanks are interconnected, ensuring that each connected tank is supplying an equal amount.
- (c) The fuel system should be designed to prevent evaporating fuel gas from entering the system.
- (d) Each fuel tank has to withstand external loads and vibration, inertia, and any fluid pressure loads in flight without fail.
- (e) If the slosh of the fuel in the tank changes the “cg” of the aircraft noticeably, appropriate tools (Such as fuel-resistant foam/sponge) should be installed in order to reduce this slosh to acceptable limits.

Fuel Flow

• Gravity-Feed Systems

- (a) For these systems, the fuel flow rate should be 150% of the fuel that the engine draws at the takeoff phase.
- (b) Gravity is used to move fuel from the tanks to the engine in the gravity-feed system. The fuel tanks, for example, are hooked up in the wings of high-wing airplanes. The fuel tanks are located above the carburetor in this design, and the fuel is “gravity-fed” into the carburetor.

Pump-Feed Fuel Systems

- (a) If gravity cannot be used to transport fuel owing to the aircraft’s configuration, fuel pumps are equipped. The fuel tanks in the wings of low-wing aircraft, for example, are located below the carburetor. The fuel flow rate of each pump system (main and auxiliary supply) should be 125% of the amount of fuel drawn by the engine at maximum power for takeoff.
- (b) There are at least two fuel pumps onboard aircraft with fuel-pump systems. The main pump mechanism is powered by an engine, with an electrically powered auxiliary pump for starting the engine and in the event that the engine pump fails. The auxiliary pump, also called a boost pump, gives the fuel system additional reliability. A switch on the deck controls the electrically driven auxiliary pump.

Unused (Trapped) Fuel Margin

- (a) In a certain flight pattern and maneuver, this amount for each fuel tank is determined by the amount of fuel in the tank at the time when the first sign of malfunction or failure in the engine started due to poor fuel supply.
- (b) This amount cannot be more than 5% of the total capacity of the fuel tank.

Fuel Tank Tests

- (a) Each fuel tank must be resistant to 1.5 psi (0.1 bar) pressure without failure or leakage.
- (b) All components must endure to the minimum force of +9 g, -4.5 g, and 3 g on the horizontal axis,

Fuel Tank Installation

- (a) Each fuel tank should be supported in such a way that the tank loads are not point-based due to the fuel weight.
- (b) If necessary, materials that will serve as seals (dampers) should be placed between the fuel tank and its support in order to prevent fretting and abrasions caused by friction.
- (c) The materials that act as support and gaskets should be nonabsorbent in a way that prevents the fuel transfer.
- (d) Each fuel tank section must be well ventilated and kept dry in order to prevent the accumulation of flammable liquids and vapors. It should be ensured that the compartments in the fuselage of the aircraft closest to the fuel tank are ventilated and kept dry in the same way.
- (e) No fuel tank should be located close to the engine flame.
- (f) It must be approved that the leaking fuel does not drip onto the passenger/crew and that the fuel tank does not interfere with the normal movement of any part of the aircraft and the normal movements of the passenger/crew.
- (g) The fuel tank and fuel pipes should not be broken in case of structural damages that may occur due to landing with heavy loads in emergency landing conditions.

Fuel Tank Drain System

- (a) Each fuel tank must have an effective discharge capacity.
- (b) The aircraft fuel system should be placed in such a way that it can be drained directly into the sediment (rest) reservoir or box with a volume of 10% suitable for discharge.
- (c) Each fuel tank should be placed in such a way that the water in it will drain from the fuel tank at sea level.
- (d) The drain system must be easily accessible and operable.
- (e) Each fuel drain system should have manual and automatic locking means in the closed position.

Fuel Tank Fill Connection

- (a) Fuel tank fill connections should be located outside of the crew and passenger cabin.

- (b) Spilled fuel must be placed in such a way that it does not enter the fuel tank cabin or any part of the aircraft other than the tank.

Fuel Tank Caps

- (a) Each fuel tank should be capped from its upper expansion area.
- (b) Each fuel tank cap outlet should be manufactured and positioned in a way that minimizes the possibility of ice or other foreign materials closing and blocking.
- (c) Under normal conditions, it should be manufactured in a way that prevents the fuel from siphoning.
- (d) Each vent must end outside the aircraft.

Fuel Filter and Strainer

- (a) A fuel filter should be located between the fuel tank outlet and the carburetor inlet (or engine-assisted fuel pump, if present).
- (b) Each fuel strainer or filter must be easily accessible for draining and cleaning.

Fuel System Pipes and Connections

- (a) Each fuel pipe should be supported and positioned in such a way that it is not affected by the acceleration conditions in flight, fuel pressure, and intense vibration.
- (b) Each fuel pipe should have flexible properties due to the relative movements that may occur between it and parts of the aircraft.
- (c) Each flexible hose must be approved and shown to be suitable for specific flight maneuvers.
- (d) Leaks that may arise from any fuel pipes and connections should not come into contact with hot surfaces or parts that could start a fire, and should not be poured directly on any pilot/passenger.

Fuel Valves and Controls

- (a) In flight conditions, there should be controls by which the pilot can suddenly cut off the fuel supply of the engine. (NOTE: There are some emergency procedures such as engine fire during the takeoff roll, engine fire during flight, etc. In case of these emergency situations, there are different kinds of precautions to be taken depending on the type of aircraft. Besides manufacturers, the airworthiness authorities also make recommendations to the crew against engine fire emergencies. For example, Federal Aviation Administration (FAA) advises pilots to descent at the maximum allowable airspeed consistent with the currently used procedure [7].)
- (b) The fuel pipe between the fuel shutoff valve and the carburetor should be as short as possible.
- (c) Each fuel shut-off valve should have normal and key stop capability for “ON” and “OFF” positions.

8.3 Aircraft Fuel Tanks

Depending on the aircraft types, the fuel tanks may differ. Although there are numerous members of a fuel system, such as tanks, pumps, pipes, hoses, fuel control Units (FCU), generally particularly fuel tanks are the systems that shape the whole structure.

Fuel tanks are formed in a variety of sizes, forms, and places. All tanks must be isolated from vibration, which is the most common cause of corrosion and leakage, and they must be able to withstand fuel expansion due to heat. The majority of the fuel tanks are fabricated from synthetic rubber or pre-shaped, riveted aluminum alloy. To avoid leakage, the aluminum wet-wing tanks have a sealant along their seams. To keep away from leakage, the aluminum wet-wing tanks have a sealant alongside their seams. Mainly, there are three types of integral fuel tanks. These are the discrete, integral, and bladder-type fuel tanks [8, 9].

8.3.1 Discrete Tanks

For the construction of fuel tanks, many aircraft, particularly older ones, use an obvious option. It is a discrete-type fuel tank. A discrete tank is strapped into the airframe structure and is made of different materials. To prevent sloshing, the baffles are often riveted or welded into place. Discrete tanks are fuel containers that are fabricated separately and bolted or strapped to the aircraft. To prevent leaks, they are usually made of 3000 and/or 5000 series aluminum alloy or stainless steel and seam welded. Light, general aviation, and homebuilt aircraft are the only types of aircraft that use discrete tanks. Discrete tanks are normally formed like the front of an airfoil and mounted on the inboard wing leading edge, or they're set up withinside the fuselage in the back of the engine and above the pilot's feet. The most common position for fuel tanks is inside the wings. Some tanks are designed to be part of the wing's leading edge. The layout of the discrete tank is illustrated in Fig. 8.4.

If there is a leak or a fault with the tank, being able to remove it and fix or replace it is an advantage. When welding repairs are performed, it is particularly important to follow all safety procedures. This usually entails cleaning the tank with water and

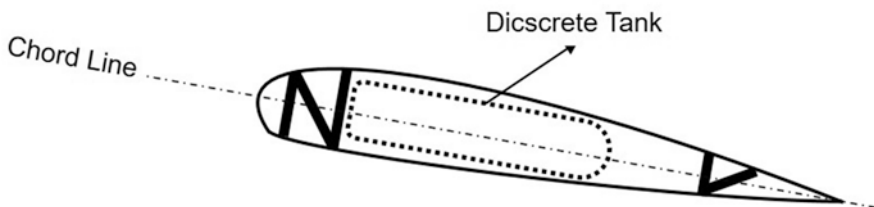


Fig. 8.4 Discrete Tank

detergent, as well as running steam or water through it for a certain amount of minutes. Fuel tanks must be pressure tested after being fixed, normally when mounted in the airframe, to avoid distortion when under pressure. It is noteworthy that the fuel tank repairs must be carried out in compliance with the manufacturer's instructions.

Advantages of the discrete tanks can be given as follows;

- Easy manufacturing which is mainly based on sheet metal forming
- Separately producing that allows mass-production in the back shops
- Easy installation of the inner systems such as quantity sensors and pipes
- Easy local reparability without pulling out the part from the mounting bay.

Disadvantages of the discrete tanks can be given as follows:

- Welding processes require more frequent NDI operations
- Rivets require fuel-resistant sealants
- Different vibration loads may affect adversely the riveted joint areas
- Leakage tendency under high impacts caused by incidents due to metal structure

Discrete tanks are generally preferred by many homebuilt air vehicles and general aviation airplanes such as Glastar N757C Aircraft.

8.3.2 Integral Tanks (Wet Wing)

Any available space is used for fuel in this system. The empty rooms amongst the spars, ribs, and stringers are sealed with non-leakage solutions. Part of the structure of the wings or fuselage is sealed with a fuel-resistant two-part sealant to form a fuel tank on many airplanes, particularly commercial-passenger category and high-performance aircraft. The insulated skin and structural parts have the most room for the least amount of weight. Since it forms a tank as a unit within the airframe structure, this type of tank is known as an integral fuel tank. A wing may be divided into different tanks for fuel management purposes, which may include a surge tank or an overflow tank, which is usually empty but sealed to hold fuel when required. Since there's no additional soft or hard case for the tank, these systems are called "wet wings" as it is illustrated in Fig. 8.5.



Fig. 8.5 Wet wing

Conventionally, the wet wings are notorious for leakage tendency. Access panels for inspection and repair of integral fuel tanks and other fuel system components are required. For repairs on large aircraft, maintenance staff physically reach the tank. For this purpose, many transport category aircraft have more than a dozen oval access panels or tank plates on the bottom surface of the wing. All fuel must be drained from an integral fuel tank before entering and conducting maintenance on it, and strict safety protocols must be followed. Fuel vapors must be purged from the tank, and the technician must use respiratory equipment. In case of leak or damage, the fire hazard is sudden, so wet wings should not be placed in ducts, weapon compartments, or close to the engine. The fire hazard can be prevented by a fuel-resistant, porous foam sponge inside the tank, but in this case, some fuel cannot be used. Approximately 2.5% of the fuel cannot be used due to the volume of the sponge material. Besides, another 2.5% portion cannot be used due to the sponge's tendency to absorb fuel. Finally, using fuel resistant sponge increases the amount of unused fuel. When using a discrete tank, subtract the wall thickness from the exterior measurements to get the actual usable internal volume.

Advantages of the integral tanks can be given as follows:

- Significant weight saving comparing with discrete and bladder tanks
- No additional effort is required for manufacturing since they are naturally integrated inside the wings and/or fuselages
- Relatively less manufacturing time since they don't require operations such as riveting, welding, bonding, etc.
- More traceable maintenance intervals which are parallelized with wing and structural check tasks
- Comparatively, easier fuel ejection process since they are directly connected to wing fuel flow lines.

Disadvantages of the integral tanks can be given as follows:

- More reliable insulation requirements because neighboring with wire-harness bundles
- Easy flammability since their periphery is lower and upper skins of the wings and/or fuselages
- Increased corrosion effect of the inner wing parts since they are wet by the fuel
- Integral tanks should not be deployed near people compartments, inlet ducts, gun bays, or engines due to the risk of fire in the event of a leak or battle damage.

Integral tanks are famously used by Rockwell B-1 Lancer aircraft. Grumman A-6 Intruder airplanes are also equipped with integral tanks. Many commercial passenger airplanes also have wet wing systems.

8.3.3 Bladder Tanks

Bladder tanks are constructed by rubber-like material (polyurethane sealant absorbed carbon-fiber fabric) bag into the aircraft structure's cavity. A bladder tank, which is made of reinforced flexible material, may be used instead of a rigid tank. A bladder tank has many of the same features and components as a rigid tank, but it can be installed through a smaller hole in the aircraft's skin. The tank, also known as a fuel cell, may be rolled up and inserted through a small opening, such as inspection access, into a specially prepared structural bay or cavity.

Bladders tanks are made up of two or three layers of rubberized material, with the inner layer serving as a non-porous fuel container and the outer layer serving as a more protective barrier against chafing, heat, and humidity. The fabric layers are made of nitrile rubber or vitthane, a urethane-based material. Heat-cured vulcanization is used to make nitriles, and the urethane bladders are cemented together. During installation, it can be unfurled to its maximum size once within. Clips or other fastening methods must be used to secure bladder tanks to the structure. In the bay, they should be smooth and wrinkle-free. It's particularly crucial that there are no wrinkles on the bottom surface, as this will prevent fuel pollutants from settling into the tank sump. The bladder tank is shown in Fig. 8.6.

One of the disadvantages of a bladder tank is the thickness of the skin. Since the rubber bag is thick, about 10% of the available fuel volume may be lost.

The bladder tanks are popular because they can be manufactured with a "self-sealing" feature. When a bullet passes through a self-sealing tank, the rubber fills in the cavity, avoiding a significant loss of fuel and a fire hazard. This feature, allows the cockpit crew to gain time for accomplishing a safe landing. Self-sealing bladder tanks provide a significant increase in aircraft survivability, as fuel tank hits account for roughly a third of all fighting losses.

In general, to account for wall thickness, internal structure, and bladder thickness in integral and bladder tanks, the usable tank volume must be reduced from the calculated value. As a rule of thumb, assume that integral wing tanks can use 85% of the volume measured to the external skin surface, and integral fuselage tanks can use 92%. When bladder tanks are used, the values for wing tanks and fuselage tanks increase to 77% and 83%, respectively [9].

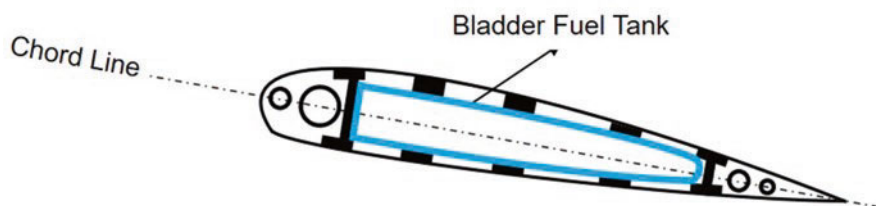


Fig. 8.6 Bladder fuel tank

Another important phenomenon inside the tank is slosh. As it was mentioned before, even the small movements of a free surface fluid in the chamber in which it is placed cause large-scale movements of that fluid. This phenomenon also occurs in land vehicles carrying liquid cargo [10]. The dynamic oscillation of the center of gravity of the fuel in the tank causes fluctuations in the fuel surface and the slosh effect in the tank. The most severe shaking is when the tank is half full [11]. The amplitude of the slosh depends heavily on the frequency, shape, and movement of the fluid in the tank [12]. During maneuvers of an aircraft, breakwaters called fuel slosh baffles are needed inside long horizontal fuel tanks [13].

The discrete tanks, wet wing, and bladder-type fuel systems are located inside the body and/or wing. Besides these tanks, there are some external ones such as drop tanks and conformal fuel tanks. External tanks are popular on modern military aircraft, and they can also be used in civilian aircraft. They are standard on modern military aircraft, and they are also sometimes found in commercial aircraft. The conformal fuel tanks are additional fuel tanks that are fitted tightly to the profile of an aircraft and extend the aircraft's range or endurance with a lower aerodynamic disadvantage than typical drop tanks.

Drop tanks were designed to be jettisoned when they were empty or in the event of a war or emergency to minimize drag and weight while increasing maneuverability and range. Drop tanks are usually disposable and easily discarded. Italian-made Blackshape Czechia-made Shark, Latvia-made Tarragon airplanes are famous for their bladder-type fuel tanks.

8.4 The Specifications of the Aircraft Fuel Tanks

Every system or component has its own specifications on an aircraft. In this section, the specifications of the aircraft fuel tanks will be described.

8.4.1 *The Safety Precautions of the Fuel Tanks*

Safety precautions have crucial importance in the fuel system. In general, all potential thermal hazards that could result in smoke and/or fire should be identified. The measurements including fuel system must be applied against hazards, at least but not limited to given as follows;

- Identification of all possible thermal hazards that may result in smoke and/or fire
- Uncontained rotor burst associated with APU and engines
- The effects of a fan blade out failure
- Flailing shaft
- Ram air turbine rotor burst
- Hydraulic accumulator burst

- Wheel and tire failure
- Fuel ignition risk
- Crashworthiness
- Tank overpressure
- Rapid decompression and aft pressure bulkhead rupture [14].

It is noteworthy that the majority of the mentioned hazards are more likely related to fuel and combustion systems.

8.4.2 *Crashworthiness Feature*

Amongst the precautions given above the crashworthiness is a vital feature for fuel tanks. This feature saves lives when applied to other aircraft systems. The capacity of an aircraft and its internal structures to shield passengers from injury in the event of a crash is known as crashworthiness. In general, injury in plane crashes is caused by three things:

- Extreme acceleration forces
- Direct damage from contact with injurious surfaces
- Exposure to environmental factors like fire, smoke, water, and chemicals, which can result in burns, drowning, or asphyxiation.

The capacity of the bladder material to bend to the severe contours needed in crashes resulting in significant structural distortions and breaks in the tank region is the real benefit of being able to withstand large strains. This capability, combined with resistance to tear propagation, would compensate for a significant loss in ultimate strength.

As a result, for a given design configuration, successful crashworthiness designs must consider all potential sources of injury and remove or minimize as many as possible. The crash-resistant fuel systems (CRFS) were introduced in 1970. Between 1970 and 1997 only fire-related death in a survivable crash was reported while 42% of fatal accidents had occurred with fire-related issues. In some studies, it was shown that the crashworthy fuel tanks had been found damage-free [15].

8.4.3 *Self-Sealing Feature*

If a traditional fuel tank is shot, it can easily leak fuel. This will not only limit the effective range of aircraft, but it will also pose a major fire threat. Damaged fuel tanks may also cause the tank to rupture, resulting in the glider's destruction or a significant change in in-flight characteristics. It was realized that adding armor to aircraft fuel tanks would be impractical due to weight constraints, so a method of preventing fuel leakage from damaged tanks was required. The first attempts to

secure the fuel tanks included the use of a metal container that was sealed on the inside or outside of the material and expanded when penetrated. The study found that the yield of the projectile, rather than a recording, was a major issue, as it is often tumbled, resulting in a wide escape hole.

The history of the self-sealing concept goes back to the Second World War era. The concept was created to prevent leakage and igniting after enemy fire damages aircraft fuel tanks or vessels. A standard tank installation, consisting of several layers of rubber and reinforcing fabric, one of vulcanized rubber and one of untreated natural rubber that can absorb fuel and swell and expand when in contact with it. Fuel spills into the layers when the fuel tank is punctured, allowing the raw layer to swell and seal the puncture. Self-sealing run-flat tires are also manufactured using a similar concept.

The role of self-sealing (bullet-sealing) composites for fuel tanks is based on three parameters:

1. The resulting puncture must be very thin.
2. After the projectile has passed, the lips of the self-sealing composite must remain in place or realign themselves so that they support each other.
3. The composite must have a fuel-sensitive layer that swells when contacted by fuel and seals the puncture, ideally across opposing lips.

Self-sealing tanks are used for the majority of jet fighters and rotary-wing aircraft. Crashworthiness is an additional characteristic of military rotary-wing fuel tanks. Since the tanks must be pressurized at such high altitudes, self-sealing is difficult. Advances in technology, such as inert foam-filled tanks to avoid detonation, have been made possible by newer technologies. This foam is an open-cell foam that divides the gas space above the remaining fuel into thousands of small spaces, none of which have enough vapor to support combustion. This foam also helps to keep fuel slosh to a minimum as will be explained in 4.3. On the military side, the self-sealing fuel tank is qualified to MIL-DTL-27422.

8.4.4 Anti-Slosh Feature

This foam material serves as an anti-slosh baffle and prevents or restricts flame and pressure wave propagation [16].

The liquid movement inside the tank is referred to as sloshing. Slosh dynamic direct on top of liquid will be determined by the liquid properties and compartment state. Limits may have an impact on the quality of a moving tank and reduce its effectiveness. Hydrodynamic load measurement in moving compartments involves two remarkable portions that are accomplished by the fluid moving at a high speed and increasing the tank speed [17]. The sloshing is usually caused by the container's motion, which is often affected by the sloshing itself (e.g., damping). In the open literature, it has been observed that many studies were examined to understand the behavior of the slosh phenomenon. The finite volume method (FVM) [18] was used

besides computational fluid dynamics (CFD) and experimental fluid dynamics (EFD) [19] to determine the principles of the slosh behavior. It is an unsteady, extremely nonlinear phenomenon that is difficult to explain in detail due to the various physics involved. As a result, some simplifications were made in both the physical and numerical models. At present, there are many fuel tank aviation-grade sponges in the market. The fuel-resistant foam establishment is illustrated in Fig. 8.7. The manmade baffles are illustrated in Fig. 8.7(a) and natural baffles of porous foam are shown Fig. 8.7(b).

The transverse baffles, a commonly used anti-slosh system, on the other hand, appear to suppress fluid slosh in the vertical vector. To be a slosh dynamics problem, the liquid must have a free surface where the liquid's dynamics can interfere with the container and dramatically alter the system dynamics. National Aeronautics and Space Administration (NASA) made some research for minimizing the slosh effect also because slosh in microgravity is important for spacecraft, particularly Earth-orbiting satellites since liquid surface tension can change the shape of the liquid slug. A significant portion of a satellite's mass is typically liquid propellant, and slosh can negatively impact satellite output in a variety of ways [20].

Other than the aircraft and aerospace industry sloshing is a problem that must be prevented for land vehicles also. Liquid sloshing has a significant negative impact on the directional dynamics and safety performance of highway tank vehicles [21].

8.4.5 Freeform Feature

When a surface shape has no continuous translational or rotational symmetry around axes, it is called freeform. The category of complex invariant surfaces includes freeform surfaces. The geometry of freeform surfaces is difficult to explain with a single universal equation, and it has a significant impact on a product's results. The industry defines many types of surfaces as freeform, such as off-centered rotational optics, toroidal, and so on. These are not true freeform surfaces mathematically, but they do have an axis that does not move through the functional surface. What follows applies to these quasi-freeform surfaces as well [22].

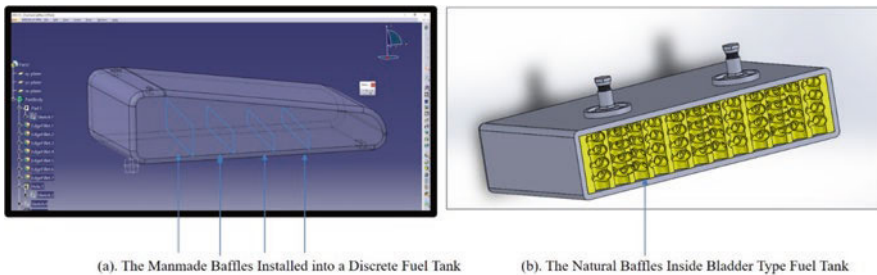


Fig. 8.7 Fuel-resistant foam works as baffle

While manufacturing the bladder-type fuel tanks, the shape has few limitations, with even the tiniest detail and most complex geometry is possible to produce. This helps the bladder tanks to fit into tight spaces and match the shape of any containment of the aircraft perfectly. In this manner, the bladder tanks are known as freeform.

8.4.6 Collapsibility/Foldability Feature

A collapsible fuel tank, with rigid top and bottom elements and foldable sidewalls. When fluid is pumped into the bladder, the top, bottom, and side walls expand, forming its original structure with solid walls to protect the bladder. Withdrawing fluid from the bladder allows it to compress, causing the walls to fold and the tank to collapse into a more compact size.

The collapsible tank lies fully flat when empty and is often rolled or folded for transportation. These tanks can be folded down to less than 5% of their total capacity. The tank may be mounted on an aircraft's fuel cell bay, and when the tank fills with the fuel it gains its original shape [23].

8.4.7 Lightweight Feature

“Lightweight part manufacturing” is a widely researched and applied concept in a variety of industries, especially in aerospace applications, and is linked to the green aviation concept. As a result of aviation's exposure to global warming and pollution, ongoing attempts to reduce aviation emissions have been made. Rising energy efficiency is one strategy for achieving this goal. While metal materials, especially aluminum alloys, remain the most common in aerospace applications, composite materials are gaining popularity and competing with aluminum alloys in a growing number of new aircraft applications.

The main structure which is a compound of carbon fiber fabric and polyurethane sealant makes the bladder-type fuel tanks remarkably lighter compared with the steel and/or aluminum fuel tanks. The lightweight structure also contributes to the bladder tank's reputation in terms of fuel saving.

8.5 Manufacturing Process of Bladder-Type Aircraft Fuel Tank

The manufacturing steps of an ultralight airplane's bladder-type fuel tank will be submitted in this chapter. A model is prepared according to the volume where the fuel tank will be placed. In this case study, an "L" shaped bladder fuel tank to be placed in the back of the rear cockpit in a tandem aircraft is considered. For the production of walls (Skin), carbon fiber material and polyurethane sealant are cured together. Inside the bladder fuel tanks, instead of baffles, porous filling material (Foam) with each tiny chamber acting as a natural baffle is used. The mentioned filling material completely fills the volume of the fuel tank. For this reason, by reducing the size of the fuel tank as much as the wall thickness—by offsetting inward—the geometry of the filling material is revealed. This method was used for the fuel cells installed in ultralight airplanes such as the T19A aircraft shown in Fig. 8.8.

Carbon fiber hand layup is a method commonly used in composite part production. Generally, the polymer material used provides compressive strength and carbon fiber provides tensile strength.

Before starting the production, the environment should be prepared per Occupational Health and Safety (OHS) regulations. The Material Requirement List (MRL) gives information about the parts, consumables, tools & devices, and test equipment necessary for the production of an ultra-light airplane's bladder-type fuel tank.



Fig. 8.8 T19A aircraft contains bladder-type fuel tank

8.5.1 *Material Requirement List—MRL*

MRL is an important preparation step for manufacturing the bladder-type aircraft fuel tank. In the following sections, the items for MRL will be provided.

Materials

Carbon fiber twill fabric:

The thickness and density may change depending on the customer requirements.

However, the minimum thickness between 0.4 and 0.6 mm and the density of 1.8 g/cm³ recommended

Matrix material/polyurethane sealant:

A fuel-resistant-type polyurethane sealant may be used for bonding. With using this material, elasticity is maintained indefinitely to enable joint movement. It has also UV resistance. It is a moisture-curing sealant, a single component that simplifies the application.

Fuel drain component:

This is a bent pipe and flanged parts designed by the engineers in terms of draining the excessive fuel. In general, the Aluminum alloys such as 2024, 7075 may be preferred.

Fuel filling component:

This flanged part is a manufactured part per the requirements fitting the area inside the wings or fuselage. In general, a threaded flange part is attached to the appropriate area of the skin.

Fuel indicating system:

The fuel quantity and fuel flow are crucial information for pilots. The fuel indicating system may be provided as a commercial-off-the-shelf (COTS) item.

Fuel tank cell foam (polyurethane):

It is the most useful system to prevent slosh. It helps reduce the surge originated from slosh creating a baffling effect. Upon receiving a sudden impact during maneuvers, the foam inside the fuel tank helps dissipate and absorb a great amount of energy of the impact, therefore reduce the risk of fuel tank rupture.

Gelcoat:

This is a flame retardant-filled resin used to protect the tank from the outside effects.

It has a special filler combination and will not drip down from vertical surfaces because of its viscosity. After the bladder tank is produced this resin should be applied to the outside of the tank.

Solvent:

Although the aircraft parts are generally manufactured in the controlled shops sometimes the raw materials require an additional cleaning process. This chemical is used for cleaning the fabric, during the raw material preparation phase.

Note: In any steps of the manufacturing, the staff should follow the information in the Material Safety Data Sheet (MSDS) and other safety documents of Occupational Health & Safety regulations.

Consumables

Wax:

It is a multipurpose wax generally used for polishing in the automotive industry.

Before spreading the fabric it is applied beneath the twill allowing easy removal.

Wooden spatula:

The wooden spatulas for spreading the polyurethane sealant. During the hand layout manufacturing process, splinterless manufacturing is an important issue for maintaining material homogeneity. The spatulas, preferably, manufactured from birch tree is recommended.

Cleaning cloth:

There is a huge variety of wipes for use throughout the manufacturing shop. Cotton (including organic cotton), ramie, silk, esparto fibers, synthetic blends, cotton blends and polyester, and microfiber are among the fibers available. Polyester clothes often confirm that it is right not to scratch any material on the surface you have to clean in the shop.

Glove (Nitrile):

This consumable is as sensitive and protective as it can be for bladder tank shop applications.

Tools and Devices

Cutting templates (cardboard, wood, or aluminum—depend on the number of productions)

Shoes (ethylene vinyl acetate)

Wet mop (for maintaining the shop floor industry)

Work suit (polyester reinforced with carbon threads)

Shop workbench (ideally, with a tempered 1 cm flat glass)

Electrical heater (2400 W infrared)

Clamps (for keeping the fabric stretched)

The gauges (ruler, miter, compasses, etc.)

Vacuum cleaner

Test Equipment

Vacuum pump (17.0 m³/h – 283 lt/min, 1HP)

Tub for leakage test (diameter: 166 cm, depth: 44 cm, 450 lt)

Digital scale (measuring capacity between 1 and 200 kg)

8.5.2 *Manufacturing Steps of an Ultra/Light Aircraft Bladder Fuel Tank*

In Tables 8.2, 8.3, 8.4, 8.5, 8.6, and 8.7, the manufacturing steps of a U/L aircraft bladder fuel tank will be submitted in the Work Control Document (WCD) format. All the manufacturing operations should be performed by certified and experienced personnel. In general, the certification process is made by the Country/National Airworthiness Authority (CAA/NAA) in accordance with the Product Organization Approval (POA-Part 21 G) regulations.

Test and Control Procedures

Per, British Civil Airworthiness Authority (BCAA), CAP 482 Section S—Small Light Aeroplanes Requirements the test steps are given below for the airplanes that have Maximum TakeOff Weight (MTOW) below 472.5 kg and experimental category. In general, the tests for leakage, pressure, and G-force are given as follows per the CAP 482 document.

- All components and equipment on the manufactured aircraft must withstand a minimum force of +9 g, –4.5 g, and 3 g on the horizontal axis,
- In the event of fuel slosh in the tank, the aircraft must be equipped to prevent the displacement of the center of gravity and to maintain the flight within the limit under safe conditions,
- Each fuel tank should withstand 1.5 psi pressure without causing any leakage or disruption [24].

Finally, high-end fuel bladders are constructed from elastomer-coated (polyurethane sealant) fabrics that are vulcanized in a single process. Mechanical resistance is ensured by the fabrics. The water tightness is provided by coating and construction engineering.

Table 8.2 The steps of the preparation of the manufacturing environment

Step	Task
10	Before starting the production, make sure the cleanroom requirements are met
20	Be sure that protective equipment such as a suit, gloves, mask, bonnets are worn in accordance with the cleanroom conditions
30	Clean all materials to be used with a nonwoven polyester cleaning cloth and a wet mop
40	Prepare the cutting template, in accordance with the exploded view of the parts to be manufactured. The material can vary per mass production number
50	Make sure the flatness of the table is at the right angle

Table 8.3 Manufacturing process of the first layer

Step	Task
10	Spread the wax on the production table
20	Wait until the wax is cured
30	Apply the solvent to the fabric to assure the fabric is cleaned
40	Wait until the solvent-applied fabric is cured
50	To make the first layer, lay the cured solvent-based fabric on the cured wax to 0° with the x-axis by hand laying
60	Fix the first layer with clamps
70	Mark the fabric according to the cutting template
80	Pour the polyurethane sealant until it exceeds the border of the marked area at least 2 cm
90	Spread polyurethane sealant until a homogenous thickness is gained
100	Switch on the heater for curing the first layer of polyurethane sealant and fabric. (Follow the instructions of the polyurethane sealant for temperature level and duration)
110	As the polyurethane sealant applied fabric is cured, switch off the heater
120	Carefully cut the polyurethane sealant applied fabric following the marked area border. (Be sure that the remained particles are cleaned promptly using a vacuum cleaner)
130	Remove the fabric meticulously
140	Clean the wax driven on the table

Table 8.4 Manufacturing process of the second layer

Step	Task
10	Spread the wax on the production table
20	Wait until the wax is cured
30	Reverse the polyurethane sealant applied fabric
40	Apply solvent to the second layer. (Do not apply solvent to the first layer)
50	Lay the cured solvent-based fabric on the cured wax to 0° with the x-axis
60	Fix the polyurethane sealant applied fabric with clamps
70	Pour the polyurethane sealant until it covers the whole surface
80	Spread polyurethane sealant until a homogenous thickness is gained
90	Before the polyurethane sealant is cured, lay the second fabric on the first layer
100	Switch on the heater for curing the first layer of polyurethane sealant and fabric. (Follow the instructions of the polyurethane sealant for temperature level and duration)
110	As the polyurethane sealant applied fabric is cured, switch off the heater
120	Control the layers are strongly bonded to each other

Note: Depending on the thickness requirement, the third or the fourth layers can be added

Table 8.5 Foam preparation

Step	Task
10	Cut the foam to fill inside the fuel tank volume tightly
20	Wrap the polyurethane sealant applied fabrics around the cut foam
30	Depending on the shape cut the flange holes for fuel-fill, fuel-supply, and fuel-drain lines/ pipes
40	For the corners and open edges apply the patches that are manufactured in the steps of the “Manufacturing first layer” section

Table 8.6 Fuel fill, drain line, supply line preparation, and fuel quantity

Step	Task
10	Mount the manufactured flanges inside and outside of the fuel-fill line, fuel-drain line, and fuel supply lines at the cut locations as illustrated in Fig. 8.9
20	For reinforcement of the flanged areas apply the polyurethane sealant with the reinforcement fabric as shown in Fig. 8.10
30	Insert the fuel quantity gauge mechanism before the fuel-drain line is closed

Table 8.7 Post-process steps

Step	Task
10	When the manufacturing process is completed, apply gelcoat to the entire outer surface and wait for it to cure.
20	Perform the load test, leakage test, and pressure test after the part manufacturing is completed.

8.6 Maintenance, Repair, and Overhaul (MRO) of the Bladder-Type Fuel

In general, during the MRO operations maintenance, repair, renewal, and testing are carried out to keep the aircraft at a fit-to-fly level. The aircraft itself and its components are subjected to MRO operations depending on the manufacturer’s relevant documents and in the certified service centers. The MRO operations are critical and they should be done in the proper time periods. The competition in the aviation industry is fierce hence the airlines take into account even cent-level costs. Maintenance and fuel consumptions are always the top drivers. As it is seen in Fig. 8.11, the fuel and maintenance costs have a direct impact on the direct operational cost (DOC) [25].

That’s why the aircraft manufacturing companies developed a novel system for increasing fuel efficiency and contrarily decreasing the DOC. For example; Airbus is concentrating on intelligent computing technologies for aircraft operations, including fuel efficiency, maintenance capabilities, and aircraft operational optimization [26].

To ensure that all aircraft are airworthy and safe to fly, they must be inspected and maintained on a regular basis. Any of the maintenance is planned ahead of time

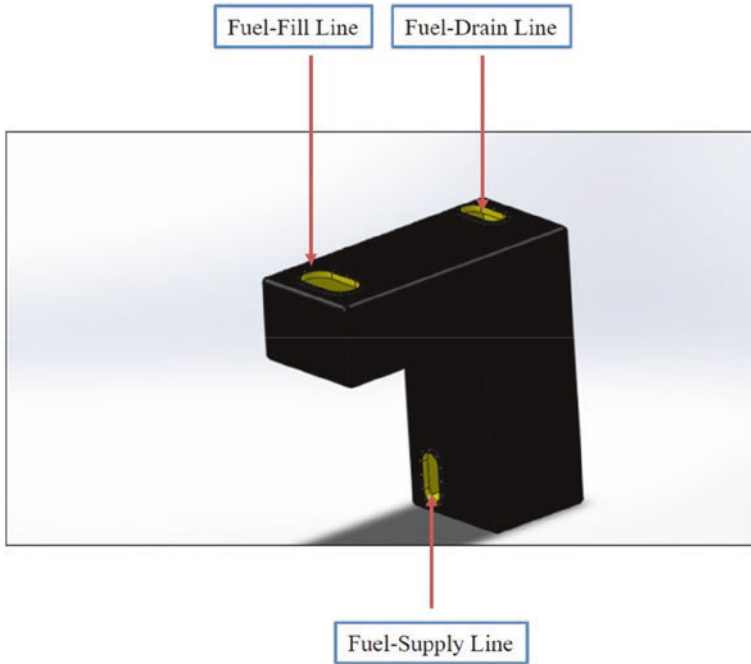


Fig. 8.9 Fuel-fill line, fuel-drain line, and fuel supply lines of an “L-shaped” bladder-type aircraft fuel tank

and is acknowledged to both the pilot and the aircraft technician. Other forms of maintenance are unexpected and unscheduled, which can be caused by problems discovered by the pilot or by an inspection performed by the aircraft maintenance personnel (AMP). It’s important for pilots and aircraft owners to consider the difference between scheduled and unscheduled aircraft maintenance.

8.6.1 *Unscheduled Maintenance Operations*

The unscheduled/planned maintenance operations, which usually result from condition-based maintenance inspections, have major consequences for spare parts inventory management, resource planning, and maintenance task execution. Unscheduled aircraft maintenance arises when a part fails or is suspected of failing, and this maintenance is unexpected by definition. It can happen after the pilot discovers a defect during the preflight inspection, as a result of an in-flight malfunction, or as a result of defects discovered during a flight-hour (FH) based (50 FH, 100 FH, 600 FH, etc.), annual, or progressive inspections.

A worn bladder fuel tank skin, a low landing gear strut, or a sheared vacuum pump are all examples of unscheduled maintenance. They are generally in-flight or

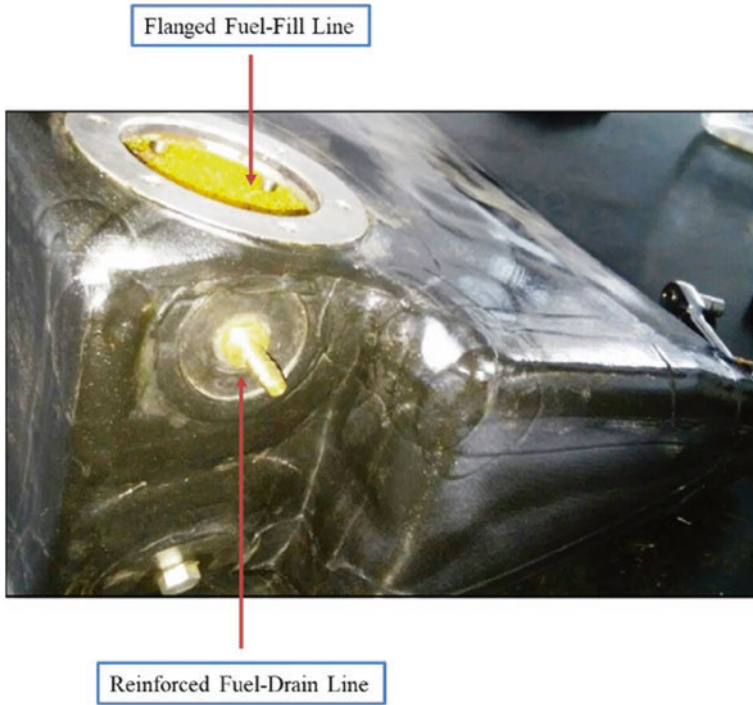


Fig. 8.10 Reinforcement of flanged areas

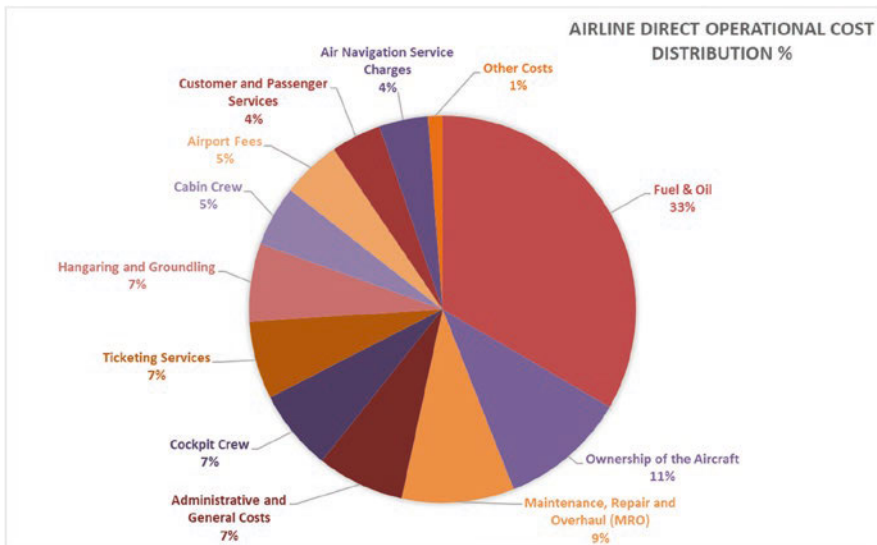


Fig. 8.11 Direct operational cost (DOC) of airlines

ground test issues like a rough running engine or a high magneto drop during engine-start-up. When the issue is discovered, the pilot would notify the relevant technician and submit a repair order. The plane would be grounded at this stage until the problems were fixed and the technician found the plane safe to fly.

8.6.2 Scheduled Maintenance Operations

Every pilot is needed to conduct various preflight tests to ensure that the aircraft is ready to fly and that no defects or malfunctions are present. When performing a preflight inspection, a pilot or student pilot must use a checklist to ensure that nothing is missed. Preflight inspections include walking around the planes and checking all major fuselage and flight control surfaces for irregularities, wear and tear, and other abnormalities that could jeopardize flight safety.

Generally, the scheduled/planned maintenance is handled in four main categories. These are A, B, C, and D levels. Although many operations in B level maintenance from these categories are transferred to A and C level, it is known that there are three different levels although four different categories. Scheduled repairs, such as inspections of different system parts, as well as structural changes and alternations, are also part of heavy maintenance, which refers to a significant redesign of aircraft structures. An aircraft is briefly taken out of revenue service during heavy maintenance, and the elapsed period is viewed as downtime. Due to the size and complexity of a significant overhaul of an aircraft, heavy maintenance is the most difficult of all maintenance categories.

8.6.3 MRO Operations of Bladder Fuel Tanks

Either unscheduled or scheduled bladder fuel tanks begin degradation, within the moment fuel is added for the first time. The additives in aviation and automotive fuels contain volatile chemicals that leach out the polymers in rubber or urethane. This degradation, which itself may take 50 or more years to render the bladder unusable, accelerates when the tanks have less than full fuel or if the aircraft is outdoors in hot, dry climates. Aftermarket additives may further degrade the bladder material.

Since the surface of the cell, which is subjected to the sun's heat and dryness as fuel is consumed, loses elasticity, hardens, and cracks, sloughing off chunks of material. Fuel back-shop staff agrees, stating that most cells fail at the top outboard leading edge, which is the most frequently dry spot. Though leaks are a concern, fuel depletion caused by particles clogging the system is also a bigger concern. Repair shop staff unanimously agree that high-octane gasoline, such as 95 octanes, causes problems with bladder fuel tanks, especially if the fuel contains alcohol. This will eliminate the use of ethanol in bladders, whether aviation-grade or otherwise.

Long-term exposure to alcohol, in any form, is a drying agent that causes premature embrittlement in rubber-based bladders.

It is worth noting that, All the MRO operations should be performed by certified and experienced personnel. In general, the certification process is made by CAA/NAA in accordance with the Maintenance Organization Approval (MOA-Part 145) regulations.

Visual Control

Fuel dripping on the bottom of the plane, accompanied by a strong odor, is normally the first sign of a leak. It should be kept in mind that the fuel sometimes travels a long distance before reaching an exit point, the source of the leak might be away from the suspected area. In general, it can be difficult to pinpoint the source of the leak as a result of fuel travel. To put it another way, the leaking Bladder fuel tank may be far away from the apparent leak. Until removing a suspected leaker, the leak route should be followed.

Removal Operations

Before removing the cell, the potential source of the leak or leaks should be thoroughly investigated. Any stains or fuel can be traced back to their original source in the wing or fuselage cavity. Leaks often do not occur near where the leak is most apparent externally due to the impact gravity has on fluid flow.

The other components of the fuel system, apart from maybe the bladder fuel tank, will leak. Leaks should be tested in the connections, hoses, and vent areas. It's also worth noting that just because a fuel tank is leaking doesn't mean it has to be replaced. On a fuel cell, there are some leaks that can be repaired. Loose hose clamps, transmitter screws, or other fasteners, broken gaskets, loose plate or filler neck bolts, and/or cracks in the filler neck or tubing may all cause leaks. The following steps should be performed during removal operations;

- The technical information should be examined: The technical data on MRO operations provided by the manufacturer should be carefully followed.
- The rough metal edges of maintenance access doors should be taped to avoid damage to the bladder fuel tank and the hands of maintenance workers.
- Let the rubber relax by loosening the clamps: The bladder fuel tank could have been on the plane for a long time, and the rubber under the clamps has hardened. Allow the tank to sit for a few minutes after loosening the clamps to allow the rubber to relax and make removal easier.
- Vacuum the tank: Since the bladder fuel tanks are collapsible, vacuuming the inside will make the removal process easier.

After the tank is removed, the bladder fuel tank bay should be inspected against foreign object damage (FOD). All FOD's should be removed, especially metal shavings, which can quickly harm a newly installed fuel cell.

Back-Shop Inspection

A test bench recommended by the manufacturer should be used for back-shop inspection. During diagnosis, pressure may be helpful to find the location of the leakage. The tank vent port, fuel drain pipe, and fuel transfer pipes on the aircraft must be sealed off during the fuel leak test to prevent air from venting outside the tank. To detect any leakage, the fuel tank is pressurized with dry air up to 20.3 psi [27].

A white cotton sheet soaked in ammonia Phenethylamine is wrapped around the cell in the final examination. The cell is filled with nearly pure alcohol, and any escaping vapors leave remarkable red spots on the board.

Repair Operations

Depending on the damaged region of the bladder fuel tank assembly, regional patches may be applied following the manufacturer company's Component Maintenance Manual (CMM) and/or Structural Maintenance Manual (SRM). If the leakage is originated from the accessories such as pipes, fasteners, clamps, flanges AMM/SRM's should be referred for performing the required repair operations. In case of a hole occurrence on the skin of the bladder, the patches advised by the manufacturer may be used. It must be kept in mind that, the repaired/patched areas will require more frequent inspections than before.

In terms of quick troubleshooting, the polyurethane spray seal (Brush-Up) method was also used albeit it is not effective for a long-term period.

Curing time depends on the manuals. However, an adequate leak check is necessary after repair or patching.

Failure to properly mount the cell will result in damage to the fuel tank or the aircraft, as well as potential leaks. The bladder fuel tank should be stored in a warm storage room or office until ready to mount if the back shop and hangar are cold. Installing the tank into the bay could be easier with the vacuum. The fuel tank would quickly slide into the cavity after being vacuumed. As the vacuum pump is removed after installation, the tank will revert to its original shape in the bay.

Following the clamping operations, the fuel-fill, fuel-drain, and fuel-supply lines should be linked according to the AMM and CMM documents. After a final visual inspection for FOD or suspicious results, the maintenance/access doors can be locked. The needed fuel can then be filled at a slower rate than during normal service.

It's worth noting that a leak check is recommended before the air vehicle is put back into operation. Although the leak check varies depending on the bladder brand, at least 8 h of on-wing monitoring is recommended.

8.7 Conclusions

The bladder fuel tanks are widely used in the aviation industry. When opposed to hard steel or plastic tanks, bladders are lightweight and portable, making them suitable for remote areas. The ability to transport and set up a portable storage system like fuel bladders has many advantages. The followings are the features of the bladder-type aircraft fuel tanks;

- Minimize the slosh effect thanks to its porous filling material
- A free-form structure that allows the unused space inside the aircraft to be used as a fuel tank
- Easy to assemble and disassemble
- Easy to MRO (Maintain, repair, and overhaul) operations
- Relatively, low maintenance cost
- Resistant to saltwater as it is produced with composite production technology
- Production processes are mature
- For post-production testing processes, no special test equipment is needed.

It is noteworthy that, with their overwhelming features the bladder-type fuel tanks will be used more widely in the aviation industry. In addition to the aviation industry, marine, subsea, automotive sectors are the strong industries for hosting the bladder fuel tanks. With the development of carbon fiber fabric, fuel-resistant soft resins, filling materials, and other fuel tank accessories, more durable bladder-type aircraft fuel tanks will be manufactured in the future. Finally, it can be easily claimed that the bladder-type fuel tanks will be more popular in industries including, aviation, aerospace, marine, and automotive in the future.

References

1. Purton, L., & Kourousis, K. (2014). Military airworthiness management frameworks: A critical review. *Procedia Engineering*, 80, 545–564. <https://doi.org/10.1016/j.proeng.2014.09.111>
2. Merzvinckas, M., Brighenti, C., Tomita, J., & De Andrade, C. R. (2020). Air conditioning systems for aeronautical applications: A review. *The Aeronautical Journal*, 124(1274), 499–532. <https://doi.org/10.1017/aer.2019.159>
3. Balli, O. (2020). Failure analysis of inlet guide vane (IGV) actuator and bellcrank assembly used on J85 turbojet engines. *Engineering Failure Analysis*, 115, 1–6. <https://doi.org/10.1016/j.engfailanal.2020.104700>
4. Smith, H. (1974). Crash-resistant fuel tanks for helicopters and general aviation aircraft. *SAE Transactions*, 83, 1549–1564. Retrieved March 27, 2021, from <http://www.jstor.org/stable/44734461>.
5. Gudmundsson, S. (2014). *General aviation aircraft design: Applied methods and procedures* (Vol. 145). Butterworth-Heinemann of Elsevier. <https://doi.org/10.1016/B978-0-12-397308-5.00001-5>
6. Pinheiro, N. R., & Góes, L. S. (2017). Modeling and simulation of a single engine aircraft fuel system. In *The 15th Scandinavian International Conference on Fluid Power, SICFP'17*, June 7–9, 2017, Linköping, Sweden.

7. Federal Aviation Administration (FAA). (2004). *Airplane flying handbook: FAA-H-8083-3B, Chapter 17: Emergency procedures*. Retrieved April 5, 2021, from https://www.faa.gov/regulations_policies/handbooks_manuals/aviation/airplane_handbook/media/19_afh_ch17.pdf.
8. Goraj, Z., & Zakrzewski, P. (2005). Aircraft fuel systems and their influence on stability margin. *Transactions of the Institute of Aviation*, 183, 29–40.
9. Raymer, D. P. (1989). *Aircraft design: A conceptual approach*. American Institute of Aeronautics and Astronautics.
10. Kandasamy, T., Rakheja, S., & Ahmed, A. K. W. (2010). An analysis of baffles designs for limiting fluid slosh in partly filled tank trucks. *Open Transportation Journal*, 4, 23–32.
11. Stengel, R. (2016). *Aeroelasticity and Fuel Slosh, Lecture notes*. Retrieved April 5, 2021, from <https://www.princeton.edu/~stengel/MAE331Lecture21.pdf>.
12. Shreeharsha, H. V., Shivakumar, S. G., & Mallikarjun, S. G. (2017). Simulation of sloshing in rigid rectangular tank and a typical aircraft drop tank. *Journal of Aeronautics & Aerospace Engineering*, 6(1), 1–9. <https://doi.org/10.4172/2168-9792.1000186>
13. Federal Aviation Administration (FAA). (2004). *Airplane flying handbook: FAA-H-8083-3B, Chapter 14: Aircraft fuel systems*. Retrieved April 5, 2021, from https://www.faa.gov/regulations_policies/handbooks_manuals/aviation/airplane_handbook/media/19_afh_ch17.pdf.
14. Langton, R., Clark, C., Hewitt, M., & Richards, L. (2010). Aircraft fuel systems. In R. Blockley & W. Shyy (Eds.), *Encyclopedia of aerospace engineering*. Wiley. <https://doi.org/10.1002/9780470686652.eae463>
15. Shanahan, D. F.. (2004, October 28–29). *Pathological aspects and associated biodynamics in aircraft accident investigation*, Basic Principles of Crashworthiness, Madrid, Spain.
16. Advisory Group for Aerospace Research and Development (AGARD). (1990). Fuel Tank Technology, AGARD Report No: 77.
17. Rohini, D. Abinaya, R., Lokesharun, D., Karthik, K., Sovishnuchringth, V., & Sivaprakash, P. (2020). IOP Conf. Ser.: Mater. Sci. Eng. 995 012044.
18. Jäger, M. (2019). *Fuel tank sloshing simulation using the finite volume method*. Springer, Germany. ISBN 978-3-658-25227-4. <https://doi.org/10.1007/978-3-658-25228-1>.
19. Frosina, E., Senatore, A., Andreozzi, A., Marinaro, G., Buono, D., Bianco, G., & Giliberti, P. (2017). Study of the sloshing in a fuel tank using CFD and EFD approaches. In *ASME/BATH 2017 symposium on fluid power and motion control*. <https://doi.org/10.1115/fpmc2017-4337>.
20. Dasgupta, A. (2011). *Effect of tank cross-section and longitudinal baffles on transient liquid slosh in partly-filled road tankers*. M.Sc. Thesis, Concordia University.
21. Kolaei, A., Rakheja, S., & Richard, M. J. (2016). An efficient methodology for simulating roll dynamics of a tank vehicle coupled with transient fluid slosh. *Journal of Vibration and Control*, 23(19), 3216–3232. <https://doi.org/10.1177/1077546315627565>
22. Chatti, S., Laperrière, L., Reinhart, G., & Tolio, T. (2019). *CIRP encyclopedia of production engineering*. <https://doi.org/10.1007/978-3-662-53120-4>.
23. Walter, R., Burhans, Jr., Ciccarello, J. L., & Stumpf, C. H. (1980). *Aircraft collapsible fuel tank*, US Patent Office.
24. British Civil Airworthiness Authority (BCAA). CAP 482 Section S—Small Light Aeroplanes Requirements.
25. Saraçyakupoğlu, T. (2019). The qualification of the additively manufactured parts in the aviation industry. *American Journal of Aerospace Engineering*, 6(1), 1–10. <https://doi.org/10.11648/j.ajae.20190601.11>
26. Valdés, R. A., Comendador, V. F. G., Sanz, A. R., & Castán, J. P. (2018). Aviation 4.0: More safety through automation and digitization. In M. Kushan (Ed.), *Aircraft technology*. IntechOpen, ISBN: 978-1-78923-645-3.
27. Behbahani-Pour, M. J., & Radice, G. (2016). Fuel leak detection on large transport airplanes. *Journal of Aeronautics & Aerospace Engineering*, 5, 174. <https://doi.org/10.4172/2168-9792.1000174>

Chapter 9

Structural Health Monitoring Method for In Situ Inspection of Landing Gears



Gökhan Haydarlar, Mesut Tekkalmaz, and Mehmet Alper Sofuoğlu

Nomenclature

CC	Correlation coefficient
CCDM	Correlation coefficient deviation metric
d	Piezoelectric charge constant [10^{-12} C/N]
E	Modulus of elasticity [GPa]
EMI	Electromechanical impedance
G	Shear modulus [GPa]
MAPD	Mean absolute percent deviation
PWAS	Piezoelectric wafer active sensor
PZT	Lead zirconate titanate
Q_m	Mechanical quality factor
RMSD	Root mean square deviation
SHM	Structural health monitoring
s	Elastic compliance coefficient [10^{-12} m ² /N]
T	Temperature [°C]
w	Angular velocity [Hz]
α	Coefficient of thermal expansion [1/K]
β	Stiffness multiplication factor
ν	Poisson's ratio
ϵ	Dielectric constant [10^{-12} F/m]
ρ	Density [kg/m ³]

G. Haydarlar (✉) · M. Tekkalmaz · M. A. Sofuoğlu
Department of Mechanical Engineering, Eskişehir Osmangazi University, Eskişehir, Turkey
e-mail: ghaydarlar@ogu.edu.tr

9.1 Introduction

Structural health monitoring (SHM) is a technique in which specific strategies are used to determine the location and size of the damage. With SHM, the response of the structural system is measured under different conditions. SHM is often used to monitor and assess structure or components' condition due to the damage and abnormalities [1]. Damage detection is the primary objective of SHM.

SHM observes the system's dynamic response with sensors' aid at regular intervals and determines the current state of operation using statistical analyzes. In the long term, outputs of this process are updated to provide information on the structure's predefined functions. SHM is used for rapid status scanning and aims to provide reliable information about the structure's integrity in real time [2].

The electromechanical impedance (EMI) technique is a new method of SHM. In this technique, the piezoelectric ceramic (PZT) sensor patch is embedded or attached to the structure via a high-strength epoxy adhesive. The conductance characteristic of the patch is obtained in the high-frequency range (30–400 kHz). This characteristic is a reference in assessing structural health. When it is desired to evaluate the health of the structure, the conductance characteristic is reacquired and compared with the reference conductance characteristic. The bonded/embedded PZT patch's conductance characteristic is obtained using a commercially available impedance analyzer. The impedance analyzer implements an alternating voltage signal of 0.5/1 V to the bonded/embedded PZT transducer over a predetermined frequency [3].

Hooker [4] investigated the change of the piezoelectric charge constants (d_{31} and d_{33}) of piezoelectric ceramics PZT 4, PZT 5A, PZT 5H between -150 °C and 250 °C and the relative thermal expansion between 25 °C and 600 °C. Sherrit et al. [5] determined the elastic, dielectric, and piezoelectric charge constants of PZT 4D ceramics at temperatures ranging from 0 °C to 100 °C. From these obtained data, they derived a function by the curve fitting method. Wolf and Trolier-McKinstry [6] performed measurements with lead zirconate titanate (PZT) thin films for the thicknesses of 2, 4, 6 μm between -55 °C and 85 °C to obtain an effective piezoelectric coefficient (40/60, 52/48, 60/40 Zr/Ti ratios). They found that films exhibited smaller dielectric, ferroelectric, and piezoelectric properties compared to other ceramic analogs. The effective piezoelectric coefficient increased with increasing temperature and the highest temperature-dependent 6 μm film was observed. Yang et al. [7] investigated temperature and adhesive thickness effects on conductance signatures. They concluded that the effect of the adhesive layer can be neglected up to two-thirds of the thickness of the PZT patch. The imaginary part of admittance at varying temperatures was studied by Grisso and Inman [8]. Siebel and Lilov [9] studied the damaged state and temperature effect using maximum correlation coefficient (CC) for changing temperature (-50 to 100 °C). Baptista et al. [10] investigated the temperature effect on EMI signals. They suggested a narrow frequency band for temperature compensation. Bukhari et al. [11] studied the parameters of the piezoelectric charge coefficient d_{15} for different ceramics (PZT, LiNbO_3 , PMN-PT) at cryogenic temperatures (between 0 K and 300 K). By introducing

harmonic signals at various frequencies, Zou et al. [12] studied the amplitude of the signals detected at different temperature. Xu et al. [13] provided a method of spectral elements to estimate admittance by considering the effect of temperature. Wandowski et al. [14] investigated the temperature effects on resistance signals using carbon fiber reinforced polymers for damaged and undamaged states. At different temperatures, Haider et al. [15] researched the material properties of the circular piezoelectric sensor. Fallahian et al. [16] introduced a new technique to identify the location in different structures via a time-domain response/optimization method. Rezvani et al. [17] investigated four simple techniques to determine the damages in structures with frequency response functions (FRF) signals, principal component analysis technique (PCA), and transmissibility.

The strength of structures decreases because of the effect of continuous loading. Because of the strength reduction, it should be assessed whether the performance of the structure is sufficient. If the structural strength falls below a certain threshold level, a sudden failure will occur, which can cause an accident. It is essential to detect the change in the structure's early stages. If the structure's change cannot be determined promptly, it can lead to severe consequences for the structure's safety. If the structures are monitored regularly or continuously, the behavior of the structures can be observed. This will contribute to design improvement studies [3].

Components in landing gears are subjected to sudden heavy loadings during takeoff and landing, in addition to various conditions such as wear, fatigue, and foreign object damage. In the current procedure, landing gears are inspected after flights and in case of damaged evidence, components are removed from the aircraft. However, in situ monitoring enables instant inspection of in-service components. In this work, the EMI method is proposed to check landing gears in service. For this purpose, a piezoelectric sensor was attached to a steel specimen to obtain the material's high-frequency response. Since aircraft are subjected to a wide subzero temperature range in cruise, the tests were conducted within a range from $-10\text{ }^{\circ}\text{C}$ to $-45\text{ }^{\circ}\text{C}$. The method was simulated by using a numerical model. After the experimental and numerical studies, the temperature effect was compensated by using three damage metrics. The genetic algorithm was used to solve the compensation algorithm.

9.2 Experimental and Numerical Method

9.2.1 *Experimental Method*

A steel block used in torque links of landing gears was used in the tests. The impedance tests were recorded using a Keysight E4990A impedance analyzer at room temperature. The measurements focused on the real part of the impedance as the real part of the impedance reflects the sensor-added sample's vibration spectrum. Using ARTICO LFE140 laboratory freezer, impedance tests of the sample were

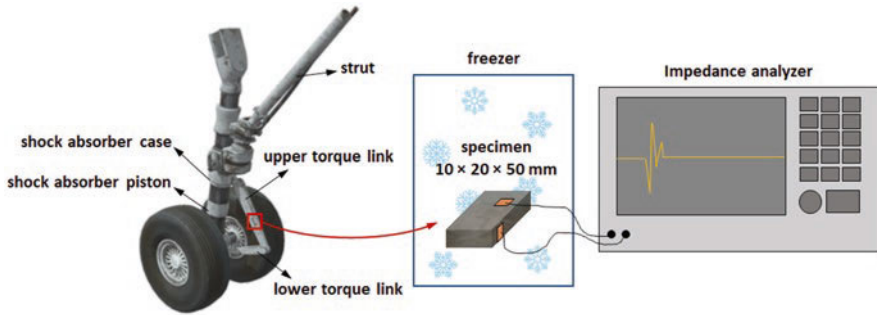


Fig. 9.1 Testing procedure

carried out at various temperatures (-10 to -45 °C at 5 °C intervals). After the experimental measurements, the real part of the impedance change was discussed using the temperature compensating algorithms. A piezoelectric sensor ($10 \times 10 \times 0.5$ mm) was attached to the host structure using M-Bond 200 adhesive. The measurements of the real part of the sample impedance at room temperature were carried out in 1000 steps in the frequency range from 2 to 80 kHz after the probes were attached. Figure 9.1 shows the schematic of the testing procedure.

9.2.2 Numerical Method

For PWAS, there are eight-node points, and the SOLID5 element with 6 degrees of freedom at each node, eight-node points for steel, and the SOLID45 element with 3 degrees of freedom at each node was used. The applied voltage value was 0 and 0.5 V, respectively. The frequency range and the number of steps were selected as in the experimental study. The solution conditions were defined. In this study, since the adhesive thickness was about half of the sensor's thickness and the studies were conducted at low excitation frequencies, the adhesive effect was neglected, according to Yang's study [7].

Since piezoelectric sensors' characteristics are not the same in all directions, they are classified as anisotropic materials. Two subscripts usually represent piezoelectric constants. X, Y, and Z directions are represented by subscripts 1, 2, 3, respectively, and the shear occurring in these directions is represented by subscripts 4, 5, 6, respectively [18].

The piezoelectric sensor's material properties were entered into the ANSYS® program using the data published by PI ceramic [19], the manufacturer of the sensors supplied for the experimental study, on the internet. The data obtained from the manufacturer cannot be directly entered into the ANSYS program. The necessary conversions should be done, as suggested in Imaoka [20].

Stiffness/Compliance Matrix

Elastic compliance (s) is defined as the strain resulting from the unit stress applied to the piezoelectric material in directions 11 and 33. Also, it can be defined as the inverse of the elasticity modulus [18].

$$[s^E] = \begin{bmatrix} s_{11} & s_{12} & s_{13} & 0 & 0 & 0 \\ s_{12} & s_{11} & s_{13} & 0 & 0 & 0 \\ s_{13} & s_{13} & s_{33} & 0 & 0 & 0 \\ 0 & 0 & 0 & s_{66} & 0 & 0 \\ 0 & 0 & 0 & 0 & s_{44} & 0 \\ 0 & 0 & 0 & 0 & 0 & s_{44} \end{bmatrix}$$

$[s^E]$ matrix is closely related to the modulus of elasticity, shear modulus, and Poisson's ratio (Eqs. 9.1–9.6).

$$E_x = \frac{1}{s_{11}^E} = E_y \quad (9.1)$$

$$E_z = \frac{1}{s_{33}^E} \quad (9.2)$$

$$G_{xy} = \frac{1}{s_{66}^E} \quad (9.3)$$

$$G_{yz} = \frac{1}{s_{44}^E} = G_{xz} \quad (9.4)$$

$$s_{12}^E = \nu U_{xy} (-s_{11}^E) \quad (9.5)$$

$$s_{13}^E = \nu U_{yz} (-s_{33}^E) \quad (9.6)$$

s_{66}^E and s_{44}^E values are not available in the manufacturer's data. These values are calculated using Eqs. (9.7)–(9.8).

$$s_{66}^E = 2(s_{11}^E - s_{12}^E) \quad (9.7)$$

$$s_{44}^E = 2(s_{33}^E - s_{13}^E) \quad (9.8)$$

In literature, there is no function or graphics related to the temperature change of these values of the PIC255 piezoelectric sensors. Therefore, these values were

determined using the equations, including the change in elasticity modulus and shear modulus with temperature.

The variation of the Poisson's ratio with temperature is neglected. It is assumed to be independent of the direction since there is no different value depending on the direction in the manufacturer's data ($NU_{xy} = NU_{xz} = NU_{yz} = \nu = 0.34$). The relationship between the shear modulus and the elastic modulus is defined in Eqs. (9.9)–(9.10).

$$G_{xy} = \frac{E_x}{[2(1+\nu)]} \quad (9.9)$$

$$G_{yz} = G_{xz} = \frac{E_z}{[2(1+\nu)]} \quad (9.10)$$

The variation of the elastic modulus with temperature is given in Eq. (9.11) [21].

$$E_p(T) = E_p - \frac{(T_0 - T) E_p}{160} \frac{E_p}{4} \quad (9.11)$$

Here E_p , is Young's modulus at the reference temperature, $E_p(T)$ is Young's modulus at the measured temperature, T is ambient temperature, T_0 is reference temperature, p is piezoelectricity. The reference temperature is 25 °C. Elasticity modulus values at the reference temperature were calculated using the values of s_{11}^E and s_{33}^E supplied by the manufacturer for the PIC255 piezoelectric sensor. Using Eq. (9.11), the elastic modulus values of the PIC255 piezoelectric sensor at varying temperatures ranging from 0 to -45 °C at 5 °C intervals were calculated. These values are given in Table 9.1.

Table 9.1 Modulus of elasticity for PZT sensor at various temperatures

Temperature (°C)	$E_x = E_y$ (GPa)	E_z (GPa)
25	62.10	48.30
0	60.16	46.79
-5	59.67	46.41
-10	59.18	46.03
-15	58.70	45.65
-20	58.21	45.28
-25	57.73	44.9
-30	57.24	44.52
-35	56.76	44.14
-40	56.27	43.77
-45	55.79	43.39

After the modulus of elasticity values was determined, shear modulus values were calculated using Eqs. (9.9)–(9.10). Shear modulus values of the PIC255 piezoelectric sensor are given in Table 9.2.

Using Eqs. (9.1)–(9.8), all the parameters in the $[s^E]$ matrix were determined for varying temperatures. These values are given in Table 9.3.

In Table 9.3, elastic compliance coefficients are given as $10^{-12} \text{ m}^2/\text{N}$ and temperature values in $^{\circ}\text{C}$. The data will be used to determine the dielectric matrix and the piezoelectric matrix $[e]$ related to the stress/electric field.

Piezoelectric Charge Constants

The matrix $[d]$ was created by taking the parameters d_{31} , d_{33} and d_{15} from the catalog values of the producer company.

$$[d] = \begin{bmatrix} 0 & 0 & d_{31} \\ 0 & 0 & d_{31} \\ 0 & 0 & d_{33} \\ 0 & 0 & 0 \\ 0 & d_{15} & 0 \\ d_{15} & 0 & 0 \end{bmatrix}$$

In the ANSYS® program, the matrix $[e]$ is the matrix that relates the mechanical stress to the electric field. Using Eq. (9.12), the manufacturer’s data has been made available for the ANSYS® program.

Table 9.2 Modulus of shear for PZT sensor at different temperatures

Temperature($^{\circ}\text{C}$)	G_{XY} (GPa)	$G_{XZ} = G_{YZ}$ (GPa)
25	23.17	18.02
0	22.44	17.45
-5	22.26	17.31
-10	22.08	17.17
-15	21.90	17.03
-20	21.72	16.89
-25	21.54	16.75
-30	21.36	16.61
-35	21.18	16.47
-40	20.99	16.33
-45	20.81	16.19

Table 9.3 Elastic compliance coefficients of the PZT sensor at varying temperatures

Temperature (°C)	s_{11}	s_{33}	s_{12}	s_{13}	s_{66}	s_{44}
25	16.10305958	20.70393370	-5.47504026	-7.03933700	43.15619968	55.48654200
0	16.62251312	21.37180260	-5.65165446	-7.26641300	44.54833515	57.27643100
-5	16.75765550	21.54555710	-5.69760287	-7.32548900	44.91051674	57.74209300
-10	16.89501333	21.72216000	-5.74430453	-7.38553400	45.27863573	58.21538900
-15	17.03464154	21.90168200	-5.79177812	-7.44657200	45.65283933	58.69650800
-20	17.17659689	22.08419600	-5.84004294	-7.50862700	46.03327966	59.18564500
-25	17.32093804	22.26977750	-5.88911893	-7.57172400	46.42011394	59.68300400
-30	17.46772565	22.45850440	-5.93902672	-7.63589100	46.81350474	60.18879200
-35	17.61702245	22.65045740	-5.98978763	-7.70115600	47.21362016	60.70322600
-40	17.76889333	22.84572000	-6.04142373	-7.76754500	47.62063413	61.22653000
-45	17.92340545	23.04437840	-6.09395785	-7.83508900	48.03472660	61.75893400

$$[e] = [s^E]^{-1} [d] \quad (9.12)$$

Simulation studies were carried out considering the change of piezoelectric charge coefficients with temperature. As a result of the trial simulation studies, although the amplitude changes were observed at varying temperatures, no difference was found in the frequency. For this reason, the variation of the piezoelectric charge coefficients with temperature was neglected. The matrix $[d]$ is defined identically for all temperatures and is expressed, as shown below.

$$[d] = \begin{bmatrix} 0 & 0 & -180 \\ 0 & 0 & -180 \\ 0 & 0 & 400 \\ 0 & 0 & 0 \\ 0 & 550 & 0 \\ 550 & 0 & 0 \end{bmatrix}$$

Using the calculated $[s^E]$ matrices, the $[e]$ matrices were calculated for varying temperatures.

The $[e]$ matrix generated for 25 °C was given below.

$$[e] = \begin{bmatrix} 0 & 0 & -7.53378 \\ 0 & 0 & -7.53378 \\ 0 & 0 & 14.19998 \\ 0 & 0 & 0 \\ 0 & 9.912232 & 0 \\ 9.912232 & 0 & 0 \end{bmatrix}$$

Dielectric Constants

The relative dielectric constant is defined as the ratio of the amount of load, the piezoelectric element can store to the amount of vacuum stored in the vacuum ($\epsilon_0 = 8.85 \times 10^{-12}$ F/m). The manufacturer data for piezoelectric materials are ϵ_{11}/ϵ_0 and ϵ_{33}/ϵ_0 . In the manufacturer's data, no graph or equation shows the dielectric constants' variation with temperature. As the piezoelectric sensor type used in our experimental study was PZT 5A, the relative dielectric constants' temperature-dependent function was derived from the plot of these values for PZT 5A [22].

The relative dielectric constants' functions for PZT 5A derived from the temperature dependence are given in Eqs. (9.13)–(9.14).

$$\varepsilon_{11} / \varepsilon_0 = 0.0103T^2 + 3.4885T + 1585.4 \quad (9.13)$$

$$\varepsilon_{33} / \varepsilon_0 = 0.0117T^2 + 3.6999T + 1681.5 \quad (9.14)$$

The coefficient of determination value (r^2) in the two derived equations is 0.99. In these equations, T represents temperature. The values of $\varepsilon_{11}/\varepsilon_0$ and $\varepsilon_{33}/\varepsilon_0$ are given in Table 9.4.

The parameters of $\varepsilon_{11}/\varepsilon_0$ and $\varepsilon_{33}/\varepsilon_0$ cannot be entered directly into the ANSYS® program from the manufacturer's catalog values. The matrix defines the manufacturer's $[\varepsilon^T]$ data.

$$[\varepsilon^T] = \begin{bmatrix} \varepsilon_{11} / \varepsilon_0 & 0 & 0 \\ 0 & \varepsilon_{11} / \varepsilon_0 & 0 \\ 0 & 0 & \varepsilon_{33} / \varepsilon_0 \end{bmatrix}$$

Equation (9.15) was used to adapt the manufacturer's data to the ANSYS® program.

$$[\varepsilon^S] = [\varepsilon^T] - [d]^t [s^E]^{-1} [d] \quad (9.15)$$

The $[\varepsilon^S]$ matrix is shown below for 25 °C.

$$[\varepsilon^S] = \begin{bmatrix} 1033.986 & 0 & 0 \\ 0 & 1033.986 & 0 \\ 0 & 0 & 801.7345 \end{bmatrix}$$

After recalculating $[s^E]^{-1}$ and $[\varepsilon^T]$ matrices for the different temperatures, $[\varepsilon^S]$ matrices are determined using Eq. (9.15).

Table 9.4 $\varepsilon_{11}/\varepsilon_0$ and $\varepsilon_{33}/\varepsilon_0$ values with respect to varying temperatures

Temperature (°C)	$\varepsilon_{11}/\varepsilon_0$	$\varepsilon_{33}/\varepsilon_0$
25	1679.05	1780.87
0	1585.40	1681.50
-5	1568.22	1663.28
-10	1551.55	1645.60
-15	1535.39	1628.48
-20	1519.75	1611.90
-25	1504.63	1595.88
-30	1490.02	1580.40
-35	1475.92	1565.48
-40	1462.34	1551.10
-45	1449.28	1537.28

Density

The equation proposed by Jyoti [21] was used to calculate the change in density at varying temperatures (Eq. 9.16). Density values of the piezoelectric sensor are given in Table 9.5.

$$\rho = \frac{\rho_0}{\left[(1 + \alpha \Delta T)^3 \right]} \tag{9.16}$$

α (coefficient of thermal expansion) has a value ranging from 4×10^{-6} (1/K) to 8×10^{-6} (1/K) given by the manufacturer catalog of the piezoelectric sensor. The value of α is assumed to be 6×10^{-6} (1/K), since the value of α is defined as the average coefficient of thermal expansion in Eq. (9.16). The values in Table 9.5 are entered into the ANSYS® program without any conversion while developing models for varying temperatures. The value was taken as 6×10^{-6} (1/K) for the steel specimen, as suggested in Kabeya [23]. The density values of the specimen are given in Table 9.6.

Modulus of Elasticity of Samples with Piezoelectric Sensor Added at Varying Temperatures

Equation (9.17) is used for the change of the elasticity modulus with temperature [23].

$$E(T) = E_0 + \frac{\partial E}{\partial T}(T - T_0) = E_0 + \beta(T - T_0) \tag{9.17}$$

Table 9.5 Density values of the piezoelectric sensor at varying temperatures

Temperature (°C)	Density (kg/m ³)
25	7800.00
0	7803.51
-5	7804.21
-10	7804.92
-15	7805.62
-20	7806.32
-25	7807.02
-30	7807.73
-35	7808.43
-40	7809.13
-45	7809.84

Table 9.6 Density values of the specimen at varying temperatures

Temperature (°C)	Density (kg/m ³)
25	7832.00
0	7835.53
-5	7836.23
-10	7836.94
-15	7837.64
-20	7838.35
-25	7839.05
-30	7839.76
-35	7840.46
-40	7841.17
-45	7841.88

Here, E_0 is Young's modulus at the reference temperature, E is Young's modulus at the measured temperature, T is the ambient temperature, T_0 is the reference temperature, and β is the linear variation of the temperature. The β value of steel was taken as -3.7×10^7 (N/m²), as proposed in Kabeya [23]. Elastic modulus values of the specimen are given in Table 9.7.

Damping Ratio

It is known that there are three types of damping: viscous damping because of energy loss, structural damping because of material properties, and friction damping because of slipping between surfaces [24]. Viscous damping occurs in low kHz piezoelectric applications [25]. In this study, the damping ratio was determined using viscous damping principles. α (Mass multiplication factor) value is 0, the β (stiffness multiplication factor) value is greater than 0, and the constant damping ratio value is 0 for viscous damping [26]. β (Stiffness multiplication factor) value is calculated by the equations proposed by Naillon et al. [27] (Eqs. 9.18–9.19).

$$\beta = \frac{1}{\omega Qm} \quad (9.18)$$

$$\omega = 2\pi f \quad (9.19)$$

Here, ω is the angular velocity in the largest mode (Hz) and Qm is the mechanical quality factor. The Qm value of the PIC 255 is given as 80 in the manufacturer's data. ω value is determined using the result of an experimental study at 25 °C.

Table 9.7 Elastic modulus values of the specimen at varying temperatures

Temperature (°C)	<i>E</i> (GPa)
25	210.000
0	210.925
-5	211.110
-10	211.295
-15	211.480
-20	211.665
-25	211.850
-30	212.035
-35	212.220
-40	212.405
-45	212.590

Damage Metrics

Damage metrics capture spectrum characteristics caused by damage and ignore changes in normal conditions. The most commonly used metrics are root mean square deviation (RMSD), mean absolute percent deviation (MAPD), correlation coefficient (CC), and correlation coefficient deviation metric (CCDM) [28].

Effective frequency shift (EFS) is a straightforward technique to compensate for the effect of temperature. By comparing the impedance obtained according to the temperature change with the reference impedance, the frequency shift is performed by forming the loop until the minimum CCDM is obtained [29].

A stochastic search technique that uses the creation of biological systems to solve problems is the genetic algorithm. The approach differs from the other approaches since arrays are used to represent the parameters. Generally, the algorithm is used to solve problems where the search space is not large [30].

The Genetic Algorithm was used in this analysis to solve the compensation algorithm. MATLAB Optimization Toolbox was used to optimize (minimize) CCDM. There are various genetic algorithm parameters to be modified (fitness scaling function, population size, the function of selection, fraction of crossover, the function of mutation, function of crossover, elite count, etc.). In this analysis, the crossover function was two-point. The crossover fraction and population size were 0.8 and 200. The function of the Gaussian type mutation was selected and the default values for the other parameters were set.

While eight different temperature levels were used in the experimental study, ten different temperature levels were used in the numerical study. As damage metrics, RMSD, MAPD, and CCDM were used. EFS/Genetic algorithm was applied. Using CCDM values, temperature compensation was carried out.

9.3 Experimental and Numerical Results

In this part, the effect of temperature on the constrained piezoelectric sensor was studied experimentally and numerically. Then, the temperature effect was compensated by the compensation algorithm.

9.3.1 Experimental Results

The room temperature measurements were taken as a reference. The measurements taken at the other temperatures were compared according to this reference measurement. Figure 9.2 presents the impedance measurement results at room temperature.

As can be seen in Fig. 9.2, the modes with the largest peak are between 40 and 80 kHz. Therefore, the room temperature experiment was repeated for 40–80 kHz, and other experiments were performed for 40–80 kHz. The results obtained at room temperature were taken as reference measurements. The measurements at the other temperatures were compared with the reference measurement. The results are shown in Fig. 9.3.

The results for the frequency ranges of 40–48 kHz, 48–56 kHz, and 73–80 kHz are shown in Figs. 9.4, 9.5, and 9.6, respectively. As a result of the experimental study, it was observed that as the temperature decreased, the peaks were shifted to the right and the amplitudes increased.

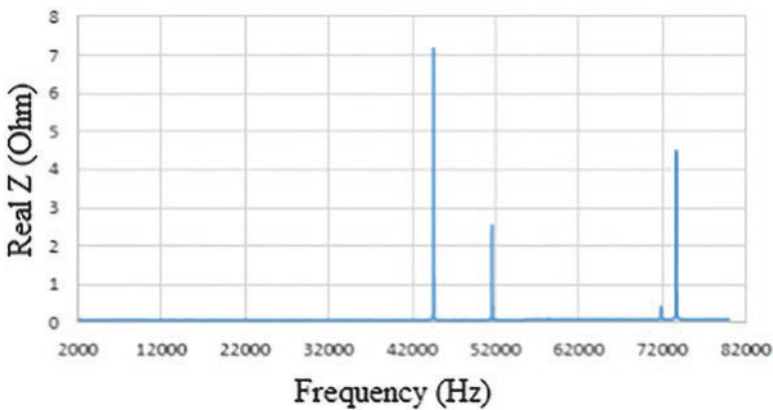


Fig. 9.2 Impedance measurements at 25 °C (experimental)

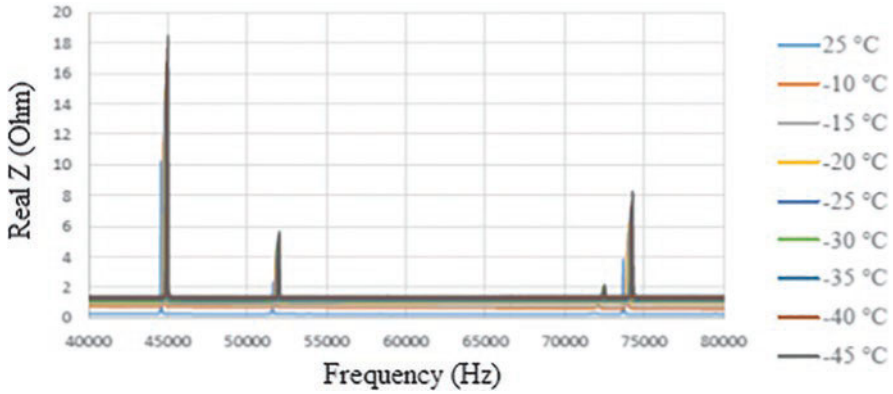


Fig. 9.3 Experimental measurement results (40–80 kHz)

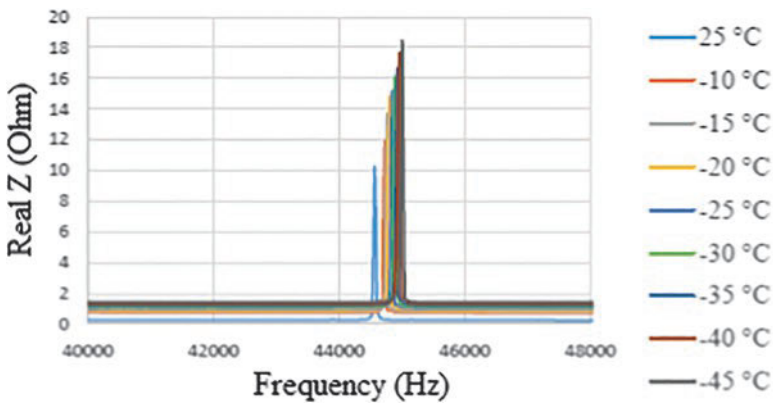


Fig. 9.4 Experimental measurement results (40–48 kHz)

9.3.2 Numerical Results

The frequency range and the number of steps were defined as the preferred number of steps (1000) and frequency range (40–80 kHz) in the experimental study. For the damping ratio, the value of α (mass multiplication factor) is 0, and the constant damping ratio value is 0 entered.

The solutions were found by determining the ω values for varying temperatures. However, no change was observed in the trial simulation results. For this reason, ω value was determined using the result of an experimental study at 25 °C. For the value of β (stiffness multiplication factor), the frequency value in the largest mode was set at 44564 Hz for the experimental study at 25 °C. After substituting this value in Eq. (9.19), the β value is calculated as 4.46×10^{-8} using Eq. (9.18).

For 25 °C, solutions for different mesh sizes were tried. The appropriate mesh size was determined by comparing the results with experimental measurements at

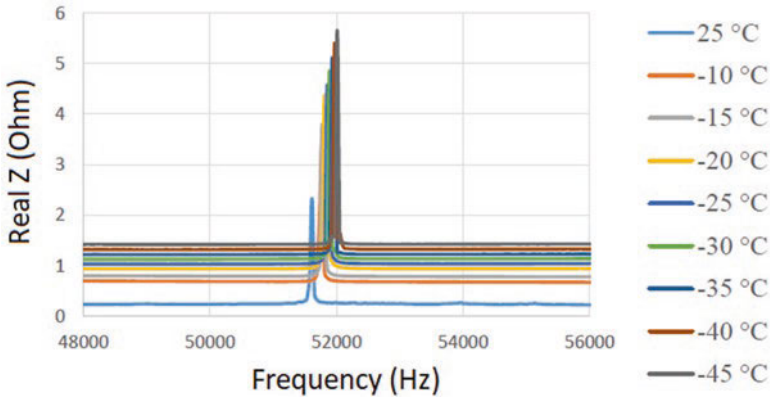


Fig. 9.5 Experimental measurement results (48–56 kHz)

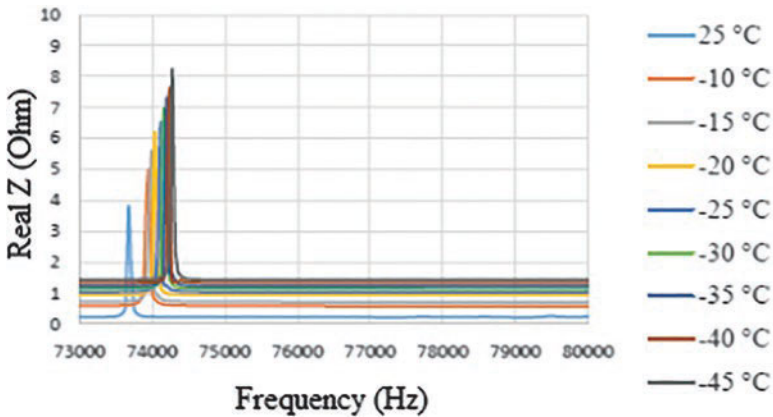


Fig. 9.6 Experimental measurement results (73–80 kHz)

25 °C. The specimen's behavior was examined at varying temperatures ranging from 0 to -45 °C with 5 °C intervals. The comparison of the results is given in Fig. 9.7. The figure shows that the amplitude values obtained from the simulation studies start from a higher level than the amplitude values obtained from the experimental study. The reason is the thickness of the specimen (10 mm), so the probe cannot be directly attached to the sample.

The suitable mesh size is 10,500 ($10,000 \times 500$). Here 10,000 is the number of mesh in the plate and 500 is the number of mesh in the sensor. Therefore, a 10,500 cell structure was chosen for simulation runs at 25 °C and different temperatures. The mesh structure is given in Fig. 9.8. The simulation results obtained for varying temperatures are shown in Fig. 9.9.

The figure shows three modes. These modes are shown in Figs. 9.10, 9.11, and 9.12 for 40–48 kHz, 48–56 kHz, and 72–80 kHz, respectively. When the

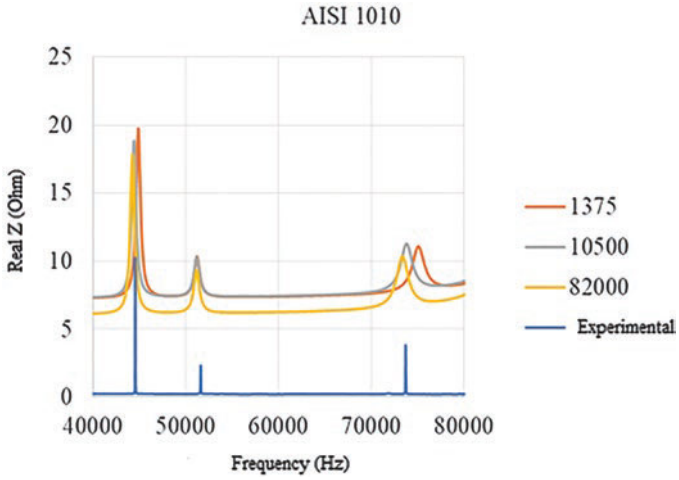


Fig. 9.7 Mesh number selection for specimen model

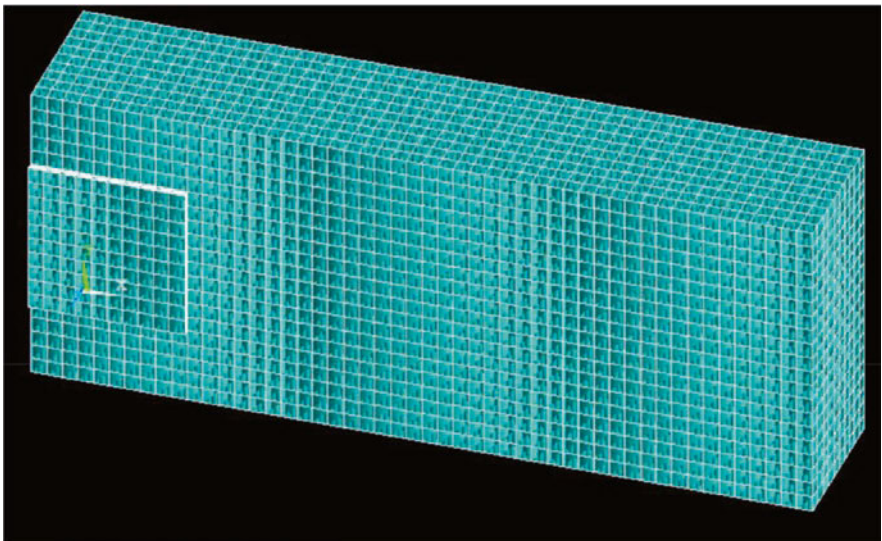


Fig. 9.8 The mesh structure of the piezoelectric sensor and specimen

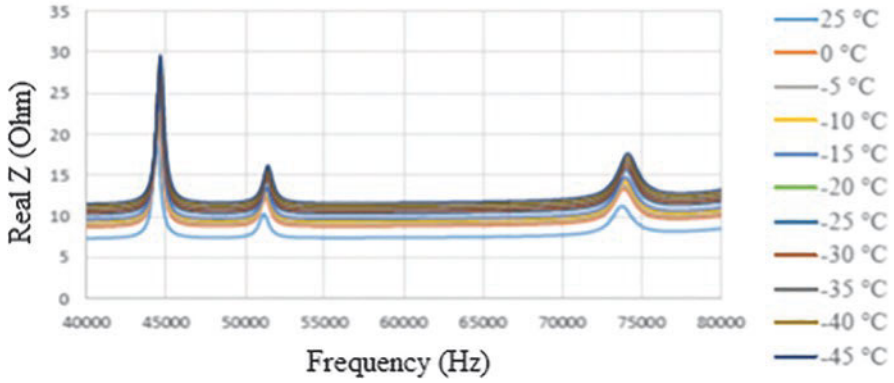


Fig. 9.9 Simulation results at varying temperatures (40–80 kHz)

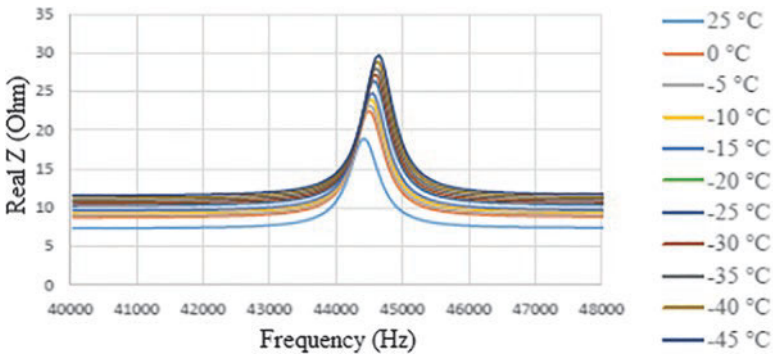


Fig. 9.10 Simulation results at varying temperatures (40–48 kHz)

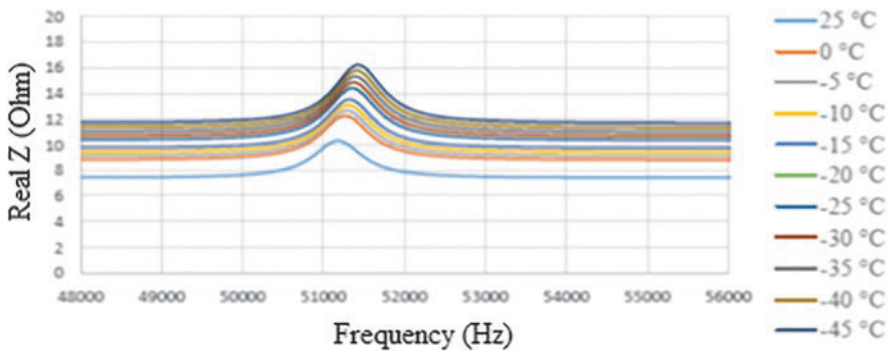


Fig. 9.11 Simulation results at different temperatures (48–56 kHz)

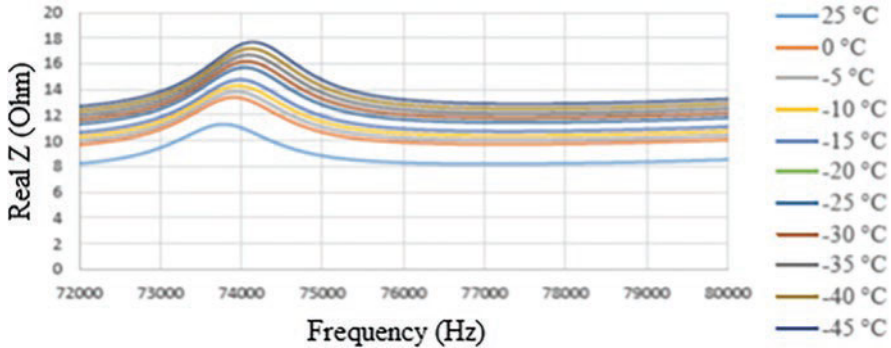


Fig. 9.12 Simulation results at different temperatures (72–80 kHz)

temperature reduces, the frequency shifts to the right and the amplitude value also increases.

The experimental and simulation results obtained at $-10\text{ }^{\circ}\text{C}$, $-30\text{ }^{\circ}\text{C}$, and $-45\text{ }^{\circ}\text{C}$ of the specimen steel are shown in Figs. 9.13, 9.14, and 9.15, respectively. Simulation and experimental results are consistent with each other.

9.3.3 *Experimental/Numerical Results in Terms of Damage Metrics (Compensated and Non-compensated)*

Experimental results that are non-compensated by three damage metrics are given in Figs. 9.16, 9.17, and 9.18. When the results were examined, the damage metric values increased as the temperature difference increased.

The experimental results, which are compensated by three damage metrics, are shown in Figs. 9.19, 9.20, and 9.21. When the results were examined, the damage metrics decreased compared to the non-compensated metrics.

Numerical results that are non-compensated by three damage metrics are given in Figs. 9.22, 9.23, and 9.24. When the results were examined, the damage metrics increased as the temperature difference increased.

The numerical results compensated according to the three damage metrics are given in Figs. 9.25, 9.26, and 9.27. When the results were examined, the damage metrics decreased compared to the non-compensated results.

Compensated real impedance graphs are shown in Figs. 9.28 and 9.29 for experimental studies and Figs. 9.30 and 9.31 for numerical studies.

The real impedance graphs moved to the right with the drop in temperature after all the effects were evaluated. As the temperature change increased, the frequency shift increased. These graphics have been compensated by sliding them to the left. The values of damage metrics have decreased since they were compensated. As the

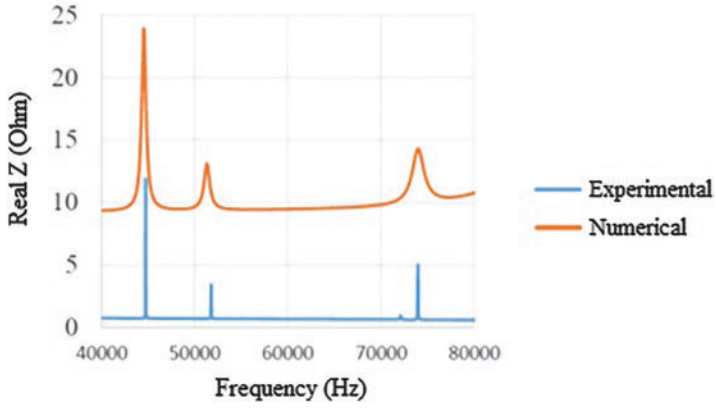


Fig. 9.13 Comparison of experimental and simulation results (-10 °C)

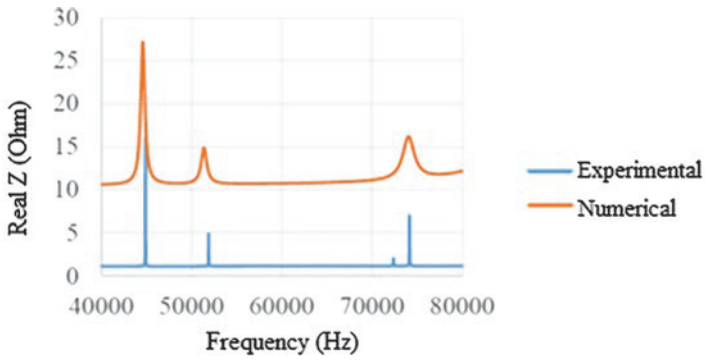


Fig. 9.14 Comparison of experimental and simulation results (-30 °C)

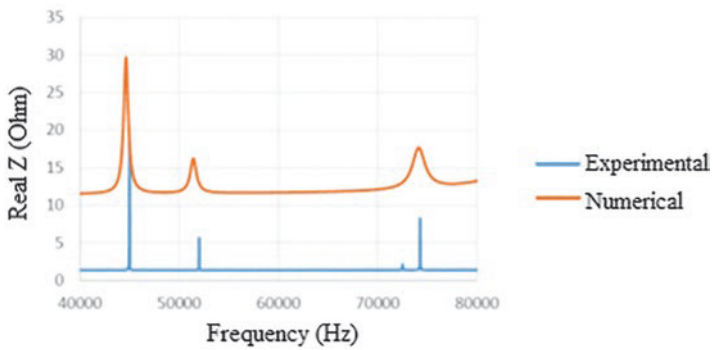


Fig. 9.15 Comparison of experimental and simulation results (-45 °C)

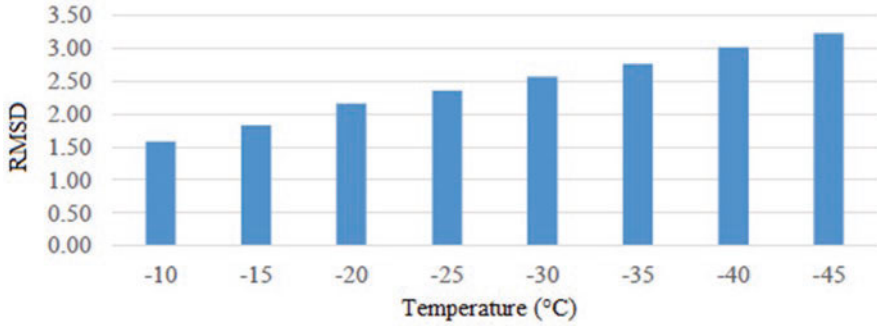


Fig. 9.16 Non-compensated RMSD damage metric values of experimental results at different temperature values

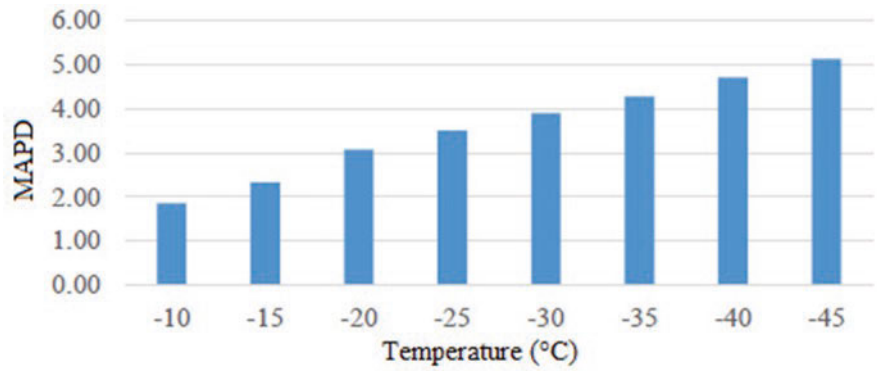


Fig. 9.17 Non-compensated MAPD damage metric values of experimental results at varying temperature values

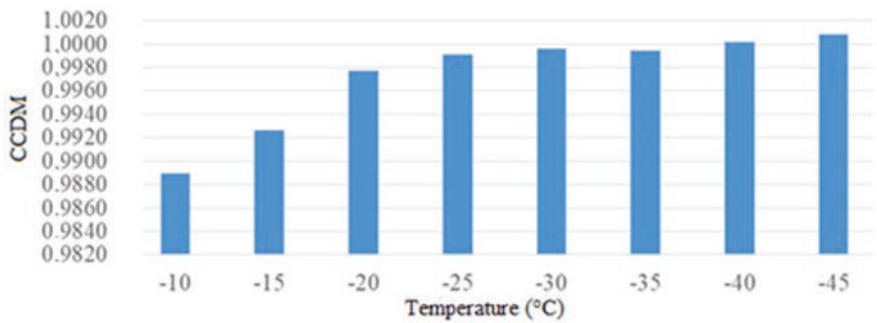


Fig. 9.18 Non-compensated CCDM values of experimental results at varying temperature values

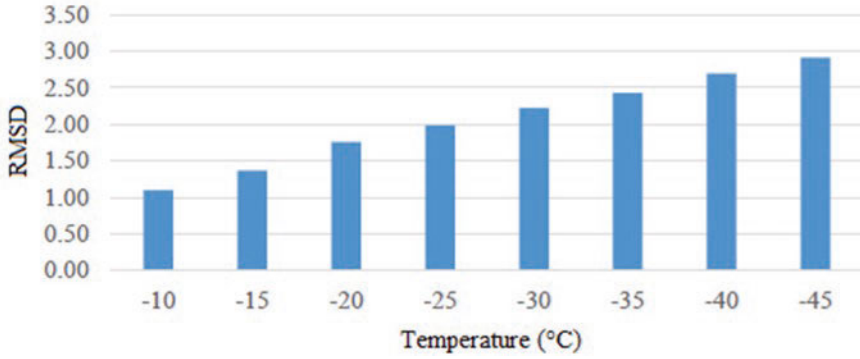


Fig. 9.19 Compensated RMSD damage metric values of experimental results at varying temperatures

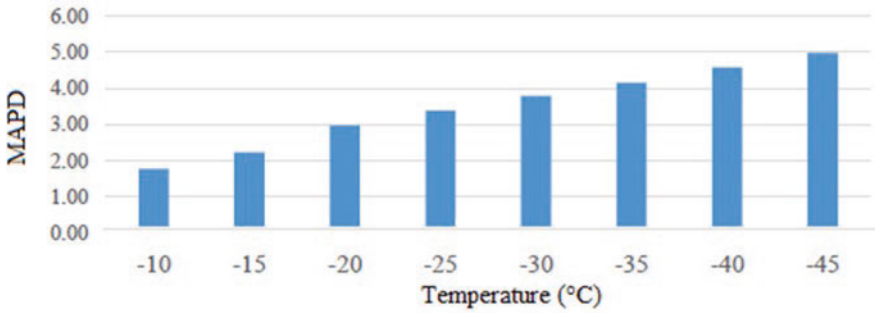


Fig. 9.20 Compensated MAPD damage metric values of experimental results at varying temperatures

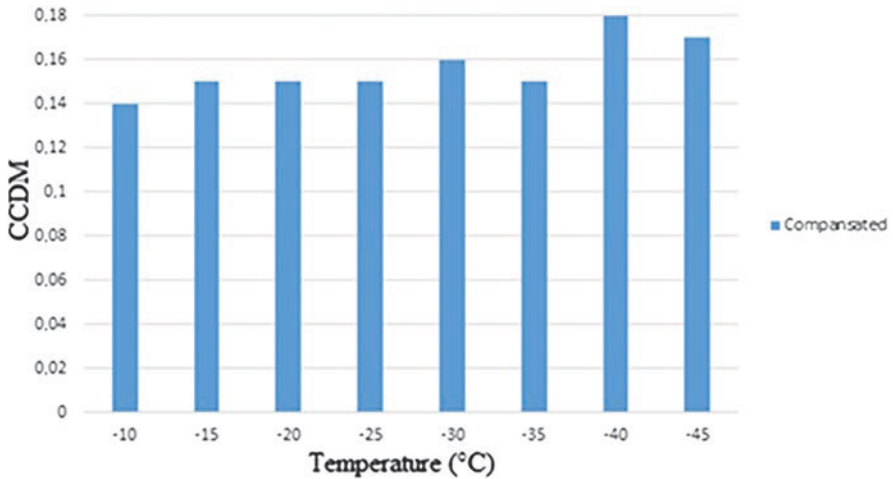


Fig. 9.21 CCDM after compensation with EFS/Genetic algorithm (Experimental)

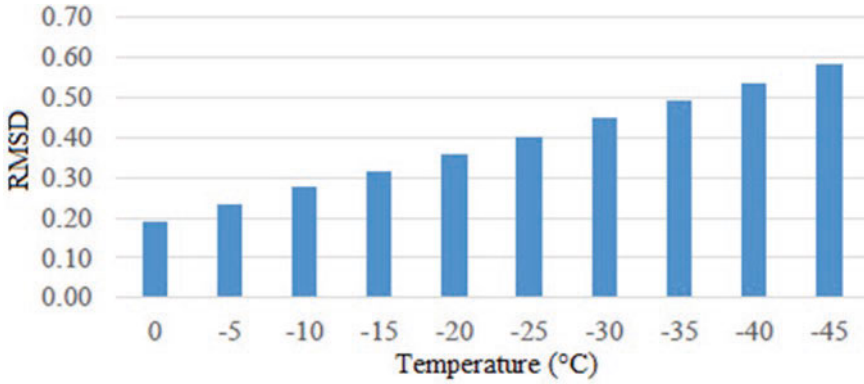


Fig. 9.22 RMSD damage metric values of simulation results at varying temperatures (non-compensated)

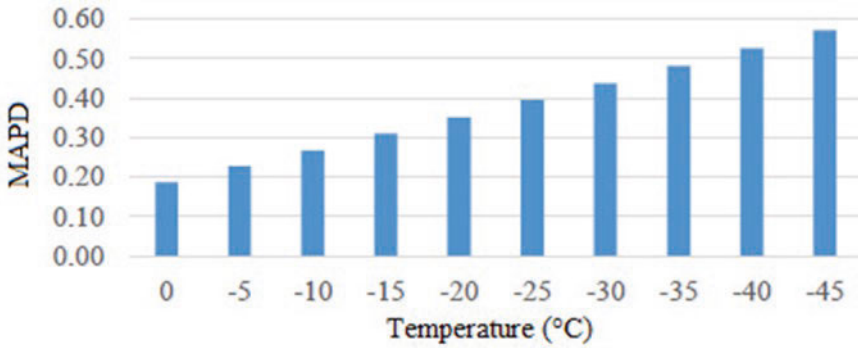


Fig. 9.23 MAPD damage metric values of simulation results at varying temperatures (non-compensated)

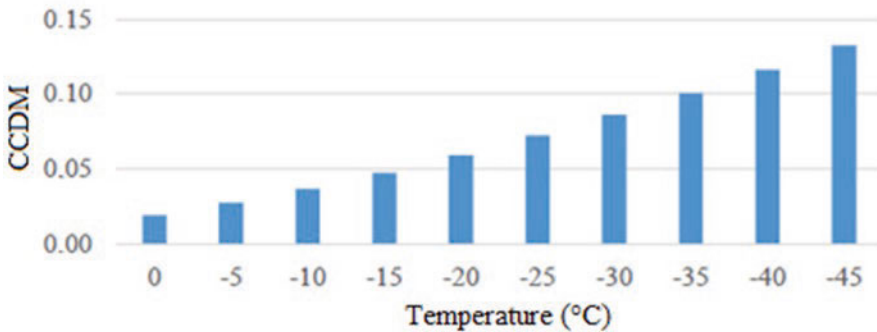


Fig. 9.24 CCDM values of simulation results at varying temperatures (non-compensated)

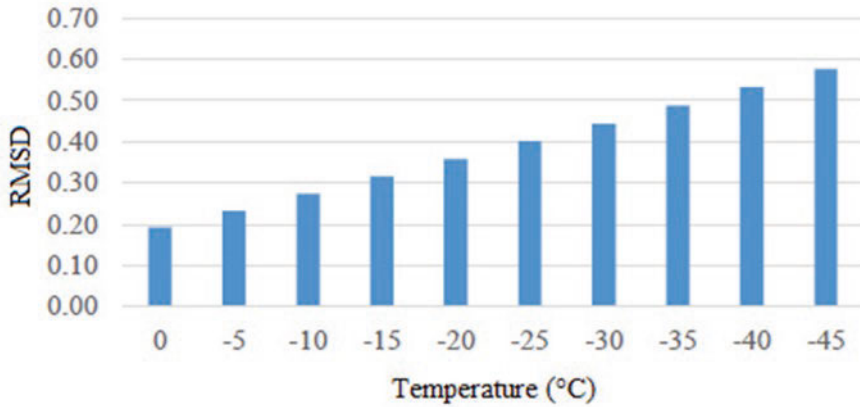


Fig. 9.25 RMSD damage metric values of simulation result at varying temperatures (compensated)

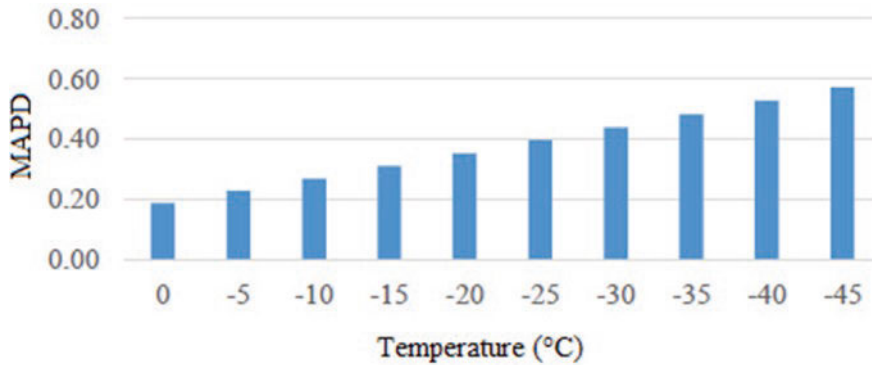


Fig. 9.26 MAPD damage metric values of simulation result at varying temperatures (compensated)

temperature decreased, the real impedance values increased. The findings are consistent with existing literature [10, 13–15].

9.4 Conclusions

Piezoelectric sensors are added to the structure to ensure that the health of the structure is monitored simultaneously. It is known that temperature changes the material properties of the piezoelectric sensors. In this work, the EMI method is proposed to check landing gears in service. In comparison with the room temperature results, variations in the real part of the impedance between -10 and -45 °C were

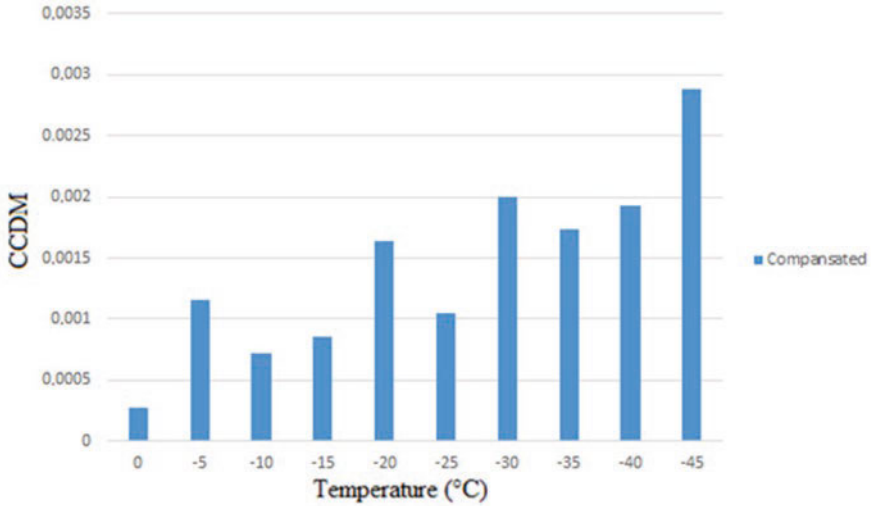


Fig. 9.27 CCDM after compensation with EFS/Genetic algorithm (Numerical)

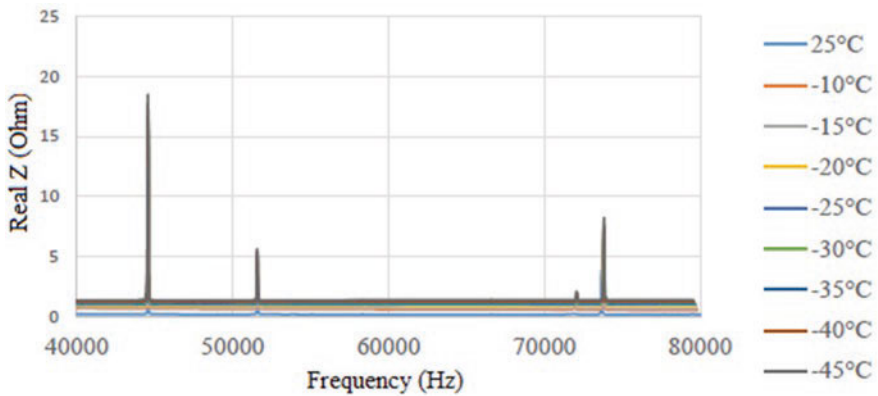


Fig. 9.28 Compensated impedance charts in the 40–80 kHz frequency range at varying temperatures (Experimental study)

evaluated. It has been seen that as the temperature reduces, the frequency shifts to the right (increases) and the amplitude increases. The change has been compensated via EFS/Genetic algorithm.

In this research, a finite element model considering the temperature effect on the piezoelectric sensor and specimen was proposed. The behavior of the constrained piezoelectric sensor was investigated. Changes in the real part of the impedance were evaluated by comparing them with the results of the room temperature. It has been noted that as the temperature decreases, the frequency shifts to the right (increases) and the amplitude increases.

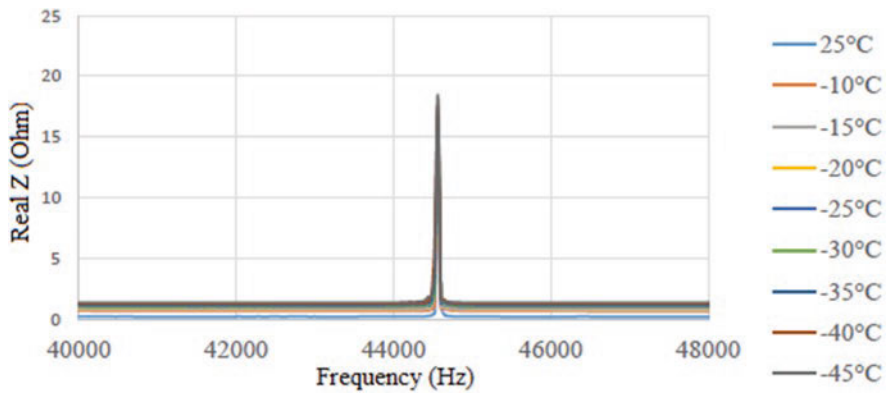


Fig. 9.29 Compensated impedance charts in the 40–48 kHz frequency range at varying temperatures (Experimental study)

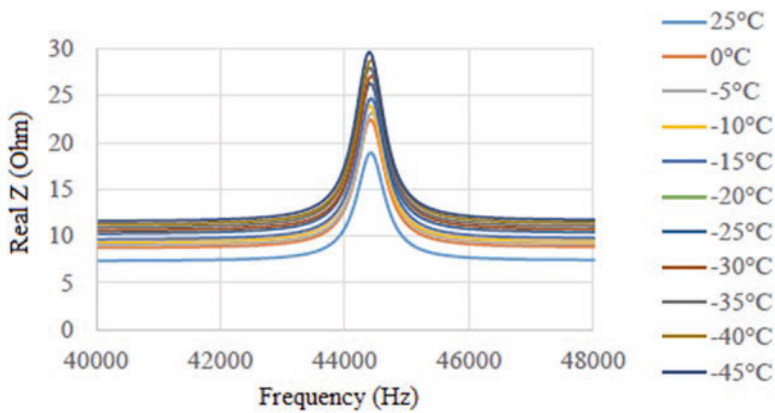


Fig. 9.30 Compensated impedance charts in the 40–48 kHz frequency range at varying temperatures (Simulation study)

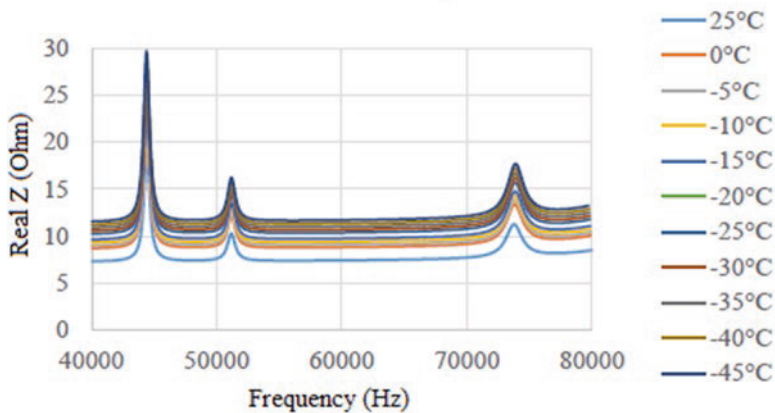


Fig. 9.31 Compensated impedance charts in the 40–80 kHz frequency range at varying temperatures (Simulation study)

Experimental and simulation results are consistent. In future studies, different studies can be performed by selecting a wider range of temperatures. For the determination of the size effect, experiments and simulations can be repeated several times. Furthermore, by studying defective samples' behavior at varying temperatures, two effects can be evaluated together.

Acknowledgments and Funding This work was supported by the Scientific Research Projects Commission of Eskişehir Osmangazi University with the project number 201715A119.

References

1. Aktan, A. E., Helmicki, A. J., & Hunt, V. J. (1998). Issues in health monitoring for intelligent infrastructure. *Smart Materials and Structures*, 7(5), 674–692.
2. Doebling, S. W., Farrar, C. R., & Prime, M. B. (1998). A summary review of vibration-based damage identification methods. *The Shock and Vibration Digest*, 30(2), 91–105.
3. Shankar, R. (2009). *An integrated approach for structural health monitoring*. PhD thesis, Indian Institute of Technology Delhi.
4. Hooker, M. W. (1998). *Properties of PZT-based Piezoelectric Ceramics between 150 and 250 °C*. Technical Report, National Aeronautics and Space Administration.
5. Sherrit, S., Yang, G., Wiederick, H., & Mukherjee, B. (1999). Temperature dependence of the dielectric, elastic and piezoelectric material constants of lead zirconate titanate ceramics. In *Proceedings of the international conference on smart materials, structures and systems*.
6. Wolf, R. A., & Trolier-McKinstry, S. (2004). Temperature dependence of the piezoelectric response in lead zirconate titanate films. *Journal of Applied Physics*, 95(3), 1397–1406.
7. Yang, Y., Lim, Y. Y., & Soh, C. K. (2008). Practical issues related to the application of the electromechanical impedance technique in the structural health monitoring of civil structures: I. *Experiment*. *Smart Materials and Structures*, 17(3), 1–14.
8. Grisso, B. L., & Inman, D. J. (2010). Temperature corrected sensor diagnostics for impedance-based SHM. *Journal of Sound and Vibration*, 329(12), 2323–2336.
9. Siebel, T., & Lilov, M. (2013). Experimental investigation on improving electromechanical impedance based damage detection by temperature compensation. *Key Engineering Materials*, 569, 1132–1139.
10. Baptista, F. G., Budoya, D. E., de Almeida, V. A., & Ulson, J. A. (2014). An experimental study on the effect of temperature on piezoelectric sensors for impedance-based structural health monitoring. *Sensors (Basel)*, 14(1), 1208–1227.
11. Bukhari, S., Islam, M., Haziot, A., & Beamish, J. (2014). Shear piezoelectric coefficients of PZT, LiNbO₃ and PMN-PT at cryogenic temperatures. *Journal of Physics: Conference Series*, 568(3).
12. Zou, D., Liu, T., Liang, C., Huang, Y., Zhang, F., & Du, C. (2015). An experimental investigation on the health monitoring of concrete structures using piezoelectric transducers at various environmental temperatures. *Journal of Intelligent Material Systems and Structures*, 26(8), 1028–1034.
13. Xu, G., Xu, B., Xu, C., & Luo, Y. (2016). Temperature effects in the analysis of electromechanical impedance by using spectral element method. *Multidiscipline Modeling in Materials and Structures*, 12(1), 119–132.
14. Wandowski, T., Malinowski, P. H., & Ostachowicz, W. M. (2016). Delamination detection in CFRP panels using EMI method with temperature compensation. *Composite Structures*, 151, 99–107.

15. Haider, M. F., Giurgiutiu, V., Lin, B., & Yu, L. (2017). Irreversibility effects in piezoelectric wafer active sensors after exposure to high temperature. *Smart Materials and Structures*, 26(9).
16. Fallahian, S., Joghataie, A., & Kazemi, M. (2017). Structural damage detection using time domain responses and teaching-learning-based optimization (TLBO) algorithm. *Scientia Iranica*, 25(6), 3088–3100.
17. Rezvani, K., Maia, N. M. M., & Sabour, M. (2018). A comparison of some methods for structural damage detection. *Scientia Iranica*, 25(3), 1312–1322.
18. Türker, Ö. (2009). *Designing and manufacturing of Pz/Polymer based smart beams which compatible active vibration control*. MSc Thesis, Istanbul Technical University.
19. PI Ceramic. Retrieved from <https://www.piceramic.com/en/products/piezoceramic-materials/#c15162>.
20. Ansys tip of the week: Conversion of piezoelectric material data. Retrieved from <http://ansys.net/ansys/tips/Week13%TNT%Conversion%of%Piezoelectric%Material%Data.pdf>.
21. Jyoti, A. (2008). *Modelling and analysis of PZT Micro power generator*. PhD Thesis, Auburn University.
22. Piezo System Inc. Retrieved from <http://www.piezo.com/catalog8.pdf>.
23. Kabeya, K. I. (1998). *Structural health monitoring using multiple piezoelectric sensors and actuators*. MSc Thesis, VirginiaTech University.
24. Cai, C., Zheng, H., Khan, M. S., & Hung, K. C. (2002). Modeling of material damping properties in ANSYS. In *CADFEM users' meeting & ANSYS conference*.
25. Nader, G., Silva, E. C. N., & Adamowski, J. C. (2004). Effective damping value of piezoelectric transducer determined by experimental techniques and numerical analysis. In *ABCMSymposium series in mechatronics*.
26. Lerch, R. (1990). Simulation of piezoelectric devices by two-and three-dimensional finite elements. *IEEE transactions on ultrasonics, ferroelectrics, and frequency control*, 37(3), 233–247.
27. Naillon, M., Coursant, R., & Besnier, F. (1983). Analysis of piezoelectric structures by a finite-element method. *Acta Electronica*, 25(4), 341–362.
28. Giurgiutiu, V. (2014). *Structural health monitoring with piezoelectric wafer active sensors*. Elsevier.
29. Rabelo, D. S., Steffen, V., Neto, R. M. F., & Lacerda, H. B. (2017). Impedance-based structural health monitoring and statistical method for threshold-level determination applied to 2024-T3 aluminum panels under varying temperature. *Structural Health Monitoring*, 16(4), 365–381.
30. Goldberg, D. E. (1989). Genetic algorithms in search, optimization, and machine learning. *Addison Wesley*, 102(36).

Chapter 10

Major Units and Systems in Aircraft



Tamer Saraçyakupoğlu

Nomenclature

ABS	Air bleed system
ADG	Accessory drive gearbox
AFCS	Automatic flight control system
AGL	Above ground level
AHRS	Attitude heading and reference systems
AOG	Aircraft on the ground
APU	Auxiliary power unit
APS	Auxiliary power system
ATC	Air traffic controller
COTS	Commercial off-the-shelf
CVR	Cockpit voice recorder
DH	Decision height
DOC	Direct operational cost
DME	Distance-measuring equipment
EASA	European Aviation Safety Agency
ECB	Electronic control box
ECS	Environmental control system
EGPWS	Enhanced ground proximity warning system
ELT	Emergency locator transmitter
EPS	Environmental protection system
FAA	Federal Aviation Administration
FC	Flying hour/flight cycle

T. Saraçyakupoğlu (✉)

Standoff Jammer Aircraft Project Department, Turkish Aerospace Industries, Ankara, Turkey

e-mail: dr.tamer@tamersaracyakupoglu.com.tr

FDR	Flight data recorder
FMS	Flight management system
FH	Flying hour/flight hour
ICAO	International Civil Aviation Organization
ILS	Instrument landing system
IM	Inner marker
MM	Middle marker
MFD	Multifunction display
MRO	Maintenance, repair, and overhaul
NAA	National Airworthiness Authorities
NWS	Nose wheel steering
OM	Outer marker
OLS	Optical landing system
PAC	Passenger air-conditioner
PAPI	Precision approach path indicators
PFD	Primary flight display
QRH	Quick reference handbook
RH	Relative humidity
RVR	Runway visual range
TOGA	Takeoff go-around mode
ULB	Underwater locator beacon
VASI	Visual approach slope indicators
VOR	VHF omnidirectional radio range

Subscripts

V_{APP} Approach velocity

10.1 Introduction

A common commercial passenger aircraft includes approximately three to six million parts and units. These parts and units may vary depending on the certificated aircraft type. To give an idea, a Boeing B747-400, which is a very famous large body, consists of approximately six million parts that almost half of them are fasteners [1]. However, the freighter adaptations would have a lot fewer parts than the passenger commercial ones.

The airplanes operate in a challenging environment. That's why all the parts and components should be produced for running under extraordinary conditions. It's a stiff requirement for aviation safety. For instance, while cruising at 33.000 ft flight level, the outside temperature is about -55°C and the outside pressure is about 1/4 Atm. Besides the aircraft is under static and dynamic loads which may adversely influence the structure and lead to a fatigue failure. Each part and component of the aircraft dynamically reacts to the loads acting. This reaction is effective during all flight phases such as

taxi-roll, landing, climb, cruise, and approach, etc. [2]. For meeting the requirements of the mentioned challenging conditions, in the airborne-part manufacturing facilities, the meticulously prepared tests are carried out by the technical staff.

From an assembly perspective, the components and units are combined with manufactured and standard parts. In other words, these are the building blocks of assemblies. The airplane is the highest assembly which is generally called “top assembly.” It is made up of commercial off-the-shelf (COTS) parts, loose objects, and standard parts like fasteners and consumables. For sure there are many systems and sub-systems in an air vehicle. Some of the main components subjected to this study are given as follow:

- Auxiliary power unit (APU)
- Environmental control system (ECS)
- Black box (flight data recorder (FDR) and cockpit voice recorder (CVR))
- Auto-pilot system

It needs to be underlined that, the abovementioned systems may vary depending on the type of aircraft. Independently, whether they are auto-controlled or manually-controlled systems, in the cabin, cargo, or avionics bay, these systems have numerous interfaces in the cockpit panel. Finally, every system is optimized in terms of weight, functionality, and cost-effectivity before implementation. Also, hazardous analyses are performed for figuring out the necessity of the systems.

10.2 Auxiliary Power Unit (APU)

The main duty of the APU is to allow the aircraft to be self-sufficient in terms of pneumatic and electrical power especially during ground operations before main engines run. It is also used during the flight phases in case the main generators are out of order. In other words, the function of the APU differs whether it is operated on the ground or in-flight. If a pneumatic impairment occurs in the main engine, then APU supplies the pressurized and later on conditioned air for cabin pressurization and ice protection for the airframe. The cabin and cockpit require livable conditions in terms of sufficient breathable air and eligible ambient temperature. It is a direct flight safety issue. Without, APU, it is not allowed to long-range flights by the airworthiness authorities. Thanks to APU providing redundancy, the twin-engine jets can fly long distances over the ocean.

10.2.1 *The Flow Mechanism of the APU*

Figure 10.1 illustrates a schematic diagram of a traditional APU, which demonstrates how inlet air is sucked into the APU and separated into two streams [3]. It is noticeable that the left side of the centrifugal compressor is engaged to a pneumatic

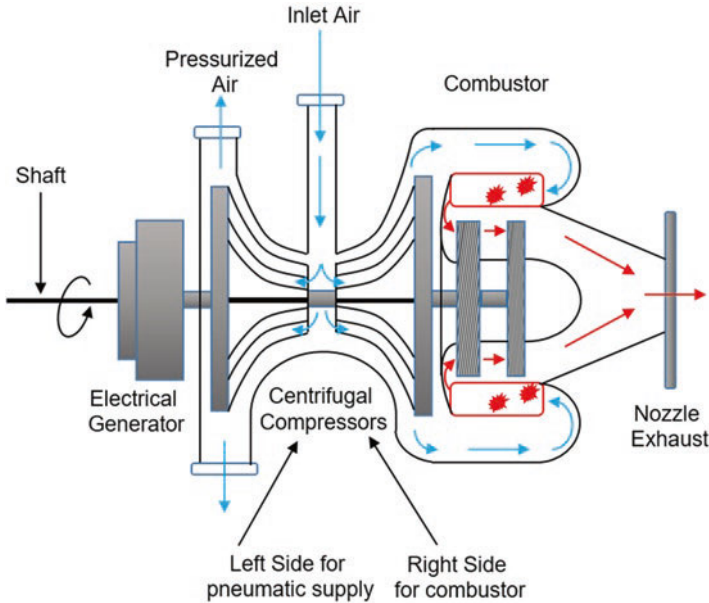


Fig. 10.1 A Typical APU's running mechanism

supply while the right side feeds the combustor. In some models, the electrical generator has a clutch that waits at the idle position when not used.

As shown in Fig. 10.1, a stream passes via a centrifugal compressor located in the middle, which supplies highly pressurized air to a combustion chamber, where fuel is burned. In terms of fuel consumption, it can be said that, during a typical flight, the APU could burn up to 2% of the total used fuel. The hot gases power an axial turbine engine that has two stages. The mentioned hot gases produce shaft power before leaving the exhaust nozzle. It is noteworthy that APUs are generally found at the fuselage tail cone's aft end of the aircraft [4].

As an axial turbine engine, more appropriately called "a turboshaft engine," an APU needs a lot of fresh air to operate as all other turbine engines do. They are "air-breathing" and "fuel-drinking" engines. Generally, there are air intake doors on the top side of the tail cone. These doors are generally motorized. They open when the APU is started. During operation, the secondary air stream is compressed by a second centrifugal compressor that is powered by the primary shaft. The air pressure is boosted to around 50 psi there. Later on, pressurized air is released to power pneumatic and cabin Environmental Control System (ECS). When the electric power generated by the main engine is below the desired level, then the main power shaft of the APU drives the electric generator and hence feeds the aircraft's electrical harness [5].

In some documents, the system may be called as Auxiliary Power System (APS). The APS is an enlarged system that includes an APU engine [6]. As it is illustrated

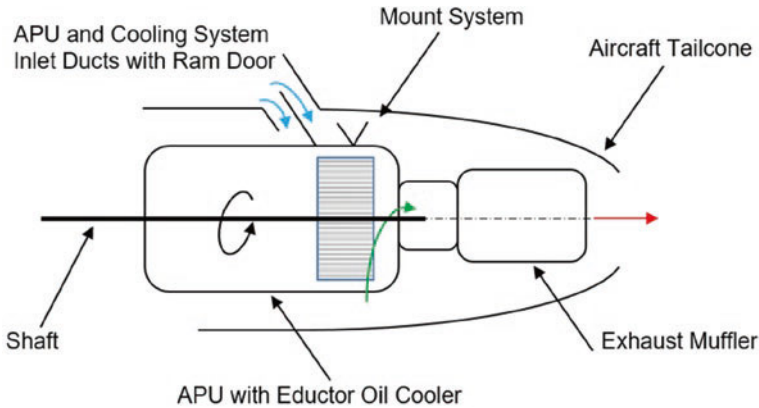


Fig. 10.2 The Schematic of APS

in Fig. 10.2, the APS consists of APU, the mounting system, the ducts that route air into and out of the APU, and the cooling system.

The APU operations may be considered in two ways: on the ground and during flight. On the ground, the APU supplies the air for the environmental conditioning system and running the engines. Besides, it provides electrical power aircraft's inner electrical harness. During the takeoff roll, any aircraft requires maximum power. The APU feeds air to air-conditioning hence preventing a reduction in engine thrust which is crucial during takeoff. During the flight, the APU is the main backup unit that supports the electrical system and air-conditioning. Also in any engine failure during flight, the APU can be used to restart the engines [7]. The APU may be ignited by the power of the aircraft's batteries or a normal electrical system. Eventually, running the APU may be permitted throughout a typical flight envelope that includes the phases such as climb, cruise, descent, and approach.

In some cases, there are additional electronically governed systems equipped with APUs. For example, for a commonly used commercial passenger aircraft such as Airbus A320, the APU's main component is a single-shaft gas turbine that generates bleed air while providing mechanical shaft power to the Accessory Drive Gearbox (ADG). In an Airbus A320, the APUs are controlled by the Electronic Control Box (ECB) which is a full-authority digital electronic controller. The ECB governs the most crucial settings of APU which are given as follow:

- Starts the sequence and keeps track of it
- Monitors the speed and temperature
- Detects the bleed air's flow and temperature
- Puts in order the shutdown stages
- Manages the auto-shutdown function.

In a typical gas turbine engine, the inlet air duck is used for sucking the air. External air can reach the compressor inlet through the air intake and an electrically controlled flap. The electric starter is controlled by the ECB as mentioned

previously. As the air intake is wide open, for engaging the starter, the “master-switch” and the “start-push-button” are both activated simultaneously.

The fuel supply for APU is an important issue because it may adversely impact the reserve fuel level. For managing the fuel level, state-of-art devices are implemented in modern airplanes. In this manner, the features of fuel systems of the A320 APU can be defined as follow:

- The APU is supplied via the left fuel supply line.
- Tank pumps are usually adequate to provide the appropriate pressure.
- When “no pressure” is sensed in the fuel-flow system, the APU fuel pump initiates automatically.
- The ECB is in charge of the fuel supply.

In terms of cooling, it is noteworthy that, the APU has integral independent lubrication and cooling system. The APU’s lubrication system is not powered by the main engines hence it doesn’t affect the main engines’ performance in terms of power generation. The APU’s, IGV control bleed airflow is controlled by a fuel-pressure-powered actuator. In response to aircraft requests, the ECB regulates the actuator. It is noteworthy for APU’s Air Bleed System (ABS) specification that the air bleed system operates on a fully automatic basis. APU’s shaft rotational speed may reach 99% for maintaining the ambient cabin temperature between -18°C and $+35^{\circ}\text{C}$.

To perform a regular shutdown, the cockpit crew employs the controls on the APU panel. In the event of an emergency shutdown, the following precautions may be taken;

- The APU fire handle may be activated by the cockpit crew. It will directly shut down the engine,
- The APU’s shutoff pushbutton located on the interphone panel under the nose fuselage may be activated by the ground crew.

Since the APU is located in the tail cone, it requires special attention for fire control. In the event of a fire in the APU compartment, the following items are realized in the written sequence;

- APU fire alarms are activated automatically
- A warning sound comes in the cockpit
- The Avail light turns on automatically
- The Master-Switch’s light turns on
- The APU is turned off
- The fire extinguisher in the APU bay is activated.

In any circumstances, when the plane is on the ground, the APU can be operated without the need for cockpit crew monitoring. Naturally, it requires mutual communication between ground and cockpit crew. During the flight, while the system is in electrical emergency mode, the APU will not start for a limited time in general 45 s. This buffer time is required for regulating to exchange of electrical flow from main engines to APU.

It needs to be highlighted that the APU is used in vessels and road vehicles that other than, aviation industry. For operational specifications and life estimations, there are many studies and etudes for aircraft, vessel, and land vehicle APUs. Especially for the Maintenance, Repair, and Overhaul (MRO) operations of the APUs, there are many studies in the open literature [8, 9]. It is noteworthy that, during the lifespan, the cost of MRO operations is two to three times higher than ownership prices [9]. It is acceptable for calculation of the Direct Operational Cost (DOC) of APU.

The APUs, like all other aircraft subsystems, must be maintained based on the intervals to meet the desired operational demands. Scheduled maintenance ensures that the APU performs as expected and does not fail. Even if a malfunction occurs, MRO processes are performed to ensure that faulty equipment is recovered quickly. Then the APU is subjected to unscheduled maintenance. The MRO cost is also an important issue. Each segment of scheduled or unscheduled maintenance tasks has a cost associated with it. One option to decrease costs is to automate the diagnosis process by the sensors that don't interfere with the aircraft's functionality but yet collect useful data about the APU. Some developed acoustic sensors are used to collect a wide range of data and contribute to better issue diagnosis. For APU and general structure MRO operations, by removing human engagement from the diagnostic loop, such diagnostic devices can speed up the recovery process, minimize labor-hours spent for troubleshooting, and ultimately reduce Aircraft on the Ground (AOG) time [10].

10.3 Environmental Control System (ECS)

The aircraft is a sealed container, and the cabin air-conditioning should maintain the specifications of 22 ± 2 °C, 90 ± 10 kPa, and $60 \pm 10\%$ relative humidity (RH). These parameters are closely related to external circumstances during flight and taxi. Sometimes the external conditions may be very severe in terms of temperature, pressure, ozone, etc. In general, ECS ensures the ventilation, pressurization, cooling, heating, humidification, dehumidification, demisting, and disinfection systems are running appropriately. The conditioned air enters the cabin and cockpit via wall floor, ceiling grills, and directional outlets in the overhead panel, and exits through the collection ducts under the seats [11, 12].

As it was mentioned previously, that the ECS is in charge of a variety of activities, including pressurizing and ventilation the cabin, managing pressure, and maintaining the temperature in the cabin and cockpit. Mainly, the ECS maintains cabin temperature, pressure, and humidity while also providing air to the anti-ice system and passenger air-conditioner (PAC). Filters, air pumps, humidifiers, driers, valves, and other components are included in the ECS [13].

Air pressure and temperature are important issues for a human to breathe. The air pumps compress the air inside the cabin. The entire aircraft is pressurized with 250 kPa bleed air from the engine compressor, which is located upstream of the

combustion chambers. The temperature of the air is decreased from 180 °C to a breathable level through a precooler unit located in the PAC system. Outflow valves regulate cabin pressure to keep it above 75 kPa, simulating a flight altitude of 7800 ft. Thanks to PAC, the passengers and personnel are expected to be at this level of comfort. The pressurization control system has pneumatic members that are extremely reliable. Any rapid change necessitates an emergency procedure.

While performing these activities inside the cabin, the aircraft also needs some systematic regulations outside. The EPS, on the other hand, is utilized to protect against extreme temperatures, high wind and turbulence, water and ice deposition, radiation, electrical shock, and biological assault from microbes to birds.

It's worth noting that the ECS is implemented not only in airplanes but also in submarines and spaceships. Mainly, the ECS typically includes the following subsystems:

- Window defogging
- Fire protection
- Sanitation and water supply
- Ergonomics of cabin furnishings
- Entertainment systems in the cabin
- Lighting.

Like ECS, there's a similar system called environmental protection system (EPS). The ECS is primarily concerned with the interior of the aircraft, whereas the EPS is responsible for the external environment.

A Boeing 747-400, for instance, has roughly $V_{\text{air}} = 886 \text{ m}^3$ of air. Every 350 s, the air in the Boeing 747-400 is circulated. The remaining half is pulled by fans through special. High-Efficiency Particulate Arresting (HEPA) filters to hold the particles before being evacuated from the aircraft through an outflow valve positioned under the seats. The HEPA filter traps the majority of microorganisms and particles. However, aerosol particles smaller than 0.3 μm (300 nm) cannot be entirely removed by the filter due to the HEPA filter's size limitation. Filters no longer meet the standards of the HEPA filter as their "removal effectiveness" steadily diminishes during operation, and they must be replaced periodically. The mentioned filters' remove and replace periods are adjusted based on the flying hour (FH) and flight cycle (FC) parameters at relevant maintenance intervals. For ensuring hygiene and providing livable conditions it is critical to remove the aerosols. That's why HEPA filters are changed frequently even at high costs [14].

10.4 Black Box (Flight Data Recorder (FDR) and Cockpit Voice Recorder (CVR))

The flight data and aural recording systems have two units called flight data recorder (FDR) and cockpit voice recorder (CVR). Flight recorders are also called "black boxes." In general, they are colored bright orange to aid for being "easy-noticeable"

after an accident. It was named as a black box indicating that the inner mechanism was unknown [15, 16]. When both types of recorders are installed, they are occasionally merged into a single unit as combination recorders per International Civil Aviation Organization (ICAO) regulations. To give detail, both Federal Aviation Administration (FAA) and European Aviation Safety Agency (EASA) member countries have to obey the rules ordered by ICAO. Also, National Airworthiness Authorities (NAA) have to follow rules dictated by FAA, EASA, and ICAO which is relevant.

10.4.1 The Flight Data Recorder (FDR)

FDR is a device that records particular information of aircraft flight conditions. This information may include, velocity, flight path, altitude, heading, engine power, bank angle, direction, flap position, and other operational data. It needs to be highlighted that, any change is logged with a timestamp so the pilots' intentions and activities could be inspected in a sequence.

An FDR's role is to report and record data from several aircraft sensors onto a media that can withstand an accident. The FDRs were first employed in the 1950s. At that time, a metal foil was used as the recording medium in several first-generation FDRs. This metal foil was kept safe in a crash-proof cage put in the plane's rear end. FDRs were mandated to be painted bright orange or bright yellow beginning in 1965 to make them easier to locate at a crash site as was mentioned previously.

In the case of deepwater incidents, the most contemporary FDR systems have an Emergency Locator Transmitter (ELT), and some current, modern recorders also have an Underwater Locator Beacon (ULB) to aid for easy noticing. When the recorder is submerged in water, a component known as a "pinger" activates automatically. It sends out a 37.5 kHz acoustic signal that can be detected by a proper receiver. These transmissions are detectable in all but the deepest oceanic depths with the most recent recorders, but because they are battery-powered, they can only transmit for a limited time.

There are two types of FDR recording mechanisms: digital and analog. Digital data is made up of discrete quantized time (Timestamp), frequency, and amplitude values. Continuous processes with no quantized or discrete deviations make up analog information. As a result, the recorded information is ready for decoding in both systems.

By airworthiness side, an FDR is mandatory for multiengine, turbine-powered aircraft carrying more than 10 passengers [17]. Newly produced airplanes are required by law to monitor at least 88 essential data, including time, altitude, air-speed, heading, and aircraft attitude. In addition, certain FDRs can track over 1000 other in-flight parameters that can help with the inquiry. Anything from flap position to autopilot mode or even smoke alarms can be observed. Regulations mandate that an FDR verification control be performed on an annual basis to ensure that all mandatory parameters are captured. The recorder is typically put in the tail area of the

aircraft, which is the most crash-survivable zone. Survivability is the most important issue for FDR for reaching the required data in it [18].

Investigators can utilize the data generated by the FDR system to assess if an accident was caused by a cockpit crew error, an external incident (such as severe meteorological impacts), or a fault with airplane equipment. Furthermore, these data aids in the enhancement of airplane system design and the ability to foresee possible problems which may increase synchronically with the age of the airplane. Using FDR data to monitor the wear condition of an engine could be an example. Analyzing the data could help in deciding whether or not to replace the engine before it fails.

10.4.2 The Cockpit Voice Recorder (CVR)

The CVR is the other major unit of the black box. CVR's main duty is to log the auditory signals in the flight panel in case of accidents and/or incidents investigations. It records and stores the aural signals (Comments and communication elements) that are transmitted or received from the pilots' headset microphones and earphones. For storing the audio signals, in the beginning, analog magnetic tapes were used. Two reels with the magnetic tape reversing at both ends were used in these early devices. But later on, with the development of technology, CVR took place of the magnetic tape.

The CVRs used in commercial air vehicles have the capability of recording aural signals from four channels for up to 2 h on average. Literature studies show that 2 h of recording is generally enough for aircraft crash investigations. One of the most important features of the CVR is having durability against severe impacts like FDR. In a similar way to FDRs, CVRs are tested against challenging situations also. The modern CVRs are equipped with a solid-state memory which is governed by digital recording techniques. This technology makes them damage-resistant, moisture-proof, and durable against vibration. CVR's chassis is manufactured by the strong and durable material, also the survived memory module. It is worth to be underlined that although the rest of the aircraft was substantially damaged, all data was collected from the accident referred to [18].

In some models, CVRs are fed by the electrical hardware of air vehicles. But in many modern types, they have an inner battery that feeds the CVR. With the malfunction of the wire-harness CVR continues to record and store the voice with the help of the inner battery. Relatively, decreased power requirements of solid-state recorders, it is possible to use small-sized inner batteries.

By the airworthiness side, under ICAO regulations, aircraft manufacturers and operation companies should obey two crucial rules regarding CVR management. The CVR should be capable of preserving the data collected during the last 2 h of flight for the air vehicles given as follow:

- The air vehicles with a maximum takeoff weight are above 5700 kg and an airworthiness certificate is issued after January 01, 1990,

- The helicopters for which the individual certificate of airworthiness was originally granted on or after January 1, 1990

Following the further ICAO regulations, effective January 1, 2007, all aircraft that use data link communications are obliged to be equipped with a CVR to record all data link interactions to and from the aircraft on a flight recorder. Naturally, the CVR should be connected to the cockpit audio and the lowest recording time must be equal to the CVR operation time. The content of the information itself is important but the “timestamp” is also crucial information for aircraft crash investigations. Because of this need, any additional information relevant to data link communications such as “creation time” is also stored in CVR.

10.5 Autopilot System

The word autopilot is used by combining the words “auto” and “pilot.” An autopilot is a device that guides an airplane without the cockpit crew’s controlling input. In the beginning, the autopilots were used to limit the maintaining a consistent heading and altitude, but today’s autopilots can handle every aspect of the flight envelope. It is also from takeoff to landing. The most recent autopilots are directly connected to the Flight Management System (FMS). Also, the auto-thrust/auto-throttle system is a crucial feature of the FMS.

An autopilot system detects and controls the direction, bank angle, altitude, and speed of the aircraft. It converts what it detects into a numerical structure. For instance, in terms of altitude, it compares the numerical value obtained by measuring it with the reference values given in the algorithm in its memory. After benchmarking, it moves on to the decision-making process; if the aircraft is lower than the reference value, it generates signals to climb. Or vice versa, if the aircraft is higher than the reference value, it generates signals to dive. If the set value and current state, deviate even one degree on the compass from the direction it takes the action for yaw movement. At the end of the process, the system activates the actuators on the control surfaces (such as an aileron, flap, horizontal stabilizer, vertical stabilizer, tail rudder).

It should be underlined that the autopilot that is connected to navigation systems has the capability of controlling the air vehicles at all times during the flight. If the aircraft is equipped with an auto-thrust/auto-throttle system, the required power can be automatically adjusted upon takeoff and hence climb safely taken into account its weight and environmental conditions. The purpose is to ensure the aircraft flies at the demanded speed. The air vehicle then en routes at the desired flight level. The thrust is automatically regulated to attain and maintain the demanded speed. Namely, the aircraft sits in the en route pattern and follows the flight plan’s itinerary. If the aircraft is not equipped with an auto-throttle/auto-thrust system, then the cockpit crew should accomplish all power activities necessary for safe flight maneuvers.

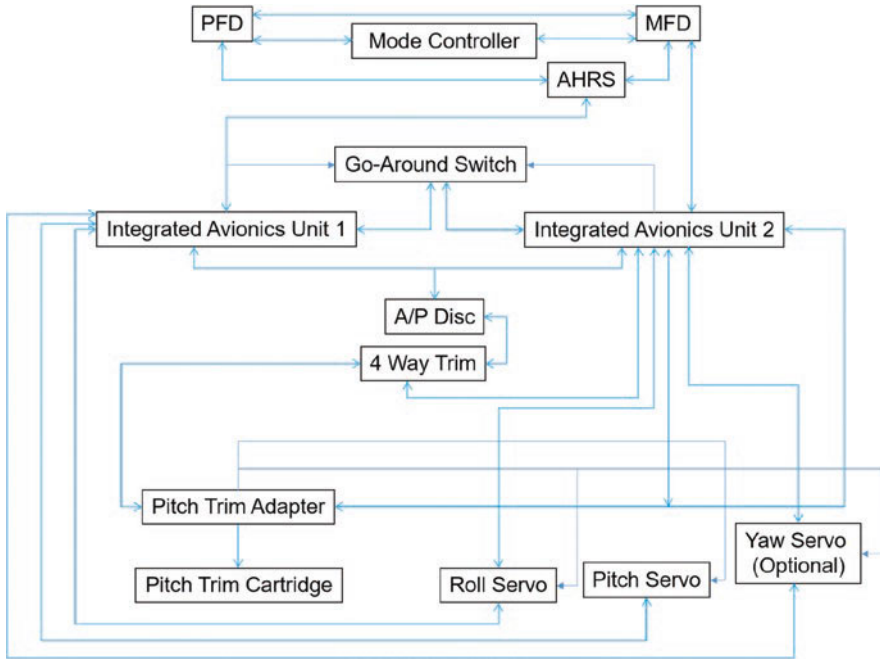


Fig. 10.3 The general architecture of automatic flight control system (AFCS)

There are certain differences between general aviation aircraft and commercial passenger aircraft autopilot systems. In an aircraft registered under general aviation rules, the Automatic Flight Control System (AFCS) is used as “automatic piloting.” The modern general aviation AFCS is sophisticatedly integrated with digital Attitude Heading and Reference Systems (AHRS) and navigational aids such as localizer and glideslope. The AFCS has a slightly different system architecture than analog autopilot systems. Mainly the architecture of the AFCS is based on the philosophy of the intelligent servos govern some of the error correction calculations, and functionality is distributed among several interconnected computers. A control panel connects the servos to dedicated avionics computers and display unit computers. Nevertheless, in an AFCS there is no central autopilot computer [19]. In Fig. 10.3, the general philosophy of AFCS is given.

By making suitable inputs to the autopilot or FMS, the cockpit crew can intervene at any time throughout the flight. In an adverse aircraft situation, the pilot can deactivate the autopilot and resume manual control by pushing a simple switch on the control panel. Modern aircraft include an additional switch or throttle position that allows the pilot to convert from approach to

Take-Off Go-Around mode (TOGA) in an instant time as required. The cockpit crew, should deactivate the autopilot and perform the “missed approach emergency procedure” manually if the aircraft does not have an autonomous go-around option.

10.5.1 Autoland System

As similar to autopilot, the word autoland is used by combining the words “auto” and “landing.” Autoland systems are used to allow landing in circumstances that were too severe for any type of visual landing. However, they can be employed whenever the cockpit crew desires. The autoland system mainly consists of autopilot(s), auto-thrust/auto-throttle, radio altimeters, and nose wheel steering (NWS) controller. The auto-brake system is frequently utilized in conjunction with an autonomous landing, even though it is not part of the autoland system.

According to aircraft manufacturer Boeing Company, the most dangerous phases of any flight are the final approach and landing. Roughly more than half of all fatal accidents occur in these two phases. According to the annual “Boeing Statistical Summary of Commercial Jet Airplane Accidents Worldwide Operations 1959–2019,” 29% of all serious accidents occurred on the phase of “final approach to land.” In the second row, 24% of the serious incidents occurred during landing. As shown in Fig. 10.4, there’s significant friction between landing gear tires and runway [20]. This friction causes the tire to melt. For decreasing the first touch tire melting, there is an angle between the tires and runway surface.

Autoland is a term that defines a system that completely automates the landing phase of an aircraft’s while still allowing the cockpit crew to supervise and monitor the procedure. During the last stages of the approach, the pilots undertake a monitoring position and will only act if a system failure or emergency occurs as well as taxiing the aircraft off the runway and to the parking place after a safe landing.

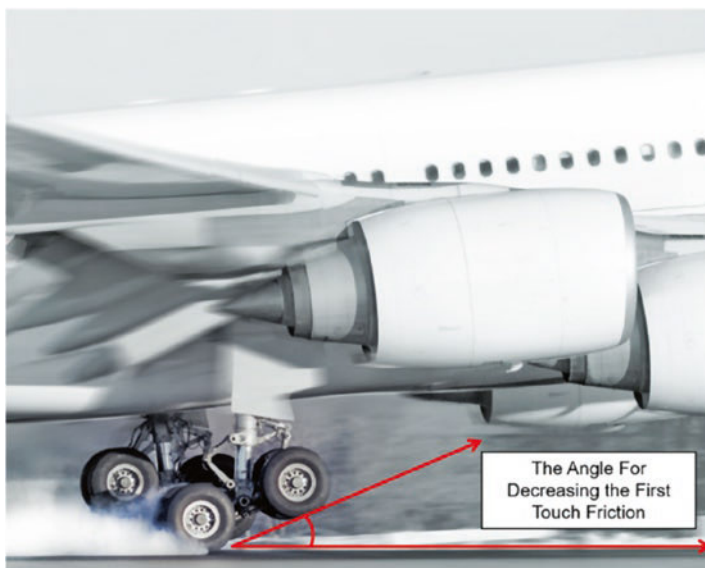


Fig. 10.4 The first touch of the tires

Certain autoland systems, such as Boeing's "fail-passive-system" on the B-737/700 NG, need the cockpit crew to maneuver the aircraft during the runway rollout stage after landing because the autopilot is not coupled to the rudder. On the contrary, the autoland system on the Airbus A-320 and A330 families controls the aircraft onto the runway, first with the rudder and then with the Nose Wheel Steering (NWS) leading aircraft to slow down safely. Without the need for a pilot, a full stop on the centerline can be achieved using the auto-brake. If the NWS is not available, the Quick Reference Handbook (QRH) states that the autopilots must be deactivated as soon as the plane touches down, and the cockpit crew must control the aircraft throughout the rollout.

The cockpit crew should set the Flight Management System (FMS) to establish the aircraft for landing, and then engage the auto-thrust/auto-throttle systems as usual. The autoland system then controls the engine power settings and provides inputs to the aircraft flight controls to maintain the proper approach profile and land the aircraft safely without the need for cockpit crew's intervention. During a manual approach and landing, several systems require the pilot to lower thrust to sometimes to the idle position. When the aural warning calls "Retard" originated from the Enhanced Ground Proximity Warning System (EGPWS), then the cockpit crew adjusted the thrust lever and control the directional changes for a safe landing [21]. Nevertheless, before this time, the auto-thrust/auto-throttle has already lowered the thrust to idle. The retard call is a reminder to the pilot to adjust the thrust levers to the required thrust as it is required. The pilot should select reverse thrust settings in all circumstances. After landing, the autopilots will be turned off so that the aircraft may taxi away from the runway.

The approach can be terminated at any time by activating the TOGA switches or, on an Airbus, by moving the thrust levers to the TOGA position. The autopilot may or may not disconnect at this moment, relying on the aircraft type and autopilot system installed. It can be claimed that almost all modern commercial passenger air vehicles are capable of autoland, which can conduct to TOGA feature.

10.5.2 Instrument Landing System (ILS)

The ILS is a sophisticated runway approach assistance. The Runway Visual Range (RVR) is very important for both landing and takeoff. The RVR is the distance over which a pilot flying on the runway's centerline may see the runway surface markings or lights identifying the runway. In severe weather conditions where the cloud ceiling is low and RVR is poor, ILS allows the aircraft to approach the runway precisely and land safely on the runway. Its philosophy is based on two radio beams that offer both vertical and horizontal direction to the cockpit crew throughout a landing approach. There are two important inputs for an ILS approach: the glideslope and the localizer.

The Glideslope (GS) provides information about the vertical descent profile, while the localizer (LOC) gives azimuth guidance. Marker beacons, Precision

Approach Path Indicators (PAPI) Visual Approach Slope Indicators (VASI), and other high-intensity runway lights may also be used as ILS aids. However, the former ILS are more likely to have been superseded in recent years by a Distance-Measuring Equipment (DME) built into the ILS or one located elsewhere on the airfield, such as with a VHF Omni-Directional Radio Range (VOR) [22]. Figure 10.5 depicts a precision approach using an ILS for an A330-300 type aircraft.

As shown in Fig. 10.6a, the ILS localizers are usually positioned at the runway’s end; they emit two slim crossing beams. One of these beams is emitted slightly from the right side of the runway centerline while the other one is slightly emitted from the left side. They define the “on LOC” indication in the flight deck where they overlap. It is the equipment that broadcasts horizontally on the runway surface and

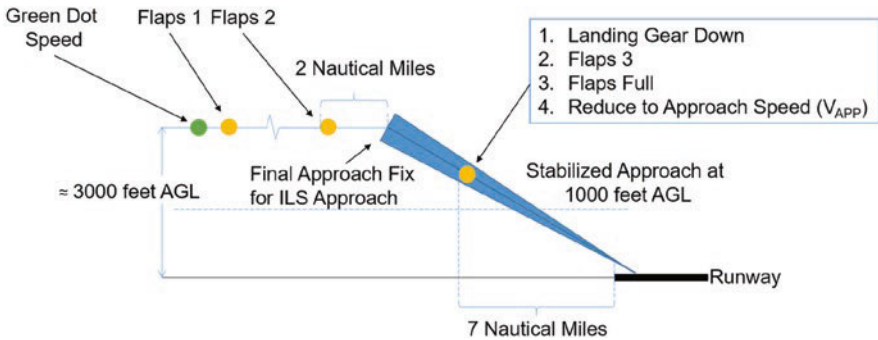


Fig. 10.5 Depict of a generic ILS-approach for Airbus A330-300

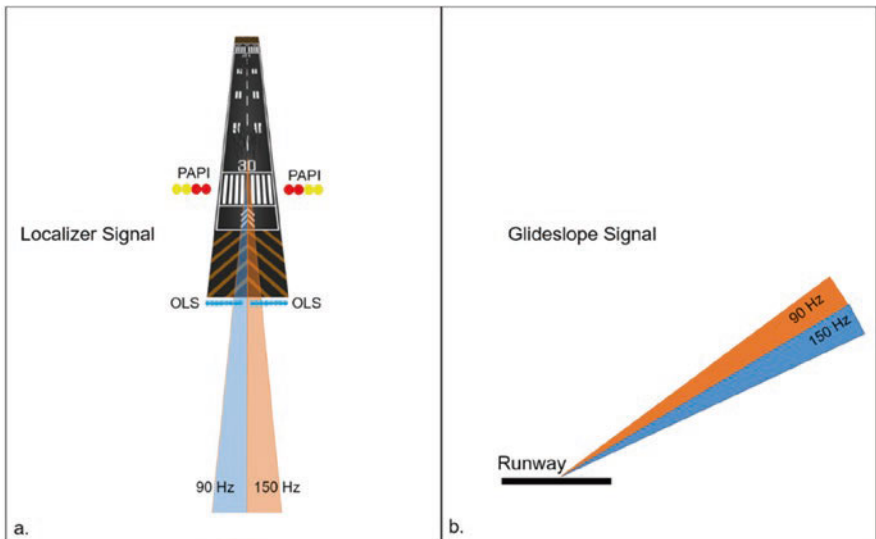


Fig. 10.6 (a) The illustration of the localizer signals and (b) illustration of the localizer signals

in the opposite direction of the landing direction. It leads the aircraft in the direction of the runway axis. It is located 1000 ft (300 m) from the runway end. Localizer transmitters broadcast signals down to 25 nm. In other words, the aircraft starts to receive the signal from 25 nautical miles from the runway extension. It solely gives the runway direction information to the aircraft. The pilot receives data from airborne equipment that shows the aircraft's deviation from the runway centerline [23].

As shown in Fig. 10.6b, The ILS glideslope instruments are also usually installed on the airfield. Similar to, localizer, two narrow intersecting beams are emitted. One of these beams is emitted slightly below the required vertical profile while the other one is emitted slightly above the required vertical profile. They define the “on GS” indication in the flight deck where they overlap. The displacement of the airplane above or below the GS is shown by aircraft equipment. The glideslope instruments are normally positioned so that the glideslope offers a runway threshold crossing height of around 50 ft. The standard GS angle is 3° . However, the modifications may be performed to satisfy specific approach requirements such as terrain or noise reduction [23].

For the ILS approach, three markers are placed on the ILS approach track at predetermined locations from the airport. During the approach pattern, the first marking beacon is the Outer Marker (OM). The OM is often situated 5 nautical miles from the threshold. The following marker beacon is the Middle Marker (MM), which is often situated 1 nautical mile from the threshold. And the final marker is the inner marker (IM). The IM is located at the threshold of the runway.

In a flight envelope, during the approach phase, the pilots follow the ILS guidance until they reach the Decision Height (DH). The DH is the specified lowest height where pilots decide to land or go around. If the RVR is poor or the runway is not eligible for a safe landing then the cockpit crew should initiate a missed approach procedure. In other words, unless the stated visual reference is accessible at the DH may the approach be resumed; otherwise, a go-around process must be initiated.

Special ILS approach categories have been established to allow properly qualified pilots. Also, the special ILS approach requires specifically equipped aircraft and appropriately equipped runways with competent ILS systems to carry out an ILS approach without acquiring a visual reference. Depending on the DH and RVR features, the ILS systems are categorized. The mentioned categories are given in Table 10.1.

Table 10.1 ILS Categories

Category	DH	RVR
Category I	>200 ft	>1800 ft
Category II	Between 100 and 200 ft	ICAO: > 1200 ft. EASA: > 1000 ft
Category III A	<100 ft	<700 ft
Category III B	<50 ft	ICAO: Between 150 and 700 ft. EASA: Between 250 and 700 ft
Category III C	No limit	None

It is noteworthy that there are no DH or RVR constraints while landing in Category IIIC because it is a full autoland with roll-out guidance along the runway centerline. Because of issues with ground maneuver after landing, this category is not currently offered regularly.

In case of an adverse situation, the signal transmission is automatically shut off. In this case, the cockpit crew has an instant display that the ILS is inoperative. Also, Air Traffic Controller (ATC) provides adequate information about the ILS if necessary. All ILS systems are subjected to frequent calibration flights to ensure that signals are being relayed appropriately.

10.6 Conclusions

Aviation safety is combined with two elements: flight safety and ground safety. The ultimate target of aviation safety is the study and practice of managing risks for preventing accidents and incidents through scientific researches. In general, for ensuring aviation safety there are methods used based on the reactive, proactive, and predictive approaches. While designing a component, aviation safety is considered as the main concern while the technical features are shaped accordingly.

Air vehicles are operated under extremely challenging conditions which force aviation safety. For ensuring flight and ground safety air vehicles should be equipped with state-of-art devices. In this chapter, general information regarding APU, ECS, FDR, CVR, and auto-pilot system including ILS has been provided. It is noteworthy that the abovementioned systems are a small part of an aircraft system though they were selected from a crucial equipment perspective. Auxiliary power unit (APU) takes the main engines' role in terms of providing air into the aircraft on the ground. It may be considered as a not vital function. But, in the sky, if the main engines fail, it has a vital role in providing power for the engine re-start procedure. The ECS regulates the environmental conditions for both passengers and cockpit crew. It regulates the oxygen in the cockpit and cabin. Needless to emphasize the cockpit crew cannot operate the aircraft without ECS. The black box is one of the most famous components of an aircraft. It includes the FDR and CVR. When a crash occurs the investigators search for a black box that enlightens the investigation experts. Finally, autopilot and auto-landing systems control the aircraft when the cockpit crew needs to concentrate on other issues such as communication, managing the warning, and caution messages.

In the conclusion, the air vehicles are equipped with system aids given at least but not limited to given in this chapter. In the future with the development of technology, these systems will be more sophisticated and will support aviation safety.

References

1. Science Based Life. Retrieved June 1, 2021, from <https://sciencebasedlife.wordpress.com/2011/07/25/extreme-engineering-the-boeing-747/>.
2. Gurgen, S., Kushan, M. C., & Diltemiz, S. F. (2016). Fatigue failure in aircraft structural components. In *Handbook of materials failure analysis with case studies from the aerospace and automotive industries*. Elsevier.
3. Sforza, P. (2014). Chapter 8—Refined weight and balance estimate. In P. Sforza (Ed.), *Commercial airplane design principles* (pp. 320–321). Butterworth-Heinemann.
4. Greatrix, D. R. (2012). Gas turbine engines: Fundamentals. *Powered Flight*, 147–231. https://doi.org/10.1007/978-1-4471-2485-6_6
5. Ahmed, U., Ali, F., & Jennions, I. (2021). A review of aircraft auxiliary power unit faults, diagnostics and acoustic measurements. *Progress in Aerospace Sciences*, 124, 100721. <https://doi.org/10.1016/j.paerosci.2021.100721>
6. Lavieille, M., Brown, D., & Vieuille, F. (2011). Numerical modeling and experimental validation of the acoustic efficiency of treated ducts on an aircraft auxiliary power system. In *AIAA 2011–2810. 17th AIAA/CEAS aeroacoustics conference (32nd AIAA aeroacoustics conference)*. <https://doi.org/10.2514/6.2011-2810>.
7. Altuntas, O., Ekici, S., Yalin, G., & Karakoc, T. H. (2014). Comparison of Auxiliary Power Unit (APU) and Ground Power Unit (GPU) with life cycle analysis in ground operations: A case study for domestic flight in Turkey. *Applied Mechanics and Materials*, 629, 219–224. <https://doi.org/10.4028/www.scientific.net/AMM.629.219>
8. Yabsley, A., & Ibrahim, Y. (2008). Study on maintenance contribution to Life Cycle Costs: Aircraft Auxiliary Power Unit example. In *2008 IEEE international conference on industrial technology*. <https://doi.org/10.1109/icit.2008.4608331>.
9. Saracyakupoglu, T., & Ates, M. (2020). A methodological research on the correlation between the airborne part manufacturing system and aircraft maintenance operations. *Journal of Green Engineering*, 20(12), 13734–13742.
10. Vunnam, K., & Bouldin, B. (2012). *APU exhaust muffler design improvements through conjugate heat transfer CFD analysis* (Heat transfer, Parts A and B) (Vol. 4). <https://doi.org/10.1115/gt2012-68850>
11. Ozdemir, Y., Ozgoren, M., & Goktepel, I. (2016). Energy analysis for an air-conditioning system of a commercial aircraft: Case study for airbus A330. *International Journal of Energy Applications and Technologies*, 3(2), 60–67.
12. IATA. Cabin Air Quality. Retrieved June 1, 2021, from <https://www.iata.org/en/youandiata/travelers/health/cabin-air/>.
13. Martínez, I. (2011). *Aircraft environmental control*. Retrieved June 3, 2021, from <http://web-server.dmt.upm.es/~isidoroto3/Aircraft%20ECS.pdf>.
14. Min-Ho Lee, W. Y. (2019). Performance assessment of HEPA filter against radioactive aerosols from metal cutting during nuclear decommissioning. *Nuclear Engineering and Technology*, 52(5), 1043–1050.
15. Grose, V. L. (2013). Aircraft flight data recorders. *Encyclopedia of Forensic Sciences*, 327–334. <https://doi.org/10.1016/b978-0-12-382165-2.00129-x>
16. Milosovski, G. (2008). *Improvement Of Aircraft Accident Investigation Through Expert Systems, Doctorate Thesis*. Royal Melbourne Institute of Technology.
17. FAA. (2009). *Advisory circular, airworthiness and operational approval of digital flight data recorder systems*. Retrieved June 5, 2021, from https://www.faa.gov/documentLibrary/media/Advisory_Circular/AC20-141.pdf.
18. Swedish Accident Investigation Authority. (2016). *Accident in Oajevágge, Norrbotten County, Sweden on 8 January 2016 involving the aeroplane SE-DUX of the model CL-600-2B19, operated by West Atlantic Sweden AB*. Retrieved June 7, 2021, from https://www.havkom.se/assets/reports/RL-2016_11e.pdf.

19. Aeronautics Guide Website. Retrieved June 7, 2021, from <https://www.aircraftsystemstech.com/p/automatic-flight-control-system-afcs.html>.
20. Boeing Website. Statistical Summary of Commercial Jet Airplane Accidents, Worldwide Operations, 1959–2019. Retrieved June 7, 2021, from http://www.boeing.com/resources/boeingdotcom/company/about_bca/pdf/statsum.pdf.
21. Skybrary Website. Retrieved June 5, 2021, from <https://www.skybrary.aero/index.php/Autoland>.
22. Struempfel, C., & Lehmann, O. (2017). Challenges and potentials of aircraft noise modeling using enhanced aircraft performance parameters and flight deck procedures. In *INTER-NOISE 2017—46th international congress and exposition on noise control engineering, Hong Kong*, Vol. 255.
23. Boldmethod Website. *How to fly a perfect ILS approach*. Retrieved June 11, 2021, from <https://www.boldmethod.com/learn-to-fly/maneuvers/how-to-fly-a-perfect-ils-approach/>.

Chapter 11

Vibration-Assisted Machining of Aerospace Materials



Ramazan Hakkı Namlu and Bahram Lotfi Sadigh

Nomenclature

1D	One dimension
2D	Two dimension
3D	Three dimension
CD	Cutting direction
kHz	Kilohertz
LUVAM	Longitudinal ultrasonic vibration-assisted machining
MQL	Minimum quantity lubrication
UAM	Ultrasonic assisted machining
UVAM	Ultrasonic vibration-assisted machining
VAM	Vibration-assisted machining
VD	Vibration direction

Greek

φ_0	Initial angle
w	Angular velocity

R. H. Namlu (✉) · B. L. Sadigh
Department of Manufacturing Engineering, Atılım University, Ankara, Turkey
e-mail: ramazan.namlu@atilim.edu.tr

11.1 Introduction

Intense market competitions, enhanced performance requirements, or new technology developments demand new products with much efficient design, higher stability, improved functionality, etc. One of the oldest human dreams is to fly and sense the incredible feeling of being free in the sky and to be able to have interstellar journeys, travel to other planets, discover the vast universe, and maybe meet any other living alien species or even civilizations. Not so long ago, even flying was considered an inaccessible human ability, but as science and technology developed, it became a daily routine. However, the endless human desire to discover even more pushes the edges of known science and technology to reach even more challenging distant targets. Aerospace is one of the frontier industrial sectors requiring higher technologies and consumes new products in different aspects like producing better aircraft, space ships, satellites, etc. For instance, today, aircraft are evolving rapidly to be faster, environmentally friendly, economical, durable, or have better maneuverability or reliability. These qualities require lighter, more robust materials with some superior mechanical, electrical, or chemical properties. Traditional materials such as steel and aluminum alloys cannot meet these demands sufficiently. Therefore, new materials with excellent requested properties are needed.

Examples of these materials are engineering alloys, composites, and superalloys. They provide these required specifications with their superior characteristics; Ti-6Al-4V and Inconel 718 have high wear resistance, which is needed to eliminate air friction. Composite materials have lightweights with high durability required for removing the heavyweight effect on aircraft fuel. No need to say to produce parts out of these materials require some shaping. Many manufacturing processes make the end product from raw materials such as forging, casting, and machining. Machining is one of the most commonly used manufacturing processes in several fields. It is a subtractive manufacturing process, and since it shapes the product by removing chips from the workpiece, direct mechanical contact between the tool and the workpiece is inevitable. Thus, these new materials' mentioned superior mechanical properties become an obstacle for machining operations; and, the process's efficiency reduces severely.

Modern machining methods are mainly turning, milling, drilling, and grinding. Their history dates back to the middle of the nineteenth century. After the invention of the steam engine, developments in machining methods gain speed. Machining processes with 100 years of history are the most widespread and commonly used manufacturing processes in the industry. Nevertheless, as mentioned before, the new advanced materials are quite different from the materials that have been used in years. Machining that kind of materials is challenging due to their material characteristics; for example, these materials' high wear resistance is not a desired feature for machining. Cutting tools can be worn out more quickly, and tool life decreases severely. These kinds of materials are categorized as difficult-to-cut materials due to their low machinability. However, it is still needed to form these materials, so that it is required to develop machining processes' capabilities to deal with such problems.

There are new techniques called hybrid machining methods that are invented to cope with low machinability problems. Nontraditional machining methods take advantage of traditional machining processes and add new technological developments to enhance efficiency by providing chemical, thermal, or mechanical energy sources to the chip removal process to reduce the cost and improve product quality.

Vibration-assisted machining is one of these nontraditional machining processes that use mechanical energy sources to facilitate the process. The process is generally carried out by adding high frequency and low amplitude vibrations to the chip removal process. The first use of vibration-assisted machining is developed in the 1960s. However, it gained popularity at the beginning of the 2000s. The main reason for these 40 years of unpopularity is the lack of need for such processes in those years. However, as mentioned before, with new and advanced materials, the benefits of vibration-assisted machining are required today.

Vibration-assisted machining has many advantages over the traditional machining process. It can decrease the cutting forces so that the required power is reducing; the tool life lasts longer; therefore, cutting tool cost is getting lower, and surface finish is smoother than the traditional machining process.

In this chapter, a detailed literature survey on the effects of vibrations on the performance of various machining processes, including turning, milling, drilling, and cutting advanced aerospace materials, is systematically summarized and discussed. At the end of this chapter, a case study is provided to understand the topic deeply.

11.2 Classification of Vibration-Assisted Machining Systems

In most vibration-assisted machining applications, the vibration frequency is in the ultrasonic range (more than 20 kHz) called ultrasonic-assisted machining. The ultrasonic-assisted devices are mainly divided into three groups: one-directional ultrasonic vibration-assisted devices (1D UVAM), 2-D ultrasonic vibration-assisted devices (2D UVAM), and finally, 3-D ultrasonic vibration-assisted devices (3D UVAM). They are categorized based on the vibration directions of the tool and/or the workpiece. There are numerous studies about 1D UVAM and 2D UAM, but there is a lack of research on 3D UVAM. Nowadays, 3D UVAM researches are getting more popular. 1D UVAM and 2D UVAM have two subgroups, as shown in Fig. 11.1. can be divided into two subgroups. “Vertical direction of cutting” and “axial direction of cutting” are subgroups of 1D UVAM [1, 2], while “Elliptical vibration-assisted machining” and “spindle vibration-assisted machining” are subgroups of 2D UVAM [3, 4]. 3D UVAM has not been a subgroup yet and it mainly contains cutting tool vibration [5]. It is crucial to study these three categories in detail as each one’s effects on process outputs are quite different. 1D UVAM’s vibrations can be either longitudinal and torsional direction, in 2D UVAM the vibrations are in both directions. Longitudinal vibrations are mostly seen as depth of cut directions but torsional vibrations are generally in feed directions.

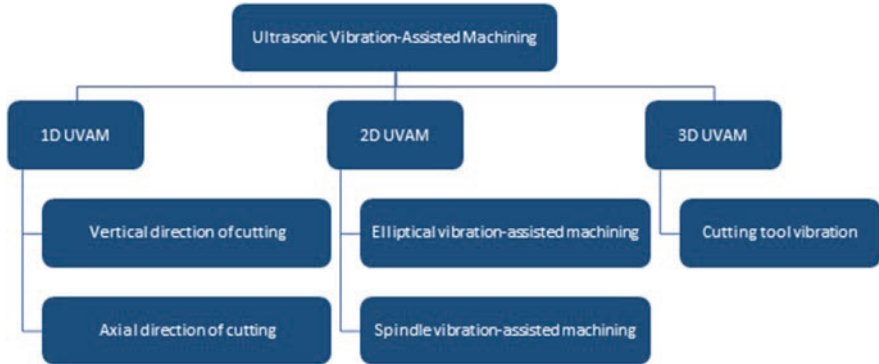


Fig. 11.1 Classification of ultrasonic vibration-assisted machining

Frequency is essential for vibration-assisted machining. There are two main system behaviors when applying the frequency to the process. They are categorized as resonant and nonresonant systems. Both of the systems have some benefits and weaknesses. Nonresonant type systems cannot gain high frequencies. Their working limit is around 11 kHz [6]. But resonant-type systems can achieve up to 40 kHz frequency [7]. This difference is based on their working principles. Resonant vibration implemented systems work at the system's natural frequency, which means the system can operate at ultrasonic frequencies. However, nonresonant type systems' frequency and amplitude values should change through time [7]. Generally, the system's process efficiency increases with increasing frequency; in other words, resonant type systems give a better cutting performance. Also, changing the frequency and amplitude values of the nonresonant type systems may lead to complex tool movements and difficult to solve analytical models. Vibration-assisted machining process is used in different kind of machining applications. Figure 11.2 shows the detailed classifications.

It is important to understand the different vibration directions in UVAM, as can be seen in Fig. 11.3 vibrations in different directions can be applied for each axis. These applied vibrations can be applied on each axis on their own, or multiple axes can be applied in combination with each other. Which direction to vibrate generally depends on the process to be applied. For example, in drilling operations, since the cutting tool moves only in the Z-axis direction, it may be sufficient to give the vibrations in the longitudinal direction. However, if a more complex operation such as milling is applied, it may be more useful to vibrate in more than one axes [7]. In the UVAM literature, it is still being investigated whether vibration in which axes is beneficial for which process.

Multiple phases occur when applying vibration during cutting. As seen in Fig. 11.4, it can be seen that there is a three-stage cutting during a feed direction cutting.

Stage 1: While the cutting tool is moving in the cutting direction (CD), it is pulled back toward the vibration direction (VD) due to the applied vibration.

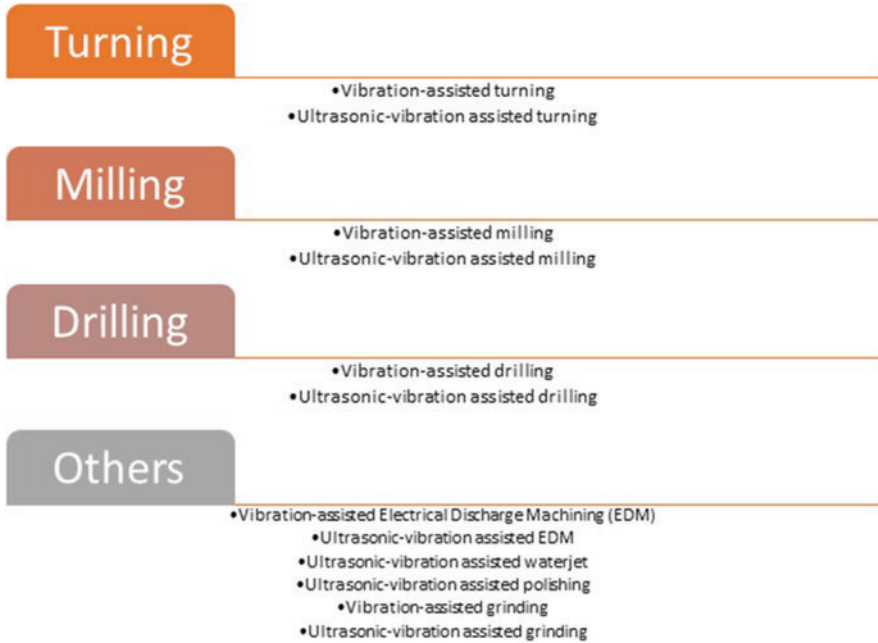


Fig. 11.2 Different vibration-assisted machining processes

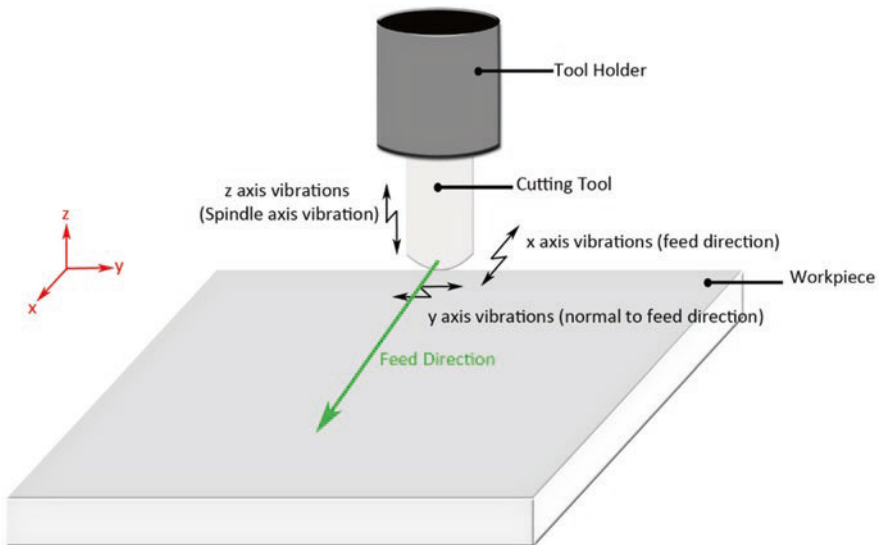


Fig. 11.3 Possible vibration directions

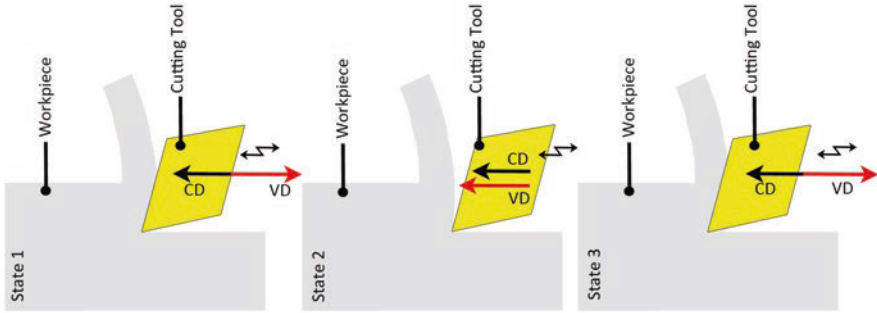


Fig. 11.4 Cutting stages of feed direction vibrations

Stage 2: The cutting tool retracting in the VD direction momentarily moves away from the workpiece completely. At this point, the cutting forces theoretically decrease to zero. The cutting tool finds time to cool down by getting away from the heat generated during cutting.

Stage 3: The cutting tool continues to advance in the CD direction. The VD direction no longer moves backward but forwards because the vibrations are harmonic.

This cycle continues until the interrupt ends.

11.2.1 One-Dimensional UVAM (1D UVAM) Method

1D UVAM methods are the most commonly used UVAM method because of their basic configuration and application. There is plenty of research about 1D UVAM available in the literature. Zhong and Ling conducted diamond turning experiments on metal matrix composite (MMC) reinforced with SiC particles which is the desired material for the aerospace manufacturing industry due to its high strength and light weightness. Outcomes of research reveal that the surface roughness of the MMC is enhanced using ultrasonic vibration compared to traditional machining [8].

Shen et al. [9] conducted micro-end-milling experiments with ultrasonic vibration-assisted milling of aluminum alloy. According to their research, the surface roughness of the bottom of the slots is higher when ultrasonic vibrations are used; however, at surfaces of vertical sidewalls, the roughness decreased with the help of ultrasonic vibrations. Aluminum alloys are widely used in the aerospace sector for their lightweight. However, different aluminum alloys have different material properties. Most aluminum alloys have low strength, but some aluminum alloys have high strength in aviation. One of the most common is the 2024-T3 aluminum alloy; it has high strength and high fatigue resistance and is generally used in aircraft structures like wings and fuselage. Another one is 6061-T6 aluminum alloy, which has excellent corrosion resistance together with good weldability. This material is used in aircraft landing mats, the aircraft's body, and other structural

components. 7075 is another aluminum alloy that is used in the aerospace industry. It has high strength with good machinability [10].

Nath and Rahman [11] researched the ultrasonic vibration-assisted turning of Inconel 718. They reveal that after applying vibrations, cutting forces and the tool flank wear are decreased. Therefore, the tool life is increased four to eight times over the conventional turning method, and surface roughness enhances around 75–85%. It is important to note that Inconel 718 is a highly demanded material for the aerospace industry sector due to its high corrosion resistance, good creep, and fatigue strength even at high temperatures (around 700 °C) [12]. Its excellent properties at elevated temperatures are used in gas turbine engines and rockets where high-temperature resistance with good mechanical properties is needed. More than 30% of an aircraft engine's total weight is made by Inconel 718 [13]. Due to its high hardness and low thermal conductivity of the Inconel 718 is considered a difficult-to-cut material, and the application of UVAM can improve the conditions for machining this alloy.

Hsu et al. investigated the performance of UVAM on MAR-M247 nickel-based superalloy. This material is demanded in aircraft applications due to its good mechanical properties at low (−200 °C) and elevated (700 °C) temperatures [14]. However, its machining is challenging due to heat accumulation on tip of the tool when the process occurs, which leads to built-up edge formation, which is an undesirable phenomenon. It is found out that since ultrasonic-assisted milling creates an intermittent contact, the cutting temperature is reduced, and consequently, it leads to higher tool life and better surface roughness.

Sofuoğlu et al. [15] investigated the ultrasonic-assisted turning on another important aerospace alloy which is Hastelloy-X. When ultrasonically assisted turning is used, it positively affects surface roughness and stable cutting depth. However, the cutting tool tip temperature is getting a little higher due to external energy implementation.

Grooving tungsten carbide with ultrasonic vibrations to investigate the ductile chip formation studied by Liu et al. [16]. The results reveal that the critical value of cutting depth for the transition from ductile to brittle in UVAM grooving is around three times larger than the conventional grooving process. Tungsten carbide materials pose high hardness, good resistance to wear, and excellent toughness; therefore, they are widely used in the aviation industry [17].

Ostasevicius et al. [18] researched ultrasonic-assisted end milling of stainless steel and titanium alloy, with ultrasonic vibrations. This research shows that surface roughness is decreased compared to ultrasonic-assisted end-milling operation compared to conventional end-milling operation. One of the most used titanium alloys in the aerospace industry is Ti-6Al-4V which has high wear resistance and adequate strength to weight ratio [19]. The properties mentioned above make this material a suitable substance to get used mostly in jet engine parts. On the other hand, this high wear resistance and low thermal conductivity make this material difficult to cut [20]. Nevertheless, as can be seen in the example given, with the application of ultrasonic vibrations, the cutting performance can be increased significantly in machining difficult-to-cut material.

Babitsky et al. [21] conducted a series of experiments about ultrasonic vibration-assisted drilling of carbon fiber/resin composite material. They gave ultrasonic vibrations to a standard twist drill with a longitudinal transducer. Resultant cutting forces decreased up to 90% compared to conventional drilling applications in these experiments. Carbon fiber composite materials show good strength, high stiffness, and strength-to-weight ratio properties; therefore, they make these materials much desired in aircraft where lightweight with good strength is needed [22]. They have some advantages over traditional materials, such as shorter manufacturing cycles, low energy consumption, and manufacturing cost [23]. As shown in the example, UVAM dramatically increases machining applications' performance on carbon fiber composite materials. This research made a series of drilling experiments with and without ultrasonic vibrations on aluminum material. The research shows when ultrasonic vibrations are applied on the exit of the drilled hole, the size of cratering is lower with respect to traditional drilling. The fall of the cutting forces significantly affects the deformation of the drilling process.

Halim et al. [24] investigated ultrasonic-assisted milling of carbon fiber-reinforced plastic as well. In ultrasonic-assisted milling, cutting forces are 10% lower than the traditional process and machining temperature decreases. Carbon fiber-reinforced plastic has desirable properties for the aerospace sector, such as good strength and high stiffness to weight ratio. In some aerospace applications, carbon fiber reinforced plastic can reduce the total mass up to 40% compared to aluminum and with the same material properties. This makes it possible to be replaceable with aluminum in the aerospace application where lightweight is needed.

11.2.2 Two-Dimensional UVAM (2D UVAM) Method

Another method of implementing ultrasonic vibrations in metal-cutting processes is the two-dimensional UVAM (2D UVAM) method. 2D UVAM method improves cutting performance much better than the 1D UVAM method in many cases. Since its design and implementation are relatively complicated compared to 1D UVAM methods, the usage of 2D UVAM methods is beginning after decades of the invention of 1D UVAM methods. In aircraft and general aerospace materials, 2D UVAM methods have some significant advantages over traditional machining; therefore, many studies have investigated the effects of 2D methods on machining materials with low machinability.

One of the earliest researches in this field is done by Shamoto et al., which is about the ultraprecision turning of hardened die stainless steel with 2D UVAM [25]. In this research, a novel elliptical vibration device with a feedback control system is developed, and as a result of controlled vibration shape accuracy of 0.2 μm is reached. Also, with vibration control, more steady cutting forces are obtained. Stainless steels are commonly used in aerospace applications because of their high corrosion resistance and their ability to maintain their mechanical properties within a wide temperature range. Some of their used application in aircraft applications are fuel tanks, exhaust systems, and landing gear components [26].

Another study is done by Liu et al. [27]. Their research is based on rotary ultrasonic elliptical machining of carbon fiber-reinforced plastics. In the experiments, holes on carbon fiber reinforced plastic are drilled. Compared to conventional drilling, 2D ultrasonic vibrated drilling requires lower cutting forces due to the elliptical separating cutting mechanism. Also, washing away the chips is more accessible because ultrasonic vibrations have some cleaning effect. The intermittent cutting mechanism decreases the excessive heat on the cutting tool tip, leading to a reduction in tool wear and an enhancement in tool life. Similarly, due to improved surface quality on the edges of holes, more precise drilled holes are obtained.

Another research on the application of 2D UVAM on carbon fibre-reinforced plastics is a rotary ultrasonic elliptical machining is done by Geng et al. [28]. This time the machining process is side milling. According to their experiments' outputs, the side machined surfaces' quality is better in rotary ultrasonic elliptical machining than conventional milling and this could be due to rotary ultrasonic elliptical machining's separating cutting mode. Besides, as a result of an intermittent cutting mechanism, lower cutting forces and decreased tool wear are obtained from rotary ultrasonic elliptical machining process.

Suzuki et al. [29] studied the elliptical vibration machining of tungsten alloy, and outcomes show that tool wear and adhesion are decreased using this method compared to conventional machining. Tungsten alloys are well known for aerospace applications due to their capability in operating normally at elevated temperatures.

Tungsten alloy machining is the subject of another study conducted by Guo et al. [7]. They researched micro polishing of tungsten carbide materials with a magnetostrictive vibrating device. The device gives two-dimensional elliptical vibrations to the cutting process. As a result of giving 9.2 kHz circular vibrations in the polishing process, surface roughness values of 9 nm R_z and 1 nm R_a are obtained. These results are better than experiments with lateral vibrations. The study confirms that two-directional vibration is better than one directional vibration in polishing tungsten carbide alloys. Tungsten carbide materials have a higher weight; however, they are most widely used in counterweight and balancing the mass in rotorcraft blades due to their higher resistance to wear. This high resistance to wear, machining of this material is a challenging issue [30]. This is where ultrasonic vibration-assisted machining has come into play, and with the help of ultrasonic vibrations, the machining process performance is enhanced considerably.

Ding et al. [31] developed a 2D vibration-assisted micro-end-milling technique and implemented it on aluminum 6061 alloys. Their proposed model consists of two piezoelectric actuators to give the vibrations. In this research, the results from simulations and experimental studies are compared. Besides, an integrated model to simulate surface generation is developed. The simulation study agreed with the experimental results. According to the outcomes, the data obtained with a suitable and smooth simulation can be compatible with the experimental data under conditions where 2D vibrations are given. In light of this information, it can be said that the number of experiments can be reduced, and simulations can be studied instead. Hence, the necessity to make the excessive number of experiments is eliminated, and by simulating the various cutting conditions, reliable results are obtained, and the required time and budget are reduced.

Yin et al. [32] developed a unique ultrasonic elliptical vibratory device and made an experimental study on LY12 aluminum alloy. According to their study, average cutting forces are decreased by 65% in elliptical vibration cutting than conventional cutting. In surface roughness results, it is indicated that the average R_a value is $0.08 \mu\text{m}$ in ultrasonic elliptical vibration cutting and it is improved with respect to conventional cutting. LY12 aluminum alloy is a widely used material in aircraft structures. It is classified as “hard aluminum” due to its ingredients. It has high strength and heat resistance at a certain level. Its strength is higher than 2024 and 7075 aluminum alloys at temperatures above 125°C . However, corrosion resistance of the LY12 aluminum alloy is poor, which is not acceptable in aerospace applications, and in most cases, to eliminate this shortcoming, it needs to be coated.

11.2.3 Three-Dimensional UVAM (3D UVAM) Methods

As seen in the previous sections, studies have been carried out on 1D and 2D vibrations for years and these studies continue today. 3D vibration methods have become an increasingly popular subject of research in the last few years. In general, methods with 2D vibrations are observed to increase their process performance compared to 1D vibrations, and methods with 3D vibrations are also studied from this perspective. However, like every developing technology, 3D vibration methods have many missing or unknown points. Tracking the tool trajectory becomes more complicated than 1D and 2D methods. Some 3D vibration methods have run with closed-loop control using displacement sensors and have been able to achieve smoother motions.

Methods with 3D vibration are not widely used in macro machining yet. However, there are 3D vibration methods developed for micromachining processes recently [33]. Micromachining is also a widely used process in aerospace applications. Successful results have been obtained in applying 3D vibrations in the micromachining of Ti-6Al-4V [34].

11.2.4 Differences Between Different Vibration-Assisted Methods

As mentioned before, there are multiple methods and applications in vibration-assisted machining. According to the working principle, there are resonant and non-resonant systems. Considering the vibration axes, there are 1D, 2D, and 3D vibrational systems. Each method has its weaknesses and strengths.

If we compare resonant systems and nonresonant systems, resonant systems generally operate with vibration frequencies at the ultrasonic level; therefore, it is very advantageous to machining difficult-to-cut materials. Considering that materials such as Ti-6Al-4V, Inconel 718, etc., are difficult to cut class in aerospace materials, they are very suitable for this sector. Also, considering that they operate at a fixed frequency, it is an advantage that resonant systems are more straightforward in terms of installation and application. However, the basic principle of working at this fixed frequency value is to operate at the system's natural frequency. This can turn into a disadvantage by limiting the frequency values that can be studied. Besides, closed-loop control is also challenging to obtain as it operates at high frequencies.

In nonresonant systems, the working area limitation is more flexible since it can be applied at the variable frequency and amplitude values. Likewise, since closed-loop control can be obtained more efficiently, it is possible to follow the used movements more accurately. However, in 2D and 3D systems, movement accuracy may not be obtained since the operation of transducers independent from each other at different frequencies will cause the coupling effect. The necessity of establishing complex systems to get rid of this situation can be seen as another disadvantage.

Considering systems in which the number of axes to which vibrations are given varies, it can be said that systems with 1D vibration systems can be worked more stable with the simple structure of the systems, easy installation, and noncomplex movements. However, considering most 2D and 3D vibrating systems, it is seen that systems with 1D vibration are higher in terms of process efficiency. However, the complex structure of the systems with vibrations in more than one axis, the coupling effect problem, and the related movements that are difficult to control are among these systems' weaknesses.

11.3 Kinematics of Vibration-Assisted Machining

In order to explain the effects of UVAM, it's crucial to understand its kinematics. The tool tip's (C_0) trajectory equations of CM as follows where r is the cutting tool radius (mm), n is the spindle speed (r/min);

$$x(t) = r \sin(2\pi nt) \quad (11.1)$$

$$y(t) = r \cos(2\pi nt) \quad (11.2)$$

$$z(t) = 0 \quad (11.3)$$

There can be three harmonic vibration directions which consist of X, Y, and Z directions. When vibrations are applied in all axis, tooltip trajectories from equations above turns into this [35];

$$x(t) = r \sin\left(\frac{2\pi nt}{60} + \frac{A_T}{r} \cos(2\pi ft) + \varphi_0\right) \quad (11.4)$$

$$y(t) = r \cos\left(\frac{2\pi nt}{60} + \frac{A_T}{r} \cos(2\pi ft) + \varphi_0\right) + v_y t \quad (11.5)$$

$$z(t) = A_L \sin(2\pi ft) \quad (11.6)$$

v_y is the feed rate (mm/min), A_T is the amplitude of torsional direction (μm), A_L is the amplitude of longitudinal direction (μm) and finally, φ_0 is the initial angle (rad) which is zero at the beginning. Eq. (11.1) helps to find out the angular velocity w as;

$$w = \frac{2\pi n}{60} - 2\pi f \frac{A_T}{r} \sin(2\pi ft) \quad (11.7)$$

If $2\pi f \frac{A_T}{r} > \frac{2\pi n}{60}$, at frequency f there will be a separation between the cutting tool and the workpiece. However, when $2\pi f \frac{A_T}{r} < \frac{2\pi n}{60}$, the cutting process becomes continuous. So that there is a critical speed, which can be found as:

$$n_{\text{critical}} = \frac{60 f A_T}{r}$$

It is important to note that this critical rotation speed is very crucial to calculate whether the vibration system implements discontinuous cutting or continuous cutting. If the critical cutting speed is passed, the benefits of the vibration system cannot be achieved [35].

Equations (11.4)–(11.6) are essential to understand the how vibrated cutting process occurs. It is vital to know the vibration effect on the cutting tooltip. For further investigation, let's assume that we have longitudinal vibrations that are used in a UVAM process. When longitudinal vibrations are implemented, only the Z direction harmonic vibration is applied, therefore only Eq. (11.6) is used. In order to see the other ultrasonic vibrations effect, it is important to find out the velocity v_z and acceleration a_z :

$$z_{\text{LUVAM}}(t) = A_L \sin(2\pi ft + \varphi_0) \quad (11.8)$$

$$v_{z\text{LUVAM}}(t) = A_L 2\pi f \cos(2\pi ft + \varphi_0) \quad (11.9)$$

$$a_{z\text{LUVAM}}(t) = -A_L (2\pi f)^2 \sin(2\pi ft + \varphi_0) \quad (11.10)$$

The velocity v_z and acceleration a_z can be used for finding the cutting tool tip trajectory with the aim of investigating the process better, for example, they can be

used for what will happen when different number of cutter is used or velocity changes. This kinematic analysis can be applied for X and Y direction vibrations too.

11.4 Machining Characteristics of Vibration-Assisted Machining

The effects of applying vibrations on various axes on machining hard-to-cut materials are discussed in previous sections. However, it is essential to examine the outputs of operational efficiency and quality during and after machining. These outputs directly affect the operation's stability, the quality of the manufactured part, the power spent during production, and the production cost. Examples of these include cutting force, surface quality, and tool life. In this section, the outputs obtained while vibration-assisted machining is applied to aerospace manufacturing materials are examined.

11.4.1 Surface Roughness

Surface roughness is a factor that directly affects surface quality. Damages in surface quality and subsurface affect the quality of the produced part, which is crucial in aerospace products. High surface roughness in features such as aircraft wings or tails can adversely affect the outflow. Due to such situations, it is necessary to investigate the effect of any process on surface quality. Many studies are conducted on vibration-assisted machining and its impact on surface quality.

Since 1D methods are the first vibration-assisted methods that emerged, early studies are made on these methods [36]. Generally, improved surface quality is observed compared to traditional machining processes if ultrasonic vibrations are applied on many different materials in the same cutting conditions or cutting tool types. This result is attributed to multiple reasons. One of them is that chip formation is smoother, discrete, and discontinuous in vibration-assisted machining, so the chips removed during the process leave fewer marks on the surface. Another important issue is reduced built-up edge formation in vibration-assisted machining, which decreases the traces created by the cutting tool on the machined surface. The intermittent cutting mechanism in vibration-assisted machining processes lessens the period cutting tool in contact with the workpiece, which reduces the friction and temperature in the cutting zone. Reduction in the cutting zone temperature decreases tool temperature and tool wear and consequently enhances the machined surface quality.

Vibration parameters also have an impact on surface quality. In a study which conducted by Lian et al. on aluminum alloy [37], it is observed that after a certain point, any increase in ultrasonic vibration amplitude negatively affects the surface

quality. Therefore, it is more important to use the optimum value rather than increasing the amplitude continuously. Zhu et al. also performed a similar experiment on Ti-6AL-4V using vibration-assisted machining. Results show that the surface quality increased up to 45% [38], and again this result is obtained in specific vibration amplitude. SiCp/Al composite material, a composite used in turbine rotor blades, skins, and truss of aircraft.

11.4.2 Tool Life

Tool life and tool wear concepts have an important place as machining outputs. The cutting tool wears out due to friction, and after a particular time, the dull cutting tool becomes unusable. The cutting tool's cost is one of the most important parameters for calculating total process cost, especially when machining hard-to-cut materials used in the aerospace sector in the issue. Machine tools need to be consumed continuously, and a large number of tools are needed to carry out machining processes. The cost of the cutting tool itself and the period of production downtime when changing the cutting tool is an additional cost. For such reasons, reducing tool wear and increasing the cutting tool's life can make a massive contribution to the production cost. Most of the materials used in the aerospace manufacturing sector are classified as difficult to cut materials and cause the tool life to expire in a short time. Hence, any technological advancements that reduce tool wear and increase tool life are greatly appreciated by manufacturers, especially those active in the aerospace industry. Many studies on vibration-assisted machining have revealed that this hybrid method reduces tool wear compared to traditional methods. Ibrahim et al. [39] observed that tool wear is reduced around 40% in vibration-assisted milling compared to conventional milling. The research conducted by Janghorbanian et al. [40] on AISI 304 material shows that when the appropriate cutting speed is selected, the tool life is longer in vibration-assisted machining compared to traditional machining. According to work, not getting the same effect at each cutting speed is the change in the impact between the cutting tool and the workpiece. If the optimum value is not found, this will adversely affect tool wear.

According to the study published by Zhang et al. [41], tool wear in the high-speed ultrasonic vibrating cutting of titanium alloy material is reduced compared to conventional machining. However, the rate of this reduction decreases as the cutting speed increases. While the highest tool wear difference in dry cutting is found at 200 m/min cutting speed, there is hardly any difference in cutting speed of 350 m/min. This is thought to be due to exceeding critical cutting speed or getting too close to that value, where ultrasonic vibrations lose their effect in the turning process. At the experiments with cutting fluids, tool life increases in both conventional machining and ultrasonic vibration-assisted machining compared to dry cutting. It is also detected that the tool life increased 2.3 times in ultrasonic vibration-assisted machining. According to this result, it is seen that the use of coolant can be recommended to see the performance-enhancing effect of ultrasonic vibrations fully.

11.4.3 Cutting Forces

Cutting forces are one of the most important outcomes of a machining operation. Some performance parameters such as the power spent in the machining operation, process stability, and specific cutting energy are calculated based on measured cutting forces. Cutting forces are measured with a dynamometer and in machining operations using different axes, cutting forces appear in different directions. For example, while the cutting force generated in the drilling process is only in the Z direction, the cutting force can be seen in three different X, Y, and Z axes in milling operations. Regardless of the axis, the decrease in the cutting force causes the resultant cutting force to decrease. The formula of the resultant cutting force is as follows:

$$F_R = \sqrt{F_X^2 + F_Y^2 + F_Z^2} \quad (11.11)$$

Lower cutting forces mean less power and energy consumption as well as a more stable operation. As stated before, less power and energy leads to cost savings in the manufacturing of parts. It has been observed in many studies that cutting forces can be decreased in vibration-assisted machining to cut materials with low machinability.

In a study conducted by Peng et al. [42], the high-speed ultrasonic vibrating cutting method is investigated in the turning process of hardened steel. Compared to the traditional method, the average principal and thrust shear forces decrease under all conditions when ultrasonic vibrations are applied. The reduction in principal cutting forces can be up to 70%, while the reduction in thrust cutting forces can be as high as 80%. The reason for the decrease in cutting forces is explained by intermittent cutting mechanism in vibration-assisted machining. In addition, both cutting forces increased with increasing feed and cutting depth.

In a study conducted by Peng et al. [43], the high-speed ultrasonic vibrating cutting method of Inconel 718 material is investigated in turning operation. When ultrasonic vibrations are applied, it is observed that the cutting forces generally decrease compared to the traditional method. However, the cutting force differences between the traditional method and the ultrasonic vibrating method decrease as the feed increases. This situation can be explained as follows: in each cutting cycle, an intermittent cutting occurs because of vibration. The cutting tool separates from the workpiece and moves back and contacts the workpiece. The separation state is called the non-cutting stage, and the recontacting process is called the cutting stage. Non-cutting stage time decreases as the feed increases. In this case, the cutting stage, that is, the time in contact between the cutting tool and the workpiece increases. In general, the cutting tool–workpiece separation space is decreasing. This process gets closer to the continuous cutting process as the feed increases. This explains why the difference in cutting forces decreases as the feed increases.

Zhang et al. [41] investigated the effect of vibration-assisted machining on the turning of titanium alloy materials. The traditional method and the ultrasonic vibration method are compared at different cutting speeds. It is seen that in the ultrasonic-assisted machining process, the cutting forces are less than the conventional

machining process. The highest difference between the cutting forces is at 200 m/min with 40%. However, it is observed that the cutting force decreases even further in higher cutting speeds. This situation is thought to be due to the decrease in the tool-workpiece separation time mentioned earlier. Besides, it is observed that both the primary cutting force and thrust cutting force increase as the cutting speed increases. In the research, tool wear is also examined, and it is stated that the cutting forces decrease the tool wear as they affect the adhesion.

According to Llanos et al. [44], in an ultrasonic-assisted milling operation on Ti-6Al-4V, a titanium alloy used in the aerospace sector, the cutting forces decrease compared to conventional milling. According to the standard deviation of the reduction in the cutting force components F_t (tangential force), F_a (axial force), and in F_r (radial force) values, the tangential force decreases by 4.76%, axial force by 8.6%. Finally, the radial force decreases by 9.04%.

Another study on Ti-6Al-4V material is carried out by Ni et al. [45] differently from other studies; the use of ultrasonic vibration-assisted milling methods together with a new cooling system, minimum quantity lubrication (MQL), is investigated in this study. Although ultrasonic vibration-assisted milling alone reduces cutting forces compared to conventional milling, it is observed that cutting forces are reduced at a much higher rate when the MQL technique also is applied. The rate of reduction in cutting forces ranging from 10 to 40% in ultrasonic vibration-assisted milling is increased to 30 to 55% when MQL and ultrasonic vibration-assisted milling are used together. This situation can be explained as follows. During the intermittent cutting caused by ultrasonic vibrations, a gap occurs between the workpiece and the cutting tool. At this time, MQL can penetrate the gap formed when applied to the cutting area as an aerosol spray. Cavitation occurs with ultrasonic vibrations, which increases the effectiveness of both MQL and ultrasonic vibration-assisted milling.

11.4.4 Other Benefits and Limitations of VAM

As seen in the previous sections, VAM provides significant benefits in many outputs. Apart from the previously mentioned surface roughness, cutting forces, and tool wear, it also directly affects many other outputs. Chip shapes are one of them, as it is known, chip formations have an important place in the machining process and affect many variables from process stability to tool life. In studies on VAM, it has been observed that there is a noticeable improvement in chip formations. In the study, thinner chip thickness and higher shear angle were obtained when VAM was used, and this was considered as the main factor in the reduction of cutting forces, which is the other output of the study. In addition, high shear angle and thin chip thicknesses led to a decrease in shear plane resistance to cutting and also reduced shear deformation. Apart from surface roughness, surface integrity is also an important factor in examining surface quality. In this regard, VAM appears to be a very beneficial process. In a study on the use of VAM in CFRP material [28], the

following findings were obtained; when VAM is used in the side surface section, the surface integrity is less impaired, and fiber pullout, which is an important factor for surface integrity in composite materials, is decreased. In addition, the trace left by the cutting tool on the surface has also decreased, thus a smoother surface has been obtained.

Although VAM has many positive aspects, it also has some limitations. In processes using resonant vibrations, it is necessary to stay at high frequencies consistently. In order to remain stable at these frequencies, a perfect control mechanism must be used. This requires a decent control process. Although high efficiency is achieved with resonant vibrations, the use of more complex systems can also present problems. Another problem with 2D UVAM and 3D UVAM is phase lag. In systems using more than one transducer or piezoelectric ring, vibration movements can also act independently of each other, since there is more than one vibration source. This creates phase lag, which can reduce process efficiency. Another point is that the benefits of using VAM in every material and process have not been investigated yet, which causes us to draw conclusions on the limited number of materials we have.

11.5 Case Study (Longitudinal Vibrated Ultrasonic-Assisted Milling of Ti-6Al-4V)

11.5.1 Introduction

In the previous sections, various experiments and their results from the literature are surveyed. In order to dig more into the details of vibration-assisted machining, in this section, the milling process performed on Ti-6Al-4V material by ultrasonic vibration in the longitudinal direction [46] is examined.

Ti-6Al-4V is a material commonly used in aircraft construction, as mentioned in previous chapters. This material's properties, such as wear resistance, good strength-to-weight ratio, high fatigue strength, have made it one of the indispensable materials of the aerospace manufacturing industry. The chemical, physical, and mechanical properties of this material are given in Tables 11.1, 11.2, and 11.3, respectively [47]. Unfortunately, some of these material properties make it difficult to machining and put it in the difficult-to-cut materials category. These features include low thermal conductivity and high wear resistance. Due to its high wear resistance, very high friction occurs between the cutting tool and the workpiece. This friction generates heat and the low thermal conductivity of the material keeps the generated heat in the cutting zone. Therefore, a heat concentration occurs in the cutting zone and this accumulated heat causes the cutting tool tip to lose strength, wear quickly, and consequently, make its tool life shorter and deteriorate the machined surface with high surface roughness. Many alternative processes are tried to eliminate such undesirable situations; one of them is vibration-assisted machining. Techniques such as

ultrasonic vibration-assisted turning [15], ultrasonic vibration-assisted milling [45], along feed direction are tested in the machining of Ti-6Al-4V material, and successful results are obtained.

In this case study, the effect of ultrasonic vibrations given in the Z-axis (in the *longitudinal* direction) in the milling process is experimentally investigated. The cutting force results during the experiments are inspected. In addition, two different depth of cuts for finishing and rough cutting operations are studied in this research.

11.5.2 Material and Method

The workpiece used in the experiments is Ti-6Al-4V Grade 5. In order to perform the finish cut and rough cut experiments, samples in different sizes are 90 mm × 55 mm × 15 mm dimension samples are prepared for the finishing operations, and 80 mm × 60 mm × 70 mm dimension samples are prepared for the rough cutting experiments.

TiAlN coated solid carbide milling cutters, one of the most suitable cutting tools for cutting Ti-6Al-4V [46], are used in the experiments. Tool diameters are 10 mm and have a 35° helix angle. After each experiment, a new cutting tool is used to eliminate the tool wear effect in the following experiments. The cutting tool's detailed view can be seen in Fig. 11.5, properties of the cutting tool can be seen in Table 11.4. Experiments are made on the VTEC brand 4-axis CNC milling machine depicted in Fig. 11.6.

In the study, ultrasonic vibrations are given by an ultrasonic tool holder. The ultrasonic tool holder can be seen in Fig. 11.7. The ultrasonic tool holder can convert the electrical energy it receives into mechanical, i.e., vibration energy, through the transducers. This electricity is also transmitted with the help of an ultrasonic generator. Other technical details about the ultrasonic tool holder can be seen in Table 11.5. The ultrasonic system in the experiments is a resonant vibration system, the vibration frequency is fixed at 19 kHz, and the 10 μm amplitude value has been selected.

In all experiments, the samples are attached to the dynamometer in order to measure the cutting forces. The samples attached to the dynamometer can be seen in Fig. 11.8. 926B model Kistler brand dynamometer is used to measure the cutting

Table 11.1 Chemical composition of Ti-6Al-4V

Component	wt%
Al	6
Fe (Max)	0.25
O	Max 0.2
Ti	90
V	4

Table 11.2 Physical properties of Ti-6Al-4V

Property	Typical value
Density g/cm ³ (lb/cu in)	4.42 (0.159)
Melting range °C ± 15 °C (°F)	1649 (3000)
Specific heat J/kg.°C (BTU/lb./°F)	560 (0.134)
Volume electrical resistivity ohm.cm (ohm.in)	170 (67)
Thermal conductivity W/m.K (BTU/ft.h.°F)	7.2 (67)

Table 11.3 Mechanical properties of Ti-6Al-4V

Property	Minimum value	Typical value
Tensile strength MPa (ksi)	897 (130)	1000 (145)
0.2% Proof stress MPa (ksi)	828 (120)	910 (132)
Elongation over 2 in. %	10	18
Reduction in area %	20	
Elastic modulus GPa (Msi)		114 (17)
Hardness Rockwell C		36

forces. 5070A type charge amplifier is also used to amplify the signals coming from the sensors in the dynamometer, and 5697A1 type data acquisition is used to transfer the data obtained with the amplified signals to the computer. The dynamometer's sensor placement and how it calculates the cutting forces from these sensors are given in Fig. 11.9 [48].

Another subject investigated in this research besides ultrasonic vibration-assisted milling is minimum quantity lubrication (MQL). MQL is one of the new operations used to increase efficiency in machining processes, such as vibration-assisted machining. MQL is a technology that generally mixes a minimal amount of oil with air and transmits the aerosol formed at high pressure to the cutting zone through a nozzle. Traditional cutting fluids consume up to 2000 L/h flow rate; however, MQL provides a significant advantage by minimizing this consumption. In the study, MQL is used at a 50 mL/h flow rate. This low consumption causes minor damage to the environment, better protects the operator's health, and reduces oil consumption costs [49]. In addition, it has been shown in many studies that MQL is more efficient than traditional cutting fluids in many issues such as cutting force, surface quality, tool wear [49]. Ester-based oil is used in the MQL system; it is aimed to minimize the friction between the cutting tool and the workpiece with the high lubricating properties of these oils. The spraying pressure of MQL is 8 bar and a 5 mm diameter nozzle is used.

Calculation of the three forces F_x , F_y , F_z

Fig. 11.5 Cutting tool used in the experiments



Table 11.4 Properties of cutting tools

Brand model	STOCK-64551
Base material	Carbide
Coating	TiAlN
Number of cutting edge	4
Diameter (mm)	10
Helix angle	35°

$$F_x = F_{x1+2} + F_{x3+4}$$

$$F_y = F_{y1+4} + F_{y2+3}$$

$$F_z = F_{z1} + F_{z2} + F_{z3} + F_{z4}$$

MQL and ultrasonic tool holder can be seen in Fig. 11.10. The general scheme of the experimental setup is given in Fig. 11.11.

In order to see the interaction of all experimental parameters with each other, a full factorial experimental design is applied; 0.3 mm cutting depth is chosen for the finishing operations and 3 mm cutting depth for the rough cutting experiments. Cutting speed and feed values are the values recommended by the cutting tool manufacturer. The entire experimental design can be seen in Table 11.6.

11.5.3 Results

It is possible to detect ultrasonic vibrations through cutting force measurements. Figure 11.12 shows the Z-axis's cutting forces in one of the experiments without ultrasonic vibrations, i.e., conventional milling. As expected in the slot milling process, the forces on the Z-axis are very close to zero. On the other hand, Fig. 11.13 shows the Z-axis forces in one experiment with ultrasonic vibration-assisted milling. As can be seen, the Z-axis forces are slightly increased and move very frequently due to the ultrasonic vibration in the longitudinal direction. It is observed that this is caused by the separation of the cutting tool and workpiece 19,000 times per second (19 kHz). As a result of these data, the presence of ultrasonic vibrations is visible. Although ultrasonic vibrations in the longitudinal direction are most pronounced in the Z-axis forces, as expected, their effect can also be seen in the other



Fig. 11.6 CNC Milling Center used in the experiments

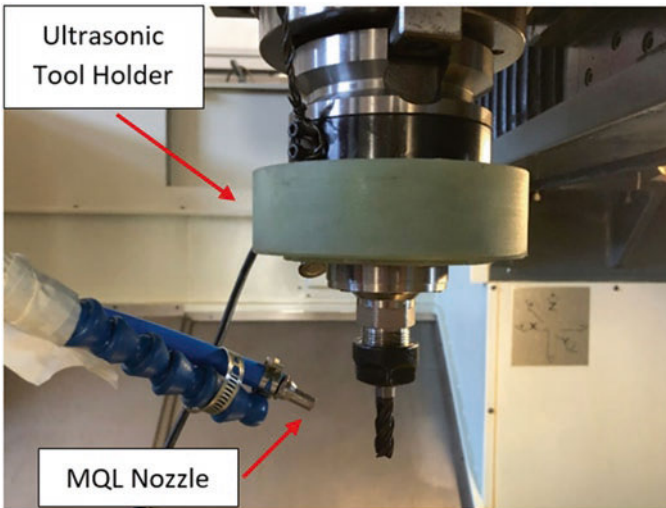


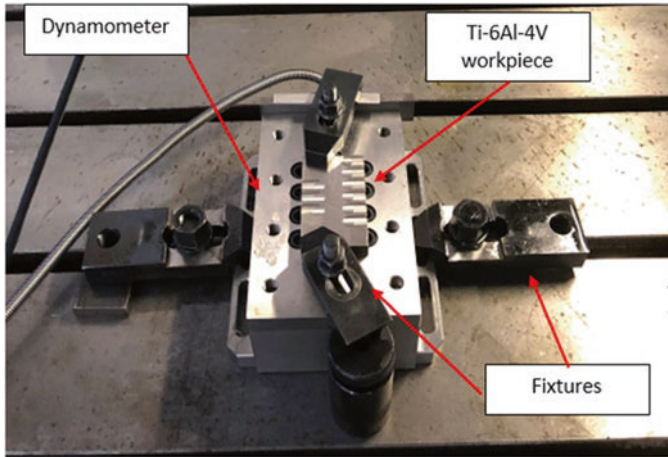
Fig. 11.7 The ultrasonic tool holder used in the experiments

direction forces. Figures 11.14 and 11.15 show the X direction's cutting forces in two different experiments with and without ultrasonic vibration. In Fig. 11.14, sharper peaks are seen, with more fluctuations due to vibration. The presence of ultrasonic vibrations affected the X direction's cutting forces, but it is seen that this interaction is not at the level in the Z-axis.

In cutting force measurements, quite different results are found between finish and rough cutting operations. In the finishing operations using ultrasonic

Table 11.5 Technical parameters of the ultrasonic vibration system

Technical parameters	Values
Tool holder type	BT50
Working frequency	15–21 kHz
Amplitude	10 μm or more
Matching tool	2–13 mm

**Fig. 11.8** Dynamometer and workpiece placement

vibration-assisted milling, it is observed that the cutting forces are higher than conventional milling regardless of any other variable, and the difference is found to be around 20% on average. In addition, as the speed and feed increase, the difference in cutting forces between ultrasonic-assisted milling and conventional milling also increases. It is observed that the lowest cutting forces are obtained from the combination of traditional milling and MQL combined. The highest cutting forces are observed in the experiments where ultrasonic vibration-assisted milling and dry cutting are used together. MQL always gives lower cutting forces than dry cutting, regardless of all other parameters. It is also detected that shear forces tend to increase with increasing cutting speed and feed.

The cutting force outputs of the rough cutting experiments show that in all experiments using ultrasonic vibration-assisted milling, the cutting force is always lower than conventional milling and the difference is around 25%. Like finishing operations, as the feed and cutting speed increase, the differences in cutting force between traditional milling and ultrasonic vibration-assisted milling tend to increase. The lowest cutting forces are achieved from MQL and ultrasonic vibration-assisted milling combinations. The highest cutting forces are obtained with conventional milling and dry cutting combination. The coolant effect is the same as in finishing

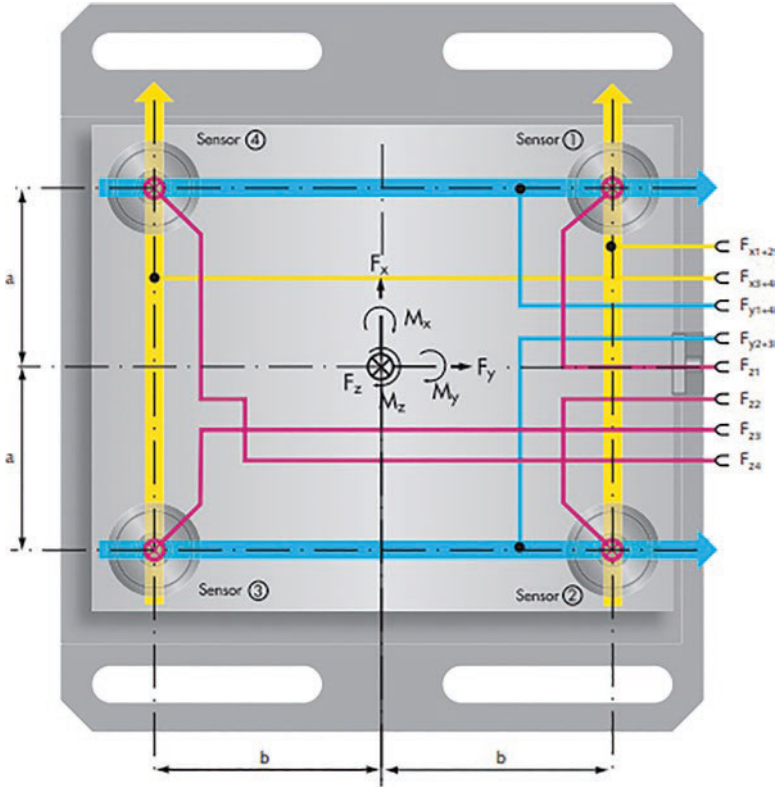


Fig. 11.9 Sensor placements of dynamometer

operations, and in experiments using MQL, lower cutting forces are always obtained compared to dry cutting. Cutting forces tend to increase as the cutting speed and feed increase. Results are given for finish and rough cutting operations in Figs. 11.16 and 11.17.

11.5.4 Discussion

Results show that finish and rough cutting operations have different outputs as can be shown in Figs. 11.16 and 11.17. While the cutting forces are expected to decrease in ultrasonic vibration-assisted milling, the finish cut results do not fit this case. The main reason for this is thought to be the ultrasonic vibrations in the longitudinal axis. It is known that the amplitude of ultrasonic vibrations is $10\ \mu\text{m}$. In finish cut experiments, the depth of cut is taken as $0.3\ \text{mm}$, but this value in the rough cutting experiments is $3\ \text{mm}$. In this case, the ultrasonic vibration amplitude is proportionally closer to the depth of cut in the finish cut than in the rough cut. Considering the

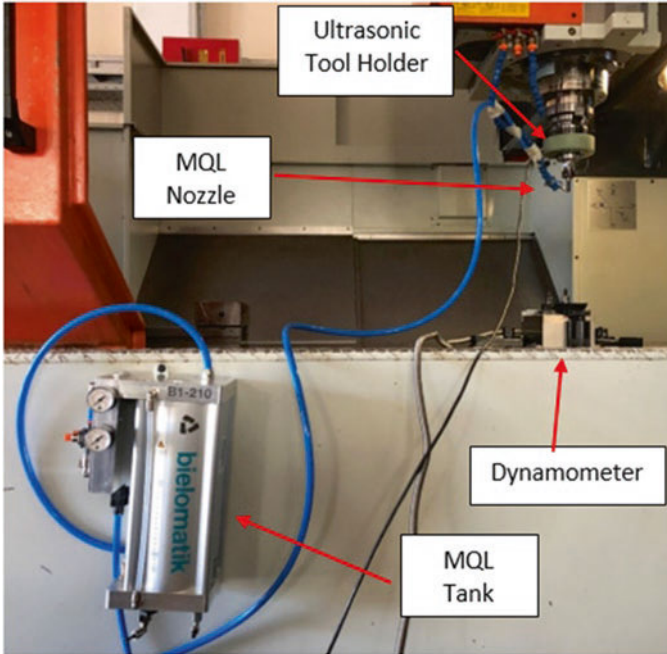


Fig. 11.10 MQL and ultrasonic vibration system together

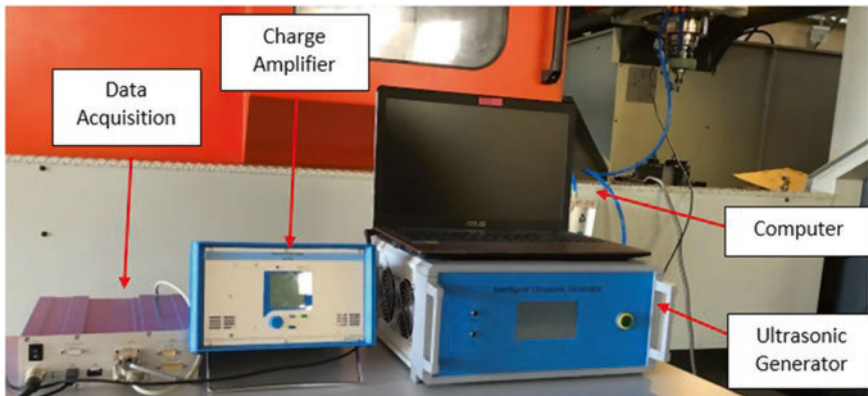


Fig. 11.11 Experimental setup

vibration-assisted machining mechanism, it is known that the cutting tool tip engages with the workpiece to the frequency value per second and with a retraction equal to the amplitude value. In this case, these impacts create a “hammering effect” on the surface. This hammering effect tends to increase the forces in the Z-axis and the forces in the other direction. In finishing operations, since cutting forces are smaller than rough cut, the hammering effect has a considerable impact on the

Table 11.6 Design of experiments

RPM/cutting speed (m/min)	Feed (mm/tooth)	Depth of cut (mm)	Frequency (kHz)	Amplitude (μm)
1500/47.12	0.03	0.3	19	10
1500/47.12	0.04	0.3	19	10
1500/47.12	0.05	0.3	19	10
1500/47.12	0.03	0.3	–	–
1500/47.12	0.04	0.3	–	–
1500/47.12	0.05	0.3	–	–
1500/47.12	0.03	3	19	10
1500/47.12	0.04	3	19	10
1500/47.12	0.05	3	19	10
1500/47.12	0.03	3	–	–
1500/47.12	0.04	3	–	–
1500/47.12	0.05	3	–	–
2000/62.9	0.03	0.3	19	10
2000/62.9	0.04	0.3	19	10
2000/62.9	0.05	0.3	19	10
2000/62.9	0.03	0.3	–	–
2000/62.9	0.04	0.3	–	–
2000/62.9	0.05	0.3	–	–
2000/62.9	0.03	3	19	10
2000/62.9	0.04	3	19	10
2000/62.9	0.05	3	19	10
2000/62.9	0.03	3	–	–
2000/62.9	0.04	3	–	–
2000/62.9	0.05	3	–	–
2500/78.5	0.03	0.3	19	10
2500/78.5	0.04	0.3	19	10
2500/78.5	0.05	0.3	19	10
2500/78.5	0.03	0.3	–	–
2500/78.5	0.04	0.3	–	–
2500/78.5	0.05	0.3	–	–
2500/78.5	0.03	3	19	10
2500/78.5	0.04	3	19	10
2500/78.5	0.05	3	19	10
2500/78.5	0.03	3	–	–
2500/78.5	0.04	3	–	–
2500/78.5	0.05	3	–	–

results; therefore, it increases overall cutting forces in vibration-assisted finishing operations. This phenomenon has positive effects like reducing the temperature and friction in the cutting zone due to the instant separation of the cutting tool from the surface of the workpiece. However, the hammer effect's negative side is dominant. In this case, it can be thought that the resultant cutting force may increase



Fig. 11.12 Z-direction cutting forces in traditional milling (finish cut)

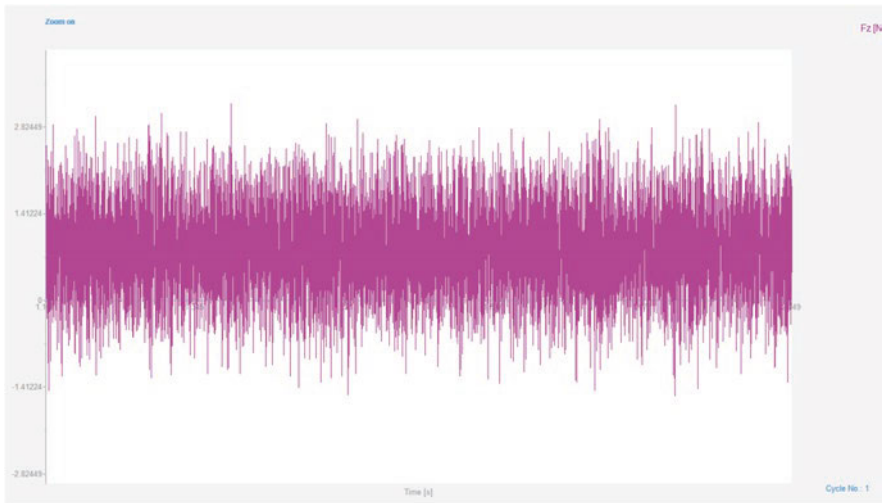


Fig. 11.13 Z-direction cutting forces in ultrasonic vibration-assisted milling (finish cut)

accordingly. But, in traditional milling, since the cutting forces will not be exposed to this “hammering effect,” it is predicted that lower cutting forces may occur. If we look at the rough cut results, the previously mentioned amplitude ratio to the depth of cut is relatively high this time. Although the hammer effect is still valid, it is thought that it is reaching a level that can now be ignored due to higher cutting forces. At this point, the positive effects such as reducing friction can now suppress the hammer effect, which reduces the cutting forces.

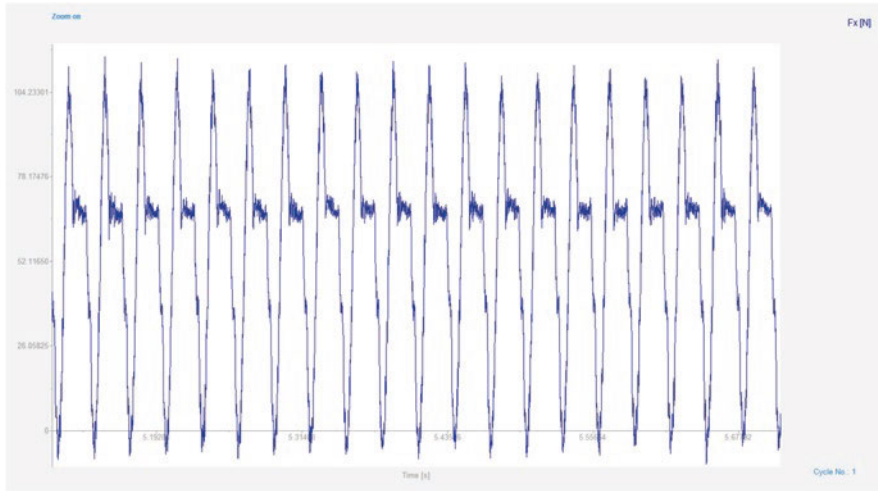


Fig. 11.14 X-direction cutting force in ultrasonic-vibration assisted milling (finish cut)

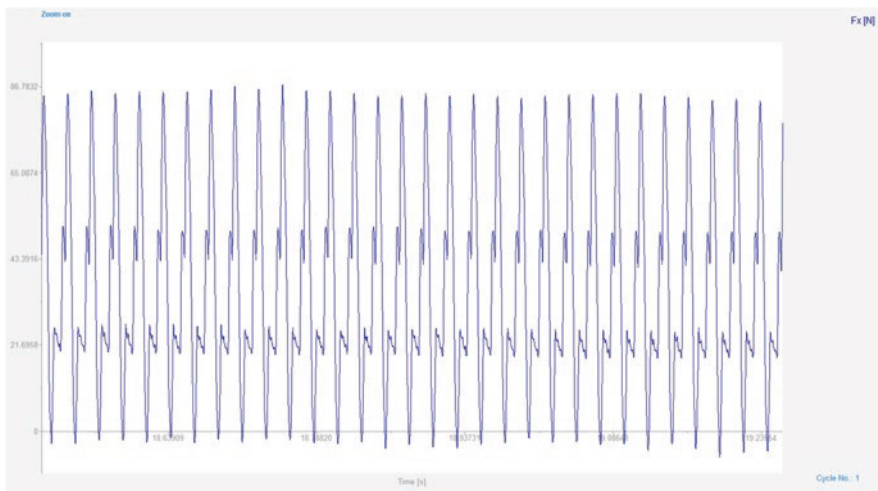


Fig. 11.15 X-direction cutting forces in traditional milling (finish cut)

Due to the intermittent cutting mechanism, recurrent separations of tool and workpiece happen, and consequently, a gap between the cutting tool and workpiece is created. Simultaneous application of MQL in the process helps aerosols penetrate even more to space between tool and part and cool down cutting zone temperature more than traditional processes, and thus the cutting forces are decreased. Therefore, the efficiency of the MQL also increases thanks to ultrasonic vibrations.

The effects of feed and cutting speed, which are other cutting parameters, on cutting forces can be explained as follows. In almost all experiments, regardless of

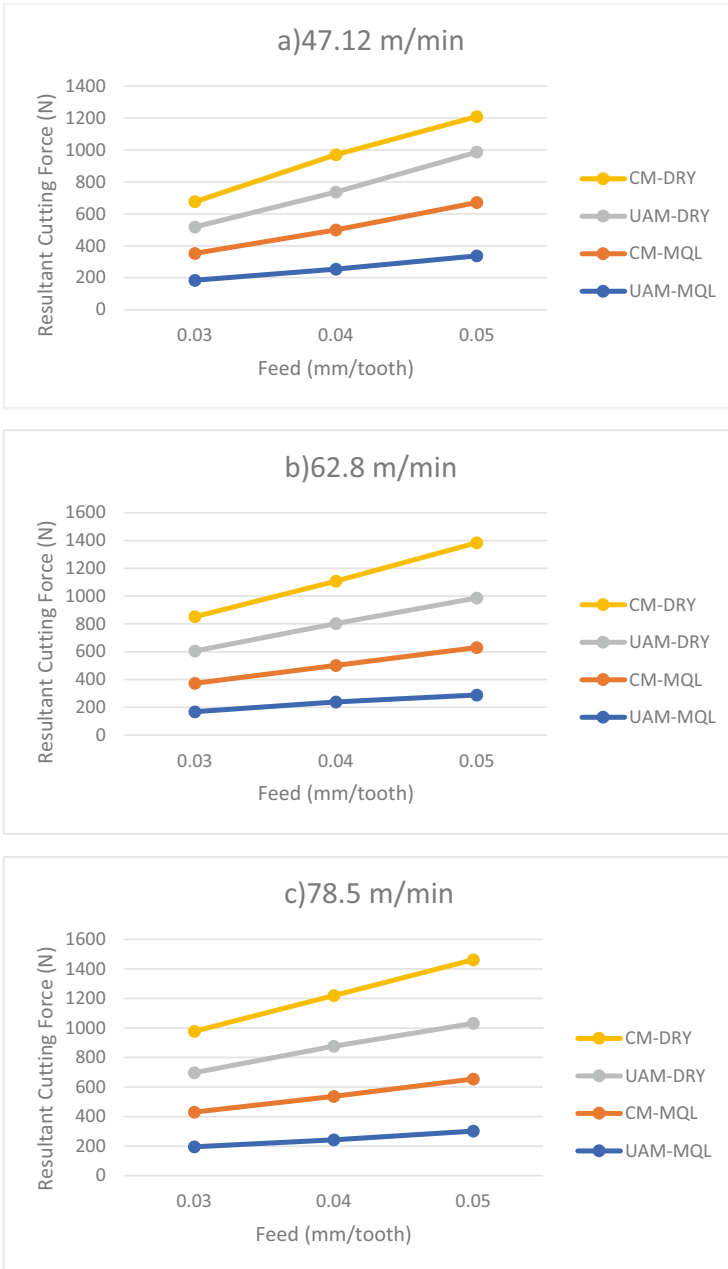


Fig. 11.16 Cutting force results of rough cut

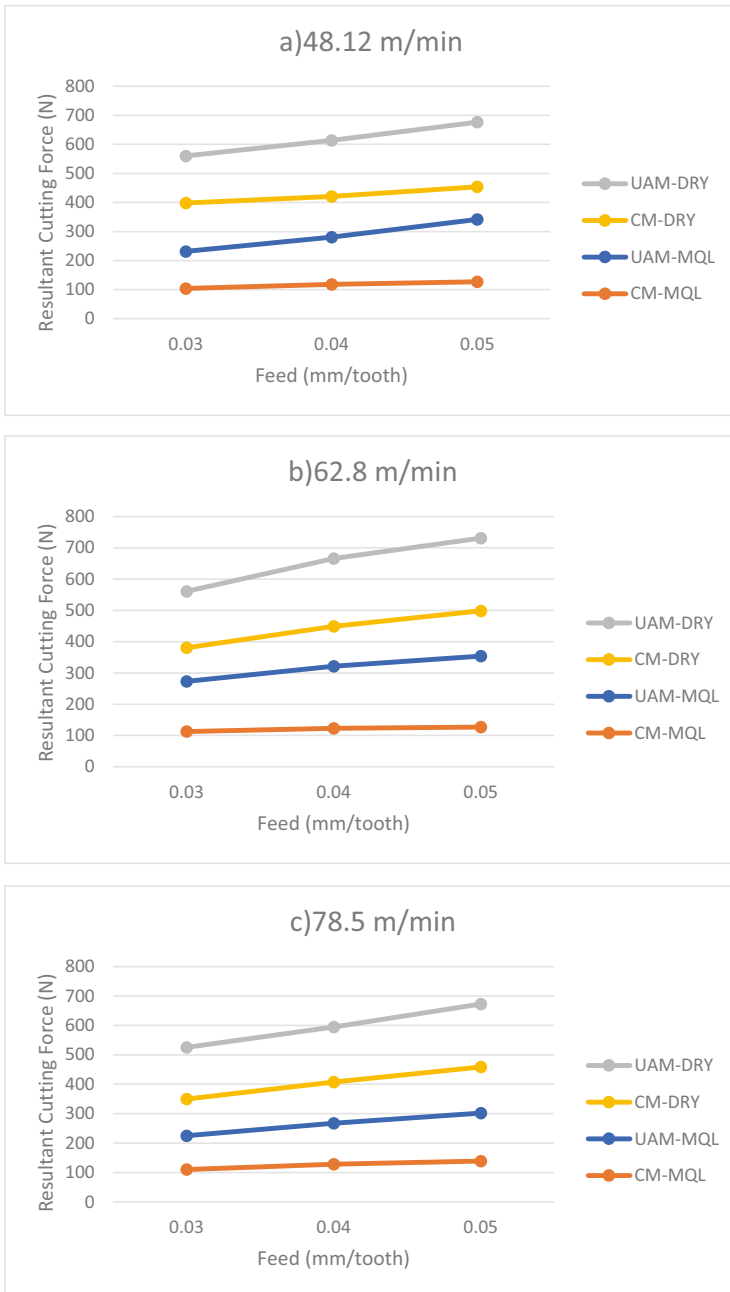


Fig. 11.17 Cutting force results of the finish cut

different parameters, as the feed and cutting speed increase, the cutting force also increases. The “Material Removal Rate” (MRR), indicates the amount of removed material by the cutting tool’s teeth, increases by an increase in feed or cutting speed. The increase in MRR means that more chips are in contact with the cutting tool’s surface, the friction increases with the increased contact area, which leads to an increase in the cutting force.

11.6 Conclusions

In this chapter, a broad literature survey on various vibration-assisted machining applications on aerospace materials is given, and in the end, an example case study is examined. Vibration-assisted machining is an emerging technology that still needs to be investigated for industry applications, especially in the aerospace sector. Research on these materials has shown that vibration-assisted machining is a promising developing technology for the machining processes. Outputs of vibration-assisted machining studies on aerospace manufacturing materials can be listed as follows;

- In general, vibration-assisted machining applications reduce tool wear and increase cutting tool life, decreasing the manufacturing cost.
- In many studies, it is observed that the surface quality obtained after vibration-assisted machining is better than that obtained by traditional methods. In this way, the need for secondary operation for surfaces is reduced.
- Many studies show that vibration-assisted machining reduces the cutting forces; therefore, it decreases the required power for machining operations, consequently making the process more stable and efficient.
- A limited number of studies report that the application of vibration-assisted machining has positive effects on subsurface phenomena such as residual stresses. Considering that residual stresses are of great importance in critical parts of aircraft (e.g., aircraft wings), vibration-assisted machining applications can be recommended in this case.
- The fatigue life effect is highly important in aerospace applications since most aircraft’s parts, and other aviation vehicles are constantly exposed to dynamic loads. Although the studies of vibration-assisted machining on fatigue life are limited, it is reported that it positively affects fatigue life.
- Studies prove that vibration-assisted machining has more uniform and smooth chip formations than traditional machining methods and contributes to operation by reducing burr formations, especially in hole drilling.

11.7 Future Studies

Vibration-assisted machining is a subject that is researched and applied more frequently in recent years and it still has some problems and areas that need to be studied. The first of these is the examination of vibration-assisted machining applications across a broader aerospace material spectrum. Until now, vibration-assisted machining studies are done on difficult-to-cut materials, composite materials, and aluminium alloys, but many materials used in aerospace production have not yet been tried. Filling this gap is essential in finding out whether traditional machining methods or vibration-assisted machining will be a more efficient production method in all aerospace materials.

Another area to be studied is to examine which number of axes vibrated in vibration-assisted machining is more efficient. Most of the researches on the vibration-assisted machining processes studied the effects of single-dimensional vibrations, and investigations on two-dimensional vibrations are limited. Studies over three-dimensional vibrations are pretty rare. However, current studies show that processes with 2D vibrations are often more efficient than methods with 1D vibrations, as seen in previous chapters. The processes with 3D vibrations are still very new and it is needed to work on this subject to compare 3D vibrations results with 1D or 2D vibrations. In this case, it is expected that the number of works on multidimensional vibrations increase in the near future. Moreover, the simplification of 2D and 3D vibrating processes is another area that needs to be studied, since they have a more complex structure than those that give 1D vibrations. Besides, mathematical modeling related to vibration-assisted machining is generally limited to areas such as tooltip trajectory and cutting forces and it is seen that more comprehensive modeling studies are needed. In addition to mathematical models, simulation applications are not sufficient and they fall far behind current machining processes simulations.

Today, the increase in artificial intelligence applications inevitably affected the manufacturing sector. However, artificial intelligence studies are quite limited in vibration-assisted machining applications [50]. The increase of these applications can accelerate the analysis of the previously mentioned mathematical modeling and simulation applications.

Studies on fatigue life, residual stresses, chip formations in vibration-assisted machining processes, and the differences in applying this method compared to traditional machining processes are quite rare.

Vibration-assisted machining is generally classified within nontraditional hybrid manufacturing method. The possible combination for applying vibrations on manufacturing processes is not only traditional machining processes but also it can be combined with nontraditional processes like electrical discharge machining (EDM), micro-machining, high-speed machining, etc. [51].

References

1. Liu, S., Chen, T., & Wu, C. (2016). Rotary ultrasonic face grinding of carbon fiber reinforced plastic (CFRP): A study on cutting force model. *The International Journal of Advanced Manufacturing Technology*, 89(1–4), 847–856. <https://doi.org/10.1007/s00170-016-9151-x>
2. Wang, H., Hu, Y., Cong, W., & Hu, Z. (2019). A mechanistic model on feeding-directional cutting force in surface grinding of CFRP composites using rotary ultrasonic machining with horizontal ultrasonic vibration. *International Journal of Mechanical Sciences*, 155, 450–460. <https://doi.org/10.1016/j.ijmecsci.2019.03.009>
3. Niu, Y., Jiao, F., & Zhao, Bo & Gao., G. (2019). Investigation of cutting force in longitudinal-torsional ultrasonic-assisted milling of Ti-6Al-4V. *Materials*, 12(12), 1955. <https://doi.org/10.3390/ma12121955>
4. Tang, X., Liu, Y., Shi, S., Chen, W., & Qi, X. (2017). Development of a novel ultrasonic drill using longitudinal-bending hybrid mode. *IEEE Access*, 5, 7362–7370. <https://doi.org/10.1109/access.2017.2696566>
5. Zhang, C., & Song, Y. (2019). Design and kinematic analysis of a novel decoupled 3D ultrasonic elliptical vibration assisted cutting mechanism. *Ultrasonics*, 95, 79–94. <https://doi.org/10.1016/j.ultras.2019.03.012>
6. Zheng, L., Chen, W., & Huo, D. (2020). Review of vibration devices for vibration-assisted machining. *The International Journal of Advanced Manufacturing Technology*, 108, 1631–1651. <https://doi.org/10.1007/s00170-020-05483-8>
7. Yang, Z., Zhu, L., Zhang, G., Ni, C., & Lin, B. (2020). Review of ultrasonic vibration-assisted machining in advanced materials. *International Journal of Machine Tools and Manufacture*, 156, 103594. <https://doi.org/10.1016/j.ijmachtools.2020.103594>
8. Zhong, Z. W., & Lin, G. (2005). Ultrasonic assisted turning of an aluminium-based metal matrix composite reinforced with SiC particles. *The International Journal of Advanced Manufacturing Technology*, 27(11–12), 1077–1081. <https://doi.org/10.1007/s00170-004-2320-3>
9. Shen, X.-H., Zhang, J., Xing, D. X., & Zhao, Y. (2011). A study of surface roughness variation in ultrasonic vibration-assisted milling. *The International Journal of Advanced Manufacturing Technology*, 58(5–8), 553–561. <https://doi.org/10.1007/s00170-011-3399-y>
10. Dursun, T., & Soutis, C. (2014). Recent developments in advanced aircraft aluminum alloys. *Materials & Design*, 1980-2015(56), 862–871. <https://doi.org/10.1016/j.matdes.2013.12.002>
11. Nath, C., & Rahman, M. (2008). Effect of machining parameters in ultrasonic vibration cutting. *International Journal of Machine Tools and Manufacture*, 48(9), 965–974. <https://doi.org/10.1016/j.ijmachtools.2008.01.013>
12. Davis, J. R. (2000). *ASM specialty handbook: Nickel, cobalt, and their alloys*. ASM International, OH 44073–0002, USA, p. 442.
13. Qi, H., Azer, M., & Ritter, A. (2009). Studies of standard heat treatment effects on microstructure and mechanical properties of laser net shape manufactured INCONEL 718. *Metallurgical and Materials Transactions A*, 40(10), 2410–2422. <https://doi.org/10.1007/s11661-009-9949-3>
14. Hsu, C. Y., Huang, C. K., & Wu, C. Y. (2006). Milling of MAR-M247 nickel-based superalloy with high temperature and ultrasonic aiding. *The International Journal of Advanced Manufacturing Technology*, 34(9–10), 857–866. <https://doi.org/10.1007/s00170-006-0657-5>
15. Sofuoğlu, M. A., Çakır, F. H., Gürgen, S., Orak, S., & Kuşhan, M. C. (2017). Experimental investigation of machining characteristics and chatter stability for Hastelloy-X with ultrasonic and hot turning. *The International Journal of Advanced Manufacturing Technology*, 95(1–4), 83–97. <https://doi.org/10.1007/s00170-017-1153-9>
16. Liu, K., Li, X. P., Rahman, M., & Liu, X. D. (2004). Study of ductile mode cutting in grooving of tungsten carbide with and without ultrasonic vibration assistance. *The International Journal of Advanced Manufacturing Technology*, 24(5–6), 389–394. <https://doi.org/10.1007/s00170-003-1647-5>
17. Liu, K., & Li, X. (2001). Ductile cutting of tungsten carbide. *Journal of Materials Processing Technology*, 113(1–3), 348–354. [https://doi.org/10.1016/s0924-0136\(01\)00582-9](https://doi.org/10.1016/s0924-0136(01)00582-9)

18. Ostasevicius, V., Gaidys, R., Dauksevicius, R., & Mikuckyte, S. (2013). Study of vibration milling for improving surface finish of difficult-to-cut materials. *Strojniški Vestnik – Journal of Mechanical Engineering*, 57(06), 351–357. <https://doi.org/10.5545/sv-jme.2012.856>
19. Mayers, J. R., Bobberger, H. B., & Froes, F. H. (1984). *Journal of Materials*, 36(10), 50–60.
20. Ezugwu, E. O., & Wang, Z. M. (1997). Titanium alloys and their machinability—A review. *Journal of Materials Processing Technology*, 68(3), 262–274. [https://doi.org/10.1016/S0924-0136\(96\)00030-1](https://doi.org/10.1016/S0924-0136(96)00030-1)
21. Babitsky, V. I., Astashev, V. K., & Meadows, A. (2007). Vibration excitation and energy transfer during ultrasonically assisted drilling. *Journal of Sound and Vibration*, 308(3–5), 805–814. <https://doi.org/10.1016/j.jsv.2007.03.064>
22. Kim, K.-W., Kim, D.-K., Kim, B.-S., An, K.-H., Park, S.-J., Rhee, K. Y., & Kim, B.-J. (2017). Cure behaviors and mechanical properties of carbon fiber-reinforced nylon6/epoxy blended matrix composites. *Composites Part B: Engineering*, 112, 15–21. <https://doi.org/10.1016/j.compositesb.2016.12.009>
23. Takagaki, K., Hisada, S., Minakuchi, S., & Takeda, N. (2016). Process improvement for out-of-autoclave prepreg curing supported by in-situ strain monitoring. *Journal of Composite Materials*, 51(9), 1225–1237. <https://doi.org/10.1177/0021998316672001>
24. Halim, N. F. H. A., Ascroft, H., & Barnes, S. (2017). Analysis of tool wear, cutting force, surface roughness and machining temperature during finishing operation of ultrasonic assisted milling (UAM) of carbon fibre reinforced plastic (CFRP). *Procedia Engineering*, 184, 185–191. <https://doi.org/10.1016/j.proeng.2017.04.084>
25. Shamoto, E., Suzuki, N., Moriwaki, T., & Naoi, Y. (2002). Development of ultrasonic elliptical vibration controller for elliptical vibration cutting. *CIRP Annals*, 51(1), 327–330. [https://doi.org/10.1016/S0007-8506\(07\)61528-5](https://doi.org/10.1016/S0007-8506(07)61528-5)
26. Garrison, W. M. (1990). Ultrahigh-strength steels for aerospace applications. *JOM*, 42(5), 20–24. <https://doi.org/10.1007/bf03220942>
27. Liu, J., Zhang, D., Qin, L., & Yan, L. (2012). Feasibility study of the rotary ultrasonic elliptical machining of carbon fiber reinforced plastics (CFRP). *International Journal of Machine Tools and Manufacture*, 53(1), 141–150. <https://doi.org/10.1016/j.ijmactools.2011.10.007>
28. Geng, D., Zhang, D., Xu, Y., He, F., Liu, D., & Duan, Z. (2015). Rotary ultrasonic elliptical machining for side milling of CFRP: Tool performance and surface integrity. *Ultrasonics*, 59, 128–137. <https://doi.org/10.1016/j.ultras.2015.02.006>
29. Suzuki, N., Haritani, M., Yang, J., Hino, R., & Shamoto, E. (2007). Elliptical vibration cutting of tungsten alloy molds for optical glass parts. *CIRP Annals*, 56(1), 127–130. <https://doi.org/10.1016/j.cirp.2007.05.032>
30. Jahan, M. P., Rahman, M., & Wong, Y. S. (2011). A review on the conventional and micro-electrodischarge machining of tungsten carbide. *International Journal of Machine Tools and Manufacture*, 51(12), 837–858. <https://doi.org/10.1016/j.ijmactools.2011.08.016>
31. Ding, H., Chen, S. J., & Cheng, K. (2011). Dynamic surface generation modeling of two-dimensional vibration-assisted micro-end-milling. *International Journal of Advanced Manufacturing Technology*, 53, 1075–1079. <https://doi.org/10.1007/s00170-010-2903-0>
32. Yin, Z., Fu, Y., Xu, J., Li, H., Cao, Z., & Chen, Y. (2016). A novel single driven ultrasonic elliptical vibration cutting device. *The International Journal of Advanced Manufacturing Technology*, 90(9–12), 3289–3300. <https://doi.org/10.1007/s00170-016-9641-x>
33. Zhu, Z., To, S., Ehmann, K. F., & Zhou, X. (2017). Design, analysis, and realization of a novel piezoelectrically actuated rotary spatial vibration system for micro-/nanomachining. *IEEE/ASME Transactions on Mechatronics*, 22(3), 1227–1237. <https://doi.org/10.1109/tmech.2017.2682983>
34. Lotfi, M., Sajjadi, S. A., & Amini, S. (2019). Wettability analysis of titanium alloy in 3D elliptical ultrasonic assisted turning. *International Journal of Lightweight Materials and Manufacture*, 2(3), 235–240. <https://doi.org/10.1016/j.ijlmm.2019.05.0012>
35. Pang, Y., Feng, P., Wang, J., Zha, H., & Xu, J. (2021). Performance analysis of the longitudinal-torsional ultrasonic milling of Ti-6Al-4V. *The International Journal of Advanced Manufacturing Technology*, 113, 1255–1266. <https://doi.org/10.1007/s00170-021-06682-7>

36. Moriwaki, T., Shamoto, E., & Inoue, K. (1992). Ultraprecision ductile cutting of glass by applying ultrasonic vibration. *CIRP Ann. - Manuf. Technol.*, *41*, 141–144. [https://doi.org/10.1016/S0007-8506\(07\)61171-8](https://doi.org/10.1016/S0007-8506(07)61171-8)
37. Lian, H., Guo, Z., Huang, Z., Tang, Y., & Song, J. (2013). Experimental research of Al6061 on ultrasonic vibration assisted micro-milling. *Procedia CIRP*, *6*, 561–564. <https://doi.org/10.1016/j.procir.2013.03.056>
38. Zhu, L., Ni, C., Yang, Z., & Liu, C. (2019). Investigations of micro-textured surface generation mechanism and tribological properties in ultrasonic vibration-assisted milling of Ti–6Al–4V. *Precision Engineering*, *57*, 229–243. <https://doi.org/10.1016/j.precisioneng.2019.04.010>
39. Ibrahim, M. R., Rahim, Z., Rahim, E., Tobi, L., Cheng, K., & Ding, H. (2017). An experimental investigation of cutting temperature and tool wear in 2 dimensional ultrasonic vibrations assisted micro-milling. *MATEC Web of Conferences*, *95*, 07005. <https://doi.org/10.1051/mateconf/20179507005>
40. Janghorbanian, J., Razfar, M. R., & Abootorabi Zarchi, M. M. (2013). Effect of cutting speed on tool life in ultrasonic-assisted milling process. *Proceedings of the Institution of Mechanical Engineers, Part B: Journal of Engineering Manufacture*, *227*(8), 1157–1164. <https://doi.org/10.1177/0954405413483722>
41. Zhang, X., Peng, Z., Li, Z., Sui, H., & Zhang, D. (2020). Influences of machining parameters on tool performance when high-speed ultrasonic vibration cutting titanium alloys. *Journal of Manufacturing Processes*, *60*, 188–199. <https://doi.org/10.1016/j.jmapro.2020.10.053>
42. Peng, Z., Zhang, X., & Zhang, D. (2021). Effect of radial high-speed ultrasonic vibration cutting on machining performance during finish turning of hardened steel. *Ultrasonics*, *111*, 106340.
43. Peng, Z., Zhang, X., & Zhang, D. (2021). Performance evaluation of high-speed ultrasonic vibration cutting for improving machinability of Inconel 718 with coated carbide tools. *Tribology International*, *155*, 106766.
44. Llanos, I., Campa, Á., Iturbe, A., Arrazola, P. J., & Zelaieta, O. (2018). Experimental analysis of cutting force reduction during ultrasonic assisted turning of Ti6Al4V. *Procedia CIRP*, *77*, 86–89. <https://doi.org/10.1016/j.procir.2018.08.227>
45. Ni, C., & Zhu, L. (2019). Investigation on machining characteristics of TC4 alloy by simultaneous application of ultrasonic vibration assisted milling (UVAM) and economical-environmental MQL technology. *Journal of Materials Processing Technology*, *278*, 116518. <https://doi.org/10.1016/j.jmatprotec.2019.116518>
46. Namlu, R. H., Sadigh, B. L., & Kiliç, S. E. (2021). An experimental investigation on the effects of combined application of ultrasonic assisted milling (UAM) and minimum quantity lubrication (MQL) on cutting forces and surface roughness of Ti-6AL-4V. *Machining Science and Technology*, *25*(5), 738–775. <https://doi.org/10.1080/10910344.2021.1971706>.
47. Boyer, R., Welsch, G., & Collings, E. W. (1994). *Materials properties handbook: Titanium alloys*. ASM International.
48. Kistler Instrumente AG. (2004). *Data sheet, 3 component force link* (type 9317B).
49. Namlu, R.H. Yilmaz, O.D., Kilic S.E., Cetin B. (2019) Investigating the effect of cutting conditions on machining performance of Al 6061-T6 alloy. In *10th international congress on machining*, pp. 293–304.
50. Namlu, R., Turhan, C., Sadigh, B., & Kılıç, S. (2021). Cutting force prediction in ultrasonic-assisted milling of Ti–6Al–4V with different machining conditions using artificial neural network. *Artificial Intelligence for Engineering Design, Analysis and Manufacturing*, *35*(1), 37–48. <https://doi.org/10.1017/S0890060420000360>
51. Xu, L., Na, H., & Han, G. (2018). Machinability improvement with ultrasonic vibration-assisted micro-milling. *Advances in Mechanical Engineering*, *10*(12), 168781401881253. <https://doi.org/10.1177/1687814018812531>

Chapter 12

Potential of Incremental Forming Techniques for Aerospace Applications



Ricardo J. Alves de Sousa, D. G. Afonso, F. Rubino, and A. K. Behera

12.1 Definition of Incremental Forming Processes

The Incremental Sheet Forming process (ISF) has been majorly studied since the beginning of the 2000s, despite the fact it has been patented much before that, in 1967 by Lezsak. In simple terms, a sheet, clamped all around its perimeter, is formed using a stylus—usually in the form of a hemispherical punch—into the final work-piece by a series of small continuous incremental deformations. The process can provide asymmetrical geometries, contrarily to other incremental forming technologies such as spinning. Tool motion is controlled entirely by CNC technology and no die is needed as is in traditional, press-based sheet metal forming. The deformation is performed by applying pressure on the surface of the sheet, forcing it to deform gradually. The metal sheet is usually restrained by a blank-holder to avoid displacement and the flow of material into the forming area. Therefore, the whole forming operation is undertaken through the blank's thinning.

The removal or simplification of the die in the manufacturing process decreases the cost per piece for small batches even if manufacturing times increase

R. J. Alves de Sousa (✉) · D. G. Afonso
TEMA: Centre for Mechanical Technology and Automation, Department of Mechanical Engineering, University of Aveiro, Aveiro, Portugal
e-mail: rsousa@ua.pt

F. Rubino
Department of Chemical, Energetic and Mechanical Technology, King Juan Carlos University, Madrid, Spain
e-mail: felice.rubino@urjc.es

A. K. Behera
Thornton Science Park, University of Chester, Chester, UK
e-mail: a.behera@chester.ac.uk

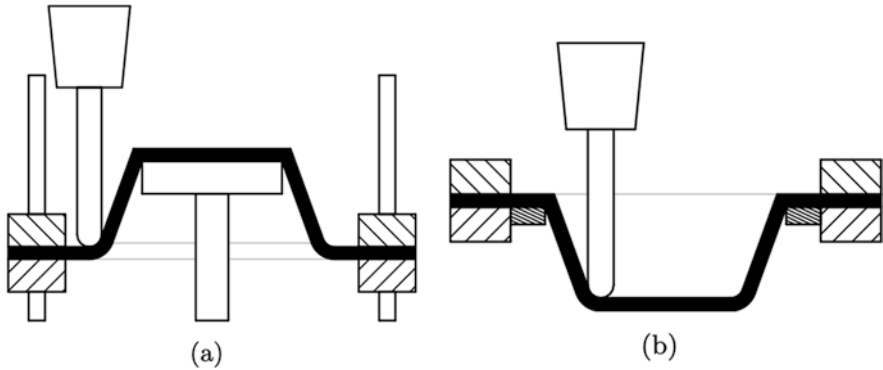


Fig. 12.1 Two main types of incremental forming processes: (a) two-point (with partial die) and (b) single point

significantly [1]. The differences in the forming principle lead to a loss of accuracy due to continuous spring back and differ the possible achievable part design, once forming vertical walls may reveal a cumbersome task. Incremental forming processes can be considered ideal for customized parts, or development prototypes reducing time to market, which may be ideal for the aerospace industry.

An unaccountable number of works dealing with the process and its variants, for diverse types of materials and processing parameters have been published, aiming to achieve consistent results making possible the process dissemination in an industrial environment. Some works focused on condensing all the information generated by the scientific community such as the pivotal work of Jeswiet et al. [1] and the updates made by Behera et al. [2] or Duflou et al. [3].

From the many process variants, single-point (SPIF) and two-point (TPIF) incremental forming variants have been used more intensively. The SPIF variant requires the use of a so-called backing plate (Fig. 12.1b) in order to facilitate the initial stages of bending the flat sheet into a cavity. The TPIF variant can appear in many forms such as with partial die (Fig. 12.1a) or with a counter-tool. Naturally, the die-less, single tool SPIF variant is much easier to implement and more cost-effective. However, TPIF, despite its complexity in terms of control and higher costs, brings more potential in terms of flexibility regarding forming strategies.

12.2 Incremental Forming Machinery

To perform incremental forming there are a few indispensable requirements. One of them is the need for CNC-controlled three-axis kinematics. The most straightforward way to implement Incremental Forming technology into the academic or industrial environment is by adapting a CNC milling machine (which is part of virtually every shop) to perform SPIF. To do so the table must be provided with a fixture to clamp the sheet over its edges; in some cases, the tool holder might be

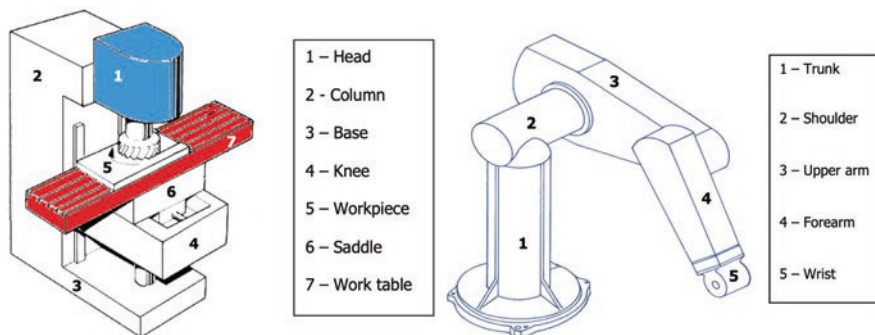


Fig. 12.2 Typical milling machine (left) and serial kinematics robot (right)

reinforced to withstand the lateral and compressive forces during the ISF process, since they are much larger than cutting operation forces. Another approach resorts to serial kinematics robots, which have much less limitations in terms of space and work envelope. However, serial-kinematics robots lack stiffness and positioning errors tend to add up. Schematics for both solutions are given in Fig. 12.2.

Besides adapting machinery, dedicated, in-house prototypes have been developed. They may provide reasonable travel speed, working volume, stiffness, and instrumentation. High speeds, large working volumes, sufficient stiffness, and high load capacity are favorable. The machines proposed all over the last years varied in type, ranging from simple 3-axis models to parallel kinematics ones [4]. Amino company [5] has made the most recognized attempt to provide a commercial solution for ISF machines. They have developed a series of commercial models, but with limited success. Other manufactures have been also providing customized ISF machinery on request [6].

In conclusion, the choice of a proper ISF setup will depend on a number of factors related to initial investment, the number of parts to be produced, academic or industrial environment, material to be formed and forces to be required and desired geometries.

12.3 Incremental Forming: Materials and Process Limitations

Like most material forming processes, the SPIF process is characterized by inherent process limits beyond which material failure occurs [7]. Typically, the forming limits in terms of achievable stretch are higher for SPIF compared to conventional stamping operations [8]. A significant increase in strain values is reported, as illustrated in Fig. 12.3. The higher forming limits were initially explained by the fact that plastic deformation is localized. This has been further elaborated in later studies, that indicate the effect of through-the-thickness shear (TTS) that creates a

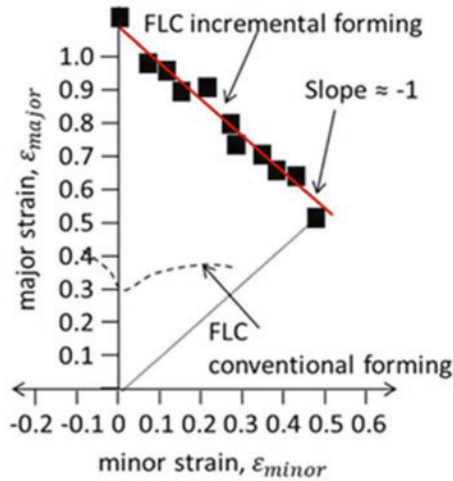


Fig. 12.3 Observed forming limit curve for incremental forming for 1.21 mm thick AA 1050-O sheets formed into truncated pyramids [1]. Reprinted by permission from Elsevier

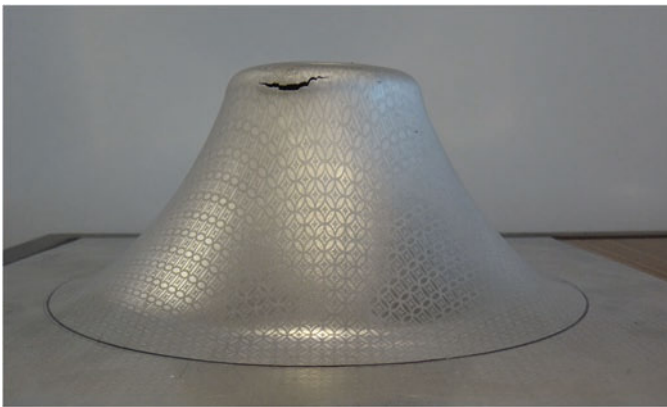


Fig. 12.4 Fracture of a formed component; cone with continuously varying wall angle, with step down of 0.5 mm

stabilizing effect [9]. Other studies suggest that the strain paths are serrated due to cyclic and localized plastic deformation [10]. Experimental evidence indicates that necking is avoided before failure occurs. Forming limits are approximated using straight lines with a slope of -1 [11]. Several empirical forming limit curves are now available.

Typically, for a particular material with a specific thickness, and being formed by a hemispherical tool of a specific diameter, a critical wall angle of failure can be established. This is usually done by either making conical shapes with increasing wall angle in steps until failure occurs or a variable wall angle geometry (Fig. 12.4),

Table 12.1 Failure wall angles of common aerospace alloys [12]

Material	Aerospace application	Specimen geometry	Tool dia (mm)	Thickness (mm)	Maximum achievable wall angle
Al 2024-T3	Wings and fuselages	Truncated cone	10	1	42
AA 3003-O	Fin stock	Truncated cone	10	2	76
Ti grade 2	Airframe skins	Truncated cone	10	0.5	47
TiAl6V4	Aircraft engine blades, compressor wheels, impeller pumps, and connecting rods	Truncated cone	10	0.6	32

where the wall angle of failure can be determined from the depth at which failure occurs [7]. Table 12.1 lists failure wall angles for various materials and thicknesses that are typically used in aerospace applications. Process parameters that affect the forming limits include sheet thickness, tool diameter, lubrication conditions, and toolpath strategies. It has been observed that the failure wall angle increases for reduced tool diameter, reduced step-down increment, higher feed rate, and higher sheet thickness [13]. At higher tool diameters, the stress triaxiality ratio was found to increase and necking was found to occur prior to fracture [14]. The ratio between the initial sheet thickness to the tool diameter has been found to affect the various stabilizing mechanisms that explain the increased formability in SPIF.

Additionally, several analyses have been performed to understand the failure mechanisms in SPIF. An extended M-K analysis with non-zero stress tensor components was tried out [15]. Further studies suggest using a detailed membrane analysis suggested a failure mechanism consistent with stretching combined with shearing [11]. It was suggested that typical assumptions used in the conventional forming analysis that lead to the FLC are not satisfied in SPIF. Additional mechanisms that can explain the failure behaviors in SPIF include bending, cyclic straining, and hydrostatic stress [8]. In SPIF, bending and stretching occur simultaneously as the sheet curves underneath the tool. The phenomenon of cyclical straining has been observed experimentally by taking a cross section of the formed wall that shows serrations in the strain history when plotted against the principal strains. Formability is enhanced due to the cyclic straining, which can be proven by carrying out detailed constitutive modeling of the process. Likewise, hydrostatic stresses can enable material to strain significantly without damage; however, although these have been included in models, they are not sufficient to explain all the strain hardening that occurs during the process. Studies on TTS in prolonging necking have shown that the effect of TTS in prolonging necking is dependent on the shear direction [16]. Another study has also shown that meridional stresses under plane strain conditions led to failure by cracking [17]. The failure occurred due to excessive thinning without the presence of necking. Another theory that has been suggested is the “noodle theory” that proposed that localized small deformations were distributed leading to enhanced forming limits [10].

12.4 Incremental Forming for Low Batches or Prototypes

Nowadays rapid prototyping methods are encountering an expanding usage as a cost-effective alternative to the conventional processes for low-volume production of spare parts. Indeed, rapid prototyping allows to ensure the precise assembling of parts in new products, enhance the cost-effectiveness of low-volume production and receive feedback in the minimum time [18, 19]. Among several technologies, ISF has gained interest and has been bringing many benefits for small series production and in rapid prototyping of products [20]. Potential applications for ISF are dental and medical prosthesis or devices, sculpture and architecture, automotive customized parts, aerospace, etc. (Figs. 12.5 and 12.6).

The deformation process during ISF has been deemed more time consuming than the other conventional forming processes, however, this technology offers intriguing advantages in rapid prototyping: production of sheet metal parts directly starts from the CAD 3D models to the complete traditional product without intermediate stages required for the design and the manufacturing of molds, and, in addition, allows to achieve greater formability of material sheets.

Practical examples showing the use of incremental forming for the production of functional parts in the industry are still rare, but the published literature documenting the application of ISF to manufacture a large variety of parts, having growing shape complexity, seems to be increasing in recent years [3, 21]. It points out that the process is better controlled and gradually approaching the flexible forming technique envisaged in the early research publications.

Up to date, a few examples are reported in the literature showing the application of the ISF method to manufacture components and demonstrating at the same time the capabilities and the maturity of this process for prototype development and rapid testing. Adam and Jeswiet [21] in their work reported the production of several components, such as automotive guards, engine components as well as patient-fitted medical devices. The authors also proposed design rules for the designing of parts and the implementing of incremental forming. These guidelines allow translating



Fig. 12.5 Rapid prototyping and customized products from ISF

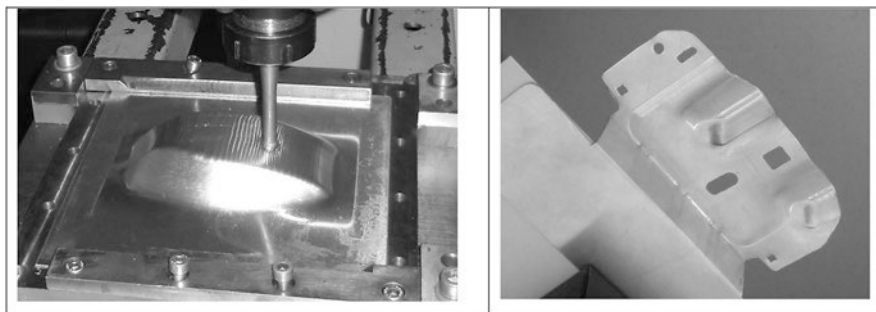


Fig. 12.6 Incremental sheet forming for automobile shapes (left: tank; right: fender after trimming and cutting operations)

the forming limitations of the material sheets to design constraints and then, producing usable prototypes. Design rules proposed by the authors can be summarized as [5]: (1) all parts must fit within the working volume of the machine used; (2) keep the design simple and avoid changes in part shape from concave to convex (parts having double curvature can be manufactured but required additional complexity in the setup of the process and of the CNC machine); (3) each material has a maximum wall angle for a single pass, wall angles should keep below this threshold for the material used.

By adopting these rules, rapid prototypes can be manufactured by using conventional three-axis milling machines, CNC furtherly allows applying high-precision features to complex-shaped parts.

Other examples of ISF reported by different sources include the case study of Jeswiet et al. [22], which employed incremental forming to manufacture a solar cooker cavity. The study aimed to demonstrate the possibility of extending ISF to low-income countries' applications.

Authors demonstrated that ISF can be successfully used to make specific metal parts meeting the customer's requests. At the same time, ISF also proved to be much less expensive than conventional methods, saving the costs of making the set of dies to manufacture the part and reducing the amount of time required by the lay-up of fiber-glass layers. Adam and Jeswiet [21] recently explored the manufacturing of customized parts for heating, ventilation, and air conditioning (HVAC) systems by using the ISF process. Prototypes of baffles, airflow management system (AFMS) display (to house sensor hardware), and shroud parts having specific flow patterns were produced with ISF [3].

Barimani-Varandi et al. [23] evaluated the feasibility of ISF in the rapid prototyping of polycarbonate aircraft canopies. Integral canopies (that are single parts without frames in order to enhance the ability of the pilots to detect and identify) utilized in the fourth-generation fighters are usually produced in very small batches and need to meet specific requirements to be assembled in the aircraft structures (especially in case of training or military aircraft). These aspects make the conventional forming processes of polymers, such as blow molding, injection, or

compression, not cost-effective due to the high energy requirements and high cost of machinery, equipment, and tools. ISF, conversely, is a suitable candidate and several research teams have successfully applied it to the forming of polymeric sheets [24, 25]. The results of their study demonstrated the ISF is a promising technology for the manufacturing of integral canopies allowing to produce samples with appropriate transparency and higher geometric accuracy by designing proper tool-path strategies, specific tools, and post-forming treatments.

As mentioned, ISF is suitable for the one-of-a-kind manufacturing of patient-fitted implants or medical devices. Indeed, the medical field represents a sector where products can be considered to some extent as unique. Although many products (implants, prostheses, internal or external devices, etc.) are classified as similar, intrinsic natural differences of each individual push the research interest to the product with the high level of specificity and customization in order to guarantee the best performance. Ambrogio et al. [24] employed ISF to manufacture high-customized ankle support tailored to the patients. The authors proposed a reverse engineering approach to manufacture the customized foot orthosis starting from the patient's ankle in order to minimize the clearance between the patient's ankle and the support, which can lead to an improper stabilization of the limb. Similarly, in [21] different steps were followed in a "round design" approach: the cycle starts from the patients acquiring the ankle geometry by using a laser scanner, then the data are processed and a 3-D model (virtual and CAD) of the body part is built. The CAD model, before being converted in CAM language, needs to match the constraints of the forming process (formability, toolpath strategy, wall angle, etc.). Figure 12.7 depicts the typical components in the CAD-to-part approach for a bus seat mold.

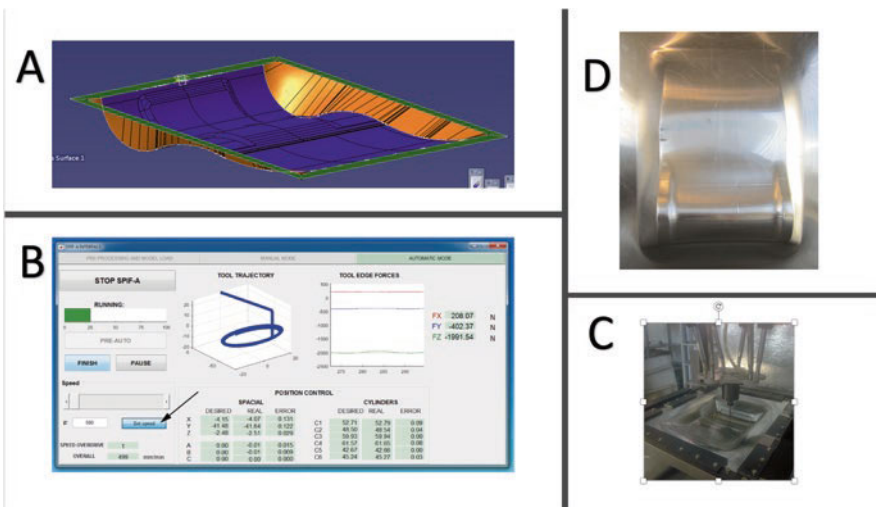


Fig. 12.7 A back-seat mold for a commercial bus. From CAD (a), man-machine interface (b), forming process (c) to formed part (d)

Other studies documented the usage of ISF to produce skull implants using different materials (biocompatible metals and polymers) and obtaining a satisfactory fitting of the customized parts, without the need for further adjustment during the surgery [26–29]. The application of ISF to manufacture highly customized parts and small batches for aerospace and aeronautical industries has been explored in the very recent year. Trzepieciński et al. investigated the possibilities to produce U-shaped stiffening ribs in AA2024-T3 [30]. Authors pointed out that particular care needs to be paid in the selection of the forming parameters, especially in the tool path, in order to deal with the low formability of the high strength alloys employed in the aeronautics and aerospace, not only the aluminum alloy 2024 but also the 7075 alloy, the AZ31B magnesium alloy, and the Ti6Al4V and TiAl2Mn1.5 titanium alloys, to cite but a few [31, 32]. Gupta et al. [33, 34] and Mohanraj et al. [35] studied the manufacturing of C-channel for vibration testing of an airframe and asymmetrical curvilinear part, respectively, by means of ISF. Despite authors in their works being able to demonstrate that ISF is potentially able to manufacture very complex geometries, they observed geometrical errors, due to excessive thinning and elastic spring-back, detrimental for the accuracy of the parts required in the aerospace applications. To mitigate these phenomena and achieve the geometries with the required tolerances, authors highlighted the relevance to adopt novel approaches, consisting not only in different tool path strategies or optimization of process parameters but also in post-forming operations, with a larger number of experiments.

The further potential application for the ISF process is represented by architecture. Decorative elements (Fig. 12.8) or architectural linings represent a



Fig. 12.8 SPIF manufactured decorative elements for facades

continuously growing domain for ISF facilities, which can afford the request for specific and high-customized products.

Despite the fact that ISF has been the object of intense research and development activities for more than three decades [36], the technology of ISMF applied in rapid prototyping still represents a hot topic for the scientific community and several issues need to be addressed. First of all, the accuracy of formed products with respect to the CAD 3-D model is still limited; the surface roughness of the parts is high and often above the design requirements; heat generation and friction forces between tool and sheet are significant and not easily predictable, it can lead to unexpected influence on the parts in terms of formability, final properties of the deformed products and even to failure of the part. Finally, the ISF is still characterized by low productivity [37]. On the other hand, the advancements in the manufacturable shapes and the improvement of tolerances control have promoted the diffusion of ISF in medical implant categories, which can benefit from the one-of-a-kind shaping abilities of the incremental forming. The high added value of these applications can pave the way for broader use of SPIF in industrial practice and developments in more competitive application areas, thus opening perspectives for broader use of single point incremental forming in industrial practice.

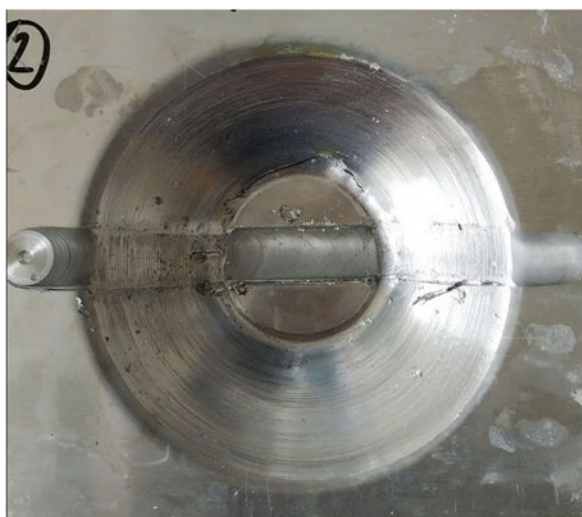
12.5 Combing ISF with Welding Techniques

In the past decades, incremental sheet forming has been suggested for the manufacturing of components and parts from aerospace to automotive and biomedical applications, as described in the previous paragraph [38, 39]. Among those, in the past years, several studies explored the use of incremental sheet forming as a post-weld process. The interest by researchers and industry is derived from the growing demand from aeronautic and automotive industries for novel solutions for designing lighter vehicles (cars and airplanes mainly) in order to reduce fuel consumption and meet safety environmental regulations. It resulted in the adoption of lightweight materials (aluminum and magnesium alloys primarily, but also titanium) as structural materials and in novel construction strategies, such as tailored welded blanks [40]. However, the conventional forming of welded plates has always been limited by the significant reduction in their formability, which is lower than the base materials joined [41]. Deep-drawing tests pointed out that forming limit curves and minimum major strain value in TWBs of the same material, but different thickness, are strongly influenced by the thickness ratio increase, higher the thickness ratio lower the formability of the TWBs, while in case of dissimilar parental materials, formability is influenced by the mismatching in mechanical properties between the materials and between weld region and base material (this last also strongly related to the welding process adopted) [42, 43]. In this scenario, the incremental forming strategy may be a suitable alternative to produce complex sheet metal parts with high depths.

First attempts of combining incremental forming and welding have been made on different materials; aluminum alloys (but in some extent also steels) were mainly investigated by researcher, joined by fusion, and solid-state welding processes. Aluminum alloys, indeed, and especially the 2xxx, 6xxx, 7xxx, and 8xxx series have encountered a growing diffusion in the aerospace and aeronautic industry. The 2000 series possess higher damage tolerance and longer-term durability, being suitable for aerospace applications. Among those, the 2024-T3 has excellent fracture toughness and fatigue crack propagation characteristics and, hence, it has been the most widely used alloys in fuselage construction. The 6000 series is mainly-adopted thanks to their good corrosion resistance and improved machinability (they showed a good formability and weldability), with respect to the 2xxx and 7xxx series. Within the 6xxx series, the 6013 and 6050 alloys are used to produce fuselage skin, stringers, and seat parts (e.g. backrest and armrests). The 7000 series alloys are being used for their superior strength-to-weight ratio (w.r.t.) the other Al alloys; therefore, they are employed for flight-critical airframe structural components, such as wheels and landing gear links, wing and fuselage skins. 8xxx series alloys are mainly used for their low density and high-temperature performances [44].

An example is shown in Fig. 12.9. Ambrogio et al. [45] explored the effect of the welding process on the local mechanical properties of 6181-T4 aluminum alloy with particular attention to the formability when the welded blanks are subjected to single point incremental forming (SPIF) process. Blanks were joined by means of friction stir welding (FSW), which is a solid-state weld process and demonstrated to be able to reduce the occurrence of defects and obtain sound joints characterized by remarkable mechanical performances, whereas conventional fusion welding processes, like TIG or laser, may result in weak joints. SPIF results on unwelded and welded sheets showed a reduction of formability, here represented as the maximum slope of the wall inclination angle [46], which dropped from 58.75°, reached with

Fig. 12.9 SPIF truncated cone manufactured from 6082-T6 friction stir welded blanks



the bulk sheet, to 50° . Welded blanks failed at 58° but were successfully formed with the lower values. Authors argued that the presence of weld line reduced the strength of the materials and introduced critical points, which led to a premature failure, localized indeed in the weld bead. The slight drop registered in the experiments by the authors suggested that FSW was able to reduce the brittleness of material in the joint, typical in the fusion welding of aluminum alloys, resulting in better formability. However, the work was preliminary, although promising, investigation, and the FSW can be furtherly optimized to achieve more effective results.

Silva et al. [47] also investigated the application SPIF process on TWBs joined by FSW. In this study 1.5 and 2 mm thick AA1050-H11 aluminum alloy sheets have been employed in different configurations. Authors also proposed the utilization of a dummy sheet to avoid, or limit, the occurrence of galling phenomena due to the contact between tool and aluminum sheets that cause local surface damages. A dummy sheet, indeed, prevents direct tool/sheet contact and improves the final surface quality of the sheet metal blank. The authors confirmed that the SPIF can be combined with TWBs produced by FSW to manufacture complex metal parts, achieving satisfactory forming depths. In particular, homogenous 2 mm-thick welded sheet demonstrated a good formability showing crack outside the welding joint in case of and reaching a maximum wall angle of approximately 80° , very close to the 82° registered by the reference material without welding, for the truncated cones, and a wall angle of 75° and 77° for TWB and unwelded blank, respectively in case of truncated pyramids (where the failure occurred simultaneously at the corners in the weld line and outside it). Poorer results, conversely, have been observed for uniform thinner and for no-uniform welded sheets, which showed catastrophic failures in the weld line for reduced values of wall angle, however, the mechanisms behind the failures were not fully understood due to the high scattering in the data. Further studies are, thus, necessary to evaluate the formability of TWBs, not only in the case of non-uniform sheets but also for dissimilar materials.

Alinaghian et al. [48] studied the formability of 2 mm thick 6061 aluminum alloy sheet TWBs welded by FSW and then formed by SPIF. They optimized FSW parameters, such as welding direction (i.e., rolling, transverse and diagonal directions), rotational speed, plunge depth, and travel speed by response surface methodology for greater formability. The same methodology was used to find the optimal configuration of forming parameters (i.e. spindle speed, feeding rate, and axial step) for the welded blank fabricated adopting the optimal FSW parameter combination. SPIF results showed that, as far as FSW parameters, the spindle speed of the FSW tool has the highest influence together with the welding direction, meanwhile feeding rate and plunge depth have a limited effect on the formability. For the material tested, joins along the diagonal direction, and welded with 1600 rpm as rotary speed obtained a higher value of bowl height. As far as the incremental forming parameter, all showed a comparable influence on the formability of the welded sheet. Best results were reached with a non-rotary tool.

Ebrahimzadeh et al. [49] investigated the formability of the FSWed AA5083 alloy blank through the ISF process. Authors also carried out a comparison between SPIF and Two Point Incremental Forming (TPIF). Like [48], response surface

methodology was applied to find out the effect of incremental forming factors (i.e. tool rotation, feeding rate and step down) on the dimensional accuracy of the formed part and minimum thickness. They observed that regardless of the wall angles reached with the different configurations of parameters, TPIF increased the formability of AA5083 friction stir welded blanks by 38 and 40% with respect to SPIF. The forming process also influenced the failure of the welded sheet. In SPIF cracks occurred in the middle of the weld line suggesting that, as expected, welding negatively affects the formability, and the tear is parallel to it. On the other hand, in TPIF the crack moves beyond the weakest zone thanks to the action of the supportive die and then propagates perpendicularly to the weld line.

Besides the research works reported above which investigated the formability of similar FSWed sheets, limited contributions dealing with the application of SPIF on dissimilar welded sheets are available in the literature, despite the great interest in the formed parts having tailored properties. Fusion-welded or FSWed sheets with different materials or thicknesses represent a common strategy to obtain tailored properties in welded components. Although the formability reduction of the welded sheets is well known and reported in the literature, proper jointing of dissimilar sheets by FSW and forming of the tailored sheets without reduction of the formability can be achieved. In this scenario, a study of the integration of fusion welding and incremental forming was proposed by Rattanachan et al. [50] which applied the SPIF on St37 steel and SUS304 steel dissimilar welded blanks joined by the laser welding process. The two steels showed distinct forming behaviors as the effect of the different chemical compositions and properties, with the St37 that demonstrated a formability twice the SUS 304 (50 mm dome height against 25 mm). In the welded sheet, the failure occurred on the welded line, triggered by the mismatch in the strength of the two alloys, at 25 mm of deformed height, similar to that of SUS 34. In this case, the less formable material dictated the formability of the welded part. Authors argued that changing the position of the welded line of the TWBs in the fixture could lead to forming with success the dissimilar TWBs.

Ghadmode et al. [51] investigated the incremental forming of dissimilar TIG-welded AA5052-H32 and AA6061-T6 aluminum alloys. The formability of parental materials and the welded sheet was tested at different values of the wall angles (from 40° up to 70°). The two parental materials showed distinct formability due to the different compositions and mechanical properties. AA5050 alloy, characterized by lower values of yield and tensile strength than AA 6061 alloy, was successfully formed up to 65° of wall angle with a maximum forming depth of 115.47 mm, while the other material failed at 50°, reaching a depth of 52 mm (at 45°). All TWBs behaved similarly to AA6061-T6 (Fig. 12.10). Authors argued that, even though there are two materials available in TWBs, weld follows the forming behavior of stronger material, i.e., AA6061-T6. No successfully forming has been obtained and failure occurred already at a wall angle of 40°. All TWBs failed in the weld zone: deterioration in the weld strength due to the increase in average grain size and the residual porosity are quoted as the reason behind the failures of TIG-welded blanks [41, 52, 53]. Additionally, the failures observed in the weld zone were brittle in nature. The authors also observed that reduction of porosity and mitigation of the

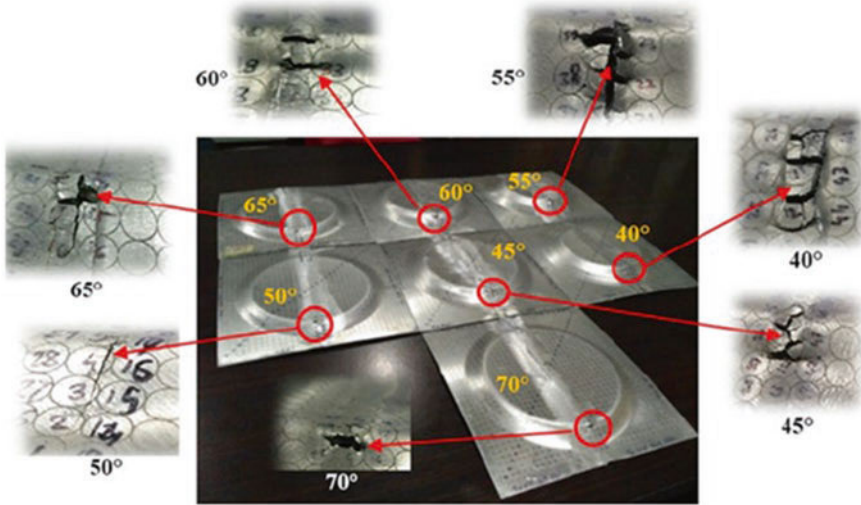


Fig. 12.10 TWBs formed by SPIF (wall angle ranging from 40° to 70°) [51]. Reprinted by permission from Springer

brittleness by means of post-weld heat treatment would be beneficial to the formability of the welded blank, which was successfully formed at 45° and showed improvement in thickness distribution, close to that observed for the parental 6061 alloys. Results of [51] seem promising for the integration of incremental forming with welding processes, however, more study is required to assess the effects of microstructural chemical composition and morphology of weld beads on the formability of aluminum alloy TWBs. In addition, the approach proposed by the authors to mitigate the deterioration of weld strength and the low formability paves the way for further experimentation.

The formability of dissimilar AA 6061 and AA 5083 welded blanks during SPIF (SPIF) was also investigated by Tayebi et al. [54]. According to [50, 51], the forming behavior of the welded sheet depends on the parental materials and the matching between their properties. In this case, 6061 and 5083 alloys showed similar forming limit angles, between 60° and 62.5°. Similar values were attained by the FSWed sheet. It means that, differently from the fusion welding processes [50, 51], FSW had no significant effect on the formability. Surprisingly, different from previous works [41] that reported a reduction in the maximum wall angle of FSWed samples, in this case, any reduction in formability was observed. Authors claimed that it could be attributed to a proper selection of process parameters and FSW tool design. Additionally, tensile analysis of FSWed blank pointed out that, despite the yield and tensile strength reduced by almost 50% w.r.t the parental materials, the welded region acquired a higher ductility than the seamless sheets made achieving also a higher elongation at break. It explains why material formability and forming limit of the angle of FSWed blanks are very close to the 5083 and 6061 parental

materials. As a confirmation of these observations, the failure in 5083/6061 welded sheets occurred far from the weld region (cracks started in AA60661), pointing out that the FSW process could be a benefit for the strength and the formability of the part.

12.6 Incremental Forming as Rapid Tooling

In addition to the application for low batches or prototypes manufacturing, ISF has a potential field of application as a rapid tooling (RT) process. The RT concept is overall defined as a combination of processes to produce tools and molds for conventional manufacturing processes in less time and at a lower cost relative to traditional machining methods (Equbal et al., [55]). Although being largely associated with additive manufacturing, RT is not only the result of layer-by-layer fabrication. The leading characteristics should ensure a shorter and less expensive tool development and fabrication time than conventional tooling, at the cost of smaller tool life and wider tolerances [56]. In such a way, RT processes are linked to flexible manufacturing systems, with parts manufactured from CAD models without considerable dedicated tools in a short time. Being compatible with FMSs, ISF processes can be seen analogously to AM technologies and considered rapid smart manufacturing processes.

Two main classifications of RT are indirect and direct methods. Indirect tooling processes use patterns to produce tools. Direct tooling implies the ability to fabricate tools directly from a rapid manufacturing machine. With the possibility of working with mid-to-high strength materials, ISF has a potential application as a direct RT method.

The use of sheet metal and other thin-walled molds has considerable application in industrial processes, particularly in the processing of thermoplastics and composite materials. These tools have usually attractive weight/strength ratios with low material costs and, when applicable, low thermal inertia. However, conventional manufacturing processes have limited geometric freedom or are very time-consuming and expensive. Furthermore, traditional RT techniques, using AM processes, struggle to achieve thin geometric features, becoming weak competitors for mold manufacture.

The ISF processes have great potential for the fabrication of these geometries. Thus, as refereed, ISF processes are highly suitable for direct hard tooling. In such a way, different ISF techniques can be used for the development of sheet metal molds for various manufacturing processes. The manufactured parts, either from aluminum alloys, steel, or other materials, can be used in multiple cycles. Still, it is important to consider a correct sizing of the part's strength and stiffness in both a mechanical and thermal way. It is also important to refer that often the ISF technologies must coexist with others to achieve the desired geometry and properties.

A sheet metal tool should be designed to mimic the operation of conventional tools. Thus, it must consider both the correct geometry of the target part as well as

the possible manufacturing process awareness as material shrinkage, de-molding possibilities, and clamping and positioning systems. Besides, the sheet metal parts geometric limitations must be considered, exploring not only the ISF potential but also other flexible forming techniques.

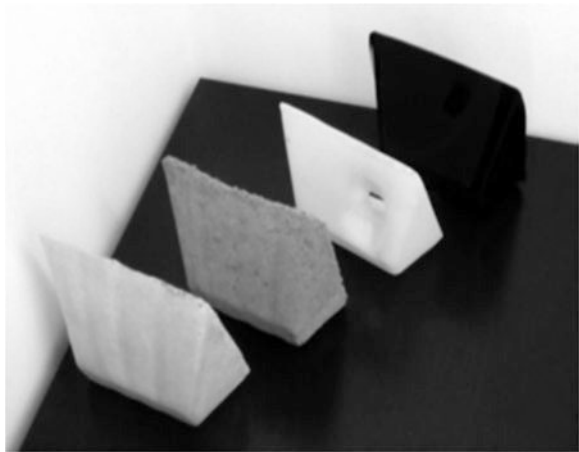
From the mechanical point of view, the tool development should consider its operation loading in the material and thicknesses selection, including the possible use of supports and reinforcements. The thermal behavior of the parts may also influence the tool design. Further, the tool's thermal behavior understanding helps to validate their use and define process cycle time.

Under the aerospace engineering field, ISF rapid tooling expands the process application. In one way, the development of tools allows the processing of a wide variety of materials, such as polymers and polymer-based composites. In another way, the fast development time is highly suitable for low batch production of those parts. Several studies have been published exploring the use of low-pressure polymer processing with sheet metal tools manufactured using SPIF. Research varies from proof-of-concept evaluations to industrial applications.

The authors have used a multi-slope geometry to test the SPIF made tools for thermoforming, roto-molding, contact molding, and compression molding. The 180×180 mm with a 30° wall and three 70° walls were designed to allow cutting tensile specimens from both the top face, high and low slope walls. The geometry suffered slight adjustment for each process to explore the viability of using sheet metal tools in different features typical from those processes. Conventional tooling was also developed and the manufactured parts via the two approaches were compared. Figure 12.11 presents a fiber-glass epoxy molded part, an agglomerated cork with a polyurethane resin, a low-density polyethylene roto-molded part, and a thermoformed acrylic part.

The parts accuracy, detail, and surface quality were compared between the ones made using sheet metal tools and the ones made using conventional tooling. The tool performance was also compared, looking for the ability to support all

Fig. 12.11 Parts manufactured with sheet metal rapid tools



mechanical and thermal loads. Table 12.2 presents a comparative analysis with a qualitative assessment of the sheet metal tools.

Other similar studies have been developed to validate the sheet metal tools concept and to address solutions for identified issues. To overcome the mechanical disadvantage of sheet metal tools, Appermont et al. added a porous mixture to the box support of a sheet metal thermoforming tool. This supporting method adds the benefit that heating elements can be placed very close to the sheet metal mold, before pouring the porous mixture [57]. To overcome the low surface quality and aluminum-formed material adherence, Alabanda et al. [58] tested using the dummy method on pre-painted aluminum with a non-stick resin was used in SPIF to form thermoforming tools with satisfactory results.

In addition to simple geometries used in the referred tests, the possibility of sheet metal molds for the manufacture of complex parts was tested. Camara [59] developed a shower bath thermoforming mold using AA1050-O using two different backing plates and a multistage tool path to achieve the high slope wall angles, while the present authors developed a mold for the tourism bus back seat, shown in Fig. 12.7.

12.7 Future Directions in Aerospace Industry

Although incremental forming has been used so far for a few isolated aerospace application case studies and demonstrators, with promising results, large-scale use by the aerospace sector has been lacking. A number of aerospace materials have not yet been tested for formability studies. Part of the challenge is the slowness of the incremental forming process, lack of process capabilities for large-scale parts in many industries, and the inherent limitations of ISF in terms of forming limits, accuracy, and wall thickness variations. Among the applications that have been shown successfully tested are airfoils and fuselage components. Recently, the authors of this work produced tunnel-type parts made from 2 mm thick AA1050 sheets using SPIF (Fig. 12.12), while Gupta and Jeswiet [60] formed C-channels designed for the vibrational testing of airplane fuselage systems with 2.54 mm thick, AA3003-O sheets using intermediate shapes. Earlier, Behera et al. [61] used a mesh-morphing strategy combined with sequencing of toolpaths to create an airfoil component (Fig. 12.13).

Table 12.2 Comparative analysis of molded parts and tools

Manufacturing process	Part accuracy	Part detail	Surface quality	Tool performance
Thermoforming	Fair	Poor	Fair	Good
Roto-molding	Good	Poor	Fair	Good
Roto-casting	Fair	Poor	Poor	Good
Hand layup	Good	Fair	Fair	Good
Compression molding	Fair	Good	Good	Poor

Fig. 12.12 Tunnel-type parts using ISF technology

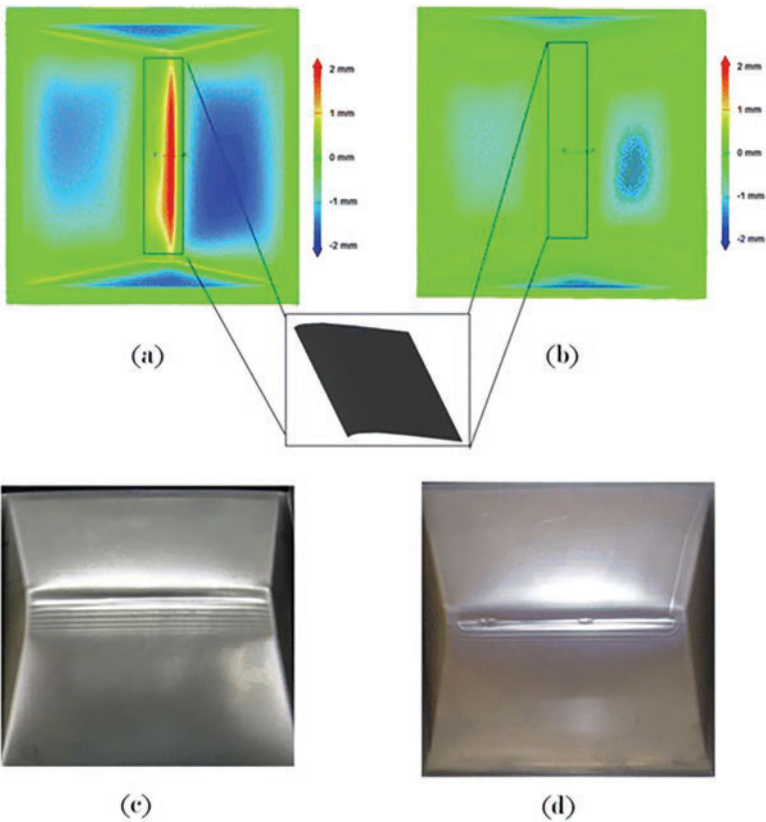


Fig. 12.13 Airfoils using a mesh morphing strategy [62]. Reprinted by permission from Springer

In the following considerations and given the great number of key contributions regarding ISF over the last few years, the reader is encouraged to verify references [7, 12, 13, 17, 62–80], linked to the topics referred to in the next paragraph.

A key concern in aerospace parts manufacture is that of accuracy. To overcome the issues of spring back in incremental forming and the over forming of negative curvature surfaces, feature-based approaches or other advanced techniques have been tried out on parts formed on milling machines. These approaches include detection of features on 3D CAD models of STL files, forming graphs by connecting features, and taking intelligent toolpath compensation strategies to overcome the anticipated deformations. Additionally, anticipating deformations using finite-element modeling or using regression equations. There is also current interest in forming large-scale components. This can be facilitated by high feed rate incremental forming or hybridization with other processes such as electromagnetic incremental forming combined with stretch forming. Initial studies on forming polymers and composites have been successful. To overcome forming limits, heat-assisted techniques such as using lasers and double-sided forming processes have been tried out. Likewise, there is significant interest to manufacture tunnel-shaped parts, which are different from the conventional formed parts which are container-like (Fig. 12.12).

References

1. Jeswiet, J., Micari, F., Hirt, G., Bramley, A., Dufloy, J., & Allwood, J. (2005). Asymmetric single point incremental forming of sheet metal. *Cirp Annals-Manufacturing Technology*, 54(2), 623–649.
2. Behera, A. K., de Sousa, R. A., Ingarao, G., & Oleksik, V. (2017). Single point incremental forming: An assessment of the progress and technology trends from 2005 to 2015. *Journal of Manufacturing Processes*, 27, 37–62. <https://doi.org/10.1016/j.jmapro.2017.03.014>
3. Dufloy, J. R., Habraken, A. M., Cao, J., Malhotra, R., Bambach, M., Adams, D., Vanhove, H., Mohammadi, A., & Jeswiet, J. (2018). Single point incremental forming: State-of-the-art and prospects. *International Journal of Material Forming*, 11, 743–773. <https://doi.org/10.1007/s12289-017-1387-y>
4. Alves de Sousa, R. J., Ferreira, J. A. F., Sa de Farias, J. B., Torrao, J. N. D., Afonso, D. G., & Martins, M. A. B. E. (2014). SPIF-A: On the development of a new concept of incremental forming machine. *Structural Engineering and Mechanics*, 49(5), 645–660. <https://doi.org/10.12989/SEM.2014.49.5.645>
5. Amino Corporation. Retrieved from <https://www.amino.co.jp/product/dieless-nc-forming-machine.html>.
6. EURECAT, Technological Center of Catalunya. Retrieved from <https://eurecat.org/wp-content/uploads/2019/10/MECO-ISF-BLAU-03-ENG-DIGITAL.pdf>.
7. Behera, A. K. (2013). *Shape feature taxonomy development for toolpath optimisation in incremental sheet forming*. PhD Thesis. Katholieke Universiteit Leuven.
8. Emmens, W., & Van den Boogaard, A. (2009). An overview of stabilizing deformation mechanisms in incremental sheet forming. *Journal of Materials Processing Technology*, 209(8), 3688–3695.
9. Jackson, K., & Allwood, J. (2009). The mechanics of incremental sheet forming. *Journal of Materials Processing Technology*, 209(3), 1158–1174.
10. Malhotra, R., Xue, L., Belytschko, T., & Cao, J. (2012). Mechanics of fracture in single point incremental forming. *Journal of Materials Processing Technology*, 212(7), 1573–1590.
11. Silva, M., Skjødt, M., Martins, P. A., & Bay, N. (2008). Revisiting the fundamentals of single point incremental forming by means of membrane analysis. *International Journal of Machine Tools and Manufacture*, 48(1), 73–83.

12. Verbert, J. (2010). *Computer aided process planning for rapid prototyping with incremental sheet forming techniques*. PhD Thesis. Katholieke Universiteit Leuven., Leuven.
13. Bhattacharya, A., Maneesh, K., Venkata Reddy, N., & Cao, J. (2011). Formability and surface finish studies in single point incremental forming. *Journal of Manufacturing Science and Engineering*, 133(6).
14. Silva, M. B., Nielsen, P. S., Bay, N., & Martins, P. (2011). Failure mechanisms in single-point incremental forming of metals. *The International Journal of Advanced Manufacturing Technology*, 56(9), 893–903.
15. Allwood, J., Shouler, D., & Tekkaya, A. E. (2007). *The increased forming limits of incremental sheet forming processes*. Paper presented at the Key Engineering Materials.
16. Eyckens, P., Van Bael, A., & Van Houtte, P. (2009). Marciniak–Kuczynski type modelling of the effect of through-thickness shear on the forming limits of sheet metal. *International Journal of Plasticity*, 25(12), 2249–2268.
17. Montanari, L., Cristino, V., Silva, M., & Martins, P. (2013). A new approach for deformation history of material elements in hole-flanging produced by single point incremental forming. *The International Journal of Advanced Manufacturing Technology*, 69(5–8), 1175–1183.
18. Khazaali, H., & Fereshteh-Saniee, F. (2018). Application of the Taguchi method for efficient studying of elevated-temperature incremental forming of a titanium alloy. *Journal of the Brazilian Society of Mechanical Sciences and Engineering*, 40(2), 43.
19. Valle, P. D., Amorim, F. L., Da Costa, D. D., & Marcondes, P. V. (2018). Experimental investigations on the incremental sheet forming of commercial steel ASTM A653 CS-A G90 to predict maximum bending effort. *Journal of the Brazilian Society of Mechanical Sciences and Engineering*, 40(6), 322.
20. Allwood, J. M., King, G. P. F., & Dufloy, J. (2005). A structured search for applications of the incremental sheet forming process by product segmentation. *Proceedings of the Institution of Mechanical Engineers, Part B: Journal of Engineering Manufacture*, 219, 239–244.
21. Adams, D., & Jeswiet, J. (2014). Design rules and applications of single-point incremental forming. *Proceedings of the Institution of Mechanical Engineers, Part B: Journal of Engineering Manufacture*, 229(5), 754–760.
22. Jeswiet, J., Dufloy, J. R., Szekeres, A., & Lefebvre, P. (2005). Custom manufacture of a solar cooker—A case study. *Advanced Materials Research*, 6–8, 487–492. <https://doi.org/10.4028/www.scientific.net/AMR.6-8.487>
23. Barimani-Varandi, A., Nasrabadi, M. K., Ravan, B. A., & Javadi, M. (2021). Rapid prototyping of aircraft canopy based on the incremental forming process. *Journal of the Brazilian Society of Mechanical Sciences and Engineering*, 43, 59. <https://doi.org/10.1007/s40430-021-02811-1>
24. Durante, M., Formisano, A., & Lambiase, F. (2018). Incremental forming of polycarbonate sheets. *Journal of Materials Processing Technology*, 253(57–63), 25.
25. Durante, M., Formisano, A., & Lambiase, F. (2019). Formability of polycarbonate sheets in single-point incremental forming. *The International Journal of Advanced Manufacturing Technology*, 102(5–8), 2049–2062.
26. Dufloy, J. R., Behera, A. K., Vanhove, H., & Bertol, L. S. (2013). Manufacture of accurate titanium Cranio-facial implants with high forming angle using single point incremental forming. *Key Engineering Materials*, 549, 223–230. <https://doi.org/10.4028/www.scientific.net/KEM.549.223>
27. Bagudanch, I., Lozano-Sánchez, L. M., Puigpinós, L., Sabater, M., Elizalde, L. E., Elías-Zúñiga, A., & Garcia-Romeu, M. L. (2015). Manufacturing of polymeric biocompatible cranial geometry by single point incremental forming. *Procedia Engineering*, 132, 267–273. <https://doi.org/10.1016/j.proeng.2015.12.494>
28. Göttmann, A., & Korinth, M. (2012). Manufacturing of cranial implants using incremental sheet metal forming. In *Proceedings 1st internat. conf. on design and processes for medical devices PROMED*, pp. 287–290.

29. Lu, B., Xu, D. K., Liu, R. Z., Ou, H., Long, H., & Chen, J. (2015). Cranial reconstruction using double side incremental forming. *Key Engineering Materials*, 639, 535–542. <https://doi.org/10.4028/www.scientific.net/KEM.639.535>
30. Trzepieciński, T., Krasowski, B., Kubit, A., & Wyrzyński, D. (2018). Possibilities of application of incremental sheet-forming technique in aircraft industry. *Scientific Letters of Rzeszow University of Technology - Mechanics*, 1(2018), 87–100.
31. Fan, G., Gao, L., Hussain, G., & Wu, Z. (2008). Electric hot incremental forming: A novel technique. *International Journal of Machine Tools and Manufacture*, 48(15), 1688–1692.
32. Kleiner, M., Geiger, M., & Klaus, A. (2003). Manufacturing of lightweight components by metal forming. *CIRP Annals*, 52, 521–542.
33. Gupta, P., Szekeres, A., & Jeswiet, J. (2021). Manufacture of an aerospace component with hybrid incremental forming methodology. *International Journal of Material Forming*, 14, 293–308.
34. Gupta, P., Szekeres, A., & Jeswiet, J. (2019). Design and development of an aerospace component with single-point incremental forming. *The International Journal of Advanced Manufacturing Technology*, 103, 3683–3702.
35. Mohanraj, R., & Elangovan, S. (2020). Incremental sheet metal forming of Ti–6Al–4V alloy for aerospace application. *Transactions of the Canadian Society for Mechanical Engineering*, 44(1), 56–64.
36. Jeswiet, J., Micari, F., Hirt, G., Bramley, A., Duflou, J., & Allwood, J. (2005). Asymmetric single point incremental forming of sheet metal. *CIRP Annals*, 54(2), 88–114. [https://doi.org/10.1016/s0007-8506\(07\)60021-3](https://doi.org/10.1016/s0007-8506(07)60021-3)
37. Duc-Toan, N., & Long, H. (2019, August 22). *Rapid prototyping for sheet metal products, mass production processes, anil akdogan and ali serdar vanli*. IntechOpen. <https://doi.org/10.5772/intechopen.88435>. Retrieved from from <https://www.intechopen.com/books/mass-production-processes/rapid-prototyping-for-sheet-metal-products>.
38. Scheffler, S., Pierer, A., Scholz, P., Melzer, S., Weise, D., & Rambousek, Z. (2019). Incremental sheet metal forming on the example of car exterior skin parts. *Procedia Manufacturing*, 29, 105–111.
39. Peter, I., Fracchia, E., Canale, I., & Maiorano, R. (2019). Incremental sheet forming for prototyping automotive modules. *Procedia Manufacturing*, 32, 50–58.
40. Seo, D., Kim, H., Heo, Y., Kim, N., & Kim, H. Y. (2000). Forming and drawing characteristics of tailor welded sheets in a circular draw bead. *Journal of Materials Processing Technology*, 105, 294–301.
41. Xue, S., Zhou, J., & He, Y. Q. (2011). Tensile testing on formability of different gauge tailor-welded blanks. *The Open Materials Science Journal*, 5, 89–92.
42. Padmanabhan, R., Baptista, A. J., Oliveira, M. C., & Menezes, L. F. (2007). Effect of anisotropy on the deep-drawing of mild steel and dual-phase steel tailor-welded blanks. *Journal of Materials Processing Technology*, 184, 288–293.
43. Zadpoor, A. A., Sinke, J., & Benedictus, R. (2007). Mechanics of tailor welded blanks: An overview. *Key Engineering Materials*, 344, 373–382.
44. Kaushik, Y. (2015). A review on use of aluminium alloys in aircraft components. *I-Manager's Journal on Material Science*, 3(3), 33–38.
45. Ambrogio, G., Fratini, L., & Micari, F. Incremental forming of friction stir welded tailored sheets. In *Proceedings of the ASME 8th biennial conference on engineering systems design and analysis*. Volume 4: Fatigue and fracture, heat transfer, internal combustion engines, manufacturing, and technology and society. Torino, Italy. July 4–7, 2006. pp. 757–762. ASME. <https://doi.org/10.1115/ESDA2006-95375>.
46. Ambrogio, G., Filice, L., Fratini, L., & Micari, F. (2003). Some relevant correlations between process parameters and process performance in incremental forming of metal sheets, In *Proceedings of the 6th esaform conference on material forming*, pp. 175–178.

47. Silva, M. B., Skjoedt, M., Vilac, P., Bay, N., & Martins, P. A. F. (2009). Single point incremental forming of tailored blanks produced by friction stir welding. *Journal of Materials Processing Technology*, 209, 811–820. <https://doi.org/10.1016/j.jmatprotec.2008.02.057>
48. Alinaghian, I., Ranjbar, H., & Beheshtizad, M. A. (2017). Forming limit investigation of AA6061 friction stir welded blank in a single point incremental forming process: RSM approach. *Transactions of the Indian Institute of Metals*, 70, 2303–2318. <https://doi.org/10.1007/s12666-017-1093-y>
49. Ebrahimzadeh, P., Baseri, H., & Mirnia, M. J. (2018). Formability of aluminum 5083 friction stir welded blank in two-point incremental forming process. *Proceedings of the Institution of Mechanical Engineers, Part E: Journal of Process Mechanical Engineering*, 232(3), 267–280. <https://doi.org/10.1177/0954408917692370>
50. Rattanachan, K., Sirivedin, K., & Chungchoo, C. (2014). Formability of tailored welded blanks in single point incremental forming process. *Advanced Materials Research*, 979, 339–342. <https://doi.org/10.4028/www.scientific.net/amr.979.339>
51. Ghadmode, M. M., Patil, A. R., Sonawane, B. U., & Mulay, A. (2021). Analysis of TIG-welded aluminum alloys during single point incremental forming at different wall angles. In H. K. Dave & D. Nedelcu (Eds.), *Advances in manufacturing processes. Lecture notes in mechanical engineering*. Springer. https://doi.org/10.1007/978-981-15-9117-4_15
52. Wang, X., Wang, K., Shen, Y., & Kai, H. (2008). Comparison of fatigue property between friction stir and TIG welds. *Journal of University of Science and Technology Beijing*, 15(3), 280–284.
53. Fadaeifard, F., Matori, K. A., Garavi, F., Al-Falahi, M., & Sarrigani, G. V. (2016). Effect of post weld heat treatment on microstructure and mechanical properties of gas tungsten arc welded AA6061-T6 alloy. *Transactions of the Nonferrous Metals Society of China*, 26, 3102–3114.
54. Tayebi, P., Fazli, A., Asadi, P., & Soltanpour, M. (2019). Formability analysis of dissimilar friction stir welded AA 6061 and AA 5083 blanks by SPIF process. *CIRP Journal of Manufacturing Science and Technology*, 25, 50–68. <https://doi.org/10.1016/j.cirpj.2019.02.002>
55. Equbal, A., Sood, A. K., & Shamim, M. (2015). Rapid tooling: A major shift in tooling practice. *Manufacturing and Industrial Engineering*, 14(3–4).
56. Tackett, E. (2012). *Rapid tooling*. Saddleback College Advanced Technology Center.
57. Appermont, R., Van Mieghem, B., Van Bael, A., Bens, J., Ivens, J., Vanhove, H., Behera, A. K., & Dufloy, J. (2012). Sheet-metal based molds for low-pressure processing of thermoplastics. In *Proceedings of the 5th bi-annual PMI conference*, Vol. 5, pp 383–388.
58. Rodriguez-Alabanda, O., Narvaez, M. A., Guerrero-Vaca, G., & Romero, P. E. (2018). Manufacturing of non-stick molds from pre-painted aluminum sheets via single point incremental forming. *Applied Sciences - Special Issue Mechanical Behaviour of Aluminium Alloys*, 8(6), 1002.
59. Camara, J. (2009). *Single point incremental forming*, IST—UTL Master Thesis.
60. Gupta, P., & Jeswiet, J. (2019). Manufacture of an aerospace component by single point incremental forming. *Procedia Manufacturing*, 29, 112–119.
61. Behera, A. K., Gu, J., Lauwers, B., & Dufloy, J. R. (2012). Influence of material properties on accuracy response surfaces in single point incremental forming. *Key Engineering Materials*, 504–506, 919–924. <https://doi.org/10.4028/www.scientific.net/KEM.504-506.919>
62. Behera, A. K., Lauwers, B., & Dufloy, J. R. (2013). Tool path generation for single point incremental forming using intelligent sequencing and multi-step mesh morphing techniques. *International Journal of Material Forming*, 8(4), 517–532. <https://doi.org/10.1007/s12289-014-1174-y>
63. Behera, A. K., Lauwers, B., & Dufloy, J. R. (2012a). Advanced feature detection algorithms for incrementally formed sheet metal parts. *Transactions of Nonferrous Metals Society of China*, 22, S315–S322. [https://doi.org/10.1016/S1003-6326\(12\)61725-7](https://doi.org/10.1016/S1003-6326(12)61725-7)
64. Behera, A. K., Lauwers, B., & Dufloy, J. R. (2012b). An integrated approach to accurate part manufacture in single point incremental forming using feature based graph topology.

- Key Engineering Materials*, 504–506, 869–876. <https://doi.org/10.4028/www.scientific.net/KEM.504-506.869>
65. Behera, A. K., Lauwers, B., & Dufloy, J. R. (2014). Tool path generation framework for accurate manufacture of complex 3D sheet metal parts using single point incremental forming. *Computers in Industry*, 65(4), 563–584.
 66. Bagudanch, I., Garcia-Romeu, M., & Sabater, M. (2015). Incremental forming of polymers: Process parameters selection from the perspective of electric energy consumption and cost. *Journal of Cleaner Production*.
 67. Behera, A. K., Afonso, D., Murphy, A., Jin, Y., & de Sousa, R. A. (2018). Accuracy analysis of incrementally formed tunnel shaped parts. In *Recent advances in intelligent manufacturing* (pp. 40–49). Springer.
 68. Behera, A. K., Lu, B., & Ou, H. (2015). Characterization of shape and dimensional accuracy of incrementally formed titanium sheet parts with intermediate curvatures between two feature types. *The International Journal of Advanced Manufacturing Technology*, 1–13. <https://doi.org/10.1007/s00170-015-7649-2>
 69. Behera, A. K., Vanhove, H., Lauwers, B., & Dufloy, J. R. (2011). Accuracy improvement in single point incremental forming through systematic study of feature interactions. *Key Engineering Materials*, 473, 881–888. <https://doi.org/10.4028/www.scientific.net/KEM.473.881>
 70. Behera, A. K., Verbert, J., Lauwers, B., & Dufloy, J. R. (2013). Tool path compensation strategies for single point incremental sheet forming using multivariate adaptive regression splines. *Computer-Aided Design*, 45(3), 575–590. <https://doi.org/10.1016/j.cad.2012.10.045>
 71. Cui, X., Mo, J., Li, J., Xiao, X., Zhou, B., & Fang, J. (2016). Large-scale sheet deformation process by electromagnetic incremental forming combined with stretch forming. *Journal of Materials Processing Technology*, 237, 139–154.
 72. Duchene, L., Guzman, C. F., Behera, A. K., Dufloy, J., & Habraken, A. M. (2013). Numerical simulation of a pyramid steel sheet formed by single point incremental forming using solid-shell finite elements. *Sheet Metal*, 2013(549), 180–188. <https://doi.org/10.4028/www.scientific.net/KEM.549.180>
 73. Dufloy, J., Callebaut, B., Verbert, J., & De Baerdemaeker, H. (2008). Improved SPIF performance through dynamic local heating. *International Journal of Machine Tools and Manufacture*, 48(5), 543–549.
 74. Dufloy, J. R., Callebaut, B., Verbert, J., & De Baerdemaeker, H. (2007). Laser assisted incremental forming: Formability and accuracy improvement. *Cirp Annals-Manufacturing Technology*, 56(1), 273–276. <https://doi.org/10.1016/j.cirp.2007.05.063>
 75. Lu, B., Chen, J., Ou, H., & Cao, J. (2013). Feature-based tool path generation approach for incremental sheet forming process. *Journal of Materials Processing Technology*, 213(7), 1221–1233. <https://doi.org/10.1016/j.jmatprotec.2013.01.023>
 76. Vanhove, H., Mohammadi, A., Guo, Y. S., & Dufloy, J. R. (2014). *High-speed single point incremental forming of an automotive aluminium alloy*. Paper presented at the Key Engineering Materials.
 77. Verbert, J., Behera, A. K., Lauwers, B., & Dufloy, J. R. (2011). Multivariate adaptive regression splines as a tool to improve the accuracy of parts produced by FSPIF. *Key Engineering Materials*, 473, 841–846. <https://doi.org/10.4028/www.scientific.net/KEM.473.841>
 78. Emmens, W. C., & Van den Boogaard, A. (2007). *Strain in shear, and material behaviour in incremental forming*. Paper presented at the Key Engineering Materials.
 79. Nguyen, D. T., Yang, S. H., Jung, D. W., Choi, T. H., & Kim, Y. S. (2011). Incremental sheet metal forming: Numerical simulation and rapid prototyping process to make an automobile white-body. *Steel Research International*, 7, 795–805.
 80. Ambrogio, G., De Napoli, L., Filice, L., Gagliardi, F., & Muzzupappa, M. (2005). Application of incremental forming process for high customised medical product manufacturing. *Journal of Materials Processing Technology*, 162-163, 156–162. <https://doi.org/10.1016/j.jmatprotec.2005.02.148>

Chapter 13

Welding of Dissimilar Materials in Aerospace Systems



Seyed Reza Elmi Hosseini, Fábio A. O. Fernandes, António B. Pereira,
and Zhuguo Li

13.1 Introduction

Dissimilar welding of metals is an important challenge for several industries, especially the aerospace industry [1]. The aerospace industry has driven the generation of many alloys and dissimilar combinations [2, 3]. In past years, the aerospace system has been shifting to the manufacturing of more energy-effective products. Energy efficiency may be attained by mass reduction. To realize this target, lighter material(s), like high-strength steel, aluminum (Al) alloys, magnesium (Mg) alloys, titanium (Ti) alloys, and composites are replacing heavier steels. The new variety of materials applied led to a requisite for efficient routes of welding dissimilar materials [1, 4–7].

Some examples of dissimilar materials that have been welded involve uranium stainless steel (SS), Ni-stainless steel, Be–Ni, Be–SS, thorium dioxide-dispersion strengthened-Ni alloys, Zr–steel, Cu–Monel, steel to SS, steel to brass, steel to copper, copper to brass, and die-cast zinc to Al [8–10]. Welds between Be and metals like Ti, SS, and Al are experienced in the space vehicle system, where Be is an

S. R. Elmi Hosseini

School of Metallurgy and Materials Engineering, Iran University of Science and Technology (IUST), Narmak, Tehran, Iran

F. A. O. Fernandes · A. B. Pereira (✉)

TEMA: Centre for Mechanical Technology and Automation, Department of Mechanical Engineering, University of Aveiro, Aveiro, Portugal

e-mail: abastos@ua.pt

Z. Li

Shanghai Key Laboratory of Materials Laser Processing and Modification, School of Materials Science and Engineering, Shanghai Jiao Tong University, Shanghai, China

attractive metal due to its resistance to damage by impact with meteors, its low density, its stiffness under load, and its high heat capacity [2, 3].

Elevated strength Al alloys are employed extensively in aerospace applications because of their high mechanical properties and low mass compared with other materials like steel. Ti has a big strength-to-weight ratio in addition to resistance to corrosion which causes another material to be used in these areas. By enhancing the utilization of these materials, there is a requisite to find more innovative and effective ways for welding these dissimilar materials [1, 11]. Mg alloys are the lightest structural materials with some unique properties that steel does not possess, such as high specific strength, specific elastic modulus, damping capacity, low density, and recyclability. They are called “Green” materials of the twenty-first century and are being introduced into aerospace [12].

Dissimilar welding of Al and steel has collected broad acceptance in the aerospace system, as it may lead to a notable mass reduction in the system and obtain the required characteristics. Nevertheless, it is very difficult to join steel to Al because of their metallurgical dissimilarity, big differences in their thermal expansion coefficient, and the brittle intermetallic compounds (IMCs) formation. Austenitic SS and an Al–Cu alloy are applied in the manufacturing of bimetallic adaptors in the satellite launch structures. These adaptors are utilized as transition welds between Al tanks and SS piping. Although these adaptors are commonly manufactured by explosive welding, an accepted bonding at the transition area is very tough to fulfill. Furthermore, this technique is much expensive, and this needs some safety measures. The trouble in welding is typical because of the brittle IMC formation in the bonding area that results in weak joint tensile strength. To decrease the IMC layer thickness and to reach elevated tensile strength, the heat input (H.I.) value near the bonding area should be managed [10, 13, 14].

Dissimilar joints are not limited to metallic materials alone. Joining thermoplastic matrix materials to thermosetting composites is a highly relevant concept offering the highest flexibility to polymer design engineering. Similarly, metal-to-polymer joints offer the benefit of ductility and strength of the metal with corrosion resistance and the lightweight of the polymer. The joining of lightweight dissimilar materials, like metals and polymers, is important in the design of hybrid structures. With the increased thrust on the development of lightweight structures in aerospace sectors, the possibility of getting a good dissimilar joint is highly relevant [15].

For aerospace applications, the welding of Al to Mg is of specific interest. Mg provides the largest mass savings possibility as this is 35% and 75% lighter than aluminum and steel, respectively. This also has very high vibration and noise dampening properties. Nevertheless, the specific stiffness of Al is more than Mg. Therefore, there are many applications for hybrid structures that would need welding of Mg and Al constituents together [1]. Six applications that need the dissimilar welding of metals/alloys are:

1. Increasing the resistance to wet corrosion in one area vs. another area, for example, in the corrosion conditions side of a structure, vessel, pipe, or part.

2. Increasing the resistance to dry corrosion by sulfurization or oxidation scaling in one area vs. another area, for example, in the sulfur-rich side of a structure, vessel, pipe, part, or the high-temperature atmosphere.
3. Increasing the resistance to abrasive wear/adhesive in one area vs. another area.
4. Increasing thermal or electrical conductivity or resistivity/insulation in one area vs. another area, for example, at a laminate, external surface, interior surface, or in a core.
5. Decreasing the weight by applying lower density, but less stiff or strong of the metal/alloy.
6. Increasing the resistance to ballistic penetration, for example, in multilayer armors [16, 17].

Dissimilar welding of the materials causes significant challenges that welding is not possible from time to time. This issue is basically due to the difference in physical, mechanical, metallurgical, and chemical properties of materials being welded. Differences in thermal conductivity, coefficient of thermal expansion, melting point, and so on can cause fracture at the joints even during the welding. Welding is an important manufacturing technique that produces a broad area of products being applied in aerospace systems. Nevertheless, welding techniques are very multidimensional and complex in terms of workmen's skill, materials, and technique, which cause the production of the desired joint very difficult [15, 18].

13.2 Dissimilar Liquid State Welding for Aerospace Systems

13.2.1 Dissimilar GMAW in Aerospace Systems

The possibility of control of the joint thermal cycle and joint isotherm has caused the GMAW technique suitable for usage in several challenging sectors of the aerospace constituents. The successful utilization of this technique is usually noted in the joining of tubular constituents with the thickness of around 0.5 mm of the sheet products, modern ferrous/nonferrous alloys, as well as the dissimilar metal surfacing of the steel. The quality of this technique regarding the transfer and thermal behavior of metal depositions enhances the quality of the product particularly about porosity, weld geometry, weld chemistry, microstructure, and stress development and inclusion in the weldment [19].

13.2.2 Dissimilar GTAW in Aerospace Systems

Tungsten inert gas (TIG) or gas tungsten arc welding (GTAW) technique is one of the most widely adopted processes in industries for joining similar/dissimilar metals. The increasing demand for the quality of the weld has caused this process to be

very attractive for joining smaller sections to huge pressure vessels for critical applications. TIG process has become an essential process in industries because of its versatility and its capability to manufacture big quality joints with low equipment costs [20].

GTAW was developed by Russell Meredith at Northrop Aviation in the early 1940s and came into widespread use during World War II with the need to replace riveting for difficult-to-weld metals as Al and magnesium, and Ti alloys in aircraft and also to weld reactive metals; later it was extended to join a broad scale of metallic materials like SSs, Ni alloys, and so on. Using a DC power source with the negative electrode and tungsten electrode, a stable and efficient heat source (arc) was produced, which resulted in excellent welds. Helium gas was selected to provide the necessary shielding since it was the only readily available inert gas at that time. This process is also known as the Heli-arc process or nonconsumable electrode welding process [20–22].

A TIG weld is sound, smooth, strong, ductile, uniform, and bright. These characteristics make it ideal for use in industries such as aerospace products [23]. Joints of high quality and strength could be produced on thin, light, and dissimilar materials with minimal corruption or distortion of the parent metals. The technique does not create a spatter or spark, and the joints are as clean as could be because of no flux usage, which is why this is the process of choice in aerospace systems. There is no slag included. Since there is a little smoke generation, the weld has an acceptable view of the technique and creates fine joints [24].

Flexibility is obtained by using GTAW as the technique to let the filler metal additions and heat source be controlled individually. The technique may be utilized with/without an intermediate layer as needed by the particular application. The exceptional control of the weld penetration could be kept. Joints could be formed in any position, and the utilizations are usually unlimited. The technique can produce autogenous welds with few defects, spatter-free, and generally with superior quality at high speed. An extra advantage is a relatively inexpensive power source may be applied [25]. Since the shielding gas used in this process is transparent, the welder may detect the welding pool obviously because it is created during the welding process. Welding can be performed in all positions [23].

The process control is regularly attained now by switching the joining process current between very low and big level values, or pulsing, to regulate H.I. as well as the molten pool behavior and then its following solidification. Low frequencies (1–10 Hz) result in the thermal pulsing that prepares difficult welds to be formed in thin materials with unequal thermal capacity, due to either dissimilar geometry (thin to thick) or various thermal conductivity (carbon steel to SS), that was impossible with DC. Pulsing at stronger amounts of frequency values (1–10 kHz) in GTAW controls over arc directionality as well as affects grain growth during molten pool solidification [26].

Plasma arc welding is a close relative of gas tungsten. This equipment can weld nearly all metals in all positions and offers better directional control of the arc than GTAW with a smaller heat-affected zone (HAZ) [22].

13.2.3 Dissimilar Flash Welding in Aerospace Systems

The aircraft industry utilizes flash welding in the manufacturing of control assemblies, landing gear, and hollow propeller rings and blades for rocket casings and jet engines. Flash welding is widely used to join rings for aircraft engines, bandsaw blades, window frames, steel rails, and a wide variety of parts [27]. In addition to the low carbon steels, metals that are flash joined involve low alloy steels, tool steels, SSs, Al alloys, Mg alloys, copper alloys, and Ni alloys. Ti alloys could be flash welded; however, an inert gas cover to displace air from around the weld is recommended to reduce embrittlement. Flash welding could be utilized for welding several ferrous/nonferrous alloys as well as different dissimilar metals with a high quality of the joint. Dissimilar metallic materials can be joined by flash welding if their upsetting and flashing properties are similar. Some dissimilarities could be overcome with selections of joining variables, a difference in the initial extensions between the clamping electrodes, and adjustment of flashing distance. Some examples of this process are the welding of Al to Cu or steel to Ni alloy [8, 10, 28].

Flash welding is an economical and rapid process. This can produce uniform and high-quality joints [10, 28]. Many developments have been recently incorporated into the technique, which resulted in the soundness of the final product, dimensional strength of the final assembly of the product, and the external upsets removal by stripping dies or by machining/grinding [8].

13.2.4 Dissimilar Laser Welding in Aerospace Systems

Laser welding is an energy beam-assisted fusion welding process that includes the application of a laser beam with big power to melt and weld two similar/dissimilar metals. The benefits of laser welding over conventional arc welding methods include narrow HAZ, high-welding speed, ease to be automated, low distortion, single-pass weldability of thick sections and flexibility with the controlled bead size, weldability the dissimilar materials, and less contamination [29, 30].

The particular interest in laser welding lies in its ability for dissimilar welding of materials with different thickness values, compositions, and/or chemical/physical properties for industrial applications, especially in aerospace systems. Today, aerospace application relies on lasers for a noncontact and clean source of heating/fusion for welding of sheets. Laser welding applies to both organic/inorganic and similar or dissimilar materials with big productivity, precision, and versatility that could only be matched by electron-beam welding. Furthermore, laser-assisted welding could be performed in the atmosphere with appropriate shrouding, unlike the vacuum methods required in electron-beam welding [29, 30].

Studies on dissimilar laser welding have been continued for several years, while many challenges are remaining unsolved yet. A specific challenge is the brittle IMCs formation in the weldments. Understanding of material behavior in the

joining of dissimilar materials is complicated than joining similar materials, especially due to a big difference in two parent materials properties [31]. The most important research was performed on the laser welding of Al to steel and Al to Ti. Al–Ti combination has a significant application in aircraft systems [32].

Dissimilar materials have high application in large structures of the aircraft system. Laser welding of dissimilar materials has an application in the seat track. Nowadays, Al is applied for the seat tracks. Nevertheless, to prevent flaws formation due to the presence of liquids within the passenger cabin, it is desired to employ Ti instead of Al in the top region of the seat track. As the remaining seat track should be formed of Al (particularly due to the cost), laser welding for Al–Ti seat tracks was promoted. Although laser welding of dissimilar materials found large applications in aerospace systems, the trend goes toward the use of composites like CFRP in this industry [32].

13.2.5 Dissimilar Electron Beam Welding in Aerospace Systems

Electron beam welding (EBW) may create narrow, deep, and parallel-sided joints with low values of H.I. and narrow HAZs in a broad variety of metals. When initially employed in industrial applications in the 1950s, EBW was done in a vacuum. In this condition, EBW was employed due to its capability to create elevated quality welds in materials that are considered entirely tough to weld (e.g., superalloys, oxidizable metals, SSs, and refractory metals). This formed EBW suited for application in the aerospace system. During the 1960s, the capability to apply the EBW method for non-vacuum and medium-vacuum joining applications was promoted [33]. It has been considered which there are about 3000 electron-beam welders in operation in all of the worlds of which roughly 15% with both aircraft and aerospace-related tasks [34].

EBW is applied to weld not only difficult-to-weld materials but also common materials like steels (less than 150 mm in thick), Al (less than 305 mm in thick), and Cu (less than 100 mm in thick). These metals (in thickness values scaling from foil to plate) could be EB welded. Furthermore, EBW could be used to weld several combinations of dissimilar alloys [8, 9]. Temperatures up to 100,000 °C are generated by EBW machines. At such high temperatures, the machine can accurately vaporize metals and ceramics. The welds have high strength and purity [35]. Many alloys are important for use in high-temperature service in industries such as aerospace or any application requiring high strength and resistance to oxidation and corrosion [33].

This is capital-intensive equipment however able to form a quality joint with low distortion and H.I. as well as to weld parts with a dissimilar thickness which permitted engineers to redesign samples with fewer joints or even to produce in novel

routes. There are few benefits in replacing the arc welding process with electron beam welding [36].

The copper and steel are not very compatible components for mixing in a weld, the EBW process has been found to be especially well suited to make dissimilar welding between copper and the steel. In aerospace applications, various joints of these metals, such as heat exchanger tubes, copper cavities, and copper beamlines with conflate stainless-steel flanges are done by EBW [37].

As reflective alloys like copper and Al include several free electrons, they are very susceptible to be welded by electron beam welding compared to laser beam welding. High penetration and low distortion could be obtained with elevated welding speed values [21].

Electron Beam Braze Welding

Electron-beam braze welding (EBBW) is a specific brazing technique that is useful in some applications. The elements to be welded are heated to a suitable temperature by defocusing the electron beams. This technique is always done in a high vacuum environment [10^{-4} to 10^{-5} torr] and is very similar to EBW. EBBW has many advantages. Most of these advantages relate to performing the process in a vacuum. Flux is not required to assure the brazing filler-metal flow. This eliminates the requisite for post braze cleaning and also any suggestion related to entrapment of the flux. Refractory metals and the metals are sensitive to oxygen, difficult to wet, or those no effective fluxes are available could be welded by EBBW. Welds are retained free from oxidation. Distortion is retained to a minimum because the heating is very localized. This localized heating allows thin constituents to be welded as well as constituents of dissimilar thickness/mass.

EBBW has some limitations. The size of constituents that could be welded is limited by the vacuum chamber size. Materials include elements with high vapor pressure such as Zn could not be welded because they are volatilized in a vacuum during the method. EBBW is very practical for the brazing of small assemblies. Most applications are found in the aerospace industry [38].

13.3 Dissimilar Solid-State Welding for Aerospace Systems

13.3.1 Dissimilar Microwave Welding in Aerospace Systems

This welding method depends on the heat created by microwave frequency radiation. The parts being welded are held together at a pressure of 35–70 kPa, and afterward, the interfaces are irradiated by the electromagnetic radiation by well-focused horn antennas. To absorb electromagnetic energy, the polymer should involve a polar group. To achieve viable heating, either a low-conductivity polymer or a

nonconducting must dope with a conducting polymer/adhesive film that contains polar/electron-withdrawing groups could be placed at the weld interface. This welding technique is simple, fast, clean, and very efficient in terms of energy conversion. Therefore, short joining times are counted. Dissimilar materials could be welded, and employing a microwave adhesive will let the repair of thermoset/thermoplastic-based composites. This welding method could be very beneficial for in situ repairing of structures, particularly on space structures [9].

13.3.2 Dissimilar Magnetic Pulse Welding in Aerospace Systems

Magnetic pulse welding is a solid-state joining process that is well suited for big volume joining of dissimilar/hard-to-join metals. A quick emerging impact welding process similar to explosive welding, magnetic pulse welding creates a solid-state join by producing contact at elevated pressures and through removing the oxide layer by the angle and speed of impact. Complete bonding could be provided by pressing two surfaces together at high pressure to provide a joint between the metals. This technique has been studied for the joining of axisymmetric parts. Many scientists have now focused on the field of magnetic pulse welding because of the application of this process to weld flat sheets of dissimilar/hard-to-weld metals in aerospace constituents [8].

13.3.3 Dissimilar Explosion Welding in Aerospace Systems

The dissimilar metal joining features of explosive welding (EXW) is available to a wide industrial application by the concept of joining transition welds. Transition weld constituents are created by explosion welders at their production equipment and then produced in the form of tubular couplings, blocks, or strips for application in the conventional joining of dissimilar metals. Its common utilization is Ti/SS for aerospace and aircraft applications.

Solid-state welds need clean surfaces; in EXW, the effect of the materials provides this by removing the layers of an oxide layer. EXW is well suited for joining dissimilar/difficult-to-join metals, but due to safety and cost concerns, it has many applications mainly for low production volume [8]. Due to the unique noise vibration and safety inspection, explosive welding is carried out in isolated facilities. The main products are huge clad plates [9].

13.3.4 Dissimilar Forge Welding in Aerospace Systems

Forge welding is commonly used to low alloy and carbon steels at the welding temperature of 1125 °C. Low carbon steels may be applied in as-joined conditions; however, low alloy steels and medium carbon steels usually are given a full-heat treatment after welding. In these cases, where the full-heat treatment is impossible, the hardening occurred because of the rapid cooling, and induction heating can be employed to temper the weldment. The other metals joined by the forge welding technique include high alloy steels, Ni-base alloys, cobalt-base alloys, Al alloys, tungsten, and Ti alloys. Applications of this technique involve welding cans, rods, bars, tubes, rails, aircraft gear, and chains. The forge welding method is competitive with friction welding and flash welding [8].

13.3.5 Dissimilar Ultrasonic Welding in Aerospace Systems

Ultrasonic welding (USW) is a quasi-solid-state method that creates a joint by a high-frequency vibration to the weld because it is held at an elevated clamping force. Weld strength equals the base metal strength. In USW, the weldment temperature is not increased to the melting point. Consequently, there is no nugget alike that is created in the resistance welding method. Most ductile metals can be welded together. USW is a technique that awaits thorough exploration. An important understanding is required for the methods that happen at the bonding interface.

The advantages of USW are: • Permits joining of thin materials to thick materials • Permits dissimilar metal joints • Provides joints with good thermal and electrical conductivity • Joins metals without the heat of fusion • Provides efficient energy use • Typically requires no filler material, flux, or special atmosphere • Typically requires no special cleaning processes • Welds through most oxides.

To make a good joint with USW, three points need to be considered:

1. Welds should be lap joined, not butt joined.
2. Thin sections are needed adjacent to the welding tip.
3. Better results are provided with nonferrous alloys.

USW is employed in the aerospace application. Military applications of USW in the aircraft system are explained in MIL-STD 1947 [9, 39].

Applications of USW are considerable, finding utilizations in the aerospace industry. Although almost of metals may be joined with USW, the broadest current employees involve different alloys of Cu, Al, Mg, and related softer alloys, involving silver and gold. Some dissimilar metallic combinations (like Cu and Ni) are readily joined with USW. It is applied to form welds between metal sheets, plates, wires, foils, ribbons, and flat surfaces. Figure 13.1 shows some dissimilar metallic combinations that currently could be ultrasonically joined. The technique, which

x	Zr alloys																	
	x	W alloys																
	x	x	Ti alloys															
			x	Sn														
	x	x		x	Ta alloys													
x				x	x	Ag alloys												
				x	x	Si												
	x	x		x	x	x	Pt alloys											
				x	x		x	Pd										
	x	x		x			x	x	x	Ni alloys								
x	x	x		x			x		x	x	Mo alloys							
		x			x						x	Mg alloys						
x	x	x		x	x		x	x	x	x		x	Fe alloys					
x	x	x			x	x	x	x	x			x	x	Au				
							x						x	Ge				
x	x	x		x	x		x	x	x	x	x	x	x	x	Cu alloys			
		x												x	x	Be alloys		
x	x	x	x	x	x	x	x	x	x	x	x	x	x	x	x	x	Al alloys	
Zr	W	Ti	Sn	Ta	Ag	Si	Pt	Pd	Ni	Mo	Mg	Fe	Au	Ge	Cu	Be	Al	

Fig. 13.1 Dissimilar combination of ultrasonic weldments. Blank areas show combinations that have not been effectively welded or in that joining has not been aimed

may also be employed for welding plastics, is finding broader applications in that area than in metals welding [9, 39].

13.3.6 Dissimilar Brazing in Aerospace Systems

The brazing process is used for a variety of reasons to join various materials. In numerous instances, the motivation is to weld dissimilar materials to provide the maximum advantage of both materials or to produce the most cost- or weight-effective joint. By applying the appropriate weld design, the resulting braze may perform better than either of the base materials being welded. Applications of brazing cover the entire range of manufactured products, from inexpensive toys to the greatest quality aircraft engines as well as aerospace machines [25].

The covered materials involve carbon/alloy steels by copper brazing alloys, high-temperature and heat resistance steels by Ni brazing alloys, nonferrous alloys including Cu and Al alloys, and dissimilar metals involving hard-metal cutting tools. There are numerous intermediate layers in which the correct selection is important to success [27].

The most modern diffusion brazing techniques are employed in aerospace application, especially for brazements including Ti, Ni, Co, and Al alloys. Nevertheless, numerous similar/dissimilar combinations could be diffusion welded, as diffusion is counted in all brazing techniques, from a lesser to the greater extent [9].

The applications of brazing/soldering have enhanced in volume with the introduction of modern structural ceramic materials. A considerable emphasis is placed on the utilization of ceramic materials in aerospace systems. A complete

understanding and characterization of the current brazing/soldering methods for welding dissimilar materials will supply the extra growth of these methods and the welding of ceramics reliably [9].

Filler Materials

The filler materials selection is an important parameter that usually receives low attention at the welding of aerospace materials. Filler materials or intermediate materials are often chosen on the chemistry match basis. Nevertheless, other inspections sometimes take preference, like control of ferrite in the welding of SSs, control of residual stress/distortion in high strength steels, the optimization of elevated temperature properties at Ni-base superalloys, strength optimization in Al welding, and environmental resistance optimization in brazing/adhesive bonding. The filler materials selection for dissimilar material welding needs a careful inspection. The formation effect of detrimental compounds in the base materials is a parameter when some alloys are used. A specific corrosion/wear resistance will sometimes conduct with the use of a specific welding consumable [9].

In conventional brazing of dissimilar materials, the material having the higher expansion coefficient is made the outer element of the joint. Joint tolerances are used that do not allow the gap between the surfaces to become too great for capillary flow. Additional problems occur in the brazing of dissimilar materials when one part of the joint is carbon or graphite. Carbons and graphite have little/no ductility and are relatively weak at the tensile loading. These conditions are usually compensated for in metal-to-graphite welds by brazing the graphite with a transition part of a metal, such as Mo, Ta, or Zr with an expansion coefficient near that of the graphite. This transition part could be brazed to metal if needed. This reduces shear fracture in the graphite by transferring the stresses resulting from the big thermal expansion difference to the metallic constituents.

Many dissimilar combinations can be brazed, even those with metallurgical incompatibility that precludes welding. Important criteria to be considered start with differences in thermal expansion. When a metal/alloy with an elevated thermal expansion is surrounding a low thermal expansion metal/alloy, the clearance may exist at room temperature that is satisfactory for the capillary flow. Inversely, if a low expansion metal is surrounding a high expansion metal, no clearance can exist at the brazing temperature [2].

Thin sections of metals that deform easily when stressed, such as Cu or Ni, have also been effectively employed for brazing the dissimilar metals. Metals that have strong tendencies to form carbides (titanium, zirconium, silicon, and chromium) were discovered to wet graphite if they are molten. A commercial intermediate metal regularly employed for brazing of graphite is copper–silver–clad Ti wire. Also, graphite is readily wetted by Mo disilicide, Ti, and Zr. In recent years, the requirements of the aerospace industry have resulted in the development of several additional filler metals. In general, these filler metals incorporate substantial quantities of carbide-forming elements. They include 48Ti-48Zr-4Be, 35Au-35Ni-30Mo,

70Au-20Ni-10Ta, Ni-clad Ti, 54Ti-21 V-25Cr, 43Ti-42Zr-15Ge, and 47Ti-48Zr-5Nb. Additionally, the filler metal 49Ti-49Cu-2Be has been recommended for the brazing of graphite as well as oxide ceramics. The filler metals mentioned previously wet graphite and most metals well in either a vacuum or an inert atmosphere (pure argon or helium) or span a fairly wide range in brazing temperatures, from 1000 °C for 49Ti-49Cu-2Be to 1350 °C for 35Au-35Ni-30Mo [2].

Vacuum Brazing

Several brazing amounts of the heat resistant alloys, especially precipitation-hardenable alloys that contain Ti and Al, are performed in a vacuum. The vacuum brazing on the scale of 13 mPa proved an appropriate brazing condition for most of the Ni-base superalloys. By gases removal to an adequate low pressure, involving gases which are produced during heating to the brazing temperature, clean surfaces are provided. A vacuum is especially helpful in the manufacturing of samples in the aerospace field. The maximum pressure for effective brazing depends on some parameters that are determined by the base metals composition, the intermediate layer composition, and the gas remains in the evacuated chamber.

Vacuum brazing is an economical technique for fluxless brazing of several similar/dissimilar metal combinations. The vacuum is particularly suited for the brazing of huge, continuous zones where:

1. solid/liquid fluxes may not be removed appropriately from the interface after the brazing,
2. gas atmosphere is not efficient due to its inability to remove gas produced from the close-fitting brazing interface. This is very interesting to mention that a vacuum chamber evacuated to 1.3 mPa includes 0.00000132% of the residual gases based on the starting pressure of 100 kPa [9].

Dissimilar Brazing of Al-base Alloys

Diffusion bonding of Al alloys is difficult, due to the presence of a film of surface oxide. The surface oxide could be disrupted by using the big deformation/elevated temperature, for instance, roll bonding. Nevertheless, for low deformation diffusion bonding, similar or dissimilar intermediate layers have been employed. The particular processes to be followed for Al alloys are different, depending on the system of the alloy. For Al-Mg-Si alloys (like Al-0.6Mg-0.9Si-0.5Mn), diffusion bonding without an intermediate layer has yielded the tensile strength of 145 MPa at 550 °C welding temperature. Nevertheless, this induces the constituent's deformation. This is very attractive to employ silver or copper intermediate layers that could be used as a foil or a coating. These intermediate layers could be applied to produce a transient liquid phase (eutectic) or a solid-state joint. Much care requires to be taken to make sure that the rate of the heating is not too slow as to permit the intermediate

layer to be diffused away before the eutectic temperature is achieved. Solid-state diffusion joints formed with silver or copper have yielded the strength of the joint to the 85 MPa for the bonding temperature of 450 °C. Much attention needs to be considered to the diffusion bonding of alloys which are of interest for the aerospace systems, that is, 7010, 7475, and 8090. The alloys welding without an intermediate layer is possible if oxide disruption may happen during the welding. Some successes have been attained by the welding of 7475 alloys with a rough surface, by the alloy surface grinding in an Ar atmosphere before the welding, as well as by the grit blasting with the particles of alumina followed by the chemical cleaning in a hot 30 wt. % NaOH. The times of the long welding are employed for this alloy and then the big strength has been achieved by performing the welding at 515 °C at a load of 5 MPa for 5 h, followed by a post-weld heat treating to T6 condition. In conditions where intermediate layers are employed for this alloy, the metal that has depicted the highest promise is Zn.

Al–Li alloys are attracting high applications in aerospace systems, as Li significantly enhances the elastic modulus of Al, by roughly 6% for each wt. % of lithium addition, and simultaneously declines its density by 3%. In aerospace utilizations, developments in particular strength and modulus may lead directly to the weight-saving [9].

Dissimilar Brazing of Titanium-Base Alloys

Titanium and titanium alloys are used widely for aerospace hardware. Commercially brazed assemblies include jet engine inlet vanes, hydraulic tubing or fittings, honeycomb sandwich panels, and heat exchangers [38].

Figure 13.2 shows a large front fan turbojet engine with fan blades of 6Al-4V titanium base metal. Each blade has a wraparound skin and a corrugated core member, which are brazed in a vacuum with brazing filler metal Ti-15Cu-15Ni. Titanium plumbing systems that provided additional weight savings were a logical outgrowth from brazed high-pressure fluid line joints and fittings of stainless steel used on the XB-70 supersonic airplane and the lunar excursion modules. Application of hinged induction heating tools and protective argon atmosphere permitted rapid, reliable brazes to be made in the production of U.S. Air Force and Navy high-performance aircraft. One wide-body jetliner utilizes more than 250 brazed joints involving commercially pure titanium tubing and Ti-6Al-4 V fittings and brazing filler metal 90Ag-10Pd. Tubing sizes include 1/4 in., 5/16 in., 3/8 in., and 1/2 in.

Titanium joints brazed with brazing filler metal 82Ag-9Pd-9Ga offer improved producibility and metallurgical compatibility. The results are satisfactory with respect to impulse fatigue, burst, and corrosion tests. In yet another illustration, a U.S. supersonic transport prototype design relied heavily on high-efficiency honeycomb structures. One very promising material for the fuselage, wing, and control surfaces was metallurgically bonded titanium sandwich panels.

Honeycomb cores in supersonic plane wings were made of commercially pure 0.002 in. thick titanium foil; facings were chemically milled Ti-6Al-4V alloy

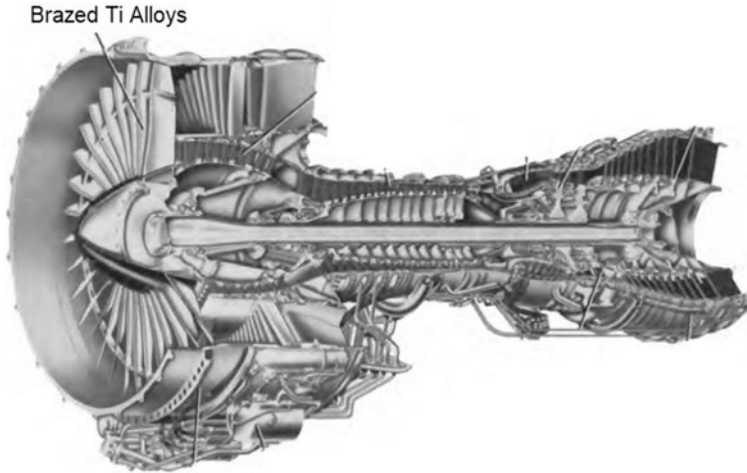


Fig. 13.2 Large fan turbojet engine with brazed sheet metal vanes. Reprinted by permission from Elsevier

measuring 0.010 in. in thickness. Type 3003 Al alloy foil was preplaced between all faying surfaces. This assembly was brazed successfully using ribbon-heated ceramic tooling and an argon atmosphere. The U.S. Air Force F15 aircraft also had this Al-brazed titanium alloy honeycomb sandwich system. In addition, honeycomb structures made with Ti-3Al-2.5 V alloy core and Ti-6Al-4 V alloy face sheets have been fabricated using diffusion brazing techniques.

One of these applications is the lightweight jet engine fan case. It is 75 in. in diameter and 22 in. long. Successful joining of dissimilar metal combinations has been attained with titanium, stainless steel, and copper. For example, a brazed transition part located between a Ti tank and a SS feed line was assessed during the space program course. Ti-6Al-4V alloy was vacuum-induction brazed to Type 304L SS with brazing intermediate layer AWS BAu-4 (Au-18 Ni). The brittle IMCs formation was reduced by heating the joint rapidly and holding it at brazing temperature for a minimum of time. The same routes have been employed to build welds between Ti and mild-steel, tool steel, and other metals [38].

Alloy promotion investigations are conducted to develop a brazing intermediate layer to weld Ti to SS for other uses in the space program. Brazing filler metal Pd-9.0Ag-4.2Si was used to braze stainless steel to titanium in a vacuum at 1360 °F. Excellent flow properties were exhibited by this brazing filler metal. Titanium alloys have been brazed successfully to carbon-steel and austenitic SS with brazing filler metal 48Ti-48Zr-4Be. The alloy Ti-3Al-1.5Mn is brazed to a Cu-0.8Cr alloy by an Ag-based brazing intermediate layer. Three brazing intermediate layers were assessed during these programs: AWS BAg-8 (Ag-28Cu), AWS BAg-37 (Ag-40Cu-35Zn), and 68Ag-27Cu-5Sn. The welds were brazed in the vacuum at 1520 °F for 5 min. At these instances, the shear strength values of 28.4–38.3 ksi were provided. The brazing temperature and heating rate were

critical. For the maximum weld strength, the brazing temperature must be controlled at the range of 1518–1526 °F. A method for vacuum brazing of Cu-plated Ti has been promoted. The Cu was electroplated on the Ti-3Al-1.3Mn alloy surface after the surface was hydrided in a sulfuric acid solution. The hydriding of the titanium surface removed hydrogen or hydrogen compounds, thereby creating an effective surface for the copper plate. Joints have also been made between the Ti alloy and (1) pure copper, (2) stainless steel, and (3) Ni-based alloy using brazing filler metal 68Ag-27Cu-5Sn. The welds were brazed at the range of 1400–1500 °F for 15–20 min. The average shear strength was 28 ksi [38].

It is worth mentioning that employing the Ag-based brazing intermediate layers have found many utilizations in brazing Ti as well as Ti to dissimilar metals which are broadly applied in aerospace systems. Commercially pure Ti (CP Ti) has been effectively brazed by Incusil-ABA (Ag-27.2Cu-12.5In-1.25 Ti) in a high vacuum furnace, at a temperature less than the “beta transus,” the α to the β phase transformation temperature. The holding time and brazing temperature are found to manage the shear strength of the brazed welds. The shear strength of the joints reported a tendency to be increased with an increase in the holding time. The joint strength changes with the brazing factors to a big extent depending on the reaction layer thickness between the brazed alloy and the substrate. The best results were obtained when the thickness value was the minimum value to reach a good wetting as well as interaction at the Ti/braze alloy interface area [40].

Dissimilar Brazing of Beryllium-Base Alloys

Brazing is also used in the fabrication of complex and high-performance aerospace hardware made of beryllium. Because of its remarkable modulus-to-weight ratio and commercial availability of large wrought sheet sizes, beryllium is used for spacecraft structure and instrument payloads. These are brazed using several brazing filler metals in general use that strong yield joints with good manufacturability are needed.

Sleeves of Fe-29Ni-17Cu alloy were first brazed to the beryllium base using brazing filler metal BAg-19 (Ag-7Cu-0.2Li). The electrical lead throughs were then arc welded to the sleeves. In yet another example, a primary structural brazement of beryllium was the main support ring for a satellite instrument. Beryllium sheet fins were brazed to a machined beryllium case with brazing filler metal AWS BAg-19 (92.5Ag-7.5Cu-0.2Li). A stainless-steel transition ring was brazed to each end of the beryllium housing using the same brazing filler metal.

Numerous dissimilar metal combinations with beryllium have been brazed successfully. Stainless steel tubes have been brazed to beryllium end caps with brazing filler metal (49Ti-49Cu-2Be). This filler metal readily wet the beryllium, and the joints exhibited adequate strength for the applications provided the brazing time was kept sufficiently short to minimize the formation of IMCs. Induction brazing in a vacuum was used to make this assembly. Beryllium window assemblies for X-ray tubes have been vacuum brazed into Monel retainers with silver-based brazing filler

metal AWS BAg-8a. All assemblies were vacuum tight and suitable for use in X-ray tubes.

Other vacuum brazing applications include multiwalled beryllium sandwich structures for antennas, space hulls, and interstage adapters. In addition, 303 SS pressure fittings were welded to a 0.080 in. (2.03 mm) thick beryllium sheet by the silver intermediate layer. The weld was a eutectic diffusion brazed weld at 1690 °F for 20–30 min in the vacuum. The brazing process temperature and the time at temperature should be kept to a minimum to obtain high joint strengths when a silver filler metal is used. Beryllium has also been brazed to 304 L SS to express the possibility of welding these alloys for nuclear systems. The steel surface was coated with a thin layer of brazing intermediate layer AWS BAg-8 (Ag-28Cu) by vapor deposition techniques. The brazing temperature was 1510 °F (821 °C). Lap shear strengths ranged from 14.2 to 20.5 ksi (98–141 MPa) [38].

Dissimilar Brazing of Ti–Al IMCs

Ti–Al IMCs have several excellent characteristics: low density, high elastic modulus, good oxidation resistance, and high-temperature strength. They are therefore very suitable for employing high-temperature structural materials in the aviation and aerospace fields. The mechanical properties of Ti–Al IMCs are strongly affected by their microstructures. High internal stress is easily produced in the joint if Ti–Al IMCs are used in brazing dissimilar materials. In the fusion welding process, the joint composition is complicated, and brittle IMCs and hot cracking often appear in the joint. Hence, the commonly used welding methods for joining Ti–Al IMCs to dissimilar materials are brazing and diffusion bonding [41].

13.3.7 Dissimilar Diffusion Bonding in Aerospace Systems

Several similar/dissimilar materials could be welded by diffusion bonding. Nonetheless, the method has some limitations [42]. Many industries employ the diffusion bonding technique, especially aerospace application. The engine mounts of the space-shuttle vehicles were designed to have 28 diffusion bonded Ti parts, scaling from huge frames to the interconnecting tubes. This structure is capable of withstanding three million pounds of thrust. Tubes of 203 mm² were produced with diffusion bonding in length values up to 457 cm. The gas turbine system has utilized diffusion bonding to make a Ti-6%Al-4%V constituent for a modern high thrust engine. This application marked the first use of diffusion bonding in a rotating engine species [10]. Ti has the rather unnormal characteristic of being capable to solvate its oxide at a specific temperature (roughly 1000 °C). Other metals/alloys that could be diffusion bonded are Ni alloys, low carbon steels, and Al alloys, although the persistent-oxide associated with Al should be dealt with. Dissimilar metallic combinations and also many similar and dissimilar combinations of

ceramics could be diffusion bonded. Some ceramic materials may even be diffusion bonded to some metals [43].

In the case of diffusion welding, it is very important that the melting temperature is not gained, and the intermediate layer is not required. Diffusion welding happens as a result of the interface atoms diffusion at the bonded materials [40].

Diffusion Welding of Al-Base Alloys

Aluminum is the most common metal used as dissimilar welding in the aerospace industry. The diffusion bonding of Al to Cu and Ti results in the IMCs formation at the bonding interface. With Cu, it has been found that the Al/copper IMCs may reach 15 μm in thickness before the reduction in the weld strength happens. The parent Al strength was not attained, even before the extreme growth of the IMCs, which proposes that full bonding could be attained only after the time necessary for considerable IMCs formation. Nevertheless, Al to Ti diffusion welds may reach the tensile strength which equals to that of the parent Al, and it is stated that IMCs thickness values of up to 10 μm could be tolerated. A silver interlayer could be employed to develop bonding between the Al and the Ti such that the parent Al strength could be attained in lower welding times [9].

13.3.8 Dissimilar Friction Welding in Aerospace Systems

Friction welding (FRW) is a solid-state joining method that uses the heat produced by compressive forces generated by materials rotating together in a friction mode, which is one of the highly productive and economical techniques for welding similar and a wide variety of dissimilar metals like Al to steel. Shielding gases, flux, and filler metal are not required.

It is widely used in aerospace component fabrication. It is often the only practical alternative available in the joining domain to overcome the problems encountered during the welding of the materials with broadly varying physical properties. The major benefits of FRW are low-production time, high-materials saving, and the feasibility of the dissimilar metals/alloys welding [15, 23, 42].

Generally, the welding of carbon/low-carbon steels is not problematic, and there are ways to do it successfully. But the same thing cannot be said about medium-carbon and alloy steels. But they could be friction welded. The success depends on the strict control of parameters because of the possibility of difficulties because of their hardening properties. For instance, the steel stamping is friction joined to the steel rod's shoulder. Similarly, Ni-based alloys are joined to steel compression wheels using friction welds for their applications in the aerospace sector [15].

Cu- and Ni-base alloys are usually friction welded. Also, Cu alloys are used in a dissimilar welding utilization with Al. For inertia welding, surface speeds are close to twice those of the carbon steels due to the big thermal conductivity of Cu. Welding

forces and flywheel energies are roughly 50% of those applied for carbon steel. For direct drive friction welding, bigger surface speeds would be needed for Cu, given its big thermal conductivity. The welding force would be lower because it is for inertia welding.

Ni-base alloys are almost welded by the inertia welding technique, particularly in the aerospace system. Surface speed is less than that of steel, typically no bigger than 50% of the carbon steel. Nevertheless, due to increased high-temperature properties, welding forces and flywheel energies are roughly double those needed for carbon steels. After inertia welding, the weld in heat-treatable Ni-base alloys is almost subjected to the solution annealing and then aging treatments [8].

FRW could be used to weld a broad scale of similar/dissimilar materials, including metals/alloys, some metal–matrix composites, plastics, and ceramics. The parts made by friction welding have many applications in aerospace systems. Many parts from tong-holds on the forging billets to the aircraft engine constituents are friction welded in production [10].

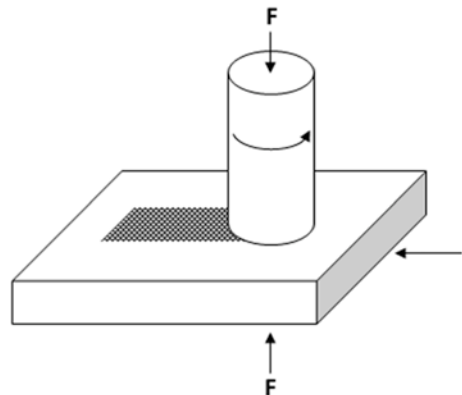
Friction Surfacing

This technique variation employs rotational motion of one part and at the same time adds a motion in the perpendicular direction to the rotation axis. This method is employed to deposit material in the solid state to a different configuration from flat plates to circular/cylindrical shapes. This variation is depicted in Fig. 13.3.

Dissimilar Friction Stir Welding in Aerospace Systems

Friction stir welding (FSW) is a solid-state welding method that needs a low degree of weld preparation, low degree of the post-weld dressing, and provides welds with big fatigue and tensile strength. Other advantages involve fewer defects compared with the fusion weldings and the capability to weld dissimilar alloys. The process

Fig. 13.3 Friction surfacing



has attracted an important interest in some main industrial sections, especially aerospace [4, 16]. The technique suggests many benefits like big joint strength and the capability to make dissimilar welds. Other positive features are the big environmental agreement and that no intermediate layer or shielding gas is needed [44].

The strongest interest in this process has been from the aerospace application, beginning the FSW development study in the early 1990s on structures like the Delta rocket-fuel tank of the Boeing, aircraft design (airbus), and external fuel-tank section (NASA). These organizations have formed a big forward step in FSW. In the 1990s, eclipse aviation designed a processing method for producing small jets integrating the intensive employment of the FSW process in the main assembling of eclipse 500 jets. They removed 70% of rivets on the aircraft structure by the welding overlap connections in 7075, 2024, or dissimilar 7075 to 2024 alloys. Therefore, they were able to perform a production speed of 4 aircrafts per day, which then led to important and reduced leading times for the customers [4]. The major rationale for using FSW in the manufacturing of aerospace constituents is weight and time savings, which translates directly to cost savings. Decreasing weight prepares bigger speeds/declined fuel consumption [44].

The principle of this process is based on a rotating tool that plasticizes the metallic material by using friction-induced heat [45]. The most significant of interest factors in the FSW method are rotation speed, travel speed, forging load, tool geometry, tool material, tool plunge depth, tool tilt angle, joint gap, and offset of tool pin [1, 18].

Strong performance materials like Ti alloys and Ni-based superalloys and adaptive materials like piezoelectric ceramics, shape memory polymers, shape memory alloys, and carbon fibers could only be applied in this process where they are essential [46]. The FSW on the soft (like Al/Mg) and hard (like Fe/Ni) alloys combinations is of specific interest in aerospace systems. These parameters lead to asymmetry in heat generation, as well as the material flow, and then lead to heterogeneous weld formation [10, 13, 14]. Improvement in tool materials has permitted FSW to be effectively used to weld elevated temperature and hard materials like steels, Ti, and Ni-based alloys [47]. Although this process is well suited for welding Al alloys, this has also been effectively applied with copper and its alloys, magnesium and its alloys, metal matrix composite materials of the mentioned metals, Pb, SSs, and dissimilar metallic combinations [16, 48].

The dissimilar materials combinations, such as Al to steel, Al to Mg, and Ni-base superalloy to steel, prepare an appropriate application with the great properties of both materials. A barrier is placed during the joining of dissimilar materials is the brittle IMCs formation, which decreases the integrity and strength of the weld. Recent attempts on decreasing such deleterious phases by the FSW process have led to the execution of industrial applications. The progress formed in joining of lightweight materials, like Al and Mg alloys, fabricates the mass production of the light transportation vehicles possible and then an important reduction in the fuel consumption. FSW process was suggested to join the Al to the steel in a lap configuration at different locations. Tailor blanks with different dissimilar combinations, like different Al alloys, Al and Mg alloys, Al and steel, were investigated by FSW for the

aircraft systems [46]. FSW on dissimilar big strength elevated-corrosion-resistant aluminum alloys may give higher flexibility for aerospace structures design. Extra expanding it for dissimilar welding of Mg and Al alloys or steels and Mg alloys could more realize mass reduction.

Friction stir welding eliminates fasteners and rivets. This requires an overlap-sheet configuration. The butt weld configuration facilitates weld evaluation since a homogeneous weld with a full penetration eliminates the crack happening. Joints created by this process have stronger strength than riveted joints and less residual stress than fusion joints. The other advantage of this process in the aerospace system is that FSW welds do not suffer from color changing when anodized [44].

Dissimilar Friction Stir Welding of Al and Mg Alloys

Al alloys are broadly applied in aerospace applications because of the combination of mass reduction and strong strength. Mg alloys are also interesting in these areas because of their low density and strong strength. Consequently, it could be expected which welding of Mg alloys and Al alloys requires to be investigated for industrial applications. Nevertheless, it is very difficult to achieve dissimilar joints of these two types of alloys by typical fusion welding processes, as huge IMCs that have a negative influence on the mechanical properties of the joint, are easy to create in the joints [44].

Aircraft Fuselages and Wings in Europe

Airbus has depicted interest in FSW since 1998 and invested in many laboratories focusing on thin/thick welding of Al alloys. Airbus has matured the technique for wing and fuselage applications by validating the technological and mechanical properties of the welds by effective full-scale testing of many demonstrators, like fuselage barrel and wing rib sections. Furthermore, validation of the robustness and reproducibility of the joints improved the design, and the quality assurance in the aircraft system has been promoted. Airbus has considered several applications, and no technical show stopper has been recognized.

At the moment, the application focus must be adjusted with various applications from 1998 because of the change from Al to composite materials in several primary sections of the fuselage and wing. This obtains FSW a chance to be more promoted particularly for dissimilar alloys welding. The first flying utilization for Airbus was the FS-welded floor panel in an A400M military aircraft. There were 102 panels in the cargo-hold roughly 1 m long and different values in width. The FSWed solution was chosen as it fulfills the requirement with the least value of the weight [4].

FSWed welds have widely replaced the riveted joints in aerospace systems due to their less production cost and also some problems related to the riveting. Consequently, the FSW technique has been recognized as a key process for welding materials in wing and fuselage manufacturing. The products welded by FSW were

launched into space in the seams form of fuel tanks of the Boeing-Delta II rocket in 1999. First, rivets were employed for the joining extreme-strength Al alloys (7xxx and 2xxx series of Al alloys) as these were not suitable for joining by usual fusion joining techniques. Recently, FSW has proved to be an attractive process for welding strong-strength Al alloys and has resulted in weight saving and huge costs [18].

Dissimilar FSW of Aluminum Alloys

Strong-strength Al alloys are broadly used in aerospace systems. In aircraft structures, lower and upper portions of the wings are formed of 2xxx and 7xxx series of Al alloys, respectively, which need dissimilar welding of these Al alloys. Dissimilar joining of Al alloys is employed in different industries where constituents are needed to sustain various environmental conditions and complex loadings [18].

The fabrication of dissimilar Al alloys is very attractive for most industrial applications since we can join a less expensive alloy with a costlier material when the need arises. In fact, the joining of dissimilar materials might often be experienced in several engineering and structural-design instances, including aerospace, where the conventional fusion welding technique is not appropriate, because of the huge disparities in chemical, physical, and mechanical properties between the materials/alloys to be fabricated. Furthermore, challenges like porosity formation, slag inclusions, chemical reaction, and solidification cracking could occur during the traditional fusion welding of dissimilar alloys; however, good welds can be achieved in a few limited situations with a specific focus on weld-joints preparation, choice of filler metal, design, and process/welding parameters [15].

Sound welding of dissimilar Al alloys by using FSW increases the use of a big ratio of strength-to-weight for Al alloys in aerospace systems. This produces a light-weight transportation system that results in considerable reduction of fuel consumption [18].

FSW of 2xxx–7xxx Series Aluminum Alloys

Dissimilar welds have found significant applications in the eclipse-jet aircraft where the 7xxx series stringers alloys are lap joined to the 2xxx series exterior skins alloys [4]. Aerospace-grade Al alloys (2xxx and 7xxx) are strong-strength and heat-treatable alloys. 7xxx series of Al alloys are applied in defense applications, worm gears, missile parts, structural constituents, and aircraft fittings. Moreover, 2xxx series of Al alloys are almost used in bolts, shafts and gears, aircraft fittings, couplings, fuel tanks, missile parts, rectifier sections, pistons, structures, and worm gears. There are many applications of the mentioned two series of Al alloys. Therefore, welding of these alloys is needed in several applications. Consequently, an efficient welding technique is needed to weld these big-strength Al alloys. Dissimilar welding of these alloys is difficult because of a big difference in some properties [18].

FSW of the 6xxx–7xxx Series Aluminum Alloys

Many sections of aerospace systems use 6xxx and 7xxx series of Al alloys for producing structural constituents. Dissimilar welding of these alloys is needed for the production of various parts of space shuttles and aircrafts. Dissimilar FSW of 6xxx–7xxx series of Al alloys has been effectively used in many engineering applications with good weld properties [18].

Dissimilar Inertia Friction Welding in Aerospace Systems

Inertia friction welding (IFW) is a solid-state joining technique that welds materials by rotating and then making friction to generate heat, then lateral inducing the force to the plastically displace material and joining the parent materials together. Table 13.1 represents information about inertia friction welding is used for special applications of dissimilar-metal welding [33].

One of the most important inertia friction welding applications in aerospace systems is a dual-drive shaft (dissimilar SCMV AerMet100-IFW weld). SCMV (3.15% Cr, 0.3% C, 1.6% Mo, 0.6% Si, 0.1% Va) is employed at the turbine end of the aero-engine drive shaft; however, Aermet 100 (2.5% Cr, 0.2% C, 12.7% Co, 10.1% Ni, 3.26% Nb, 1.37% Mo, 0.01% Mn) is applied at the compressor end of the shaft, where a strong-strength alloy is needed to withstand the big torque [40].

IFW is applied in aerospace materials. However, the main parts of such welds are Ni-based superalloys and recently are Ti alloys and steels. IFW could be classified as a unique process, particularly as a welding process on the Ni-based superalloys aeroengine parts. There is a requisite for more considerable studies on the IFW of steels, Ti, and Al alloys due to their capability applications in aerospace systems. This is an attractive topic to use IFW for welding cylindrical constituents to thin noncylindrical members and also dissimilar materials. The post welding heat treatment technique in many inertia friction welds seems to be important, as the post welding heat treatment results in the mechanical properties retention, particularly

Table 13.1 Inertia friction welding of dissimilar alloys [33]

Component	Alloy dissimilar combination
Cryogenic tank fittings for fuel cells on the space shuttle	2219 Al to Type 304 L stainless steel
Turbine wheels (17 units)	Various Inconel and other high-temperature alloys to alloy steels
Connection of helicopter power source to the main rotor	Nitalloy N to maraging steel 250
Injector tubes	Haynes 188 to Inco 718
Hydraulic solenoid valves for aircraft like the F-5 and T-38	Type 300 series stainless steels to mild steel
Rocket motor case	AISI 4130 steel tubing to an investment casting

the fatigue strength properties. Also, many patents proposed new applications, such as crankshafts, gas-turbine parts, and aircraft-actuator pistons [40].

Dissimilar Linear Friction Welding in Aerospace Systems

Linear friction welding is a technique that has developed to be an important method in the last decades. There are many applications for this process both within and outside the aerospace systems. This process could be applied to weld several materials.

Many investigations have been reported at the welding Al-matrix composites and Ti and Ni aluminides. Welding factors seem to have an important effect on the temperature distribution at the welding. This property of the technique can be significant during dissimilar welding of the materials. The optimization and modification of the weldment properties and microstructure modify the welding parameters which can be one of the advantages of the technique [40].

13.4 Dissimilar Bolt Fastening in Aerospace Systems

Bolted fastening is one of the attractive joining processes in several applications in aerospace systems. These kinds of fasteners show many benefits like the simplicity of repairing and assembly. In-service responses are defined by some complex facts related to different parameters influencing durability and serviceability. One of the main causes for bolted joint failure is the preload relaxation which could be made by creep or rotational self-loosening in the thickness direction of the constituents joined. A critical point in structures including composites or plastics is obtaining an accepted strength to weight values.

Bolt loosening is known as a significant area to hinder failure in several applications, especially in similar/dissimilar joining. The preload loss induced by the creep has a harmful influence on the residual lifetime and the strength of the connections. Therefore, it is very critical to record the bolt preload in the service situations to hinder failure from the joints bolted. Several research on the composite creep were executed; however, in all of these studies, the clamp-up force was randomly chosen. Furthermore, due to the lack of a standard route, scanning times have been frequently chosen and the results were depicted in various formats, which means the different results may not be compared directly. The results of initial preload influence on composite creep show some contradictions. The creep investigation on the similar/dissimilar joints, involving the appropriate selection of the NDE method used, is required in which manufacturers and designers could meet performance and weight criteria [48].

13.5 Dissimilar Welding of Aluminum Alloys in Aerospace Systems

Dissimilar welding of Al alloys has wide applications in replacing the riveted joints of the aircraft sections. Recently, the aerospace system has promoted dissimilar welding of Al alloys. Effective dissimilar welding is a challenging topic because of the differences in metallurgical, chemical, and physical properties of the base metals. In fusion joining, the intermediate layer is needed, and its chemical composition depends on the base metal nature being joined, and then it is very difficult to select the intermediate layer for fusion joining of dissimilar Al alloys. Moreover, with the dissimilar joining of Al alloys using the fusion joining techniques, there is potential for the formation of many joining defects like distortion, porosity, voids, hot cracking, and so on. The thermal conductivity and melting temperature of various Al alloys are different because of the different alloying elements that existed in them. The joining of different types of Al alloys with acceptable thermal and mechanical properties has a great application due to their big corrosion resistance, specific strength, and thermal conductivity. Many examples could be suggested where different types of Al alloys are welded together to provide the required properties for the structures. For instance, welding of 7xxx (used to create upper wing) and 2xxx (used to make lower wing) series of Al alloy could be observed in aircraft [18].

Another example of dissimilar welding is the welding of steel with Al alloys because of its wide utilization in aerospace systems. The dissimilar welding of materials like steels and Al alloys poses several problems such as brittle IMCs formation, weak wetting of Al. AA6016-T4 alloys of the blank sheet were combined with the steel-blank sheets called mild steel (DC06), and elevated-strength steels (HSLA-340, DP 600, and AISI 1018) to make steel–Al alloy tailor welded joints [49].

Al-matrix composites are usually low cost and show strong specific strength, big wearability, and desirable design performance functionality and property. They are broadly used in aviation structure, aerospace flight, and the heat-resistant wearable sectors of the engines. Therefore, a great effort was focused on their applications and development, especially on the discontinuous reinforced Al-matrix composites such as composites with whiskers, particles, and short fibers. Furthermore, great attention has been focused on the study of secondary processing like welding. Welding is a significant technique for joining these materials. There has been considerable effort to promote appropriate techniques for joining the similar/dissimilar composite materials in literature. These techniques could be classified as: (a) fusion welding techniques such as arc welding, laser welding, shielding gas welding and electron-beam welding and (b) solid-state welding techniques such as diffusion welding, soldering, explosive welding, and friction welding [50].

13.6 Dissimilar Welding of Composites in Aerospace Systems

Composites were first employed in nonstructural constituents and now are applied in high flight-critical utilizations. Glass-reinforced plastics and carbon fiber-reinforced plastics are the broadly employed materials. In several aerospace systems, composite materials must attach to the metals, and then the problem of the dissimilar materials bonding seems to be a real issue. Two scenarios are considered: the first one is when the bonding process is a part of the initial production technique, while the second one is when it is applied for the repairing of the structural damage [40].

The Eaton Vehicle Group provides aerospace with systems and products that are designed to increase the power, vehicle efficiency, and performance, suggesting driveline expertise by its torque, transmission, and clutch management systems [48].

The other application of the welding of composites can be discussed in cladding or additive manufacturing. Clad metals are laminar composites consisting of a metal or alloy, with a metal or alloys of different chemical composition applied to one or more sides by welding casting, drawing, rolling, surfacing, chemical deposition, or electroplating. The term *dissimilar welding* here refers to the joining of alloys with different chemical compositions (for example, Al, Cu, and Ni) or alloys with different microstructures (for instance, SSs and carbon steels). Dissimilar welding comprises one/more base metals and one/more intermediate layers that make up the final weld metal after melting and mixing during welding. A series of weldments that vary in composition can exist by a single welding pass; each weld bead may have individual compositional properties. Combining a dissimilar combination of metals in a weldment permits the use of great properties from each metal, and serves the special requirements of industries especially in the aerospace industry. The welding of clad and dissimilar metals is particularly significant when the weldment is to be employed in corrosive environments or is subjected to thermal cycles in service [33].

13.7 Dissimilar Welding of Plastics in Aerospace Systems

Adhesive bonding and mechanical fastening could be applied to weld similar/dissimilar materials. For instance, mechanical fastening is used for welding a metal to a plastic, creating a permanent weld or connection. The benefits of this process are no need to surface treatment as well as disassembly of the constituents for repair and inspection. The major obstacles of this process are the enhanced mass, the existence of big concentrations of the stress around the fastener holes, and then in-service corrosion troubles. The application of mechanical fastening is considered in aerospace systems. Polymers that have similar solubility factors could be welded by solvent/fusion welding. The interdiffusion in the polymers chains plays main role in reaching the intrinsic adhesion as well as in developing chains diffusion, either by using an appropriate solvent or heating the polymers [9].

13.8 Summary

This study aimed to provide a big source of the newest information about the topics associated with the welding of different dissimilar materials in the aerospace industry. Scientists met the fact with the necessity of dissimilar welding of materials since they are looking for creative constructs or parts with outstanding properties. Sometimes a member needs a property in one zone, and another property in another zone. Enhancing the potential of dissimilar welding with high properties is enabling new processes to light-mass aerospace systems. In this work, different materials such as metals, composites, ceramics, and polymers are employed to make dissimilar material pairs. The most important welding techniques explained in this chapter that are employed in aerospace systems involve GTAW, GMAW, flash welding, big energy density techniques like electron beam welding and laser welding, as well as friction welding, diffusion welding, brazing, and ultrasonic welding.

13.9 Conclusions

This chapter has investigated the different methods employed for dissimilar welding in aerospace systems. The welding techniques explained in this work involve liquid- and solid-state weldings. GTAW, GMAW, flash welding, laser welding, and electron beam welding were the processes chosen to explain the dissimilar welding of materials in the aerospace industry. To hinder the difficulties made by fusion welding techniques, solid-state weldings such as friction welding, friction stir welding, diffusion welding, brazing, ultrasonic welding, forge welding, explosive welding, magnetic pulse welding, and microwave welding have been explained. The influence of mentioned techniques on the different dissimilar materials especially dissimilar metallic materials which used in the aerospace industry completely discussed. The dissimilar welding of aluminum alloys has been obtained separately due to the high application of Al alloys in aerospace systems. In the meantime, dissimilar welding of plastics and composites in this application was discussed.

Acknowledgments This study was supported by the projects UIDB/00481/2020 and UIDP/00481/2020-FCT-Fundação para a Ciência e a Tecnologia; and CENTRO-01-0145-FEDER-022083-Centro Portugal Regional Operational Programme (Centro2020), under the PORTUGAL 2020 Partnership Agreement, through the European Regional Development Fund.

References

1. Mishra, R., Mahoney, M. W., & Sato, Y. (2011). In Y. Hovanski & R. Verma (Eds.), *Friction stir welding and processing VI*. Wiley.
2. Schwartz, M. M. (2003). *Brazing*. ASM International.

3. Lucas, W., & Makhnenko, V. I. (2006). *Computer technology in welding and manufacturing & mathematical modelling and information technologies in welding and related processes*. E.O. Paton Electric Welding Institute.
4. Lohwasser, D., & Chen, Z. (2009). *Friction stir welding*. Woodhead Publishing Ltd..
5. Elmi Hosseini, S. R., Feng, K., Nie, P., Zhang, K., Huang, J., Chen, Y., Shu, D., Li, Z., Guo, B., & Xue, S. (2018). Fracture surface characterization of laser welding processed Ti alloy to stainless steel joints. *Welding in the World*, 62(5), 947–960.
6. Elmi Hosseini, S. R., Feng, K., Nie, P., Zhang, K., Huang, L., & Z., Kokawa, H., Guo, B., Xue, S. (2018). Enhanced strength of 304 SS-Ti6Al4V laser-welded joints containing composite interlayers. *Journal of Materials Engineering and Performance*, 27(11), 6135–6148.
7. Elmi Hosseini, S. R., Feng, K., Nie, P., Zhang, K., Huang, Li, Z., Kokawa, H., Guo, B., & Xue, S. (2019). Interlayer thickening for development of laser-welded Ti-SS joint strength. *Optics and Laser Technology*, 112, 379–394.
8. ASM Handbook. (2011). *Welding fundamentals and processes* (Vol. 06A). ASM International.
9. ASM Handbook. (1993). *Welding, brazing, and soldering* (Vol. 6). ASM International.
10. O'Brien, R. L. (1997). *Jefferson's welding encyclopedia* (18th ed.). American Welding Society.
11. Sheward, G. (1985). *High-temperature brazing in controlled atmospheres*. PERGAMON PRESS.
12. Liu, L. (2010). *Welding and joining of magnesium alloys*. Woodhead Publishing.
13. Mishra, R. S., Mahoney, M. W., Sato, Y., & Hovanski, Y. (2015). *Friction stir welding and processing VIII*. Wiley-TMS.
14. Mishra, R. S., & Sidhar, H. (2017). *Friction stir welding of 2XXX aluminum alloys including Al-Li alloys*. Butterworth-Heinemann.
15. Vora, J. J., & Badheka, V. J. (2019). *Advances in welding technologies for process development*. CRC Press.
16. Messler, R. W. (2019). *A practical guide to welding solutions overcoming technical and material*. Wiley-VCH.
17. Weitzenböck, J. R. (2012). *Adhesives in marine engineering*. Woodhead Publishing.
18. Khan, N., Siddiquee, A., & Khan, Z. (2017). *Friction stir welding dissimilar aluminium alloys*. CRC Press.
19. Ghosh, P. K. (2017). *Pulse current gas metal arc welding_ characteristics, control and applications*. Springer Singapore.
20. Chakravarthy, P., Agilan, M., & Neethu, N. (2020). *Flux bounded tungsten inert gas welding process: An introduction*. CRC Press.
21. Ion, J. C. (2005). *Laser processing of engineering materials*. Elsevier Butterworth-Heinemann.
22. Galvery, W. L. (2006). *Welding essentials—Questions and answers*. Industrial Press.
23. Bohnart, E. R. (2018). *Welding _ principles and practices*. McGraw-Hill Education.
24. Storer, J., & Haynes, J. H. (1999). *Welding manual*. Thomson Delmar Learning.
25. O'Brien, A. (2004). *Welding handbook* (Vol. 2). American Welding Society.
26. Street, J. A. (1990). *Pulsed arc welding. An introduction*. Woodhead Publishing.
27. Houldcroft, P. (1990). *An introduction to welding and related processes and a guide to their selection*. Abington Publishing.
28. Resistance Welding Manual. (2003). American Welding Society.
29. Majumdar, J. D., & Manna, I. Laser material processing. *International Materials Reviews*, 56(5/6), 341–388.
30. Majumdar, J. D., & Manna, I. (2003). *Laser processing of materials* (Vol. 28). Sadhana.
31. Lawrence, J., Pou, J., Low, D. K. Y., & Toyserkani, E. (2010). *Advances in laser materials processing*. Woodhead Publishing Limited.
32. Katayama, S. (2013). *Handbook of laser welding technologies*. Woodhead Publishing Limited.
33. O'Brien, A. (2011). *Welding handbook* (Vol. 4). American Welding Society.
34. *Recommended practices for electron beam welding and allied processes*. (2013). American Welding Society.
35. Jeffus, L. (2017). *Welding principles and applications*. Cengage Learning.

36. Houldcroft, P. T., & John, R. (2001). *Welding and cutting: A guide to fusion welding and associated cutting processes*. Woodhead Publishing.
37. Klein, R. J. (2011). *Welding processes, quality, and application*. Nova Science Publishers.
38. Paponetti, C. (2007). *Brazing handbook*. American Welding Society.
39. Ahmed, N. (2005). *New developments in advanced welding*. CRC Press_ Woodhead Pub.
40. Chaturvedi, M. C. (2012). *Welding and joining of aerospace materials*. Woodhead Publishing.
41. Sekulić, D. P. (2013). *Advances in brazing, science technology and applications*. Woodhead Publishing Limited.
42. Jenney, C. L., & O'Brien, A. (2001). *Welding handbook* (Vol. 1). American Welding Society.
43. Messler, R. W. (2004). *Principles of welding*. WILEY-VCH Verlag GmbH & KGaA.
44. Kazem Besharati Givi, M., & Asadi, P. (2014). *Advances in friction-stir welding and processing*. Woodhead Publishing.
45. Hovanski, Y., Mishra, R., Sato, Y., Upadhyay, P., & Yan, D. (2017). *Friction stir welding and processing IX*. Springer International Publishing.
46. Kumar, N., Yuan, W., & Mishra, R. S. (2015). *Friction stir welding of dissimilar alloys and materials*. Butterworth-Heinemann.
47. Mishra, R., Mahoney, M. W., Sato, Y., Hovanski, Y., & Verma, R. (2016). *Friction stir welding and processing VII*. Springer International Publishing.
48. Cloud, G.L., Backman, D. (2016) Joining technologies for composites and dissimilar materials. In *Proceedings of the 2016 annual conference*. The Society for Experimental Mechanics, Inc.
49. Na, X. (2011). *Laser welding*. Sciyo.
50. Kovacevic, R. (2012). *Welding processes*. InTech.

Chapter 14

Design, Analysis, and Production of Lattice Structures Through Powder Bed Fusion Additive Manufacturing



Ozgur Poyraz, Evren Yasa, Fatma Nur Depboylu, and Feza Korkusuz

Nomenclature

2D	Two-dimensional
3D	Three-dimensional
AM	Additive manufacturing
BCC	Body-centered cubic
BCCZ	Body-centered cubic-reinforced along Z-axis
CAD	Computer-aided design
DC	Diamond cubic
FCC	Face-centered cubic
FCCZ	Face-centered cubic along Z-axis
FEA	Finite element analysis
FEM	Finite element method
OT	Octet Truss
PBF	Powder bed fusion
SC	Simple cubic
TPMS	Triply periodic minimal surface lattice structures

O. Poyraz (✉)

Department of Mechanical Engineering, Eskişehir Technical University, Eskişehir, Turkey
e-mail: ozgurpoyraz@eskisehir.edu.tr

E. Yasa

Department of Mechanical Engineering, Eskişehir Osmangazi University, Eskişehir, Turkey

F. N. Depboylu

Department of Bioengineering, Hacettepe University Institute of Science and Technology, Ankara, Turkey

F. Korkusuz

Faculty of Medicine, Department of Sports Medicine, Hacettepe University, Ankara, Turkey

14.1 Introduction

Additive Manufacturing (AM) as an emerging technology has played an important role in the evolution of scientific and industrial practices over the past decade. Undoubtedly, the advantages offered by AM technologies in terms of research, education, design, production, and product development had a significant effect on this evolution. The creation of novel shapes, geometrical features, and 3D structures that cannot be produced cost-effectively with other conventional manufacturing techniques can now be established with AM technology for researchers, designers, and engineers. They are now considering and employing internal structural channels, generative shapes, and biomimicry to obtain improved functionalities, lightweight components, or integral assemblies. Although the designers and the engineers may manually intervene to employ the related shapes and functionalities, automated design of these is also now possible by using necessary software packages, which introduce design optimization algorithms or modules transforming the bulk volumes to porous structures by filling those volumes with lattices.

AM technologies provide the necessary abilities to cost-effectively produce the lattice structures, which have ideal details, internal recesses, and thousands of instanced cells in a single component in this respect. Powder bed fusion (PBF) family of AM technologies moreover makes this more compelling for various industries including aerospace, dental and medical use by offering a wide material range from heat resistant high strength nickel-based superalloys to biocompatible titanium structures. Successful implementation of the emerging AM technologies along with the novel design approach is only possible by using proper designs with optimized process parameters. However, there is a lack of knowledge for the fabrication of lattice structures with AM, which is relatively new compared to conventional manufacturing techniques.

This chapter presents a comprehensive review of the design, analysis, and production of lattice structures through Laser powder bed fusion (L-PBF) AM technologies to contribute to the scientific knowledge base. The first section of the chapter introduces the porous structures and the background information on the use of cellular solids as industrial materials. The design of lattice structures is described later on considering the common unit cells within the current state-of-the-art and their important dimensional characteristics. Analytical techniques used to calculate the basic attributes of lattice structures together with advanced numerical methods used for identifying their strength are briefly explained. Automated design and analysis of the lattice structures are exemplified based on the available commercial software packages. Subsequently, the production limits and challenges encountered in the L-PBF of lattice structures are illustrated and discussed taking the effect of process variables on dimensional accuracy, manufacturability, and surface quality. Finally, current and prospective use of the technology is emphasized considering various industries such as aerospace and medical.

14.2 Design and Analysis of Lattice Structures

14.2.1 Background and Development

Porous structures can be described as volumes or solids which mostly contain internal voids or spaces. These structures are often referred as cellular solids when they form an assembly of cells with solid edges or faces, packed together so that they fill a space [1]. In this context, examples of natural representatives to cellular solids are sponge, cork, honeycomb, wood, and coral. Although they are naturally formed, they may still pose orderly structures like honeycombs having hexagonal cells arrayed on a plane in two perpendicular directions. Humankind has been using these cellular structures for more than several thousand years but has only started to produce these artificially in the last century [1].

Honeycombs and foams are two earlier examples of cellular structures which can be produced artificially by conventional manufacturing methods. Among these, honeycombs can be manufactured by casting, extrusion, or expansion depending on the edge lengths of the unit cell, the size of the overall structure, and the part material, whereas the foams can be manufactured by introducing gas bubbles into the liquid material [1]. The gas bubbles can be introduced by blowing, saturation, or evaporation of agents which have low melting points relative to the parent material [2, 3]. The manufacturing techniques for foams are also dependent on the unit cell characteristics, part size, and parent material.

Examples of more advanced cellular structures including regular arrays of complex unit cell geometries are octet truss, tetrahedral lattice truss, pyramidal lattice truss, and 3-Dimensional (3D) Kagome [4] structures. They were commonly made of aluminum alloys, e.g., AA6061, by a series of conventional manufacturing techniques. In this regard, fabrication of these starts with aluminum sheets, and 2-Dimensional (2D) patterns are created first by perforating the sheets using a punch press. Subsequently, perforated sheets are folded at each pattern row by applying pressure in female dies, which have certain angles compatible with the geometry of lattice. Finally, these perforated and folded structures are brazed with filler materials, e.g. AA4343. After air-cooling to ambient temperatures, they can be heat treated via different techniques such as solutionizing [4]. Although the so-called series of fabrication techniques allow the production of 3D lattices, they have certain disadvantages such as scrapping the punched material after perforation, being limited for the minimum unit cell dimensions as a result of using dies, and risk of losing stiffness due to joining by brazing with different filler materials.

In the current state-of-the-art, the PBF family of AM technologies allows the production of lattice structures having various 2D or 3D geometries. Especially L-PBF enables manufacturing fine details with a good surface quality compared to other AM methods. By the adoption of L-PBF AM, much smaller unit cell dimensions with intricate shapes can be fabricated using a wide variety of materials including ferrous, nickel, aluminum, and titanium alloys. The amount of waste material furthermore is drastically reduced by this technology.

14.2.2 Types and Characteristics of Lattice Structures

Types of lattice structures are categorized under three main groups as strut-based lattice structures, shell lattice structures, and triply periodic minimal surface lattice structures (TPMS) [5]. The sub-categories of strut-based lattice structures are simple cubic (SC), body-centered cubic (BCC), face-centered cubic (FCC), diamond cubic (DC), and octet truss (OT) (Table 14.1) [6, 7]. Strut-based lattice structures can be reinforced or used as a combination of two sub-categories when needed. As an example, a BCC structure can be reinforced by introducing an additional strut parallel to the Z-direction and it can be named as BCCZ [7].

Researchers mostly focus on the prediction of various characteristics during the design and analysis of strut-based lattice structures. These are geometrical characteristics (strut diameter, number of struts, number of joints, cell size), physical characteristics (density or relative density), mechanical characteristics (relative elastic modulus, stress, strain, energy absorption), and thermal characteristics (conductivity or relative conductivity, diffusivity or relative diffusivity) [4, 6, 8, 9].

Geometrical characteristics are of initial interest and the number of struts (b) for (n) number of cells in a 3D arrangement can be calculated for SC using Eq. (14.1), for BCC using Eq. (14.2) and for FCC using Eq. (14.3).


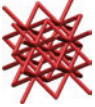
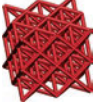
$$b = 3n(1+n)^2 \quad (14.1)$$

$$b = 8n^3 \quad (14.2)$$

$$b = 12n^2(1+2n) \quad (14.3)$$

As will be discussed in the upcoming sections of the chapter, the number of joints (j) is another important geometrical characteristic for strut-based lattice structures. This can be calculated similarly to the number of struts for (n) number of cells

Table 14.1 Strut-based lattice structures and their geometrical characteristics

Representative view of a unit cell	Designation	Number of struts for $2 \times 2 \times 2$ 3D structure	Number of joints for $2 \times 2 \times 2$ 3D structure
	SC	54	27
	BCC	64	35
	FCC	240	105

in a 3D arrangement for SC using Eq. (14.4), for BCC using Eq. (14.5), and for FCC using Eq. (14.6).

$$j = (1+n)^3 \quad (14.4)$$

$$j = (1+2n)(1+n+n^2) \quad (14.5)$$

$$j = (1+2n)(1+2n+4n^2) \quad (14.6)$$

Following the geometrical characteristics, it would be wise to consider main physical characteristics, such as density (ρ), since the lightweight opportunity offered by lattice structures is compelling both for L-PBF AM and other manufacturing techniques. Considering strut radius (r) and edge length of a unit cell (a), this can be calculated for (n) number of cells in a 3D arrangement for SC using Eq. (14.7), for BCC using Eq. (14.8) and for FCC using Eq. (14.9) [17].

$$\rho = \pi \left(\frac{r}{a} \right)^2 \left(3 + \frac{6}{n} + \frac{3}{n^2} \right) \quad (14.7)$$

$$\rho = 4 / \sqrt{3} \pi \left(\frac{r}{a} \right)^2 \quad (14.8)$$

$$\rho = \frac{\pi}{2} \left(\frac{r}{a} \right)^2 \left(24 + \frac{12}{n} \right) \quad (14.9)$$

Using the aforementioned geometrical and physical characteristics, a simple but useful assessment could be carried out by the utilization of Maxwell's stability criterion so that an initial overview can be obtained on the mechanics of the system [8]. The number of struts (b) and the number of joints (j) are used in Maxwell's criterion which can be calculated using Eq. (14.10) [8]. The value of (M) in Maxwell's criterion distinguishes the behavior of the lattice system. When it is less than zero, the lattice system is actually a mechanism without any stiffness or strength. When it is greater than zero, it demonstrates a further concept of being self-stressed. However, the value of (M) for most of the strut-based lattices used in L-PBF AM are approximately equal to or greater than zero, and these have sub-classifications referred to as bending or stretch-dominated lattice structures. FCC lattice is a proper example of stretch-dominated lattice structures [9].

$$M = b - 3j + 6 = 0 \quad (14.10)$$

Although compression testing is common for lattice structures within the current state-of-the-art, pioneer researchers considered tensile behavior, and analytical techniques were developed accordingly. In this context, the struts of lattice

structures demonstrate elastic stretching during tensile, and for metal alloys, approximately one-third of the struts carry tension [9]. This assumption can be expressed by a relation between the elasticity modulus of the solid (E_s)/lattice (E) together with their densities (ρ_s & ρ) and is presented with Eq. (14.11).

$$\frac{E}{E_s} \approx \frac{1}{3} \frac{\rho}{\rho_s} \quad (14.11)$$

Plastic yielding, fracture, or buckling can be observed beyond elastic limit and the lattice system may collapse as the result of the loading. The particular issue of buckling in stretch-dominated metal alloys is associated with the geometrical attributes of the struts and needs further attention. In this regard, slender struts having lower diameters or thicknesses and greater lengths tend to buckle before yielding. Through a generalized approach, it can be stated that strut-based lattice structures tend to buckle before yielding for cases where the ratio of lattice density to solid density is less than 0.05 [9].

Bending-dominated lattice structures, which are in the same sub-class with stretch-dominated lattice structures, mostly have a reduced number of struts and joints in comparison with its counterpart. SC is a proper example for bending-dominated lattice structures with a tendency to bend under compression and shows considerable plateau stress making them a good energy absorber. The relation between plateau stress of the lattice (σ_{pl}) and yield strength of solid ($\sigma_{y,s}$) together with their densities (ρ_s & ρ) is expressed in Eq. (14.12) [9]. Similar to stretch-dominated metal alloys, buckling needs further attention for bending-dominated lattice structures, but it cannot be generalized using simple density ratios. The stress–strain relationship of bending and stretch-dominated lattices is shown in Fig. 14.1 [10].

$$\frac{\sigma_{pl}}{\sigma_{y,s}} \propto \left(\frac{\rho}{\rho_s} \right)^{3/2} \quad (14.12)$$

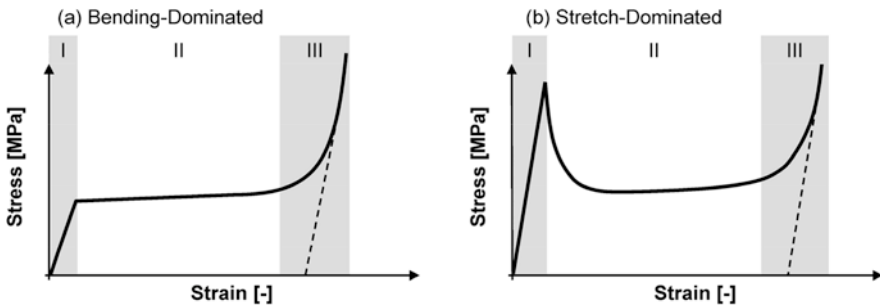


Fig. 14.1 Stress–strain relationship of (a) bending-dominated lattices and (b) stretch-dominated lattices [10]. Under the Creative Commons license

The unit cells of shell lattice structures are mostly designed by introducing plates on the closest packed plane of strut-based lattice structures [11]. Shell lattice structures, which have plate-based closed-cell geometries, demonstrate improved elastic properties than strut-based lattice structures with the same densities. However, since they have some manufacturing issues for L-PBF AM such as the difficulty of powder removal, they are not very common like strut-based lattice structures [12].

Instead of shell lattice structures, TPMS can be used to have 3D surfaces together with necessary voids and passages which facilitate easy powder removal. Moreover, the continuous form of TPMS offers other manufacturing advantages such as self-supporting unit cells [13]. Further highlights in terms of advantages provided by the utilization of TPMS are greater specific energy absorption compared to strut-based lattices and easier bone growth when used for implants [14, 15].

Common examples of TPMS include but are not limited to Schwartz Primitive, Schoen-Gyroid, and Schwartz Diamond as shown in Fig. 14.2 [16]. The topologies of these TPMS structures are defined using necessary mathematical equations and as a result of these, surface boundaries of lattices are generated.

As an example, Schwartz Primitive is developed based on a simple cubic lattice, but it uses tubes instead of struts. There are smooth transitions between the tubes and the unit cell has a mirror symmetry for all the central planes of the unit cube. As a result, it can be easily defined by Eq. (14.13), where x , y , and z stand for the dimensions of the unit cell.

$$\cos x + \cos y + \cos z = 0 \quad (14.13)$$

14.2.3 Design and Analysis

Analytical definition of all attributes of structures and components could be challenging although many principles and equations are presented for common lattice structures in the previous section. The main reasons for this are the complexity of

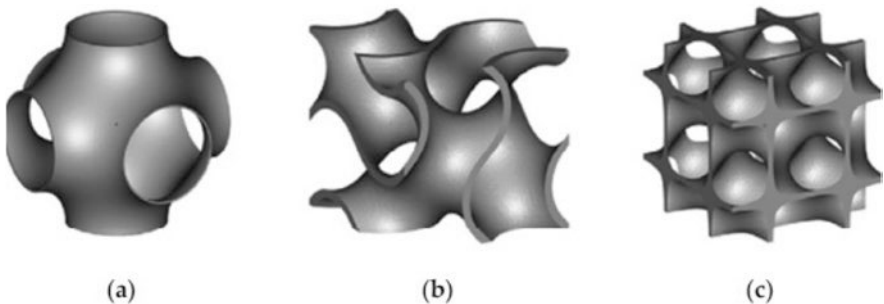


Fig. 14.2 TPMS (a) Schwartz primitive, (b) Schoen-Gyroid, and (c) Schwartz Diamond [16]. Under the Creative Commons license

product geometries made of lattice structures, variation in material properties due to primary and secondary processing, and the effect of dimensional or surface characteristics of the utilized manufacturing method on material performance. In this respect, the use of computational techniques such as computer-aided engineering (CAD) and finite element method (FEM) which can be available in commercial, noncommercial, general-purpose, or dedicated software packages could be beneficial. It is though still important to employ these software tools carefully by following proper methods and providing correct inputs.

In the current state-of-the-art, there are three common approaches for the design and analysis of the lattice structures. In the scope of these approaches design and analysis of lattice structures can be conducted separately. The design of the unit cell can be generated by finite element analysis (FEA) and/or topology optimization and applied to component geometry, or component geometry can be filled with lattices as the result of special topology optimization algorithms.

Among these three approaches, separate design and analysis of the lattice structures were the initial ones. In this approach, lattice structures are selected from a software's predefined library, the dimensions are identified by the user and the assigned volume of the component is filled with these lattice structures. Gradient lattices are also available which have identical unit cell geometry but varying dimensions, and these are beneficially used for tailoring the mechanical properties of the target components (Fig. 14.3) [21]. While lattice design options were initially offered by additive manufacturing job preparation software companies such as Materialise 3-Matic Lattice Module or Autodesk Lattice Commander, general-purpose CAD software companies like Siemens NX or PTC Creo have also started to introduce similar modules with the emergence of additive manufacturing technologies [17–20].

FEA studies are conducted as the second step of the first approach. In the scope of FEA studies, the mechanical performance of the final component or unit cell array can be simulated. When the mechanical performance of unit cells is studied, their stress-strain, force-displacement, toughness, or energy absorption behaviors are benchmarked with the bulk parts with special consideration on their cell porosity [22]. Researchers or engineers are always tempted to find the maximum porosity for minimum loss in mechanical performance to provide optimum lightweight

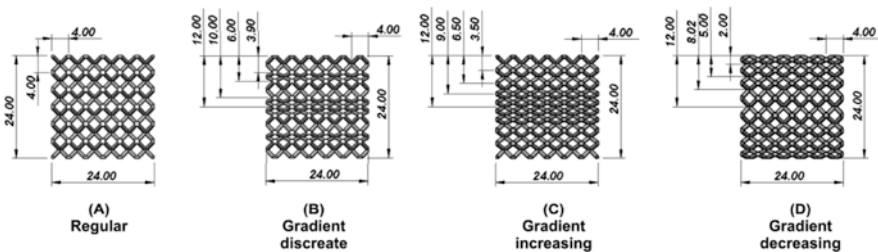


Fig. 14.3 Sample gradient configurations of a BCC lattice [21]. Under the Creative Commons license

lattice cell information to use in their designs. However, both for the final component or the unit cell analysis, the properties of parent material are needed. Examples of these material properties are parent material density, elastic modulus, Poisson ratio, and yield strength [23]. Considering the fact that, plastic yielding occurs for these slender structures, hardening curves of parent material may also be needed if it poses strain hardening. The general trend to use these structures under compressive load moreover leads to the need for further material properties such as compressive yield strength [23]. The generation of finite element meshes is another significant step for these studies and should be conducted carefully. Previous research shows that various types of mesh elements can be utilized for these studies. Among these element types, beam elements can be employed for strut-based lattice structures with the advantage of reducing the number of elements needed and thus leading to cost-effective computations. In this way, the number of elements can be reduced by nearly 1/100 compared to the number of elements when 3D meshing is applied [24]. Previous demonstrations however showed that FEA results of 3D meshed models exhibit better convergence than beam element meshed models, especially for densified regions of the stress–strain diagram [24].

As stated above, in the scope of the second approach for the design and analysis of lattice structures, the design of the unit cell can be generated by FEA and/or topology optimization and applied to component geometry. This approach predominantly employs a unit cube to have a single volume and it is meshed using fine 3D hexahedral elements [25]. All necessary parent material properties are assigned to the relevant unit cube in order to facilitate the consistency of the method. Boundary conditions of fixation and loading are also defined to the related areas of the unit cube. Finally, topology optimizations are conducted with the help of several commercial software considering objective function, design variables, and constraints [25]. The obtained unit cell geometry is arrayed along all the necessary coordinate axis to fill the final component volume with the obtained cell. Figure 14.4 shows the unit cell optimization approach with varying porosities [26].

The last approach for the design and analysis of lattice structures is to use special topology optimization algorithms and related software and fill the component geometry with lattice structures as the result of the optimization process. Examples of the related software which can be used for this approach are Altair OptiStruct and nTopology [27, 28]. These software packages basically employ traditional topology optimization algorithms, but they retain semi-dense elements instead of applying a sharp discretization which leaves only fully dense elements. Following that, the so-called semi-dense elements are converted to lattices, which have a porosity to facilitate the same stiffness as the semi-dense element. A refinement step can be introduced by the software in certain cases involving a detailed optimization where the end diameters of each lattice cell member are optimized.

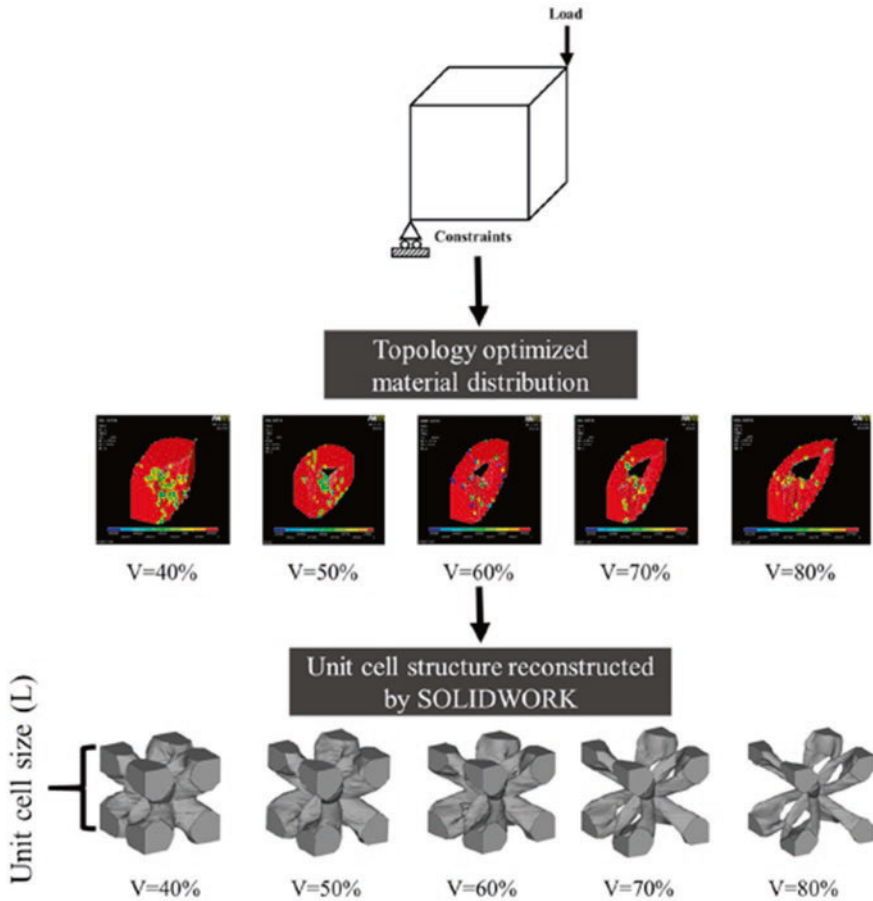


Fig. 14.4 Unit cell optimization approach with varying porosity [26]. Under the Creative Commons license

14.3 Production of Lattice Structures

Very complex geometries including internal features such as cavities and cooling channels have become possible to be manufactured from a wide range of metallic materials by the L-PBF process [5]. These complex geometries include topologically optimized bionic shapes and lattice structures which are almost impossible to produce by conventional manufacturing. With lattice structures, by controlling unit cell type, size, and distribution as well as other lattice parameters, specific material properties can be obtained. This unique advantage of lattices combined with L-PBF capabilities makes it very appealing for many industries. Among other AM technologies, L-PBF has the highest industrialization level as well as the highest maturity [29]. L-PBF has the advantages of producing almost fully dense parts with a

high resolution to be able to produce fine features and comparable mechanical properties with those of conventional processes [30–33]. On the other hand, it still has some limitations where the research in the field is focused on. These limitations include minimum feature size, process-inherent defects affecting the part performance, quality control issues, need for support structures on overhang surfaces, high cooling rates leading to residual stresses and deformations, and low surface quality. Some of these limitations also play a significant role in the manufacturability of the lattice structures.

The minimum feature size achievable in the L-PBF process, which is a critical factor for manufacturability, depends on many parameters. These include powder characteristics, e.g., particle size distribution, process parameters, laser spot size, powder coating mechanism, material, geometry, etc. In literature, there is a range of reported minimum feature size accomplished in this processing from 40 μm up to 300 μm although struts thinner than 0.1 mm are rarely reported and basically depends on machine specifications [34–38]. An example of minimum feature size in lattice structures is presented in [39] where struts with a size from 0.7 to 0.3 mm were produced. The minimum strut size that could be produced was limited to 0.35 mm. The build job with struts having a thickness of 0.3 mm could not be finished with a nominal beam focus diameter of 80–115 μm . Even the struts with a thickness of 0.35 mm were not very successfully produced because the horizontal struts were generally incomplete or irregular [39]. On the other hand, there are some smaller strut sizes achieved such as the production of 0.2 mm diameter struts by Van Bael from Ti6Al4V material with a beam spot size of 80 μm [40]. One of the limiting factors of the strut size is the recoating process. Using very small strut sizes, during the powder coating with a hard blade, the thin struts may be damaged or removed by the recoat blade leading to build [41].

L-PBF process dynamics lead to the variation of the nominal strut sizes and thicker struts. The deviation from the nominal design size depends on the melt pool formation and generally increases as the strut size is reduced. Thinner struts are usually produced with single scan tracks. Thus, the width of the melt pool determines the strut size. Depending on the utilized equipment and powder, the amount of the difference between the designed and actual strut size differs. If the melt pool width is greater than the designed strut diameter, it is not possible to accomplish the nominal diameter [40]. Moreover, the metal powder particles around the melt pool can interfere and bond the strut surfaces widening the strut size. This effect is clearly shown in Fig. 14.5 where Scanning Electron Microscopy (SEM) images of body-centered cubic lattice structures with a strut size of 0.7 mm at different magnifications are demonstrated. As shown in higher magnification, the powder particles stick to the surface deteriorating the dimensional accuracy as well as surface quality. A typical mismatch between designed and actual strut sizes is about 100 μm and needs to be taken into account during design and calculation of the volume fraction. If the strut size is designed as greater than the melt pool width of a single track and not sufficiently wide enough for two scan tracks, then it is possible to have smaller strut sizes than design values as reported in [42].

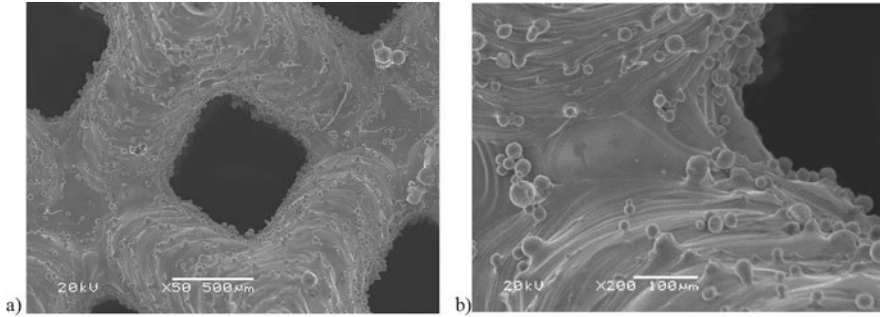


Fig. 14.5 Scanning Electron Microscopy images of body-centered cubic lattice structures with a strut size of 0.7 mm at (a) low magnification (×25) and (b) high magnification (×200)

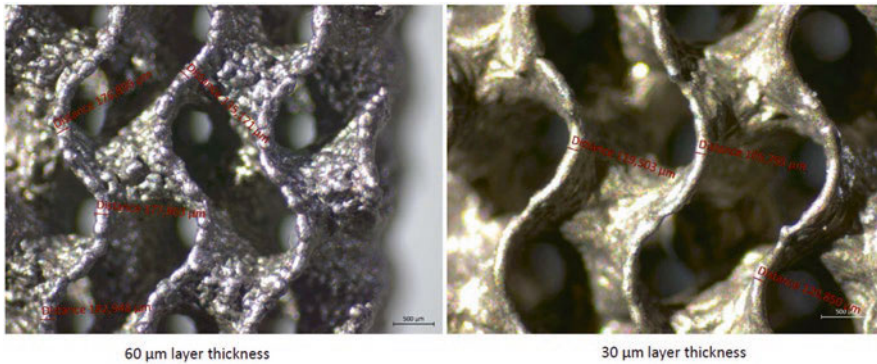


Fig. 14.6 Comparison of layer thickness on the minimum wall thickness of gyroid structures

The minimum feature size is generally encountered in lattice structures as the minimum strut size. However, in some unit cell geometries, there is no strut. For example, the gyroid structure, a member of the TPMS family, does not include any struts, but rather surfaces and thus a minimum wall thickness oriented in several different ways. As shown in Fig. 14.6, the gyroid geometry is mainly self-supporting, and very small wall thicknesses down to almost 100 μm are achievable with Ti6Al4V material. However, the geometrical accuracy and consistency of the wall thickness highly depend on the selected parameters, such as layer thickness.

Strut inclination angle plays a role in the manufacturability of the lattice structures in addition to minimum strut size. Scanning over powder or bulk material leads to a different melt pool behavior due to the variance in the thermal conductivity values of powder and bulk material. Thus, the overhang surfaces, which are not supported and have an inclination angle to the base plate lower than 45° , lead to undesired results such as sagging, bad surface quality, and even to build failure [43–46]. Forty-five degrees is a widely accepted rule-of-the-thumb, yet smaller inclination angles can be attained. Supports are not an option due to the impossibility to remove support structures after the build for lattice structures. Self-supporting

structures though need to be preferred for the manufacturability to minimize the local overheating in down-skin surfaces encountered in lattice structures [48–53]. The work undertaken with lattice structures by Leary et al. reports that it is possible to go down to 35° for different strut sizes from 0.5 to 3 mm [47]. In another study by Dong et al., it was presented that the strut size is also affected by the inclination angle of the struts in addition to the porosity [54]. In a study by Mazur et al., smaller inclination angles were possible as depicted in Fig. 14.7. The minimum printable strut angle was found to be 20° [55]. This is also consistent with the results of the study carried out by Kessler et al. with different cross-section geometries [56]. Thus, the orientation of the struts within the unit cell size and build direction plays a significant role in manufacturability as well as lattice performance.

The L-PBF process parameters also play a significant role in lattice production. The process parameters are generally optimized for maximum density but not for the best resolution limiting the manufacturability and geometrical accuracy of the lattice structures. Abele et al. have worked on optimizing the energy density for single tracks by varying laser scan speeds with strut thicknesses of 200 μm . The mismatch between the designed and actual strut size could be reduced down to 3% [42]. However, changing process parameters affecting the energy input may lead to changes in the porosity observed within the struts. In the study carried out by Sing et al., it is found that the strut size of L-PBF lattice structures is mostly influenced by the laser power in comparison to layer thickness and scanning speed while changes in laser power and other process parameters lead to changes in porosity and obtained mechanical properties [57]. Karami et al. addressed the effect of laser mode on the lattice structures and they found that the strut thickness was more uniform for pulsed laser. However, many defects, i.e., porosity and bad surface quality, were encountered with the pulsed mode due to non-optimized process parameters [58]. In another study carried out with a pulsed mode by Egan and Dowling, it is observed that rising the laser power from 50 to 150 W while using a constant exposure time, an increase of about 30% is seen in the strut diameter. While the strut size

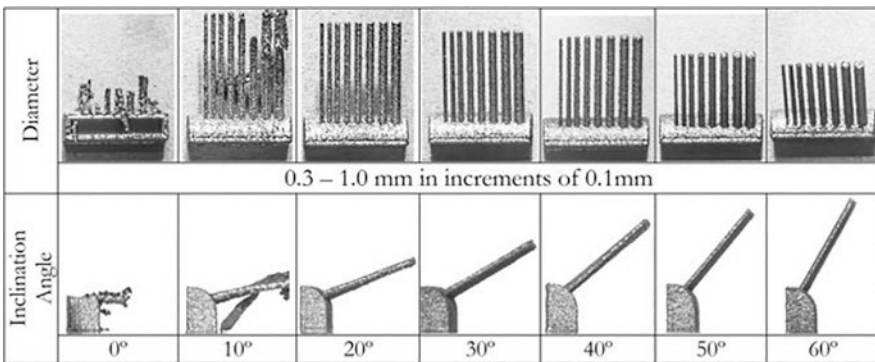


Fig. 14.7 Strut test specimens showing the possible range of inclination angles and strut sizes [55]. Reprinted by permission from Springer Nature

is increased, the relative porosity within the lattice structures is reduced from 96.3% to 89.1%. The effect of the laser beam spot size is moreover investigated and the tests led to the result that increasing the spot size 100%, the strut diameter was reduced by 17% whereas the mechanical strength was decreased by approximately 22% [59].

Lattice structures in general are built with contour exposure as single tracks. In some studies, however, the effect of hatch scanning is compared to contour exposure as shown in Fig. 14.8. Hatch scanning leads to the necking effect at nodes and unacceptable surface quality with all surfaces covered with partially melted powder particles [60] can be obtained. In the same study, the process parameters for contour scanning were investigated to understand the effect on strut size and manufacturability for a nominal strut size of 100 μm . A process window including the laser power and scan speed was generated to illustrate the relevant defects and lattice quality. A laser power between 350 W and 170 W was found to be suitably combined with an energy input greater than 2 J/mm^2 and smaller than 8 J/mm^2 . High laser power values result in overheating and excessively large struts whereas low values of laser power led to only partially built-up lattice structures and build failure. The position of the lattice structure on the base plate with respect to the airflow direction and recoating direction moreover affected the buildability as well as the mechanical performance [60].

As a summary, the process variables, as well as the powder characteristics, play a very significant role in the material properties and performance of the lattice structures. The actual struts that can be produced in the process may vary from the designed values and this mismatch shall be taken into consideration for structural analysis of the lattices. It can be compensated during the design phase provided that a good estimation can be made. However, many factors need to be considered to estimate the deviation such as powder particle size distribution, machine variables such as gas flow and powder coating, process parameters including layer thickness, laser power and scan speed, unit cell geometry/size, etc. Alternatively, it is also possible to clean the strut surfaces and reduce the strut size with different post-processes such as chemical etching. This also enables a smooth surface quality in comparison to as-built structures as shown in Fig. 14.9 [61–64].

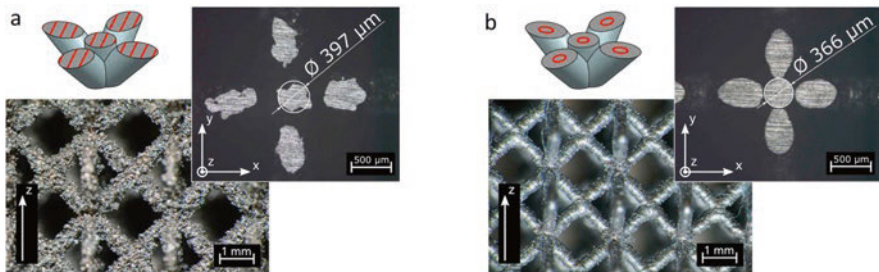


Fig. 14.8 The results of (a) hatch scanning and (b) contour exposure [60]. Reprinted with permission from Elsevier

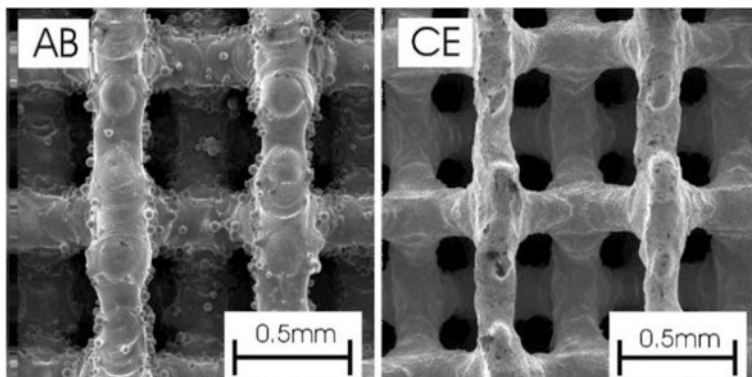


Fig. 14.9 Top surfaces of as-built (AB) and chemically etched (CE) lattice structures [64]. Reprinted with permission from Elsevier

14.4 Applications of Lattice Structures

Most of the studies conducted on utilizing lattice structures for weight reduction and tailoring mechanical properties have been focused on the compression behavior for a wide range of materials [58, 65–73]. These materials mainly include nickel superalloys (Inconel 625), Ti6Al4V, stainless steels (AISI 316 L), tool steels (1.2709), and AlSi10Mg. The purpose is generally to utilize lattice structures to reduce the weight of components while achieving part requirements. On the other hand, L-PBF has also been utilized to produce lattice structures to vary damping [74, 75], fatigue [76, 77], biocompatibility [78–81], and others.

The use of lattice structures is especially more important for aerospace and biomedical applications for different reasons. In aerospace, the lightweight design is appealing whereas in biomedical the possibility to reduce the elasticity modulus of bulk material to be closer to that of the bone is the motivation. As an example, a payload adapter structure with a hybrid approach combining solid structures coming from classical topology optimization and lattices is shown in Fig. 14.10. This enables the design of components with reduced weight while retaining structural response [82].

In biomedical applications, on the other hand, the modulus of elasticity of bone is very different than the values obtained from metallic implants leading to the stress-shielding effect associated with severe loss of bone mass [83]. This happens due to the fact that the metallic material with a higher modulus of elasticity adsorbs the load hindering bone regeneration. Therefore, the lattices are used in metallic implants to reduce the load needed for a specific deformation in the elastic region, in other words, modulus of elasticity [84]. Moreover, the hierarchical characteristic

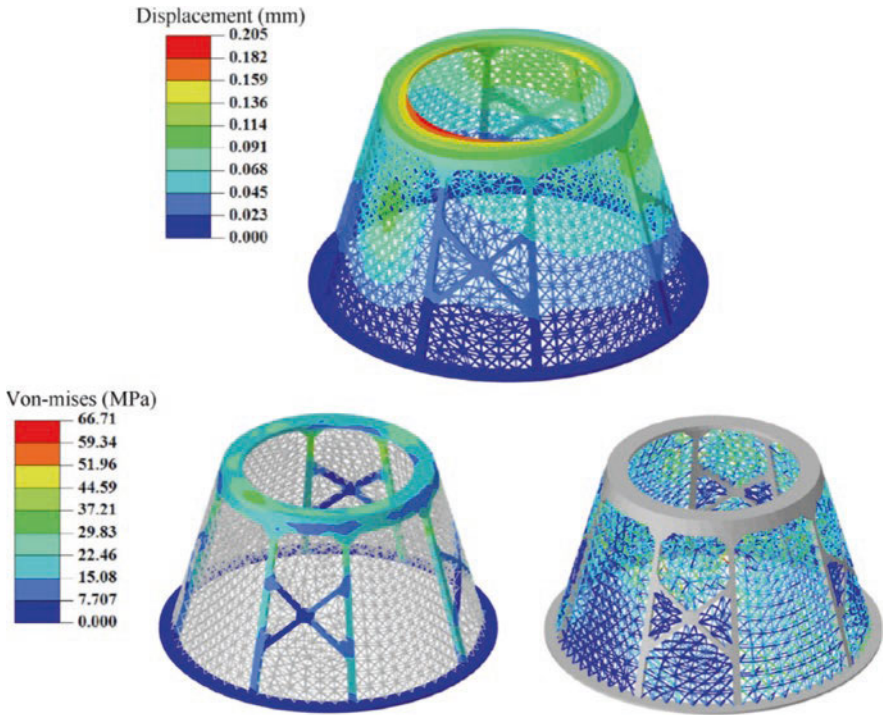


Fig. 14.10 Solid-lattice hybrid payload adapter structure [82]. Under the Creative Commons license

of the bone from macro to nanostructure can be very well represented in powder bed fusion processes as shown in Fig. 14.11 [85].

14.5 Summary and Conclusions

In this chapter, it has been demonstrated that the use of lattice structures could be beneficial in terms of achieving a decreased mass within the same volume of the component domain. However, the researchers or engineers dealing with these lattice structures should have an accurate understanding of types and characteristics, since the reduction in mass may company to the reduction in stiffness and accurate understanding may help to decide the compromise between mass and stiffness reduction. As there are several available analytical equations to calculate geometrical characteristics, computational techniques are still needed for the design and analysis of these structures. These techniques can be used according to three approaches and may be coupled with topology optimizations. The utilization of L-PBF AM technologies offers compelling advantages for the production of these lattice structures

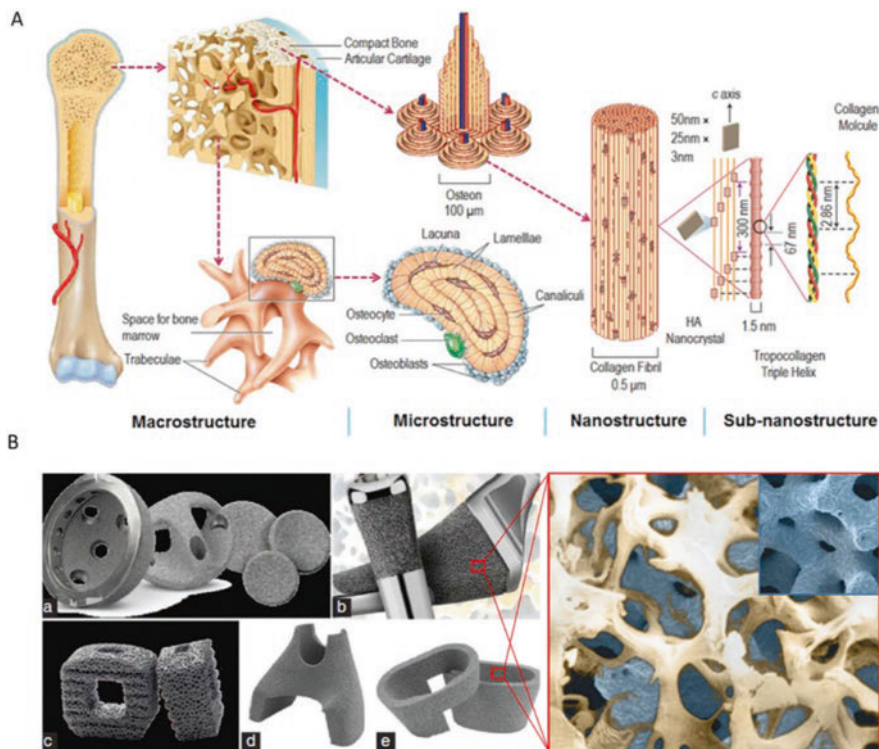


Fig. 14.11 Hierarchical structure of bone and biomimetic design of AM implants [85]. Reprinted with permission from Elsevier

compared to conventional manufacturing techniques. Still, L-PBF AM process parameters, such as laser power, should be optimized and the process limits, such as minimum diameter or inclination angle, have to be systematically studied.

Acknowledgments The authors would like to acknowledge that this literature survey was carried out in the scope of a project with a number of 120 N943 funded by the TUBITAK 2523 Program. One of the authors, Dr. Evren Yasa, would like to acknowledge that the SEM images given in Fig. 14.5 in this study are a result of research carried out under the TUBITAK ARDEB 1002 Program with a project number of 119 M781. She would also like to thank SLM Solutions GmbH for their assistance in the production of lattice structures.

References

- Gibson, L., & Ashby, M. (1997). Introduction. In *Cellular solids: Structure and properties* (Cambridge Solid State Science Series) (pp. 1–14). Cambridge University Press. <https://doi.org/10.1017/CBO9781139878326.003>
- LeMay, J. D., Hopper, R., Hrubesh, L. W., & Pekala, R. W. (1990). Low-density microcellular materials: Introduction. *MRS Bulletin*, 15(12), 19–20.

3. Suh, K. W., & Skochdopole, R. E. (1980). In Kirk-Othmer (Ed.), *Encyclopedia of chemical technology* (Vol. II, 3rd ed., p. 82).
4. Kooistra, G. W., Deshpande, V. S., & Wadley, H. N. (2004). Compressive behavior of age hardenable tetrahedral lattice truss structures made from aluminium. *Acta Materialia*, 52(14), 4229–4237.
5. Maconachie, T., Leary, M., Lozanovski, B., Zhang, X., Qian, M., Faruque, O., & Brandt, M. (2019). SLM lattice structures: Properties, performance, applications and challenges. *Materials & Design*, 183, 108137.
6. Zok, F. W., Lattice, R. M., & Begley, M. R. (2016). Periodic truss structures. *Journal of the Mechanics and Physics of Solids*, 96, 184–203.
7. Hanks, B., Berthel, J., Frecker, M., & Simpson, T. W. (2020). Mechanical properties of additively manufactured metal lattice structures: Data review and design interface. *Additive Manufacturing*, 35, 101301.
8. Maxwell, J. C. (1864). Relaxing in foam. *Philosophical Magazine*, 27(250), 1864.
9. Ashby, M. F. (2006). The properties of foams and lattices. *Philosophical Transactions of the Royal Society A: Mathematical, Physical and Engineering Sciences*, 364(1838), 15–30.
10. Austermann, J., Redmann, A. J., Dahmen, V., Quintanilla, A. L., Mecham, S. J., & Osswald, T. A. (2019). Fiber-reinforced composite sandwich structures by co-curing with additive manufactured epoxy lattices. *Journal of Composites Science*, 3(2), 53.
11. Bonatti, C., & Mohr, D. (2019). Mechanical performance of additively-manufactured anisotropic and isotropic smooth shell-lattice materials: Simulations & experiments. *Journal of the Mechanics and Physics of Solids*, 122, 1–26.
12. Tancogne-Dejean, T., Diamantopoulou, M., Gorji, M. B., Bonatti, C., & Mohr, D. (2018). 3D plate-lattices: An emerging class of low-density metamaterial exhibiting optimal isotropic stiffness. *Advanced Materials*, 30(45), 1803334.
13. Yan, C., Hao, L., Hussein, A., Young, P., & Raymont, D. (2014). Advanced lightweight 316L stainless steel cellular lattice structures fabricated via selective laser melting. *Materials & Design*, 55, 533–541.
14. Maskery, I., Aboulkhair, N. T., Aremu, A. O., Tuck, C. J., & Ashcroft, I. A. (2017). Compressive failure modes and energy absorption in additively manufactured double gyroid lattices. *Additive Manufacturing*, 16, 24–29.
15. Zadpoor, A. A. (2015). Bone tissue regeneration: The role of scaffold geometry. *Biomaterials Science*, 3(2), 231–245.
16. Pan, C., Han, Y., & Lu, J. (2020). Design and optimization of lattice structures: A review. *Applied Sciences*, 10(18), 6374.
17. Retrieved from <https://www.materialise.com/en/software/3-matic>.
18. Retrieved from <https://knowledge.autodesk.com/support/netfabb/learn-explore/caas/CloudHelp/cloudhelp/2020/ENU/NETF/files/GUID-7C5857A1-501E-406B-9632-6EEBD603FE29-htm.html>.
19. Retrieved from <https://community.sw.siemens.com/s/article/introducing-lattice-in-nx>.
20. Retrieved from https://support.ptc.com/help/creo/creo_pma/r6.0/usascii/index.html#page/part_modeling/part_modeling/part_nine_sub/To_Create_Formula_Driven_Lattice.html.
21. Sienkiewicz, J., Płatek, P., Jiang, F., Sun, X., & Rusinek, A. (2020). Investigations on the mechanical response of gradient lattice structures manufactured via SLM. *Metals*, 10(2), 213.
22. Kladovasilakis, N., Tsongas, K., & Tzetzis, D. (2021). Mechanical and FEA-assisted characterization of fused filament fabricated triply periodic minimal surface structures. *Journal of Composites Science*, 5(2), 58.
23. Helou, M., Vongbunyong, S., & Kara, S. (2016). Finite element analysis and validation of cellular structures. *Procedia CIRP*, 50, 94–99.
24. Smith, M., Guan, Z., & Cantwell, W. J. (2013). Finite element modelling of the compressive response of lattice structures manufactured using the selective laser melting technique. *International Journal of Mechanical Sciences*, 67, 28–41.

25. Xiao, Z., Yang, Y., Xiao, R., Bai, Y., Song, C., & Wang, D. (2018). Evaluation of topology-optimized lattice structures manufactured via selective laser melting. *Materials & Design*, *143*, 27–37.
26. Xu, Y., Zhang, D., Zhou, Y., Wang, W., & Cao, X. (2017). Study on topology optimization design, manufacturability, and performance evaluation of Ti-6Al-4V porous structures fabricated by selective laser melting (SLM). *Materials*, *10*(9), 1048.
27. Retrieved from <https://insider.altairhyperworks.com/design-and-optimization-of-lattice-structures-for-3d-printing-using-altair-optistruct/>.
28. Retrieved from <https://ntopology.com/resources/whitepaper-implicit-modeling-technology/#:~:text=At%20the%20core%20of%20nTopology,to%20describe%20a%20solid%20body.>
29. Retrieved from <https://tritoneam.com/wp-content/uploads/Ampower-Insights-vol.-6-New-Technologies-1.pdf>.
30. Zhang, L.-C., Attar, H., Calin, M., & Eckert, J. (2016). Review on manufacture by selective laser melting and properties of titanium based materials for biomedical applications. *Materials Technology*, *31*(2), 66–76.
31. Wenjin, W., Tor, S. B., Leong, K., Chua, C. & Merchant, A. (2016). State of the art review on selective laser melting of stainless steel for future applications in the marine industry. In *2nd international conference on progress in additive manufacturing (Pro-AM 2016) in Singapore*.
32. Zhang, B., Li, Y., & Bai, Q. (2017). Defect formation mechanisms in selective laser melting: A review. *Chinese Journal of Mechanical Engineering*, *30*, 515–527.
33. Gunasekaran, J., Sevvil, P., & Solomon, I. J. (2021). Metallic materials fabrication by selective laser melting: A review. *Materials Today: Proceedings.*, *37*(2), 252–256.
34. Guagliano, M., Previtali, B., Rampino, L., Rosa, E. & Galimberti, G. (2015). Digital aesthetic of new products obtained by selective laser melting process. In *Proceedings of the 20th international conference on engineering design, Milan, Italy*.
35. Thomas, D. (2009). *The development of design rules for selective laser melting the development of design rules for selective laser melting*. Ph.D. Thesis, University of Wales Institute, Cardiff, UK.
36. Barroqueiro, B., Andrade-Campos, A., & Valente, R. A. F. (2019). Designing self supported SLM structures via topology optimization. *Journal of Manufacturing and Materials Processing*, *3*(3), 68.
37. Sames, W. J., List, F. A., Pannala, S., Dehoff, R. R., & Babu, S. S. (2016). The metallurgy and processing science of metal additive manufacturing. *International Materials Reviews*, *61*(5), 315–360.
38. Gruber, S., Grunert, C., Mirko, R., Lopez, E., Marquardt, A., Brueckner, F., & Leyens, C. (2020). Comparison of dimensional accuracy and tolerances of powder bed based and nozzle based additive manufacturing processes. *Journal of Laser Applications*, *32*, 032016.
39. Sola, S., Defanti, S., Mantovani, S., Merulla, A., & Denti, L. (2020). Technological feasibility of lattice materials by laser-based powder bed fusion of A357.0. *3D Printing and Additive Manufacturing.*, *7*(1). <https://doi.org/10.1089/3dp.2019.0119>
40. Van Bael, S., Kerckhofs, G., Moesen, M., Pyka, G., Schrooten, J., & Kruth, J. P. (2011). Micro-CT-based improvement of geometrical and mechanical controllability of selective laser melted Ti6Al4V porous structures. *Materials Science and Engineering: A.*, *528*(24), 7423–7431.
41. Raymont, D., Yan, C., Hussein, A. & Young, P. (2011). Design and additive manufacturing of cellular lattice structures. *Innovative Developments in Virtual and Physical Prototyping*. <https://doi.org/10.1201/b11341-40>.
42. Abele, E., Stoffregen, H. A., Klimkeit, K., Hoche, H., & Oechsner, M. (2015). Optimisation of process parameters for lattice structures. *Rapid Prototyping Journal*, *21*(1), 117–127.
43. Paterson, A. E., Messimer, S. L., & Farrington, P. A. (2017). Overhanging features and the SLM/DMLS residual stresses problem. *Review and Future Research Need. Technologies*, *5*(15). <https://doi.org/10.3390/technologies5020015>

44. Cloots, M., Zumofen, L., Spierings, A. B., Kirchheim, A., & Wegener, K. (2017). Approaches to minimize overhang angles of SLM parts. *Rapid Prototyping Journal*, 23(2), 362–369. <https://doi.org/10.1108/RPJ-05-2015-0061>
45. Paggi, U., Sinico, M., Thijs, L., Dewulf, W. & Hooreweder, B. (2019). Improving the dimensional accuracy of downfacing surfaces of additively manufactured parts. In *Proceedings of the special interest group meeting on advancing precision in additive manufacturing*. Nantes, France.
46. Wang, D., Mai, S., Xiao, D., & Yang, Y. (2016). Surface quality of the curved overhanging structure manufactured from 316-L stainless steel by SLM. *International Journal of Advanced Manufacturing Technology*, 86, 781–792. <https://doi.org/10.1007/s00170-015-8216-6>
47. Leary, M., Mazur, M., Elambasseril, J., McMillan, M., Chirent, T., Sun, Y., Qian, M., Easton, M., & Brandt, M. (2016). Selective laser melting (SLM) of AlSi12Mg lattice structures. *Materials & Design*, 98, 344–357.
48. Li, S., Hassanin, H., Attallah, M. M., Adkins, N. J. E., & Essa, K. (2016). The development of TiNi-based negative Poisson's ratio structure using selective laser melting. *Acta Materialia*, 105, 75–83. <https://doi.org/10.1016/j.actamat.2015.12.017>
49. Sercombe, T. B., Xu, X., Challis, V. J., Green, R., Yue, S., Zhang, Z., & Lee, P. D. (2015). Failure modes in high strength and stiffness to weight scaffolds produced by selective laser melting. *Materials and Design*, 67, 501–508. <https://doi.org/10.1016/j.matdes.2014.10.063>
50. Alghamdi, A., Maconachie, T., Downing, D., Brandt, M., Qian, M., & Leary, M. (2020). Effect of additive manufactured lattice defects on mechanical properties: An automated method for the enhancement of lattice geometry. *International Journal of Advanced Manufacturing Technology*, 108, 957–971. <https://doi.org/10.1007/s00170-020-05394-8>
51. Wauthle, R., Vrancken, B., Beynaerts, B., Jorissen, K., Schrooten, J., Kruth, J.-P., & Van Humbeeck, J. (2015). Effects of build orientation and heat treatment on the microstructure and mechanical properties of selective laser melted Ti6Al4V lattice structures. *Additive Manufacturing*, 5, 77–84.
52. du Plessis, A., Yadroitsava, I., & Yadroitsev, I. (2018). Ti6Al4V lightweight lattice structures manufactured by laser powder bed fusion for load-bearing applications. *Optics and Laser Technology*, 108, 521–528. <https://doi.org/10.1016/j.optlastec.2018.07.050>
53. Al-Ketan, O., Rowshan, R., & Abu Al-Rub, R. K. (2018). Topologymechanical property relationship of 3D printed strut, skeletal and sheet based periodic metallic cellular materials. *Additive Manufacturing*, 19, 167–183. <https://doi.org/10.1016/j.addma.2017.12.006>
54. Dong, Z., Liu, Y., Li, W., & Liang, J. (2019). Orientation dependency for microstructure, geometric accuracy and mechanical properties of selective laser melting AlSi10Mg lattices. *Journal of Alloys and Compounds*, 791, 490–500. <https://doi.org/10.1016/j.jallcom.2019.03.344>
55. Mazur, M., Leary, M., Sun, S., Vcelka, M., Shidid, D., & Brandt, M. (2016). Deformation and failure behaviour of Ti-6Al-4V lattice structures manufactured by selective laser melting (SLM). *International Journal of Advanced Manufacturing Technology*, 84, 1391–1411. <https://doi.org/10.1007/s00170-015-7655-4>
56. Kessler, J., Balc, N., Gebhardt, A., & Abbas, K. (2017). Basic design rules of unit cells for additive manufactured lattice structures. *MATEC Web of Conferences*, 137, 02005. <https://doi.org/10.1051/mateconf/201713702005>
57. Sing, S. L., Wiria, F. E., & Yeong, W. Y. (2018). Selective laser melting of lattice structures: A statistical approach to manufacturability and mechanical behavior. *Robotics and Computer-Integrated Manufacturing*, 49, 170–180.
58. Karami, K., Blok, A., Weber, L., Ahmadi, S. M., Petrov, R., Nikolic, K., Borisov, E. V., Leeftang, S., Ayas, C., Zadpoor, A. A., Mehdipour, M., Reinton, E., & Popovich, V. A. (2020). Continuous and pulsed selective laser melting of Ti6Al4V lattice structures: Effect of post-processing on microstructural anisotropy and fatigue behaviour. *Additive Manufacturing*, 36, 101433.

59. Egan, D. S., & Dowling, D. P. (2019). Influence of process parameters on the correlation between in-situ process monitoring data and the mechanical properties of Ti-6Al-4V non-stochastic cellular structures. *Additive Manufacturing*, 30, 100890.
60. Großmann, A., Gosmann, J., & Mittelstedt, C. (2019). Lightweight lattice structures in selective laser melting: Design, fabrication and mechanical properties. *Materials Science and Engineering: A*, 766, 138356.
61. Kerckhofs, G., Pyka, G., Moesen, M., & Schrooten, J. (2012). High resolution micro-CT as a tool for 3D surface roughness measurement of 3D additive manufactured porous structures. *ProC iCT*, 77–83. <https://doi.org/10.1002/adem.201200156>
62. Pyka, G., Kerckhofs, G., Papantoniou, I., Speirs, M., Schrooten, J., & Wevers, M. (2013). Surface roughness and morphology customization of additive manufactured open porous Ti6Al4V structures. *Materials (Basel)*, 6, 4737–4757. <https://doi.org/10.3390/ma6104737>
63. Chang, S., Liu, A., Ong, C. Y. A., Zhang, L., Huang, X., Tan, Y. H., Zhao, L., Li, L., & Ding, J. (2019). Highly effective smoothing of 3D-printed metal structures via over potential electrochemical polishing. *Materials Research Letters*, 7(7), 282–289. <https://doi.org/10.1080/021663831.2019.1601645>
64. Hooreweder, B., & Kruth, J.-P. (2017). Advanced fatigue analysis of metal lattice structures produced by Selective Laser Melting. *CIRP Annals - Manufacturing Technology*, 66(1), 221–224. <https://doi.org/10.1016/j.cirp.2017.04.130>
65. Leary, M., Mazur, M., Williams, H., Yang, E., Alghamdi, A., Lozanovski, B., Zhang, X., Shidid, D., Farahbod-Sternahl, L., Witt, G., Kelbassa, I., Choong, P., Qian, M., & Brandt, M. (2018). Inconel 625 lattice structures manufactured by selective laser melting (SLM): Mechanical properties, deformation and failure modes. *Materials & Design*, 157, 179–199. <https://doi.org/10.1016/j.matdes.2018.06.010>
66. Isaenkova, M. G., Yudin, A. V., Rubanov, A. E., Osintsev, A. V., & Degadnikova, L. A. (2020). Deformation behavior modelling of lattice structures manufactured by a selective laser melting of 316L steel powder. *Journal of Materials Research and Technology*, 9(6), 15177–15184.
67. Yan, X., Lupoi, R., Wu, H., Ma, W., Liu, M., O'Donnell, G., & Yin, S. (2019). Effect of hot isostatic pressing (HIP) treatment on the compressive properties of Ti6Al4V lattice structure fabricated by selective laser melting. *Materials Letters*, 255, 126537.
68. Choy, S. Y., Sun, C.-N., Leong, K. F., & Wei, J. (2017). Compressive properties of functionally graded lattice structures manufactured by selective laser melting. *Materials & Design*, 131, 112–120.
69. Mahshid, R., Hansen, H. N., & Højbjerg, K. L. (2016). Strength analysis and modeling of cellular lattice structures manufactured using selective laser melting for tooling applications. *Materials & Design*, 104, 276–283.
70. Bari, K., & Arjunan, A. (2019). Extra low interstitial titanium based fully porous morphological bone scaffolds manufactured using selective laser melting. *Journal of the Mechanical Behavior of Biomedical Materials*, 95, 1–12.
71. Ge, J., Yan, X., Lei, Y., Ahmed, M., O'Reilly, P., Zhang, C., Lupoi, R., & Yin, S. (2021). A detailed analysis on the microstructure and compressive properties of selective laser melted Ti6Al4V lattice structures. *Materials & Design*, 198, 109292.
72. Li, Z., Nie, Y., Liu, B., Kuai, Z., Zhao, M., & Liu, F. (2020). Mechanical properties of AlSi10Mg lattice structures fabricated by selective laser melting. *Materials & Design*, 192, 108709.
73. Zhong, T., He, K., Li, H., & Yang, L. (2019). Mechanical properties of lightweight 316L stainless steel lattice structures fabricated by selective laser melting. *Materials & Design*, 181, 108076.
74. Rosa, F., Manzoni, S., & Casati, R. (2018). Damping behavior of 316L lattice structures produced by Selective Laser Melting. *Materials & Design*, 160, 1010–1018.
75. Li, C., Lei, H., Liu, Y., Zhang, X., Xiong, J., Zhou, H., & Fang, D. (2018). Crushing behavior of multi-layer metal lattice panel fabricated by selective laser melting. *International Journal of Mechanical Sciences*, 145, 389–399.

76. Mahmoud, D., Al-Rubaie, K. S., & Elbestawi, M. A. (2021). The influence of selective laser melting defects on the fatigue properties of Ti6Al4V porosity graded gyroids for bone implants. *International Journal of Mechanical Sciences.*, 193, 106180.
77. Refai, K., Brugger, C., Montemurro, M., & Saintier, N. (2020). An experimental and numerical study of the high cycle multiaxial fatigue strength of titanium lattice structures produced by Selective Laser Melting (SLM). *International Journal of Fatigue.*, 138, 105623.
78. Wally, Z. J., Haque, A. M., Feteira, A., Claeysens, F., Goodall, R., & Reilly, G. C. (2019). Selective laser melting processed Ti6Al4V lattices with graded porosities for dental applications. *Journal of the Mechanical Behavior of Biomedical Materials.*, 90, 20–29.
79. Wang, X., Xu, S., Zhou, S., Xu, W., Leary, M., Choong, P., Qian, M., Brandt, M., & Xie, Y. M. (2016). Topological design and additive manufacturing of porous metals for bone scaffolds and orthopaedic implants: A review. *Biomaterials*, 83, 127–141. <https://doi.org/10.1016/j.biomaterials.2016.01.012>
80. Deering, J., & Grandfield, K. (2021). Current interpretations on the in vivo response of bone to additively manufactured metallic porous scaffolds: A review. *Biomaterials and Biosystems.*, 2, 100013.
81. Rodgers, G. W., Van Houten, E. E. W., Bianco, R. J., Besset, R., & Woodfield, T. B. F. (2014). Topology optimization of porous lattice structures for orthopaedic implants. *IFAC Proceedings*, 47, 9907–9912.
82. Wang, C., Zhu, J., Wu, M., Hou, J., Zhou, H., Meng, L., Li, C., & Zhang, W. (2021). Multi-scale design and optimization for solid-lattice hybrid structures and their application to aerospace vehicle components. *Chinese Journal of Aeronautics.*, 4(5), 386–398.
83. Brizuela, A., Herrero-Climent, M., Rios-Carrasco, E., Rios-Santos, J. V., Pérez, R. A., Manero, J. M., & Gil Mur, J. (2019). Influence of the elastic modulus on the osseointegration of dental implants. *Materials (Basel)*, 12(6), 980. <https://doi.org/10.3390/ma12060980>
84. Luo, J. P., Huang, Y. J., Xu, J. Y., Sun, J. F., Dargusch, M. S., Hou, C. H., Ren, L., Wang, R. Z., Ebel, T., & Yan, M. (2020). Additively manufactured biomedical Ti-Nb-Ta-Zr lattices with tunable Young's modulus: Mechanical property, biocompatibility, and proteomics analysis. *Materials Science and Engineering: C*, 14, 110903.
85. Li, J., Cui, X., Hooper, G. J., Lim, K. S., & Woodfield, T. B. F. (2020). Rational design, bio-functionalization and biological performance of hybrid additive manufactured titanium implants for orthopaedic applications: A review. *Journal of the Mechanical Behavior of Biomedical Materials*, 105, 103671.

Chapter 15

Application of Wire Arc Additive Manufacturing for Inconel 718 Superalloy



G. K. Sujan, Huijun Li, Zengxi Pan, Daniel Liang, and Nazmul Alam

Nomenclature

A	Ampere (C/s)
AF	As-fabricated
AM	Additive manufacturing
AMS	Aerospace material specifications
ARP	As-received plate
bct	Body-centered tetragonal
BD	Build direction
CMT	Cold metal transfer
DCEN	Direct current electrode negative
EBM	Electron beam melting
EDM	Electrical discharge machining
EDS	Energy-dispersive X-ray spectroscopy
fcc	Face-centered cubic
GTAW	Gas tungsten arc welding
HA	Homogenization-annealed
HAP	Homogenization-annealed plate
HSA	Homogenization-solution-annealed
IN718	Inconel 718
LBM	Laser beam melting
MIG	Metal inert gas
MZ	Middle zone
NSZ	Near-substrate zone

G. K. Sujan · H. Li (✉) · Z. Pan
Faculty of Engineering and Information Sciences, University of Wollongong,
Wollongong, NSW, Australia
e-mail: huijun@uow.edu.au

D. Liang · N. Alam
Commonwealth Scientific and Industrial Research Organization (CSIRO),
Melbourne, Australia

PAW	Plasma arc welding
PDAS	Primary dendritic arm spacing
SAE	Society of automotive engineers
SDAS	Secondary dendritic arm spacing
SEM	Scanning electron microscope
TD	Transverse direction
TIG	Tungsten inert gas
TZ	Top zone
UTS	Ultimate tensile strength (MPa)
WAAM	Wire-arc additive manufacturing
WD	Welding direction
XRD	X-ray diffraction
YS	Yield strength (MPa)
γ	Gamma (Austenite)
γ'	Gamma prime
γ''	Gamma double prime
δ	Delta

15.1 Introduction

Superalloys are special class of complex solid solution and precipitation strengthening materials used in specialized applications due to the excellent ability to maintain structural integrity and mechanical strength and to resist surface degradation phenomena in high temperature and corrosive environments [1]. Among the existing major categories of superalloys, Ni-based superalloys are widely consumed in the hottest areas (combustor and turbine sections) of a modern jet aircraft comprising an estimated 50% of the total engine weight with Inconel 718 (IN718) constituting 70% of the total Ni-based superalloys [2, 3]. Besides its use in the aerospace industry, IN718 has also been utilized in oil- and gas-field applications, nuclear reactors, marine, and superconducting magnet systems [4]. It has been well recognized throughout the world as an industrially important alloy system due to the exhibition of overall better physical and chemical properties in comparison with its counterparts. It is regarded as a solution-annealed and precipitation-hardened Ni-based superalloy with the reputation of retaining its mechanical properties (high tensile, creep rupture, and fatigue strength) at cryogenic (~ -250 °C) to high (~ 700 °) temperature service conditions [5–12]. These outstanding mechanical attributes are achieved predominantly by the coherent precipitation of metastable γ'' -Ni₃(Nb,Ti) phase (ordered and bct DO₂₂ crystal structure [13–15]) providing coherency strain hardening as a result of inducing tetragonal distortion in γ matrix (Ni–Cr–Fe phase) [16, 17]. The γ' -Ni₃(Al,Ti,Nb) precipitates (coherent, ordered, and fcc L1₂ crystal structure [13, 15]) also provide a minor contribution to the strengthening through chemical or order hardening mechanism due to its lower volume fraction (~ 3 –5%) in comparison with γ'' phase (~ 10 –20%) [17–20]. Due to the presence of high Cr

content (~19 wt.%) in the alloy composition of IN718, it shows excellent oxidation resistance at high-temperature application regime [21–24] and gives splendid protection against corrosion in both dry and wet conditions [25–27]. These attributes are possible due to the formation of a passive and continuous chromia scale (Cr_2O_3) on the outer surface of the material which prohibits metal-medium contact for further metal dissolution [23, 28]. Apart from its excellent physical and chemical attributes, the superior weldability of IN718 alloy was also one of the prime reasons that cemented its importance and reputation to resist strain-age cracking either during welding or annealing condition. The reasons are the sluggish hardening response of γ'' precipitates, and the low concentration of Ti and Al resisting the rapid hardening response of γ' precipitates [29].

The fabrication of IN718 parts by wire-arc additive manufacturing (WAAM) process has been evolved into a major topic of immediate interest in the scientific and research communities [12, 30–40]. It is a type of directed energy deposition (DED) process based on inexpensive and well-known arc welding technology which deposits material in a layer-by-layer fashion in order to achieve a near-net shaped product. As IN718 alloy is an expensive and high strain-hardening material [41], the free-forming manufacturing processes, like WAAM, have decisive economic advantages over conventional fabrication methods in terms of reducing materials wastage and lowering machining cost. Besides, the WAAM process is much cheaper, user friendly, and has a higher deposition rate and production capability than that of other additive manufacturing methods [42–44]. The conventional gas tungsten arc welding (GTAW) technique has already been used and is widely popular in joining as-cast or wrought IN718 alloy components for the production of welded assemblies and repairing of damaged aircraft parts during fabrication or service conditions to prolong the engine life and minimize the associated costs related to component replacement [45, 46]. Thus, the GTAW-based WAAM system can be considered as an economically viable candidate to fabricate near-complete IN718 metal components in future. Although additive manufacturing (AM), in general, is still in the stage of infancy, the integration of AM processes with conventional manufacturing techniques has already been demonstrated to achieve the metal components with desired shape and properties [47]. The wall geometry of additively manufactured samples has experienced many complications due to its complex correlation with the processing parameters used in WAAM process. Depending on the end-use application, it is necessary to optimize the processing conditions in order to achieve the required dimensions of the fabricated components. Tsurumaki et al. [39] conducted the effects of wire feed speed and deposition current on the fabrication of IN718 thin wall geometry in repairing the damaged parts of turbine blades using metal inert gas (MIG)-based WAAM technique. It was suggested that the width and cross-sectional area of the wall followed a parabolic relationship under constant interlayer temperature and the processing parameters should be considered in such a way that would avoid the dipping phenomenon of molten metal from the thin end of the plate. The influence of welding parameters on the production of thick wall IN718 components using cold metal transfer (CMT)-based WAAM process has recently been investigated by Kindermann et al. [38]. The results showed that

decreasing the travel speed increased both the height and width of as-fabricated walls. However, decreasing the wire feeding speed decreased the wall width only without affecting the wall height. In GTAW-based WAAM process, arc current was also found to be an important parameter on the wall geometry of fabricating Ni-based superalloy [48]. Furthermore, there are reports in literature which suggest that the processing parameters used in WAAM process also influenced the microstructure and mechanical properties of Ni-based superalloys [38, 49]. Thus, a comprehensive understanding of the effects of welding parameters on wall geometry, as well as microstructure and mechanical properties of IN718 components produced by GTAW-based WAAM process is still necessary to achieve material of desirable quality and properties and to optimize the processing conditions for repeatability and reproducibility.

The microstructural evolution of as-deposited IN718 superalloy parts during WAAM process has been found to be consistent and is independent of applying various arc-welding techniques, such as GTAW [31, 32, 36, 40], MIG [30], plasma arc welding (PAW) [12, 34, 35, 37, 50], and CMT [33, 38]. A highly textured γ -matrix of dendritic morphology was developed parallel to the buildup direction with laves phase and carbide inclusions situating in the interdendritic region [12, 30, 32, 36, 38]. Carbide inclusions are not considered detrimental to mechanical strength of IN718 alloys. However, the presence of these particles was found to cause difficulty during the machining process [41, 51]. The precipitation of laves phase in wire arc additively fabricated IN718 parts is the major concern as it deteriorates the mechanical integrity of the weldments. The WAAM-IN718 alloy is susceptible to solidification and liquation cracking under improper welding conditions during fabrication providing anisotropic mechanical properties [50]. The presence of laves phase was also reported to cause fracture by initiating the micro-voids formation under loading [52]. The formation of laves phase also depletes the Nb concentration in the matrix for the precipitation of strength-hardening phases of γ'' and γ' [53]. Thus, the avoidance or elimination of laves constituents in WAAM alloy 718 is important to achieve the desired properties. The inevitability of the formation of laves constituents is commenced due to the high heat input and low cooling rate of WAAM process [54, 55] which are difficult to govern and control at present [43]. As a result, the post-deposition homogenization treatment is the best way to eliminate laves phase by dissolving it back to γ -matrix and redistributing the beneficial Nb concentration in a more uniform manner throughout the γ -matrix. Recently, Seow et al. [12] have investigated the effects of a modified homogenization-annealed (HA) condition on microstructure and mechanical properties of WAAM alloy 718. It was found that laves phases were completely dissolved into the γ -matrix. The mechanical strength of heat-treated WAAM parts (1062 MPa) was inferior to wrought products (1241 MPa, AMS 5662) as high homogenization temperature (1186 °C for 40 mins) promoted excessive grain growth of existing large columnar grains. Interestingly, it was also possible to dissolve the deleterious laves phases at 1100 °C using standard homogenization-solution-annealed (HSA) condition [12, 56]. However, the solution treatment (980 °C for 1 hour) precipitated out δ -Ni₃Nb phase in γ -matrix of WAAM parts which adversely affected the ductility and

obviously depleted the Nb amount for γ'' formation. Thus, a lower homogenization temperature of 1100 °C with only annealed condition should be more useful to subside the grain coarsening behavior and dissolve laves particles in WAAM parts than that of Seow et al. work [12]. It is also necessary to understand the influence of this modified heat treatment on structure–property relationship of WAAM parts and compares with the literature.

Apart from microstructural stability and mechanical integrity of WAAM alloy 718 components, the understanding of chemical interactions under severe service condition (such as high-temperature oxidation) is equally critical to predict their long-lasting performance and reliability. According to the general characterization of Ni–Cr–Al superalloys, IN718 forms external chromia (Cr_2O_3) scale to reach the steady-state condition with internal alumina (Al_2O_3) subscale during high-temperature oxidation [57]. In reality, the oxide-scale formation and oxidation kinetics of IN718 are much more complex due to the presence of other alloying elements (Ti, Mn, Nb) that are more susceptible to oxidation than that of Cr. Al-hatab et al. [24] suggested that the oxidation kinetics of as-received IN718 was sub-parabolic in nature and independent of temperature. On the other hand, the formation of oxide scale was found to be temperature dependent. Until 850 °C, only a thin and nonporous Cr_2O_3 layer was formed. At 950 °C, a multilayered oxide scale was observed: an external layer of Cr_2O_3 at air/alloy interface, an outermost thin layer of rutile- TiO_2 and spinel- MnCr_2O_4 at air/scale interface, an innermost layer of Nb- and Ti-enriched Ni_3Nb , and a subscale of Al_2O_3 . Recently, Sanviemvongsak et al. [58] have studied the oxidation behavior of as-fabricated laser beam melting (LBM) and electron beam melting (EBM) IN718 parts, and reported a similar observation as discussed above, except the innermost layer has been confirmed to be a thermodynamically stable rutile-type TiNbO_4 phase. The presence of this inner layer has also been reported in Nb-containing high-Cr steels at 800 °C [59]. However, in a previous study, Sanviemvongsak et al. [60] also claimed the Nb-rich inner oxide layer as non-oxidized δ (Ni_3Nb)-phase under the same experimental conditions which coincides with the results of Al-hatab et al. [24]. Due to the contradiction of results in the literature, it is necessary to identify and confirm the exact nature of innermost Nb-rich layer during high-temperature oxidation of WAAM alloy 718 by using both quantitative elemental method and phase analysis. So far, studies related to the chemical reactions of WAAM-processed IN718 superalloys under severe conditions are very scarce. Zhang and Ojo [36] investigated the corrosion performance of heat-treated WAAM IN718 alloy in acidic environments at ambient atmosphere and showed that it was more susceptible to corrosion than its wrought counterparts. The only work available in literature on the oxidation behavior of WAAM-processed IN718 alloy has recently been conducted in as-fabricated conditions at 800–900 °C by Singh, A. B. [61]. Thus, it is necessary to understand the effects of high-temperature oxidation behavior on heat-treated WAAM-processed IN718 alloy.

Based on the literature survey discussed above, the present study is attempted to fill-up the gaps in order to understand the influence of welding parameters, heat treatment and high-oxidation temperature on microstructural evolution, mechanical

properties, and oxidation behavior of single bead IN718 alloys manufactured via GTAW-based WAAM process. This manuscript uses the terms associated with AM technology according to the standard ISO/ASTM 52900:2015 [62]. The experimental works were divided into two parts. First, the effects of key processing parameters such as arc current, wire feeding speed and travel speed on the geometry, microstructure, and mechanical properties of as-fabricated single bead IN718 walls were investigated. Based on the results obtained, large single bead walls were fabricated and the effects of the modified heat treatment on microstructure and mechanical properties were studied with respect to as-fabricated conditions. Lastly, the oxidation performance of heat-treated samples in terms of oxidation rate and oxide phase formation was evaluated at 1000 °C in static furnace air up to 100 h.

15.2 Experimental Procedures

15.2.1 Raw Materials

Commercially available IN718 wire (specification of AMS 5832, Danyang Haiwei Electrothermal Alloy Co., Ltd., China) of diameter 1.2 mm was used to fabricate single bead walls in GTAW-based WAAM process. The as-received IN718 plate (denoted as ARP) of dimensions 200 × 50 × 6 mm³ (Jiangsu DZX Technology Co., Ltd., China) was used as the substrate in cold-rolled condition. The chemical composition and microstructural analysis of both wire and substrate were conducted extensively and discussed in Sect. 15.3.1.

15.2.2 Experimental Setup

A custom-made WAAM system was used to build multilayered single bead IN718 walls, as shown in Fig. 15.1. It was a semiautomatic welding assembly containing a tungsten inert gas (TIG) torch (heating source), a constant-current power source (Kemppi MasterTIG MLS™ 2000), a water coolant unit, a wire feeding device (CK Worldwide WF-3 wire feeder), and an argon (Ar) gas-shielding system. During deposition, these parts were automatically operated and controlled via a program console. After depositing a layer, the platform (substrate with deposited material) was adjusted manually along the horizontal direction in order to get back into the starting position for the deposition of the next layer. At the same time, the upper parts of the system (torch, gas-shielding system, and wire feeder) were also required manual adjustment in vertical direction in such a way that the distance between the torch tip and the deposited material surface (arc length) should remain approximately 3.5 mm. This distance was crucial to generate a stable and dense arc having adequate heat input and welding voltage. In order to maintain a stable molten

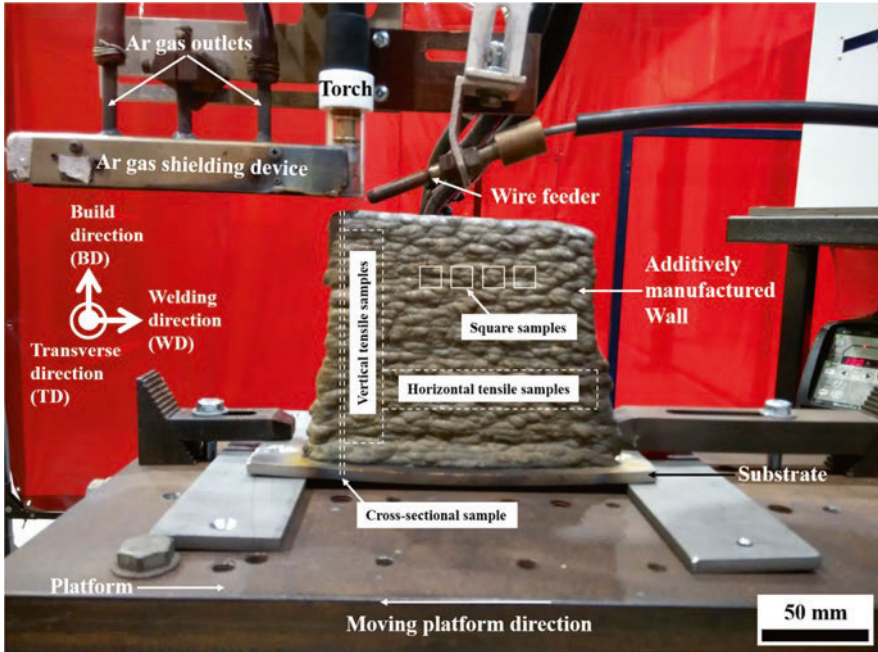


Fig. 15.1 The experimental setup and fabricated IN718 buildup wall in WAAM process. The inserted motifs represent the sample extraction places within IN718 wall

Table 15.1 General operating conditions used in WAAM system

Polarity	DCEN (Direct Current Electrode Negative)
Electrode	2% Ceriated, 2.4 mm in diameter
Arc length	~3.5 mm
Inert shielding gas	Welding grade Ar
Flow rate—TIG torch nozzle	8 L/min
Flow rate—trailing shield front	10 L/min
Flow rate—trailing shield rear	7 L/min
Pre-flow duration	3 s
Up-slope duration	2 s
Down-slope duration	1 s
Post-flow duration	30 s

puddle as well as continuous feeding of wire into it during the deposition process, the torch and the wire feeder were placed at an angle of 60° . The general operating conditions used in this study are listed in Table 15.1.

15.2.3 Process Parameters and Test Conditions

Seven single bead walls (S1 to S7) of 120 mm in length were fabricated with 30 layers for each set of conditions as shown in Table 15.2. Samples S1 to S3 were designated to study the influence of altering arc current from 120 A to 160 A at constant wire feeding rate and travel speed. Similarly, sample sets S3 to S5 were studied the effects of changing the wire feeding rate, while the arc current and travel speed were fixed at 160 A and 100 mm/min, respectively. Sample sets S3, S6 and S7 were evaluated the effects of varying travel speed at constant arc current and wire feed rate of 160 A and 1000 mm/min, respectively. In all cases, the heat input (kJ/mm) and the mass deposition rate (g/s) were calculated by considering the arc efficiency for GTAW with DCEN polarity and the density of IN718 in annealed condition as 0.77 [63] and 8.192 g/cm³ [5], respectively.

After the deposition, the front and top macrographs for the entire as-fabricated (AF) wall in all cases were collected using a digital camera setup in order to measure the wall height and width, respectively. The wire electrical discharge machining (EDM) process was used to extract all cross-sectional samples for metallographic analysis and mechanical testing. The size and shape of the samples are schematically shown in Fig. 15.2. The vertically cross-sectioned samples of 2 mm thickness (Fig. 15.2(a)) were polished according to the standard metallographic procedure for Ni-based superalloys [64] in all cases using an automatic grinding/polishing machine (Struers Tegrapol-21 equipped with TegraForce-5 and TegraDoser-5) and etched electrolytically in a 10 wt.% oxalic acid solution at 6 V for 10s. The preliminary microstructural analysis was performed at different zones along the build direction (BD) for each sample by using Nikon Eclipse LV100NDA optical microscope. Then, the key microscopic imaging and elemental composition of different microstructural features present in the wall were performed using a conventional

Table 15.2 The different processing parameters set to produce as-fabricated (AF) walls during the WAAM process

No. of samples	Parameters							
	Arc current (A)	Voltage (V)	Wire feed speed (mm/min)	Travel speed (mm/min)	No. of layers	Heat input (kJ/mm)	Mass deposition rate (g/s)	Specific deposition energy (kJ/g)
S1	120	~13	1000	100		0.72	0.154	10.12
S2	140	~13.8	1000	100		0.89	0.154	12.52
S3	160	~14.5	1000	100		1.07	0.154	15.03
S4	160	~14.5	2000	100	30	1.07	0.309	7.52
S5	160	~14.5	3000	100		1.07	0.463	5.01
S6	160	~14.5	1000	200		0.54	0.154	15.03
S7	160	~14.5	1000	300		0.36	0.154	15.03

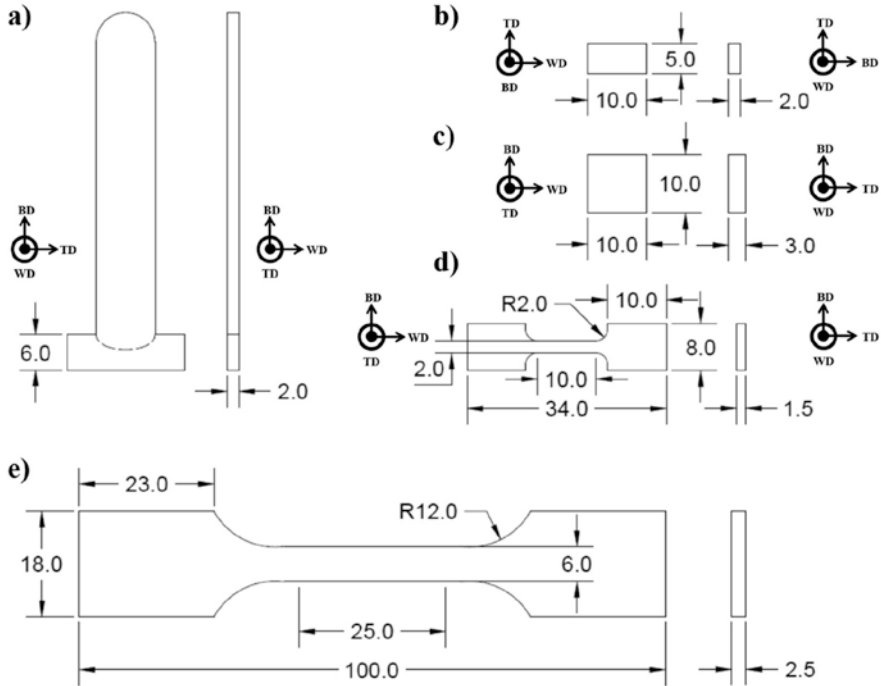


Fig. 15.2 The schematic representation of sample dimensions (in mm): (a) vertical cross-sectioned sample parallel to BD-TD plane for microstructure and microhardness study, (b) XRD samples parallel to TD-WD plane, (c) oxidation samples parallel to BD-WD plane, (d) micro-tensile samples extracted from the middle part of wall along WD, and (e) large tensile samples for heat-treatment results. *BD* build direction, *TD* transverse direction, and *WD* welding direction

tungsten filament-based SEM (JEOL JSM-6490LA)-EDS (AZtecEnergy) system at 20 kV. Later, the Vickers microhardness results were collected along the wall height (BD) at 1 kg indentation load for 10s by using the automatic Matsuzawa Via-F hardness setup. After that, the identification of crystalline phases for AF samples extracted from middle part of the wall (Fig. 15.2(b)) in all cases was done by X-ray diffraction (XRD) technique (MMA, GBC) using the monochromatic radiation of $\text{CuK}\alpha$ (1.5418 Å in wavelength). Finally, the room-temperature tensile tests of deposited samples in all cases were conducted in Instron 3367 machine at a loading rate of 1 mm/min. Due to the height limitation of deposited materials, three micro-tensile samples (Fig. 15.2(d)) were removed only along the welding direction (WD) for each case. The strain data (true strain) were collected using a contactless optical measurement system (Mercury RT) based on a single high-speed camera and real-time image processing technology.

15.2.4 The Modified Heat Treatment and Characterization

After studying the effects of processing parameters on sample geometry, two large single bead walls of physical dimensions of $\sim (125 \times 116 \times 11 \text{ mm}^3)$ were fabricated with 40 layers using the same deposition conditions in case of S5 sample (Table 15.2) as it has the largest mass deposition rate. The thermal history of the deposition process was recorded by using a radiometric stationary infrared camera (Optrix PI) equipped with real-time temperature measurement software system (Optrix PIX connect). The ambient temperature was 21.3 °C and the emissivity parameter for IN718 alloy was set to 0.285 [65]. Then, one sample was used to study the effects of modified heat treatment on microstructure and mechanical properties of WAAM-IN718 alloys. The heat treatment was carried out in a muffle furnace through two steps: (1) homogenization treatment (HA) (1100 °C for 1 h/air cooling) and (2) a continuous double aging process (720 °C for 8 h/furnace cooling at ~ 71.2 °C/h to 620 °C for 8 h/air cooling). The vertical cross-sectioned sample was used to conduct the microstructure, composition, and microhardness of HA sample. Similarly, the phase characterization was performed using XRD technique on sample parallel to TD–WD plane. Large tensile samples (Fig. 15.2(e)) were cut from both the horizontal and vertical directions of the wall according to the standard ASTM E8/E8M-13a [66] which is referred in standard ASTM F3122-14 [67]. At least, three tensile specimens were tested using the same experimental condition, and the fracture surface analysis was done by SEM. At the same time, the microstructural evolution, mechanical properties, and fracture surface analysis of heat-treated ARP samples were also studied for comparison.

15.2.5 Oxidation Study and Oxide Layer Analysis

The isothermal oxidation behavior of heat-treated WAAM-processed IN718 superalloys was performed in a laboratory muffle furnace at 1000 °C up to 100 h under static air condition. The square samples ($10 \times 10 \text{ mm}^2$) of 3 mm in thickness were cut from the middle part of the build wall parallel to the BD-WD plane (Fig. 15.2(c)). Prior to the oxidation study, all six faces of oxidation specimens were manually wet ground up to P1200 SiC paper followed by ultrasonic cleaning in ethanol solution and air drying. At the same time, high purity (99%) alumina crucibles (outer diameter: 22 mm and height: 20 mm; Toho Ceramic Technology Co., Ltd., China) were placed in a preheated furnace at 1100 °C for 30 mins to remove any moisture or volatile substances and cooled in air. Then, the weight of the unexposed specimens with crucibles was recorded using a microanalytical balance and put in a preheated furnace at 1000 °C. Later, the oxidized specimens with crucibles were weighted and the difference was considered as the weight of oxide scale. After that, top-surface morphology, composition, and identification of oxide scale were performed by using SEM and XRD, respectively. Finally, the oxidized samples were hot-mounted

(Struers CitoPress 20 with sensitive mode), polished according to standard procedure for chromium oxide, Cr₂O₃ layer [64], and etched to characterize the cross-sectional morphology and composition of oxide scale using the SEM-EDS system.

15.3 Results and Discussion

15.3.1 Raw Materials Characterization

Figure 15.3 shows the SEM cross-sectional micrographs and elemental compositions of various microstructural features for as-received wire and substrate used in this study under unetched condition, respectively. As shown in Fig. 15.3(b) and (f), the alloy composition (γ -matrix of Ni-Cr-Fe) of both wire and substrate was found to be within the specified range for Inconel 718 superalloys with SAE International standards AMS5832H [68] and AMS5597G [69], respectively. Two types of microstructural features with blocky morphology were clearly visible in both the wire and substrate cross sections as these were highly contrast in color. The bright features were found to be Nb-rich Nb(Ti)C particles (EDS results in Fig. 15.3(c) and (g)) distributing throughout the γ -matrix which are considered to be the primary carbides in IN718 superalloys due to the segregation of Nb and C during solidification [70–72]. On the other hand, randomly distributed dark precipitates were determined to be complex Ti-rich Ti(Nb)(N,C) carbonitride (EDS results in Fig. 15.3(d) and (h)) resulting at above the final eutectic temperature during solidification due to elemental segregation [72, 73]. No evidence of carbonitrides of NbC casing with TiN core has been observed in either cases which is the typical morphological feature of carbonitrides in IN718 alloys. The formation and morphology of carbonitrides during the deposition of IN718 using WAAM process are further discussed.

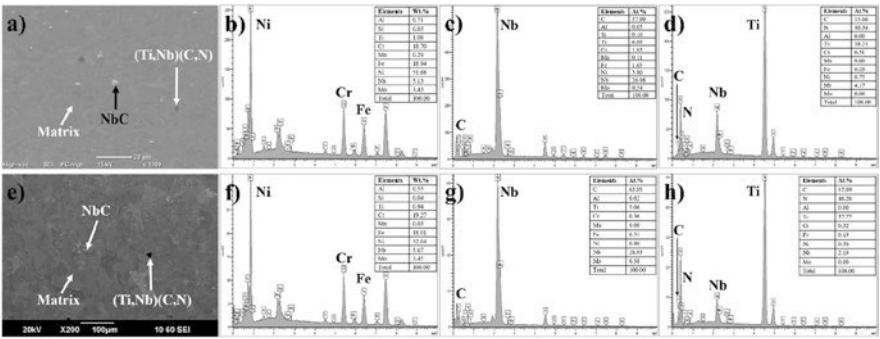


Fig. 15.3 EDS spot analyses of (b, f) matrix, (c, g) NbC, and (d, h) (Ti,Nb)(C,N) for IN718 wire (a) and substrate (e), respectively

15.3.2 Effects of Welding Process Parameters

Heat Input and Deposition Rate

The graphical representation in the influence of welding parameters on heat input, materials deposition volume, and specific deposition energy during the fabrication of Inconel 718 wall using WAAM process is shown in Fig. 15.4. The heat input is the most fundamental physical parameter used in welding which controls the quantitative value of transferred heat (J) into the weldment by unit length (mm) and the formula is given below:

$$\text{Heat input (J/mm)} = \frac{\text{Current (A)} \times \text{Voltage (V)} \times 60 \times 0.77}{\text{Travel speed (mm/min)}} \quad (15.1)$$

In Eq. (15.1), 0.77 is the arc efficiency for GTAW with DCEN polarity [63]. In general, it primarily affects the geometrical correctness and deposition defects in welded parts inducing distortion and residual stresses, and the mechanical characteristics of the welded joints altering the direction of phase transformation due to the variation in cooling rate [74]. In case of multilayered rapid prototyping process like WAAM, the situation becomes more complex as the influence of heat accumulation in subsequent layers also crucially affects the bead geometry, arc stability,

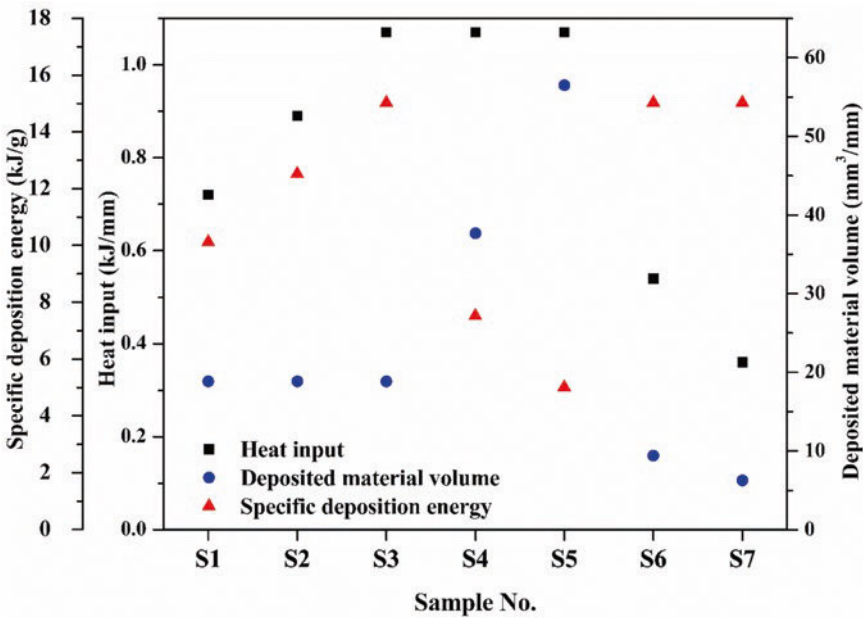


Fig. 15.4 The influence of process parameters on heat input, material volume, and deposition energy in WAAM process

oxidation, and metal transfer behavior [75]. It is seen from Fig. 15.4 that the variation in arc current and travel speed has a significant impact on heat input in GTAW-based WAAM process. Under constant travel speed (S1 to S3), increasing current resulted in higher heat inputs which conducted greater amount of heat from torch (cathode) to substrate/deposited metal (anode) to generate a large molten puddle. On the contrary, faster welding travel speeds transferred less heat into work piece per unit length due to the rapid movement of welding arc in relation to work piece and reduced weld pool size (samples S3, S6, S7). It is to be understood that the heat input was independent of wire feed speed in the GTAW-based WAAM setup conditions used in this study (S3–S5). Unlike consumable electrode (or filler metal)-related welding processes such as GMAW [74] or CMT [76], wire feed speed does not determine the current to influence the heat input in GTAW-based system. As a result, the ratio of wire feed speed to travel speed was not considered as a processing parameter in the present study unlike the work done by Yildiz et al. [76] using CMT process.

As shown in Fig. 15.4, the material deposition rate was dependent on wire feed rate and welding travel speed and can be presented using the formula as follows [76]:

$$\text{Deposited material volume (mm}^3/\text{mm)} = \frac{\text{Wire area (mm}^2) \times \text{Wire speed (mm/min)}}{\text{Travel speed (mm/min)}} \quad (15.2)$$

At constant current and travel speed (S3–S5), increasing wire feed speed increased the supply of material in the molten pool and the volume of weld metal deposition per unit length. A complete opposite result was observed in case of increasing travel speed. Under fixed current and wire feeding rate (samples S3, S6, S7), faster welding travel speeds completed the deposition of a single pass quickly and minimized the volume of deposition of material. Generally, the selection of travel speed depends on the fabrication efficiency (productivity) and the nature of welded parts [39, 74]. The rule of thumb involves proportional increase in travel speed with increasing wire feed speed (and vice versa) in order to avoid the humping effect [38, 76]. The variation in arc current did not affect the material deposition volume under constant wire speed and welding speed (samples S1 to S3) as it only ensured the supply of sufficient arc energy into the work piece to create a molten puddle and melt the feeding wire.

The specific deposition energy is a physical term recently used in AM-based processes in order to evaluate the optimal energy required to transfer into the weldment avoiding the formation of lack of fusion zone [77]. It is defined as the ratio of supplied energy (J) to deposited mass (g) and can be calculated using the formulas given below for WAAM-based process:

$$\text{Specific deposition energy (J/g)} = \frac{\text{Current (A)} \times \text{Voltage (V)}}{\text{Mass deposition rate (g/s)}} \quad (15.3)$$

$$\text{Mass deposition rate (g/s)} = \frac{\text{Density (g/cm}^3\text{)} \times \text{Wire speed (mm/min)} \times \text{Wire area (mm}^2\text{)}}{60 \times 1000} \quad (15.4)$$

It is to be noted that the specific deposition energy is independent of welding travel speed. According to previous work done by Nursyifaulkhair et al. [77], high energy supply and low feeding rate conditions under constant travel speed were suitable to obtain correct specific energy to avoid the formation of lack of fusion zone. Under the present experimental conditions, no lack of fusion zone was found in the buildup walls. As shown in Fig. 15.4, increasing arc current increased the specific energy under constant travel speed and wire feed rate (S1–S3), whereas increasing wire feeding rate decreased the specific energy under fixed current and welding speed (S3–S5).

Bead Geometry

In this part, we will elaborate the effects of different processing parameters on the weld bead geometry during the WAAM process. It is important to understand the controlling aspects of arc current, wire feed speed, and travel speed in the formation of multilayered single bead wall dimensions in terms of wall height and width. Figure 15.5 demonstrates the front and top view macrographs of the entire deposited buildup walls for different processing conditions. The front view images were used to measure the height of the walls, whereas the top view macrographs were considered to determine the width of the walls. The quantitative values of width and height of the deposited walls under different processing conditions are shown in Fig. 15.6. It is seen from Fig. 15.6 that it is possible to obtain a wide range of heights of 16.45–77.93 mm and widths of about 8.87–12.94 mm by changing the arc current, wire feed speed, and travel speed. Under constant wire feed rate and welding speed, increasing arc current from 120 A for S1 to 160 A for S3 resulted in a decrease of about 16.8% in the wall height (45.2 to 37.6 mm) and an increase of 31.2% in wall width (9.86 to 12.94 mm), respectively. Applying high currents would supply high heat input and create a wider and deeper molten puddle exerting high arc pressure from the torch into the weldment during multi-pass welding process. Since the deposited material volume would remain the same as shown in Fig. 15.4 for S1 to S3 samples, the volume compensation should be made to increase the width and decrease the height of the wall, respectively.

On the contrary, the wall height was found to be mostly affected by increasing the wire feed speed under fixed current and travel speed for samples S3–S5 as shown in Fig. 15.6. Increasing wire feed speed from 1000 mm/min for S3 to 3000 mm/min for S5 dramatically increased the wall height by 107.3% on average (37.6–77.9 mm), while the wall width was decreased only by 12.52% on average (12.94–11.32 mm). As we discussed previously, the width of the deposited walls

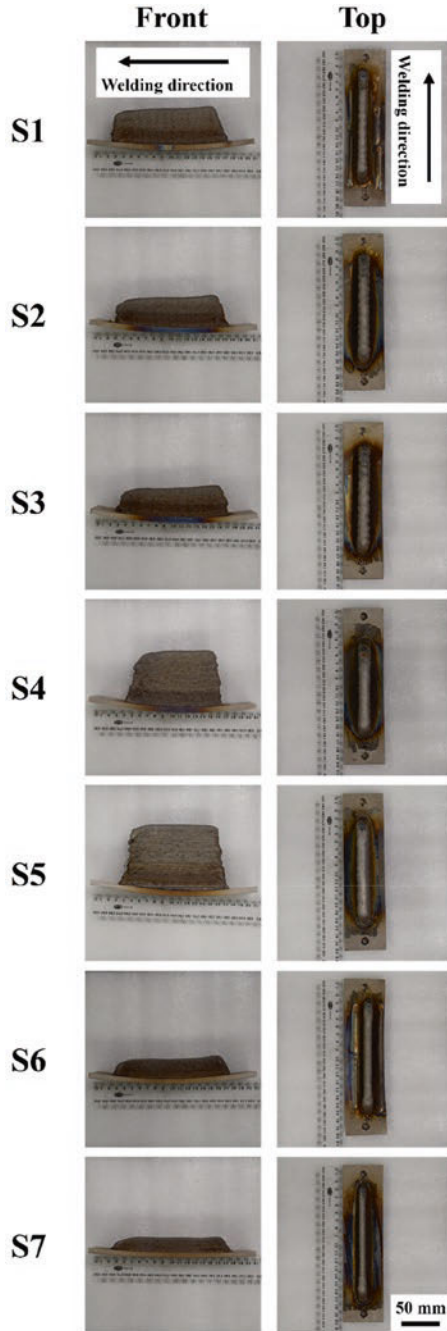


Fig. 15.5 The front and top macrostructural images of AF walls for different process parameters

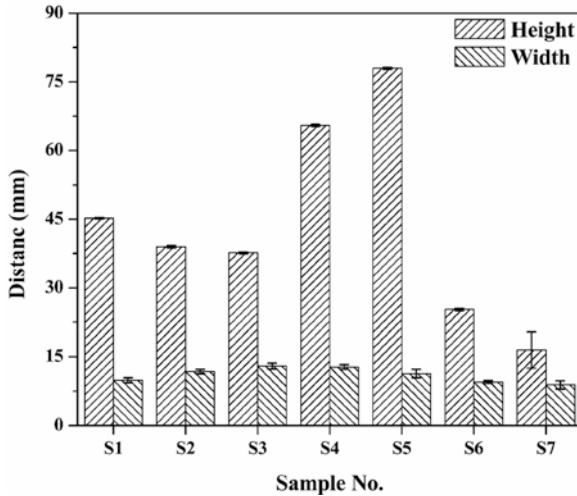


Fig. 15.6 The effects of processing parameters on the wall height and width

Table 15.3 The summary of the effect of different processing parameters on wall geometry

Effect of increasing	Wall height	Wall width
Arc current	Decreased	Increased
Wire feed speed	Increased	Decreased
Travel speed	Decreased	Decreased

was predominately affected by the arc pressure exerted into the weldment with changing arc current under constant travel speed. Thus, the logical argument would be to get constant values of wall width for S3, S4, and S5 samples under constant arc current as seen in Fig. 15.6. Since the volume of material deposition increased with increasing wire feed speed for S3 to S5 samples as shown in Fig. 15.4, the volume should be compensated with increasing the height of the manufactured walls. Finally, the investigation of changing the travel speed under constant current and wire feed speed was found to adversely affect both the width and height of the fabricated walls for S3, S6, and S7 samples as shown in Figs. 15.5 and 15.6, respectively. The height and width of the walls were decreased by 56.25% (37.6–16.45 mm) and 31.5% (12.94–8.86 mm), respectively when the travel speed was increased from 100 mm/min for S3 to 300 mm/min for S7, as shown in Fig. 15.6. Increasing travel speed reduced both the heat input and material deposition volume to create thinner and shallower weld pool under fixed current and wire feed speed. Table 15.3 summarizes the effect of different processing parameters on the wall geometry fabricated by GTAW-based AM process in this study.

As-Fabricated Macro- and Microstructural Evolution

In-depth microstructural analysis was conducted on the vertical cross-sectioned AF samples for different process parameters. Figure 15.7 gives both macroscopic and microscopic images of AF walls extracted from BD–TD plane. In all deposition conditions, the light macrographic images showed the existence of alternating light and dark patterns in the formation of interlayer boundary as a result of remelting the previously deposited layer by the subsequent deposition of a new layer. The inter-layer boundaries were seen to protrude outwardly along the deposited walls and the top part of the walls developed a convex meniscus after the deposition of the last layer due to the high cohesive attraction or surface tension of molten liquid at the liquid–air interface during welding. The wall microstructure was divided into three regions, namely the near-substrate zone (NSZ), the middle zone (MZ), and the top zone (TZ), respectively. Irrespective of welding conditions used in the present study, the microstructural evolution was found to be homogeneous across the entire wall. A typical columnar dendritic structure was developed growing continuously through the deposited layers in the upward direction, almost parallel to the BD direction.

During weld solidification, the solid IN718 substrate was acted as the heterogeneous nucleation site for the growth of the deposited IN718 filler metal retaining the same crystallographic orientation from the substrate grain. This is known as epitaxial solidification of molten weld metal on either newly formed nuclei or partly melted grain in the substrate metal. The epitaxial growth is a spontaneous solidification process of consuming liquid metal along the preferential easy growth directions such as the cube edges or $\langle 100 \rangle$ crystallographic directions for cubic metals. The conditions become more prominent when these growth directions concur with the heat dissipation direction through solid–liquid interface [78, 79]. As a result, the AF samples showed strong preferential crystalline orientation under all processing conditions in comparison with the commercial ARP sample as shown in Fig. 15.8. A preferential or random grain orientation of epitaxial growth of columnar dendritic structure can be explained from the XRD reflection intensities. The texture coefficient, $T_{c(hkl)}$ gives quantitative information about the texture in the material indicating preferred growth orientation along a particular (hkl) plane if it deviates from unity according to the following equation [80]:

$$T_{c(hkl)} = \left(I_{(hkl)} / I_{o(hkl)} \right) / \left[1 / N \sum \left(I_{(hkl)} / I_{o(hkl)} \right) \right] \quad (15.5)$$

where $I_{(hkl)}$ is the experimentally obtained relative intensity of (hkl) plane from XRD data, $I_{o(hkl)}$ is the standard XRD intensity of randomly orientated grains of (hkl) plane taken from ICDD database for austenite (reference code: 00-033-0397 and PDF index name: Chromium Iron Nickel Carbon), and N is the total number of diffraction peaks considered. Five diffractions peaks were identified within the 2θ range ($30\text{--}100^\circ$) from the ICDD data that belong to (111), (200), (220), (311), and (222) reflections respectively. The texture coefficient of each reflection was calculated and is presented in Table 15.4.

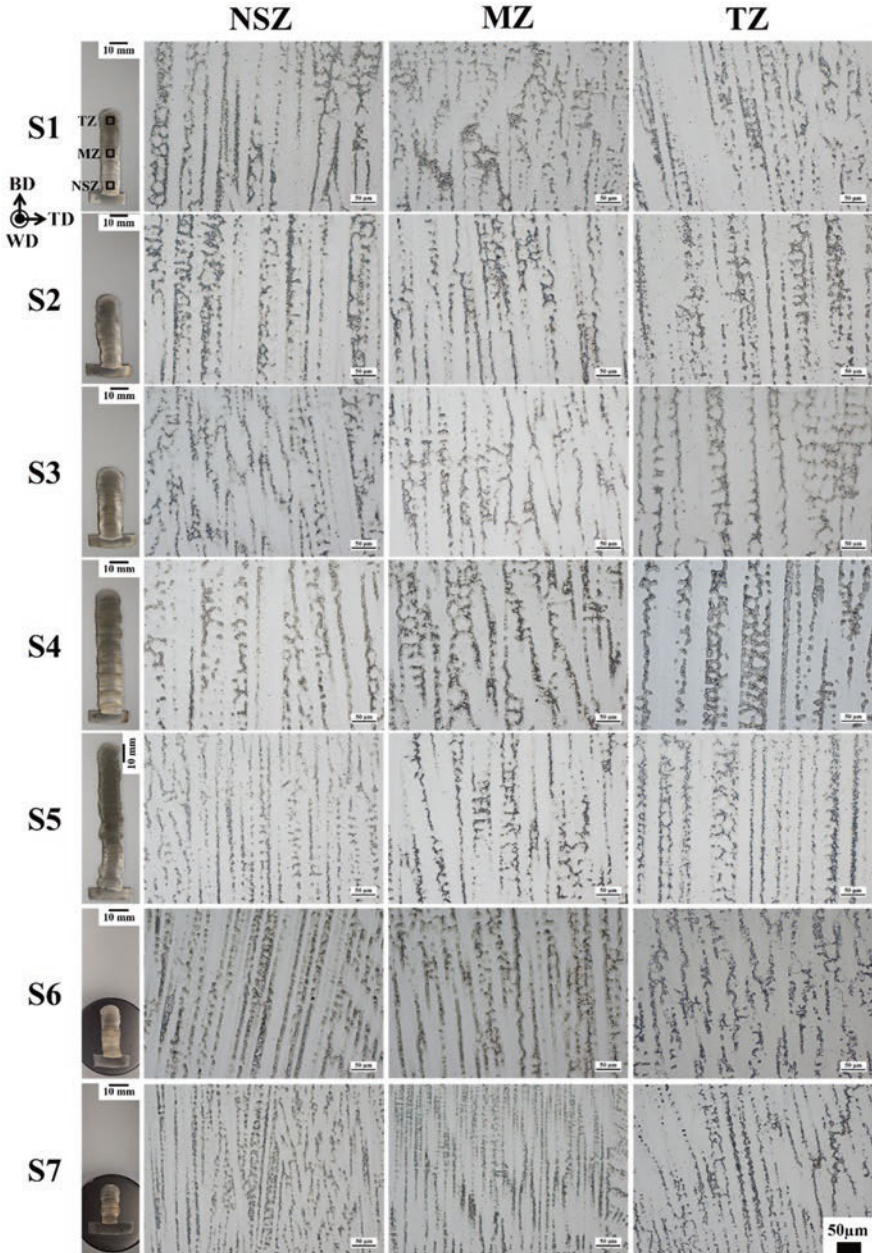


Fig. 15.7 Optical microscopic images of cross-sectional AF walls for different process parameters

From Eq. (15.5), it is seen that the value of $T_{c(hkl)} \approx 1$ represents the existence of grains in the structure having (hkl) plane in random orientation similar to the

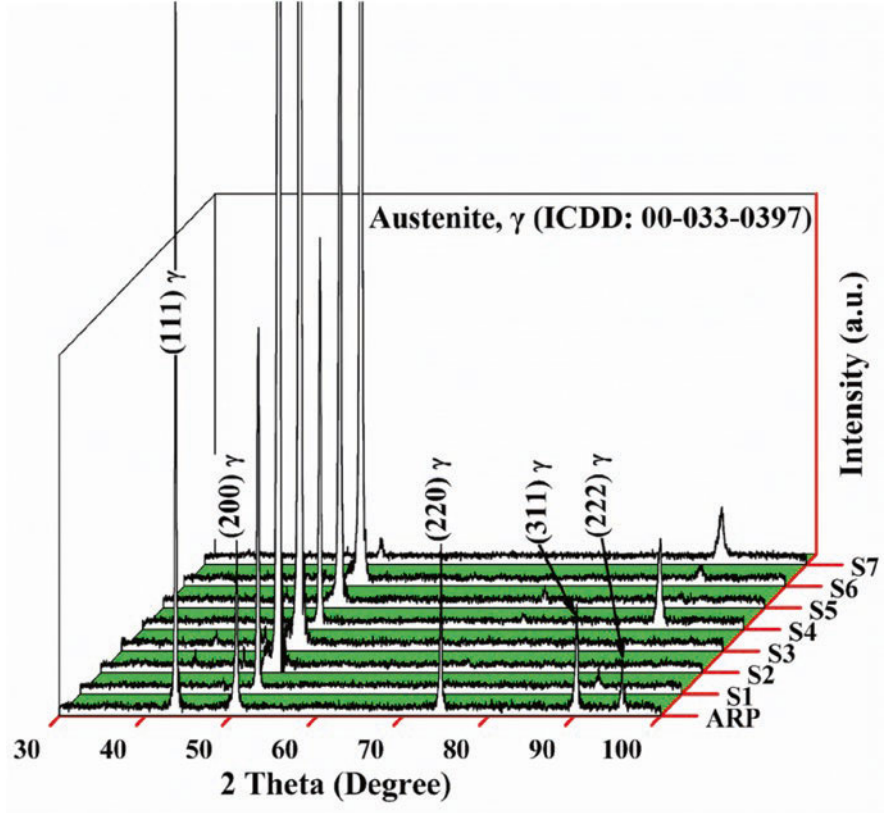


Fig. 15.8 XRD graphs of AF samples S1–S7 and as-received IN718 plate (ARP)

Table 15.4 The quantitative values of texture coefficient, $T_{c(hkl)}$ of a specific (hkl) reflection and degree of texture, σ obtained for different samples

Samples	Texture coefficient					Degree of texture σ
	$T_{c(111)}$	$T_{c(200)}$	$T_{c(220)}$	$T_{c(311)}$	$T_{c(222)}$	
ARP	1.53	0.73	1.27	0.69	0.77	0.34
S1	0	4.74	0	0.26	0	1.87
S2	0	5	0	0	0	2
S3	0	5	0	0	0	2
S4	0	3.73	0.08	1.18	0	1.44
S5	0	4.91	0.09	0	0	1.96
S6	0	4.95	0	0.05	0	1.97
S7	0	0.87	0	4.13	0	1.60

reference ICDD data. When $T_{c(hkl)} = 0$, it means the absence of grains in the structure of a specific (hkl) plane. If the value falls within the range of $0 < T_{c(hkl)} < 1$, then it indicates the lack of grains or crystallites in the microstructure having (hkl) plane in

comparison with reference ICDD data. If $T_{c(hkl)} > 1$, then the structure has preferred growth orientation of grains in the direction normal to the (hkl) plane. Since we considered five diffraction peaks in the calculation, the maximum value of $T_{c(hkl)}$ should be 5. This represents all the grains in the microstructure preferentially grew in the crystallographic direction normal to the (hkl) plane under consideration and the material is 100% textured. According to Gao et al. [81], the standard deviation (σ) of all the texture coefficient values for (hkl) planes can be considered to analyze the degree of texture using the following equation:

$$\sigma = \sqrt{\left[\frac{\sum (T_{c(hkl)} - \mu)^2}{N} \right]} \quad (15.6)$$

where μ is the arithmetic mean of $T_{c(hkl)}$ values which is 1. When $\sigma = 0$, the structure has complete random growth orientation identical to the reference ICDD data. If the value of $\sigma > 0$, then the structure has texture component with preferential growth orientation. As shown in Table 15.4, the AF samples exhibited strong texture than that of ARP sample due to the epitaxial growth of columnar structure along the BD direction.

The columnar dendritic substructure was mainly composed of primary γ core regions (DCR) having high-solidus temperature (white color) which were surrounded by low-melting point interdendritic regions, ICR (dark color) as shown in Fig. 15.7. According to Knorovsky et al. [82], the solidification of IN718 weld structure was reminiscent of binary eutectic phase diagram. The primary proeutectic γ started to crystallite from molten metal developing the DCR by rejecting solute elements at the near vicinity (or periphery) of solid–liquid dendritic interface. The extent of solute rejection or microsegregation of an alloy can be characterized by the compositional difference between the core region and periphery of solid–liquid dendritic interface. The equilibrium partition coefficient or solute redistribution coefficient, denoted as k , is used to measure the segregation potential of an alloy which is the compositional ratio of solid and liquid in equilibrium at a given temperature within the solidification range for a particular solute element. For IN718 alloy, the value of k should be less than unity due to the rejection/partition of solute to the liquid. In this study, it is possible to calculate the partition coefficient, k quantitatively for WAAM IN718 alloy using the following relationship:

$$C_s = kC_o (1 - f_s)^{k-1} \quad (15.7)$$

where C_s is the solute content at solidified volume fraction of f_s and C_o is the solute content in alloy. At the beginning of solidification ($f_s = 0$), the composition of the DCR can be considered as C_s . As shown in Fig. 15.9b, the Nb content in the DCR was found to be 2.45 wt.% in WAAM IN718 alloy in comparison with the value of 5.13 wt.% for IN718 wire in Fig. 15.3b. This gives a k value of 0.48 which is less than 1. Similar observations were also reported in early works [54, 82]. As a result, it gradually developed a highly segregated terminal liquid of solute elements just

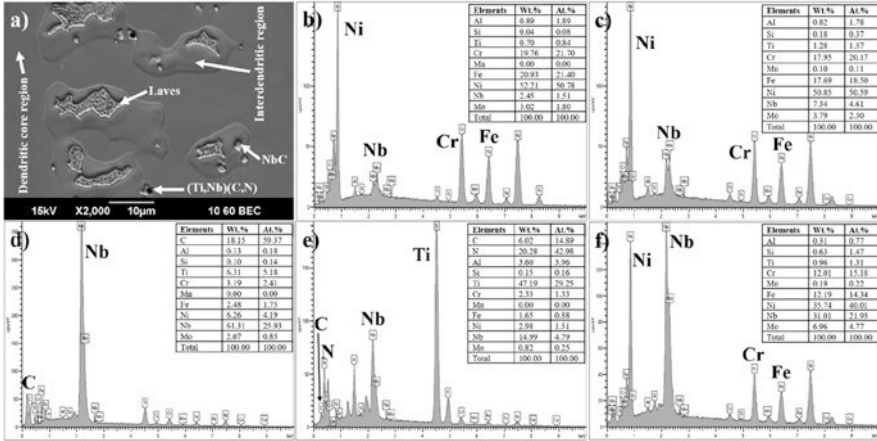


Fig. 15.9 EDS spot analysis of (b) dendritic core region (DCR), (c) interdendritic region (ICR), (d) NbC, (e) (Ti,Nb)(C,N), and (f) Laves for S5 in (a)

close to solid–liquid dendritic interface creating a solute gradient or profile to a certain distance into the molten metal. Since $k < 1$, the solute content would gradually decrease along the distance from the solid–liquid interface to the actual alloy composition (C_o) of molten metal. This would create a situation where the actual temperature of liquid at the near vicinity of interface became lower than that of the equilibrium liquidus temperature of the alloy corresponding to C_o and a positive temperature gradient (G_T) would exist as a function of distance from the interface. If the slope of this actual temperature gradient (G_T) was lower than that of the slope of line tangent drawn on liquidus temperature line at the solid–liquid interface, the liquid was undercooled and the columnar grain growth would commence. This phenomenon is known as constitutional supercooling or undercooling of liquid at the solid–liquid interface and the columnar dendritic morphology of grain growth is favored as the degree of constitutional supercooling increases into the liquid [78, 79, 83–85].

The epitaxial growth of columnar dendritic morphology of IN718 AF walls fabricated by WAAM process occurred due to the constitutional supercooling of heavy solute elements (especially Nb). This situation was fueled by the low-temperature gradient (G_T) in the liquid during solidification due to the high heat input from GTAW setup and heat accumulation from multipass deposition, and the high growth rate (V) of liquid–solid interface during solidification due to the epitaxial nucleation. The morphology parameter is defined as the ratio of G_T/V establishing the stability criterion for the evolution of columnar grain morphology at the solid–liquid interface using the concept of constitutional undercooling which can be mathematically expressed as [84, 85]:

$$G_T / V < -m_L C_o (1 - k) / k D_L = \Delta T_o / D_L \tag{15.8}$$

where m_L is the slope of liquidus line, D_L is the diffusion coefficient of solute elements in liquid, and ΔT_o is undercooling during nonequilibrium solidification. From Eq. (15.8), it is clear that lower value of G_T/V provides larger undercooled liquid zone (ΔT_o) leading to severe constitutional undercooling and yields columnar grain morphology. Also, IN718 superalloy contains several heavy solute elements (Nb, Mo, Ti) with $k < 1$ (from Eq. 15.7) and thus these elements have strong tendency to segregate preferentially at solid–liquid interface during solidification. Another important aspect is the local cooling rate at solid–liquid interface which is the product of $G_T \cdot V$ determining predominantly the secondary dendritic arm spacing (SDAS). As seen in Fig. 15.7, the microstructure of AF walls rarely developed any secondary dendritic arms under different processing conditions. The microstructures were solely made of primary γ core regions and the spacing between two core regions can be considered as the primary dendritic arm spacing (PDAS). Under constant travel speed, the PDAS of adjacent core regions was seemed to be independent of arc current (S1–S3) or wire feed speed (S3–S5). On the other hand, refined columnar grain structure was observed with increasing travel speeds for S6 and S7 samples in comparison with S3 sample. During fast welding travel speed, the supply of heat input into the molten puddle decreased. As a result, it accelerated the cooling rate and reduced the solidification time of the weldment which would provide a higher growth rate (V) of liquid–solid interface reducing the dendritic tip radius [85, 86].

The microstructural evolution of different phases in the solidified AF parts was extensively investigated in each condition. In all conditions, three types of phases were identified, namely Ti-rich Ti(Nb)(N,C) carbo-nitride, Nb-rich Nb(Ti)C, and laves phase (Ni, Cr, Fe)₂(Nb, Mo, Ti) as shown in Fig. 15.9. NbC and laves phases were mostly found in the IDR due to the strong microsegregation of solute elements (especially Nb), wherein carbo-nitrides were formed in DCR. The solidification sequence of these phase constituents in IN718 parts during WAAM can be interpreted from a previous study with varying cooling rates [87]. It was found that the phase evolution of AM parts in this study was exactly the same for slow cooling rate (0.25–55 °C/s) processes. Figure 15.10 shows a typical temperature–time profile of AF wall (S5) during the WAAM process. Since WAAM is a multipass welding process, a deposited layer is expected to experience either complete melting or partial melting or both on multiple occasions. As for example in Fig. 15.10a, the fourth layer was seen to experience complete melting by crossing the liquidus temperature on three times and partial melting by crossing the solidus or eutectic temperature on two times, respectively after subsequent depositions. The average cooling rate was determined by using the classical solution of Newton's law of cooling [88, 89] from the temperature–time profiles that were only crossed the liquidus temperature. The average cooling rate was found to be (5.03 ± 0.48) , (6.73 ± 0.49) , and (6.36 ± 0.52) °C/s for NSZ, MZ, and TZ, respectively. Thus, the solidification sequence of phase evolution at slow cooling rates from molten IN718 alloys during the WAAM process can be summarized as follows [82, 87]:

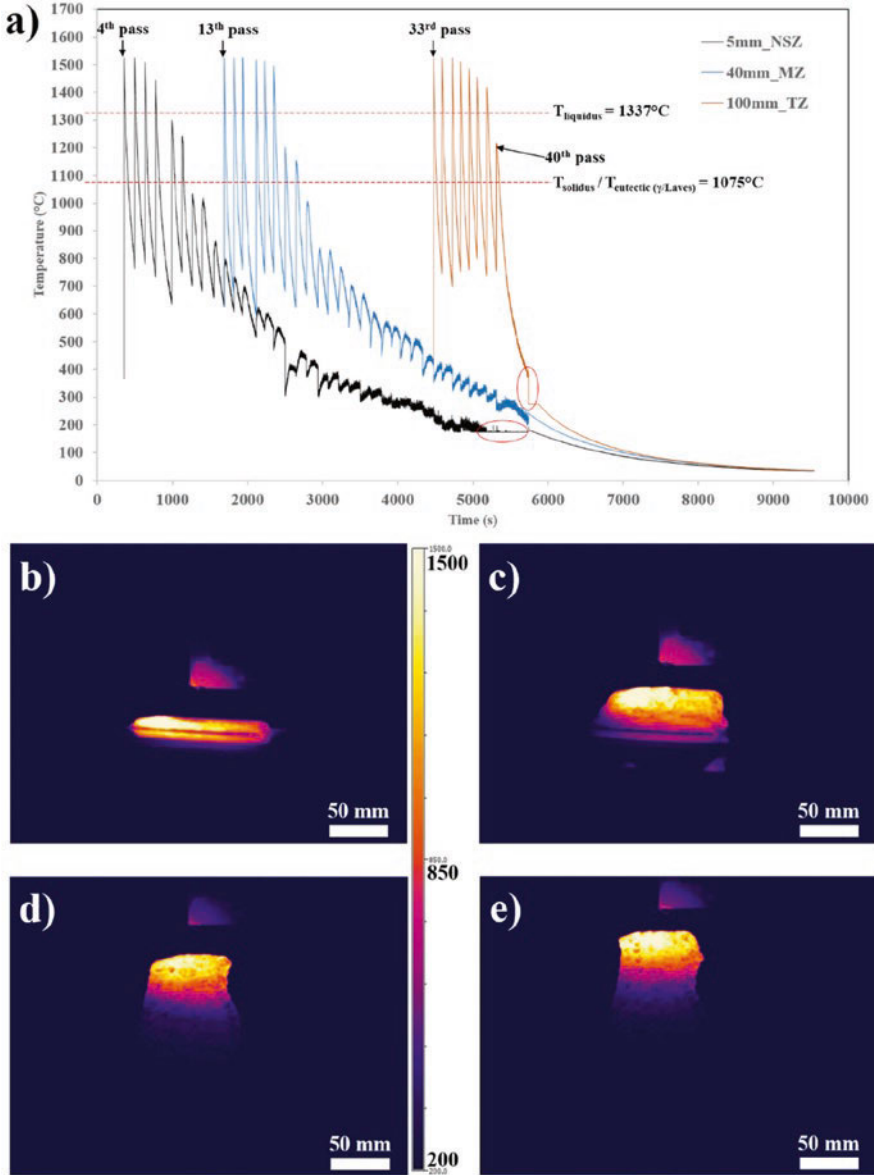
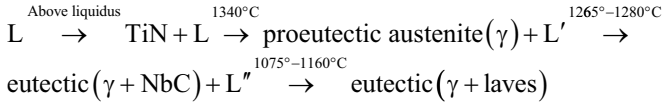


Fig. 15.10 (a) The thermal history of the deposited wall (S5) in the middle position along the buildup direction at a distance of 5 mm, 40 mm, and 100 mm from the substrate for near-substrate zone (NSZ), middle zone (MZ), and top zone (TZ), respectively. The thermal images show the temperature distribution along the wall height for (b) fourth pass, (c) 13th pass, (d) 33rd pass, and (e) 40th pass. In (a), the red color oval-shaped areas indicated the instrumental limitation on recording the full temperature profiles from 1500 °C (max) to room temperature. The recorded profiles were collected in two regimes, namely high-temperature regime (1500–200 °C) and low-temperature regime (250–0 °C), respectively. The horizontal line for NSZ in high-temperature regime indicated that the temperature was below 200 °C, whereas the vertical line for TZ indicated that the temperature was above 250 °C in low-temperature regime



The precipitation of TiN was occurred first at above liquidus temperature from the molten IN718 alloy (L) corresponding to actual alloy composition (C_o) due to the segregation of N and Ti which was a function of N concentration in alloy and temperature [73]. After crossing the liquidus point at 1340 °C, proeutectic γ started to nucleate epitaxially forming DCR as well as enriching the molten liquid (L') composition with Nb and C interdendritically. The precipitation of NbC would commence via eutectic γ/NbC reaction when the composition of C and Nb in liquid (L') reached 0.25 wt.% and 10.5 wt.%, respectively [72]. As seen in Fig. 15.9(a), NbC could develop in the form of shell with a TiN core and has been identified as carbo-nitrides. These complex particles were developed as TiN precipitates acted as nucleating sites for the formation and growth of primary NbC in IN718 alloys [72, 73]. It was assumed that the majority of C consumption happened during the eutectic γ/NbC reaction step and the remaining liquid (L'') was continued to enrich in Nb by forming proeutectic γ as the cooling proceeded. Finally, the solidification terminated at ICR via eutectic γ/laves reaction when the terminal liquid (L'') composition reached at 19.1 wt.% Nb [82]. This resulted in an Nb-enriched γ phase (Fig. 15.9c) and laves precipitates (Fig. 15.9f).

Mechanical Properties

The microhardness measurements were conducted on AF walls for each processing condition from bottom (NSZ) to top (TZ) along the centerline of the BD–TD plane (the macroscopic images are shown in Fig. 15.7). Figure 15.11(a) shows the

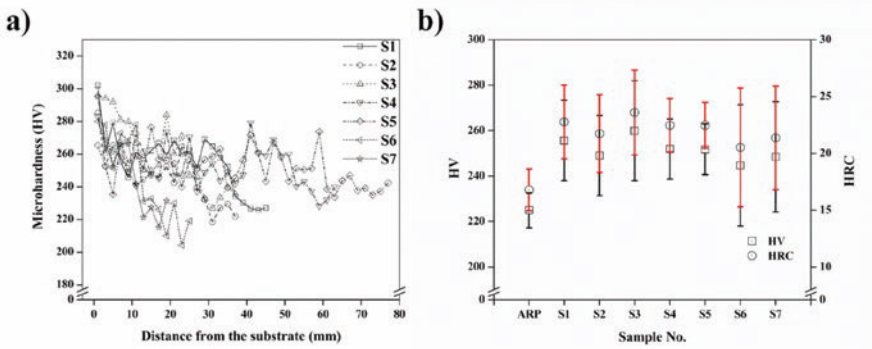


Fig. 15.11 (a) Vickers microhardness values of the AF walls as a function of the wall height for different processing conditions and (b) the average microhardness results of the AF walls S1–S7 with as-received IN718 plate (ARP) for comparison

hardness variation profiles as a function of wall height from the substrate. It is to be understood that it was difficult to specify different regions along the hardness profiles due to the wall height variation for different processing conditions. It is apparent that the hardness values were fluctuating along the wall height under all processing conditions. The highest value of microhardness resulted in the bottom (NSZ) parts of AF samples and gradually decreased as the wall height increased. This phenomenon was extensively studied by Zuo Li et al. [65] for IN718 alloys using time–temperature profiles for different regions. It was concluded that the hardness variation was originated due to the precipitation of δ , γ' , and γ'' along with laves phases in IDR. The minimum incubation time periods for these phases to precipitate in heavily segregated ICR were found to be 540 s, 124 s, and 57 s in their respective fastest temperature ranges. Under the present experimental condition, the holding times for δ , γ' , and γ'' phases during cooling were determined to be 107.9 s, 100.6 s, and 120.6 s, respectively for NSZ (Fig. 15.10a). Thus, it is assumed that the increased hardness in NSZ was established due to the presence of minor amounts of γ'' precipitates and laves phases in IDR during the solidification process of AF walls. It is noteworthy to mention that the holding times for the precipitation of these phases in MZ and TZ were lower than the required incubation time periods, and these phases did not form giving low hardness values. Figure 15.11b represents the average hardness results for AF walls under different processing conditions. It is clear that the processing parameters do not have any significant impact on overall hardness values giving only 4.7% difference from the highest value (259.89 ± 22.05 HV) for S3 to the lowest value (248.3 ± 33.34 HV) for S6. The commercial IN718 plate (ARP) showed lower hardness value of 224.97 ± 7.7 HV in comparison with AF samples under all processing conditions due to the absence of various phase constituents, especially laves phases. The effects of processing parameters on the increment of microhardness values due to the grain refinement of WAAM IN718 alloys have recently been studied [38]. In this study, it is clear that the microhardness value is more dependent on the phase constituents rather than grain boundary density. Otherwise, the ARP sample should have given the highest microhardness value as the grain size of ARP sample was much more refined than that of AF samples under any conditions (Fig. 15.14 in Sect. 15.3.3).

Figure 15.12a shows the stress–strain curves of single tensile test obtained for each processing condition. The average tensile properties, namely yield strength (YS), ultimate tensile strength (UTS), and elongation are shown in Fig. 15.12b. Like the microhardness results as shown in Fig. 15.11b, the average tensile properties do not seem to vary considerably for different processing conditions. From the discussion on microstructural evolution in section “As-Fabricated Macro- and Microstructural Evolution”, the grain morphology and phase constituents were found to be identical in nature for all processing conditions, despite the fact that a relatively finer PDAS was observed with increasing the welding travel speed. Thus, under the present experimental conditions, the effects of processing parameters on mechanical properties of AF walls were found to be similar in nature due to having identical microstructural morphology and phase constituents.

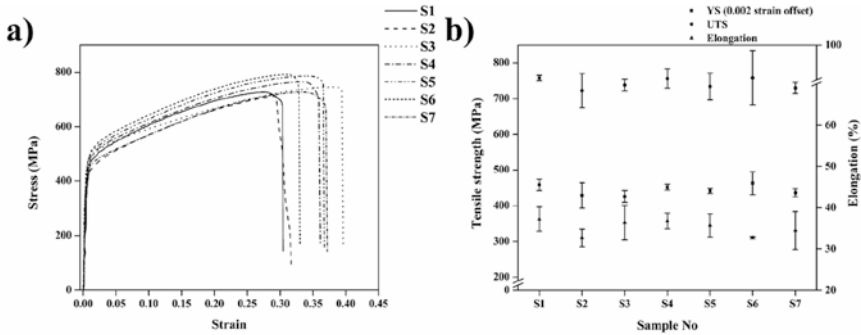


Fig. 15.12 (a) The engineering stress–strain graphs and (b) the average tensile properties of S1–S7 tensile samples loaded in welding direction at room temperature

15.3.3 Effects of Heat Treatment on Microstructure and Mechanical Properties

The purpose of performing a specific heat treatment on IN718 superalloys can be divided into two categories. First, it should homogenize or equilibrate the concentration of solute elements throughout the matrix from microstructural perspective, and second, it should precipitate out the strengthening phases to improve the mechanical properties for real-life applications.

From the microstructural point of view, it is necessary to perform a suitable heat treatment on WAAM IN718 alloys to alleviate the microstructural heterogeneity as described in section “As-Fabricated Macro- and Microstructural Evolution”. It must minimize or completely eliminate the micro-segregation of solute elements, especially Nb and redistribute the alloy composition uniformly throughout the matrix so that the strengthening precipitates (γ'' and γ') can form in uniform manner by dissolving the laves phases and eutectic γ in IDR so that Nb elements return back to matrix. Figure 15.13 shows the SEM images for AF and HA samples used in this study. Under the present heat-treatment condition, the AF sample fabricated using WAAM process has responded well by completely eliminating laves phases and Nb-enriched eutectic γ phase from the structure. The quantitative results of the fraction of phase constituents and their elemental composition have been tabulated in Tables 15.5 and 15.6, respectively. The microstructure of HA sample retained the epitaxial columnar grain morphology with primary NbC and Ti-rich carbonitrides precipitates. The matrix composition of HA sample was complementing quite well with the nominal composition of commercial wire or substrate used in this study (Fig. 15.3). These inclusions were still present in the HA structure due to their higher saturation solubility and eutectic temperatures than the heat-treatment temperature used in this study [73, 82, 87].

Figure 15.14 shows the grain size comparison between AF, ARP, and their heat-treated samples. As discussed previously, both AF and HA samples formed long

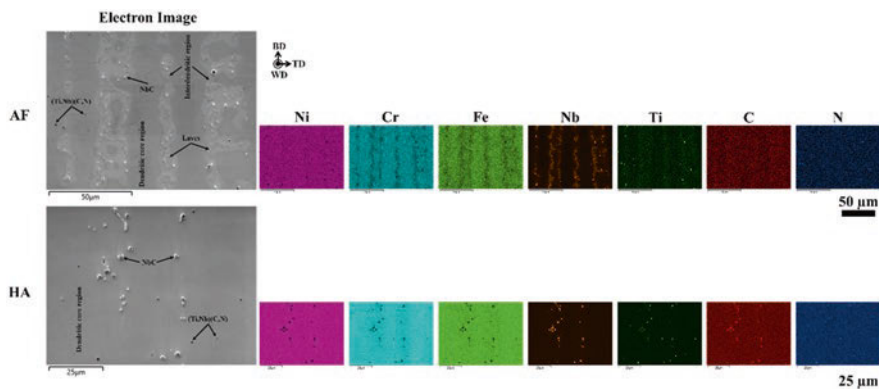


Fig. 15.13 SEM images with the corresponding maps of elemental distribution for as-fabricated (AF) and homogenization-annealed (HA) samples fabricated by the WAAM process

Table 15.5 The determination of the fraction of microstructural constituents (%) present in the AF and HA samples as shown in Fig. 13 using SEM Auto Phase Map tool

Samples	Matrix (NiFeCr)	Laves	NbC precipitates	(Ti,Nb)(C,N) precipitates
AF	97.15	2.55	0.22	0.08
HA	98.79	–	1.08	0.13

columnar grains along the BD direction with the highest thermal gradient or heat flux. The extension of these long grains seemed to occupy the entire frame of micrographs in the BD direction and the length could grow up to several millimeters. The HA sample was found to be much coarser (~3 times) than that of AF samples due to the high-temperature heat-treatment cycle used in this study. Comparing these results with the commercial IN718 alloy (ARP) and its heat-treated counterpart, the severity of grain coarsening in AF and HA samples was extremely high and this could lead to poor mechanical properties which will be discussed later in this section. The XRD curves for AF, ARP, and their heat-treated counterparts are shown in Fig. 15.15. Both AF and HA samples had strong preferred growth orientation along (200) crystal plane for γ matrix which varied quite significantly from the commercial IN718 part (ARP) and its heat-treated condition. The degree of texture for AF and HA samples was much stronger than that of ARP and HAP samples due to the epitaxial grain orientation during the WAAM process (Table 15.7). Due to the inadequate quantity of different phase constituents (<5% as shown in Table 15.5) in the samples, the detection of carbides or laves phases was not possible.

Thus, the modified heat treatment used in this study successfully eliminated the compositional heterogeneity by dissolving laves phase and eutectic γ in IDR. Severe grain coarsening occurred in HA samples due to the initially formed large columnar grain of AF samples without affecting the strong epitaxial texture during heat-treatment process.

Table 15.6 The elemental composition of the microstructural features present in different specimens

Samples	Elemental compositions											Microstructural features
	Ni	Fe	Cr	Nb	Mo	Ti	Mn	Al	Si	C	N	
AF	52.6 ± 0.6	21.07 ± 0.2	19.6 ± 0.25	2.32 ± 0.19	2.78 ± 0.34	0.65 ± 0.08	0.10 ± 0.14	0.83 ± 0.09	0.08 ± 0.06	–	–	DCR ^a
	51.1 ± 0.7	17.57 ± 0.4	17.9 ± 0.46	7.48 ± 0.73	3.40 ± 0.42	1.41 ± 0.18	0.19 ± 0.11	0.81 ± 0.03	0.15 ± 0.04	–	–	IDR ^a
	6.7 ± 6.31	2.17 ± 1.8	2.76 ± 1.71	25.7 ± 6.68	0.82 ± 0.18	4.84 ± 1.25	0.02 ± 0.03	0.27 ± 0.19	0.27 ± 0.07	56.5 ± 3.11	–	NbC ^b
	2.75 ± 1.76	1.49 ± 0.87	2.15 ± 1.16	4.48 ± 0.42	0.26 ± 0.02	32.5 ± 4.71	0.02 ± 0.03	2.59 ± 1.93	0.13 ± 0.04	14.8 ± 0.15	38.67 ± 6.0	(Ti,Nb)(C,N) ^b
HA	40.3 ± 1.1	14.1 ± 0.37	15.6 ± 0.35	21.7 ± 1.07	4.54 ± 0.33	1.46 ± 0.16	0.28 ± 0.12	0.59 ± 0.1	1.43 ± 0.1	–	–	Laves ^b
	51.39 ± 0.3	18.92 ± 0.4	18.9 ± 0.35	5.18 ± 0.49	3.28 ± 0.2	1.03 ± 0.16	0.06 ± 0.07	0.71 ± 0.02	0.17 ± 0.04	–	–	DCR ^a
	2.2 ± 0.67	1.11 ± 0.45	1.37 ± 0.43	30.13 ± 5.4	1.60 ± 0.31	5.72 ± 1.72	0.03 ± 0.04	0.11 ± 0.1	0.07 ± 0.05	57.7 ± 6.01	–	NbC ^b
	1.35 ± 0.75	0.76 ± 0.31	1.44 ± 0.64	9.02 ± 1.65	0.38 ± 0.11	39.0 ± 4.54	0.02 ± 0.03	2.91 ± 2.81	0.03 ± 0.04	13.30 ± 6.6	31.5 ± 1.01	(Ti,Nb)(C,N) ^b

^aResults are given in wt pct^bResults are given in at pct

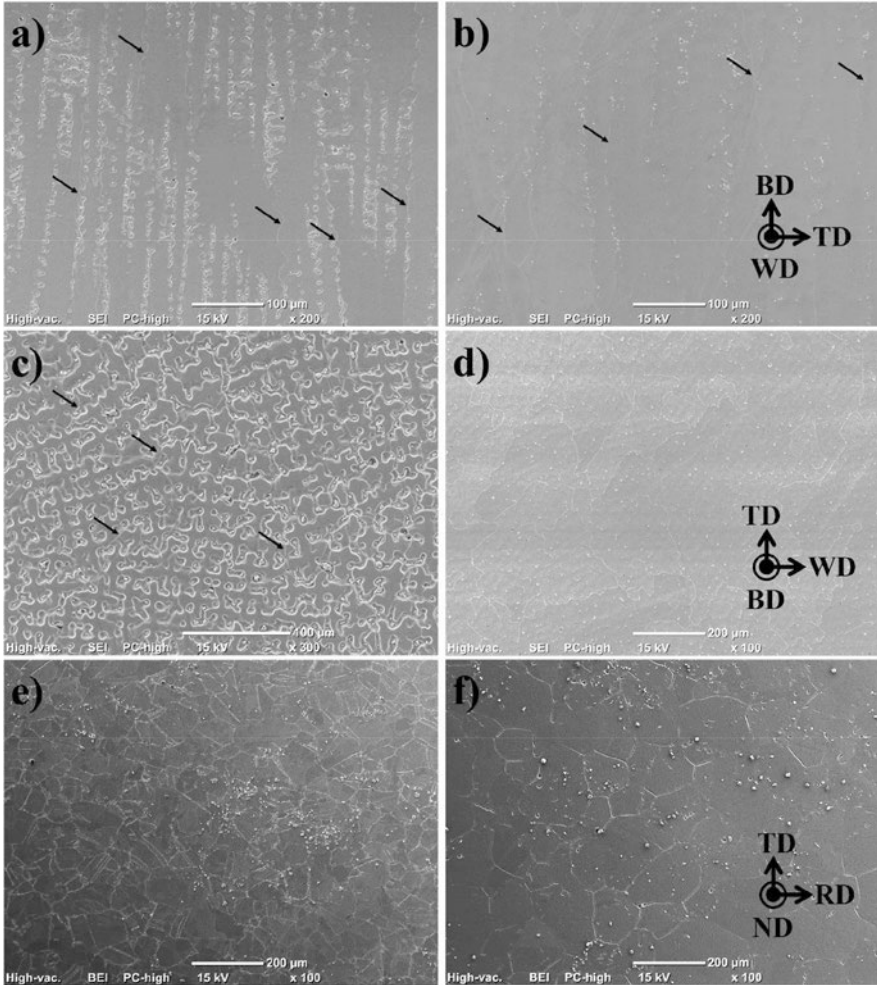


Fig. 15.14 The SEM images for (a, c) AF, (b, d) HA, (e) ARP, and (f) HAP conditions. The dark arrows indicate the presence of grain boundaries

From the prospective of physical attributes of IN718 superalloys parts in practice applications, the associated heat-treatment should enhance the mechanical strength of the IN718 alloys via precipitation hardening of γ'' and γ' [12, 35, 38]. Figure 15.16 shows the response of heat treatment in microhardness values for WAAM IN718 alloys in this study. The HA samples yielded almost double the microhardness values in comparison with AF condition along the wall height as shown in Fig. 15.16a. For HA condition, the microhardness values are more uniformly distributed along the wall height than that of AF condition. This indicates the suitability of the modified heat treatment in the dissolution of laves phases and redistribution of beneficial Nb elements in the γ matrix uniformly to precipitate out hardening phases. The

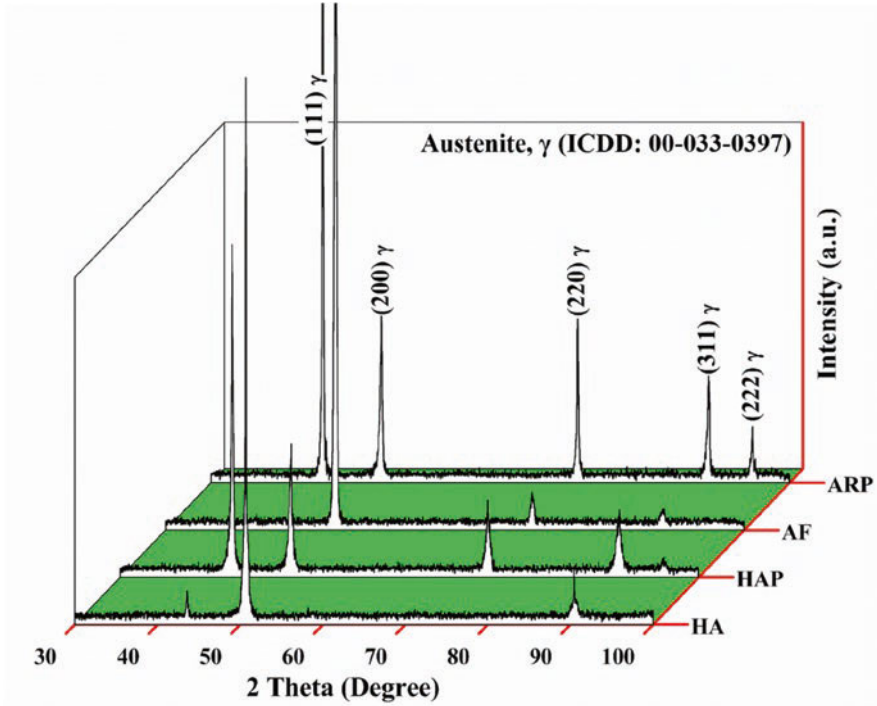


Fig. 15.15 XRD profiles for AF, HA, ARP, and HAP samples

Table 15.7 The quantitative values of texture coefficient, $T_{c(hkl)}$ of a specific (hkl) reflection and degree of texture, σ obtained for different samples as shown in Fig. 15.15

Samples	Texture coefficient					Degree of texture σ
	$T_{c(111)}$	$T_{c(200)}$	$T_{c(220)}$	$T_{c(311)}$	$T_{c(222)}$	
AF	0.0	4.65	0.24	0.12	0.0	1.83
HA	0.08	4.68	0.0	0.24	0.0	1.84
ARP	1.53	0.73	1.27	0.69	0.77	0.34
HAP	1.52	1.26	1.08	0.86	0.27	0.42

average hardness value for HA sample was measured to be 461.34 ± 4.48 HV (equivalent to 46.24 ± 0.36 HRC), which has exceeded the minimum requirements (38 HRC) for IN718 plate (47.17 ± 0.82 HRC in this study) according to the standard AMS 5597 [5]. Thus, from the microhardness results, it is clear that the presence of phase constituents in the matrix is more effective to resist the plastic deformation than that of grain boundary density which was also discussed in section “Mechanical Properties”.

The effects of heat treatment on the tensile test results of WAAM IN718 alloys are shown in Fig. 15.17 and summarized in Table 15.8. The commercial IN718 superalloy (ARP) and its heat-treated condition (HAP) were also studied for

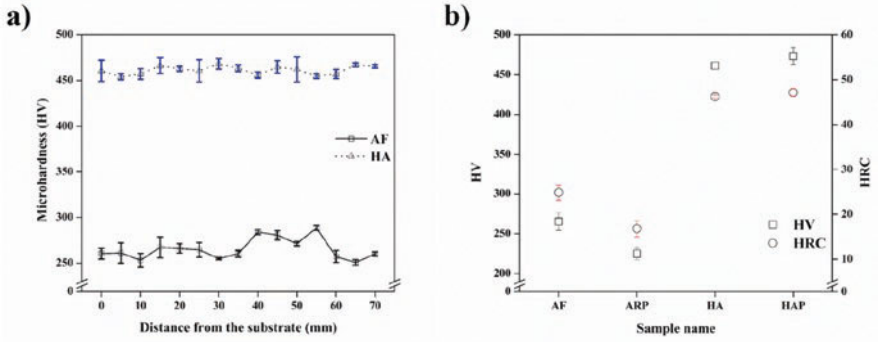


Fig. 15.16 (a) Vickers microhardness results of AR and HA conditions as a function of the wall height and (b) the average microhardness results for AF and as-received (ARP) Inconel 718 parts, and also in their respective heat-treated conditions

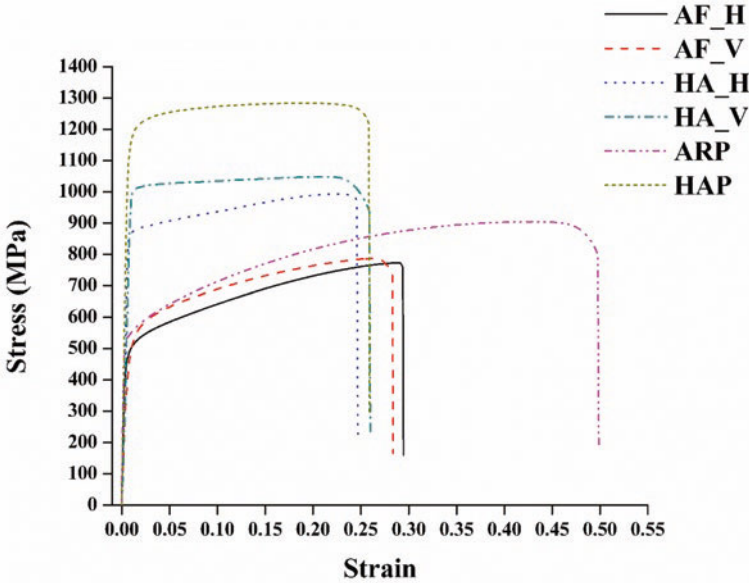


Fig. 15.17 The engineering stress–strain curves of AF and HA conditions at room temperature with ARP and HAP samples for comparison

comparison. The modified HA samples fabricated by WAAM process in this study were superior to cast IN718 alloys [90], but did not meet the minimum requirements for wrought IN718 plate (HAP in this study) in terms of YS and UTS according to the standard AMS 5597 [5]. The grain size of HA samples became too large after heat-treatment process due to the coarse columnar grain structure of AF samples produced during the WAAM process. This was negatively affected the tensile properties and outweighed the precipitation strengthening aspects of γ'' and γ' phases.

Table 15.8 The summary of tensile results of heat-treated IN718 walls fabricated by WAAM process

Samples	Tensile properties										The spread of anisotropy, R_{UTS} ($R_{\text{UTS}})^a$
	Elastic modulus (GPa)	Modulus of resilience (MJ/m ³)	Toughness (MJ/m ³)	Strain hardening exponent, n	Ductility (%)	YS (MPa)	UTS (MPa)				
AF_H ^b	157.2 ± 4.17	1.46 ± 0.03	202.74 ± 6.26	0.43 ± 0.01	30.20 ± 0.75	445.41 ± 5.45	778.02 ± 4.54				0.91 (0.996)
AF_V ^b	122.98 ± 26.96	1.40 ± 0.22	190.63 ± 6.52	0.46 ± 0.01	27.95 ± 0.42	405.39 ± 12.57	774.52 ± 12.53				
HA_H	146.73 ± 10.92	4.30 ± 0.11	219.80 ± 9.45	0.21 ± 0.01	23.42 ± 1.28	869.92 ± 10.64	995.49 ± 1.72				1.169 (1.072)
HA_V	105.30 ± 0.73	6.86 ± 0.38	251.24 ± 41.19	0.15 ± 0.02	24.62 ± 4.34	1016.82 ± 28.76	1067.15 ± 22.62				
ARP	280.04 ± 14.15	1.51 ± 0.01	403.09 ± 2.50	0.51 ± 0.05	50.08 ± 0.31	510.01 ± 4.81	906.53 ± 5.96				
HAP	206.60 ± 3.20	5.17 ± 0.18	334.40 ± 19.12	0.20 ± 0.01	25.76 ± 0.17	1123.11 ± 20.03	1282.46 ± 5.18				
AF_H [12]	–	–	–	–	17.7	421	646				1.024 (1.17)
AF_V [12]	–	–	–	–	21.3 ± 7	431 ± 39	756 ± 47				
HA_H [12]	–	–	–	–	21.1 ± 8	932 ± 2	1073 ± 36				0.918 (0.973)
HA_V [12]	–	–	–	–	19.9 ± 1	856 ± 6	1044 ± 14				
Cast AMS5383 [90]	–	–	–	–	3	724	827				
Wrought AMS5597 [5]	–	–	–	–	15	1034.21	1241.06				

^a $R_{\text{UTS}} = Y_{\text{S}}/Y_{\text{S}_H}$ ($Y_{\text{S}}/Y_{\text{S}_H}$) is the ratio of yield strength (ultimate tensile strength) in vertical and horizontal directions

^bH and V refer to the horizontal (parallel to welding direction) and vertical (parallel to build-up direction) directions, respectively

Both AF and HA samples showed weak anisotropic tensile properties (YS and UTS) in horizontal and vertical directions as the values of the spread of anisotropy are relatively close to 1. These results are well complimented with the work of Seow et al. [12] as shown in Table 15.8. The ductility of HA samples could be comparable to the wrought IN718 sample in this study as it exceeded the minimum value (15%) required to satisfy the standard AMS 5597.

Figure 15.18 shows intragranular ductile fracture mode to be the failure mechanism for AF, ARP, and their heat-treated counterparts in this study. The microvoid coalescence of dimples was found to be coarser in AF samples. It is clearly evident that the fracture path was the continuous shearing of large columnar grain structure along the buildup direction so that DCR produced cleavage facets with tear ridges for AF sample in the horizontal direction. For AF sample in the vertical direction, the fracture path was random and the dimples were more equiaxed in nature. On the other hand, a different fracture morphology was observed in the case of HA. The fracture was not so obviously aligned along the buildup direction and the continuity of the shearing pattern of columnar grains was disappeared. The dimples were not only clearly visible but also their numbers were higher and the sizes were relatively smaller in comparison with AF conditions. For ARP sample, the dimples produced were the finest. On the other hand, dimples with a flat morphology were observed along with large cleavage facets fracture surface due to the removal of carbide particle in case of HAP.

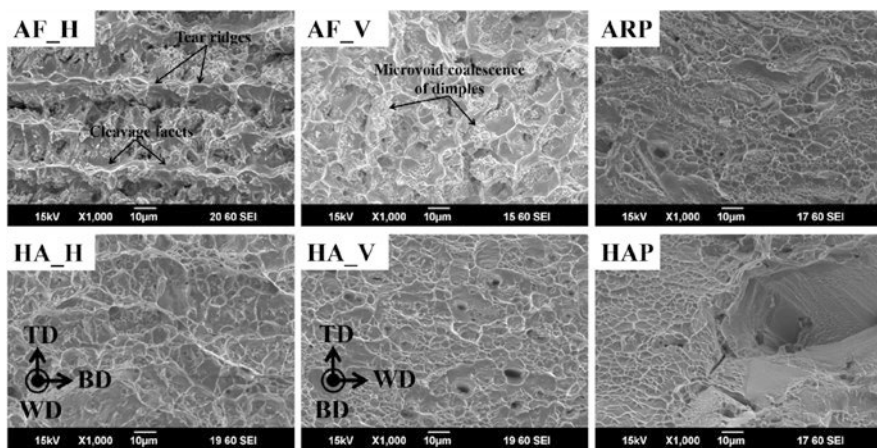


Fig. 15.18 SEM micrographs of fracture surfaces for different specimens after room temperature tensile test

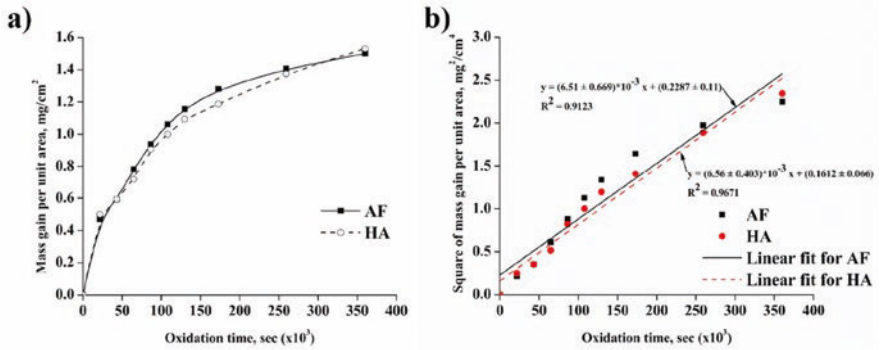


Fig. 15.19 The oxidation kinetics of AF and HA alloys at 1000 °C in ambient air upto 100 h: (a) mass gain versus oxidation time and (b) square of mass gain versus oxidation time

15.3.4 High-Temperature Oxidation Performance of WAAM IN718 Alloys

The oxidation kinetics graphs at 1000 °C are given in Fig. 15.19. Figure 15.19a gives the mass gain per unit area as a function of oxidation time for AF and HA samples. The shape of the curves can provide the nature of the oxidation rate law governing the oxide layer formation during oxidation time. It seems that the kinetic curves can be divided into two regions. The first region was a transient stage of oxidation until 48 h where the rate of oxidation was rapid due to the exposure of clean surface into the high-temperature atmosphere. After 48 h exposure time, the mass of the oxide scale reached at a steady state due to the formation of a protective oxide layer over the substrate. As a result, further oxide scale formation slowed down and the oxidation became totally diffusion controlled of inward moving oxygen anions and outward moving metal cations across the oxide layer. Under these circumstances, the oxidation curves obey the parabolic rate law and can be expressed using the following formula [91]:

$$(\Delta w / A)^2 = k_p \cdot t + C \tag{15.9}$$

where Δw is the mass gain (mg), A is the total area of the sample (cm²), k_p is the parabolic rate constant (mg²/cm⁴s), t is the exposure time (s), and C = integral constant. From Fig. 15.19b, the slope of line curve will be the value of k_p and it was found to be $(6.51 \pm 0.669) \times 10^{-6}$ and $(6.56 \pm 0.403) \times 10^{-6}$ for AF and HA samples, respectively. An identical rate of oxidation behavior was observed in both AF and HA conditions which means that the heat-treatment does not have any influence on the oxidation resistance at high-temperature regime. Specific studies related to the oxidation performance of IN718 alloys manufactured by WAAM process are scarce. Singh, A. B. [61] was found that the rate of oxidation for AF sample ($k_p = 4.675 \times 10^{-5}$ mg²/cm⁴s) was 1.47 times higher than that of commercial IN718

alloys ($k_p = 3.178 \times 10^{-5} \text{ mg}^2/\text{cm}^4\text{s}$) at 900 °C. Greene and Finfrock [21] reported a k_p value of $4.67 \times 10^{-5} \text{ mg}^2/\text{cm}^4\text{s}$ at 1000 °C for 24 h. In this study, k_p value was found to be $1.02 \times 10^{-5} \text{ mg}^2/\text{cm}^4\text{s}$ at 1000 °C up to 24 h for AF sample giving ~5 times lower oxidation rate than that of conventional IN718 alloy. Al-hatab et al. [24] reported cyclic oxidation rate, $k_p = 2.05 \times 10^{-6} \text{ mg}^2/\text{cm}^4\text{s}$ of commercial IN718 alloy at 950 °C which has the same order of magnitude, but ~3 times lower oxidation rate than that of AF sample in this study. A k_p value of $8.55 \times 10^{-4} \text{ mg}^2/\text{cm}^4\text{s}$ was reported by Kang et al. [92] at 1000 °C up to 10 h exposure time for solution-treated IN718 sample fabricated by selective laser melting (SLM) process. Calandri et al. [93] also performed an oxidation study on SLM-fabricated IN718 alloys in homogenization-treated condition and reported a k_p value of $7.5 \times 10^{-8} \text{ mg}^2/\text{cm}^4\text{s}$ at 850 °C. A direct comparison of the oxidation kinetics obtained in this study with these reports is difficult to explain. These differences in experimental results may be derived from various factors including the fabrication routes, testing conditions, surface roughness [60], grain size, or grain boundary density [58, 94]. To sum up, the wire-arc additively fabricated IN718 superalloys showed a lower parabolic oxidation kinetics (k_p). A low value of k_p indicates good oxidation behavior with long-term service life due to the slow consumption of cations from the metal alloy.

The oxide surface analysis was conducted at 1000 °C in ambient air for different oxidation times as shown in Fig. 15.20. During the early transient stage of oxidation, the exposed IN718 samples rapidly developed a thin oxide layer and covered the entire sample surface in a uniform manner. Although the mass gain of oxide layer after a certain oxidation period gives an overall oxidation rate of oxide formation (Fig. 15.19), the actual rate of oxidation can be quite complex and varies region to region microscopically. For example, the rate of oxidation at grain boundaries was faster and easier than that of matrix region providing excessive growth of oxide particles. The protrusion of oxide scale along grain boundaries was clearly visible. As the oxidation period continued to increase, the growth of oxide layer continued and thermal stresses started to develop in the oxide layer. Once the thickness of oxide scale reached a critical point where the acting thermal stresses on the oxide scale exceeded the critical spallation stress, the oxide scale could buckle and separate from the oxide/substrate interface leading to crack development and eventually spalled away under compression during cooling period [95, 96]. In this study, oxide spallation was observed after 48 h of high-temperature exposure and the intensity of spallation increased as the oxidation time increased (Fig. 15.20e and g).

The surface morphology of oxidized HA sample after 100 h was found to be a mixture of two types of oxides as shown in Fig. 15.21. The elemental composition of these elements is tabulated in Table 15.9. A Ti-enriched oxide particle (spot m) with a flat morphology and a Cr-rich oxide with small amount of Mn (spot n) were identified. The cross-sectional study of oxide scales was carried out at different oxidation times and three distinct types of oxides were identified as shown in Fig. 15.22. Under all conditions, an external oxide scale of Cr (spot p) and an internal scale of complex Ti and Nb (spot q) were developed at the air/alloy interface. As the oxidation time increased, the degree of internally formed Al-rich particles (spot r) was also increased in number and size. It is to be noted that the externally formed

Table 15.9 The elemental composition of EDS point analyses conducted in Fig. 15.21 and Fig. 15.22, respectively

EDS spots	Elemental composition in at. pct.									
	O	Al	Si	Ti	Cr	Mn	Fe	Ni	Nb	Mo
m	69.96	0.06	0.14	21.82	5.32	1.27	0.18	0.10	1.15	0.00
n	65.75	0.04	0.04	6.08	19.44	7.23	0.81	0.27	0.30	0.04
p	62.04	0.29	0.10	0.87	36.00	0.00	0.38	0.29	0.03	0.00
q	60.46	0.52	0.04	9.16	5.12	0.05	0.41	0.74	22.96	0.54
r	56.19	35.07	0.00	0.02	1.23	0.12	2.32	4.34	0.42	0.29

oxide scale was covered with Ti- and Mn-rich oxide particles at the air/scale interface as the oxidation times increased.

The XRD analysis was conducted to identify the oxide phases in this study. As shown in Fig. 15.23, the externally formed oxide scale was identified as chromia phase, Cr_2O_3 (ICSD 01-070-3766), and internally formed oxide layer was a complex rutile-type $\text{Ti}_{0.67}\text{Nb}_{1.33}\text{O}_4$ phase (ICDD 00-053-0293) at the air/alloy interface. The Al-enriched islands of oxide particles within the alloy were identified as the alumina phase, Al_2O_3 (ICSD 01-070-3319). The outermost thin layer at the air/scale interface was composed of a rutile-type TiO_2 phase (ICSD 01-077-0443) and a spinel MnCr_2O_4 phase (ICSD 01-075-1614), respectively.

The oxidation mechanism of oxide scale in IN718 superalloys can be understood by the thermodynamic stability and kinetic ability of oxide phases from Ellingham diagram at 1000 °C [97, 98]. During the initial transient stage of oxidation, externally formed chromia and internal oxidation of complex Nb and Ti layer developed mainly due to the kinetic abilities of Cr^{+3} and Nb^{+4} cations in alloy. Thermodynamically chromia is the least favorable oxide to form among all of them with high partial pressure of oxygen (Po_2) of 10^{-22} atm and less negative Gibbs free energy (ΔG°) of -523 kJ/mol. As a result, it formed at air/alloy interface where the Po_2 was significantly high (Po_2 of 0.21 atm in air). Since the Cr content in IN718 alloy was much higher than that of Ti, Nb, Mn, and Al, the outward diffusion of Cr^{+3} cations dominated the diffusion process and developed the chromia scale externally. On the other hand, both Ti^{+4} and Nb^{+4} cations have a strong affinity toward oxygen anions (O^{-2}) in the formation of rutile-type TiO_2 (0.3×10^{-27} atm, -667.44 kJ/mol) and NbO_2 (0.5×10^{-23} atm, -564.84 kJ/mol). However, in this present study, a complex Nb-rich $\text{Ti}_{0.67}\text{Nb}_{1.33}\text{O}_4$ phase formed instead of TiO_2 and NbO_2 underneath chromia scale which was also observed for Nb-containing alloys in previous studies [58, 59]. The thermodynamic data for this Nb-rich complex oxide are unknown, but the presence of this oxide in the alloy indicated that it was thermodynamically more stable than TiO_2 and/or NbO_2 . Due to the low solute content of Ti and Nb, O^{-2} anions dominated the diffusion process and thus it grew internally. Alumina phase is the most stable oxide (10^{-34} atm, -836.8 kJ/mol) at 1000 °C and formed internally within the IN718 alloy as discrete islands due to its low concentration. As the oxidation time increased, the chromia scale increased further to slow down the oxidation process as the scale growth became diffusion controlled of cations and anions

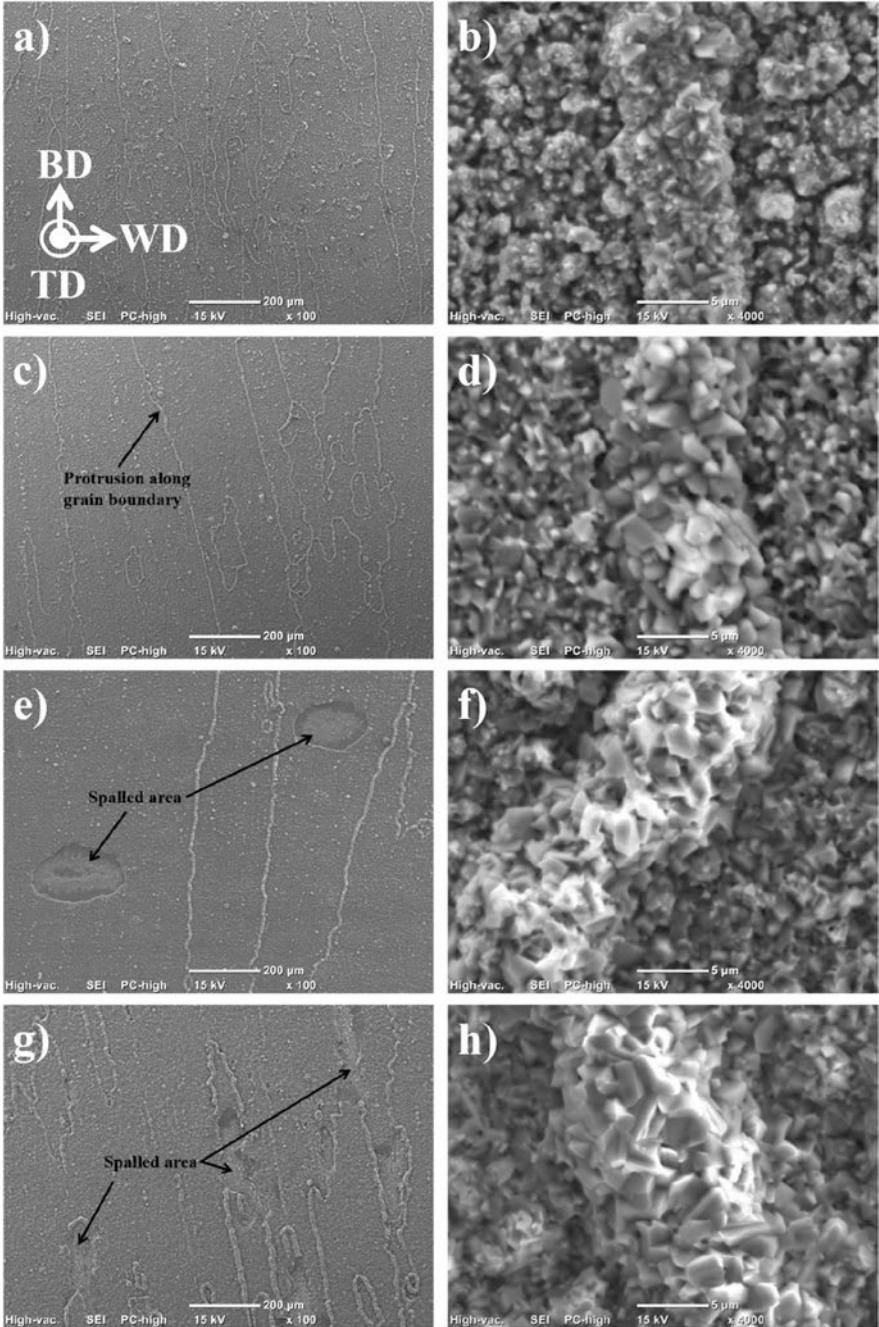


Fig. 15.20 SEM top view micrographs of oxide scale for HA samples after exposing (a, b) 6 h, (c, d) 24 h, (e, f) 48 h, and (g, h) 100 h in ambient air at 1000 °C

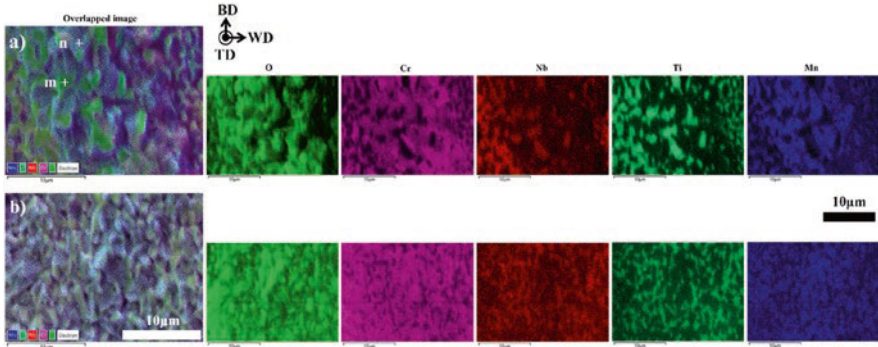


Fig. 15.21 The elemental distribution of oxide surface for HA samples after 100 h exposure at 1000 °C in ambient air: (a) protrusion along grain boundary and (b) within the matrix. EDS point analyses of m and n in (a) are mentioned in Table 15.9

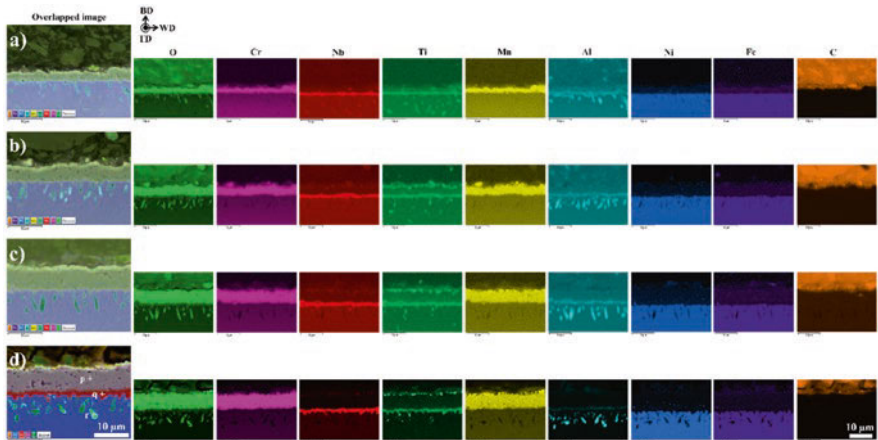


Fig. 15.22 SEM elemental mapping analysis on cross-sectioned HA samples after (a) 6 h, (b) 24 h, (c) 48 h, and (d) 100 h exposures at 1000 °C in ambient air. EDS point analyses of p, q, and r in (d) are tabulated in Table 15.9

through the scale. However, Ti^{+4} [99] and Mn^{+2} [99, 100] cations possess greater lattice diffusivity through chromia scale than Cr^{+3} cations resulting in the formation of outermost thin layer of TiO_2 and spinel $MnCr_2O_4$ (−1189.4 kJ/mol) phases.

15.4 Conclusions

The effects of welding parameters, modified heat-treatment cycle, and high-oxidation temperature on the microstructural evolution, mechanical and chemical properties of WAAM IN superalloys were extensively investigated in this work.

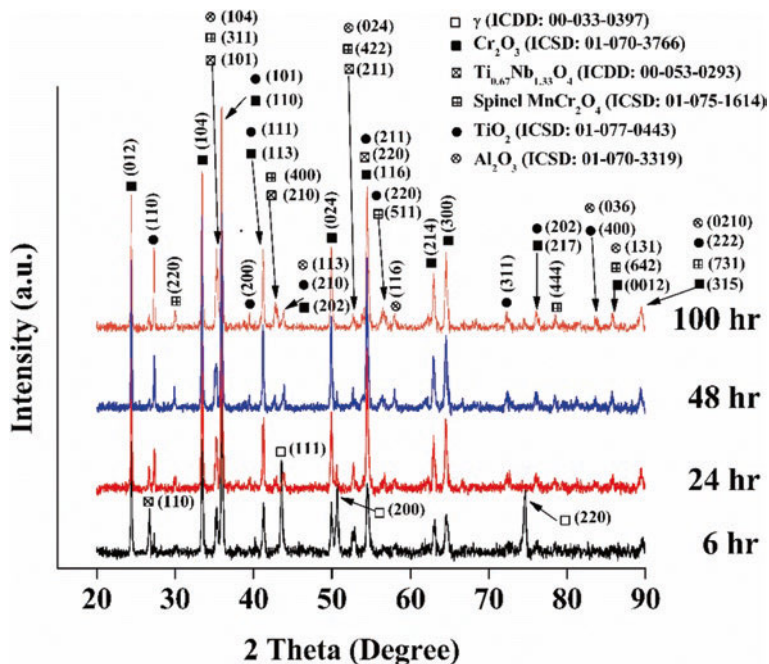


Fig. 15.23 XRD profiles of oxidized HA samples at 1000 °C in ambient air for different exposure intervals

Under the present experimental conditions, IN718 build parts were fabricated with any noticeable defects, such as lack of fusion zone. The results showed that the wall height was most affected by the wire feed speed and travel speed, whereas the width of the fabricated walls was predominantly influenced by the arc current and travel speed. The epitaxial growth of columnar dendritic morphology of AF walls under all processing conditions was formed due to the constitutional undercooling, high heat input, and slow cooling rates during GTAW-based WAAM process. The microstructure can be divided into two regions based on the compositional heterogeneity. The DCR is an Nb-depleted γ phase containing Ti-rich carbonitrides particles, whereas primary NbC and laves precipitates were formed in IDR with an Nb-enriched γ phase. The modified heat treatment used in this study was successfully eliminated the deleterious laves phases and Nb-enriched eutectic γ phase in IDR and redistributed the beneficial Nb solute elements into the matrix. WAAM IN718 alloys showed weak anisotropic properties in both AF and HA conditions. The HA samples showed superior mechanical properties to cast IN718, but inferior to commercial IN718 alloys. The high-temperature oxidation study revealed that the oxidation kinetics were independent of heat-treatment process. The oxidation kinetics followed the parabolic rate law forming a protective chromia scale externally at the air/alloy interface. The internal oxidation of Nb-rich complex $\text{Ti}_{0.67}\text{Nb}_{1.33}\text{O}_4$ phase and sub-scale of alumina phase was observed due to the high thermodynamic stability at low Po_2 .

Acknowledgments The authors acknowledge the financial support from University of Wollongong (UOW) and Commonwealth Scientific and Industrial Research Organization (CSIRO), respectively. The authors also would like to acknowledge the use of the facilities within the UOW Electron Microscopy center.

References

1. Akca, E., & Gürsel, A. (2015). A review on superalloys and IN718 nickel-based INCONEL superalloy. *Periodicals of Engineering and Natural Sciences*, 3(1), 15–27.
2. Scharfrik, R., & Sprague, R. (2004). The saga of gas turbine materials, Part III. *Advanced Materials and Processes*, 162, 33–35.
3. Pollock, T. M., & Tin, S. (2006). Nickel-based superalloys for advanced turbine engines: Chemistry, microstructure and properties. *Journal of Propulsion and Power*, 22(2), 361–374.
4. Patel, S., deBarbadillo, J., & Coryell, S. (2018). Superalloy 718: Evolution of the alloy from high to low temperature application. In *Proceedings of the 9th international symposium on superalloy 718 & derivatives: Energy, aerospace, and industrial applications*.
5. Special Metals - Inconel® alloy 718. Retrieved from <https://www.specialmetals.com/documents/technical-bulletins/inconel/inconel-alloy-718.pdf>.
6. Kwon, S. I., Bae, S. H., Do, J. H., Jo, C. Y., & Hong, H. U. (2016). Characterization of the microstructures and the cryogenic mechanical properties of electron beam welded inconel 718. *Metallurgical and Materials Transactions A*, 47(2), 777–787.
7. Chen, K., Dong, J., & Yao, Z. (2021). Creep failure and damage mechanism of inconel 718 alloy at 800–900° C. *Metals and Materials International*, 27, 970–984.
8. Kuo, C.-M., Yang, Y.-T., Bor, H.-Y., Wei, C.-N., & Tai, C.-C. (2009). Aging effects on the microstructure and creep behavior of Inconel 718 superalloy. *Materials Science and Engineering: A*, 510, 289–294.
9. Shi, J.J, Li, X., Zhang, Z.X., Cao, G.H., Russell, A.M., Zhou Z.J., Li, C.P. & Chen, G.F. (2019). Study on the microstructure and creep behavior of Inconel 718 superalloy fabricated by selective laser melting. *Materials Science and Engineering: A*, 765, 138282.
10. Ono, Y., Yuri, T., Nagashima, N., Ogata, T., & Nagao, N. (2015). Effect of microstructure on high-cycle fatigue properties of Alloy718 plates. In *IOP conference series: Materials science and engineering*.
11. Ono, Y., Yuri, T., Sumiyoshi, H., Takeuchi, E., Matsuoka, S., & Ogata, T. (2004). High-cycle fatigue properties at cryogenic temperatures in Inconel 718 nickel-based superalloy. *Materials Transactions*, 45(2), 342–345.
12. Seow, C. E., Coules, H. E., Wu, G., Khan, R. H., Xu, X., & Williams, S. (2019). Wire+ Arc Additively Manufactured Inconel 718: Effect of post-deposition heat treatments on microstructure and tensile properties. *Materials & Design*, 183, 108157.
13. Paulonis, D. F., Oblak, J. M., & Duvall, D. S. (1969). Precipitation in nickel-base alloy 718. *American Society of Metals*, 62, 611–622.
14. Hong, S. J., Chen, W. P., & Wang, T. W. (2001). A diffraction study of the γ' phase in INCONEL 718 superalloy. *Metallurgical and Materials Transactions A*, 32(8), 1887–1901.
15. Cozar, R., & Pineau, A. (1973). Morphology of γ' and γ'' precipitates and thermal stability of inconel 718 type alloys. *Metallurgical Transactions*, 4(1), 47–59.
16. Oblak, J. M., Paulonis, D. F., & Duvall, D. S. (1974). Coherency strengthening in Ni base alloys hardened by DO₂₂ γ' precipitates. *Metallurgical Transactions*, 5(1), 143–153.
17. Chaturvedi, M. C., & Han, Y.-F. (1983). Strengthening mechanisms in Inconel 718 superalloy. *Metal science*, 17(3), 145–149.
18. Han, Y.-F., Deb, P., & Chaturvedi, M. C. (1982). Coarsening behaviour of γ'' - and γ' -particles in Inconel alloy 718. *Metal Science*, 16(12), 555–562.

19. Drexler, A., Oberwinkler, B., Primig, S., Turk, C., Povoden-Karadeniz, E., Heinemann, A., Ecker, W., & Stockinger, M. (2018). Experimental and numerical investigations of the γ'' and γ' precipitation kinetics in Alloy 718. *Materials Science and Engineering: A*, 723, 314–323.
20. Munjal, V., & Ardell, A. J. (1975). Precipitation hardening of Ni-12.19 at.% Al alloy single crystals. *Acta Metallurgica*, 23(4), 513–520.
21. Greene, G. A., & Finrock, C. C. (2001). Oxidation of Inconel 718 in air at high temperatures. *Oxidation of Metals*, 55(5–6), 505–521.
22. Sadeghimeresht, E., Karimi, P., Zhang, P., Peng, R., Andersson, J., Pejryd, L., & Joshi, S. (2018). Isothermal oxidation behavior of EBM-additive manufactured alloy 718. In *Proceedings of the 9th international symposium on superalloy 718 & derivatives: Energy, aerospace, and industrial applications*.
23. Jia, Q., & Gu, D. (2014). Selective laser melting additive manufactured Inconel 718 superalloy parts: High-temperature oxidation property and its mechanisms. *Optics & Laser Technology*, 62, 161–171.
24. Al-Hatab, K. A., Al-Bukhaiti, M. A., Krupp, U., & Kantehm, M. (2011). Cyclic oxidation behavior of IN 718 superalloy in air at high temperatures. *Oxidation of Metals*, 75(3–4), 209–228.
25. Klapper, H. S., Zadorozne, N. S., & Rebak, R. B. (2017). Localized corrosion characteristics of nickel alloys: A review. *Acta Metallurgica Sinica (English Letters)*, 30(4), 296–305.
26. Luo, S., Huang, W., Yang, H., Yang, J., Wang, Z., & Zeng, X. (2019). Microstructural evolution and corrosion behaviors of Inconel 718 alloy produced by selective laser melting following different heat treatments. *Additive Manufacturing*, 30, 100875.
27. Debarbadillo, J. J., & Mannan, S. K. (2012). Alloy 718 for oilfield applications. *JOM*, 64(2), 265–270.
28. Hamdani, F. (2015). *Improvement of the corrosion and oxidation resistance of Ni-based alloys by optimizing the chromium content*. Ph.D. Thesis, INSA de Lyon (France) and Tohoku University (Japan).
29. Muralidharan, B. G., Shankar, V., & Gill, T. P. S. (1996). *Weldability of Inconel 718—A review*. Indira Gandhi Centre for Atomic Research.
30. Clark, D., Bache, M. R., & Whittaker, M. T. (2008). Shaped metal deposition of a nickel alloy for aero engine applications. *Journal of Materials Processing Technology*, 203(1–3), 439–448.
31. Baufeld, B. (2012). Mechanical properties of Inconel 718 parts manufactured by shaped metal deposition (SMD). *Journal of Materials Engineering and Performance*, 21(7), 1416–1421.
32. Jia, Z., Wan, X., & Guo, D. (2020). Study on microstructure and mechanical properties of Inconel718 components fabricated by UHFP-GTAW technology. *Materials Letters*, 261, 127006.
33. Xu, X., Ding, J., Ganguly, S., & Williams, S. (2019). Investigation of process factors affecting mechanical properties of INCONEL 718 superalloy in wire+ arc additive manufacture process. *Journal of Materials Processing Technology*, 265, 201–209.
34. Xu, X., Ganguly, S., Ding, J., Seow, C. E., & Williams, S. (2018). Enhancing mechanical properties of wire+ arc additively manufactured INCONEL 718 superalloy through in-process thermomechanical processing. *Materials & Design*, 160, 1042–1051.
35. Wang, K., Liu, Y., Sun, Z., Lin, J., Lv, Y., & Xu, B. (2020). Microstructural evolution and mechanical properties of Inconel 718 superalloy thin wall fabricated by pulsed plasma arc additive manufacturing. *Journal of Alloys and Compounds*, 819, 152936.
36. Zhang, L. N., & Ojo, O. A. (2020). Corrosion behavior of wire arc additive manufactured Inconel 718 superalloy. *Journal of Alloys and Compounds*, 829, 154455.
37. Bhujangrao, T., Veiga, F., Suárez, A., Iriondo, E., & Mata, F. G. (2020). High-temperature mechanical properties of IN718 alloy: Comparison of additive manufactured and wrought samples. *Crystals*, 10(8), 689.
38. Kindermann, R. M., Roy, M. J., Morana, R., & Prangnell, P. B. (2020). Process response of Inconel 718 to wire+ arc additive manufacturing with cold metal transfer. *Materials & Design*, 195, 109031.

39. Tsurumaki, T., Tsukamoto, S., Chibahara, H., & Sasahara, H. (2019). Precise additive fabrication of wall structure on thin plate end with interlayer temperature monitoring. *Journal of Advanced Mechanical Design, Systems, and Manufacturing*, 13(2), JAMDSM0028.
40. Clark, D., Bache, M. R., & Whittaker, M. T. (2010). Microstructural characterization of a polycrystalline nickel-based superalloy processed via tungsten-intert-gas-shaped metal deposition. *Metallurgical and Materials Transactions B*, 41(6), 1346–1353.
41. Mohsan, A. U. H., Liu, Z., & Padhy, G. K. (2017). A review on the progress towards improvement in surface integrity of Inconel 718 under high pressure and flood cooling conditions. *The International Journal of Advanced Manufacturing Technology*, 91(1–4), 107–125.
42. Williams, S. W., Martina, F., Addison, A. C., Ding, J., Pardal, G., & Colegrove, P. (2016). Wire+ arc additive manufacturing. *Materials Science and Technology*, 32(7), 641–647.
43. Cunningham, C. R., Flynn, J. M., Shokrani, A., Dhokia, V., & Newman, S. T. (2018). Invited review article: Strategies and processes for high quality wire arc additive manufacturing. *Additive Manufacturing*, 22, 672–686.
44. Pan, Z., Ding, D., Wu, B., Cuiuri, D., Li, H., & Norrish, J. (2018). Arc welding processes for additive manufacturing: A review. In *Transactions on intelligent welding manufacturing* (pp. 3–24). Springer.
45. Manikandan, S.G.K, Sivakumar, D., & Kamaraj, M. (2019). Welding the Inconel 718 superalloy: Reduction of micro-segregation and laves phases: Elsevier.
46. Sonar, T., Balasubramanian, V., Malarvizhi, S., Venkateswaran, T., & Sivakumar, D. (2020). Effect of delta current and delta current frequency on microstructure and tensile properties of gas tungsten constricted arc (GTCA)-welded Inconel 718 alloy joints. *Metallurgical and Materials Transactions A*, 51, 3920–3937.
47. Bush, D., Bodily, B., Watson, H., Chastka, M., Colvin, E., & Satoh, G. (2017). Arconic development of the ampliforge process. In *AeroMat conference and exposition*.
48. Dinovitzer, M., Chen, X., Laliberte, J., Huang, X., & Frei, H. (2019). Effect of wire and arc additive manufacturing (WAAM) process parameters on bead geometry and microstructure. *Additive Manufacturing*, 26, 138–146.
49. Yangfan, W., Xizhang, C., & Chuanchu, S. (2019). Microstructure and mechanical properties of Inconel 625 fabricated by wire-arc additive manufacturing. *Surface and Coatings Technology*, 374, 116–123.
50. Seow, C. E., Zhang, J., Coules, H. E., Wu, G., Jones, C., Ding, J., & Williams, S. (2020). Effect of crack-like defects on the fracture behaviour of Wire+ Arc Additively Manufactured nickel-base Alloy 718. *Additive Manufacturing*, 36, 101578.
51. Ezugwu, E. O., Bonney, J., & Yamane, Y. (2003). An overview of the machinability of aero-engine alloys. *Journal of Materials Processing Technology*, 134(2), 233–253.
52. Sui, S., Chen, J., Zhang, R., Ming, X., Liu, F., & Lin, X. (2017). The tensile deformation behavior of laser repaired Inconel 718 with a non-uniform microstructure. *Materials Science and Engineering: A*, 688, 480–487.
53. Radavich, J. F. (1989). The physical metallurgy of cast and wrought alloy 718. In *Superalloys 718 metallurgy and applications*.
54. Radhakrishna, C. H., & Rao, K. P. (1997). The formation and control of Laves phase in superalloy 718 welds. *Journal of Materials Science*, 32(8), 1977–1984.
55. Sivaprasad, K., & Raman, S. G. S. (2008). Influence of weld cooling rate on microstructure and mechanical properties of alloy 718 weldments. *Metallurgical and Materials Transactions A*, 39(9), 2115–2127.
56. Song, K., Yu, K., Lin, X., Chen, J., Yang, H., & Huang, W. (2015). Microstructure and mechanical properties of heat treatment laser solid forming superalloy Inconel 718. *Acta Metallurgica Sinica*, 51(8), 935–942.
57. Giggins, C. S., & Pettit, F. S. (1971). Oxidation of Ni-Cr-Al alloys between 1000° and 1200°C. *Journal of the Electrochemical Society*, 118(11), 1782–1790.
58. Sanviemvongsak, T., Monceau, D., Desgranges, C., & Macquaire, B. (2020). Intergranular oxidation of Ni-base alloy 718 with a focus on additive manufacturing. *Corrosion Science*, 170, 108684.

59. Vayyala, A., Povstugar, I., Galiullin, T., Naumenko, D., Quadackers, W. J., Hattendorf, H., & Mayer, J. (2019). Effect of Nb addition on oxidation mechanisms of high Cr ferritic steel in Ar-H₂-H₂O. *Oxidation of Metals*, 92(5–6), 471–491.
60. Sanviemvongsak, T., Monceau, D., & Macquaire, B. (2018). High temperature oxidation of IN 718 manufactured by laser beam melting and electron beam melting: Effect of surface topography. *Corrosion Science*, 141, 127–145.
61. Adria, B.S. (2020). *Oxidation resistance of additively manufactured Inconel 718 for gas turbine applications*. Master's Thesis, Carleton University.
62. ISO/ASTM 52900:2015 Additive manufacturing—General Principles—Terminology. Retrieved from <https://www.iso.org/obp/ui/#iso:std:iso-astm:52900:ed-1:v1:en>.
63. Snbacka, N. (2013). On arc efficiency in gas tungsten arc welding. *Soldagem & Inspeção*, 18(4), 380–390.
64. Li, Z., Chen, J., Sui, S., Zhong, C., Lu, X., & Lin, X. (2020). The microstructure evolution and tensile properties of Inconel 718 fabricated by high-deposition-rate laser directed energy deposition. *Additive Manufacturing*, 31, 100941.
65. Geels, K., Fowler, D. B., Kopp, W.-U., & Rückert, M. (2007). *Metallographic and materialographic specimen preparation, light microscopy, image analysis, and hardness testing*. ASTM International.
66. ASTM E8/E8M - 13a Standard Test Methods for Tension Testing of Metallic Materials. Retrieved from <https://www.astm.org/DATABASE.CART/HISTORICAL/E8E8M-13A.htm>.
67. ASTM F3122–14 Standard Guide for Evaluating Mechanical Properties of Metal Materials Made via Additive Manufacturing Processes. Retrieved from <https://www.astm.org/Standards/F3122.htm>.
68. AMS 5832H Nickel Alloy, Corrosion and Heat Resistant, Welding Wire, 52.5Ni - 19Cr - 3.0Mo - 5.1Cb(Nb) - 0.90Ti - 0.50Al - 18Fe, Consumable Electrode or Vacuum Induction Melted. Retrieved from <https://www.sae.org/standards/content/ams5832h/>
69. AMS 5597G Nickel Alloy, Corrosion and Heat Resistant, Sheet, Strip, and Plate, 52.5Ni - 19Cr - 3.0Mo - 5.1Cb(Nb) - 0.90Ti - 0.50Al - 18Fe, Consumable Electrode or Vacuum Induction Melted, 1950 °F (1066°C) Solution Heat Treatment. Retrieved from <https://www.sae.org/standards/content/ams5597g/>.
70. Mitchell, A. (2010). Primary carbides in Alloy 718. *Superalloys 718 and derivatives*.
71. Mitchell, A. (2005). The precipitation of primary carbides in IN 718 and its relation to solidification conditions. *Superalloys 718, 625, 706 and derivatives*.
72. Mitchell, A., Schmalz, A. J., Schvezov, C., & Cockcroft, S. L. (1994). The precipitation of primary carbides in alloy 718. *Superalloys 718, 625, 706 and various derivatives*.
73. Cockcroft, S. L., Degawa, T., Mitchell, A., Tripp, D. W., & Schmalz, A. (1992). Inclusion precipitation in superalloys. *Superalloys 1992*.
74. Phillips, D. H. (2016). *Welding engineering: An introduction*. Wiley.
75. Wu, B., Ding, D., Pan, Z., Cuiuri, D., Li, H., Han, J., & Fei, Z. (2017). Effects of heat accumulation on the arc characteristics and metal transfer behavior in Wire Arc Additive Manufacturing of Ti6Al4V. *Journal of Materials Processing Technology*, 250, 304–312.
76. Yildiz, A. S., Davut, K., Koc, B., & Yilmaz, O. (2020). Wire arc additive manufacturing of high-strength low alloy steels: Study of process parameters and their influence on the bead geometry and mechanical characteristics. *The International Journal of Advanced Manufacturing Technology*, 108(11), 3391–3404.
77. Nursyifaulkhair, D., Park, N., Baek, E. R., & Lee, J.-b. (2019). Effect of process parameters on the formation of lack of fusion in directed energy deposition of Ti-6Al-4V alloy. *Journal of Welding and Joining*, 37(6), 579–584.
78. Lampman, S. (1997). Weld solidification. In *Weld integrity and performance* (pp. 3–21). ASM International.
79. Lippold, J. C. (2015). Welding metallurgy principles. In *Welding metallurgy and weldability* (pp. 9–83). Wiley Online Library.

80. Barrett, C. S., & Massalski, T. B. (1966). *Structure of metals: Crystallographic methods, principles, and data*. McGraw-Hill.
81. Gao, J., Jie, W., Yuan, Y., Wang, T., Zha, G., & Tong, J. (2011). Dependence of film texture on substrate and growth conditions for CdTe films deposited by close-spaced sublimation. *Journal of Vacuum Science & Technology A: Vacuum, Surfaces, and Films*, 29(5), 051507.
82. Knorovsky, G. A., Cieslak, M. J., Headley, T. J., Romig, A. D., & Hammett, W. F. (1989). Inconel 718: A solidification diagram. *Metallurgical Transactions A*, 20(10), 2149–2158.
83. Chalmers, B. (1970). Principles of solidification. In *Applied solid state physics* (pp. 161–170). Springer.
84. Stefanescu, D. M., & Ruxanda, R. (2004). Fundamentals of solidification. In *ASM handbook (Metallography and microstructures)* (Vol. 9, pp. 71–92). ASM International.
85. Kurz, W., & Fisher, D. J. (1984). *Fundamentals of solidification*. Trans Tech Publications.
86. David, S. A., & Vitek, J. M. (1989). Correlation between solidification parameters and weld microstructures. *International Materials Reviews*, 34(1), 213–245.
87. Antonsson, T., & Fredriksson, H. (2005). The effect of cooling rate on the solidification of INCONEL 718. *Metallurgical and Materials Transactions B*, 36(1), 85–96.
88. Mondol, A., Gupta, R., Das, S., & Dutta, T. (2018). An insight into Newton's cooling law using fractional calculus. *Journal of Applied Physics*, 123(6), 064901.
89. Newton's Law of Cooling. Retrieved from <https://www.carolina.com/teacher-resources/Interactive/newtons-law-of-cooling/tr36401.tr>.
90. AMS 5383 Nickel Alloy, Corrosion and Heat-Resistant, Investment Castings, 52.5Ni - 19Cr - 3.0Mo - 5.1Cb(Nb) - 0.90Ti - 0.60Al - 18Fe, Vacuum Melted Homogenization and Solution Heat Treated. Retrieved from <https://www.sae.org/standards/content/ams5383/>.
91. Young, D. J. (2008). The nature of high temperature oxidation. In *High temperature oxidation and corrosion of metals* (pp. 1–27). Elsevier.
92. Kang, Y.-J., Yang, S., Kim, Y.-K., AlMangour, B., & Lee, K.-A. (2019). Effect of post-treatment on the microstructure and high-temperature oxidation behaviour of additively manufactured inconel 718 alloy. *Corrosion Science*, 158, 108082.
93. Calandri, M., Manfredi, D., Calignano, F., Ambrosio, E. P., Biamino, S., Lupoi, R., & Ugues, D. (2018). Solution treatment study of inconel 718 produced by SLM additive technique in view of the oxidation resistance. *Advanced Engineering Materials*, 20(11), 1800351.
94. Li, L., Gong, X., Ye, X., Teng, J., Nie, Y., Li, Y., & Lei, Q. (2018). Influence of building direction on the oxidation behavior of inconel 718 alloy fabricated by additive manufacture of electron beam melting. *Materials*, 11(12), 2549.
95. Cao, G., Li, Z., Tang, J., Sun, X., & Liu, Z. (2016). Oxidation kinetics and spallation model of oxide scale during cooling process of low carbon microalloyed steel. *High Temperature Materials and Processes*, 36(9), 927–935.
96. Evans, H. E. (1995). Stress effects in high temperature oxidation of metals. *International Materials Reviews*, 40(1), 1–40.
97. Bose, S. (2017). Oxidation. In *High temperature coatings* (pp. 45–71). Butterworth-Heinemann.
98. Elorz, J. A. P.-S., González, D. F., & Verdeja, L. F. (2019). Structural materials: Metals. In *Structural materials: Properties and selection* (pp. 21–30). Springer.
99. Abe, F., Araki, H., Yoshida, H., & Okada, M. (1987). The role of aluminum and titanium on the oxidation process of a nickel-base superalloy in steam at 800°C. *Oxidation of Metals*, 27(1), 21–36.
100. Kassim, S. A., Thor, J. A., Seman, A. A., & Abdullah, T. K. (2020). High temperature corrosion of Hastelloy C22 in molten alkali salts: The effect of pre-oxidation treatment. *Corrosion Science*, 173, 108761.

Index

A

- Accessory drive gearbox (ADG), 243
- Adaptive cycle engine (ACE), *see* Aeroengines
- Additive manufacturing (AM), 346, 352
- Advanced gas turbine engines, 128
- Advanced polymers
 - aircraft components, 66
 - carbon fiber–reinforced composite, 66
 - ceramic materials, 65
 - composite materials, 65, 67, 69
 - engineering materials, 65
 - hybrid materials, 67
 - manufacturing processes
 - autoclave processes, 83
 - automated fiber placement, 80
 - automated tape layup, 79
 - filament winding process, 82
 - pultrusion process, 81, 82
 - resin transfer molding, 79, 80
 - vacuum-assisted resin transfer molding, 81
 - satellite components, 66
 - sectors, 66
 - solar cells, 66
 - structural components
 - aircraft manufacturers, 69
 - brackets, 71
 - empennage, 77, 78
 - engine fan blades, 69, 70
 - fuselage, 76, 77
 - interiors, 72, 74
 - nacelles, 73, 74
 - technology development programs, 69
 - wings, 75, 76
 - structural materials, 65
- Advisory Council for Aviation Research and Innovation in Europe (ACARE), 116
- Aeolipile, 129, 130
- Aerobatics aircraft, 181
- Aeroengines
 - airfoil-like surfaces, 131
 - classification, 131, 132
 - design, 131
 - eco-friendly trends, 127–129
 - fuel efficiency, 137
 - jet engines (*see* Jet engines)
 - metal heat capacity, 138
 - piston, 132, 133
 - turbine inlet temperature, 138
- Aero-gas turbine engine, 139
 - Co- and Ni-based superalloys, 143
 - combustor, 141, 143
 - compressor, 140, 141
 - current and future materials, 139, 140
 - fan blades and disks, 139, 140
 - fan case, 140
 - shaft, 144, 147
 - turbine section, 142–146
- Aeronautics, 155
- Aerospace, 260
 - and aeronautical industries, 301
 - applications, 297
 - approaches, 311
 - automotive and biomedical applications, 302
 - challenge, 309
 - common alloys, 297
 - component fabrication, 333
 - industry, 317

- Aerospace (*cont.*)
 - ISF (*see* Incremental sheet forming (ISF))
 - materials, VAM (*see* Vibration-assisted machining (VAM))
- Aerospace systems
 - dissimilar welding (*see* Dissimilar welding)
- Air bleed system (ABS), 244
- Airbus, 203
- Aircraft, 128, 260
- Aircraft fuel system, 182
 - bladder tanks (*see* Bladder-type fuel tanks)
 - collector fuel tank, 184
 - component requirements, 186
 - fuel flow
 - filter, 188
 - fuel-pump systems, 186
 - gravity-feed system, 186
 - pipe and connections, 188
 - strainer, 188
 - tank caps, 188
 - tank drain system, 187
 - tank fill connections, 187
 - tank installation, 187
 - tank tests, 187
 - unused (trapped) fuel margin, 187
 - integral fuel tank, 190, 191
 - maximum fuel capacity, 184
 - operating range specifications, 184
 - safe diversion and landing, 185
 - schematic, commercial passenger aircraft, 185
 - valves and controls, 188
 - wing configuration, 184
- Aircraft fuel tanks
 - anti-slosh feature, 195–196
 - collapsibility/foldability feature, 197
 - corrosion and leakage, 189
 - crashworthiness feature, 194
 - discrete tank, 189, 190
 - freeform feature, 196–197
 - fuel system, 189
 - layout, commercial passenger aircraft, 183
 - lightweight feature, 197
 - safety precautions, 193–194
 - self-sealing feature, 194–195
 - wet wings, 190, 191
- Aircraft fuselages and wings in Europe, 336, 337
- Aircraft systems
 - challenging environment, 240
 - components, 241
 - flight phases, 240
 - “top assembly”, 241
 - units, 241
- Airfoils, 309, 310
- Air traffic controller (ATC), 255
- Air vehicles, 181
 - pneumatic, hydraulic and fuel, 181
 - weight, 182
- Airworthiness authorities, 182
- Al and Mg alloys, 336
- Al-base alloys, 328, 329, 333
- Alien species, 260
- Al–Li alloys, 329
 - 8090T852 alloys, 5
 - airliner, 6
 - applications
 - fuselage, 17, 18
 - lower wing structures, 20
 - upper wing structures, 18–20
 - aviation industry, 2
 - basic structural materials, 3
 - chemical contents, 4
 - corrosion properties, 16, 17
 - density, 4
 - international space station (ISS), 5
 - material properties, 2
 - mechanical properties, 2, 6
 - aircraft, 11
 - anisotropy problems, 13
 - chemical compositions, 12
 - crack tip shielding, 13
 - drawbacks, 12
 - environmental and operating conditions, 11
 - fatigue behavior, 13, 14
 - fatigue crack growth behavior, 15
 - metallurgical and processing properties, 12
 - plane stress fracture toughness, 15
 - possessing superior corrosion-resistant characteristics, 12
 - R-curve values, 15, 16
 - strength vs. ductility, 12
 - structural components, 10
 - thermomechanical processes, 13
 - types of loadings, 11
 - microstructural properties
 - elements, 8
 - formations, 9
 - grain boundaries, 8
 - heat treatment parameters, 8
 - material properties, 8
 - mechanical properties, 7
 - optical microstructural images, 10
 - planar shear motion, 7
 - secondary defects, 9
 - thermal stability, 10
 - types of formations, 10

- vacancy-rich clusters, 9
- Mig-29M fighter, 5
- powder metallurgy and casting, 3
- production, 6, 7
- ultralight materials, 2
- welded fuel tank, 5
- Al–Mg–Si alloys, 328
- Aluminum alloys, 264, 303, 304, 337, 340
- AM implants, 361
- Amino company, 295
- AM technologies, 346, 347, 354
- ANSYS® program, 214, 217, 220
- Anti-ice system, 245
- Aramids, 91
- Artificial intelligence applications, 289
- Attitude heading and reference systems (AHRS), 250
- Autoland system, 251, 252
- Automated fuel balancing, 185
- Automatic flight control system (AFCS), 250
- Automatic piloting, 250
- Automotive guards, 298
- Autopilot system, 249
- Auxiliary power system (APS), 242
- Auxiliary power unit (APU), 255
 - flow mechanism, 241–245
 - pneumatic and electrical power, 241
- Aviation, 127
- Aviation CO₂ emissions, 128
- Axial direction of cutting, 261

B

- Ballistic penetration, 319
- Bending-dominated lattice structures, 350
- Be–Ni, 317
- Beryllium-base alloys, 331, 332
- Be–SS, 317
- Beta transus, 331
- Bio-based resins, 117
- Bio-composites, 118
- Biomass valorization, 118
- Bismaleimides, 75
- Black boxes, 246
- Bladder-type aircraft fuel tank
 - carbon fiber hand layup, 198
 - filling material, 198
 - manufacturing steps, 198
 - U/L aircraft bladder fuel tank, 201–203, 205
 - material requirement list (MRL)
 - consumables, 200
 - materials, 199–200
 - test equipment, 201
 - tools and devices, 200

- T19A aircraft, 198
- test and control procedures, 201
- Bladder-type fuel tanks, 192
 - clips/other fastening methods, 192
 - disadvantages, 192
 - discrete tanks and wet wing, 193
 - fuel cell, 192
 - layers, rubberized material, 192
 - rubber-like material bag, 192
 - “self-sealing” feature, 192
- Body-centered cubic (BCC), 348, 349, 352
- Body-centered cubic-reinforced along Z-axis (BCCZ), 348
- Boeing Company, 251
- Bolt fastening, 339
- Brazing
 - advantages, 326
 - in aerospace application, 326
 - Al-base alloys, 328, 329
 - applications, 326
 - beryllium-base alloys, 331, 332
 - carbon/alloy steels, 326
 - filler materials, 327, 328
 - Ti–Al IMCs, 332
 - titanium-base alloys, 329–331
 - vacuum, 328
- Brittle intermetallic compounds (IMCs)
 - formation, 318
- Build direction (BD), 374

C

- CAD 3-D model, 300, 302, 311
- Can-type combustion chamber, 142
- Carbon emissions, 127
- Carbon fiber hand layup, 198
- Carbon fiber–reinforced plastics (CFRP), 68, 266, 267, 341
- Carbon fibers, 91
- Carbon/low-carbon steels, 333
- CERN Large Hydrogen Collider, 57
- Chemical etching, 358
- Chip formations, 289
- Civilian-based certification, 182
- Clad metals, 341
- Closed-loop control, 269
- CNC milling center in experiments, 279
- CNC milling machine, 294
- Cockpit voice recorder (CVR), 246, 248, 249
- CO₂ emissions, 127, 128
- Cold metal transfer (CMT), 369
- Collapsible fuel tank, 197
- Commercial bus, 300
- Commercially pure Ti (CP Ti), 331
- Commercial off-the-shelf (COTS), 241

Commercial passenger aircraft, 181, 183
 Composites, 341
 Compression testing, 349
 Computational techniques, 352
 Computer-aided engineering (CAD), 352
 Conventional milling, 278
 Coolant effect, 280
 Correlation coefficient (CC), 223
 Correlation coefficient deviation metric (CCDM), 223
 Crash-resistant fuel systems (CRFS), 194
 Critical engine technologies, 128
 Cu-and Ni-base alloys, 333
 Cu–Monel, 317
 Cutting direction (CD), 262
 Cutting force measurements, 278, 279
 Cutting forces, 273, 274
 Cutting stage, 273
 Cutting tools, 260

D

Decision height (DH), 254
 γ core regions (DCR), 386
 Design for additive manufacturing (AM), 361
 Diffusion bonding, 332, 333
 Diffusion welding
 Al-base alloys, 333
 Diglycidyl ether of bisphenol-A (DGEBA), 118
 Directed energy deposition (DED), 369
 Direct operational cost (DOC), 245
 of airlines, 205
 Discrete tanks, 189, 190, 193
 Dissimilar liquid state welding
 EBW, 322, 323
 flash welding, 321
 GMAW, 319
 GTAW, 319, 320
 laser welding, 321, 322
 Dissimilar solid-state welding
 brazing (*see* Brazing)
 explosion welding, 324
 forge welding, 325
 magnetic pulse welding, 324
 microwave welding, 323, 324
 USW, 325, 326
 Dissimilar welding
 Al, 318
 aluminum alloys, 340
 applications, 318
 bolt fastening, 339
 brittle IMCs formation, 318

composites, 341
 diffusion bonding, 332, 333
 elevated strength Al alloys, 318
 energy efficiency, 317
 FRW (*see* Friction welding (FRW))
 joining thermoplastic matrix materials, 318
 liquid state welding, 319–323
 metals, 317
 plastics, 341
 solid-state welding (*see* Dissimilar solid-state welding)
 steel, 318
 uranium SS, 317
 Distance-measuring equipment (DME), 253
 Drilling, 260
 Drop tanks, 193
 Dry corrosion, 319
 Dynamometer, 276, 280, 281

E

Eclipse aviation, 335
 Eco-friendly aeroengines
 economic catastrophes, 146
 environmental impact parameters, 148
 implementation of composites, 148
 LCA, 147
 normalized effect values, 149
 sustainability assessment, composites, 148
 Ecological and Multifunctional Composites for Aircraft Interior and Secondary Structures (ECO-COMPASS), 120
 Effective frequency shift (EFS), 223
 Elastic compliance coefficients, 218
 Elasticity, 215
 Elastic modulus, 216
 Electrical discharge machining (EDM), 289
 Electromechanical impedance (EMI)
 technique, 212
 Electron-beam braze welding (EBBW), 323
 Electron beam melting (EBM), 371
 Electron beam welding (EBW), 322, 323
 Electronic control box (ECB), 243
 Elevated clamping force, 325
 Elevated strength Al alloys, 318
 Elliptical VAM, 261
 Elliptical vibration machining, 267
 Emergency locator transmitter (ELT), 247
 Energy efficiency, 317
 Engine fire, 188
 Enhanced ground proximity warning system (EGPWS), 252

- Environmental control system (ECS), 181, 182, 242, 245, 246
- Environmentally affected assessment, 148
- Environmental protection system (EPS), 246
- ERG Aerospace Corporation, 56
- Ester-based oil, 277
- European Aviation Safety Agency (EASA), 247
- Exhaust systems, 266
- Explosive welding (EXW), 324
- F**
- Fabrication techniques, 347
- Fatigue life, 289
- Federal Aviation Administration (FAA), 247
- Feed direction cutting, 262, 264
- Fe-29Ni-17Cu alloy, 331
- Fiber–metal laminates, 115
- Fiber reinforcements, 117
- Fibrous composite
 - aerospace industry, 91
 - aircraft applications, 108
 - aircraft industry, 90
 - aircraft structures, 90
 - architectures, 92–95
 - braided fabrics, 96
 - fabrication, 100, 102–104
 - fiber–matrix interface, 104, 105
 - knitted fabrics, 96
 - manufacturing technology, 90
 - material design, 90
 - materials, 91
 - matrices, 98
 - mechanical behavior, 106, 107
 - nonwoven fabrics, 92
 - polymer-based, 90
 - three-dimensional textiles preforms, 97, 98
 - types of mechanical tests, 107
 - woven fabrics, 95, 96
- Filament winding, 104
- Filler materials, 327, 328
- Finite element analysis (FEA), 71, 352, 353
- Finite element method (FEM), 352
- Finite element model, 235
- Flash welding, 321
- Flax composites, 117
- Flight-critical fuel lateral balance system, 183
- Flight data recorder (FDR), 246, 247
- Flight management system (FMS), 249, 252
- Forge welding, 325
- French aerospace engineer, 130
- French Alouette 318 C turboshaft engine, 136
- Frequency response functions (FRF)
 - signals, 213
- Friction-induced heat, 335
- Friction stir welding (FSW)
 - 2xxx–7xxx series aluminum alloys, 337
 - 6xxx–7xxx series aluminum alloys, 338
 - advantages, 334, 336
 - aerospace constituents, 335
 - aircraft fuselages and wings in Europe, 336, 337
 - aircraft systems, 336
 - Al and Mg alloys, 336
 - aluminum alloys, 337
 - development, 335
 - dissimilar materials, 335
 - eliminates fasteners and rivets, 336
 - industrial applications, 335
 - principle, 335
 - soft and hard alloys, 335
 - solid-state welding method, 334
 - Ti alloys and Ni-based superalloys, 335
- Friction surfacing, 334
- Friction welding (FRW)
 - aerospace component fabrication, 333
 - benefits, 333
 - carbon/low-carbon steels, 333
 - Cu- and Ni-base alloys, 333
 - friction surfacing, 334
 - FSW (*see* Friction stir welding (FSW))
 - IFW, 338, 339
 - linear friction welding, 339
 - Ni-base alloys, 334
 - solid-state joining method, 333
 - steel stamping, 333
- Fuel management system (FMS), 183
- Fuel tanks, 266
- G**
- Gas tungsten arc welding (GTAW), 319, 320, 369
- Gas turbine engine, 134, 140, 142–144
- Gas turbines, 130, 131, 134
- General Electric J79 afterburning turbojet engine, 135
- Genetic algorithm, 223
- Glass fiber, 91
- Glass fiber reinforced plastics (GFRP), 122
- Glass-reinforced plastics, 341
- Glideslope (GS), 252
- Glucofuranoside-based trifunctional epoxy (GFTE), 118
- GMAW, 319
- Green materials, 318
- Grinding, 260

H

Hammering effect, 282, 284
 Hans von Ohain's turbojet, 130
 Hard aluminum, 268
 Heat-affected zone (HAZ), 320
 Heat-assisted techniques, 311
 Heating, ventilation and air conditioning (HVAC) systems, 299
 Heli-arc process, 320
 Hemp/epoxy composites, 117
 Hero's Aeolipile, 130
 High-Efficiency Particulate Arresting (HEPA), 246
 High-pressure turbines (HPT), 143
 High-speed machining, 289
 High-speed ultrasonic vibrating cutting method, 273
 Homogenization-solution-annealed (HSA) condition, 370
 Honeycombs, 347
 Hybrid composites, 117
 Hybrid machining, 261

I

Inconel 718 (IN718), 260, 265, 269
See also Wire arc additive manufacturing (WAAM)
 Incremental forming
 for low batches/prototypes, 298–302
 machinery, 294–295
 materials and process limitations, 295–297
 processes, 294
 as rapid tooling (RT) process, 307–309
 and welding, 303
 Incremental sheet forming (ISF)
 application, 301
 asymmetrical geometries, 293
 conventional methods, 299
 decorative elements/architectural linings, 301
 deformation process, 298
 feasibility, 299
 in medical implant categories, 302
 potential applications, 298
 rapid prototyping and customized products, 298
 SPIF (*see* Single-point incremental forming (SPIF))
 TPIF, 294
 tunnel-type parts, 310
 with welding techniques, 302–307
 Inertia friction welding (IFW), 338, 339
 Inner marker (IM), 254

Instrument landing system (ILS), 252–255
 Integral canopies, 299, 300
 Integral fuel tank, 190, 191
 Intermediate materials, 327
 Intermittent cutting mechanism, 285
 Internal combustion engines, 133
 International Civil Aviation Organization (ICAO) regulations, 247
 International space station (ISS), 5
 Isothermal oxidation behavior, 376

J

Jet engines
 combustion process, 133
 pulsejet, 134
 turbofan, 135, 136
 turbojet, 134, 135
 turboprop/turboshaft engines, 135–137
 Joining
 lightweight dissimilar materials, 318
 thermoplastic matrix materials, 318

K

Kinematics of VAM, 269–271

L

Landing gear components, 266
 Landing gear systems
 advantages, 156–157
 Antonov AN-225 aircraft, 158
 Boeing 737 aircraft, 175, 176
 Boeing 737 landing gear control system, 173
 braking systems, 166–168
 business jets, 153
 components of tire, 171
 control lever, 173
 disadvantages, 156–157
 electric-hydraulic pumps, 172
 extend-retract system, 172
 fixed and retractable, 157, 158
 ground, 154
 hydraulic system, 173
 military jets, 153
 nose wheel steering mechanism, 177, 178
 struts
 bungee cords, 160
 rigid, 160
 shock, 161–163
 spring steel, 159, 160
 tail skid, 177, 179

- three-point configuration, 153
 - tires
 - bias ply/radial, 171
 - ply rating, 170
 - tubeless/tubed, 170
 - type classification, 169
 - water/snow, 153
 - wheels, 164, 166
 - Laser-based PBF (L-PBF), 346, 347, 349, 354, 355, 357, 359, 360
 - Laser beam melting (LBM), 371
 - Laser welding, 321, 322
 - Lattice structures, 346
 - advanced cellular structures, 347
 - applications, 359–360
 - bending-dominated, 350
 - biomedical applications, 359
 - compression testing, 349
 - design and analysis, 351–353
 - honeycombs and foams, 347
 - plastic yielding, fracture/buckling, 350
 - porous structures, 347
 - production, 354–359
 - strut-based, 348
 - types, 348
 - Life cycle assessment (LCA), 116, 147, 148
 - Light sport airplanes (LSA), 181
 - Lightweight design, 128, 129
 - Lightweight part manufacturing, 197
 - Linear friction welding, 339
 - Liquid matrix, 100
 - Liquid molding, 100
 - Localizer (LOC), 252
 - Longitudinal ultrasonic vibration-assisted
 - machining (LUVAM) of Ti-6Al-4V
 - in aircraft construction, 275
 - chemical composition, 275, 276
 - CNC milling center used in experiments, 279
 - conventional milling, 278
 - cutting force measurements, 278, 279
 - cutting force results
 - of finish cut, 280, 281, 287
 - of rough cut, 280, 281, 286
 - cutting tool used in experiments, 276, 278
 - design of experiments, 283
 - dynamometer, 276, 280, 281
 - experimental setup, 282
 - hammering effect, 282, 284
 - heat concentration, 275
 - intermittent cutting mechanism, 285
 - material's properties, 275
 - mechanical properties, 275, 277
 - ML, 277, 278, 280, 282, 285
 - MRR, 288
 - physical properties, 275, 277
 - properties of cutting tools, 276, 278
 - speed and feed increase, 280
 - ultrasonic tool holder, 276, 278, 279
 - ultrasonic vibration amplitude, 281
 - ultrasonic vibration system, 282
 - vibration-assisted finishing operations, 283
 - workpiece, 276
 - X-direction cutting force
 - in traditional milling, 279, 285
 - in ultrasonic-vibration assisted milling, 279, 285
 - Z-direction cutting forces
 - in traditional milling, 278, 284
 - in ultrasonic vibration-assisted milling, 278, 284
 - Longitudinal vibrations, 261
 - L-shaped fuel tanks, 184
 - LY12 aluminum alloy, 268
- M**
- Machining characteristics of VAM
 - benefits and limitations, 274, 275
 - cutting forces, 273, 274
 - surface roughness, 271, 272
 - tool life, 272
 - Magnetic pulse welding, 324
 - Main landing gear, 153–155, 158, 159, 163–166, 173–175, 177
 - Maintenance, repair and overhaul (MRO), 245
 - bladder-type fuel
 - Airbus, 203
 - back-shop inspection, 208
 - fuel and maintenance costs, 203, 205
 - MRO operations, 203, 207
 - preflight inspections, 206
 - removal operations, 207–208
 - repair operations, 208
 - scheduled/planned maintenance, 206
 - unscheduled/planned maintenance operations, 204
 - unscheduled/scheduled, 206
 - visual control, 207
 - Manufacturing processes, 260
 - MAR-M247 nickel-based superalloy, 265
 - Material Removal Rate (MRR), 288
 - MATLAB Optimization Toolbox, 223
 - Maxim's gigantic biplane, 129
 - Mean absolute percent deviation (MAPD), 223
 - Mesh morphing strategy, 310
 - Metal-cutting processes, 266

Metal foams and applications

aircraft applications

- AFS materials, 49
- bird/wildlife strike, 52
- closed-cell aluminum, 51
- composite material, 53
- Duocel, 48
- elements, 53
- light weighting, 47
- metallic materials, 50
- military applications, 49
- multifunctional materials, 48
- nonaluminum metal foam, 54
- open-cell foam materials, 50
- radome and leading edges, 52
- sandwich composite structures, 48
- sandwich structures, 48
- sound transmission, 50

aluminum, 28

bone and wood, 27

CFRP/carbon fiber-reinforced plastic composite structure, 27

light weighting, 27

open and close cell, 28

primary processing

- advantage, 34
- blowing agent particles, 33
- blowing agents, 31
- ceramic compound, 31
- direct and indirect, 30
- direct foaming methods, 34
- direct methods, 32
- electrodeposition, 40
- functional properties, 34
- gas bubbles, 33
- homogeneous distribution, 33
- indirect foaming method, 34
- indirect method, 32
- infiltration casting technique, 36
- liquid metal, 28, 30
- liquid state methods, 35
- macroscopic cells, 30
- metal ions, 39
- metallic deposition methods, 39
- mixed powder materials, 33
- nickel/nickel–chromium alloys, 39
- open-cell metallic structures, 34
- physical and chemical evaporation, 38
- polymer foam, 35
- porous metal production methods, 29
- powder-based process, 38
- production processes, 35
- properties, 34, 40
- sandwich structures, 34

sintering, 37

solid-state processes, 37

space holders, 37

supergravity, 36

supergravity infiltration, 36

surface tension, 28

3D printing technology, 28

vapor deposition method, 38

viscosity, 31

secondary processing

aluminum, 43

burrs and surface defects, 45

conventional and ultrasonic milling, 47

cutting, 41

effect of coating, 46

foaming, 41

heat-applying methods, 43

joining, 43–45

mechanical joining, 46

protective and homogeneous paint layer, 46

spacecraft, 54, 55, 57

Metal inert gas (MIG), 369

Metal matrix composite (MMC), 264

Metal-to-polymer joints, 318

Micro-machining, 289

Microwave welding, 323, 324

Middle marker (MM), 254

Mild steel (DC06), 340

Military air vehicles, 183

Military-based certification, 182

Milling, 260

Minimum quantity lubrication (MQL), 277, 278, 280, 282, 285

Multiaxial carbon fiber fabrics, 109

Multiaxial warp-knitting (MWK), 98

N

National Airworthiness Authorities (NAA), 247

National composite center (NCC), 75

Natural composites

advantages, 114

aerospace component, 116, 117

aerospace industry, 115, 116, 122

aircraft composites, 120

aircraft industry, 122

aluminum alloy, 118

bio and synthetic fiber composites, 121

bio-based thermosets, 118

bio-resins, 114, 119

carbon fiber reinforcement, 119

characteristics, 113

- CO₂ emissions, 118
- cognitive values, 113
- epoxy composites, 119
- greenhouse gas emissions, 114
- hybrid composites, 120
- inorganic materials, 122
- laminated composites, 115
- mechanical properties, 120
- multifunctional materials, 113
- nanofillers, 119
- natural fillers, 119
- renewable resources, 114
- semi-structural and structural applications, 114
- synthetic fibers, 120
- wood and natural-based fabrics, 114
- Ni-base alloys, 334
- Ni-based superalloys, 143, 368, 370, 374
- Nickel-based superalloy, 137
- Ni-stainless steel, 317
- Nonconsumable electrode welding process, 320
- Non-cutting stage, 273
- Nonresonant systems, 269
- Nonresonant type systems, 262
- Nontraditional machining methods, 261
- Nonwoven fabrics, 92
- Nose landing gear, 156, 158, 162, 164, 166, 172, 174, 176
- Nose wheel steering (NWS), 252

- O**
- Octet truss (OT), 348
- One-dimensional UVAM (1D UVAM), 264–266
- Optical microscopy techniques, 7
- Original gas turbine engine, 129
- Outer marker (OM), 254

- P**
- Passenger air-conditioner (PAC), 245
- Phase change material (PCM), 54
- PIC255 piezoelectric sensor, 217
- Piezoelectric ceramic (PZT), 212
- Piezoelectric sensors, 234
- Piston aeroengines, 132, 133
- Plastics, 341
- Plastic yielding, fracture/buckling, 350
- Poisson's ratio, 215
- Polyacrylonitrile (PAN), 91
- Poly-ether-ether-ketone (PEEK), 71
- Polyimide, 75
- Polylactic acid (PLA), 117
- Polymer matrix, 101, 104, 105
- Porous structures, 347
- Powder bed fusion (PBF), 346, 347, 360
- Precision approach path indicators (PAPI), 252–253
- Primary dendritic arm spacing (PDAS), 388
- Principal component analysis technique (PCA), 213
- Process efficiency, 269
- Pulsejet, 134

- Q**
- Quick reference handbook (QRH), 252

- R**
- Radiation heat transfer, 56
- Ramjet engine, 134
- Rapid tooling (RT) process, 307
- Rear pressure bulkhead (RPB), 108
- Refueling aircrafts, 182–183
- Reinforcement, 67
- Research and innovation activity (RIA), 120
- Residual stresses, 289
- Resin injection molding (RIM), 117
- Resonant systems, 269
- Resonant-type systems, 262
- Rising energy efficiency, 197
- Rocket, 133
- Root mean square deviation (RMSD), 223
- Runway visual range (RVR), 252

- S**
- Scanning electron microscopy, 7
- Schwartz primitive, 351
- Secondary dendritic arm spacing (SDAS), 388
- 2xxx–7xxx Series aluminum alloys, 337
- 6xxx–7xxx Series aluminum alloys, 338
- Shear modulus, 215
- Shell lattice structures, 351
- Shielding gas, 335
- Significant area, 339
- Single-dimensional vibrations, 289
- Single-point incremental forming (SPIF), 294, 297, 301–306, 308, 309
- Smart manufacturing, 307
- Solid-lattice hybrid payload adapter structure, 360
- Solid-state joining method, 333
- Solid-state joint, 328
- Solid-state welding method, 334

- SPIF process, 295
 - Spindle VAM, 261
 - Stainless steel, 266
 - Stainless steel open-cell metal foam (S-S CMF), 53
 - Steel stamping, 333
 - Stress-strain relationship, 350
 - Strong-strength Al alloys, 337
 - Structural health monitoring (SHM)
 - components, 213
 - conductance characteristic, 212
 - damage metrics, 223
 - CCDM, 235
 - CCDM values, 233
 - compensated MAPD, 232
 - compensated RMSD, 232
 - EFS/Genetic algorithm, 232
 - MAPD, 233, 234
 - non-compensated CCDM values, 231
 - non-compensated MAPD, 231
 - non-compensated RMSD, 231
 - RMSD, 233, 234
 - temperature difference, 229
 - temperatures, 236
 - damping ratio, 222
 - density, 221
 - dielectric constants, 219, 220
 - effective piezoelectric coefficient, 212
 - elasticity modulus, 221, 223
 - experimental method, 213, 214
 - experimental results, 224, 226
 - genetic algorithm, 213
 - maximum cross-correlation (CC), 212
 - numerical method, 214
 - numerical results
 - amplitude values, 226
 - experimental and simulation results, 230
 - frequency range, 225
 - mesh number selection, 227
 - number of steps, 225
 - temperatures, 228, 229
 - piezoelectric charge constants, 217, 219
 - statistical analyzes, 212
 - stiffness/compliance matrix, 215–218
 - strength of structures, 213
 - temperature effects, 213
 - Strut-based lattice structures, 348
 - Strut inclination angle, 356
 - Superalloys, 145
 - Supersaturated solid solution (SSSS), 7
 - Surface roughness, 271, 272
 - Sustainability, 113, 114, 116–118, 120, 122
- T**
- 2024-T3 aluminum alloy, 264
 - 6061-T6 aluminum alloy, 264
 - Take-Off Go-Around mode (TOGA), 250
 - Thermal Barrier Coatings (TBC), 138
 - Thermal conductivity, 319
 - Thermoelectric generator (TEG), 54
 - Thermoplastic polymers, 99
 - Thermoplastics, 98
 - Thermosets, 98
 - Thermosetting polymers, 98
 - Thorium dioxide-dispersion strengthened-Ni alloys, 317
 - 3-Dimensional (3D), 347, 349, 353
 - Three-dimensional UVAM (3D UVAM), 268
 - Ti-6Al-4V, 260, 265, 269
 - Ti-Al IMCs, 332
 - Ti-Al-based alloys, 144
 - Titanium alloy materials, 273
 - Titanium-base alloys, 329–331
 - Tool life, 272
 - Topology optimization, 352, 353, 359, 360
 - Traditional RT techniques, 307
 - Transient liquid phase, 328
 - Transmissibility, 213
 - Triply periodic minimal surface lattice structures (TPMS), 348, 351, 356
 - Tungsten alloy, 267
 - Tungsten carbide materials, 265
 - Tungsten inert gas (TIG), 319, 320, 372
 - Turbine material technology, 138
 - Turbofan engines, 135, 136, 139
 - Turbojet engines, 134, 135
 - Turboprop engines, 135, 136
 - Turboshaft engines, 135, 136, 142, 242
 - Turning, 260
 - 2-Dimensional (2D), 347
 - Two-dimensional UVAM (2D UVAM), 266–268
 - 2D vibration-assisted micro-end-milling technique, 267
 - Two-point incremental forming (TPIF), 294, 304, 305
- U**
- Ultimate tensile strength (UTS), 391
 - Ultra-advanced composites, 147
 - Ultrahigh molecular weight polyethylene (UHMWPE) fiber, 91
 - Ultraprecision turning, 266
 - Ultrasonic-assisted end milling, 265

- Ultrasonic-assisted machining (UAM), 261, 273
 - Ultrasonic-assisted milling, 266
 - Ultrasonic-assisted turning, 265
 - Ultrasonic elliptical vibratory device, 268
 - Ultrasonic tool holder, 276, 278, 279
 - Ultrasonic vibration amplitude, 281
 - Ultrasonic vibration-assisted drilling, 266
 - Ultrasonic vibration-assisted machining (UVAM)
 - classification, 261, 262
 - feed direction cutting, 262, 264
 - literature, 262
 - longitudinal (*see* Longitudinal ultrasonic vibration-assisted machining (LUVAM) of Ti-6Al-4V)
 - 1D, 264–266
 - 3D, 268
 - 2D, 266–268
 - VD, 262, 263
 - Ultrasonic vibration-assisted milling, 276, 278–281, 284, 285
 - Ultrasonic vibration-assisted turning, 276
 - Ultrasonic vibration system, 282
 - technical parameters, 276, 280
 - Ultrasonic welding (USW), 325, 326
 - Underwater locator beacon (ULB), 247
 - Unit cell optimization approach, 353, 354
 - Uranium SS, 317
- V**
- Vacuum-assisted resin transfer molding (VARTM), 104
 - Vacuum brazing, 328
 - Vertical direction of cutting, 261
 - VHF Omni-Directional Radio Range (VOR), 253
 - Vibration-assisted finishing operations, 283
 - Vibration-assisted machining (VAM), 277, 288
 - advantages, 261
 - applications, 268, 289
 - benefits, 261
 - classifications, 262, 263
 - development, 261
 - frequency, 262
 - kinematics, 269–271
 - machining applications, 262
 - machining characteristics, 271–275
 - and nonresonant systems, 269
 - resonant and nonresonant systems, 268
 - resonant systems, 269
 - UAM, 261
 - UVAM (*see* Ultrasonic vibration-assisted machining (UVAM))
 - Vibration direction (VD), 262, 263
 - Vibration energy, 276
 - Visual approach slope indicators (VASI), 253
- W**
- Welding
 - Al to Mg, 318
 - dissimilar materials (*see* Dissimilar welding)
 - Wet corrosion, 318
 - Wet wings, 190, 191
 - Wire arc additive manufacturing (WAAM)
 - aerospace industry, 368
 - anisotropic mechanical properties, 370
 - as-fabricated macro- and microstructural evolution
 - degree of texture, 385
 - epitaxial growth, 387
 - epitaxial solidification, 383
 - equilibrium partition coefficient, 386
 - grains, 386
 - interlayer boundaries, 383
 - light macrographic images, 383
 - liquid–air interface, 383
 - liquid–solid interface, 387
 - liquidus temperature, 388
 - morphology parameter, 387
 - precipitation of NbC, 390
 - precipitation of TiN, 390
 - process parameters, 384
 - regions, 383
 - solidification sequence, 388
 - solid–liquid dendritic interface, 386, 387
 - solid–liquid interface, 383, 387
 - solute redistribution coefficient, 386
 - texture coefficient, 383, 385
 - thermal history, 389
 - bead geometry, 380, 382
 - deposition rate, 378–380
 - experimental setup, 372
 - fabrication of IN718, 369
 - heat input, 378–380
 - heat-treated samples, 372
 - heat treatment
 - anisotropy, 399
 - dimples, 399
 - elemental composition, 392, 394
 - elemental distribution, 393
 - epitaxial grain orientation, 393

- Wire arc additive manufacturing (WAAM) (*cont.*)
 - fracture surfaces, 399
 - grain boundaries, 395
 - intragranular ductile fracture mode, 399
 - matrix composition, 392
 - micrographs, 393
 - microhardness values, 395
 - microstructural constituents, 393
 - microstructural heterogeneity, 392
 - phase constituents, 392
 - physical attributes, 395
 - quantitative values, 396
 - stress–strain curves, 397
 - tensile results, 398
 - tensile test results, 396
 - XRD profiles, 396
 - high-temperature oxidation performance
 - alumina phase, 402
 - chromia scale, 402
 - elemental composition, 401, 402
 - elemental distribution, 404
 - factors, 401
 - grain boundaries, 401
 - kinetic curves, 400
 - mass gain vs. oxidation time, 400
 - mechanism, 402
 - surface analysis, 401
 - surface morphology, 401
 - XRD analysis, 402
 - homogenization-annealed (HA)
 - condition, 370
 - mechanical attributes, 368
 - mechanical integrity, 371
 - mechanical properties, 390, 391
 - metal dissolution, 369
 - microstructural evolution, 370
 - microstructural stability, 371
 - microstructure and mechanical properties, 370
 - modified heat treatment and characterization, 374, 376
 - non-oxidized δ (Ni_3Nb)-phase, 371
 - oxidation behavior, 371
 - oxidation kinetics, 371
 - oxidation study, 375, 376
 - oxide layer analysis, 375, 376
 - oxide-scale formation, 371
 - physical and chemical attributes, 369
 - physical and chemical properties, 368
 - post-deposition homogenization treatment, 370
 - processing parameters, 369, 372, 374, 375
 - raw materials, 372, 377
 - superalloys, 368
 - test conditions, 374, 375
 - Woven fabrics, 95, 96
- X**
- X-ray diffraction (XRD) technique, 375
- Y**
- Yield strength (YS), 391
 - Young's modulus, 216
- Z**
- Zr–steel, 317